POLISH ANATOMICAL SOCIETY

FOLIA MORPHOLOGICA

Vol. 80   2021   No. 4

V M
VIA MEDICA

https://journals.viamedica.pl/folia_morphologica

FOLIA MORPHOLOGICA

EDITORIAL ADVISORY BOARD

V M
VIA MEDICA

R E V I E W   A R T I C L E

Morphological and functional characteristics of satellite glial cells in the peripheral nervous system

A. Milosavljević[1], J. Jančić[2], A. Mirčić[1], A. Dožić[3], J. Boljanović[4], M. Milisavljević[4], M. Ćetković[1]

[1]Institute of Histology and Embryology, Faculty of Medicine, University of Belgrade, Serbia
[2]Clinic of Neurology and Psychiatry for Children and Youth, Faculty of Medicine, University of Belgrade, Serbia
[3]Institute of Anatomy, Faculty of Dental Medicine, University of Belgrade, Serbia
[4]Laboratory for Vascular Anatomy, Institute of Anatomy, Faculty of Medicine, University of Belgrade, Serbia

Satellite glial cells are specialised cells that form a functional perineuronal sheath around sensory ganglion neurons. There are a large number of studies that reveal the morphological and functional characteristics of these cells. Satellite glial cells have been studied both in intact ganglions and in tissue cultures, using light and transmission electron microscopy, immunohistochemical and other methods. Satellite glial cells have polygonal form; they are mononuclear and have developed synthetic organelles, numerous receptors, adhesion molecules and ion channels, which enable them to interact with adjacent neurons, as well as transmit signals in the ganglions of the peripheral nervous system. Based on the literature data, satellite glial cells thanks to their characteristics can receive signals from other cells and react to changes in their surroundings.
Previous studies have investigated the potential role of satellite glial cells in the formation of the blood-nervous tissue barrier of the peripheral nervous system, as well as in the neuropathic pain genesis. Some recent discoveries support the fact that satellite glial cells can participate in controlling of local viral infections and protecting pseudounipolar neurons from mentioned infections. (Folia Morphol 2021; 80, 4: 745–755)

Key words: satellite glial cell, sensory ganglion, peripheral nervous system, pseudounipolar neuron

INTRODUCTION

A large number of scientists are researching the morphology and function of satellite glial cells and the number of studies is increasing and increasing. The application of histochemical and electron microscopic methods in satellite glial cell research can contribute to the identification of complex mechanisms of functioning of these cells, as well as their role in numerous diseases of the peripheral nervous system ganglions [29, 38, 44, 50, 58]

Satellite glial cells continually envelop neurons in peripheral nervous system ganglions. They completely encircle the ganglionic neurons in the form of one, and rarely two or three concentric layers, and together form morphological and functional units. The extracellular space between them and neurons has a diameter of

only 20 nm. Satellite glial cells are small, flattened, and interconnected by gap junctions [47, 49, 50]. The multiplication of satellite glial cells and the formation of several of their layers were registered after the experimental disruption of the axons of the ganglion neurons [17, 41].

The close relationships between satellite and ganglia cells also allow them to communicate with each other. One of the main messengers in this communication is nitrogen monoxide [62, 66]. The protective role of satellite glial cells is also reflected in the secretion of individual neurotrophins, which help the survival of ganglion neurons [66, 74].

MORPHOLOGICAL CHARACTERISTICS OF SATELLITE GLIAL CELLS

Short history of satellite glial cells

Small perineuronal cells, which form a cell envelope around the body of neurons in sensory ganglions, were first mentioned by Valentine, in 1836 [67]. Even Ramon y Cajal himself named these cells several times [54]. In the late 1950s, the term satellite cell was widely accepted. As the term satellite cells also refers to skeletal muscle fibre progenitor cells, the authors agreed to name them satellite glial cells, with the recommendation that their exact location should be specified (e.g. satellite glial cells of trigeminal ganglion) [50].

Until the discovery of the electron microscope, various controversies arose as to whether the body of each neuron of the sensory ganglion was surrounded by satellite glial cells, since light microscopy has not always shown this in the past [29]. The advent of electron microscopy resolved these disputes, showing that the body of each nerve cell in the sensory ganglion is surrounded by a continuous sheath composed of discrete satellite glial cells [50]. Because the arrangement of satellite glial cells and the thickness of the sheath they build may vary in different areas and in different species, the fact that once these structures were below the resolution of light microscopy explains a different interpretation of the structure of the perineuronal sheath [44, 58]. Along with the development of the electron microscope, the resolution power of the light microscopy has grown, and even today, with light microscopy methods, at different cross-sectional levels, we can clearly see that satellite glial cells completely envelop sensory neurons [29, 38].

Organization of the satellite glial cells in sensory ganglia

In sensory ganglions, connective tissue sharply separates satellite glial cells' sheath belonging to one neuron from the sheaths belonging to other neurons (Figs. 1, 2). The outer surface of satellite glial cells, the one facing the interstitial connective tissue, is covered by a basal lamina (Figs. 1A, B). This surface is generally flatter than the one facing the neuron. In the peripheral parts of the cytoplasm of satellite glial cells, dense amorphous plaques may also be encountered, whose structure and function are still poorly understood. In the rabbit spinal ganglions, large voids (lacunae) have occasionally been observed, just below the outer surface of the satellite glial cell plasmalemma [49]. It has been observed that cilia and microvilli can be projected into these voids [49]. These lacunar spaces have been observed only in animal models and their significance has not been demonstrated so far [49].

Satellite glial cells have polygonal form; they are mononuclear (Figs. 1C, D), and have developed synthetic organelles, numerous receptors, adhesion molecules and ion channels, which allow them to interact with adjacent neurons as well as to transmit signals in the ganglions of the peripheral nervous system [17]. They have very expressed granular endoplasmic reticulum, mitochondria, Golgi apparatus, lysosomes, peroxisomes [18, 20, 43]. The expressed cytoskeletal components are microtubules and intermediate filaments, as well as occasionally present cellular inclusions such as lipofuscin granules [5, 44, 45].

The cell membranes of satellite glial cells differ in thickness from the cell membranes of neurons [50]. In cell membranes of satellite glial cells treated with the freeze-section procedure, sets of orthogonally arranged particles were found [42]. The distance between these particles is about 7 nm [16]. Similar structures have been observed in astrocytes, ependymal cells of higher vertebrates, while they have never been recognised within the cell membranes of oligodendrocytes or neurons [25, 55]. These structures are much rarer in satellite glial cell membranes than in astrocyte membranes [25]. These structures were later shown to be constructed from the aquaporin-4 protein, a membrane protein involved in the transport of water across the cell membrane [55, 69].

Satellite glial cells possess long and branched cytoplasmic extensions, especially on surfaces facing neurons [64]. Because of the large number of cytoplasmic extensions of both neurons and satellite glial cells, it is very difficult to determine precisely the boundary between neurons and satellite glial cells. In the past, these cytoplasmic extensions were thought
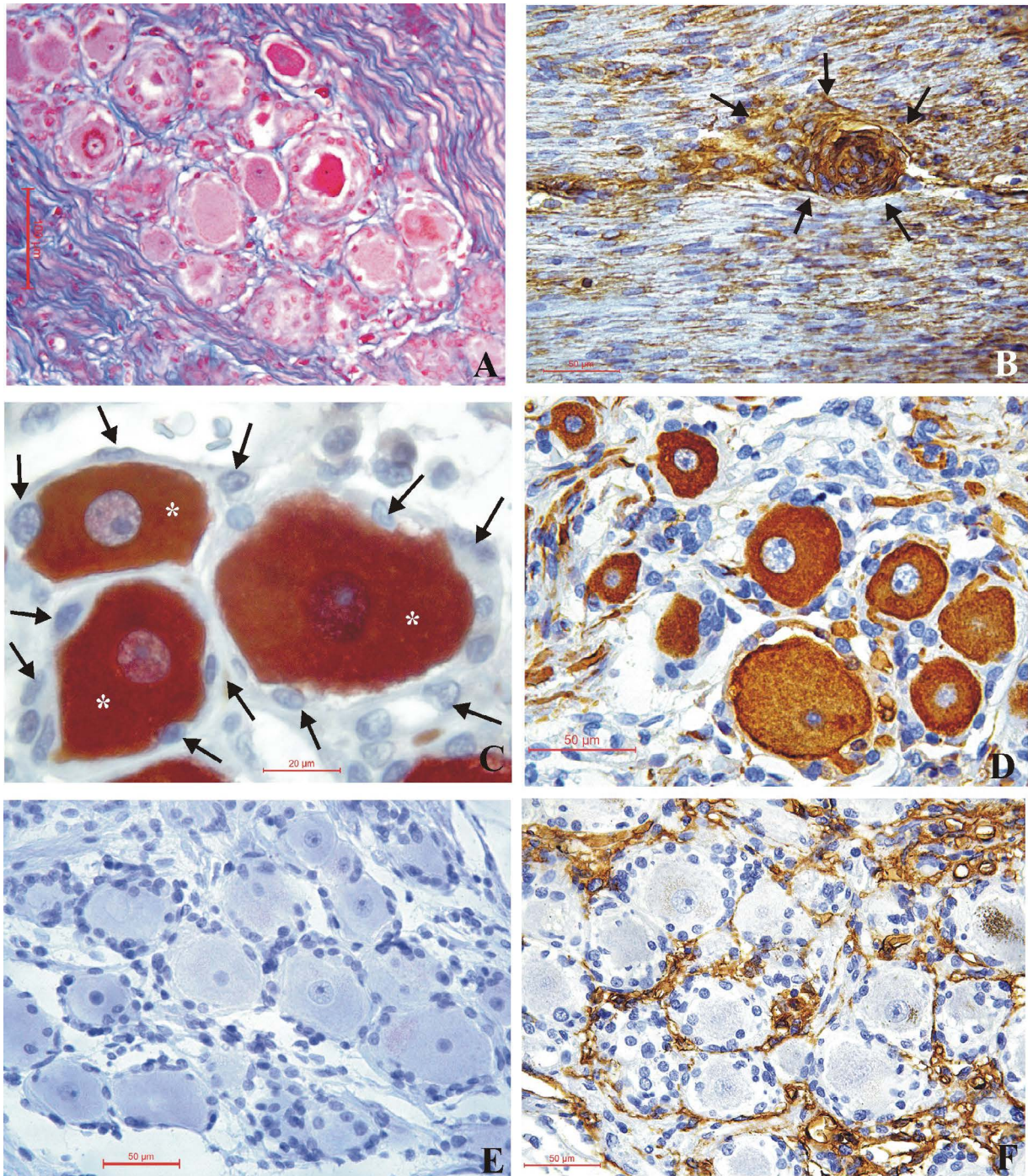
Figure 1. Histological characteristics of the human sensory ganglia; **A.** Dorsal root, spinal sensory ganglion containing clusters of round and oval neurons surrounded by many satellite glial cells (SGC). Fascicles of nerve fibres (red) are followed by bundles of collagen fibres (blue) which also separate SGC-neuron units (Trichrome Masson staining); **B.** Vimentin immunoreactivity detected in the cytoplasm of SGC (arrows), covering an ectopic, displaced neuron in the trigeminal nerve; **C.** Intense neuron specific enolase immunoreactivity in neurons (asterisks) of the trigeminal ganglion; SGC (arrows) are negative; **D.** Immunoreactivity against neurofilament protein in pseudounipolar neurons of the trigeminal ganglion; SGC do not show immunoreactivity; **E.** The cell bodies of foetal trigeminal ganglion (32 weeks gestational age) surrounded by numerous SGC (Haematoxylin staining); **F.** Numerous capillaries immunostained against CD34 (endothelial cells protein) around the SGC covering trigeminal neurons.

to be the result of deformation of satellite glial cells due to the use of different procedures [46]. Even after prolonged *in vitro* cultivation of sensory ganglions, satellite glial cells have been shown to retain shapes similar to those observed in *in vivo* conditions [5, 64, 73]. Their cytoplasmic extensions may be ring-shaped
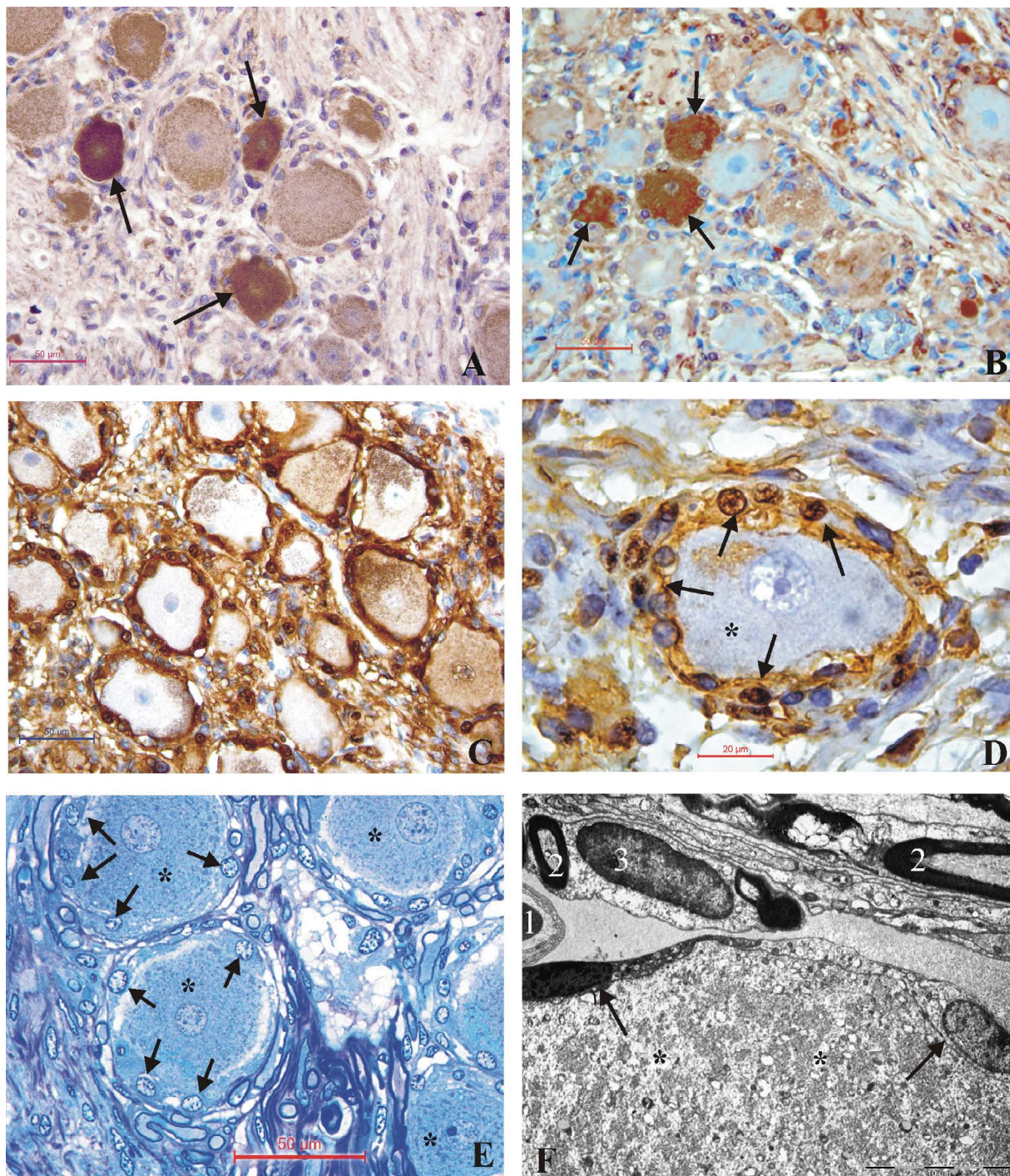
Figure 2. Histology of the sensory ganglia; **A.** Calcitonin gene related peptide (CGRP) immunoreactivity in small to medium-sized neurons of the human dorsal root ganglion (arrows); satellite glial cells (SGC) are not stained; **B.** Substance P immunoreactivity in small to medium-sized neurons of the human geniculate ganglion (arrows); SGC are negative; **C.** S-100 proteins immunoreactivity was detected in all SGC, but in few neurons of the human trigeminal ganglion; **D.** Higher magnification of SGC positive for S-100 proteins (arrows), and negative human ganglionic trigeminal cell (asterisk); **E.** Semithin section of a rat trigeminal ganglion; trigeminal neurons (asterisks) and SGC (arrows) are shown (Toluidine blue staining); **F.** Electron microscopy of the section through the trigeminal neuron (asterisks) of a rat and two SGC (arrows) in close contact; 1 — capillary; 2 — myelinated nerve fibres; 3 — Schwann cell.

or may have a lamellar shape [5, 73]. Extensions in cilia are also described in the literature [45]. These cilia lack a central microtubule pair and show only nine pairs of peripheral microtubules, as well as in neurons, in Schwann cells and astrocytes [45]. Finding specific receptors on the solitary cilia of particular

neurons supports the hypothesis that they are sensory specialisations [8, 26, 76].

Embryonic development of the satellite glial cells

Satellite glial cells of the sensory ganglia share a common embryonic origin with neurons [33]. Satellite glial cells of the spinal ganglia originate from the neural crest, and partly from neuroepithelial cells that migrate from the spinal cord [27, 61].

Levi [33], who has studied ganglion development in many species, concluded that neuronal differentiation always precedes differentiation of satellite glial cells in sensory ganglions. In the earliest stages of sensory ganglion development, undifferentiated, rounded cells at different stages of cell division can be observed [33].

These still undifferentiated cells may be single, or in small groups, among still immature neurons [44]. In the early stages of embryonic development, one satellite glial cell is connected to multiple neurons, and then, as development takes place, each nerve cell is completely enveloped by satellite glial cells, which form a functional sheath around it (Fig. 1E) [44].

Satellite glial cells: the blood-nervous tissue barrier of the peripheral nervous system

Due to the characteristic arrangement of satellite glial cells and their relationships with the surrounding structures, we can conclude that all the molecules from the blood vessels of the interstitial connective tissue must pass through the sheath built by satellite glial cells to reach neurons (Fig. 1F, 2F) [1]. Neurons in the sensory ganglion lack the presence of the blood-nervous tissue barrier (as it is present in the central nervous system). As a consequence, the satellite glial cells' sheath is the only to control the transfer of molecules to neurons [22]. Therefore, it is reported in literature, that satellite glial cells represent the blood-nervous tissue barrier of the peripheral nervous system, although there is a partial movement of substances from the connective tissue vessels to the neuron [22, 65]. In the 1960s, Novikof et al. [39] and a group of scientists proved the presence of enzymes such as acetylcholinesterase and nucleoside transferase in the spaces between satellite glial cells and neurons [65]. The origin of these two enzymes has been discussed a lot and the most accepted is the theory that these enzymes are generated in the bodies of neurons and then released into mentioned intercellular spaces at axonal terminals [39]. These enzymes have been hypothesized to have hydrolytic properties, due to which they could degrade substances that have a potentially negative effect on neural activities [39]. Hypotheses have also been claimed for the interaction of these enzymes with transport ATPases; however, there are is more detailed data on this topic in the literature [39, 65]. The striking length and curvature of the path between the basal lamina and the neural surface slows the diffusion of the substances through the perineuronal sheath [22]. The barrier function of the perineuronal sheath may be particularly important when neuronal moving substances are toxic. In old age, this function may be impaired [39]. Satellite glial cells are thought to influence the composition and density of these enzymes and other substances in intercellular spaces, which can control the flow of matter to the neuron they surround [39].

Molecular markers of satellite glial cells

We can safely say that satellite glial cells express a large number of proteins and adhesion molecules on their surface [2, 31, 36, 40, 56, 59, 62, 63, 70, 78]. Molecular markers are essential for the identification of satellite glial cells, especially when intercellular relationships are disturbed (e.g. in dissociated cell culture) (Figs. 2A, B) [59]. Among these markers is protein S100, which is also present in Schwann cells (Figs. 2C, D) [59]. The multi-selective markers of satellite glial cells are glutamate-aspartate transporter and glutamine synthetase [23].

The guanylate cyclase is also located within satellite glial cells [31]. This enzyme is activated by nitric oxide (NO) released by neurons after an axonal lesion [62]. The NO precursor, arginine, has been detected in satellite glial cells, so satellite cells are thought to supply the neurons with the arginine required to produce NO [2]. Other molecules that synthesize satellite glial cells are cytokine tumour necrosis factor-alpha [40, 63] and prostaglandins [70].

Relationships between satellite glial cells

In certain regions of the sensory ganglions, adjacent satellite glial cells interconnect, while in other regions, forming a sheath around the common cell, their lamellar extensions overlap [50]. Where numerous lamellar extensions overlap, multiple lamellar extensions may belong to the same cell, so it can sometimes be observed that the number of these lamellar extensions is greater than the number of satellite glial cells themselves (Figs. 2E, F) [49, 50].

Cracks between the membranes of adjacent satellite glial cells can measure 15 to 20 nm in diameter [49]. These cracks open into a narrow space below the basal lamina at one end, and into a narrow space between neurons and closely spaced satellite glial cells at the other [44, 49]. This potential pathway between the interstitial connective tissue of the ganglia and the surface of the neuron usually has a long and twisted flow, even in areas where the perineuronal sheath is thin, and is thought to have some functional significance [44, 49, 50].

Satellite glial cells are linked to other satellite glial cells within the same perineuronal sheath by adherent, occludent connections and nexuses [35, 47]. Adherent connections are small structures that resemble a button. These compounds have also been described between adjacent Schwann cells [13]. Nexuses, as connections present between satellite glial cells have been discovered by tissue freezing techniques [42]. These connections have also been found in satellite glial cells of autonomic ganglions [14]. The presence of structures similar to occludent connections has also been demonstrated [14]. Specifically, in some studies, thin filament structures called strands have been observed within the plasmalemma of satellite glial cells, which exhibit the same morphological characteristics as those structures and proteins that create occludent connections in other tissues [14, 47]. They were detected by the freeze-section technique, at the plasmalemma level of satellite glial cells [14]. Some scientists also call them macula occludens [14]. Such threads are interpreted as the basic elements of tight, occludent connections. Their presence has also been demonstrated in satellite glial cells of autonomic ganglions [14, 70].

All of the previously mentioned types of connections probably contribute to the adhesion between satellite glial cells [42, 48]. Moreover, these relationships have other important roles. The inner diameter of the nexus channel (about 1.2 nm in size) not only allows the intercellular passage of ions, but also the transfer of molecules with molecular weights up to about 1 kD (e.g. signalling molecules, amino acids and glucose) [14, 42, 48]. Information about the compounds and connections that form satellite glial cells are scarce.

Connexin-43 has been identified in satellite glial cells of trigeminal ganglions of rats [71], murine spinal ganglions [53], as well as in guinea pig ganglions and human spinal ganglions [35]. In perineuronal satellite cells of the spinal ganglions connexin-36 is also identified [51].

FUNCTIONAL CHARACTERISTICS OF SATELLITE GLIAL CELLS

Perineuronal homeostasis

Satellite glial cells play a major role in homeostasis of the perineuronal environment [49]. Neural activity causes an increase in extracellular potassium concentration, resulting in increased nerve excitability [23]. Satellite glial cells on their surface express K^+ channels, which play a central role in extracellular potassium uptake [23, 77]. Thanks to nexuses, satellite glial cells rapidly distribute potassium ions among adjacent cells, thereby establishing perineuronal homeostasis [24].

Glutamate is the major neurotransmitter present in sensory ganglion neurons, but it is important to emphasize that high levels of glutamate are neurotoxic [23]. Satellite glial cells express glutamate transporters on their surface; so that if high concentrations of glutamate are released from neurons into the perineuronal space, it is satellite glial cells that will remove excess glutamate from mentioned area [6, 23, 60]. In this way, they maintain glutamate concentrations below neurotoxic levels in the perineuronal microenvironment [6]. Satellite glial cells, which contain the enzyme glutamine synthetase, convert glutamate to glutamine [23, 60]. Glutamine is then returned to neurons and converted again to glutamate, using their phosphate glutaminases [60]. Since neurons use glutamate for synaptic transmission, we can say that the metabolism of sensory ganglion neurons itself is largely dependent on their interaction with neighbouring satellite glial cells [6].

In addition to the glutamate transporter, satellite glial cells also express gamma-aminobutyric acid receptors on their surface, which can induce the depolarisation of neurons by sensory ganglions [23, 60]. Due to the existence of these transporters, satellite glial cells can control the concentration of gamma-aminobutyric acid in the perineuronal microenvironment, and thus protect the neurons themselves from the effects of excessive concentrations of this acid [4, 79].

Neuroprotective role of satellite glial cells

The neuroprotective role of satellite glial cells has been repeatedly demonstrated [64]. The NO-cGMP pathway plays a major role in neuronal protection [62, 66]. NO is generated in the bodies of neurons, thanks to the enzyme NO synthetase, which is present in the bodies of the neurons of the dorsal roots of the spinal ganglion [62, 66]. Whether NO plays a protective or

toxic role depends on its concentration as well as on its receptor concentration, soluble guanylate cyclase (sGC) [62]. Across the NO receptor, cyclic guanosine monophosphate (cGMP) activation occurs in satellite glial cells, and it is thought that its generation by satellite glial cells may limit various degenerative changes at the neuronal level and facilitate their survival in pathological conditions [62, 66]. Specifically, in nerve injury, many more ganglion neurons express the presence of NO synthase, whereas satellite glial cells express cGMP [66]. Thus, activation of cGMP, v62 the receptor for NO, can limit or even reverse degenerative changes at the neuronal level [62, 66]. It is thought that the interaction between NO, sGC and cGMP expressed by satellite glial cells facilitates the survival of injured neurons [66].

There are also studies showing that inhibition of NO synthase leads to an increase in degenerative changes in neurons and glia [62]. In recent years, several studies have reported the antiapoptotic effect of NO and cGMP in cultures of neurons and non-neuronal cells. Although these observations suggest that the NO-cGMP pathway is crucial in protecting neurons, the precise mechanism of these processes is poorly understood [66].

Phagocytic activity of satellite glial cells

Based on previous studies, it has been observed that fragments of degenerate cells are found within satellite glial cells, both in the sensory and autonomic ganglions [37, 48, 52]. These findings suggest that satellite glial cells have phagocytic capacity, as demonstrated by culturing these cells in vitro [75, 77].

The role of satellite glial cells in the immune system

Satellite glial cells in the ganglion also have immune system functions [68]. They have a leukocyte phenotype, with macrophage characteristics so that they control local virus-specific T cells and protect ganglion cells infected with herpes virus from damage as well as uninfected cells from infection [68].

Satellite glial cells and herpes simplex virus

The most studied viral infection affecting the sensory ganglion is the herpes simplex virus (HSV) infection [10, 15, 21, 82]. During initial infection, the virus travels by retrograde axonal transport to the bodies of sensory ganglion neurons, in which latent infection is established [10]. Sensory ganglion neurons are capa-

ble of supporting complete viral replication with the production of mature enveloped particles [10, 15]. Unlike neurons, HSV infections are rarely detected in satellite glial cells in vivo; these cells have been shown to contain only undeveloped viral particles [10, 21]. In vivo, sensory ganglion neurons typically exhibit the following structural changes associated with HSV infection: nucleolus disruption and nuclear membrane reduplication [10]. Structural changes of organelles have been observed less frequently (some changes in mitochondria and dilatation of cisterns of the endoplasmic reticulum have been observed) [82].

In vivo neurons infected with herpes simplex persist, while in culture they are destroyed by the virus [81]. Infected neurons are usually found scattered within the ganglion. The virus does not spread from infected neurons to adjacent neurons probably because satellite cells form a barrier to the interneuronal spread of the virus within the ganglion [32]. In the vestibular ganglion, the viral particles cannot propagate from neurons to satellite glial cells because they cannot pass through the distended myelin sheath [72]. In the sensory ganglions of experimentally infected mice, satellite glial cells proliferate, and an increase in the number of these cells probably facilitates neuronal survival [15].

Satellite glial cells and herpes zoster virus

In acute varicella-zoster virus infection, in sensory ganglions, both neurons and satellite glial cells contain viral particles [80]. In the latent phase, viral particles are localised in sensory ganglion neurons and rarely in satellite glial cells [34]. Varicella-zoster virus (VZV) can induce fusion formation between a neuron and its satellite glial cells [57].

Specifically, there are studies detailing the mechanisms of action of VZV itself, as well as the supporting role of satellite glial cells in replication of this virus [57]. Nucleocapsid formation occurs in the bodies of neurons and satellite glial cells as well as virions located in cytoplasmic vacuoles [57]. Certain varicella zoster proteins (immediate-early [IE]) regulatory proteins, early ORF47 kinase, glycoprotein gE) are expressed both on the surface of satellite glial cells and on the surface of VZV-infected sensory neurons [57]. Viral genomic DNA has been detected in both nuclei of infected neurons and in nuclei of satellite glial cells that express a specific type of IE protein, called IE63 [57], on its surface. These surface proteins are thought to result in the fusion of cell membranes of satellite glial cells and neurons, as well as the

transfer of certain proteins and virions from neurons to satellite glial cells and vice versa [57]. This fusion allows rapid replication of the virus in the satellite glial cells themselves, and, much more importantly, the faster spread of the virus to the uninfected neurons (supported by the very fact that one sensory neuron surrounds a larger number of satellite glial cells, and hence the spread of the virus faster and more efficient) [57]. Direct VZV infection of satellite glial cells could also occur during primary VZV infection, when the virus can gain access to sensory ganglions via the haematogenous pathway via VZV infection of T cells [15, 57]. This pathway of spread increases the ability of the virus to establish latency [57].

The role of satellite glial cells in neuropathic pain

Peripheral nerve injury and inflammation of peripheral tissues increase the excitability of sensory ganglion neurons, thereby causing their spontaneous activity [7]. This is a major factor in the generation and maintenance of neuropathic pain [9]. As described previously, in the sensory ganglions of adult vertebrates, each nerve cell body is tightly enveloped in a single sheath of satellite glial cells, which are completely surrounded by connective tissue, thus forming a discrete unit [30]. Therefore, satellite glial cells are the only cells in direct contact with the bodies of sensory neurons. Because satellite glial cells are highly sensitive to changes in neurons, and because they have the ability to modulate neural excitability, these cells are thought to play an important role in the development and maintenance of neuropathic pain [12, 19, 71]. There are several mechanisms underlying the contribution of satellite glial cells to the hyperexcitability of sensory ganglion neurons, and thus to the development and maintenance of neuropathic pain. Because neurons are the target of lesions, changes in satellite glial cells occur secondary to neuronal changes, upon activation of signalling mechanisms between damaged neurons and associated satellite glial cells. Neuron-released adenosine triphosphate can activate purinergic receptors on satellite glial cells, which can lead to cytokine synthesis (e.g., interleukin 1p and tumour necrosis factor-alpha) [12]. Thus released cytokines can enhance nerve excitability, as demonstrated in several experiments. There is research in which topical application of the interleukin 1 receptor antagonist has acted on the physiological threshold of sensory ganglion neurons and allowed the reduction of peripheral neuropathic pain [12].

Peripheral nerve injury and facial inflammation increase the excitability of trigeminal ganglion neurons [19, 71]. Under such conditions, these neurons release K^+ into the perineuronal microenvironment [23, 77]. The K^+ concentration within this space is primarily regulated by the K^+ channel Kir4.1, which is expressed by satellite glial cells [11]. However, peripheral nerve injury and facial inflammation, regulated by Kir4.1 channels expressed on satellite glial cells, can result in disruption of K^+ homeostasis within the perineuron microenvironment [11, 23, 77]. Increasing extracellular K^+ leads to an increase in neural excitability, which may further exacerbate neuropathic pain [11, 77].

Taken together, all these mechanisms indicate that Kir4.1 channels, expressed on satellite glial cells, have a role in the development and maintenance of neuropathic pain. Since the Kir4.1 channel has been shown to be involved in glutamate homeostasis, it is thought that it could contribute to neuropathic pain and this additional mechanism [11]. If glutamate is the major neurotransmitter of sensory ganglion neurons released into the perineuronal microenvironment, impaired glutamate homeostasis caused by reduction of the Kir4.1 channel may lead to an increase in extracellular glutamate and consequently to an increase in neural excitability [11].

Certain studies have shown that the number of communicative connections between satellite glial cells increases after injury to the nerves themselves [17, 41]. An increased number of connections between satellite glial cells may cause changes in the perineuronal microenvironment and thus contribute to the creation or maintenance of neuropathic pain [7, 17]. As evidence of support to this hypothesis, research has been conducted that showed that communicative linkage blockers restore nerve excitability to baseline, control levels and thus reduce neuropathic pain [7, 12]. Moreover, the application of polymerisation chain reaction method and the use of informational RNA, as a connexin neutralizer 43, a major structural component of satellite glial cell communicative connections, reduce the number of these connections at the trigeminal ganglion level and produces analgesia [53]. Following nerve injury or inflammation, neurotrophic factors increase the excitability of sensory ganglion neurons and thus contribute to neuropathic pain [28]. Satellite glial cells also express neurotrophic factors and their receptors on their surfaces, thus regulating neuropathic pain [74, 83]. There is also an additional mechanism

by which satellite glial cells may be involved in the creation and maintenance of neuropathic pain. Over the past decade, a large number of studies have been conducted on the relationships and connections between glial cells and neuropathic pain [7, 9, 11, 12, 19, 30, 71]. Satellite glial cells have been found to undergo different changes when neuropathic pain occurs. Each of these changes inspired a specific hypothesis about the mechanisms by which satellite glial cells contribute to the development and maintenance of neuropathic pain. However, decisive experiments that confirm or refute these hypotheses are lacking, and therefore this topic itself is insufficiently elucidated and confirmed [7, 9, 11, 12].

There has been recently conducted study which started examining the role of satellite glial cells in systemic inflammation [3]. It has been hypothesized that satellite glial cells must play a role in chronic pain and that systemic inflammatory responses lead to changes in these cells, as do local injury. The study was conducted in mice whose systemic inflammation was induced by lipopolysaccharide injection intraperitoneally [3]. Satellite glial cells of mice dorsal ganglions were detected by immunohistochemical methods and electron microscopy [3, 44]. Within days of lipopolysaccharide injection, changes were observed in satellite glial cells, in the form of a large increase in the number of their cellular extensions, as well as an increase in the communicative connections between them. Twice the sensitivity of satellite glial cells to ATP has also been observed. The conclusion of this study is that changes in satellite glial cell levels are caused by systemic inflammation, similar to those caused by local injury [3].

CONCLUSIONS

Satellite glial cells are a structure much more significant rather than simple morphological enclosure of the neuron. A continuous layer of satellite glial cells protects neurons and maintains homeostasis in their microenvironment, which corresponds to a form of blood-nervous tissue barrier.

Satellite glial cells have many different receptors binding, among other things, various substances with nociceptive effect. After excitation, the satellite glial cells release molecules of inflammation, cytokines and NO, leading to sensitisation and activation of neurons. Thus, activation of neurons and satellite glial cells in a certain part of the ganglion triggers an inflammatory cascade involving other neurons and

satellite glial cells. This phenomenon was observed in the development of the pain syndromes and could be also the possible underlying mechanism of chronic pain. Subsequently, the sGC are seen as potential targets in the practical application of the pain therapy.

The progress in understanding the sGC morphology, and increasing knowledge of SGC capacities in ganglionic neurons homeostasis, both enable new perspectives of further research in this field. First, sGC have immune system properties. They control local virus-specific T cells and protect ganglionic cells. Protective function of sGC needs to be evaluated in viral infections other than herpes virus, for example in the very topical and deadly coronavirus infection. Second, instead of using animal cells, sGC from human sensory ganglions, may represent a promising objective for therapeutic studies in pain research in experimental laboratories. Third, a comparative study between sGC from different types of ganglions, particularly autonomic, would be a promising research with original scientific importance.

Funding

Conflict of interest: None declared

REFERENCES

1. Anzil AP, Blinzinger K, Herrlinger H. Fenestrated blood capillaries in rat cranio-spinal sensory ganglia. Cell Tissue Res. 1976; 167(4): 563–567, doi: 10.1007/BF00215185, indexed in Pubmed: 1083768.
2. Aoki E, Semba R, Kashiwamata S. Evidence for the presence of L-arginine in the glial components of the peripheral nervous system. Brain Res. 1991; 559(1): 159–162, doi: 10.1016/0006-8993(91)90300-k, indexed in Pubmed: 1782556.
3. Blum E, Procacci P, Conte V, et al. Systemic inflammation alters satellite glial cell function and structure. A possible contribution to pain. Neuroscience. 2014; 274: 209–217, doi: 10.1016/j.neuroscience.2014.05.029.
4. Brown DA, Galvan M. Influence of neuroglial transport on the action of gamma-aminobutyric acid on mammalian ganglion cells. Br J Pharmacol. 1977; 59(2): 373–378, doi: 10.1111/j.1476-5381.1977.tb07502.x, indexed in Pubmed: 189874.
5. Bunge MB, Bunge RP, Peterson ER, et al. A light and electron microscope study of long-term organized cultures of rat dorsal root ganglia. J Cell Biol. 1967; 32(2): 439–466, doi: 10.1083/jcb.32.2.439, indexed in Pubmed: 10976233.
6. Carozzi VA, Canta A, Oggioni N, et al. Expression and distribution of 'high affinity' glutamate transporters GLT1, GLAST, EAAC1 and of GCPII in the rat peripheral nervous system. J Anat. 2008; 213(5): 539–546, doi: 10.1111/j.1469-7580.2008.00984.x, indexed in Pubmed: 19014361.
7. Cherkas PS, Huang TY, Pannicke T, et al. The effects of axotomy on neurons and satellite glial cells in mouse trigeminal ganglion. Pain. 2004; 110(1-2): 290–298, doi: 10.1016/j.pain.2004.04.007, indexed in Pubmed: 15275779.
8. Chudler EH, Anderson LC, Byers MR. Trigeminal ganglion neuronal activity and glial fibrillary acidic protein immunoreactivity after inferior alveolar nerve crush in the adult rat. Pain. 1997;

73(2): 141–149, doi: 10.1016/S0304-3959(97)00088-2, indexed in Pubmed: 9415499.

9. Devor M, Seltzer Z. Pathophysiology of damaged nerves in relation to chronic pain. In: Wall PD, Melzack R (eds) Textbook of pain. Churcill Livingston, London 1999: 129–164.

10. Dillard SH, Cheatham WJ, Moses HL. Electron microscopy of zosteriform herpes simplex infection in the mouse. Lab Invest. 1972; 26(4): 391–402, indexed in Pubmed: 4336537.

11. Djukic B, Casper KB, Philpot BD, et al. Conditional knock-out of Kir4.1 leads to glial membrane depolarization, inhibition of potassium and glutamate uptake, and enhanced short-term synaptic potentiation. J Neurosci. 2007; 27(42): 11354–11365, doi: 10.1523/JNEUROSCI.0723-07.2007, indexed in Pubmed: 17942730.

12. Dubový P, Klusáková I, Svízenská I, et al. Satellite glial cells express IL-6 and corresponding signal-transducing receptors in the dorsal root ganglia of rat neuropathic pain model. Neuron Glia Biol. 2010; 6(1): 73–83, doi: 10.1017/S1740925X10000074, indexed in Pubmed: 20519054.

13. Eames RA, Gamble HJ. Schwann cell relationships in normal human cutaneous nerves. J Anat. 1970; 106(Pt 3): 417–435, indexed in Pubmed: 5423938.

14. Elfvin LG, Forsman C. The ultrastructure of junctions between satellite cells in mammalian sympathetic ganglia as revealed by freeze-etching. J Ultrastruct Res. 1978; 63(3): 261–274, doi: 10.1016/s0022-5320(78)80051-3, indexed in Pubmed: 682227.

15. Elson K, Speck P, Simmons A. Herpes simplex virus infection of murine sensory ganglia induces proliferation of neuronal satellite cells. J Gen Virol. 2003; 84(Pt 5): 1079–1084, doi: 10.1099/vir.0.19035-0, indexed in Pubmed: 12692271.

16. Gotow T, Yoshikawa H, Hashimoto PH. Distribution patterns of orthogonal arrays and alkaline phosphatase in plasma membranes of satellite cells in rat spinal ganglia. Anat Embryol (Berl). 1985; 171(2): 171–179, doi: 10.1007/BF00341411, indexed in Pubmed: 3985366.

17. Hanani M. Satellite glial cells in sensory ganglia: from form to function. Brain Res Brain Res Rev. 2005; 48(3): 457–476, doi: 10.1016/j.brainresrev.2004.09.001, indexed in Pubmed: 15914252.

18. Hanker JS, Romanovicz DK, Moore GH. Peroxisomes in satellite, Schwann and laminarcells associated with trigeminal sensory neurons. J Cell Biol. 1974; 63: 131a.

19. Herman SP, Klein R, Talley FA, et al. An ultrastructural study of methylmercury-induced primary sensory neuropathy in the rat. Lab Invest. 1973; 28(1): 104–118, indexed in Pubmed: 4569929.

20. Hess A. The fine structure of young and old spinal ganglia. Anat Rec. 1955; 123(4): 399–423, doi: 10.1002/ar.1091230403, indexed in Pubmed: 13292772.

21. Hill TJ, Field HJ. The interaction of herpes simplex virus with cultures of peripheral nervous tissue: an electron microscopic study. J Gen Virol. 1973; 21: 123–133, doi: 10.1099/0022-1317-21-1-123, indexed in Pubmed: 4357369.

22. Holtzman E, Peterson ER. Uptake of protein by mammalian neurons. J Cell Biol. 1969; 40(3): 863–869, doi: 10.1083/jcb.40.3.863, indexed in Pubmed: 5765774.

23. Hösli E, Hösli L. Autoradiographic localization of the uptake of [3H]- GABA and [3H]L-glutamic acid in neurones and glial cells of cultured dorsal root ganglia. Neurosci Lett. 1978; 7(2-3): 173–176, doi: 10.1016/0304-3940(78)90163-5.

24. Huang TY, Cherkas PS, Rosenthal DW, et al. Dye coupling among satellite glial cells in mammalian dorsal root ganglia. Brain Res. 2005; 1036(1-2): 42–49, doi: 10.1016/j.brainres.2004.12.021, indexed in Pubmed: 15725400.

25. Jessen KR, Thorpe R, Mirsky R. Molecular identity, distribution and heterogeneity of glial fibrillary acidic protein: an immunoblotting and immunohistochemical study of Schwann cells, satellite cells, enteric glia and astrocytes. J Neurocytol. 1984; 13(2): 187–200, doi: 10.1007/BF01148114, indexed in Pubmed: 6726286.

26. Jessen KR, Thorpe R, Mirsky R. Molecular identity, distribution and heterogeneity of glial fibrillary acidic protein: an immunoblotting and immunohistochemical study of Schwann cells, satellite cells, enteric glia and astrocytes. J Neurocytol. 1984; 13(2): 187–200, doi: 10.1007/BF01148114, indexed in Pubmed: 6726286.

27. Jones D. Studies on the origin of sheath cells and sympathetic ganglia in the chick. Anat Rec. 1939; 73(3): 343–357, doi: 10.1002/ar.1090730309.

28. Julius D, Basbaum AI. Molecular mechanisms of nociception. Nature. 2001; 413(6852): 203–210, doi: 10.1038/35093019, indexed in Pubmed: 11557989.

29. King JS. A light and electron microscopic study of perineuronal glial cells and processes in the rabbit neccortex. Anat Rec. 1968; 161(1): 111–123, doi: 10.1002/ar.1091610112, indexed in Pubmed: 4174123.

30. Krawczyk WS, Wilgram GF. Hemidesmosome and desmosome morphogenesis during epidermal wound healing. J Ultrastruct Res. 1973; 45(1): 93–101, doi: 10.1016/s0022-5320(73)90035-x, indexed in Pubmed: 4750505.

31. Kummer W, Behrends S, Schwarzlmüller T, et al. Subunits of soluble guanylyl cyclase in rat and guinea-pig sensory ganglia. Brain Res. 1996; 721(1-2): 191–195, doi: 10.1016/0006-8993(96)00097-2, indexed in Pubmed: 8793100.

32. LaVail JH, Topp KS, Giblin PA, et al. Factors that contribute to the transneuronal spread of herpes simplex virus. J Neurosci Res. 1997; 49(4): 485–496, indexed in Pubmed: 9285524.

33. Levi G. La capsula delle cellule dei gangli sensitivi. Penetrazione di fibre collagene nel loro protoplasma. Monit Zool Ital. 1907; 18: 153–158.

34. Levin MJ, Cai GY, Manchak MD, et al. Varicella-zoster virus DNA in cells isolated from human trigeminal ganglia. J Virol. 2003; 77(12): 6979–6987, doi: 10.1128/jvi.77.12.6979-6987.2003, indexed in Pubmed: 12768016.

35. Liu W, Glueckert R, Linthicum FH, et al. Possible role of gap junction intercellular channels and connexin 43 in satellite glial cells (SGCs) for preservation of human spiral ganglion neurons: a comparative study with clinical implications. Cell Tissue Res. 2014; 355(2): 267–278, doi: 10.1007/s00441-013-1735-2, indexed in Pubmed: 24241398.

36. Magnusson S, Ekström J, Elmér E, et al. Heme oxygenase-1, heme oxygenase-2 and biliverdin reductase in peripheral ganglia from rat, expression and plasticity. Neuroscience. 1999; 95(3): 821–829, doi: 10.1016/s0306-4522(99)00466-2.

37. Matthews MR, Raisman G. A light and electron microscopic study of the cellular response to axonal injury in the superior cervical ganglion of the rat. Proc R Soc Lond B Biol Sci. 1972; 181(1062): 43–79, doi: 10.1098/rspb.1972.0040, indexed in Pubmed: 4402334.

38. Moses HL, Beaver DL, Ganote CE. Electron microscopy of the trigeminal ganglion. I. Comparative ultrastructure. Arch Pathol. 1965; 79: 541–556, indexed in Pubmed: 14301977.

39. Novikoff AB, Quintana N, Villaverde H, et al. Nucleoside phosphatase and cholinesterase activities in dorsal root ganglia and peripheral nerve. J Cell Biol. 1966; 29(3): 525–545, doi: 10.1083/jcb.29.3.525, indexed in Pubmed: 4225492.

40. Ohtori S, Takahashi K, Moriya H, et al. TNF-alpha and TNF-alpha receptor type 1 upregulation in glia and neurons after peripheral nerve injury: studies in murine DRG and spinal cord. Spine (Phila Pa 1976). 2004; 29(10): 1082–1088, doi: 10.1097/00007632-200405150-00006, indexed in Pubmed: 15131433.

41. Pannese E, Ledda M, Cherkas PS, et al. Satellite cell reactions to axon injury of sensory ganglion neurons: increase in number of gap junctions and formation of bridges connecting previously separate perineuronal sheaths. Anat Embryol (Berl). 2003; 206(5): 337–347, doi: 10.1007/s00429-002-0301-6, indexed in Pubmed: 12698360.

42. Pannese E, Luciano L, Iurato S, et al. Intercellular junctions and other membrane specializations in developing spinal ganglia: a freeze-fracture study. J Ultrastruct Res. 1977; 60(2): 169–180, doi: 10.1016/s0022-5320(77)80063-4, indexed in Pubmed: 886640.

43. Pannese E. Biology and pathology of perineuronal satellite cells in sensory ganglia. Adv Anat Embryol Cell Biol. 2018: 1–63, doi: 10.1007/978-3-319-60140-3_1.

44. Pannese E. Electron microscopical study on the development of the satellite cell sheath in spinal ganglia. J Comp Neurol. 1969; 135(4): 381–422, doi: 10.1002/cne.901350403, indexed in Pubmed: 5768883.

45. Pannese E. Number and structure of perisomatic satellite cells of spinal ganglia under normal conditions or during axon regeneration and neuronal hypertrophy. Z Zellforsch. 1964; 63(4): 568–592, doi: 10.1007/bf00339491.

46. Pannese E. Observations on the morphology, submicroscopic structure and biological properties of satellite cells (s.c.) in sensory ganglia of mammals. Z Zellforsch. 1960;

52: 567–597, doi: 10.1007/BF00339847, indexed in Pubmed: 13732495.

47. Pannese E. The histogenesis of the spinal ganglia. Adv Anat Embryol Cell Biol. 1974; 47(5): 7–97, doi: 10.1007/978-3-662-10338-8_2, indexed in Pubmed: 4420826.

48. Pannese E. The response of the satellite and other non-neuronal cells to the degeneration of neuroblasts in chick embryo spinal ganglia. Cell Tissue Res. 1978; 190(1): 1–14, doi: 10.1007/BF00210032, indexed in Pubmed: 688330.

49. Pannese E. The satellite cells of the sensory ganglia. Adv Anat Embryol Cell Biol. 1981; doi: 10.1007/978-3-642-67750-2.

50. Pannese E. The structure of the perineuronal sheath of satellite glial cells (SGCs) in sensory ganglia. Neuron Glia Biol. 2010; 6(1): 3–10, doi: 10.1017/S1740925X10000037, indexed in Pubmed: 20604977.

51. Pérez Armendariz EM, Norcini M, Hernández-Tellez B, et al. Neurons and satellite glial cells in adult rat lumbar dorsal root ganglia express connexin 36. Acta Histochem. 2018; 120(3): 168–178, doi: 10.1016/j.acthis.2017.11.005, indexed in Pubmed: 29224922.

52. Pilar G, Landmesser L. Ultrastructural differences during embryonic cell death in normal and peripherally deprived ciliary ganglia. J Cell Biol. 1976; 68(2): 339–356, doi: 10.1083/jcb.68.2.339, indexed in Pubmed: 942724.

53. Procacci P, Magnaghi V, Pannese E. Perineuronal satellite cells in mouse spinal ganglia express the gap junction protein connexin43 throughout life with decline in old age. Brain Res Bull. 2008; 75(5): 562–569, doi: 10.1016/j.brainresbull.2007.09.007, indexed in Pubmed: 18355632.

54. Ramón y Cajal S. Histologie du système nerveux de l'homme & des vértébrés. A. Maloine, Paris. 1909, doi: 10.5962/bhl.title.48637.

55. Rash JE, Yasumura T, Rash JE, et al. Direct immunogold labeling of aquaporin-4 in square arrays of astrocyte and ependymocyte plasma membranes in rat brain and spinal cord. Proc Natl Acad Sci USA. 1998; 95(20): 11981–11986, doi: 10.1073/pnas.95.20.11981, indexed in Pubmed: 9751776.

56. Rashid MH, Inoue M, Matsumoto M, et al. Switching of bradykinin-mediated nociception following partial sciatic nerve injury in mice. J Pharmacol Exp Ther. 2004; 308(3): 1158–1164, doi: 10.1124/jpet.103.060335, indexed in Pubmed: 14634040.

57. Reichelt M, Zerboni L, Arvin AM. Mechanisms of varicella-zoster virus neuropathogenesis in human dorsal root ganglia. J Virol. 2008; 82(8): 3971–3983, doi: 10.1128/JVI.02592-07, indexed in Pubmed: 18256143.

58. Rosenbluth J, Palay SL. The fine structure of nerve cell bodies and their myelin sheaths in the eighth nerve ganglion of the goldfish. J Biophys Biochem Cytol. 1961; 9: 853–877, doi: 10.1083/jcb.9.4.853, indexed in Pubmed: 13743432.

59. Sandelin M, Zabihi S, Liu Li, et al. Metastasis-associated S100A4 (Mts1) protein is expressed in subpopulations of sensory and autonomic neurons and in Schwann cells of the adult rat. J Comp Neurol. 2004; 473(2): 233–243, doi: 10.1002/cne.20115, indexed in Pubmed: 15101091.

60. Schon F, Kelly JS. Autoradiographic localisation of [3H]GABA and [3H]glutamate over satellite glial cells. Brain Res. 1974; 66(2): 275–288, doi: 10.1016/0006-8993(74)90146-2.

61. Sharma K, Korade Z, Frank E. Late-migrating neuroepithelial cells from the spinal cord differentiate into sensory ganglion cells and melanocytes. Neuron. 1995; 14(1): 143–152, doi: 10.1016/0896-6273(95)90248-1, indexed in Pubmed: 7826632.

62. Shi TJS, Holmberg K, Xu ZQ, et al. Effect of peripheral nerve injury on cGMP and nitric oxide synthase levels in rat dorsal root ganglia: time course and coexistence. Pain. 1998; 78(3): 171–180, doi: 10.1016/s0304-3959(98)00124-9.

63. Shimeld C, Whiteland JL, Williams NA, et al. Cytokine production in the nervous system of mice during acute and latent infection with herpes simplex virus type 1. J Gen Virol. 1997; 78 (Pt 12): 3317–3325, doi: 10.1099/0022-1317-78-12-3317, indexed in Pubmed: 9400983.

64. Shimizu Y. The satellite cells in cultures of dissociated spinal ganglia. Z Zellforsch. 1965; 67(2): 185–195, doi: 10.1007/BF00344468, indexed in Pubmed: 5327663.

65. Shinder V, Devor M. Structural basis of neuron-to-neuron cross-excitation in dorsal root ganglia. J Neurocytol. 1994; 23(9): 515–531, doi: 10.1007/BF01262054, indexed in Pubmed: 7815085.

66. Thippeswamy T, McKay JS, Morris R, et al. Glial-mediated neuroprotection: evidence for the protective role of the NO-cGMP pathway via neuron-glial communication in the peripheral nervous system. Glia. 2005; 49(2): 197–210, doi: 10.1002/glia.20105, indexed in Pubmed: 15390094.

67. Valentin G. Über den Verlauf und die letzten Enden der Nerven. Nova acta phys med acad Caesar Leopol Carol Breslau u Bonn. 1836; 18: 51.

68. van Velzen M, Laman JD, Kleinjan A, et al. Neuron-interacting satellite glial cells in human trigeminal ganglia have an APC phenotype. J Immunol. 2009; 183(4): 2456–2461, doi: 10.4049/jimmunol.0900890, indexed in Pubmed: 19635905.

69. Verbavatz JM, Ma T, Gobin R, et al. Absence of orthogonal arrays in kidney, brain and muscle from transgenic knockout mice lacking water channel aquaporin-4. J Cell Sci. 1997; 110 (Pt 22): 2855–2860, indexed in Pubmed: 9427293.

70. Vesin MF, Urade Y, Hayaishi O, et al. Neuronal and glial prostaglandin D synthase isozymes in chick dorsal root ganglia: a light and electron microscopic immunocytochemical study. J Neurosci. 1995; 15(1 Pt 1): 470–476, indexed in Pubmed: 7529829.

71. Vit JP, Jasmin L, Bhargava A, et al. Satellite glial cells in the trigeminal ganglion as a determinant of orofacial neuropathic pain. Neuron Glia Biol. 2006; 2(4): 247–257, doi: 10.1017/s1740925x07000427, indexed in Pubmed: 18568096.

72. Wakisaka H, Kobayashi N, Mominoki K, et al. Herpes simplex virus in the vestibular ganglion and the geniculate ganglion: role of loose myelin. J Neurocytol. 2001; 30(8): 685–693, doi: 10.1023/a:1016577700280, indexed in Pubmed: 12118156.

73. Waxman SG, Dichter MA, Hartwieg EA, et al. Recapitulation of normal neuro-glial relations in dissociated cell cultures of dorsal root ganglia. Brain Res. 1977; 122(2): 344–350, doi: 10.1016/0006-8993(77)90300-6.

74. Wetmore C, Olson L. Neuronal and nonneuronal expression of neurotrophins and their receptors in sensory and sympathetic ganglia suggest new intercellular trophic interactions. J Comp Neurol. 1995; 353(1): 143–159, doi: 10.1002/cne.903530113, indexed in Pubmed: 7714245.

75. Wilkinson R, Leaver C, Simmons A, et al. Restricted replication of herpes simplex virus in satellite glial cell cultures clonally derived from adult mice. J Neurovirol. 1999; 5(4): 384–391, doi: 10.3109/13550289909029479, indexed in Pubmed: 10463860.

76. Woodham P, Anderson PN, Nadim W, et al. Satellite cells surrounding axotomised rat dorsal root ganglion cells increase expression of a GFAP-like protein. Neurosci Lett. 1989; 98(1): 8–12, doi: 10.1016/0304-3940(89)90364-9, indexed in Pubmed: 2710403.

77. Wu HH, Bellmunt E, Scheib JL, et al. Glial precursors clear sensory neuron corpses during development via Jedi-1, an engulfment receptor. Nat Neurosci. 2009; 12(12): 1534–1541, doi: 10.1038/nn.2446, indexed in Pubmed: 19915564.

78. Xian CJ, Zhou XF. Neuronal-glial differential expression of TGF-alpha and its receptor in the dorsal root ganglia in response to sciatic nerve lesion. Exp Neurol. 1999; 157(2): 317–326, doi: 10.1006/exnr.1999.7063, indexed in Pubmed: 10364443.

79. Young J, Brown DA, Kelly JS, et al. Autoradiographic localization of sites of [3H] -aminobutyric acid accumulation in peripheral autonomic ganglia. Brain Res. 1973; 63: 479–486, doi: 10.1016/0006-8993(73)90128-5.

80. Zerboni L, Arvin A. Neuronal subtype and satellite cell tropism are determinants of varicella-zoster virus virulence in human dorsal root ganglia xenografts in vivo. PLoS Pathog. 2015; 11(6): e1004989, doi: 10.1371/journal.ppat.1004989, indexed in Pubmed: 26090802.

81. Ziegler RJ, Herman RE. Peripheral infection in culture of rat sensory neurons by herpes simplex virus. Infect Immun. 1980; 28(2): 620–623, doi: 10.1128/iai.28.2.620-623.1980, indexed in Pubmed: 6249745.

82. Ziegler RJ, Pozos RS. Ultrastructural effects of herpes simplex virus type 2 infection of rat dorsal root ganglia in culture. J Neuropathol Exp Neurol. 1977; 36(4): 680–692, doi: 10.1097/00005072-197707000-00004, indexed in Pubmed: 196052.

83. Zimmerman E, Karsh D, Humbertson A. Initiating factors in perineuronal cell hyperplasia associated with chromatolytic neurons. Z Zellforsch. 1971; 114(1): 73–82, doi: 10.1007/BF00339466, indexed in Pubmed: 5541844.

755

REVIEW ARTICLE

VIA MEDICA

Can the kisspeptin help us in the understanding of pathology of some neurodegenerative brain diseases?

N. Melka[1], A. Pszczolinska[1], I. Klejbor[2, 3], B. Ludkiewicz[1], P. Kowiański[1, 3], J. Moryś[3, 4]

[1]Department of Anatomy and Neurobiology, Faculty of Medicine, Medical University of Gdansk, Poland
[2]Department of Anatomy, Jan Kochanowski University of Kielce, Poland
[3]Department of Clinical Anatomy and Physiology, Institute of Health Sciences, Pomeranian University of Slupsk, Poland
[4]Department of Normal Anatomy, Faculty of Medicine and Dentistry, Pomeranian Medical University in Szczecin, Poland

It is already known that the discovery of kisspeptin was a revolutionary step in the understanding of neuroendocrine regulation of reproduction. Kisspeptin is one of the main moderators of the gonadotropic axis, but the kisspeptin gene is known to be expressed in various regions of the central nervous system. The activity of kisspeptin is not limited to hypothalamic pituitary gonadal axis; it participates in the regulation of multiple neuronal circuits in the limbic system. The limbic system is a part of the brain involved in behavioural and emotional reactions, and disturbances in its functioning may be the source of some psychiatric as well as degenerative disorders. In the present review, we summarise the current state of knowledge concerning the role of kisspeptin in the limbic system and a new hope for the treatment of disturbances in its functioning. (Folia Morphol 2021; 80, 4: 756–765)

Key words: kisspeptin, hypothalamus, limbic system, neurodegenerative disease

INTRODUCTION

Kisspeptin (KP), a protein named after the famous chocolates 'Kisses', has revolutionised both our knowledge of hypothalamic pituitary gonadal (HPG) axis [29, 56, 90] and the understanding of neuroendocrine regulation of reproduction [29, 56, 90]. Kisspeptin bases on the principle of feedback which allows for the maintaining of homeostasis in various physiological states of the body. The first information about the KP protein and its influence on the function of HPG axis appeared at the end of the 20th century during the studies on the function of dynorphin A and neurokinin B [15, 48]. The HPG works mainly due to the interaction and integration of brain and gonadal signals [44, 104]. In the rat, the oestrogen receptor is not present on gonadotropin-releasing hormone (GnRH) neurons [47]; consequently, gonadal feedback must be realised by the intermediate signalling pathway. The protagonist of this route is KP [38, 50, 51, 56, 89]. Kisspeptin plays a decisive role in the control of fertility by initiating and regulating the process of puberty and pituitary secretion. Since 2005, it has been known to be the strongest activator of the HPG axis [43]. Depriving KP or its receptor weakens fertility and reproductive physiology [28, 30, 89], while enhancement of the mutation function in
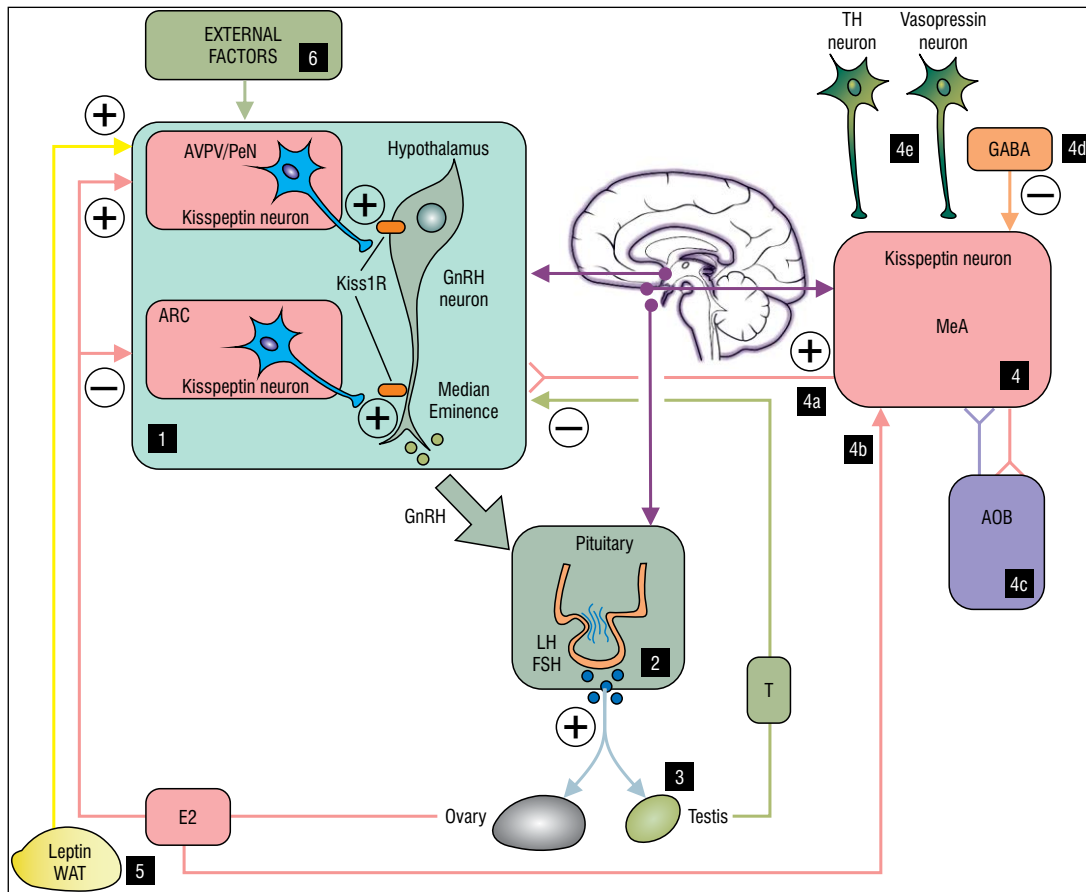
Figure 1. Diagram summarizing the integrated function of the major populations of kisspeptin neurons. **1.** The primary functions of hypothalamic kisspeptin are its roles in stimulating reproduction and mediating sex steroid feedback signalling. Kisspeptin neurons are situated in the anterior ventral periventricular region (AVPV), periventricular nucleus (PeN) and arcuate nucleus (ARC) of the hypothalamus. The diagram shows the effect of kisspeptin neurons on GnRH neurons depending on the place of occurrence. In the case of AVPV/PeN, it is a body cell, while for ARC, it is a median eminence. Sex steroid hormones inhibit the expression of Kiss1 in the ARC and induce expression in the AVPV/PeN. When sex steroids are low, Kiss1 expression increases in ARC and decreases in AVPV/PeN. Major elements having reproductive control are hypothalamic GnRH neurons that release GnRH into the bloodstream system. GnRH influences FSH and LH gonadotropins, which in turn regulate gonadal function [29, 56, 90, 103]; **2.** Pituitary: synthesize and secrete gonadotropin hormones [luteinizing hormone (LH) and follicle-stimulating hormone (FSH)]; **3.** Gonads: gamete generation and the production of sex hormones such as oestrogen and testosterone; **4.** The third big population of kisspeptin neurons (in addition to those present in the hypothalamus) is present in the medial nucleus of amygdala (medial amygdala, MeA) [42]; **4a.** Kisspeptin neurons from MeA send axons to the preoptic area of hypothalamus (POA) where many GnRH neurons are present [78]; **4b.** Oestradiol (E2) acts on MeA kisspeptin neurons via oestrogen receptor α (Erα) [95, 96]; **4c.** Kisspeptin neurons in MeA are reciprocally linked to the accessory olfactory bulb (AOB) [57, 78]; **4d.** Kisspeptin neurons in MeA are downregulated by GABA signalling via gamma-aminobutyric acid B (GABAB) receptor [34]; **4e.** Kisspeptin neurons in MeA get projections from vasopressin and tyrosine hydroxylase (TH) neurons [78]; **5.** Leptin, produced by white adipose tissue (WAT), has a stimulating effect on the activity of GnRH hypothalamic neurons. Kisspeptin neurons are present in the group of intermediate neurons that have leptin receptors [86]; **6.** Effect of external factors on kisspeptin neurons in hypothalamus, like stress, age, nutrition, and pheromones [85, 88].

the KISS1R results in premature maturation [100]. In immature rats, administration of KP induced the onset of maturation, while administration of its antagonist delayed it [77].

Kisspeptin is encoded by the kisspeptin gene (KISS1/Kiss1 gene) [63]. This neuropeptide performs different roles in brain functions. It is dynamically regulated by neuronal activity and increases synaptic transmission for a long time [6]. The kisspeptin gene is expressed in the central nervous system [21, 36, 56, 64, 65]

as well as in many other organs [10]. Kisspeptins are the products of KISS1 gene, which operate trough the G-protein coupled receptor GPR54 [37] and are essential for stimulation of GnRH secretion and induction of puberty (Fig. 1). This receptor is highly expressed in the brain areas related to memory and emotions, including the hippocampus and amygdala [7]. The wide distribution of KP fibres, as well as the KP receptor in central and peripheral nervous system, is a reason for these proteins being involved in

the regulation of multiple neuronal circuits and has been reported in a large number of physiological, as well as pathophysiological conditions of the reproductive system [18, 90, 105], diabetes [52, 53, 90], adiposity [45, 50] and suppression of metastasis in various neoplasm [17, 61], locomotor activity [98], and anxiety [98].

In all examined mammalian species, the localisation of hypothalamic KP neurons is mostly similar. They are generally placed in the anteroventral periventricular nucleus (AVPV) and the preoptic periventricular nucleus (PeN), dorsomedial nucleus (DMN), and arcuate nucleus (ARN) [1, 20, 32, 41, 66]. A studied species contains at least two types of KP neurons in the hypothalamus [66], and another one in the medial amygdala of rodents [96]. The KP neurons are observed mainly in the preoptic/rostral hypothalamus in various mammalian species, including rodents [20, 42, 92, 93], sheep [36, 41], pigs [101], nonhuman primates [91, 102, 106] as well as human [84]. Due to different role of KP neurons, they additionally contain various neurotransmitters/neuromodulators or their precursors like galanin [55, 79], enkephalin [79], dopamine [19] or GABA and glutamine [26]. Additionally, in the human, KP neurons, the co-expression of neuropeptides including neurokinin B [48], substance P [49] and cocaine- and amphetamine-regulated transcript CART were observed. The different co-transmitters present in the KP neurons suggest its multimodal functions and involvement in various behavioural activities in the brain structures.

Leptin, discovered in 1994, is known to be produced by white fatty tissue (WAT) [110] and to have a major indirect effect on excitation of HPG axis. This stimulatory effect on the HPG axis is performed through the KP interneurons located in the anterior part of the hypothalamus which also possess the receptors for leptin [12, 13, 50]. Additionally, many regulatory factors influence the hypothalamic KP neurons and consequently, the release of KP. Energy reserves are essential for reproductive success. As a result, metabolic factors tightly control the synthesis and release of KP [71].

LIMBIC SYSTEM

In 2011 scientists began to examine KP and its effects outside the hypothalamus more closely. The expression of KP was also found in other components of the limbic brain structures, like amygdala [2, 24,

57, 60, 78, 95], hippocampus [6–8, 62] and olfactory system [78]. There are very few records regarding the expression of KISS1 mRNA in the striatum [62, 67].

The limbic system is a set of structures in the brain that are involved in memory and emotions as well as in reproductive behaviours [81]. However, the precise link connecting those functions is still elusive and undefined. Defects in the functioning of the limbic system can be a source of many diseases. In the past years, KP emerged as physiological regulator of GnRH neurons and, hence, of the HPG axis. Some reviews summarized this function of KP; however, they focused mainly on the presence and role of KP in the hypothalamus [38, 50, 51, 56, 83]. There are some reports presenting other functions of KP such as decreasing food intake, as well as being one of the new hypothalamic anorexigenic factors [94].

Emotion and sexual responses are fundamental in human behaviour. Researchers have shown KP as a link between the brain and the reproductive axis [24]. Kisspeptin administration enhances limbic and paralimbic system activity [24]. What is more, KP reduces sexual aversion and noticeably increases brain activity [24]. The author emphasizes KP participation in limbic system activity, behaviour, and modulation of sex hormones [24]. On top of it, KP administration decrease negative mood [24]. The results indicate that KP also shows antidepressant-like effects [24]. Kisspeptin administration activates components of the reward system such as the hippocampus, amygdala and the cingulate and enhances the activity of this system [24]. Additional research shows, that KP increases emotional and sexual processing and decreases sexual aversion. This gives green light to the kisspeptin-based therapies for emotional and psychosexual disorders [23].

The reaction of other species is also interesting. Kisspeptin, via activation of the HPG axis, as well as modulation of releasing testosterone, has indirect effects on aggressive and territorial behaviour in male lizards [72].

BEHAVIOURAL AND NEURAL REACTIONS TO EMOTIONS

The amygdala, emotional centre of the brain, is a part of the limbic system. It is closely related to anxiety, fear, reward, stress, and social behaviour [81]. The medial nucleus of amygdala (MeA) is a most important brain region in sexual and emotional reaction [81] in which Kiss1 neurons were first described in
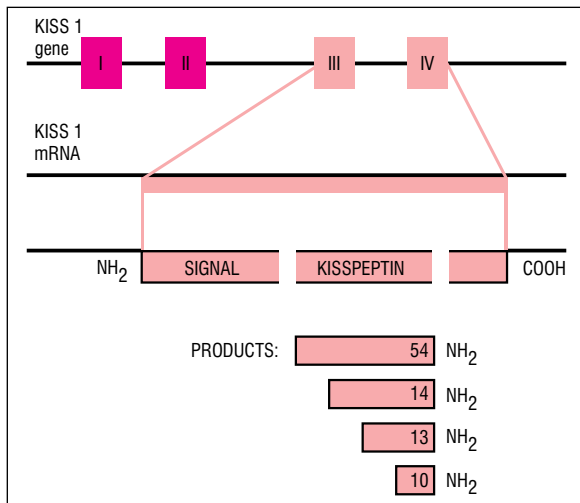
Figure 2. Kisspeptins are a family of small but important peptides that play a key role in the regulation of neuroendocrine reproductive function through the nervous pathways. The diagram demonstrates products of the KISS1 gene. Presented are the precursor kisspeptin-145 and the functional kisspeptin fragments: kisspeptin-54 and shorter peptides such as kisspeptin-14, kisspeptin-13, kisspeptin-10 (suffix showing the number of amino acids).

male mice in 2004 [42]. Neurons of MeA contain a lot of steroid hormone receptors which interact with the sex hormones and transfers olfactory information to areas closely related to KP like hypothalamic nuclei engaged in reproduction and defence (Fig. 2) [57]. Many studies on the amygdala indicate involvement of this structure in the regulation of female reproductive cycles and sexual behaviour [60]. It is known that the KP neurons present in MeA are the third largest population of these neurons in the brain [42, 96]. Today we know that MeA kisspeptin neurons are regulated by sex steroids (E2 via receptor) [95, 96] and GABA (via receptor) [34]. MeA kisspeptin neurons send efferent projections to the hypothalamus [78, 109] and are also interconnected with the accessory olfactory bulb (AOB) [57, 78]. Additionally, they receive projections from vasopressin and TH neurons [78]. All this suggests that KP plays a much larger role in the regulation and functioning of the nervous system.

Kim et al. [60] were first to test the effect of sex steroids on rodent's MeA Kiss1 neurons. In the MeA, as in the AVPV/PeN, Kiss1 levels are highly regulated and dependent on the level of sex steroids [60]. According to Stephens et al. [95], Kiss1 expression in MeA neurons rises at puberty, and it is compatible with developmental level of sex steroids. The author's showed that Kiss1 expression in the amygdaloid body

is present only in pubertal period and is not expressed in MeA in the neonate or in the prepubertal period [95]. There is a relationship and dependence between amygdala KP signalling and the HPG axis. This is evidenced by observations on the direct KP administration into the medial amygdala which stimulate a luteinizing hormone (LH) secretion [22]. In turn, KP antagonist decreases in LH secretion.

Activation of KP neurons localized in the posterodorsal part of the medial amygdala (MePD) affects both social interaction and sexual partner preference in male mice [2]. Research on the activation of medial amygdala KP neurons shows increases of time spent by male mice investigating females [2]. It indicates a key role played by MePD kisspeptin in sexual and motivation behaviour.

THE MISSING LINK: WHEN THE SMELL MEETS EMOTION

Olfactory bulbs are an important part of the sexual behavioural system due to the presence of direct olfactory pathways to the corticomedial nuclei of the amygdala [58]. Within the olfactory system, two distinct sensory systems can be distinguished; the main olfactory system and accessory olfactory system [78]. The accessory olfactory bulb projects to MeA kisspeptin neurons [78] which are usually called "vomeronasal" amygdala [58]. This indicates the role of KP neurons in the processing of and responding to fragrance and pheromone information. Pheromones are detected and processed by accessory olfactory system which has been functionally linked to reproductive behaviour [11]. Next, signals triggered by pheromones in the accessory olfactory system are transmitted to hypothalamus [46]. The connection between the olfactory signals and the reproductive neuroendocrine axis is indicated by the latest results obtained by Aggarwal's team [3]. Hellier et al. [46] indicates that a reproductive success is an effect of close relationship of pheromone stimulation. Interestingly, the exact anatomical location of the KP receptor has not been described in the olfactory system so far.

Results obtained by Yang et al. [108] confirm the effect of KP on the structures of the limbic system. It is known that KP receptors are present in brain structures involved in emotions. The administration of KP significantly affects the reception of aromatic stimuli. The activity of the main olfactory network as well as structures such as the hippocampus and amygdala increase due to the nice smell [108]. In various neu-

rodegenerative diseases, the impairment of olfactory functions is observed [4, 33]. In the Alzheimer's or Parkinson's disease, the loss of olfaction may precede memory or motor disturbances [35]. To administer proper neuroprotective therapies, an early recognition of degenerative symptoms of the nervous system is necessary [87]. According to the role of KP in the olfactory and limbic structure, we might suspect that kisspeptins are a novel therapeutic potential in neurodegenerative diseases as well as reproductive disturbances.

FUNCTION OF KISSPEPTIN IN HIPPOCAMPUS

The functional role of KP in the hippocampus is still unknown. Many studies prove that KP works in the hippocampus as a neuropeptide neuromodulator [6, 42, 54, 99]. GPR54 is strongly expressed in the granular cell of hippocampal dentate gyrus [6–8], which is the first step of the hippocampal trisynaptic circuit. Lee et al. [62] showed that GPR54 density in the hippocampus is very high in the granule cell of the dentate gyrus, whereas it is barely detectable in the pyramidal cells of CA1 and CA3. Kisspeptin in the hippocampus rises the synaptic transmission via the activation of mitogen-activated protein kinases (MAPK)-related signalling pathway in granular cell of the dentate gyrus [8]. According to some authors, this regulatory system can play a role in the pathogenesis of epilepsy [6, 7]. Arai et al. [6–8] indicate that the neuronal activity strongly affects the expression of KP. They observed the greatest changes in KP expression after kainate injection [7], which is often used to obtain the model of temporal lobe epilepsy. Arai et al. [7] suggest the existence of positive feedback loop in the hippocampal formation. The excitability of granular cells is increased by the release of KP, which in turn has the effect of increasing the expression of KP [7]. The peptide system can play a role in epilepsy.

The dentate gyrus of the hippocampus is one of main neurogenic niches in the adult brain. Neural stem cells are located in this place and produce progenitors that travel near their final location like granular cell layer of the dentate gyrus [14]. The continuous addition of new granule cell population in the dentate gyrus has the potential to make a preferential participation to neural circuit transformation. There is possibility that KP and GPR54 are recruited to regulate neurogenesis in combination with other neurotrophic factors [63, 64]. This is supported by

the antimetastatic actions of KP [63, 64]. The observations carried out by Arai et al. [8] show that activation of GPR54 by metastin reversibly increases excitatory synaptic transmission in the granule cells of dentate gyrus.

NEW THERAPEUTIC APPROACH TO THE TREATMENT OF RECOGNITION MEMORY DISORDERS

The Alzheimer's disease (AD) is associated with a loss of cognitive function due to the progressive loss of neurons and their synapses. Given the increasing incidence of AD, finding new effective therapeutic strategies is now of the utmost importance. The GPR54 mRNA is highly expressed in the hippocampus [6], what may indicate that KP might be engaged in learning and memory processes. Hippocampus has a critical role in control of learning and memory, and its damage causes dysfunction in the processing of memory, memory consolidation and recognition [80]. As the role of KP and GPR54 in recognition processes was unclear, Jiang et al. [54] were the first to undertake research into the relationship of the KP/GPR54 system in memory recognition. His research was inspired by a Telegdy and Adamik report [99] in which he pointed that KP makes learning and memory consolidation in mice easier.

In 2012 Milton et al. [68] underlines that AD involves changes in the functioning of the HPG axis. He shows that KP might be a factor preventing neurotoxicity of amyloid-β peptide in vitro. Milton was the first to show in vitro interaction of KP with amyloid-β peptide that suggests a potential role of KP in AD pathology [16]. Milton et al. [68] is a mastermind of the idea of using KP peptides in preventing, detecting and treating of diseases including Alzheimer's, Creutzfeldt-Jakob disease and type 2 diabetes. Three years later, Jiang et al. [54] shows that the injection of KP-13 into the lateral ventricle and hippocampus activates receptors GPR54, prolongs the memory retention, makes easier the creation of object recognition memory, and improves memory deficit.

The pyramidal neurons of the CA1 sector of the hippocampus are particularly damaged during AD [97]. After the injection of amyloid-β into the hippocampus, KP-13 shows neuroprotective effects, alleviates disorders, has positive effects on improving spatial memory, and significantly prevents neuronal loss [59]. Further research is needed to determine whether the neuroprotective effects of KP against

amyloid-β peptide toxicity are via direct binding to amyloid-β peptide or via the receptor.

The wide expression of KP in structures involved in memory mechanisms and learning processes suggests interactions with cholinergic systems. Babaei et al. [9] indicate therapeutic function of KP. The injection of KP-13 into lateral cerebral ventricle had a positive effect on memory and facilitated spatial learning in induced AD. This endogenous peptide has an important role in alleviating the cognitive deficit by increasing the cholinergic response. As KP interacts with many neuropeptides involved in learning and memory, its action may be mediated through these receptor systems, which should be further investigated. Gamma-aminobutyric acid (GABA) is an example here. This is a key neurotransmitter and is closely related to behavioural disorders. Studies have shown that administration of KP highly reduces the level of GABA in the limbic system in humans [25]. Kissorphin, a peptide derived from KP-10, prevents acute impairment of memory, cognitive functions, and short-term spatial learning due to ethanol administration [39].

However, Kiss1 expression is inhibited during metabolic stress [82, 86]. It is suggested that an attenuation of KP signalling reduces metabolism as KP levels are inversely proportional to insulin secretion [5]. A decrease in KP signalling causes a decrease in brain metabolism [5].

BEHAVIOURAL THEORY OF DEPRESSION AND KISSPEPTIN

The limbic system seems to be involved in severe mental illnesses such as schizophrenia and depression. Base for depression is still incompletely understood and little is known about its pathogenesis [75]. One of the reasons is the lack of consensus on the pathology and aetiology of depression. Some symptoms' characteristics for depression are impossible to be modelled on laboratory animals. As of today, the criteria for identifying animal models of depression are based on actions of antidepressant drugs and responses to stress [107]. Animal models played big roles in the development of antidepressant drugs. Two of the most frequently used examinations are the open field test and the forced swim test. The open field is a very popular animal model of anxiety-like behaviour. The forced swim test is a behavioural test for rodents and is one of the most frequently used tests for evaluation of antidepressant drugs [76]. Tana-

ka et al. [98] and Telegdy and Adamik [99] showed that KP-13 strongly influenced activity, climbing and swimming times. In this study, KP-13 displayed antidepressant-like effects in a forced swimming test [98]. In open field test, the injection of KP-13 into lateral cerebral ventricles stimulates the HPA axis which is the most important adaptive neuroendocrine system [40]. Kisspeptin-13 in the open field test has a big impact on behaviour in rats. In addition, KP-13 induces hyperthermia [27]. This suggests a potential role for KP in thermogenesis.

The observations carried out by Adekunbi et al. [2] focused on KP neuronal population in MeA which is involved in anxiety response. Adekunbi et al. [2], in contrast to Telegdy and Adamik's results [99], showed that the selective activation of MeA kisspeptin neurons reduced anxiety in mice. Injection of KP-13 in rats reduced time spent in the open arms of the elevated-plus maze. Adekunbi's mice were less anxious which was evidenced by longer exploratory time in the open arms of the elevated plus maze [2]. Similar results were obtained in another experiment regarding the effect of KP on anxiety behaviour in male mice. Delmas et al. [31] focused on the role of KISS1R signalling in anxiety behaviour. Research shows a tendency for decreased anxiety behaviour in rapport to the elevated plus maze. Such differences in specificity likely result from differences between the two species. Further work is necessary to answer the questions about the role of KP signalling in anxiety in various species, as KP has an antidepressant role not only in rodents. Ogawa et al. [73] indicates that interaction between KP and the serotonergic system plays an important role in the modulation of fear in zebrafish. Later studies by his team showed that the blockade of serotonin receptors abolished the effect of KP, which modulated the serotonergic system through glutamatergic neurotransmission [69, 70, 74]. The role of kisspeptin-based therapy requires further study and explanation as there are clear links between KP and anxiety.

CONCLUSIONS

Today, KP is undoubtedly one of the basic proteins regulating not only the mechanisms underlying reproductive functions, but also the neuronal networks that integrate sexual and emotional behaviour with reproductive functions (Fig. 3). To date, most of the data concentrate on the sexual role of KP in the central nervous system, so it will be of great interest in
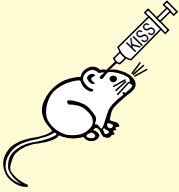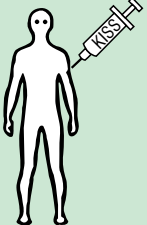
Figure 3. Summary of therapeutic roles of kisspeptin.

the coming years to investigate its role in emotion and memory function in healthy condition as well as in the diseases. The results indicating the therapeutic role of KP in neuropsychiatric and neurodegenerative diseases represent a promising path for the development of research into this problem. Future studies will, undoubtfully, investigate the influence of KP on behaviours in various species including humans and attempt to delineate the precise neuronal pathways involved. Furthermore, with a better understanding of these processes, there may emerge potential therapeutic applications to aid patients with various neurodegenerative, emotional or psychosexual diseases.

REFERENCES

1. Adachi S, Yamada S, Takatsu Y, et al. Involvement of anteroventral periventricular metastin/kisspeptin neurons in estrogen positive feedback action on luteinizing hormone release in female rats. J Reprod Dev. 2007; 53(2): 367–378, doi: 10.1262/jrd.18146, indexed in Pubmed: 17213691.
2. Adekunbi DA, Li XF, Lass G, et al. Kisspeptin neurones in the posterodorsal medial amygdala modulate sexual partner preference and anxiety in male mice. J Neuroendocrinol. 2018; 30(3): e12572, doi: 10.1111/jne.12572, indexed in Pubmed: 29356147.
3. Aggarwal S, Tang C, Sing K, et al. Medial amygdala kiss1 neurons mediate female pheromone stimulation of luteinizing hormone in male mice. Neuroendocrinology. 2019; 108(3): 172–189, doi: 10.1159/000496106, indexed in Pubmed: 30537700.
4. Aguilar Martínez N, Aguado Carrillo G, Saucedo Alvarado PE, et al. Clinical importance of olfactory function in neurodegenerative diseases. Rev Médica del Hosp Gen México. 2018; 81(4): 268–275, doi: 10.1016/j.hgmx.2017.05.007.
5. Andreozzi F, Mannino GC, Mancuso E, et al. Plasma kisspeptin levels are associated with insulin secretion in nondiabetic individuals. PLoS One. 2017; 12(6): e0179834, doi: 10.1371/journal.pone.0179834, indexed in Pubmed: 28636637.
6. Arai AC, Orwig N. Factors that regulate KiSS1 gene expression in the hippocampus. Brain Res. 2008; 1243: 10–18, doi: 10.1016/j.brainres.2008.09.031, indexed in Pubmed: 18834866.
7. Arai AC, Xia YF, Suzuki E, et al. Cancer metastasis-suppressing peptide metastin upregulates excitatory synaptic transmission in hippocampal dentate granule cells. J Neurophysiol. 2005; 94(5): 3648–3652, doi: 10.1152/jn.00590.2005, indexed in Pubmed: 16222076.
8. Arai AC. The role of kisspeptin and GPR54 in the hippocampus. Peptides. 2009; 30(1): 16–25, doi: 10.1016/j.peptides.2008.07.023, indexed in Pubmed: 18765263.
9. Babaei P, Pourmir M, Babaei P, et al. Kisspeptin-13 ameliorates memory impairment induced by streptozotocin in male rats via cholinergic system. Physiology and Pharmacology. 2016; 20(1): 38–47.
10. Bhattacharya M, Babwah AV. Kisspeptin: beyond the brain. Endocrinology. 2015; 156(4): 1218–1227, doi: 10.1210/en.2014-1915, indexed in Pubmed: 25590245.
11. Boehm U, Zou Z, Buck LB. Feedback loops link odor and pheromone signaling with reproduction. Cell. 2005; 123(4): 683–695, doi: 10.1016/j.cell.2005.09.027, indexed in Pubmed: 16290036.
12. Brown RE, Imran SA, Ur E, et al. KiSS-1 mRNA in adipose tissue is regulated by sex hormones and food intake. Mol Cell Endocrinol. 2008; 281(1-2): 64–72, doi: 10.1016/j.mce.2007.10.011, indexed in Pubmed: 18069123.
13. Castellano JM, Bentsen AH, Mikkelsen JD, et al. Kisspeptins: bridging energy homeostasis and reproduction. Brain Res. 2010; 1364: 129–138, doi: 10.1016/j.brainres.2010.08.057, indexed in Pubmed: 20800054.
14. Cayre M, Canoll P, Goldman JE. Cell migration in the normal and pathological postnatal mammalian brain. Prog Neurobiol. 2009; 88(1): 41–63, doi: 10.1016/j.pneurobio.2009.02.001, indexed in Pubmed: 19428961.
15. Cheng G, Coolen LM, Padmanabhan V, et al. The kisspeptin/neurokinin B/dynorphin (KNDy) cell population of the arcuate nucleus: sex differences and effects of prenatal testosterone in sheep. Endocrinology. 2010; 151(1): 301–311, doi: 10.1210/en.2009-0541, indexed in Pubmed: 19880810.
16. Chilumuri A, Ashioti M, Nercessian AN, et al. Immunolocalization of kisspeptin associated with amyloid-β deposits in the pons of an Alzheimer's disease patient. J Neurodegener Dis. 2013; 2013: 879710, doi: 10.1155/2013/879710, indexed in Pubmed: 26317001.
17. Ciaramella V, Della Corte CM, Ciardiello F, et al. Kisspeptin and cancer: molecular interaction, biological functions, and future perspectives. Front Endocrinol (Lausanne). 2018; 9: 115, doi: 10.3389/fendo.2018.00115, indexed in Pubmed: 29662466.
18. Clarke H, Dhillo WS, Jayasena CN. Comprehensive review on kisspeptin and its role in reproductive disorders. Endocrinol Metab (Seoul). 2015; 30(2): 124–141, doi: 10.3803/EnM.2015.30.2.124, indexed in Pubmed: 26194072.
19. Clarkson J, Herbison AE. Dual phenotype kisspeptin-dopamine neurones of the rostral periventricular area of the third ventricle project to gonadotrophin-releasing

hormone neurones. J Neuroendocrinol. 2011; 23(4): 293–301, doi: 10.1111/j.1365-2826.2011.02107.x, indexed in Pubmed: 21219482.

20. Clarkson J, Herbison AE. Postnatal development of kisspeptin neurons in mouse hypothalamus; sexual dimorphism and projections to gonadotropin-releasing hormone neurons. Endocrinology. 2006; 147(12): 5817–5825, doi: 10.1210/en.2006-0787, indexed in Pubmed: 16959837.

21. Clarkson J, d'Anglemont de Tassigny X, Colledge WH, et al. Distribution of kisspeptin neurones in the adult female mouse brain. J Neuroendocrinol. 2009; 21(8): 673–682, doi: 10.1111/j.1365-2826.2009.01892.x, indexed in Pubmed: 19515163.

22. Comninos AN, Anastasovska J, Sahuri-Arisoylu M, et al. Kisspeptin signaling in the amygdala modulates reproductive hormone secretion. Brain Struct Funct. 2016; 221(4): 2035–2047, doi: 10.1007/s00429-015-1024-9, indexed in Pubmed: 25758403.

23. Comninos AN, Demetriou L, Wall MB, et al. Modulations of human resting brain connectivity by kisspeptin enhance sexual and emotional functions. JCI Insight. 2018; 3(20), doi: 10.1172/jci.insight.121958, indexed in Pubmed: 30333302.

24. Comninos AN, Wall MB, Demetriou L, et al. Kisspeptin modulates sexual and emotional brain processing in humans. J Clin Invest. 2017; 127(2): 709–719, doi: 10.1172/JCI89519, indexed in Pubmed: 28112678.

25. Comninos AN, Yang L, O'Callaghan J, et al. Kisspeptin modulates gamma-aminobutyric acid levels in the human brain. Psychoneuroendocrinology. 2021; 129: 105244, doi: 10.1016/j.psyneuen.2021.105244, indexed in Pubmed: 33975151.

26. Cravo RM, Margatho LO, Osborne-Lawrence S, et al. Characterization of Kiss1 neurons using transgenic mouse models. Neuroscience. 2011; 173: 37–56, doi: 10.1016/j.neuroscience.2010.11.022, indexed in Pubmed: 21093546.

27. Csabafi K, Jászberényi M, Bagosi Z, et al. Effects of kisspeptin-13 on the hypothalamic-pituitary-adrenal axis, thermoregulation, anxiety and locomotor activity in rats. Behav Brain Res. 2013; 241: 56–61, doi: 10.1016/j.bbr.2012.11.039, indexed in Pubmed: 23219969.

28. d'Anglemont de Tassigny X, Fagg LA, Dixon JPC, et al. Hypogonadotropic hypogonadism in mice lacking a functional Kiss1 gene. Proc Natl Acad Sci U S A. 2007; 104(25): 10714–10719, doi: 10.1073/pnas.0704114104, indexed in Pubmed: 17563351.

29. De Bond JAP, Smith JT. Kisspeptin and energy balance in reproduction. Reproduction. 2014; 147(3): R53–R63, doi: 10.1530/REP-13-0509, indexed in Pubmed: 24327738.

30. de Roux N, Genin E, Carel JC, et al. Hypogonadotropic hypogonadism due to loss of function of the KiSS1-derived peptide receptor GPR54. Proc Natl Acad Sci U S A. 2003; 100(19): 10972–10976, doi: 10.1073/pnas.1834399100, indexed in Pubmed: 12944565.

31. Delmas S, Porteous R, Bergin DH, et al. Altered aspects of anxiety-related behavior in kisspeptin receptor-deleted male mice. Sci Rep. 2018; 8(1): 2794, doi: 10.1038/s41598-018-21042-4, indexed in Pubmed: 29434234.

32. Desroziers E, Mikkelsen J, Simonneaux V, et al. Mapping of kisspeptin fibres in the brain of the pro-oestrous rat. J Neuroendocrinol. 2010; 22(10): 1101–1112, doi: 10.1111/j.1365-2826.2010.02053.x, indexed in Pubmed: 20673302.

33. Devere R. Smell and taste in clinical neurology: Five new things. Neurol Clin Pract. 2012; 2(3): 208–214, doi: 10.1212/CPJ.0b013e31826af199, indexed in Pubmed: 29443306.

34. Di Giorgio NP, Semaan SJ, Kim J, et al. Impaired GABAB receptor signaling dramatically up-regulates Kiss1 expression selectively in nonhypothalamic brain regions of adult but not prepubertal mice. Endocrinology. 2014; 155(3): 1033–1044, doi: 10.1210/en.2013-1573, indexed in Pubmed: 24424047.

35. Doty R. Olfactory dysfunction in Parkinson disease. Nat Rev Neurol. 2012; 8(6): 329–339, doi: 10.1038/nrneurol.2012.80.

36. Franceschini I, Lomet D, Cateau M, et al. Kisspeptin immunoreactive cells of the ovine preoptic area and arcuate nucleus co-express estrogen receptor alpha. Neurosci Lett. 2006; 401(3): 225–230, doi: 10.1016/j.neulet.2006.03.039, indexed in Pubmed: 16621281.

37. Franssen D, Tena-Sempere M. The kisspeptin receptor: A key G-protein-coupled receptor in the control of the reproductive axis. Best Pract Res Clin Endocrinol Metab. 2018; 32(2): 107–123, doi: 10.1016/j.beem.2018.01.005, indexed in Pubmed: 29678280.

38. Funes S, Hedrick JA, Vassileva G, et al. The KiSS-1 receptor GPR54 is essential for the development of the murine reproductive system. Biochem Biophys Res Commun. 2003; 312(4): 1357–1363, doi: 10.1016/j.bbrc.2003.11.066, indexed in Pubmed: 14652023.

39. Gibula-Tarlowska E, Kotlinska JH. Kissorphin improves spatial memory and cognitive flexibility impairment induced by ethanol treatment in the Barnes maze task in rats. Behav Pharmacol. 2020; 31(2&3): 272–282, doi: 10.1097/FBP.0000000000000557, indexed in Pubmed: 32168027.

40. Goncharova ND. Stress responsiveness of the hypothalamic-pituitary-adrenal axis: age-related features of the vasopressinergic regulation. Front Endocrinol (Lausanne). 2013; 4: 26, doi: 10.3389/fendo.2013.00026, indexed in Pubmed: 23486926.

41. Goodman RL, Lehman MN, Smith JT, et al. Kisspeptin neurons in the arcuate nucleus of the ewe express both dynorphin A and neurokinin B. Endocrinology. 2007; 148(12): 5752–5760, doi: 10.1210/en.2007-0961, indexed in Pubmed: 17823266.

42. Gottsch ML, Cunningham MJ, Smith JT, et al. A role for kisspeptins in the regulation of gonadotropin secretion in the mouse. Endocrinology. 2004; 145(9): 4073–4077, doi: 10.1210/en.2004-0431, indexed in Pubmed: 15217982.

43. Han SK, Gottsch ML, Lee KJ, et al. Activation of gonadotropin-releasing hormone neurons by kisspeptin as a neuroendocrine switch for the onset of puberty. J Neurosci. 2005; 25(49): 11349–11356, doi: 10.1523/JNEUROSCI.3328-05.2005, indexed in Pubmed: 16339030.

44. Handa RJ, Burgess LH, Kerr JE, et al. Gonadal steroid hormone receptors and sex differences in the hypothalamo-pituitary-adrenal axis. Horm Behav. 1994; 28(4): 464–476, doi: 10.1006/hbeh.1994.1044, indexed in Pubmed: 7729815.

45. Harter CJL, Kavanagh GS, Smith JT. The role of kisspeptin neurons in reproduction and metabolism. J Endocrinol. 2018; 238(3): R173–R183, doi: 10.1530/JOE-18-0108, indexed in Pubmed: 30042117.

46. Hellier V, Brock O, Candlish M, et al. Female sexual behavior in mice is controlled by kisspeptin neurons. Nat Commun. 2018; 9(1): 400, doi: 10.1038/s41467-017-02797-2, indexed in Pubmed: 29374161.

47. Herbison AE, Theodosis DT. Localization of oestrogen receptors in preoptic neurons containing neurotensin but not tyrosine hydroxylase, cholecystokinin or luteinizing hormone-releasing hormone in the male and female rat. Neuroscience. 1992; 50(2): 283–298, doi: 10.1016/0306-4522(92)90423-y, indexed in Pubmed: 1359459.

48. Hrabovszky E, Ciofi P, Vida B, et al. The kisspeptin system of the human hypothalamus: sexual dimorphism and relationship with gonadotropin-releasing hormone and neurokinin B neurons. Eur J Neurosci. 2010; 31(11): 1984–1998, doi: 10.1111/j.1460-9568.2010.07239.x, indexed in Pubmed: 20529119.

49. Hrabovszky E, Borsay BÁ, Rácz K, et al. Substance P immunoreactivity exhibits frequent colocalization with kisspeptin and neurokinin B in the human infundibular region. PLoS One. 2013; 8(8): e72369, doi: 10.1371/journal.pone.0072369, indexed in Pubmed: 23977290.

50. Hussain MA, Song WJ, Wolfe A, et al. Glucagon regulates hepatic kisspeptin to impair insulin secretion. Cell Metab. 2014; 19(4): 667–681, doi: 10.1016/j.cmet.2014.03.005, indexed in Pubmed: 24703698.

51. Irwig MS, Fraley GS, Smith JT, et al. Kisspeptin activation of gonadotropin releasing hormone neurons and regulation of KiSS-1 mRNA in the male rat. Neuroendocrinology. 2004; 80(4): 264–272, doi: 10.1159/000083140, indexed in Pubmed: 15665556.

52. Izzi E, Comninos A, Clarke S, et al. Kisspeptin stimulates insulin secretion and modulates serum metabolites in humans. Endocrine Abstracts. 2018, doi: 10.1530/endo-abs.59.oc3.1.

53. Izzi-Engbeaya C, Comninos AN, Clarke SA, et al. The effects of kisspeptin on β-cell function, serum metabolites and appetite in humans. Diabetes Obes Metab. 2018; 20(12): 2800–2810, doi: 10.1111/dom.13460, indexed in Pubmed: 29974637.

54. Jiang JH, He Z, Peng YL, et al. Kisspeptin-13 enhances memory and mitigates memory impairment induced by Aβ1-42 in mice novel object and object location recognition tasks. Neurobiol Learn Mem. 2015; 123: 187–195, doi: 10.1016/j.nlm.2015.05.010, indexed in Pubmed: 26103138.

55. Kalló I, Mohácsik P, Vida B, et al. A novel pathway regulates thyroid hormone availability in rat and human hypothalamic neurosecretory neurons. PLoS One. 2012; 7(6): e37860, doi: 10.1371/journal.pone.0037860, indexed in Pubmed: 22719854.

56. Kauffman AS. Coming of age in the kisspeptin era: sex differences, development, and puberty. Mol Cell Endocrinol. 2010; 324(1-2): 51–63, doi: 10.1016/j.mce.2010.01.017, indexed in Pubmed: 20083160.

57. Keshavarzi S, Sullivan RKP, Ianno DJ, et al. Functional properties and projections of neurons in the medial amygdala. J Neurosci. 2014; 34(26): 8699–8715, doi: 10.1523/JNEUROSCI.1176-14.2014, indexed in Pubmed: 24966371.

58. Kevetter GA, Winans SS. Connections of the corticomedial amygdala in the golden hamster. I. Efferents of the "vomeronasal amygdala". J Comp Neurol. 1981; 197(1): 81–98, doi: 10.1002/cne.901970107, indexed in Pubmed: 6164702.

59. Khonacha SE, Janahmadi M, Motamedi F. Kisspeptin-13 Improves Spatial Memory Consolidation and Retrieval against Amyloid-β Pathology. Iran J Pharm Res. 2019; 18(Suppl1): 169–181, doi: 10.22037/ijpr.2019.112199.13599, indexed in Pubmed: 32802097.

60. Kim J, Semaan SJ, Clifton DK, et al. Regulation of Kiss1 expression by sex steroids in the amygdala of the rat and mouse. Endocrinology. 2011; 152(5): 2020–2030, doi: 10.1210/en.2010-1498, indexed in Pubmed: 21363930.

61. Kim TH, Cho SG. Kisspeptin inhibits cancer growth and metastasis via activation of EIF2AK2. Mol Med Rep. 2017; 16(5): 7585–7590, doi: 10.3892/mmr.2017.7578, indexed in Pubmed: 28944853.

62. Lee DK, Nguyen T, O'Neill GP, et al. Discovery of a receptor related to the galanin receptors. FEBS Lett. 1999; 446(1): 103–107, doi: 10.1016/s0014-5793(99)00009-5, indexed in Pubmed: 10100623.

63. Lee JH, Miele ME, Hicks DJ, et al. KiSS-1, a novel human malignant melanoma metastasis-suppressor gene. J Natl Cancer Inst. 1996; 88(23): 1731–1737, doi: 10.1093/jnci/88.23.1731, indexed in Pubmed: 8944003.

64. Lee JH, Welch DR. Identification of highly expressed genes in metastasis-suppressed chromosome 6/human malignant melanoma hybrid cells using subtractive hybridization and differential display. Int J Cancer. 1997; 71(6): 1035–1044, doi: 10.1002/(sici)1097-0215(19970611)71:6<1035::aid-ijc20>3.0.co;2-b, indexed in Pubmed: 9185708.

65. Lehman MN, Hileman SM, Goodman RL. Neuroanatomy of the kisspeptin signaling system in mammals: comparative and developmental aspects. Adv Exp Med Biol. 2013; 784: 27–62, doi: 10.1007/978-1-4614-6199-9_3, indexed in Pubmed: 23550001.

66. Lehman MN, Merkley CM, Coolen LM, et al. Anatomy of the kisspeptin neural network in mammals. Brain Res. 2010; 1364: 90–102, doi: 10.1016/j.brainres.2010.09.020, indexed in Pubmed: 20858464.

67. Martínez-Fuentes AJ, Molina M, Vázquez-Martínez R, et al. Expression of functional KISS1 and KISS1R system is altered in human pituitary adenomas: evidence for apoptotic action of kisspeptin-10. Eur J Endocrinol. 2011; 164(3): 355–362, doi: 10.1530/EJE-10-0905, indexed in Pubmed: 21169415.

68. Milton NGN, Chilumuri A, Rocha-Ferreira E, et al. Kisspeptin prevention of amyloid- peptide neurotoxicity in vitro. ACS Chem Neurosci. 2012; 3(9): 706–719, doi: 10.1021/cn300045d, indexed in Pubmed: 23019497.

69. Nathan FM, Ogawa S, Parhar IS. Kisspeptin1 modulates odorant-evoked fear response via two serotonin receptor subtypes (5-HT1A and 5-HT2) in zebrafish. J Neurochem. 2015; 133(6): 870–878, doi: 10.1111/jnc.13105, indexed in Pubmed: 25818845.

70. Nathan FM, Ogawa S, Parhar IS. Neuronal connectivity between habenular glutamate-kisspeptin1 co-expressing neurons and the raphe 5-HT system. J Neurochem. 2015; 135(4): 814–829, doi: 10.1111/jnc.13273, indexed in Pubmed: 26250886.

71. Navarro VM. Metabolic regulation of kisspeptin: the link between energy balance and reproduction. Nat Rev Endocrinol. 2020; 16(8): 407–420, doi: 10.1038/s41574-020-0363-7, indexed in Pubmed: 32427949.

72. Neuman-Lee L, Greives T, Hopkins GR, et al. The role of the kisspeptin system in regulation of the reproductive endocrine axis and territorial behavior in male side-blotched lizards (Uta stansburiana). Horm Behav. 2017; 89: 48–54, doi: 10.1016/j.yhbeh.2016.12.006, indexed in Pubmed: 28017596.

73. Ogawa S, Nathan FM, Parhar IS. Habenular kisspeptin modulates fear in the zebrafish. Proc Natl Acad Sci U S A. 2014; 111(10): 3841–3846, doi: 10.1073/pnas.1314184111, indexed in Pubmed: 24567386.

74. Ogawa S, Parhar IS. Biological significance of kisspeptin-Kiss 1 receptor signaling in the habenula of teleost species. Front Endocrinol (Lausanne). 2018; 9: 222, doi: 10.3389/fendo.2018.00222, indexed in Pubmed: 29867758.

75. Pandya M, Altinay M, Malone DA, et al. Where in the brain is depression? Curr Psychiatry Rep. 2012; 14(6): 634–642, doi: 10.1007/s11920-012-0322-7, indexed in Pubmed: 23055003.

76. Petit-Demouliere B, Chenu F, Bourin M. Forced swimming test in mice: a review of antidepressant activity. Psychopharmacology (Berl). 2005; 177(3): 245–255, doi: 10.1007/s00213-004-2048-7, indexed in Pubmed: 15609067.

77. Pineda R, Aguilar E, Pinilla L, et al. Physiological roles of the kisspeptin/GPR54 system in the neuroendocrine control of reproduction. Prog Brain Res. 2010; 181: 55–77, doi: 10.1016/S0079-6123(08)81005-9, indexed in Pubmed: 20478433.

78. Pineda R, Plaisier F, Millar RP, et al. Amygdala kisspeptin neurons: putative mediators of olfactory control of the gonadotropic axis. Neuroendocrinology. 2017; 104(3): 223–238, doi: 10.1159/000445895, indexed in Pubmed: 27054958.

79. Porteous R, Petersen SL, Yeo SH, et al. Kisspeptin neurons co-express met-enkephalin and galanin in the rostral pe-

riventricular region of the female mouse hypothalamus. J Comp Neurol. 2011; 519(17): 3456–3469, doi: 10.1002/cne.22716, indexed in Pubmed: 21800299.

80. Preston AR, Eichenbaum H. Interplay of hippocampus and prefrontal cortex in memory. Curr Biol. 2013; 23(17): R764–R773, doi: 10.1016/j.cub.2013.05.041, indexed in Pubmed: 24028960.

81. Rajmohan V, Mohandas E. The limbic system. Indian J Psychiatry. 2007; 49(2): 132–139, doi: 10.4103/0019-5545.33264, indexed in Pubmed: 20711399.

82. Roa J, Tena-Sempere M. Connecting metabolism and reproduction: roles of central energy sensors and key molecular mediators. Mol Cell Endocrinol. 2014; 397(1-2): 4–14, doi: 10.1016/j.mce.2014.09.027, indexed in Pubmed: 25289807.

83. Roseweir AK, Kauffman AS, Smith JT, et al. Discovery of potent kisspeptin antagonists delineate physiological mechanisms of gonadotropin regulation. J Neurosci. 2009; 29(12): 3920–3929, doi: 10.1523/JNEUROSCI.5740-08.2009, indexed in Pubmed: 19321788.

84. Rumpler É. Identification of species-specific and general features in the anatomy of the kisspeptin neuron system. PhD Thesis Semmelweis University, Budapest 2021.

85. Saedi S, Khoradmehr A, Mohammad Reza JS, et al. The role of neuropeptides and neurotransmitters on kisspeptin/kiss1r-signaling in female reproduction. J Chem Neuroanat. 2018; 92: 71–82, doi: 10.1016/j.jchemneu.2018.07.001, indexed in Pubmed: 30008384.

86. Sanchez-Garrido MA, Tena-Sempere M. Metabolic control of puberty: roles of leptin and kisspeptins. Horm Behav. 2013; 64(2): 187–194, doi: 10.1016/j.yhbeh.2013.01.014, indexed in Pubmed: 23998663.

87. Sarkar S, Raymick J, Imam S. Neuroprotective and therapeutic strategies against parkinson's disease: recent perspectives. Int J Mol Sci. 2016; 17(6), doi: 10.3390/ijms17060904, indexed in Pubmed: 27338353.

88. Scott CJ, Rose JL, Gunn AJ, et al. Kisspeptin and the regulation of the reproductive axis in domestic animals. J Endocrinol. 2018 [Epub ahead of print], doi: 10.1530/JOE-18-0485, indexed in Pubmed: 30400056.

89. Seminara SB, Messager S, Chatzidaki EE, et al. The GPR54 gene as a regulator of puberty. N Engl J Med. 2003; 349(17): 1614–1627, doi: 10.1056/NEJMoa035322, indexed in Pubmed: 14573733.

90. Skorupskaite K, George JT, Anderson RA. The kisspeptin-GnRH pathway in human reproductive health and disease. Hum Reprod Update. 2014; 20(4): 485–500, doi: 10.1093/humupd/dmu009, indexed in Pubmed: 24615662.

91. Smith JT, Shahab M, Pereira A, et al. Hypothalamic expression of KISS1 and gonadotropin inhibitory hormone genes during the menstrual cycle of a non-human primate. Biol Reprod. 2010; 83(4): 568–577, doi: 10.1095/biolreprod.110.085407, indexed in Pubmed: 20574054.

92. Smith JT, Cunningham MJ, Rissman EF, et al. Regulation of Kiss1 gene expression in the brain of the female mouse. Endocrinology. 2005; 146(9): 3686–3692, doi: 10.1210/en.2005-0488, indexed in Pubmed: 15919741.

93. Smith JT, Dungan HM, Stoll EA, et al. Differential regulation of KiSS-1 mRNA expression by sex steroids in the brain of the male mouse. Endocrinology. 2005; 146(7): 2976–2984, doi: 10.1210/en.2005-0323, indexed in Pubmed: 15831567.

94. Stengel A, Wang L, Goebel-Stengel M, et al. Centrally injected kisspeptin reduces food intake by increasing meal intervals in mice. Neuroreport. 2011; 22(5): 253–257, doi: 10.1097/WNR.0b013e32834558df, indexed in Pubmed: 21386700.

95. Stephens SBZ, Chahal N, Munaganuru N, et al. Estrogen stimulation of Kiss1 expression in the medial amygdala involves estrogen receptor-α but not estrogen receptor-β. Endocrinology. 2016; 157(10): 4021–4031, doi: 10.1210/en.2016-1431, indexed in Pubmed: 27564649.

96. Stephens S, Kauffman A. Regulation and possible functions of kisspeptin in the medial amygdala. Front Endocrinol. 2017; 8, doi: 10.3389/fendo.2017.00191.

97. Takamura R, Mizuta K, Sekine Y, et al. Modality-Specific impairment of hippocampal CA1 neurons of alzheimer's disease model mice. J Neurosci. 2021; 41(24): 5315–5329, doi: 10.1523/JNEUROSCI.0208-21.2021, indexed in Pubmed: 33980545.

98. Tanaka M, Csabafi K, Telegdy G. Neurotransmissions of antidepressant-like effects of kisspeptin-13. Regul Pept. 2013; 180: 1–4, doi: 10.1016/j.regpep.2012.08.017, indexed in Pubmed: 22999921.

99. Telegdy G, Adamik Á. The action of kisspeptin-13 on passive avoidance learning in mice. Involvement of transmitters. Behav Brain Res. 2013; 243: 300–305, doi: 10.1016/j.bbr.2013.01.016, indexed in Pubmed: 23348107.

100. Teles MG, Bianco SDC, Brito VN, et al. A GPR54-activating mutation in a patient with central precocious puberty. N Engl J Med. 2008; 358(7): 709–715, doi: 10.1056/NEJMoa073443, indexed in Pubmed: 18272894.

101. Tomikawa J, Homma T, Tajima S, et al. Molecular characterization and estrogen regulation of hypothalamic KISS1 gene in the pig. Biol Reprod. 2010; 82(2): 313–319, doi: 10.1095/biolreprod.109.079863, indexed in Pubmed: 19828777.

102. Trujillo MV, Kalil B, Ramaswamy S, et al. Estradiol upregulates kisspeptin expression in the preoptic area of both the male and female rhesus monkey (Macaca mulatta): implications for the hypothalamic control of ovulation in highly evolved primates. Neuroendocrinology. 2016; 105(1): 77–89, doi: 10.1159/000448520.

103. Tsatsanis C, Dermitzaki E, Avgoustinaki P, et al. The impact of adipose tissue-derived factors on the hypothalamic-pituitary-gonadal (HPG) axis. Hormones (Athens). 2015; 14(4): 549–562, doi: 10.14310/horm.2002.1649, indexed in Pubmed: 26859602.

104. Tsigos C, Chrousos GP. Hypothalamic-pituitary-adrenal axis, neuroendocrine factors and stress. J Psychosom Res. 2002; 53(4): 865–871, doi: 10.1016/s0022-3999(02)00429-4, indexed in Pubmed: 12377295.

105. Wahab F, Atika B, Shahab M, et al. Kisspeptin signalling in the physiology and pathophysiology of the urogenital system. Nat Rev Urol. 2016; 13(1): 21–32, doi: 10.1038/nrurol.2015.277, indexed in Pubmed: 26620614.

106. Watanabe Y, Uenoyama Y, Suzuki J, et al. Oestrogen-induced activation of preoptic kisspeptin neurones may be involved in the luteinising hormone surge in male and female Japanese monkeys. J Neuroendocrinol. 2014; 26(12): 909–917, doi: 10.1111/jne.12227, indexed in Pubmed: 25283748.

107. Yan HC, Cao X, Das M, et al. Behavioral animal models of depression. Neurosci Bull. 2010; 26(4): 327–337, doi: 10.1007/s12264-010-0323-7, indexed in Pubmed: 20651815.

108. Yang L, Demetriou L, Wall M, et al. OR06-2 kisspeptin enhances brain processing of olfactory and visual cues of attraction in men. J Endocr Soc. 2019; 3(Suppl_1), doi: 10.1210/js.2019-or06-2.

109. Yeo SH, Kyle V, Morris PG, et al. Visualisation of Kiss1 Neurone Distribution Using a Kiss1-CRE Transgenic Mouse. J Neuroendocrinol. 2016; 28(11), doi: 10.1111/jne.12435, indexed in Pubmed: 27663274.

110. Zhang Y, Proenca R, Maffei M, et al. Positional cloning of the mouse obese gene and its human homologue. Nature. 1994; 372(6505): 425–432, doi: 10.1038/372425a0, indexed in Pubmed: 7984236.

R E V I E W   A R T I C L E

Neuroglia — development and role in physiological and pathophysiological processes

M. Cichorek[1]*●, P. Kowiański[2]*●, G. Lietzau[2]●, J. Lasek[1]●, J. Moryś[3]●

[1]Department of Anatomy and Physiology, Pomeranian University of Słupsk, Poland
[2]Department of Anatomy and Neurobiology, Faculty of Medicine, Medical University of Gdansk, Poland
[3]Department of Normal Anatomy, Pomeranian Medical University, Szczecin, Poland

The dynamic development of studies on neuroglia in recent years indicates its previously underestimated role in maintaining proper brain function, both in physiological and pathological conditions. The use of modern research methods such as single-cell techniques as well as in vivo and in vitro models enriched the state of our knowledge. The most important issues regarding the maturation and development of neuroglia include cooperation between glial cell groups and with neurons in neurogenesis, neuroregeneration, (re)myelination and how the early developmental roles of glia contribute to nervous system dysfunction in neurodevelopmental and neurodegenerative disorders.

There is still growing evidence emphasizing the importance of astroglia in maintaining the brain physiological homeostasis, regulation of immune response, cerebral blood flow, and involvement in the reactive neurogliosis, precisely adapted to the nature of pathological stimulus and the depth of tissue damage. The important issues related to the function of oligodendrocytes include explanation of the mechanisms of interaction between the glial cells and myelinated axons, important not only in myelination, but also in development of cognitive processes and memory. Further studies are required for understanding the mechanisms of demyelination occurring in several central nervous system (CNS) diseases. An interesting area of research is related with explanation of the NG2 glia function, characterised by significant proliferative potential and ability to differentiate in both in physiological conditions and in pathology, as well as the presence of synaptic neural-glial connections, which are especially numerous during development. The increasing knowledge of microglia comprises the presence of specialised subsets of microglia, their role the myelination process and neurovascular unit functioning. We are only beginning to understand how microglia enter the brain and develop distinct functional states during ontogeny.

This review summarises the current state of knowledge on the development and role in the CNS of different, heterogeneous cell populations defined by a common term neuroglia. (Folia Morphol 2021; 80, 4: 766–775)

Key words: astrocytes, microglia, NG2 cells, neurovascular unit, oligodendrocytes

Address for correspondence: Dr. M. Cichorek, Medical University of Gdansk, Faculty of Medicine, Department of Embryology, ul. Dębinki 1, 80–211 Gdańsk, Poland, tel: +48 58 349 1496, e-mail: miroslawa.cichorek@gumed.edu.pl; Prof. P. Kowiański, Medical University of Gdansk, Faculty of Medicine, Department of Anatomy and Neurobiology, ul. Dębinki 1, 80–211 Gdańsk, Poland, tel: +48 58 349 1819, e-mail: przemyslaw.kowianski@gumed.edu.pl

*These authors contributed equally to this work.

INTRODUCTION

The increasing evidence suggests previously overlooked, important role of neuroglia in the brain physiological and pathological processes [92, 94]. This justifies the need to abandon the "neurocentric" perspective in understanding the nervous tissue functioning. In physiological conditions, the neuroglia participates in developmental processes including neuro-, glio- and synaptogenesis, in control of metabolic processes, immune response and myelination of nerve fibres [14]. It is also involved in the brain functional integration, through the modulation of neuroplasticity and shaping cognitive and memory processes. Other important issues comprise gliotransmission and regulation of the cerebral blood flow. Following, a synthetic summary of the most important information regarding neuroglial development, morphology and function is presented. The neurglial cells consist of three main types, astrocytes, oligodendrocytes and microglia.

GLIAL CELLS ORIGIN

Based on the developmental origin, two groups of central nervous system (CNS) glial cells can be distinguished: macroglia and microglia. Macroglia (i.e. astrocytes, oligodendrocytes), like neurons, originate from the epithelium of the neural tube (neuroectoderm). Microglia, in contrast, derive from mesoderm of the yolk sac wall [52, 60].

Macroglia

During the fourth week, embryonic disc follows morphological changes, as the result of ongoing differentiation of the germ layer cells. At that time, the neurulation takes place and, in a result, the neural tube (primordium for CNS) forms on the basis of neuroectodermal cells. After closing the anterior and posterior neuropores, the neural tube cells proliferate and follow differentiation into neurons and macroglial cells. The neural tube wall is formed by a pseudostratified epithelium with high rate of proliferation from the inner cavity side (future ventricles and central canal). Cytodifferentiation of the neural tube wall cells leads to an emergence of neurons and macroglia. Early glial cells called radial glial cells (glial progenitor cells) build pathways for neurons migration and are precursors for astrocytes and oligodendrocytes [19, 52, 77]. It is also a time of neuronal functional differentiation into motoneurons and interneurons, and glia provide metabolic and structural support to these neurons [19, 77]. Neuronal number during embryogenesis is modulated by a programmed cell death that is crucial for proper CNS development. Neuronal death is a result of a balance between the prosurvival and death-inducing factors, and glial cells are active players in this process [52]. Since other types of glia, such as astrocytes and oligodendrocytes, are generated during late embryogenesis after neuroblasts have produced most neurons, microglia constitute the main population of glial cells during early embryogenesis [52].

Microglia

Early entry and the brain colonization enables microglia to perform critical roles in regulating important events of early brain development, e.g. neurons' survival, phagocytosis of dying neurons, synaptogenesis, angiogenesis, axons development [78]. Microglia originate from the embryonic erythromyeloid progenitors of the yolk sac, and not from the haematopoietic stem cells [54]. These cells of the macrophage nature arise early in embryogenesis (during the fourth week) and invade the developing neural tube, where they differentiate as the result of factors action provided by their neural niche [64]. Yolk sac is the embryonic membrane where the vasculogenesis process takes place. As the result of this process first embryonic vessels and blood cells are being formed [19, 77]. Thus, from fourth to eighth week yolk sac is the place of the embryonic haematopoiesis. Primitive macrophages reach the blood vessels and also the neural tube [8, 84]. Microglia constitute the first and main population of glial cells during early embryogenesis, thus, their differentiation is strongly linked to the neural tissue maturation. Once invading the forming central nervous system, in this early embryogenesis, the microglial cells expand via proliferation without input of foetal monocytes or bone marrow-derived progenitors during later developmental stages [54, 95]. Thus, microglia self-renew via proliferation and are not replaced by bone marrow-derived cells in the healthy brain. Only in the case of injury, inflammation, disease or blood brain barrier break down, these cells are supported by infiltrating bone-marrow-derived monocytes [54, 95]. Therefore, microglia show a high ability to proliferation during prenatal and postnatal stages to expand and distribute in the developing CNS, but in adult stage there is a decline in proliferation [62, 86].

In addition to microglia located inside the nervous tissue (parenchyma), there are CNS-associated mac-

rophages located in meninges, perivascular area, and choroid plexus that also originate from the yolk sac progenitors [32]. Yolk-sac primary macrophages are heterogeneous even before brain colonisation. However, role of these other macrophages remains largely unknown [89]. Only choroid plexus macrophages are replaced over time by the circulating monocytes [32].

GLIAL CELLS CHARACTERISTIC

Astrocytes

Apart from the star-shaped cellular body, reflected in the name of this class of neuroglia, characteristic features of the astrocytes include presence of the intermediate filaments (e.g. glial fibrillary acidic protein and vimentin) building their cytoskeleton, perivascular projections and gap junctions, and presence of glutamate and GABA transporters [46–48]. Among their characteristic features are also specific properties of energy metabolism and lack of electrical excitability [43, 49]. Apart from the protoplasmic and fibrous astrocytes, there are several other types distinguished, defined by different structure and immunocytochemical characteristics [63]. The differences in the morphology and biochemical features reflect considerable variability in astrocytic function, which is still only partially disclosed.

In physiological conditions, astrocytes have several functions mainly related with maintaining the physiological homeostasis [44, 79, 80]. Among them, the most important are: regulation of metabolic processes in the brain tissue (e.g. regulation of glucose metabolism, ion concentration, water content, and pH), structural support (creating functional barriers, territorial domains and syncytial structures), brain development (proliferation, gliogenesis, neuroplasticity), intercellular communication (gliotransmission, regulation of synaptic transmission and plasticity), neuroprotection and brain defence (regulation of cerebral blood flow, protection against glutamatergic excitotoxicity, and inflammatory response).

One of the most important features of astrocytes, which determines their function in pathological conditions, is greater than in the case of other neuroglial subpopulations resistance to decrease in oxygen and glucose concentrations [98]. This enables preserving anaerobic glycolysis and ATP production in the area of brain damage and, consequently, supporting the neuronal metabolic functions [59]. Due to the abovementioned features, astrocytes are involved in processes initiated in the brain tissue by pathological stimuli and

defined as the reactive neurogliosis [80]. This neuroglial response comprises the morphological changes, changes in gene expression, activation of signalling pathways, activation of the inflammatory reactions, and interactions among the various neuroglial populations initiated by the damaging factor [2, 26, 80]. However, on the contrary to the previously accepted views, it is not regarded as a stereotypical reaction independent of the nature of the pathological stimulus [2, 13, 79]. The astrocytic response is multipotent and context-dependent, optimally adapted to the type of injury, its intensity and the time passed since its initiation [2, 55, 79]. The processes involved in the reactive neurogliosis are both of destructive and protective character [45, 55]. Each of them reaches its maximal intensity at the specific time-point determining the further fate of the damaged tissue, as well as potential therapeutic measures. The destructive effects of astrogliosis include an exacerbation of the inflammatory response resulting from pro-inflammatory cytokine production, release of reactive oxygen species and excitotoxic glutamate, and impairment of the blood-brain barrier (BBB) function [79, 81]. The protective effects include an excitotoxic glutamate uptake, protection against the oxidative stress by free radical scavenging, the BBB repair and reduction of the vasogenic oedema, and neurotrophin release [25, 27, 79]. Another characteristic feature of the reactive neurogliosis is presence of phenotypical characteristics not observed in the resting conditions and an expression of several antigens typical for the earlier stages of the cellular lineage development [10–12]. All these processes enable restoration of the functions impaired by the pathological stimuli and demarcation of the destructive effects of damage, meanwhile protecting the intact brain tissue areas. The fact that astrocytes communicate with neurons and the vascular system after injury makes them potentially useful in future regenerative therapeutic strategies.

Oligodendrocytes

The morphological classification of oligodendrocytes is based on a diversity of their body shapes, number of processes, and size of myelinated axons [17, 66]. According to these criteria, four morphological types of oligodendrocytes are distinguished. Additionally, the non-myelinating oligodendrocytes, such as perineuronal satellite oligodendrocytes and, according to some researchers, NG2 glial cells can be identified [16, 67]. The most important function

of oligodendrocytes is production of myelin sheath. The number of the neuronal extensions myelinated by a single oligodendrocyte unit may reach up to 30 axons [70]. However, this number shows great variability. The close relationship between the oligodendrocyte and the myelinated fragments of the axons enables an interaction that occurs through the ligand- and voltage-gaited ion channels and receptors, which is important for communication between oligodendrocytes and neurons [15, 18, 72]. This direct structural relationship affects, on the one hand, the course of the myelination process and, on the other hand, the conduction of the action potential along the axon. The mutual contact between the oligodendrocyte and neuronal axon determines the maintenance of the physiological efficiency of oligodendrocytes, protecting them against damage resulting from the excessive concentration of neurotransmitters or the excessive activity of ion channels [15, 18]. It has been reported that effectiveness of this communication is the highest in the oligodendrocyte progenitor cells (OPC) and gradually decreases during the ontogenic development [29].

In pathological conditions, oligodendrocyte functional impairment is manifested by a demyelination. It might be a result of improper immunological response induced by external and internal stimuli occurring in the course of demyelinating diseases (e.g. multiple sclerosis) [76]. The myelin damage has also been demonstrated during aging and in some neuropsychological illnesses, such as schizophrenia or bipolar disorder, as well as in the course of Alzheimer's disease and cognitive disorders [7, 30, 51].

Microglia

In the prenatal and early postnatal phase, microglia actively participate in brain development by stimulating neurogenesis and gliogenesis (e.g. oligodendrocytes), and the brain vasculature. Microglia regulate the neural circuit wiring, apoptosis and survival of neurons, synapse formation and functioning, and myelination [52, 78]. Thus, microglia are considered either a causal or a contributing factor to almost all brain disorders, from neurodevelopmental disorders to neurodegeneration. In humans and mice, microglia represent around 10% of the adult CNS cells, with variable cell density across distinct CNS regions [53, 69]. We are only starting to understand how microglia enter the brain and develop distinct functional states during ontogeny.

Under homeostatic conditions microglia are long-lived, self-renewing cells that constantly control the CNS environment [54, 95]. Little is known about microglia specific role in the brain during normal growth and development. Microglia activation is a common feature in neurological disorders based on inflammation, demyelination or neuronal structure degeneration, and also in glioma development [54, 60, 95]. Microglia are the glial cells that form the first line of immune defence in the brain and spinal cord. Tissue damage induces activation of microglia cells which secrete a broad range of cytokines with either pro- or anti-inflammatory properties [52, 95]. Activated microglia can influence other glial cells and increase the BBB permeability [52, 95]. Thus, activated microglia enhance their phagocytic functions in order to clear the damaged tissue from remnants of myelin, cellular debris, apoptotic bodies, and pathogens [52, 78].

Microglia have been distinguished based on their morphology and surface molecules presence, which proves that they are a heterogeneous cell population within the CNS [35]. Additionally, one can observe a variety of biologically important functions of these cells, supported by the presence of specialised subsets of microglia. It has been postulated that there are three microglial developmental stages: early microglia (high rate of proliferation and differentiation), pre-microglia linked to neuronal development, and adult microglia [4]. Animal studies using mice model of brain development have shown that early during postnatal development a CD11c^{+} microglia are involved in the myelination process [82, 96], and that this cell population is of special importance in progress of different CNS diseases and during aging [4].

There have been trials to define a precise molecular signature of microglial cells [52, 78]. Microglia have a unique gene signature determined by the microglia-specific genes, such as Tmem119, P2ry12, Sall1, and Olfml3 [5]. Microglia also express many genes shared by macrophages, including CD11b, CD45, and CX3CR1 [4, 5]. Results of animal studies have indicated that microglia subtypes emerge in brain regions or disease development [61]. Interestingly, there has been observed a regional heterogeneity of microglia in the human brain [9]. Each brain region represents a distinct niche (i.e. has its own neuronal populations, glial cells content, extracellular matrix components). During brain angiogenesis, microglia secret factors that influence vascular growth [57].

Two signalling pathways are crucial for microglial development: one involves colony stimulating factor 1 receptor (CSF1R) and the second one — transforming growth factor beta (TGF-beta). Studies have shown that deletion or inhibition of the CSF1R during mice development results in loss of microglia [36, 86]. CSF1R has two ligands, interleukin 34 (IL-34) and CSF1. Both are expressed in the CNS, but each of them has a different source established postnatally, e.g. grey matter microglia depend on neuronal IL-34 production, while white matter microglia depend on CSF1 secreted by astrocytes after birth [36, 86]. Loss of TGF-beta signalling in adult microglia results in their hyperactivation after birth and impairment of microglial expansion throughout the developing CNS [36, 86]. Thus, microglial cells need neurons to survive and differentiate. Neurons secret the cytokines IL-34 and CSF1 that influence the CSF1R pathway, as well as ligands for TGF-beta signalling [42].

Another major factor influencing microglial biology is the gut microbiome. Results of studies in the germ-free mice have shown maturation disturbances of adult microglia [86]. Signals from the microbiome affect microglia mainly during postnatal development, whereas embryonic microglia are less sensitive to the microbiota [36, 86].

Like other tissue-resident macrophages, microglia phagocytize cell debris, respond to inflammatory factors, and patrol the local microenvironment. Microglia influence the nervous tissue through a different cellular functions controlled by intrinsic and extrinsic factors. During development, microglia participate in synaptogenesis, modulate axonal growth, secrete factors that support the postnatal survival of the cortical neurons, e.g. insulin-like growth factor 1 (IGF-1). Microglia also are involved in the physiological functions in the adult CNS, as they constantly control their environment.

Animal studies have shown that amoeboid microglia in white matter are essential for proper oligodendrocyte homeostasis and myelinogenesis [82, 96]. Wlodarczyk et al. [96] discovered a new role for of CD11c^{+} microglia in promoting the CNS myelination. The molecule CD11c is a classic dendritic cell surface marker and only very few microglial cells in the normal adult brain express a detectable level of this protein. This subset of microglia also express sevenfold more mRNA for IGF-1 than their CD11c counterparts, and it has significantly higher levels compared with neurons, astrocytes, and oligodendrocyte precursor cells [96].

This population of microglia predominates in the primary areas of the brain myelination and its selective depletion provides to myelin formation disturbances [96]. It has also been suggested that early after birth the white matter microglial cells differ from the grey matter microglial cells [82].

NG2 cells

NG2 glial cells are classified as a distinct fourth population of neuroglia, accounting for approximately 5% of neuroglial population and identified by the co-expression of chondroitin sulphate proteoglycan NG2 and platelet-derived growth factor receptor alfa [67, 71]. Most of them are thought to represent oligodendrocyte lineage [73, 99]. Some authors consider them to be the OPC, sometimes even using the terms OPC and NG2 glia interchangeably. In the adult brain they remain as the NG2 glial cells or differentiate into oligodendrocytes, although this feature varies among the brain areas [67, 71].

The most important features of NG2 glia are the significant proliferative capacity and differentiation potential still present in the adult brain [23, 24, 91]. In physiological conditions, they allow to maintain a stable number of NG2 cells and oligodendrocytes [67, 71]. Other functions of NG2 cells in physiological conditions include: regulation of the cell migration, re-myelination and efficiency of synaptic conduction, and keeping the energetic metabolism at the adequate level [28, 40, 74]. The NG2 glia form synapses receiving the GABA-ergic and glutamatergic neuronal inputs [22]. The role of the neuro-glial synapses is most probably related to increase of proliferation and oligodendrocyte differentiation [22]. Another characteristic feature of the NG2 neuroglia is an occurrence of spontaneous and evoked synaptic currents, although their function is unknown [6].

The most important features of NG2 glia in pathological conditions are: the significant proliferative potential and differentiation ability preserved in adulthood, which enable their contribution to the re-population of different neuroglial classes reduced due to destructive processes in the CNS [38, 90]. This role has been demonstrated in many experimental models of brain lesion, both *in vitro* and *in vivo* [24, 33, 65, 90, 97]. The ability of NG2 cells to differentiate into astrocytes and oligodendrocytes [37, 91], as well as their contribution to increasing NG2 glia population have been proved by several authors [67, 71]. However, the NG2 cells ability to differentiate

into neurons, suggested by some authors, has not been commonly accepted [87, 88]. Reassuming, the morphological features of the NG2 glia response and its proliferation potential depend on the type of pathological stimulus and degree of tissue damage [90]. The function of NG2 glia in pathological conditions is only partially understood and requires further intensive research. The proliferative and differentiative potential of NG2 glia could be attractive for development of regenerative medicine therapeutic strategies.

NEUROVASCULAR UNIT

Regulation of physiological processes in the CNS requires involvement of all structural components of the nervous tissue. This is particularly evident in the case of the regulation of cerebral blood flow, characterised by enormous dynamics and requiring adaptation of changes to the current biochemical conditions in the brain, as well as to the physiological parameters, determining the state of the circulatory system [100].

The concept of the neurovascular unit (NVU) has proven useful in studies on the structure and function of the brain tissue in physiological and pathological conditions [31, 41, 75]. This theoretical model comprehensively describes morphological and functional relationships occurring among three main components of brain tissue: neurons, neuroglia and cerebral vessels. Apart from neurons, the NVU consists of the vascular endothelial cells, smooth muscle cells of the vascular wall, pericytes, astrocytes and perivascular macrophages [1, 20, 57]. The unquestionable value of the NVU model in explaining the essence of many physiological and pathological processes, as well as its usefulness in elucidating the complex regulatory mechanisms occurring between its components, results from the interaction of several structures. Among them one could encounter: tripartite synapses (ensuring the possibility of the synaptic activity modulation by the astrocyte) [3, 34], astrocytic perivascular end-feet (enabling direct action of the astrocyte on the vascular wall) [85], and vascular tight junctions (being an essential component of the BBB) [1]. Astrocytes control the maintenance of these tight-junctions by secreting factors, e.g. sonic hedgehog protein (Shh), beta-catenin. However, the activated astrocytes can disrupt the local BBB allowing an entry of the peripheral immune cells. The efficient functioning of the NVU is also a result of action the

signalling systems based on gliotransmission [93] and Ca^{2+} oscillations [50, 68, 101]. The NVU is characterised by involvement of its elements in numerous biochemical processes, heterogeneous resistance of its constituents to metabolic disorders occurring in the course of CNS diseases, differentiated participation in the immune response induced by pathological stimuli and, finally, by different proliferative and regenerative potential of the cellular lineages [31, 41]. The NVU concept has proven to be very useful in research on several issues, such as regulation of the cerebral blood flow, status of the BBB, dysfunctions of the neurotransmitter systems and signalling pathways. It has also proven its value in the studies on coexistence of different pathological processes, as well as diseases at different stages in patients of various age, such as atherosclerosis, hyperlipidaemia, Alzheimer's, cardiovascular and inflammatory diseases [21, 41, 50, 75]. Steliga et al. [83] have also suggested that the NVU could be a source of biomarkers useful for cerebral stroke diagnostics.

The crosstalk between microglia and astrocytes in the BBB is crucial during inflammatory processes in the CNS. Microglia and astrocytes are activated into the pro-inflammatory phenotype and the anti-inflammatory phenotype [56, 58]. Activated into the M1 phenotype microglia produce pro-inflammatory factors, such as IL-1 and TNF-alfa that activate astrocytes. Subsequently, microglia change morphology, i.e. take an amoeboid shape and increase ability to phagocytosis [58]. As a macrophages, microglial cells function also in M2 phenotype secreting anti-inflammatory factors, such as IL-10, TGF-beta. In general, the M1-like phenotype is considered to be associated with tissue destruction (including NVU), while the M2-like phenotype is involved in repair and regeneration [57, 58]. Experimental trials have been taken to inhibit the activity of the proinflammatory phenotype of microglia and augment the activity of the anti-inflammatory phenotype of microglia, e.g. in stroke [39].

CONCLUSIONS

The last decade of research has shed a new light on glial identity and activities. It is now a well-established fact that glial cells are a very heterogeneous group of the CNS cells interacting with each other and having multiple interactions with other CNS elements to control their development and functioning. Glial cells isolated from different brain regions show age-

and region-dependent differences in transcriptomic profiles. It has been suggested the appearance of homeostatic and reactive glial subtypes could be of great importance for understanding many CNS pathologies. Thus, the molecular characteristic of a particular glial subtype in its anatomical environment is a key to understand glial cells role in both homeostatic and pathological conditions.

Funding

Conflict of interest: None declared

REFERENCES

1. Abbott NJ, Patabendige AAK, Dolman DEM, et al. Structure and function of the blood-brain barrier. Neurobiol Dis. 2010; 37(1): 13–25, doi: 10.1016/j.nbd.2009.07.030, indexed in Pubmed: 19664713.

2. Anderson MA, Ao Y, Sofroniew MV. Heterogeneity of reactive astrocytes. Neurosci Lett. 2014; 565: 23–29, doi: 10.1016/j.neulet.2013.12.030, indexed in Pubmed: 24361547.

3. Araque A, Parpura V, Sanzgiri RP, et al. Tripartite synapses: glia, the unacknowledged partner. Trends Neurosci. 1999; 22(5): 208–215, doi: 10.1016/s0166-2236(98)01349-6, indexed in Pubmed: 10322493.

4. Benmamar-Badel A, Owens T, Wlodarczyk A. Protective microglial subset in development, aging, and disease: lessons from transcriptomic studies. Front Immunol. 2020; 11: 430, doi: 10.3389/fimmu.2020.00430, indexed in Pubmed: 32318054.

5. Bennett ML, Bennett FC, Liddelow SA, et al. New tools for studying microglia in the mouse and human CNS. Proc Natl Acad Sci U S A. 2016; 113(12): E1738–E1746, doi: 10.1073/pnas.1525528113, indexed in Pubmed: 26884166.

6. Bergles DE, Jabs R, Steinhäuser C. Neuron-glia synapses in the brain. Brain Res Rev. 2010; 63(1-2): 130–137, doi: 10.1016/j.brainresrev.2009.12.003, indexed in Pubmed: 20018210.

7. Bernstein HG, Keilhoff G, Dobrowolny H, et al. Perineuronal oligodendrocytes in health and disease: the journey so far. Rev Neurosci. 2019; 31(1): 89–99, doi: 10.1515/revneuro-2019-0020, indexed in Pubmed: 31323013.

8. Bian Z, Gong Y, Huang T, et al. Deciphering human macrophage development at single-cell resolution. Nature. 2020; 582(7813): 571–576, doi: 10.1038/s41586-020-2316-7, indexed in Pubmed: 32499656.

9. Böttcher C, Schlickeiser S, Sneeboer MAM, et al. Human microglia regional heterogeneity and phenotypes determined by multiplexed single-cell mass cytometry. Nat Neurosci. 2019; 22(1): 78–90, doi: 10.1038/s41593-018-0290-2, indexed in Pubmed: 30559476.

10. Bramanti V, Tomassoni D, Avitabile M, et al. Biomarkers of glial cell proliferation and differentiation in culture. Front Biosci (Schol Ed). 2010; 2: 558–570, doi: 10.2741/s85, indexed in Pubmed: 20036968.

11. Buffo A, Rite I, Tripathi P, et al. Origin and progeny of reactive gliosis: A source of multipotent cells in the injured brain. Proc Natl Acad Sci USA. 2008; 105(9): 3581–3586, doi: 10.1073/pnas.0709002105, indexed in Pubmed: 18299565.

12. Buffo A, Rolando C, Ceruti S. Astrocytes in the damaged brain: molecular and cellular insights into their reactive response and healing potential. Biochem Pharmacol. 2010; 79(2): 77–89, doi: 10.1016/j.bcp.2009.09.014, indexed in Pubmed: 19765548.

13. Burda JE, Sofroniew MV. Reactive gliosis and the multicellular response to CNS damage and disease. Neuron. 2014; 81(2): 229–248, doi: 10.1016/j.neuron.2013.12.034, indexed in Pubmed: 24462092.

14. Butt A, Verkhratsky A. Neuroglia: Realising their true potential. Brain Neurosci Adv. 2018; 2: 2398212818817495, doi: 10.1177/2398212818817495, indexed in Pubmed: 32166166.

15. Butt AM, Fern RF, Matute C. Neurotransmitter signaling in white matter. Glia. 2014; 62(11): 1762–1779, doi: 10.1002/glia.22674, indexed in Pubmed: 24753049.

16. Butt AM, Hamilton N, Hubbard P, et al. Synantocytes: the fifth element. J Anat. 2005; 207(6): 695–706, doi: 10.1111/j.1469-7580.2005.00458.x, indexed in Pubmed: 16367797.

17. Butt AM, Ibrahim M, Berry M. Axon-myelin sheath relations of oligodendrocyte unit phenotypes in the adult rat anterior medullary velum. J Neurocytol. 1998; 27(4): 259–269, indexed in Pubmed: 10640184.

18. Butt AM, Kalsi A. Inwardly rectifying potassium channels (Kir) in central nervous system glia: a special role for Kir4.1 in glial functions. J Cell Mol Med. 2006; 10(1): 33–44, doi: 10.1111/j.1582-4934.2006.tb00289.x, indexed in Pubmed: 16563220.

19. Carlson BM. Nervous system. In human embriology and develomental biology. 6th ed. Elsevier, Philadelphia 2019: 216–235.

20. Carmignoto G, Gómez-Gonzalo M. The contribution of astrocyte signalling to neurovascular coupling. Brain Res Rev. 2010; 63(1-2): 138–148, doi: 10.1016/j.brainresrev.2009.11.007, indexed in Pubmed: 19948187.

21. Czuba E, Steliga A, Lietzau G, et al. Cholesterol as a modifying agent of the neurovascular unit structure and function under physiological and pathological conditions. Metab Brain Dis. 2017; 32(4): 935–948, doi: 10.1007/s11011-017-0015-3, indexed in Pubmed: 28432486.

22. De Biase LM, Nishiyama A, Bergles DE. Excitability and synaptic communication within the oligodendrocyte lineage. J Neurosci. 2010; 30(10): 3600–3611, doi: 10.1523/JNEUROSCI.6000-09.2010, indexed in Pubmed: 20219994.

23. Dimou L, Gallo V. NG2-glia and their functions in the central nervous system. Glia. 2015; 63(8): 1429–1451, doi: 10.1002/glia.22859, indexed in Pubmed: 26010717.

24. Dimou L, Simon C, Kirchhoff F, et al. Progeny of Olig2-expressing progenitors in the gray and white matter of the adult mouse cerebral cortex. J Neurosci. 2008; 28(41): 10434–10442, doi: 10.1523/JNEUROSCI.2831-08.2008, indexed in Pubmed: 18842903.

25. Dringen R, Brandmann M, Hohnholt MC, et al. Glutathione-dependent detoxification processes in as-

trocytes. Neurochem Res. 2015; 40(12): 2570–2582, doi: 10.1007/s11064-014-1481-1, indexed in Pubmed: 25428182.

26. Escartin C, Galea E, Lakatos A, et al. Reactive astrocyte nomenclature, definitions, and future directions. Nat Neurosci. 2021; 24(3): 312–325, doi: 10.1038/s41593-020-00783-4, indexed in Pubmed: 33589835.

27. Frade J, Pope S, Schmidt M, et al. Glutamate induces release of glutathione from cultured rat astrocytes--a possible neuroprotective mechanism? J Neurochem. 2008; 105(4): 1144–1152, doi: 10.1111/j.1471-4159.2008.05216.x, indexed in Pubmed: 18182055.

28. Franklin R, Gilson J, Blakemore W. Local recruitment of remyelinating cells in the repair of demyelination in the central nervous system. J Neurosci Res. 1997; 50(2): 337–344, doi: 10.1002/(sici)1097-4547(19971015)50:2<337::aid-jnr21>3.0.co;2-3, indexed in Pubmed: 9373042.

29. Fröhlich N, Nagy B, Hovhannisyan A, et al. Fate of neuron-glia synapses during proliferation and differentiation of NG2 cells. J Anat. 2011; 219(1): 18–32, doi: 10.1111/j.1469-7580.2011.01392.x, indexed in Pubmed: 21592101.

30. Giotakos O. Is psychosis a dysmyelination-related information-processing disorder? Psychiatriki. 2019; 30(3): 245–255, doi: 10.22365/jpsych.2019.303.245, indexed in Pubmed: 31685456.

31. Girouard H, Iadecola C. Neurovascular coupling in the normal brain and in hypertension, stroke, and Alzheimer disease. J Appl Physiol (1985). 2006; 100(1): 328–335, doi: 10.1152/japplphysiol.00966.2005, indexed in Pubmed: 16357086.

32. Goldmann T, Wieghofer P, Jordão MJ, et al. Origin, fate and dynamics of macrophages at central nervous system interfaces. Nat Immunol. 2016; 17(7): 797–805, doi: 10.1038/ni.3423, indexed in Pubmed: 27135602.

33. Hackett AR, Yahn SL, Lyapichev K, et al. Injury type-dependent differentiation of NG2 glia into heterogeneous astrocytes. Exp Neurol. 2018; 308: 72–79, doi: 10.1016/j.expneurol.2018.07.001, indexed in Pubmed: 30008424.

34. Halassa MM, Fellin T, Haydon PG. Tripartite synapses: roles for astrocytic purines in the control of synaptic physiology and behavior. Neuropharmacology. 2009; 57(4): 343–346, doi: 10.1016/j.neuropharm.2009.06.031, indexed in Pubmed: 19577581.

35. Hanisch UK. Functional diversity of microglia — how heterogeneous are they to begin with? Front Cell Neurosci. 2013; 7: 65, doi: 10.3389/fncel.2013.00065, indexed in Pubmed: 23717262.

36. Henneke P, Kierdorf K, Hall LJ, et al. Perinatal development of innate immune topology. Elife. 2021; 10, doi: 10.7554/eLife.67793, indexed in Pubmed: 34032570.

37. Honsa P, Pivonkova H, Dzamba D, et al. Polydendrocytes display large lineage plasticity following focal cerebral ischemia. PLoS One. 2012; 7(5): e36816, doi: 10.1371/journal.pone.0036816, indexed in Pubmed: 22590616.

38. Honsa P, Valny M, Kriska J, et al. Generation of reactive astrocytes from NG2 cells is regulated by sonic hedgehog. Glia. 2016; 64(9): 1518–1531, doi: 10.1002/glia.23019, indexed in Pubmed: 27340757.

39. Hsuan YCY, Lin CH, Chang CP, et al. Mesenchymal stem cell-based treatments for stroke, neural trauma, and heat stroke. Brain Behav. 2016; 6(10): e00526, doi: 10.1002/brb3.526, indexed in Pubmed: 27781140.

40. Hughes EG, Kang SH, Fukaya M, et al. Oligodendrocyte progenitors balance growth with self-repulsion to achieve homeostasis in the adult brain. Nat Neurosci. 2013; 16(6): 668–676, doi: 10.1038/nn.3390, indexed in Pubmed: 23624515.

41. Iadecola C. The neurovascular unit coming of age: a journey through neurovascular coupling in health and disease. Neuron. 2017; 96(1): 17–42, doi: 10.1016/j.neuron.2017.07.030, indexed in Pubmed: 28957666.

42. Kana V, Desland F, Casanova-Acebes M, et al. CSF-1 controls cerebellar microglia and is required for motor function and social interaction. J Exp Med. 2019; 216(10): 2265–2281, doi: 10.1084/jem.20182037, indexed in Pubmed: 31350310.

43. Khakh BS, Deneen B. The emerging nature of astrocyte diversity. Annu Rev Neurosci. 2019; 42: 187–207, doi: 10.1146/annurev-neuro-070918-050443, indexed in Pubmed: 31283899.

44. Khakh BS, Sofroniew MV. Diversity of astrocyte functions and phenotypes in neural circuits. Nat Neurosci. 2015; 18(7): 942–952, doi: 10.1038/nn.4043, indexed in Pubmed: 26108722.

45. Khoshnam SE, Winlow W, Farbood Y, et al. Pathogenic mechanisms following ischemic stroke. Neurol Sci. 2017; 38(7): 1167–1186, doi: 10.1007/s10072-017-2938-1, indexed in Pubmed: 28417216.

46. Kimelberg HK, Nedergaard M. Functions of astrocytes and their potential as therapeutic targets. Neurotherapeutics. 2010; 7(4): 338–353, doi: 10.1016/j.nurt.2010.07.006, indexed in Pubmed: 20880499.

47. Kimelberg HK. Functions of mature mammalian astrocytes: a current view. Neuroscientist. 2010; 16(1): 79–106, doi: 10.1177/1073858409342593, indexed in Pubmed: 20236950.

48. Kimelberg HK. The problem of astrocyte identity. Neurochem Int. 2004; 45(2-3): 191–202, doi: 10.1016/j.neuint.2003.08.015, indexed in Pubmed: 15145537.

49. Köhler S, Winkler U, Hirrlinger J. Heterogeneity of astrocytes in grey and white matter. Neurochem Res. 2021; 46(1): 3–14, doi: 10.1007/s11064-019-02926-x, indexed in Pubmed: 31797158.

50. Kowiański P, Lietzau G, Steliga A, et al. The astrocytic contribution to neurovascular coupling--still more questions than answers? Neurosci Res. 2013; 75(3): 171–183, doi: 10.1016/j.neures.2013.01.014, indexed in Pubmed: 23419863.

51. Kuhn S, Gritti L, Crooks D, et al. Oligodendrocytes in development, myelin generation and beyond. Cells. 2019; 8(11), doi: 10.3390/cells8111424, indexed in Pubmed: 31726662.

52. Lago-Baldaia I, Fernandes VM, Ackerman SD. More than mortar: glia as architects of nervous system development and disease. Front Cell Dev Biol. 2020; 8: 611269, doi: 10.3389/fcell.2020.611269, indexed in Pubmed: 33381506.

53. Lawson LJ, Perry VH, Dri P, et al. Heterogeneity in the distribution and morphology of microglia in the normal adult mouse brain. Neuroscience. 1990; 39(1): 151–170, doi: 10.1016/0306-4522(90)90229-w, indexed in Pubmed: 2089275.

54. Li Q, Barres BA. Microglia and macrophages in brain homeostasis and disease. Nat Rev Immunol. 2018; 18(4): 225–242, doi: 10.1038/nri.2017.125, indexed in Pubmed: 29151590.

55. Liddelow SA, Barres BA. Reactive astrocytes: production, function, and therapeutic potential. Immunity. 2017; 46(6): 957–967, doi: 10.1016/j.immuni.2017.06.006, indexed in Pubmed: 28636962.

56. Liddelow SA, Guttenplan KA, Clarke LE, et al. Neurotoxic reactive astrocytes are induced by activated microglia. Nature. 2017; 541(7638): 481–487, doi: 10.1038/nature21029, indexed in Pubmed: 28099414.

57. Liebner S, Dijkhuizen RM, Reiss Y, et al. Functional morphology of the blood-brain barrier in health and disease. Acta Neuropathol. 2018; 135(3): 311–336, doi: 10.1007/s00401-018-1815-1, indexed in Pubmed: 29411111.

58. Liu LR, Liu JC, Bao JS, et al. Interaction of microglia and astrocytes in the neurovascular unit. Front Immunol. 2020; 11: 1024, doi: 10.3389/fimmu.2020.01024, indexed in Pubmed: 32733433.

59. Magistretti PJ, Allaman I. A cellular perspective on brain energy metabolism and functional imaging. Neuron. 2015; 86(4): 883–901, doi: 10.1016/j.neuron.2015.03.035, indexed in Pubmed: 25996133.

60. Martins-Macedo J, Lepore AC, Domingues HS, et al. Glial restricted precursor cells in central nervous system disorders: current applications and future perspectives. Glia. 2021; 69(3): 513–531, doi: 10.1002/glia.23922, indexed in Pubmed: 33052610.

61. Masuda T, Sankowski R, Staszewski O, et al. Microglia heterogeneity in the single-cell era. Cell Rep. 2020; 30(5): 1271–1281, doi: 10.1016/j.celrep.2020.01.010, indexed in Pubmed: 32023447.

62. Matcovitch-Natan O, Winter DR, Giladi A, et al. Microglia development follows a stepwise program to regulate brain homeostasis. Science. 2016; 353(6301): aad8670, doi: 10.1126/science.aad8670, indexed in Pubmed: 27338705.

63. Matyash V, Kettenmann H. Heterogeneity in astrocyte morphology and physiology. Brain Res Rev. 2010; 63(1-2): 2–10, doi: 10.1016/j.brainresrev.2009.12.001, indexed in Pubmed: 20005253.

64. Menassa DA, Gomez-Nicola D. Microglial dynamics during human brain development. Front Immunol. 2018; 9: 1014, doi: 10.3389/fimmu.2018.01014, indexed in Pubmed: 29881376.

65. Moshrefi-Ravasdjani B, Dublin P, Seifert G, et al. Changes in the proliferative capacity of NG2 cell subpopulations during postnatal development of the mouse hippocampus. Brain Struct Funct. 2017; 222(2): 831–847, doi: 10.1007/s00429-016-1249-2, indexed in Pubmed: 27306788.

66. Murtie JC, Macklin WB, Corfas G. Morphometric analysis of oligodendrocytes in the adult mouse frontal cortex. J Neurosci Res. 2007; 85(10): 2080–2086, doi: 10.1002/jnr.21339, indexed in Pubmed: 17492793.

67. Nishiyama A, Komitova M, Suzuki R, et al. Polydendrocytes (NG2 cells): multifunctional cells with lineage plasticity. Nat Rev Neurosci. 2009; 10(1): 9–22, doi: 10.1038/nrn2495, indexed in Pubmed: 19096367.

68. Parri HR, Crunelli V. The role of Ca2+ in the generation of spontaneous astrocytic Ca2+ oscillations. Neuroscience. 2003; 120(4): 979–992, doi: 10.1016/s0306-4522(03)00379-8, indexed in Pubmed: 12927204.

69. Pelvig DP, Pakkenberg H, Stark AK, et al. Neocortical glial cell numbers in human brains. Neurobiol Aging. 2008; 29(11): 1754–1762, doi: 10.1016/j.neurobiolaging.2007.04.013, indexed in Pubmed: 17544173.

70. Ransom BR, Butt AM, Black JA. Ultrastructural identification of HRP-injected oligodendrocytes in the intact rat optic nerve. Glia. 1991; 4(1): 37–45, doi: 10.1002/glia.440040105, indexed in Pubmed: 1828785.

71. Richardson WD, Young KM, Tripathi RB, et al. NG2-glia as multipotent neural stem cells: fact or fantasy? Neuron. 2011; 70(4): 661–673, doi: 10.1016/j.neuron.2011.05.013, indexed in Pubmed: 21609823.

72. Rivera AD, Chacon-De-La-Rocha I, Pieropan F, et al. Keeping the ageing brain wired: a role for purine signalling in regulating cellular metabolism in oligodendrocyte progenitors. Pflugers Arch. 2021; 473(5): 775–783, doi: 10.1007/s00424-021-02544-z, indexed in Pubmed: 33712969.

73. Rivers LE, Young KM, Rizzi M, et al. PDGFRA/NG2 glia generate myelinating oligodendrocytes and piriform projection neurons in adult mice. Nat Neurosci. 2008; 11(12): 1392–1401, doi: 10.1038/nn.2220, indexed in Pubmed: 18849983.

74. Robins SC, Kokoeva MV. NG2-Glia, a new player in energy balance. Neuroendocrinology. 2018; 107(3): 305–312, doi: 10.1159/000488111, indexed in Pubmed: 29506015.

75. Schaeffer S, Iadecola C. Revisiting the neurovascular unit. Nat Neurosci. 2021; 24(9): 1198–1209, doi: 10.1038/s41593-021-00904-7, indexed in Pubmed: 34354283.

76. Schirmer L, Schafer DP, Bartels T, et al. Diversity and function of glial cell types in multiple sclerosis. Trends Immunol. 2021; 42(3): 228–247, doi: 10.1016/j.it.2021.01.005, indexed in Pubmed: 33593693.

77. Schoenwolf GC, Bleyl SB, Brauer PR, Francis-West PH. Development of the central nervous system. Larsen's human embryology. 6th ed. Elsevier, Philadelphia 2020: 191–227.

78. Sharma K, Bisht K, Eyo UB. A comparative biology of microglia across species. Front Cell Dev Biol. 2021; 9: 652748, doi: 10.3389/fcell.2021.652748, indexed in Pubmed: 33869210.

79. Sofroniew MV, Vinters HV. Astrocytes: biology and pathology. Acta Neuropathol. 2010; 119(1): 7–35, doi: 10.1007/s00401-009-0619-8, indexed in Pubmed: 20012068.

80. Sofroniew MV. Astrocyte reactivity: subtypes, states, and functions in CNS innate immunity. Trends Immunol. 2020; 41(9): 758–770, doi: 10.1016/j.it.2020.07.004, indexed in Pubmed: 32819810.

81. Sofroniew MV. Molecular dissection of reactive astrogliosis and glial scar formation. Trends Neurosci. 2009; 32(12): 638–647, doi: 10.1016/j.tins.2009.08.002, indexed in Pubmed: 19782411.

82. Staszewski O, Hagemeyer N. Unique microglia expression profile in developing white matter. BMC Res Notes. 2019; 12(1): 367, doi: 10.1186/s13104-019-4410-1, indexed in Pubmed: 31262353.

83. Steliga A, Kowiański P, Czuba E, et al. Neurovascular unit as a source of ischemic stroke biomarkers-limitations of experimental studies and perspectives for clinical application. Transl Stroke Res. 2020; 11(4): 553–579,

doi: 10.1007/s12975-019-00744-5, indexed in Pubmed: 31701356.

84. Stremmel C, Schuchert R, Wagner F, et al. Yolk sac macrophage progenitors traffic to the embryo during defined stages of development. Nat Commun. 2018; 9(1): 75, doi: 10.1038/s41467-017-02492-2, indexed in Pubmed: 29311541.

85. Takano T, Tian GF, Peng W, et al. Astrocyte-mediated control of cerebral blood flow. Nat Neurosci. 2006; 9(2): 260–267, doi: 10.1038/nn1623, indexed in Pubmed: 16388306.

86. Thion MS, Low D, Silvin A, et al. Microbiome influences prenatal and adult microglia in a sex-specific manner. Cell. 2018; 172(3): 500–516.e16, doi: 10.1016/j. cell.2017.11.042, indexed in Pubmed: 29275859.

87. Torper O, Götz M. Brain repair from intrinsic cell sources: turning reactive glia into neurons. Prog Brain Res. 2017; 230: 69–97, doi: 10.1016/bs.pbr.2016.12.010, indexed in Pubmed: 28552236.

88. Torper O, Ottosson DR, Pereira M, et al. In vivo reprogramming of striatal NG2 glia into functional neurons that integrate into local host circuitry. Cell Rep. 2015; 12(3): 474–481, doi: 10.1016/j.celrep.2015.06.040, indexed in Pubmed: 26166567.

89. Utz SG, See P, Mildenberger W, et al. Early fate defines microglia and non-parenchymal brain macrophage development. Cell. 2020; 181(3): 557–573.e18, doi: 10.1016/j. cell.2020.03.021, indexed in Pubmed: 32259484.

90. Valny M, Honsa P, Kriska J, et al. Multipotency and therapeutic potential of NG2 cells. Biochem Pharmacol. 2017; 141: 42–55, doi: 10.1016/j.bcp.2017.05.008, indexed in Pubmed: 28522408.

91. Valny M, Honsa P, Waloschkova E, et al. A single-cell analysis reveals multiple roles of oligodendroglial lineage cells during post-ischemic regeneration. Glia. 2018; 66(5): 1068–1081, doi: 10.1002/glia.23301, indexed in Pubmed: 29393544.

92. Verkhratsky A, Ho MS, Zorec R, et al. The concept of neuroglia. Adv Exp Med Biol. 2019; 1175: 1–13, doi: 10.1007/978-981-13-9913-8_1, indexed in Pubmed: 31583582.

93. Verkhratsky A, Kettenmann H. Calcium signalling in glial cells. Trends Neurosci. 1996; 19(8): 346–352, doi: 10.1016/0166-2236(96)10048-5, indexed in Pubmed: 8843604.

94. Verkhratsky A, Sofroniew MV, Messing A, et al. Neurological diseases as primary gliopathies: a reassessment of neurocentrism. ASN Neuro. 2012; 4(3), doi: 10.1042/AN20120010, indexed in Pubmed: 22339481.

95. Werner Y, Mass E, Ashok Kumar P, et al. Cxcr4 distinguishes HSC-derived monocytes from microglia and reveals monocyte immune responses to experimental stroke. Nat Neurosci. 2020; 23(3): 351–362, doi: 10.1038/s41593-020-0585-y, indexed in Pubmed: 32042176.

96. Wlodarczyk A, Holtman IR, Krueger M, et al. A novel microglial subset plays a key role in myelinogenesis in developing brain. EMBO J. 2017; 36(22): 3292–3308, doi: 10.15252/embj.201696056, indexed in Pubmed: 28963396.

97. Zhao JW, Raha-Chowdhury R, Fawcett JW, et al. Astrocytes and oligodendrocytes can be generated from NG2+ progenitors after acute brain injury: intracellular localization of oligodendrocyte transcription factor 2 is associated with their fate choice. Eur J Neurosci. 2009; 29(9): 1853–1869, doi: 10.1111/j.1460-9568.2009.06736.x, indexed in Pubmed: 19473238.

98. Zhou YD. Glial regulation of energy metabolism. Adv Exp Med Biol. 2018; 1090: 105–121, doi: 10.1007/978-981-13-1286-1_6, indexed in Pubmed: 30390287.

99. Zhu X, Hill RA, Dietrich D, et al. Age-dependent fate and lineage restriction of single NG2 cells. Development. 2011; 138(4): 745–753, doi: 10.1242/dev.047951, indexed in Pubmed: 21266410.

100. Zonta M, Angulo MC, Gobbo S, et al. Neuron-to-astrocyte signaling is central to the dynamic control of brain microcirculation. Nat Neurosci. 2003; 6(1): 43–50, doi: 10.1038/nn980, indexed in Pubmed: 12469126.

101. Zonta M, Carmignoto G. Calcium oscillations encoding neuron-to-astrocyte communication. J Physiol Paris. 2002; 96(3-4): 193–198, doi: 10.1016/s0928-4257(02)00006-2, indexed in Pubmed: 12445896.

VIA MEDICA

R E V I E W   A R T I C L E

Corona mortis, aberrant obturator vessels, accessory obturator vessels: clinical applications in gynaecology

S. Kostov[1], S. Slavchev[1], D. Dzhenkov[2], G. Stoyanov[2], N. Dimitrov[3], A. Yordanov[4]

[1]Department of Gynaecology, Medical University Varna, Bulgaria
[2]Department of General and Clinical Pathology, Forensic Medicine and Deontology, Division of General and Clinical Pathology, Faculty of Medicine, Medical University Varna "Prof. Dr. Paraskev Stoyanov", Varna, Bulgaria
[3]Department of Anatomy, Faculty of Medicine, Trakia University, Stara Zagora, Bulgaria
[4]Department of Gynaecologic Oncology, Medical University Pleven, Bulgaria

Corona mortis (CMOR) is a heterogeneous and often dubious term that causes much confusion in medical literature, especially in regard to its modern day significance in pelvic surgery. Some authors define CMOR as any abnormal anastomotic vessel between the external iliac and obturator vessels, whereas others define it as any vessel coursing over the superior pubic branch, regardless whether it is a vascular anastomosis, an accessory obturator vessels, an obturator vessel related to the external iliac system or a terminal small vessel. There is no standard classification of CMOR and obturator vessels variations, although there are multitudes of classifications describing the diverse variations in the obturator foramen region. We define accessory obturator, aberrant obturator vessels and CMOR as different structures, as CMOR is an anatomical term that reflects a clinical situation rather than an anatomical structure. A new clinical classification for aberrant, accessory obturator vessels and CMOR is proposed regarding the anatomical variations, and the location of vessels to the deep femoral ring. The clinical significance of accessory obturator, aberrant vessels and CMOR is delineated in oncogynaecological and urogynaecological surgery. (Folia Morphol 2021; 80, 4: 776–785)

Key words: corona mortis, aberrant obturator vessels, accessory obturator vessels, deep femoral ring, oncogynaecology, urogynaecology

INTRODUCTION

Corona mortis (CMOR) is defined as any abnormal anastomotic vessels between the external iliac and obturator vessels [38]. Studies have shown that the definition of CMOR is heterogeneous and causes much confusion in medical literature [38]. Although in the past CMOR was defined as arterial anastomosis between an external iliac and an obturator artery, currently in medical reports the widely accepted definition includes the arterial and/or venous vascular anastomosis between an obturator and an external iliac vessel [2]. Moreover, some authors define CMOR as a connection between the external and internal iliac system, whereas others define it as any vessel coursing over the superior pubic branch, regardless whether it is a vascular anastomosis, an accessory obturator

vessels, an obturator vessel related to the external iliac system or a terminal small vessel [1, 2, 11, 36, 38]. Additionally, there is no standard classification of CMOR and obturator vessels variations, although there are multitudes of classifications describing the diverse variations in the obturator foramen region [1, 15, 36]. Studying CMOR is crucial because of its association with a high risk of severe haemorrhage during surgeries. Various gynaecological procedures carry the risk of CMOR injury. The aim of this study is to define accessory obturator vessels (ACOVs), aberrant obturator vessels (AOVs) and CMOR. Moreover, we propose a new classification for the clinical use and delineate the clinical significance of ACOVs, AOVs and CMOR in oncogynaecological and urogynaecological surgery.

OBTURATOR ARTERY ANATOMY AND VARIATIONS

In the majority of cases, the obturator artery (OA) is a branch of the anterior division of the internal iliac artery [49]. It runs anteriorly and inferiorly on the pelvic wall and lies longitudinally to the obturator foramen on the medial part of the obturator internus muscle. The OA is located cranially to the obturator vein and caudally to the obturator nerve (ON) (Fig. 1) [33, 49, 54].

The ureter lies medial to it. The OA gives branches within the pelvis before piercing the obturator foramen [8, 21, 33, 40, 49, 54]. The OA gives branches to the obturator internus muscle, psoas muscle and to the iliac fossa for the iliacus muscle and the ilium. Sometimes the inferior vesical artery is replaced by caudal branch of the OA. The pubic branch arises before the obturator canal and runs cranially over the pubis to anastomoses with the pubic branch of the inferior epigastric artery and the contralateral artery (Fig. 2) [8, 21, 24, 33, 39, 40, 42, 49, 54].

There is, perhaps, no artery of proportionate size having as variable origin as the OA (Table 1) [1, 4, 8, 21, 23, 24, 33, 39, 40, 42, 49, 54].

Although studies reported different percentages for the OA origin variations, in the majority of cases the most common OA origin is from the IIA, followed by the inferior epigastric, external iliac artery, femoral artery [8, 21, 33, 39, 40, 54]. When the OA arises from the IIA, it descends almost horizontally to the obturator foramen, whereas when the OA arises from the external iliac system, it crosses vertically over the superior pubic ramus and the external iliac vein. OA arising from the inferior epigastric artery is the com-
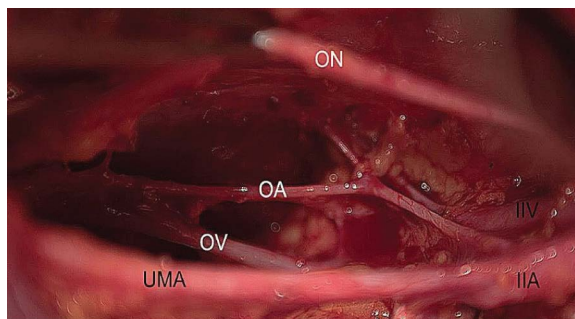
Figure 1. Obturator nerve, artery and vein topographical anatomy — open surgery (right pelvic side wall); ON — obturator nerve; OA — obturator artery; OV — obturator vein; IIV — internal iliac vein; IIA — internal iliac artery; UMA — umbilical artery.

Figure 2. Obturator fossa anatomy — open surgery (right pelvic side wall); EIA — external iliac artery; EIV — external iliac vein; IIV — internal iliac vein; IIA — internal iliac artery; UA — uterine artery (cut and ligated); UR — ureter; UMA — umbilical artery; ON — obturator nerve; OA — obturator artery; OV — obturator vein; OF — obturator foramen; OIM — obturator internus muscle; BOIM — branch of obturator artery for obturator internus muscle.

Table 1. Obturator artery (OA) origin variations [1, 4, 8, 21, 23, 24, 33, 39, 40, 42, 49, 54]

Origin from internal iliac artery (IIA)
OA arises separately from IIA before bifurcation
OA arises from the anterior division of IIA
OA arises from inferior gluteal artery
OA arises from internal pudendal artery
OA arises from posterior division of IIA
Origin from external iliac artery (EIA)
OA arises directly from EIA
OA is a branch of inferior epigastric artery
OA arises as a double root from both IIA and EIA

monest source of aberrant obturator artery (AOA) [33]. The incidence of an AOA arising from the inferior epigastric artery ranges from 20% to 34% [33].

Such an AOA has a great clinical significance. It is of a great calibre and has atypical passage through the superior pubic ramus. This artery passes posterior to the lacunar ligament and coursed the superior pubic ramus vertically to enter the obturator foramen. Therefore, OA arising from inferior epigastric artery is susceptible to injury during the dissection of the preperitoneal space using endoscissors or stapling of the mesh [23, 33]. Berberoglu et al. [4] reported on such an artery with diameter of 2.2 mm. Darmanis et al. [11] reported that an AOA originating from the inferior epigastric artery or external iliac artery is present in 20–30% of hemipelvises and it is of a greater diameter on average than a CMOR when it is present. OA arising from the external iliac artery is rare type of OA origin — 1–2% [1, 8, 21, 23, 39, 40, 33, 54]. Other authors also reported on an AOA arising from inferior epigastric artery running superior to the inguinal ligament and lateral or medial to the femoral ring [2, 33]. In conclusion, an AOA arising from the inferior epigastric artery is an extremely relevant substitute of the corona mortis.

Obturator artery can arise as a common trunk with most of the internal and external iliac arteries. Although rare, the OA shares a common trunk with the inferior epigastric and the deep circumflex iliac artery. The trunk can arise in the femoral or external iliac region [40]. Although some authors reported more OA origin anomalies in females, the majority of studies showed no statistically significant difference between genders [39].

We define an AOA as an artery that originates from an external iliac artery or its branches and pierce the obturator membrane, not participating in anastomosis. There is no other OA.

An accessory OA is the presence of an extra OA in addition to the normal counterpart. An accessory OA pierces the obturator membrane, not participating in anastomosis [11, 37, 38]. We propose a simple classification of the aberrant and accessory obturator arteries with clinical significance (Fig. 3) [8].

In Figure 3, we divide type I and type II regarding the AOA location to the deep femoral ring, as an AOA medial to the deep femoral ring is closer to the urogynaecological field during surgery. An AOA lateral to the deep femoral ring is closer to the operative field during oncogynaecological procedures. Therefore, the probability of intraoperative injury depends on the locations of the AOA and the type of surgery. Type IV is included as it is of clinical significance in
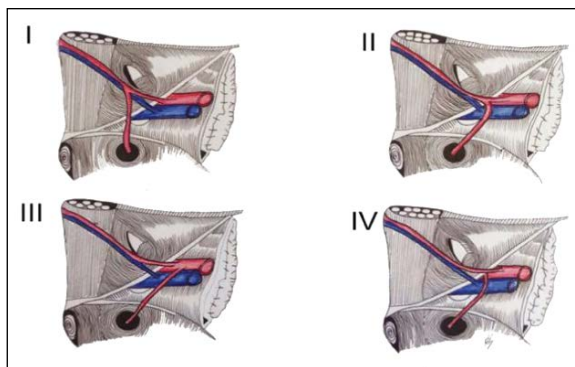
Figure 3. Aberrant obturator artery (AOA) classification; Type I — AOA arising from the inferior epigastric artery. AOA is located medial to the deep femoral ring; Type II — AOA arising from the inferior epigastric artery. AOA is located lateral to the deep femoral ring; Type III — AOA arising from the external iliac artery; Type IV — AOA arising from the femoral artery.

oncogynaecology. Clinical applications of an AOA are described below. The accessory obturator artery classification is the same as the AOA one, except that there is a normal OA, arising from the IIA.

OBTURATOR VEIN ANATOMY AND VARIATIONS

The obturator vein (OV) arises in the adductor region and passes through the obturator foramen. It then proceeds posteriorly and superiorly on the lateral pelvic wall below the OA and drains into the internal iliac vein [8, 21, 33, 39, 40, 49, 54]. As mentioned above the obturator nerve (ON), OA, and OV run in that order, from above to below, in the lateral pelvic wall and piercing the obturator foramen. However, in medical literature different order in the neurovascular bundle has been described. In a study of 150 hemipelvises of 84 embalmed adult Korean cadavers, Won et al. [54] described the order ON-OV-OA in 5 cadavers and OA-ON-OV in 3 cadavers. In 25 of the specimens, two of these three structures (ON, OA, and OV) were twisted around each other in the lateral pelvic wall.

Classic anatomy texts pay less attention to the variations of veins than arteries. There are many reports of the OA origin variations, but less importance is given to the OV drain variations. It is believed that venous anomalies are more probable than an arterial one [29, 36].

We define an aberrant obturator vein as a vein that passes through the obturator foramen and drains in the external iliac vein or its tributaries, not participating in anastomosis. There is no other OV.
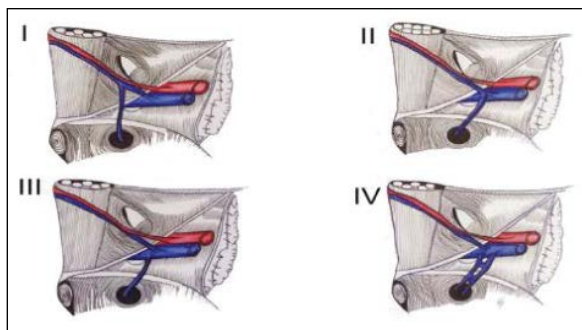
Figure 4. Aberrant obturator vein classification; Type I — aberrant obturator vein drains in the inferior epigastric vein. Aberrant obturator vein is located medial to the deep femoral ring; Type II — aberrant obturator vein drains in the inferior epigastric vein. Aberrant obturator vein is located lateral to the deep femoral ring; Type III — aberrant obturator vein drains in the external iliac vein; Type IV — double aberrant obturator vein drains in the external iliac vein.

An accessory OV is the presence of an extra OV in addition to the normal counterpart. An accessory OV passes through obturator membrane, not participating in anastomosis. We propose simple classification with a clinical significance of the aberrant and the accessory OVs (Fig. 4) [26, 54].

In Figure 4, we divide type I and type II regarding location to the deep femoral ring. An aberrant OV medial to the deep femoral ring is most likely to be injured during urogynaecology operations, whereas an aberrant OV lateral to the deep femoral ring during oncogynaecology procedures. Type IV is included, as the chance of damaging double aberrant OV is greater during pelvic lymphadenectomy. A double aberrant OV is located lateral to the deep femoral ring. Missankov et al. [26] reported in a cadaveric study, 2% of type IV of all specimens. The accessory OV classification is the same as the aberrant OV one, except that there is a normal OV, draining in the IIV.

CMOR

In medical literature, there is no consensus on CMOR terminology [41]. Berberoglu et at. [4] stated that some authors referred to the term "corona mortis" as the anastomosis between the OA and the pubic branch of the inferior epigastric artery, whereas others defined CMOR as the pubic branch of the OA [29]. Moreover, terms such as aberrant, accessory, communicating, variant obturator vessels were used to clarify CMOR [12, 31, 38, 41]. Additionally, some authors termed CMOR as any vessel coursing over the superior pubic branch, regardless whether it is a vascular anastomosis, an obturator

vessel related to the external iliac system or a terminal small vessel [2, 36].

We prefer to keep the description by Darmanis et al. [11], Sanna et al. [38] and Drewes at al. [12], as the term "corona mortis" is any abnormal anastomotic vessel, located behind the superior pubic ramus and on the posterior aspect of the lacunar ligament, between an obturator vessel (part of to the internal iliac system) and an external iliac vessel [11, 12, 38]. CMOR should measure 2 mm or more [32, 46]. CMOR could be in close relationship with the loose edge of the lacunar ligament and the neck of the femoral hernia sac [4, 11, 32, 41]. The close relation between CMOR, lacunar ligament and femoral ring could become a matter of great concern to the orthopaedic surgeon, urologist, gynaecologist and general surgeon [32]. Sarikcioglu et al. [41] measured the average distance between the arch of the lacunar ligament and the CMOR and found this average to be 12.18–3.55 mm. Accessory obturator and AOVs are excluded as these originate from the external iliac or inferior epigastric system and pierce the obturator membrane, not participating in anastomosis [38]. Our concept of separation is that CMOR is an anatomical term that reflects a clinical situation rather than an anatomical structure [2]. Therefore, CMOR, AOVs and ACOVs are at various risk of damage during different surgical procedures. We proposed a clinical classification of CMOR (Fig. 5). Type III CMOR is shown in Figure 6.

CLINICAL APPLICATIONS OF AOVS, ACOVS AND CMOR IN GYNAECOLOGY

In oncogynaecology, Selcuk et al. [43] reported that the term "corona mortis'' was questionable. They concluded that the retro-pubic vascular anastomoses were easily seen after a careful and tiny dissection over the external iliac artery below the inguinal ligament. In their opinion, an injury to CMOR rarely occurs during pelvic lymphadenectomy as they had only 6 CMOR injuries among 96 pelvic lymphadenectomies. The bleeding was easily controlled [43]. According to other authors CMOR is exposed and at risk of injury during pelvic lymphadenectomy [15, 32]. In our opinion, there is a low risk of damaging CMOR during pelvic lymphadenectomy at the external iliac region for endometrial, ovarian and cervical cancer. Anatomical landmarks for performing systematic oncogynaecological pelvic lymphadenectomy in the external iliac region are: ventrally — drain of deep
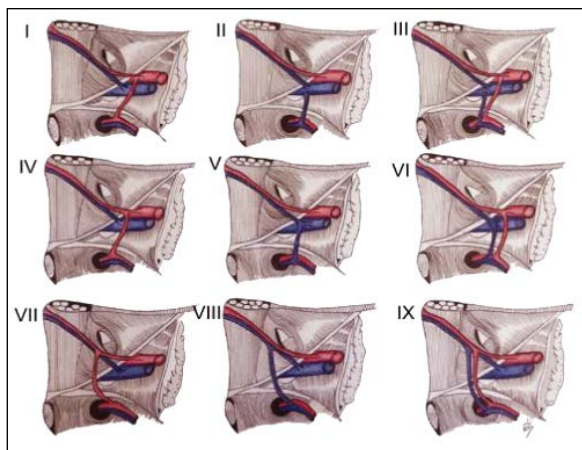
Figure 5. Corona mortis (CMOR) classification; Type I — CMOR between obturator artery (OA) and external iliac artery; Type II — CMOR between obturator vein (OV) and external iliac vein; Type III — CMOR between both obturator vessels and external iliac vessels; Type IV — CMOR between inferior epigastric artery and OA; Type V — CMOR between inferior epigastric vein and OV; Type VI — CMOR between both obturator vessels and inferior epigastric vessels (Type IV, V and VI anastomotic vessels are located lateral to the deep femoral ring); Type VII — CMOR between OA and inferior epigastric artery; Type VIII — CMOR between OV and inferior epigastric vein; Type IX — CMOR between both obturator vessels and inferior epigastric vessels (Type VII, VIII and IX anastomotic vessels are located medial to the deep femoral ring).

Figure 6. Arterial corona mortis (CMOR) and venous CMOR between obturator artery/vein and external iliac artery/vein. Fresh cadaver. Type III; PMM — psoas major muscle; EIA — external iliac artery; EIV — external iliac vein; gGFN — genital branch of genitofemoral nerve; fGFN — femoral branch of genitofemoral nerve; DCIV — deep circumflex iliac vein; IEV — inferior epigastric vein; IEA — inferior epigastric artery; IL — inguinal ligament; FR — deep femoral ring; OF — obturator foramen; ON — obturator nerve; OA — obturator artery(severed during dissection); OV — obturator vein; aCMOR — arterial corona mortis; vCMOR — venous corona mortis; SPS — superior pubic ramus.

Figure 7. Venous corona mortis between obturator vein and inferior epigastric vein (right pelvic side wall). The distance between deep circumflex iliac vein and inferior epigastric vein is measured — 11 mm. Embalmed cadaver. Type V; EIA — external iliac artery; EIV — external iliac vein; PMM — psoas major muscle; OIM — obturator internus muscle; IIA — internal iliac artery; UA — uterine artery; UMA — umbilical artery; ON — obturator nerve; OA — obturator artery; OV — obturator vein; B — bladder; PS — pubic symphysis; IEV — inferior epigastric vein; DCIV — deep circumflex iliac vein; vCMOR — venous corona mortis.

Figure 8. Arterial and venous corona mortis (CMOR) between external iliac and obturator vessels (left pelvic side wall). Rare case of CMOR proximal to the deep circumflex iliac vein. Fresh cadaver. Type III; EIA — external iliac artery; EIV — external iliac vein; PMM — psoas major muscle; PMIM — psoas minor muscle; FN — femoral nerve; IIN — ilioinguinal nerve; gGFN — genital branch of genitofemoral nerve; fGFN — femoral branch of genitofemoral nerve; DCIV — deep circumflex iliac vein; ON — obturator nerve; OA — obturator artery; OV — obturator vein; OF — obturator foramen; FR — deep femoral ring; aCMOR — arterial corona mortis; vCMOR — venous corona mortis; IL — inguinal ligament; PL — pectineal ligament; IEV — inferior epigastric vein; IEA — inferior epigastric artery.

circumflex iliac vein (DCIV), dorsally — common iliac artery bifurcation, laterally — genitofemoral nerve on the iliopsoas muscle, medially — obliterated umbilical artery [9, 43]. DCIV is ventral border as removal of circumflex iliac nodes distal to the DCIV in external iliac region for cervical cancer (FIGO stage Ia, IIa) is not

necessary for three reasons — might not be regional lymph nodes, greater risk of lymphedema and low metastatic rate [52]. Studies reported similar findings for endometrial and ovarian cancer [30, 48, 50]. Therefore, visualisation of DCIV is enough to complete ventral dissection in the external iliac region. The DCIV drains in the external iliac vein, approximately 1 cm proximal to the inferior epigastric vein, so injury to CMOR should be avoided (Figs. 7, 8).

As shown in Figure 7, the DCIV is proximal to the inferior epigastric vein. The distance between vessels was measured — 11 mm (Fig. 7). Consequently, during pelvic oncogynaecological lymphadenectomy at the external iliac region, injury to the CMOR distal to the DCIV is less likely to occur, especially for anastomotic vessels between the obturator and the inferior epigastric system. In medical literature, there are no studies comparing the frequency of AOVs, ACOVs, and CMOR distal or proximal to the DCIV. However, figures from the majority of studies showed CMOR, AOVs, ACOVs to be distal to the DCIV [15, 31, 39, 41]. Nevertheless, meticulous dissection should be performed until the level of the DCIV is reached (Fig. 8).

The risk of injury of AOVs, ACOVs and CMOR is high during pelvic lymphadenectomy in the obturator region. Anatomical landmarks for performing pelvic lymphadenectomy in the obturator region are: cranially — caudal wall of the external iliac vein, caudally — the obturator vessels, ventrally — the pubic bone together with the levator ani and the obturator muscle, where the obturator nerve leaves the pelvis through the obturator canal, dorsal — the common iliac vessels bifurcation, medial — the urinary bladder, lateral — the obturator internus muscle [9]. Meticulous and careful lymph node dissection is required in the ventral and caudal border of obturator region in order to preserve AOVs, ACOVs, and CMOR. As shown in Figure 8, the risk of damaging CMOR is elevated in the obturator and external iliac region during pelvic lymphadenectomy. CMOR is proximal to the deep circumflex iliac vein, as the anastomosis is between obturator and external iliac system.

The origin of an AOA from the femoral artery is rare and no prevalences have been established [24]. However, studies reported the rate of AOA arising from the femoral artery to be between 0.15% and 1.66% [1, 24, 33, 40]. In Figure 3 we included an AOA arising from the femoral artery (type IV), as it is of major clinical significance in two oncogynaecological procedures: inguinofemoral lymphadenectomy and sentinel lymph node biopsy in the inguinofemoral region [49]. The lymphatic system in the inguinal region can be divided into two distinct groups: superficial and deep inguinal lymph nodes. The superficial inguinal lymph nodes are located beneath the Camper fascia and superficial to the fascia lata of the thigh, whereas the deep inguinal nodes lie beneath the fascia lata along the femoral vein [7]. An AOA arising from the femoral artery is at high risk of injury during superficial and deep inguinal lymph nodes dissection. The uppermost deep inguinal lymph node located within the femoral canal and under the inguinal (Poupart) ligament is called Cloquet's node [3]. Cloquet's node was believed to be the link between inguinal and iliac/obturator nodes and the sentinel lymph node for vulvar cancer [44]. Currently, studies report that Cloquet's node has no particular surgical relevance and is considered an inconstant lymph node, being absent in approximately 50% of the cases and, when present, unilateral in approximately 30% [6, 25]. Although Cloquet's node is not consistently present, an examination for its presence should be performed by cranial retraction of the inguinal region over the femoral canal [5]. A Cloquet's node dissection carries the risk of injuring an AOA arising from femoral artery, medial circumflex femoral artery or profunda femoral. Although the node is medial to an AOA arising from femoral artery, the surgeon should be familiar with OA origin anomalies in the region.

In our opinion, ACOVs and AOVs are at higher risk of injury than CMOR in the external iliac region, as they are more likely to occur proximal to the DCIV and lateral to the deep femoral ring. AOVs cross the superior pubic ramus more obliquely and at a posterior position compared to CMOR [11]. Moreover, damage to ACOV and AOVs could be more precarious than CMOR. In the majority of cases, the average diameter of AOVs is greater than CMOR [11, 18, 54]. ACOVs, AOVs and CMOR lateral to the deep femoral ring are at major risk of damage during pelvic lymphadenectomy, as they are in the surgical field.

In urogynaecology, AOVs, ACOVs and CMOR are at risk of injury during stress urinary incontinence procedures — minimally invasive midurethral sling — the tension-free vaginal tape (TVT), Transobturator tape (TOT), TVT Secur (a single-incision sling device) and retropubic colposuspension — Burch procedure.

For many years, Burch colposuspension (first introduced in 1961) was a well-accepted technique for surgical management of stress urinary incontinence (SUI), especially when it was associated with urethral hypermobility. It was considered as the "gold standard" for the treatment of SUI [52]. Burch procedure surpassed in popularity in the early 2000s after the advent of the minimally invasive midurethral sling [14]. Although antimesh media and statements by the United States Food and Drug Administration in recent years have led to some patients requesting mesh-free surgery, Burch procedure remains an op-

tion for secondary treatment of SUI [19, 52]. Burch colposuspension is performed through laparotomy or laparoscopy [52].

The Retzius (retropubic) space is dissected. Once the retropubic space is dissected, the bladder neck and the pubocervical fascia are identified. The surgeon places 2 bilateral nonabsorbable sutures through the pubocervical fascia and vaginal muscularis, without passing through the vaginal epithelium — one at the level of the midurethra and other at the urethrovesical junction. Sutures are fixed to the Cooper's pubic ligament [19, 53].

Cooper [10] originally described Pectineal ligament or Cooper's pubic ligament. He stated that the Cooper's ligament was a ligamentous expansion, which formed a remarkably strong ridge above the iliopectineal line [10, 47]. There is no consensus about the origin of pectineal ligament. Faure et al. [13] reported that the pectineal ligament adhered to the periosteum of the superior pubic ramus, covered the pectineal line of the pubis, and stretched dorsally from the pubic tubercle and the iliopubic eminence [13, 47]. The pectineal ligament was the dorsal border of the deep femoral ring and the lacunar (Gimbernat) ligaments formed the medial border [34]. Steinke et al. [47] reported that the pectineal ligament was attached ventrally to the pectineus muscle and it was attached to both the iliopsoas fascia and obturator fascia, whereas dorsally both fasciae were free of the pectineal ligament. Cranially, the pectineal ligament was connected to the inguinal ligament by the lacunar ligament [47]. Faure et al. [13] concluded that the mean length of pectineal ligament was 53 mm. It was thicker in two regions — at its medial insertion or between the external iliac vessels and the pubic spine [13]. They reported that during Burch colposuspension stitches should be located near to the iliac vessels and 4 cm lateral to the medial insertion of the ligament, where it has its greatest thickness [13]. According to other study, the medial part of pectineal ligament close to the pubic tubercle was the thickest section and it became thinner while extending laterally [34]. In a study of 11 female unembalmed female cadavers, Kinman et al. [19] reported that the mean distance from the most lateral stitch in Cooper's pubic ligament to the obturator bundle was 25.9 ± 7.6 mm and to the external iliac vessels was 28.9 ± 9.3 mm, and in some instances, these structures were less than 15 mm away. Pulatoglu et al. [34] measured the total length of the pectineal ligament — 5.9 ± 0.76 cm on the left and

Figure 9. Arterial and venous corona mortis (CMOR) between inferior epigastric and obturator vessels (left pelvic side wall). CMOR is located medial to the deep femoral ring. Fresh cadaver. Type IX; CIA — common iliac artery; PMM — psoas major muscle; IIA — internal iliac artery; EIV — external iliac vein; EIA — external iliac artery; IIN — ilioinguinal nerve; FN — femoral nerve; gGFN — genital branch of genitofemoral nerve; fGFN — femoral branch of genitofemoral nerve; ON — obturator nerve; OA — obturator artery; OV — obturator vein; OF — obturator foramen; PL — pectineal ligament; FR — deep femoral ring; vCMOR — venous corona mortis; aCMOR — arterial corona mortis; IL — inguinal ligament; DCIV — deep circumflex iliac vein.

6.5 ± 1.14 cm on the right side. From the midpoint of the right pectineal ligament, the mean distance to the right CMOR was 2.37 ± 0.63 cm and the mean distance to the left CMOR was 2.15 ± 0.48 cm [34].

From these studies, we can conclude that during Burch colposuspension, AOVs, ACOVs and CMOR are at great risk of injury, especially if they pass medial to the deep femoral ring (Fig. 9).

In Figure 9, CMOR is located medial to the deep femoral ring and in close proximity to the most lateral stitch in the pectineal ligament. The incidence of AOVs, ACOVs and CMOR medial to the deep femoral ring varies in medical literature (5–42.5%). A recent study reported that the AOA lay medial to the deep femoral ring in 10% of cases [23]. Skandalakis and Skandalakis [45] stated 40% percentage of AOA passing medial to the deep femoral ring. Another study reported an artery that passed through the medial side of the deep femoral ring in 5% of the specimens observed. Moreover, there were comparatively larger veins, which ran medially to the deep femoral ring and opened into the external iliac vein (found in 42.5%) [8]. Injury of AOVs, ACOVs and CMOR lateral to the deep femoral ring during Burch colposuspension is possible, but less likely to occur. In the majority of cases AOVs, ACOVs and CMOR are located lateral to the deep femoral ring (60–90%) [23, 33, 45].

Furthermore, AOVs, ACOVs and CMOR are at risk of damaged during operations for vaginal wall de-

scent, uterovaginal prolapse and neovaginal reconstruction [34, 47]. Studies reported that pectopexy for pelvic organ prolapse is feasible procedure because the surgeon used a wide area in the pelvis and the strong nature of the pectineal ligament would decrease the postoperative recurrence rates [17, 34]. The pectineal ligament is the target for neovaginal attachment in Mayer-Rokitansky-Küster-Hauser syndrome. The syndrome is related with uterus aplasia and variable degrees of vaginal hypoplasia of its upper portion. Although different materials are used for creation of neovaginal attachment, sigmoid grafts are most common [28, 47].

Minimally invasive procedures, such as the TVT sling (introduced in 1998), the TOT sling (2002) and the TVT-Secur are used for treatment of SUI [46]. They involve the placement of slings under the midurethra through a retropubic (TVT) or transobturator (TOT) approach [46]. The TVT is considered a minimally invasive procedure that involved passage of needles through small vaginal and suprapubic skin incisions [27]. The TOT is a minimally invasive procedure, based on an entirely new concept of positioning of tape under the middle urethra horizontally through the obturator foramen [20]. The TVT-Secur is less invasive short tape method as anchoring the minitape in the obturator muscle avoids a full needle passage. The TVT-Secur has two suggested approaches — U-retropubic and lateral Hammock (obturator) [22]. In the U-approach, the tape is pushed along the periost behind the arc of the pubic bone at an angle of 45°, whereas in the Hammock Approach, the tape is pushed towards the obturator foramen [14]. Although TOT (the retropubic space is not entered, the needle tip penetrates the obturator externus muscle, the obturator membrane, and then rotates around the medial aspect of the pubic ramus) is associated with lower rate of AOVs, ACOVs and CMOR injury, studies reported damage to these vessels in all type of sling procedures [14, 20, 22, 27, 35, 46]. Montoya et al. [27] stated that during TVT-Secur procedure, the closest distance from the 45° and 90° anchor points to the ACOV was 1.6 and 1.5 cm, respectively. They described ACOV and CMOR as the same structure [27]. In a cadaveric study, Stavropoulou-Deli [46] stated that the average distance from the symphysis pubis to arterial CMOR was 52.4 mm and venous CMOR was 46.7 mm [27]. Darmanis et al. [11] reported an average distance between the CMOR and the symphysis pubis 40 mm – 96 mm, while Tor-
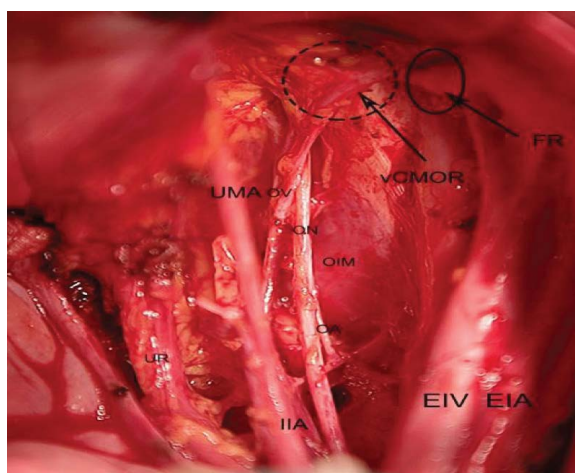
Figure 10. Venous corona mortis (CMOR) between OV and inferior epigastric vein. The anastomosis is located medial to the deep femoral ring — open surgery. Type V; EIV — external iliac vein; EIA — external iliac artery; IIA — internal iliac artery; UR — ureter; UMA — umbilical artery; ON — obturator nerve; OA — obturator artery; OV — obturator vein; OIM — obturator internus muscle; FR — deep femoral ring; vCMOR — venous corona mortis.

netta et al. [51] reported 30 mm – 90 mm [11, 36, 51]. The majority of authors concluded that average distance from the symphysis pubis to AOVs, ACOVs and CMOR exceeded 30 mm [25, 46]. Consequently, during TVT and TVT-Secur (U-approach) the tape is placed at a distance of 25 mm – 30 mm from the symphysis pubis [14, 46]. Larsson et al. [22] reported a complication of CMOR during TVT-Secur procedure [20]. Authors commented Larsson et al. [22] case and concluded that the injury of the CMOR happened in the attempt to place the TVT-Secur™ more upwardly, similar to the tape applied in the U position [14, 16, 20]. Gobrecht et al. [14] stated that the 45°-angle insertion could damage the AOVs, ACOVs and CMOR. Injuring the AOVs, ACOVs and CMOR could be avoided by inserting the tape in either a 0° angle (classic retropubic TVT) or a 90° angle (TVT-O, obturator) [14]. In our opinion, injury to AOVs, ACOVs and CMOR during TVT-sling procedures is more likely to occur if they are located medial to the deep femoral ring, as the closer proximity to the symphysis pubis (Fig. 10).

CONCLUSIONS

Aberrant obturator vessels, ACOVs and CMOR are encountered during different types of gynaecological operations. Intraoperative injury to AOVs, ACOVs and CMOR depends on the type of surgery and vessels' location behind the superior pubic ramus, and posterior aspect of the lacunar ligament. Our new

clinical classification might help gynaecologist to be familiar with AOVs, ACOVs, CMOR variations and to avoid injury during surgery.

Acknowledgements

Conflict of interest: None declared

REFERENCES

1. Al Talalwah W. A new concept and classification of corona mortis and its clinical significance. Chin J Traumatol. 2016; 19(5): 251–254, doi: 10.1016/j.cjtee.2016.06.004, indexed in Pubmed: 27780502.

2. Ates M, Kinaci E, Kose E, et al. Corona mortis: in vivo anatomical knowledge and the risk of injury in totally extraperitoneal inguinal hernia repair. Hernia. 2016; 20(5): 659–665, doi: 10.1007/s10029-015-1444-8, indexed in Pubmed: 26621137.

3. Balega J, Van Trappen PO. The sentinel node in gynaecological malignancies. Cancer Imaging. 2006; 6: 7–15, doi: 10.1102/1470-7330.2006.0002, indexed in Pubmed: 16520291.

4. Berberoğlu M, Uz A, Ozmen MM, et al. Corona mortis: an anatomic study in seven cadavers and an endoscopic study in 28 patients. Surg Endosc. 2001; 15(1): 72–75, doi: 10.1007/s004640000194, indexed in Pubmed: 11210207.

5. Bogliatto F, Bornstein J. Surgical procedures of preneoplastic and neoplastic conditions. Vulvar Disease. 2019: 401–412, doi: 10.1007/978-3-319-61621-6_59.

6. Borgno G, Micheletti L, Barbero M, et al. Topographic distribution of groin lymph nodes. A study of 50 female cadavers. J Reprod Med. 1990; 35(12): 1127–1129, indexed in Pubmed: 2283629.

7. Cesmebasi A, Baker A, Du Plessis M, et al. The surgical anatomy of the inguinal lymphatics. Am Surg. 2015; 81(4): 365–369, indexed in Pubmed: 25831182.

8. Chung S, Chengtsin LIU. The origin of the obturator artery and the blood vessels related to the femoral ring. Acta Anat Sinica. 1964; 2: 181–187.

9. Cibula D, Abu-Rustum NR. Pelvic lymphadenectomy in cervical cancer--surgical anatomy and proposal for a new classification system. Gynecol Oncol. 2010; 116(1): 33–37, doi: 10.1016/j.ygyno.2009.09.003, indexed in Pubmed: 19837449.

10. Cooper A. The anatomy and surgical treatment of inguinal and congenital hernia. Edinb Med Surg J. 1806; 2(6): 241–251.

11. Darmanis S, Lewis A, Mansoor A, et al. Corona mortis: an anatomical study with clinical implications in approaches to the pelvis and acetabulum. Clin Anat. 2007; 20(4): 433–439, doi: 10.1002/ca.20390, indexed in Pubmed: 16944498.

12. Drewes PG, Marinis SI, Schaffer JI, et al. Vascular anatomy over the superior pubic rami in female cadavers. Am J Obstet Gynecol. 2005; 193(6): 2165–2168, doi: 10.1016/j. ajog.2005.07.033, indexed in Pubmed: 16325635.

13. Faure JP, Hauet T, Scepi M, et al. The pectineal ligament: anatomical study and surgical applications. Surg Radiol Anat. 2001; 23(4): 237–242, doi: 10.1007/s00276-001-0237-1, indexed in Pubmed: 11694967.

14. Gobrecht U, Kuhn A, Fellman B. Injury of the corona mortis during vaginal tape insertion (TVT-Secur™ using the U-Approach). Int Urogynecol J. 2011; 22(4): 443–445, doi: 10.1007/s00192-010-1355-2, indexed in Pubmed: 21243484.

15. Han Y, Liu P, Chen C, et al. A digital anatomical study of the corona mortis in females. Minim Invasive Ther Allied Technol. 2017; 26(2): 111–118, doi: 10.1080/13645706.2016.1236818, indexed in Pubmed: 27830594.

16. Hubka P, Svabik K, Martan A, et al. A serious bleeding complication with injury of the corona mortis with the TVT-Secur procedure: two cases of contact of TVT-S with the corona mortis during cadaver study. Int Urogynecol J. 2010; 21(9): 1179–1180, doi: 10.1007/s00192-010-1190-5, indexed in Pubmed: 20532870.

17. Kale A, Biler A, Terzi H, et al. Laparoscopic pectopexy: initial experience of single center with a new technique for apical prolapse surgery. Int Braz J Urol. 2017; 43(5): 903–909, doi: 10.1590/S1677-5538.IBJU.2017.0070, indexed in Pubmed: 28727377.

18. Kashyap S, Diwan Y, Mahajan S, et al. The majority of corona mortis are small calibre venous blood vessels: a cadaveric study of north indians. Hip Pelvis. 2019; 31(1): 40–47, doi: 10.5371/hp.2019.31.1.40, indexed in Pubmed: 30899714.

19. Kinman CL, Agrawal A, Deveneau NE, et al. Anatomical relationships of burch colposuspension sutures. Female Pelvic Med Reconstr Surg. 2017; 23(2): 72–74, doi: 10.1097/SPV.0000000000000341, indexed in Pubmed: 27682747.

20. Kocjancic E, Crivellaro S, Oyama IA, et al. Transobturator tape in the management of female stress incontinence: clinical outcomes at medium term follow-up. Urol Int. 2008; 80(3): 275–278, doi: 10.1159/000127340, indexed in Pubmed: 18480630.

21. Kumar D, Rath G. Anomalous Origin of Obturator Artery from the Internal Iliac Artery. Int J Morphol. 2007; 25(3), doi: 10.4067/s0717-95022007000300028.

22. Larsson PG, Teleman P, Persson J. A serious bleeding complication with injury of the corona mortis with the TVT-Secur procedure. Int Urogynecol J. 2010; 21(9): 1175–1177, doi: 10.1007/s00192-010-1103-7, indexed in Pubmed: 20179906.

23. Lau H, Lee F. A prospective endoscopic study of retropubic vascular anatomy in 121 patients undergoing endoscopic extraperitoneal inguinal hernioplasty. Surg Endosc. 2003; 17(9): 1376–1379, doi: 10.1007/s00464-003-8800-y, indexed in Pubmed: 12802654.

24. Leite TF, Pires LA, Goke K, et al. Corona Mortis: anatomical and surgical description on 60 cadaveric hemipelvises. Rev Col Bras Cir. 2017; 44(6): 553–559, doi: 10.1590/0100-69912017006001, indexed in Pubmed: 29267551.

25. Micheletti L, Preti M. Surgery of the vulva in vulvar cancer. Best Pract Res Clin Obstet Gynaecol. 2014; 28(7): 1074––1087, doi: 10.1016/j.bpobgyn.2014.07.011, indexed in Pubmed: 25132277.

26. Missankov AA, Asvat R, Maoba KI. Variations of the pubic vascular anastomoses in black South Africans. Acta Anat

(Basel). 1996; 155(3): 212–214, doi: 10.1159/000147807, indexed in Pubmed: 8870790.

27. Montoya TI, Street JJ, Corton MM. Anatomic relationships of single-incision midurethral slings. Am J Obstet Gynecol. 2013; 208(1): 75.e1–75.e5, doi: 10.1016/j.ajog.2012.10.004, indexed in Pubmed: 23099191.

28. Morcel K, Camborieux L, Guerrier D. Programme de Recherches sur les Aplasies Müllériennes. Mayer-Rokitansky-Küster-Hauser (MRKH) syndrome. Orphanet J Rare Dis. 2007; 2: 13, doi: 10.1186/1750-1172-2-13, indexed in Pubmed: 17359527.

29. Nayak SB, Deepthinath R, Prasad AM, et al. A South Indian cadaveric study on obturator neurovascular bundle with a special emphasis on high prevalence of 'venous corona mortis'. Injury. 2016; 47(7): 1452–1455, doi: 10.1016/j.injury.2016.04.032, indexed in Pubmed: 27156835.

30. Ohba Y, Todo Y, Akashi D, et al. Incidence of metastasis in the circumflex iliac nodes distal to the external iliac nodes in ovarian cancer. Gynecol Oncol. 2012; 126(3): 387–390, doi: 10.1016/j.ygyno.2012.05.031, indexed in Pubmed: 22664060.

31. Okcu G, Erkan S, Yercan HS, et al. The incidence and location of corona mortis: a study on 75 cadavers. Acta Orthop Scand. 2004; 75(1): 53–55, doi: 10.1080/00016470410001708100, indexed in Pubmed: 15022807.

32. Pellegrino A, Damiani GR, Marco S, et al. Corona mortis exposition during laparoscopic procedure for gynecological malignancies. Updates Surg. 2014; 66(1): 65–68, doi: 10.1007/s13304-013-0245-9, indexed in Pubmed: 24390752.

33. Pick J, Anson B, Ashley F. The origin of the obturator artery. A study of 640 body-halves. Am J Anat. 1942; 70(2): 317–343, doi: 10.1002/aja.1000700206.

34. Pulatoğlu Ç, Doğan O, Medisoğlu MS, et al. Surgical anatomy of the pectineal ligament during pectopexy surgery: The relevance to the major vascular structures. Turk J Obstet Gynecol. 2020; 17(1): 21–27, doi: 10.4274/tjod.galenos.2020.21284, indexed in Pubmed: 32341826.

35. Rajan S, Kohli N. Retropubic hematoma after transobturator sling procedure. Obstet Gynecol. 2005; 106(5 Pt 2): 1199–1202, doi: 10.1097/01.AOG.0000161063.55834.27, indexed in Pubmed: 16260571.

36. Rusu MC, Cergan R, Motoc AG, et al. Anatomical considerations on the corona mortis. Surg Radiol Anat. 2010; 32(1): 17–24, doi: 10.1007/s00276-009-0534-7, indexed in Pubmed: 19636491.

37. Sakthivelavan S, Sendiladibban S, Aristotle S, et al. Corona mortis: a case report with surgical implications. Int J Anat Var. 2010; 3: 103–105.

38. Sanna B, Henry BM, Vikse J, et al. The prevalence and morphology of the corona mortis (Crown of death): A meta-analysis with implications in abdominal wall and pelvic surgery. Injury. 2018; 49(2): 302–308, doi: 10.1016/j.injury.2017.12.007, indexed in Pubmed: 29241998.

39. Sañudo JR, Mirapeix R, Rodriguez-Niedenführ M, et al. Obturator artery revisited. Int Urogynecol J. 2011; 22(10):

1313–1318, doi: 10.1007/s00192-011-1467-3, indexed in Pubmed: 21655978.

40. Sañudo JR, Roig M, Rodriguez A, et al. Rare origin of the obturator, inferior epigastric and medial circumflex femoral arteries from a common trunk. J Anat. 1993; 183 (Pt 1): 161–163, indexed in Pubmed: 8270471.

41. Sarikcioglu L, Sindel M, Akyildiz F, et al. Anastomotic vessels in the retropubic region: corona mortis. Folia Morphol. 2003; 62(3): 179–182, indexed in Pubmed: 14507043.

42. Selçuk İ, Tatar İ, Fırat A, et al. Is corona mortis a historical myth? A perspective from a gynecologic oncologist. J Turk Ger Gynecol Assoc. 2018; 19(3): 171–172, doi: 10.4274/jtgga.2018.0017, indexed in Pubmed: 29699960.

43. Selçuk İ, Uzuner B, Boduç E, et al. Pelvic lymphadenectomy: Step-by-step surgical education video. J Turk Ger Gynecol Assoc. 2020; 21(1): 66–69, doi: 10.4274/jtgga.galenos.2019.2018.0167, indexed in Pubmed: 30905139.

44. Shen P, Conforti AM, Essner R, et al. Is the node of Cloquet the sentinel node for the iliac/obturator node group? Cancer J. 2000; 6(2): 93–97, indexed in Pubmed: 11069226.

45. Skandalakis L, Skandalakis J. Surgical Anatomy and Technique. A Pocket Manual. 3rd ed. Springer-Verlag, New York 2009: 689–701.

46. Stavropoulou-Deli A, Anagnostopoulou S. Corona mortis: anatomical data and clinical considerations. Aust N Z J Obstet Gynaecol. 2013; 53(3): 283–286, doi: 10.1111/ajo.12076, indexed in Pubmed: 23551084.

47. Steinke H, Wiersbicki D, Völker A, et al. The fascial connections of the pectineal ligament. Clin Anat. 2019; 32(7): 961–969, doi: 10.1002/ca.23445, indexed in Pubmed: 31381189.

48. Takeshita S, Todo Y, Okamoto K, et al. Incidence of metastasis in circumflex iliac nodes distal to the external iliac nodes in cervical cancer. J Gynecol Oncol. 2016; 27(4): e42, doi: 10.3802/jgo.2016.27.e42, indexed in Pubmed: 27102250.

49. Tantchev L. Corona mortis: clinical and anatomical details. AkushGynecol. 2019; 58(1): 24–28.

50. Todo Y, Yamazaki H, Takeshita S, et al. Close relationship between removal of circumflex iliac nodes to distal external iliac nodes and postoperative lower-extremity lymphedema in uterine corpus malignant tumors. Gynecol Oncol. 2015; 139(1): 160–164, doi: 10.1016/j.ygyno.2015.07.003, indexed in Pubmed: 26186910.

51. Tornetta P, Hochwald N, Levine R. Corona mortis. Clin Orthop Relat Res. 1996; 329: 97–101, doi: 10.1097/00003086-199608000-00012.

52. Veit-Rubin N, Dubuisson J, Ford A, et al. Burch colposuspension. Neurourol Urodyn. 2019; 38(2): 553–562, doi: 10.1002/nau.23905, indexed in Pubmed: 30620096.

53. Vincent RL, Miles M. Laparoscopic Burch colposuspension for stress urinary incontinence: When, how, and why? OBG Manag. 2003; 15(2): 20–34.

54. Won HS, Kim JH, Lee UY, et al. Topographical relationships between the obturator nerve, artery, and vein in the lateral pelvic wall. Int Urogynecol J. 2016; 27(2): 213–218, doi: 10.1007/s00192-015-2806-6, indexed in Pubmed: 26224385.

R E V I E W   A R T I C L E

Anatomical review of the mandibular lingula for inferior alveolar nerve block

D.-Y. Choi[1] , M.-S. Hur[2]

[1]Department of Dental Hygiene, Catholic Kwandong University, Gangneung, South Korea
[2]Department of Anatomy, Catholic Kwandong University College of Medicine, Gangneung, South Korea

The purpose of this study was to perform a review of the literature related to the anatomy of the mandibular lingula and to provide information to improve the execution of effective anaesthesia of the inferior alveolar nerve in clinical practices of the mandible.

Prognathic mandibles have a lingula that is located more posterior and superior than non-prognathic mandibles. Most of the lingulae are located above the occlusal plane, but it is occasionally located at or below the occlusal plane. The lingula of the triangular shape was generally located slightly more superior and posterior than other shapes.

The mandibular lingula is an important anatomical landmark, and accurate information for exact lingula features is required during inferior alveolar nerve block anaesthesia. Proper evaluation of the lingula is key to effective anaesthesia and decreases the failure rate of the inferior alveolar nerve in clinical practices of the mandible. (Folia Morphol 2021; 80, 4: 786–791)

Key words: **mandible, inferior alveolar nerve, nerve block, anatomy, morphology, location**

INTRODUCTION

The mandibular lingula is often used clinically to approximate the location of the mandibular foramen. It is a salient structure with a tongue-shaped bony projection on the medial surface of the mandibular ramus near the mandibular foramen [23]. The mandibular foramen is the orifice of the mandibular canal, through which penetrates the inferior alveolar nerve, located inferiorly and posteriorly to the lingula. Thus, the mandibular lingula and mandibular foramen were considered as ideal anatomical landmarks for the surgeon, not only during inferior alveolar nerve block but also during surgical procedures such as orthognathic surgery [25].

The inferior alveolar nerve block is a widely used anaesthesia technique for the mandible. The most commonly used technique is called the direct approach, which includes inserting the needle into the pterygomandibular space by penetrating the buccinator muscle [12]. Once in this space, the aim is to put the local anaesthetic agent near the inferior alveolar nerve before it enters the mandibular foramen. The failure rate of the inferior alveolar nerve block has been reported to range from 10% to 39% [18]. This high failure rate can be attributed to various morphologies of the anatomical structures close to the inferior alveolar nerve, poor anaesthesia technique, psychological fear, or pathology [3].

The lingula is used for recognizing the site for injection of local anaesthetics or excision of the nerve for facial neuralgia [23]. Insufficient knowledge of the anatomy of the medial aspect of the mandibular ramus could be a reason for the failure of the inferior alveolar nerve block or complications such as nerve injury and haemorrhage [10, 11]. It is possible to avoid these complications when the clinician is able to identify the lingula correctly.

Several methodologies have been used to study the anatomical features of mandibular fractures in many previous studies. They include examination of the dry mandible, panoramic radiograph, and three-dimensional image obtained from cone-beam computed tomography (CBCT). An investigation into the anatomical structures of the dry mandible to the naked eye has been used for a long time to clarify its morphology as a traditional method. Because a dry mandible can be measured directly, the measurement results are relatively accurate. Recently, examination of anatomical structures has become possible using radiography. Panoramic radiography provides useful information for locating the position of the mandibular lingula and the mandible [9]. However, measurements from panoramic radiographs have been disputed because of considerable distortions or methodological errors, although, it may be possible to reduce most of the distortions when using the standardised positioning of the head and the use of a bite block [14]. Three-dimensional images obtained from CBCT were reconstructed using a computer. This allows for a complex measurement of the distance to be taken more easily because it is possible to make a virtual line or plane and set up various anatomic landmarks in the three-dimensional images.

The differences in study design, origin, and age of the investigated specimens could account for the highly variable results. Thus, the purpose of this study was to perform a review of the literature related to the anatomy of the mandibular lingula and to provide information to improve the execution of effective anaesthesia of the inferior alveolar nerve in clinical practices of the mandible.

MORPHOLOGY OF THE MANDIBULAR LINGULA

Various shapes of the lingula have been reported by many authors. These different morphological shapes were classified into several types according to the previously reported studies. Lima et al. [15] classi-fied the mandibular lingulae into three types based on its shape: triangular, rectangular, or trapezoid. Fabian [6] reported five types of lingula based on shape and size: large nodular, small nodular, large triangular, small triangular, and small bony spicule type.

Most studies were performed using the classification proposed by Tuli et al. [23], according to whom, the shapes of the lingula were classified into four different types:
— triangular type: has a wide base and a narrow rounded or pointed apex;
— truncated type: has a quadrangular top;
— nodular type: is nodular with variable size;
— assimilated type: is completely incorporated into the ramus of the mandible.

The distribution and frequency of the four different morphological types of lingula varied among different authors, according to population and race. A study using Indian dry mandibles [23] showed that the triangular type (68.5%) was the most common, followed by truncated (15.8%), nodular (10.9%), and assimilated (4.8%). Other studies on the North Indian population [4, 19] were of the same order. Likewise, Lopes et al. [16] reported that the most common shape of the lingula was the triangular type (41.3%) in a study of the Brazilian population, followed by truncated (36.3%), assimilated (11.9%), and nodular (10.5%). Similarly, Desai et al. [5] reported triangular type (51%) as the most common and assimilated (12%) as the least common.

However, other studies reported that the nodular type was the most common. Sekerci and Sisman [20] studied the shape of the lingula using CBCT data of an adult Turkish population and reported that the nodular type was most common, present in 51.2% of cases, while the truncated, triangular, and assimilated types were present in 32%, 14.1%, and 2.7% of cases, respectively. In other studies by Senel et al. [21] and Ahn et al. [1], the nodular type was the most prevalent, at 32.5% and 32.8%, respectively. These studies showed that the triangular type was more common than truncated.

In contrast, the most prevalent shape of lingula was truncated type and the least prevalent shape was assimilated type, according to the results of studies on Thai populations. Jansisyanont et al. [8] studied dried Thai adult mandibles and reported that the truncated type (46.2%) was the most common. This result was similar to that of Kositbowornchi et al. [14] who also reported that the most prevalent shape of the lingula was the truncated type (47.22%).

Table 1. Comparison between previous studies

Author (year) [Reference]	Population	Gender	ML–AM			ML–PM			ML–IM			ML–MN		
			Right	Left	Total	Right	Left	Total	Right	Left	Total	Right	Left	Total
Woo et al. (2002) [24]	Korean	Total			18.6									19.8
Jansisyanont et al. (2009) [8]	Thai	Male	20.9	20.6	20.6	18.2	18.4	18.0				16.9	16.8	16.6
		Female	20.2	20.1		17.4	17.3					16.0	15.9	
Samanta and Kharb (2012) [19]	Indian	Total	20.0	20.2	20.0	14.9	15.2	15.0				15.3	15.6	
Monnazzi et al. (2012) [17]		Total			16.5			14.6			27.1			16.4
Sekerci and Sisman (2014) [20]	Turkish	Male	18.2	17.3	16.8	13.6	14.0	13.0	35.5	36.3	33.4	17.2	15.9	15.3
		Female	16.0	15.6		12.4	12.0		30.9	30.9		14.0	14.2	
Senel et al. (2015) [21]		Total	18.4	18.7	18.5	16.7	17.1	16.9	37.6	39.1	38.3	18.1	18.1	18.1
Lima et al. (2016) [15]		Total	18.7	20.0		15.8	15.8		33.5	33.9		16.6	16.3	
Zhou et al. (2017) [25]		Male						18.2			35.3			15.7
		Female						17.0			30.5			15.5
Aps et al. (2018) [3]		Total	18.0	18.1		14.9	15.0		27.2	27.4		15.9	15.5	

ML–AM — mean distance between the mandibular lingula and the anterior border of the mandible; ML–PM — mean distance between the mandibular lingula and the posterior border of the mandible; ML–IM — mean distance between the mandibular lingula and the inferior border of the mandible; ML–ML — mean distance between the mandibular lingula and the mandibular notch; CBCT — cone-beam computed tomography

An elaborate description of the morphology of the triangular type has been illustrated by Tuli et al. [23]. The tip of the lingula in the triangular type was directed towards the mandibular condyle in 89.4% of cases and towards the posterior border of the ramus in 10.6% of cases. Then, they described that the anterior or upper border of the lingula in the triangular type was attached to the mandibular ramus in 88.5% of cases and well separated from the mandibular ramus in 11.5% of cases. They also depicted more details of the truncated type. The lingula in the truncated type had 3 borders — superior, inferior, and posteriorand between them were superior and inferior angles, directed towards the mandibular condyle and the posterior border of ramus, respectively. The posterior border of the lingula was slightly convex upwards in 69.2%, straight in 19.2%, and concave in 11.5% of cases.

LOCATION OF THE MANDIBULAR LINGULA

The position of the lingula has been described using several reference points or lines, such as the anterior and posterior border of the mandibular ramus, the deepest point of the mandibular notch, inferior border of the mandible, and the plane parallel to the occlusal plane (Table 1). The location of the lingula is affected by various factors, such as gender, age, and ethnicity. Even so, the mandibular lingula maintained the ratio location in a more posterior and superior position related to the central point of the mandibular ramus [15, 17, 19, 21, 24]. This was valid in all analysed gender and age groups, despite the entire mandibular growth [3], and whether the mandible was dentulous or edentulous [13]. It is also commonly proposed that the measurements in females were shorter than those observed in males [8, 20, 25].

The location of the lingula varies significantly with the skeletal pattern. Prognathic mandibles have a lingula that is located more posterior and superior than non-prognathic mandibles [2, 22]. Jung et al. [9] evaluated the location of the lingula in skeletal class I and class III patients using panoramic radiographs and concluded that most of the lingulae coincide with the level of the coronoid notch in skeletal class I patients and higher than the coronoid notch in class III patients.

Most of the lingulae are located above the occlusal plane, but it is occasionally located at or below the occlusal plane. According to Jansisyanont et al. [8], it was found that 80.1% of lingulae were above the occlusal plane and 19.9% of them were below the occlusal plane. Zhou et al. [25] found that only 0.8% of the lingulae were below the occlusal plane and 0.8% of them levelled with the occlusal plane. Aps et al. [3] studied the location of the mandibular lingula using CBCT data of paediatric patients who were 6 to 18 years old. All subjects were categorised according to age (6–9, 10–13, and 14–18 years old), and the lingulae were compared with the occlusal plane. In

total, 8.9% of the lingulae were located at or below the occlusal plane. As age increased, this anatomical feature showed a tendency to decrease. The number of lingulae below the occlusal plane is more numerous in the youngest group, while it is relatively unusual in adolescents between the ages of 14 and 18 years (Table 2).

A relationship has been discovered between the location of the lingula and its shape in the mandibular ramus. The lingula of the triangular shape was generally located slightly more superior and posterior than other shapes. It is important to consider this trend when performing surgical procedures including the mandibular ramus [9].

CLINICAL CONSIDERATIONS RELATED TO INFERIOR ALVEOLAR NERVE BLOCK

As there is a great degree of variability regarding the position of the mandibular lingula; it is difficult to define the accurate needling position and depth during the inferior alveolar nerve block. If the position of the lingula in the mandibular ramus can be confirmed, it will be much easier to achieve successful anaesthesia of the inferior alveolar nerve.

The location of the lingula was investigated, and the ideal injection point for inferior alveolar nerve block was suggested in previous studies. The horizontal distance from the anterior border of the mandibular ramus to the mandibular lingula (or mandibular foramen) was measured. The mean values are recommended as injection sites to deliver anaesthesia as safely and as effectively as possible (Table 3) [3, 7, 8, 20].

The recommended injection point varied among the different authors. Some reasons may explain why there are different values for each study. All subjects used in the studies had individual variations in anatomy. Some of the mandibles had a very pointed tip of the lingula, leading to a large length, while others had distinctly different lingula shapes on either side. Such anatomical variations may confuse the resulting distance and explain why there are different values for each study. Second, for the lingula to be fully visualised, the opacity and brightness of the CBCT images were adjusted. The manipulation of the image may have caused variability in some measurements. Another reason relates to the ethnic and racial backgrounds of the patients.

The proposed vertical location of the ideal injection site for the inferior alveolar nerve was based on the occlusal plane as a reference plane. Jansisyanont

Table 2. Percentage of the lingula at or below the occlusal plane

Author (year) [Reference]	Ages [years]	Study design	At or below the occlusal plane (%)
Jansisyanont et al. (2009) [8]	18–83	Dry mandible	19.9%
Zhou et al. (2017) [25]	18–36	CBCT	1.6%
Aps et al. (2018) [3]	6–18	CBCT	8.9%
	6–9		6.1%
	10–13		2.5%
	14–18		0.4%

CBCT — cone-beam computed tomography

Table 3. Mean values of horizontal location of the lingula or the mandibular foramen and the ideal injection point from anterior mandible (AM) for inferior alveolar nerve block suggested in previous studies

Author (year) [Reference]	Study design	Mean distance [mm]		Suggested injection point from AM
		ML–AM	MF–AM	
Jansisyanont et al. (2009) [8]	Dry mandible	20.6		20.6
Sekerci et al. (2014) [20]	CBCT	16.77		16.7
Findik et al. (2014) [7]	CBCT		R: 15.27 L: 15.41	15
Aps et al. (2018) [3]	CBCT	R: 18.0 L: 18.12		18

ML–AM — mean distance between the mandibular lingula and the anterior border of mandible; MF–AM — mean distance between the mandibular foramen and the anterior border of the mandible; AM — anterior border of mandible; CBCT — cone-beam computed tomography; L — left; R — right

et al. [8] and Sekerci et al. [20] measured the distance between the lingula and occlusal plane. The mean values were recommended as an injection site. Aps et al. [3] recommended a larger distance from the occlusal plane than other studies. They classified patients into three groups according to age and estimated the location of the lingula related to the occlusal plane. As age increased, the mean value of the distance from the occlusal plane to the lingula increased. The maximum distance also increased with age. They suggested that clinicians should theoretically aim at the maximum value (14 mm above all age groups) from the occlusal plane for mandibular block anaesthesia. Aiming for the maximum value from the occlusal plane as opposed to the mean value would prevent the clinician from injecting the needle too low and causing failure of the nerve block (Table 4).

Table 4. Mean values of vertical location of the lingula and the ideal injection point from the occlusal plane for inferior alveolar nerve block suggested in previous studies

Author (year) [Reference]	Study design	ML–OC [mm]			Suggested injection point from occlusal plane
		Mean	Minimum	Maximum	
Jansisyanont et al. (2009) [8]	Dry mandible	4.5	0.6	13.1	4.5
Sekerci et al. (2014) [20]	CBCT	3.6	1.3	8.2	3.6
Aps et al. (2018) [3]	CBCT	R: 5.11 L: 4.43	R: –2.77 L: –5.93	R: 13.29 L: 13.65	14

ML–OC — distance between the mandibular lingula and the occlusal plane; CBCT — cone-beam computed tomography; L — left; R — right

The mandibular lingula is an important anatomical landmark, and accurate information for exact lingula features is required during inferior alveolar nerve block anaesthesia. Proper evaluation of the lingula is key to effective anaesthesia and decreases the failure rate of the inferior alveolar nerve in clinical practices of the mandible.

Funding

Conflict of interest: None declared

REFERENCES

1. Ahn BS, Oh SH, Heo CK, et al. Cone-beam computed tomography of mandibular foramen and lingula for mandibular anesthesia. Imaging Sci Dent. 2020; 50(2): 125–132, doi: 10.5624/isd.2020.50.2.125, indexed in Pubmed: 32601587.
2. Akcay H, Kalabalık F, Tatar B, et al. Location of the mandibular lingula: Comparison of skeletal Class I and Class III patients in relation to ramus osteotomy using cone-beam computed tomography. J Stomatol Oral Maxillofac Surg. 2019; 120(6): 504–508, doi: 10.1016/j.jormas.2019.07.013, indexed in Pubmed: 31404678.
3. Aps JKM, Gazdeck LY, Nelson T, et al. Assessment of the location of the mandibular lingula in pediatric patients using cone beam computed tomography images. . J Dent Child (Chic). 2018; 85(2): 58–65, indexed in Pubmed: 30345955.
4. Asdullah M, Ansari AA, Khan MH, et al. Morphological variations of lingula and prevalence of accessory mandibular foramina in mandibles: A study. Natl J Maxillofac Surg. 2018; 9(2): 129–133, doi: 10.4103/njms.NJMS_13_16, indexed in Pubmed: 30546225.
5. Desai VC, Desai S, Shaik HS. Morphological study of mandible. J Pharmaceut Sci Res. 2014; 6(4): 175.
6. Fabian FM. Observation of the position of the lingula in relation to the mandibular foramen and the mylohyoid groove. Ital J Anat Embryol. 2006; 111(3): 151–158, indexed in Pubmed: 17312921.
7. Findik Y, Yildirim D, Baykul T. Three-dimensional anatomic analysis of the lingula and mandibular foramen: a cone beam computed tomography study. J Craniofac Surg. 2014; 25(2): 607–610, doi: 10.1097/SCS.0b013e-3182a30ec3, indexed in Pubmed: 24448541.
8. Jansisyanont P, Apinhasmit W, Chompoopong S. Shape, height, and location of the lingula for sagittal ramus osteotomy in Thais. Clin Anat. 2009; 22(7): 787–793, doi: 10.1002/ca.20849, indexed in Pubmed: 19644966.
9. Jung YH, Cho BH, Hwang JJ. Location and shape of the mandibular lingula: Comparison of skeletal class I and class III patients using panoramic radiography and cone-beam computed tomography. Imaging Sci Dent. 2018; 48(3): 185–190, doi: 10.5624/isd.2018.48.3.185, indexed in Pubmed: 30276155.
10. Kanno CM, de Ol, Cannon M, et al. The mandibular lingula's position in children as a reference to inferior alveolar nerve block. J Dent Child (Chic). 2005; 72(2): 56–60, indexed in Pubmed: 16294933.
11. Keros J, Kobler P, Baucić I, et al. Foramen mandibulae as an indicator of successful conduction anesthesia. Coll Antropol. 2001; 25(1): 327–331, indexed in Pubmed: 11787558.
12. Khoury JN, Mihailidis S, Ghabriel M, et al. Applied anatomy of the pterygomandibular space: improving the success of inferior alveolar nerve blocks. Aust Dent J. 2011; 56(2): 112–121, doi: 10.1111/j.1834-7819.2011.01312.x, indexed in Pubmed: 21623801.
13. Kim HJ, Lee HY, Chung IH, et al. Mandibular anatomy related to sagittal split ramus osteotomy in Koreans. Yonsei Med J. 1997; 38(1): 19–25, doi: 10.3349/ymj.1997.38.1.19, indexed in Pubmed: 9100479.
14. Kositbowornchai S, Siritapetawee M, Damrongrungruang T, et al. Shape of the lingula and its localization by panoramic radiograph versus dry mandibular measurement. Surg Radiol Anat. 2007; 29(8): 689–694, doi: 10.1007/s00276-007-0270-9, indexed in Pubmed: 17960323.
15. Lima FJC, Oliveira Neto OB, Barbosa FT, et al. Location, shape and anatomic relations of the mandibular foramen and the mandibular lingula: a contribution to surgical procedures in the ramus of the mandible. Oral Maxillofac Surg. 2016; 20(2): 177–182, doi: 10.1007/s10006-016-0547-4, indexed in Pubmed: 26781719.
16. Lopes P, Pereira G, Santos A. Morphological analysis of the lingula in dry mandibles of individuals in Southern Brazil. J Morphol Sci. 2017; 27(3-4).
17. Monnazzi MS, Passeri LA, Gabrielli MFR, et al. Anatomic study of the mandibular foramen, lingula and antilingula in dry mandibles, and its statistical relationship between the true lingula and the antilingula. Int J Oral Maxillofac Surg. 2012; 41(1): 74–78, doi: 10.1016/j.ijom.2011.08.009, indexed in Pubmed: 21955366.

18. Nusstein J, Reader Al, Beck FM. Anesthetic efficacy of different volumes of lidocaine with epinephrine for inferior alveolar nerve blocks. Gen Dent. 2002; 50(4): 372–5; quiz 376, indexed in Pubmed: 12640855.

19. Samanta P, Kharb P. Morphological analysis of the lingula in dry adult human mandibles of north Indian population. J Cranio-Maxillary Diseases. 2012; 1(1): 7, doi: 10.4103/2278-9588.102467.

20. Sekerci AE, Sisman Y. Cone-beam computed tomography analysis of the shape, height, and location of the mandibular lingula. Surg Radiol Anat. 2014; 36(2): 155–162, doi: 10.1007/s00276-013-1150-0, indexed in Pubmed: 23793815.

21. Senel B, Ozkan A, Altug HA. Morphological evaluation of the mandibular lingula using cone-beam computed tomography. Folia Morphol. 2015; 74(4): 497–502, doi: 10.5603/FM.2015.0114, indexed in Pubmed: 26620512.

22. Tengku Shaeran TA, Shaari R, Abdul Rahman S, et al. Morphometric analysis of prognathic and non-prognathic mandibles in relation to BSSO sites using CBCT. J Oral Biol Craniofac Res. 2017; 7(1): 7–12, doi: 10.1016/j.jobcr.2016.10.007, indexed in Pubmed: 28316914.

23. Tuli A, Choudhry R, Choudhry S, et al. Variation in shape of the lingula in the adult human mandible. J Anat. 2000; 197 (Pt 2): 313–317, doi: 10.1046/j.1469-7580.2000.19720313.x, indexed in Pubmed: 11005723.

24. Woo SS, Cho JY, Park WH, et al.. A study of mandibular anatomy for orthognathic surgery in Koreans. J Korean Ass Oral Maxillofacial Surgeons. 2002; 28(2): 126–131.

25. Zhou C, Jeon TH, Jun SH, et al. Evaluation of mandibular lingula and foramen location using 3-dimensional mandible models reconstructed by cone-beam computed tomography. Maxillofac Plast Reconstr Surg. 2017; 39(1): 30, doi: 10.1186/s40902-017-0128-y, indexed in Pubmed: 29109943.

VIA MEDICA

R E V I E W   A R T I C L E

Tensor vastus intermedius: a review of its discovery, morphology and clinical importance

T. Franchi (ID)

The University of Sheffield Medical School, Sheffield, United Kingdom

Background: This review aims to summarise the relevant literature surrounding the tensor vastus intermedius, a newly discovered muscle, and to discuss its morphology and potential clinical importance. No such review currently exists in the literature.

Materials and methods: A comprehensive literature search regarding the tensor vastus intermedius was performed using PubMed and Google Scholar in July 2020. Principles of Evidence-Based Anatomy and the Anatomical Quality Assessment Tool were employed to ensure a high-level review. All relevant papers were included and citation tracking was performed to uncover further publications.

Results: The tensor vastus intermedius is found in the anterior compartment of the thigh and has a similar morphology to the other vasti muscles. It has four main variations and a consistent neurovascular supply. The muscle has been implicated in a number of case reports and surgical procedures, which are described in detail in this paper.

Conclusions: In the 4 years since the tensor vastus intermedius was formally described, a significant amount of work has been done to help us understand its structure and function. Further efforts are needed to gain a full picture as to its clinical importance. As such, it is recommended that this muscle should be acknowledged in anatomical education. (Folia Morphol 2021; 80, 4: 792–798)

Key words: tensor vastus intermedius, quadriceps femoris muscle group, quinticeps, extensor apparatus of the knee, anatomical discovery

INTRODUCTION

The musculature of the human body has been a fascination of anatomists for many centuries. In book two of his groundbreaking work *De Humani Corporis Fabrica Libri Septem*, Andreas Vesalius intricately catalogued the structure and function of each muscle he observed during dissection [26]. Indeed, the 14 muscle-men engravings found in this book are still considered to be "arguably the most important of all illustrations in the history of medical science" [16]. Whilst anatomy's long history means that the

discovery of novel gross anatomy is now extremely unlikely [17], the development of new instruments and techniques does allow for original perspectives on familiar structures [19].

The standard characterisation of the quadriceps femoris muscle found in leading anatomy textbooks describes the group as being formed by the rectus femoris, vastus lateralis, vastus intermedius and vastus medialis [7, 21]. This definition is also reflected in the standard anatomical understanding of non-specialist anatomists and clinicians. However, research
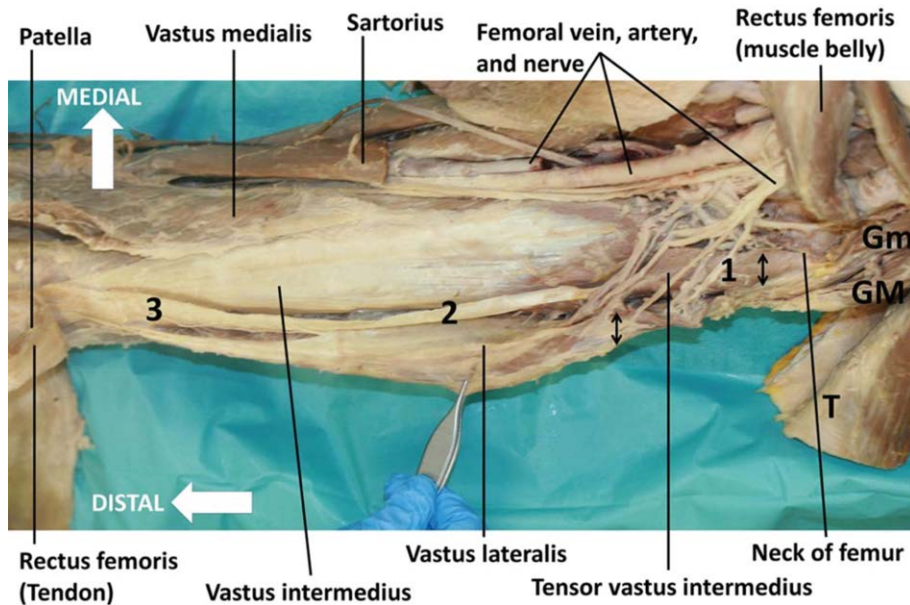
Figure 1. A dissection of tensor vastus intermedius. An anterior view of a left thigh, dissected to expose the quadriceps muscles, with rectus femoris, sartorius and tensor fasciae latae (T) transected and reflected. The muscle belly of tensor vastus intermedius (1), which can be seen between the muscle laminae of vastus lateralis and intermedius, merges into a broad aponeurosis (2) before becoming a tendinous structure (3). Gluteus medius (GM) and gluteus minimus (Gm) are also shown. (From [9] — permission to reproduce was obtained from Author and Publisher [License Number: 4895961375084]).

carried out by a Swiss/Australian group in 2016 led to the identification, characterisation and naming of an additional muscle belly — the tensor vastus intermedius [9]. The anatomy of this newly discovered muscle, which is found between the vastus lateralis and vastus intermedius, is described in detail throughout this paper.

Previous authors investigating the quadriceps femoris muscle group had already reported the possibility of an additional muscle belly, but any conclusions that were made labelled this muscle as a variation, attributable to the vastus lateralis [1, 2, 6, 27, 28]. Two of these studies reported that an additional muscle belly was observed in 29% [6] and 36% [27] of dissected thighs, respectively. Interestingly, it was noted in a later study that the separation of the muscle bellies of the quadriceps femoris would align with both evolutionary and developmental biological trends [28].

The remainder of this paper will explore and discuss the morphology of the tensor vastus intermedius, as well as its potential importance in a number of clinical settings.

MATERIALS AND METHODS

A comprehensive literature search regarding the tensor vastus intermedius was performed using Pub-Med and Google Scholar in July 2020. Principles of

Evidence-Based Anatomy were employed when conducting this narrative review in order to ensure that the synopsis of primary anatomical research presented is of a high-level [15]. When designing inclusion and exclusion criteria it was decided to include all full-length research articles, including case reports and university theses, as this is the first comprehensive review article on this topic and so it was considered appropriate to provide readers with a complete picture of the currently known research. Conference abstracts, letters to the editor and animal studies were excluded.

All studies deemed relevant for inclusion in this review were screened to assess any obvious risks of bias, by using the Anatomical Quality Assessment (AQUA) Tool [14]. No included studies were scored as high risk and therefore no studies were excluded. Citation tracking was performed to uncover further publications and, where relevant, data was extracted and is presented in the text of this paper. The papers' contents were then summarised in order to provide a critical analysis of the currently known information surrounding this muscle.

RESULTS AND DISCUSSION

Morphology

The tensor vastus intermedius is found in the anterior compartment of the thigh. It was first described
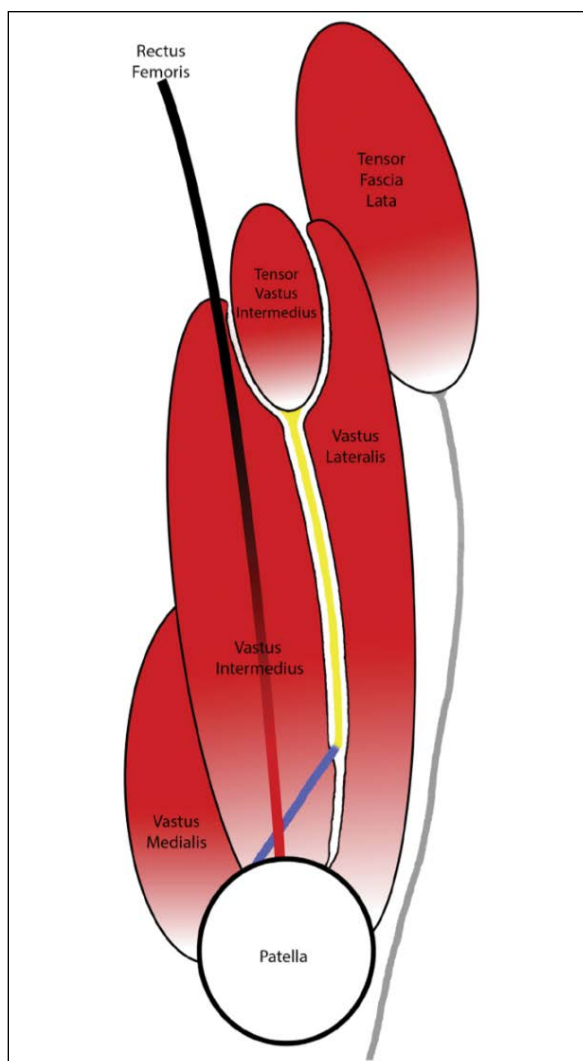
Figure 2. Schematic representation of tensor vastus intermedius. A schematic representation of the most common position for tensor vastus intermedius in relation to the quadriceps muscles and tensor fasciae latae. The aponeurosis of tensor vastus intermedius can be seen travelling between vastus lateralis and intermedius (yellow line), before becoming a tendon and turning obliquely (blue line). The iliotibial tract (grey line) is also shown. (From [22] — permission to reproduce was obtained from Author and Publisher [License Number: 4895961023137]).

as a new muscle in a cadaver study involving 26 lower limbs, in which the researchers identified a clearly separate muscle belly between vastus lateralis and vastus intermedius in 22 of 26 cases [9]. In the remaining 4 cases, proximal separation of the muscle bellies was not possible, for reasons described later in this paper. The tensor vastus intermedius is covered anteriorly by rectus femoris [9], takes origin from the anteroinferior aspect of the greater trochanter of the femur distal to the intertrochantric line, and inserts into the medial aspect of the patellar base [9]. The

position of tensor vastus intermedius in relation to its surrounding structures can be clearly seen in Figure 1.

Its morphology as a muscle follows a similar structure to the other vasti muscles, whereby it has a proximal muscle belly, which becomes a broad and flat aponeurosis before forming a tendinous structure which merges into the quadriceps femoris tendon [12]. The distal third of tensor vastus intermedius, the tendinous part, is interesting as it courses obliquely to its point of insertion [22]. This is shown in Figure 2. It has been hypothesised that this oblique nature of the tendon allows the muscle to counteract the forces produced by the medial muscles of the quadriceps femoris group [10].

Since its discovery, the anatomy of tensor vastus intermedius has been imaged and studied using both magnetic resonance imaging and sonography [12, 22]. This has allowed a better understanding of its structure in relation to the surrounding muscles, revealing a multilayered lateral extensor apparatus of the knee. This can be clearly seen in Figure 3. Indeed, the morphology of the tensor vastus intermedius between the vastus lateralis and intermedius, as well as the iliotibial band, has been described as "onion-like muscle layers" whereby "individual layers come together and lie above each other" [9, 12]. This beautiful architectural appearance has also been described as "layers of a husk of corn" [11] as the different overlying aponeurotic layers come together to form the quadriceps femoris tendon at the patella [13].

Whilst the most common form of tensor vastus intermedius is as described above, a number of studies have investigated variations in the muscle's morphology, which of course has direct implications into clinical practice. A study looking at 36 lower limbs reported the mean length of tensor vastus intermedius muscle bellies as 145.40 mm (standard deviation [SD] of 37.55 mm) and length of aponeurosis as 193.55 mm (SD of 42.32 mm), respectively [25]. Interestingly, this study also reported that both these measurements were greater in female cadavers compared to male ones.

Of even greater interest are the five distinct morphological variations described by two studies. Whilst the aponeurosis of tensor vastus intermedius is most commonly independent to vastus lateralis and intermedius, there appear to be frequent variations where it is either associated with vastus lateralis or intermedius, or both [9, 25]. In these cases, it can be more difficult to identify the muscle in question,
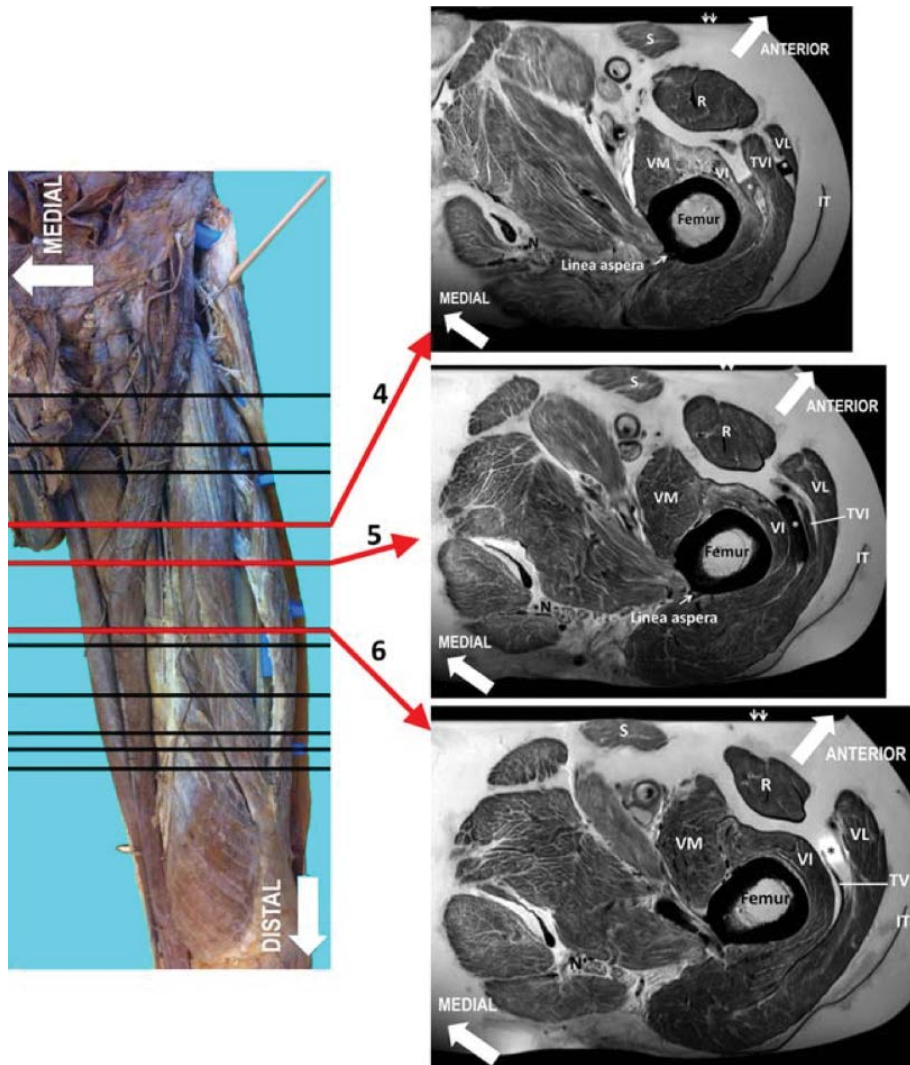
Figure 3. Magnetic resonance imaging (MRI) of tensor vastus intermedius. An anterior view of a left thigh alongside T2-weighted MRI. To allow better visualisation of muscles, foam blocks were placed between layers (marked in blue on the cadaver, and by an asterisk (*) on the MRI). Slice 4 (first MRI image) shows tensor vastus intermedius (TVI) muscle body between vastus lateralis (VL) and intermedius (VI). Slices 5 and 6 show tensor vastus intermedius thinning to an aponeurosis. Rectus femoris (R), sartorius (S), the iliotibial tract (IT) and the sciatic nerve (N) are also shown. (From [12] — permission to reproduce was obtained from Author and Publisher [License Number: 4895961225443]).

which perhaps is a factor involved in why it has only recently been described. There further appears to be a small number of cases where the tensor vastus intermedius is formed by two or more smaller intertwining muscle lamellae. The five reported variations in muscle morphology are outlined in Figure 4, and their relative prevalences are presented in Table 1. Interestingly however, a recent study investigating the tensor vastus intermedius found conflicting results when compared to the above. The study demonstrated the muscle in only seven of the 20 lower limbs studied [3], and the authors called into question the definition of this muscle. Perhaps, therefore, clarity is needed regarding the muscle's definition in order

to allow for objective and comparable research to be undertaken.

A further crucial element to consider is that of the tensor vastus intermedius' blood and nerve supply, which was critical in establishing that this muscle is indeed an independent structure and not simply a part of the vastus lateralis. The detailed dissections undertaken in the main study referred to in this paper [9], demonstrated that tensor vastus intermedius receives separate vascular supply to vastus lateralis, through individual branches from the transverse branch of the lateral circumflex femoral artery, as well as side branches from its ascending branch [4]. Similarly with regards to innervation of the tensor vastus interme-
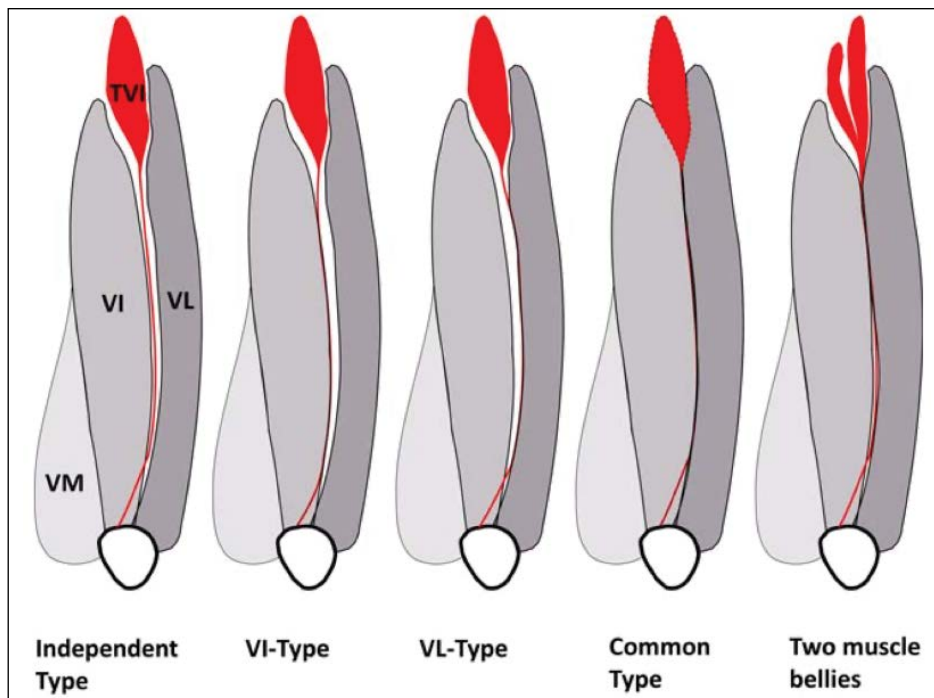
Figure 4. Variations of tensor vastus intermedius. A schematic representation of the variations in position of tensor vastus intermedius (TVI) in relation to vastus lateralis (VL) and intermedius (VI). A completely independent muscle belly and aponeurosis of tensor vastus intermedius represents the independent type. The case was labelled as VI-type if the aponeurosis was related to vastus intermedius, VL-type if related to vastus lateralis and common type if related to both muscles. In a small number of cadavers, regardless of type, there were multiple intervening muscle lamellae of the tensor vastus intermedius. These were labelled as two muscle bellies. (From [9] — permission to reproduce was obtained from Author and Publisher [License Number: 4895961375084]).

Table 1. Prevalence of tensor vastus intermedius variations

Study	Number of LLs	Independent type	VI-type	VL-type	Common type	Two muscle bellies
A	26	42.31%	23.08%	19.23%	15.38%	In 5 cases
B	36	33.33%	8.33%	30.56%	27.78%	In 3 cases
Average		37.82%	15.71%	24.89%	21.58%	13.78%

This table combines data from two studies (Study A: [9]; Study B: [25]) to provide some indication towards the prevalence of each variation of tensor vastus intermedius seen. Sixty-two lower limbs (LLs) were used between the two studies.

dius, the proximal muscle belly receives individual branches which originate from the lateral side of the posterior divisions of the femoral nerve [9, 25], with these branches being separable by dissection from the equivalent branches supplying the vastus lateralis and intermedius. Both these arteries and nerves are structures which are commonly studied by anatomy students, it would be worthwhile for teaching staff to encourage students to try and identify the muscle by tracing them on cadavers.

Based on the anatomy and morphology described above, it appears that tensor vastus intermedius has a significant role in controlling the motion of the patella, as well as in the extensor function of the knee [10]. Its aponeurosis is in close contact with the vastus intermedius and could potentially tighten it medially. In a similar fashion to the other muscles of the extensor compartment of the thigh, the tensor vastus intermedius is likely involved in both extension of the knee and prevention of flexion.

Clinical importance

Two case reports can be found in the literature that implicate the tensor vastus intermedius in the presenting pathology, and which align with the notion that the muscle is a distinct component of the extensor apparatus of the knee joint. The first [18], describes a 9-year-old girl with progressively limited knee flexion caused by an accessory quadriceps femoris muscle found between vastus lateralis and

intermedius, which in retrospect, is clearly the tensor vastus intermedius. The second and more recent case [10], comes from the authors who first described the muscle, and documents a 62-year-old woman with an isolated ruptured tensor vastus intermedius tendon following a stumble and prevention of a fall. Despite there only being two case reports to date, the fact that this muscle is only newly described combined with the fact that its anatomical appearance and relationship with vastus lateralis and intermedius makes it hard to identify, likely means that many previous injuries have simply been attributed to the vastus lateralis.

The tensor vastus intermedius has also been identified in a recent cadaver report of a seven-headed quadriceps femoris. The authors note that an awareness of this additional muscle may provide clinicians with a further differential diagnosis when investigating anterior thigh pain [23]. This novel research may therefore allow clinicians to better characterise injuries of the quadriceps femoris muscle group. To date however, the exact role of the tensor vastus intermedius in the function of the quadriceps muscle group remains unclear [24].

An understanding of the tensor vastus intermedius also has implications on surgical applications and approaches. Anterolateral thigh flaps are a versatile and widely used flap used to provide skin, muscle and fascia for reconstructions following major head and neck surgery [20], breast mastectomy or coronary bypass surgery [5]. Variation in quadriceps femoris muscle anatomy affects surgeons' ability to harvest these flaps, and indeed authors have reported a case where aberrant fusion of the vastus lateralis and intermedius prevented successful harvest of an anterolateral thigh flap mid-surgery [20]. It is very likely that this fusion represented a common type variation of tensor vastus intermedius (as previously described with reference to Fig. 4). A further example of surgical importance is seen when considering the direct anterior approach to the hip, which is commonly used in performing total hip replacement surgery. Authors have demonstrated that if a distal extension of the procedure is needed, in the case of operative complications such as femoral fracture, there is an increased risk of damaging the neurovascular bundles associated with the quadriceps femoris [8]. This potentially damages the tensor vastus intermedius, and so having a complete anatomical understanding of the muscle and its neurovasculature can al-low surgeons to make operative decisions. Finally, as the tensor vastus intermedius inserts into the patella, a better understanding of the quadriceps femoris tendon would allow improved radiological and surgical interpretation of injuries to the extensor apparatus of the knee [29].

The above case reports and surgical examples demonstrate the significance of this novel research, and the importance that properly defining and understanding the tensor vastus intermedius has on a number of clinical applications. There is therefore also an argument to be made for including this muscle in the required content when designing and delivering anatomical education programmes to anatomy and medical students.

CONCLUSIONS

Whilst discovering novel gross anatomy is rare, better characterising and understanding the structures which anatomists see still furthers our knowledge and appreciation for the human body. In the 4 years since the tensor vastus intermedius was formally described [9], a significant amount of work has been done to help us understand its structure and function. However, the answer to the latter point, specifically in relation to its contribution to the quadriceps muscle group, is still largely unanswered.

This paper has extensively described the morphology of this muscle, touching on both its anatomical variations and independent neurovascular supply. Further, the cadaver studies documenting this muscle are necessary for a number of reasons: "to better understand the biomechanical limitations of this muscle; to define the implications on surgical approaches of the hip and thigh; and to discover how this muscle can be utilised in surgical procedures" [4]. Indeed, to answer these questions, a strong understanding of the muscle's anatomy is required. Upon reflection on the anatomy of this new muscle, it appears to be similar in morphology to the plantaris muscle. Perhaps therefore there are synergies to be made between their structures and functions.

Whilst the researchers in this field are starting to gain a clearer picture of the role tensor vastus intermedius has in both normal and pathological states, further studies, both in cadavers and living participants, are needed to fully uncover the story of this newly discovered muscle.

Conflict of interest: None declared

REFERENCES

1. Becker I, Woodley SJ, Baxter GD. Gross morphology of the vastus lateralis muscle: An anatomical review. Clin Anat. 2009; 22(4): 436–450, doi: 10.1002/ca.20792, indexed in Pubmed: 19306318.

2. Becker I, Baxter GD, Woodley SJ. The vastus lateralis muscle: an anatomical investigation. Clin Anat. 2010; 23(5): 575––585, doi: 10.1002/ca.20974, indexed in Pubmed: 20309954.

3. Bonnechère B, Louryan S, Feipel V. Triceps, quadriceps or pentaceps femoris? Need for proper muscle definition. Morphologie. 2020; 104(345): 77–84, doi: 10.1016/j.morpho.2019.06.001, indexed in Pubmed: 31296371.

4. Collins CT. Anatomical investigation of the tensor vastus intermedius in the quadriceps muscle group. MSc Thesis, University of North Texas 2017.

5. Goel S, Arora J, Mehta V, et al. Unusual disposition of lateral circumflex femoral artery: Anatomical description and clinical implications. World J Clin Cases. 2015; 3(1): 85–88, doi: 10.12998/wjcc.v3.i1.85, indexed in Pubmed: 25610855.

6. Golland JA, Mahon M, Willan PL. Anatomical variations in human quadriceps femoris muscles. J Anat. 1986; 146(1): 263–264.

7. Gosling JA, Harris PF, Humpherson JR, Whitmore I, Willan PLT. Human anatomy: color atlas and textbook. Elsevier and Mosby, Missouri 2008.

8. Grob K, Monahan R, Gilbey H, et al. Distal extension of the direct anterior approach to the hip poses risk to neurovascular structures: an anatomical study. J Bone Joint Surg Am. 2015; 97(2): 126–132, doi: 10.2106/JBJS.N.00551, indexed in Pubmed: 25609439.

9. Grob K, Ackland T, Kuster MS, et al. A newly discovered muscle: The tensor of the vastus intermedius. Clin Anat. 2016; 29(2): 256–263, doi: 10.1002/ca.22680, indexed in Pubmed: 26732825.

10. Grob K, Fretz C, Kuster MS. Knee pain associated with rupture of tensor vastus intermedius, a newly discovered muscle: a case report. J Clin Case Rep. 2016; 6(7), doi: 10.4172/2165-7920.1000828.

11. Grob K, Manestar M, Filgueira L, et al. New insight in the architecture of the quadriceps tendon. J Exp Orthop. 2016; 3(1): 32, doi: 10.1186/s40634-016-0068-y, indexed in Pubmed: 27813020.

12. Grob K, Manestar M, Gascho D, et al. Magnetic resonance imaging of the tensor vastus intermedius: A topographic study based on anatomical dissections. Clin Anat. 2017; 30(8): 1096–1102, doi: 10.1002/ca.22981, indexed in Pubmed: 28833609.

13. Grob K, Manestar M, Filgueira L, et al. The interaction between the vastus medialis and vastus intermedius and its influence on the extensor apparatus of the knee joint. Knee Surg Sports Traumatol Arthrosc. 2018; 26(3): 727–738, doi: 10.1007/s00167-016-4396-3, indexed in Pubmed: 28124107.

14. Henry BM, Tomaszewski KA, Ramakrishnan PK, et al. Development of the anatomical quality assessment (AQUA) tool for the quality assessment of anatomical studies included in meta-analyses and systematic reviews. Clin Anat. 2017; 30(1): 6–13, doi: 10.1002/ca.22799, indexed in Pubmed: 27718281.

15. Henry BM, Tomaszewski KA, Walocha JA. Methods of Evidence-Based Anatomy: a guide to conducting systematic reviews and meta-analysis of anatomical studies. Ann Anat. 2016; 205: 16–21, doi: 10.1016/j.aanat.2015.12.002, indexed in Pubmed: 26844627.

16. Kemp M. A drawing for the Fabrica; and some thoughts upon the Vesalius muscle-men. Med Hist. 1970; 14(3): 277–288, doi: 10.1017/s002572730001557x, indexed in Pubmed: 4921979.

17. Kumar A, Ghosh SK, Faiq MA, et al. A brief review of recent discoveries in human anatomy. QJM. 2019; 112(8): 567–573, doi: 10.1093/qjmed/hcy241, indexed in Pubmed: 30335170.

18. Labbé JL, Peres O, Leclair O, et al. Progressive limitation of knee flexion secondary to an accessory quinticeps femoris muscle in a child: a case report and literature review. J Bone Joint Surg Br. 2011; 93(11): 1568–1570, doi: 10.1302/0301-620X.93B11.27396, indexed in Pubmed: 22058313.

19. Neumann PE. Another new organ! is this a golden age of discovery in anatomy? Clin Anat. 2018; 31(5): 648–649, doi: 10.1002/ca.23184, indexed in Pubmed: 29664145.

20. Omakobia E, Liew C, Berridge N, et al. A rare case of aberrant quadriceps muscle anatomy preventing anterolateral thigh flap harvest. JPRAS Open. 2016; 7: 19–22, doi: 10.1016/j.jpra.2016.01.002.

21. Paulsen F, Waschke J. Sobotta atlas of anatomy. Elsevier and Urban & Fischer, Munich 2018.

22. Rajasekaran S, Hall MM. Sonographic appearance of the tensor of the vastus intermedius. PM R. 2016; 8(10): 1020–1023, doi: 10.1016/j.pmrj.2016.04.002, indexed in Pubmed: 27108157.

23. Ruzik K, Waśniewska A, Olewnik Ł, et al. Unusual case report of seven-headed quadriceps femoris muscle. Surg Radiol Anat. 2020; 42(10): 1225–1229, doi: 10.1007/s00276-020-02472-0, indexed in Pubmed: 32318799.

24. Sahinis C, Kellis E, Galanis N, et al. Intra- and inter-muscular differences in the cross-sectional area of the quadriceps muscles assessed by extended field-of-view ultrasonography. Med Ultrason. 2020; 22(2): 152–158, doi: 10.11152/mu-2302, indexed in Pubmed: 32190847.

25. Veeramani R, Gnanasekaran D. Morphometric study of tensor of vastus intermedius in South Indian population. Anat Cell Biol. 2017; 50(1): 7–11, doi: 10.5115/acb.2017.50.1.7, indexed in Pubmed: 28417049.

26. Vesalius A. De humani corporis fabrica libri septem. Johannes Oporinus, Basel 1543.

27. Willan PL, Mahon M, Golland JA. Morphological variations of the human vastus lateralis muscle. J Anat. 1990; 168: 235–239, indexed in Pubmed: 2323995.

28. Willan PLT, Ransome JA, Mahon M. Variability in human quadriceps muscles: quantitative study and review of clinical literature. Clin Anat. 2002; 15(2): 116–128, doi: 10.1002/ca.1106, indexed in Pubmed: 11877790.

29. Yablon CM, Pai D, Dong Q, et al. Magnetic resonance imaging of the extensor mechanism. Magn Reson Imaging Clin N Am. 2014; 22(4): 601–620, doi: 10.1016/j.mric.2014.07.004, indexed in Pubmed: 25442025.

REVIEW ARTICLE

Anatomy of lumbar facet joint: a comprehensive review

S. Kapetanakis[1, 2], N. Gkantsinikoudis[1]

[1]Spine Department and Deformities, Interbalkan European Medical Centre, Thessaloniki, Greece
[2]Department of Minimally Invasive and Endoscopic Spine Surgery, Athens Medical Centre, Athens, Greece

Lumbar facet joints (LFJs) are diarthrodial joints which provide articulation between two adjacent lumbar vertebrae. LFJs represent complex anatomic structures with multifaceted biomechanical and functional characteristics. They are theorized as structures of crucial clinical significance since their degenerative morphologic alterations are frequently related to emergence of low back pain. Despite the emerging interest in describing LFJs anatomy in recent years, precise description of LFJs innervation remains controversial. In this comprehensive review, anatomy and biomechanical importance of LFJs and associated adjacent extra-articular structures are thoroughly presented. Furthermore, LFJs innervation in respect to current literature data is punctually analysed. Knowledge of anatomy and innervation LFJs of critical importance for clinicians and spine surgeons, so that patients are properly evaluated and related therapeutic procedures are rationally performed. (Folia Morphol 2021; 80, 4: 799–805)

Key words: lumbar vertebrae, zygapophyseal joints, mammillo-accessory ligament, biomechanics, facet joint tropism, dorsal ramus, medial branch

INTRODUCTION

Facet joints (FJ), which are also classically described as apophyseal or zygapophyseal joints, represent the only synovial joints of spine [16, 26]. They are paired diarthrodial joints, posterolaterally articulating the posterior arch between adjacent vertebral levels [26]. Lumbar facet joints (LFJs) constitute primary stabilisers of vertebral column, enabling alongside movements as extension, flexion and rotation [4, 31].

The aim of this review article is to describe the precise anatomy of LFJs according to contemporary literature data. Particular emphasis is given to innervation of LFJs.

ANATOMY OF ARTICULAR AND EXTRA-ARTICULAR ELEMENTS

Articular processes and cartilage

Lumbar facet joints are comprised by the articulation of superior and underlying adjacent vertebra via the paired inferior and superior articular processes, respectively [10, 16]. The major superior and the minor inferior articular processes (SAP and IAP) represent bony protuberances, emerging vertically from the coalescence of pedicles and laminae of respective vertebral arch, posteriorly to the ipsilateral transverse process [16, 26]. SAP and IAP are lined with articular hyaline cartilage over the subchondral

bone [26]. Hyaline cartilage of LFJs is characterised by poor vascularisation and cellular infiltration, featuring a considerable healing inability after traumatisation [24]. Articular surfaces of SAP and IAP feature a consistently different morphological pattern. Hence, SAP are characterised by a more concave articular surface, whereas IAP by a more convex one [16, 24]. In addition, orientation of SAP and IAP in sagittal and coronal planes features a noteworthy differentiation. IAP of superior vertebral level faces an anterior and lateral direction, whereas SAP lies posteriorly, facing medially [26].

LFJs articular cavity

Lumbar facet joints cavity may be anatomically divided in the FJ articular space and the FJ recesses, featuring a capacity of 1–2 mL [26, 36]. FJ space represents the anatomic space between the articular cartilage of articulating facets [36]. In contrast, FJ recesses are formed by the redundant encapsulation of LFJ by capsular ligament at the superior and inferior parts of the joint, containing adipose tissue or minor synovial villi [10]. Thorpe Lowis et al. [36] studied 19 cadaveric specimens in order to determine the precise anatomic characteristics of FJ recesses in various spinal regions. It was concluded that FJ recesses presented specific characteristics in respect to particular intervertebral levels. LFJs recesses were equally large and anteromedially and posteromedially located. The anteromedial recess was encountered superiorly, emerging over the upper end of SAP of underlying vertebra. In contrast, posteromedial recess surrounded the lower edge of IAP of supernatant vertebra. LFJs cavity featured no direct communication with the retrodural space, demonstrating an anatomically clear delimitation [36]. LFJ cavity and recesses are detectable in radiologic evaluation with magnetic resonance imaging (Fig. 1).

LFJs capsular ligament

Lumbar facet joints are, similarly to other synovial diarthrodial joints, completely encapsulated by a capsular ligament (LFCL). LFCL is histologically composed by two distinct layers: an outer layer of parallel with lateral-medial direction and densely organized collagen bundles, and an inner layer of elastic fibres with inconsistent orientation [5, 16]. Furthermore, LFCL features rich innervation with autonomic and nociceptive nerve fibres, which may reproduce pain in cases of inflammatory or mechanical irritation [26, 31].

Figure 1. Representation of facet joint cavity (red arrow) and the anteromedially located superior recess (white arrow) of L3–L4 facet joint in a normal lumbar magnetic resonance imaging.

Lumbar facet joints capsular ligament has an important role in maintaining the stability of LFJs. The presence of collagen and elastin administrates substantial mechanical support against shear and tensile forces developed during motion and vertebral loading. LFCL bears a remarkable biomechanical role during various movements of LFJs. It is extended during LFJs lateral bending or rotation. Hence, lateral-medial orientated capsular fibres feature extension along LFJs direction, providing functional resistance and stability. On the other hand, flexion or extension of LFJs is associated with emergence of crucial shear stress, transverse to LFJs direction. In this dynamic condition, LFCL fibres feature also a shear stress transverse to their alignment, providing great resistance [5].

Mammillo-accessory ligament

Mammillo-accessory ligament (MAL) represents a ligamentous structure bridging the bony mammillary (MP) and accessory processes (AP) of the lumbar vertebra bilaterally. MP constitutes a circular bony protuberance located at the posterior border of SAP. AP is, on the other side, a relatively lesser and sharpening bony structure encountered at the postero-inferior portion of each transverse process root. Ipsilateral MP and AP are connected by the ligamentous MAL (Fig. 2) [12]. MAL constitutes a portion of the medial aspect of intertransverse ligament, featuring a noteworthy tendency to ossification [31].

Shuang et al. [31] dissected 12 cadaveric specimens, in order to determine the precise anatomy of
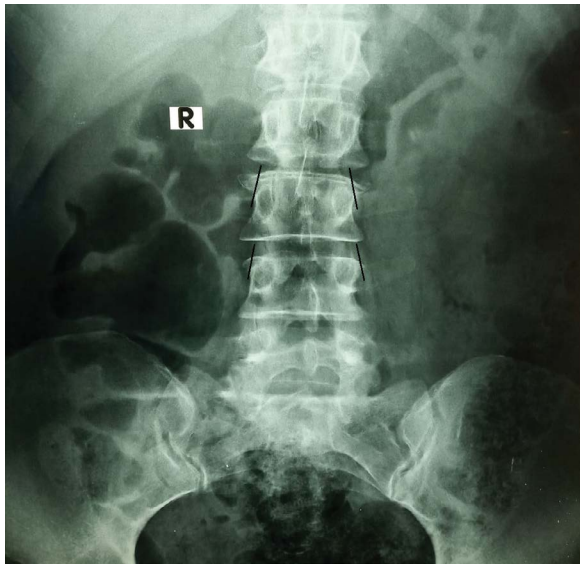
Figure 2. Conceivable representation of mammillo-accessory ligament in an anteroposterior lumbar spine radiograph.

medial branch of spinal dorsal ramus. It was inter alia concluded that the abovementioned anatomic structures form a true fibro-osseous canal, which is anatomically characterized by 4 distinct walls: a superior (MP), an inferior (AP), an anterior (the bony groove between MP and AP) and a posterior (MAL). The fibro-osseous canal displays an oblique direction, encountered at the dorsal portion of SAP and origin of transverse process [31]. In the case of MAL ossification, this canal becomes completely osseous [12, 31].

BIOMECHANICAL DATA

The three-dimensional LFJs and the anteriorly located intervertebral disc at each lumbar spine level compose an anatomic entity described as spinal segment, "three-joint complex" or articular triad [15, 16, 21, 23, 26, 32, 38]. These articular structures are theorised to constitute a single unit since the emergence of degenerative alterations in one joint has a subsequent influence on the biomechanical behaviour of the whole unit [26]. Furthermore, the harmonised function of these structures prevents potentially injurious dynamic states, warranting alongside physiological motional activity.

Functionally, the intervertebral disc is majorly responsible for the transmission of axial-compressive forces [16]. In contrast, osseous LFJs are primarily charged with the stabilization of spinal motion segment [2, 3, 16]. However, many biomechanical studies have demonstrated that LFJs also contribute

to transfer of implemented axial compressive load on the spine [1, 24, 26, 28, 32]. LFJs may bear up to 25% of this load, depending on the motion status at each case [24, 41]. However, the underlying mechanisms of this transmission remain unclear. The nearly vertical inclination of LFJs articular surfaces in conjunction with the existent low friction considerably complicates this description. Inoue et al. [16] reviewed existing literature data on the biomechanical behaviour of LFJs in various dynamic conditions. It was concluded that LFJs may contribute to axial compressive load transfer by three potential mechanisms: by articular surfaces, by LFCL and by the direct connection between the vertebral arch or the pars interarticularis and the tips of articular processes [16].

As stated above, LFJs have been delineated as the primordial lumbar spine stabilizers [22, 32]. LFJs stabilize the respective motion segment in extension and flexion, restricting also axial rotation [26, 39]. More specifically, medial and posterior portion of LFJs instates the major resistance to antero-olisthesis [3]. Comparatively, anatomic construction of LFJs relatively allows flexion-extension motions in sagittal planes, but noteworthy limits axial rotation, so that rotatory instability is prevented [32, 39].

Nevertheless, this motion-restrictive pattern may vary according to each lumbar level. This variation is majorly attributed to the differentiated LFJs orientation. LFJs are oriented 82–86 degrees in regards to the axial plane and 15–70 degrees in regards to the sagittal [5]. Nonetheless, LFJs orientation features a gradual coronal to sagittal conversion from proximal to distal levels [3]. At L1–L2 spinal motion segment, the angle between articular surfaces of SAPs is 30 degrees. However, this angle features a considerable distribution from 30 to 90 degrees in distal (L4–S1) segments. This peculiarity of LFJs orientation in distal segments is profoundly responsible for the emergence of lower resistance to rotational motion [3, 22]. Particular anatomic studies have depicted that the orientation of LFJs gradually approaches the sagittal plane with age [19]. However, the precise contribution of this alteration to further degenerative damage of spinal segment is not adequately understood [18].

LUMBAR FACET JOINTS TROPISM

Lumbar facet joints tropism (LFJT) is defined as the existing asymmetry between right and left LFJs angle [8, 13, 17, 37, 40]. Bogduk [6] initially described LFJT as the status where LFJs feature a rotational incongru-

ity in respect to axial plane, resulting in subsequent asymmetry. More recent studies identified that LFJT may be present in all planes. Therefore, LFJT may also be theorised as the subsistence of asymmetry between left and right LFJs angles in sagittal or coronal planes as well [3, 26]. This asymmetry is in the majority of cases relatively negligible, under 5 degrees in range. There is currently no universal consensus about the consideration of clinically significant LFJT. Hence, LFJs angulation may normally vary from 5 to 10 degrees [3].

Mohanty et al. [23] performed a retrospective cross-sectional study, in order to elucidate the prevalence of LFJT. For this purpose, 566 intact spinal motion segments from 124 computed tomography scans of spinal trauma patients were analysed. Results showed that LFJT featured greater prevalence in L4–L5 and L5–S1 levels, with the percentages of 47.82% and 38.5%, respectively. Authors concluded that these results may offer an explanation for the more frequent occurrence of lumbar disc herniation and related degenerative disorders as lumbar arthrosis and degenerative spondylolisthesis encountered at these levels [23]. This thesis has been also adopted from other studies in recent literature [3, 14, 26].

LUMBAR FACET JOINTS INNERVATION

Lumbar facet joints innervation is derived by the medial branch of the lumbar dorsal rami, or, as also known, posterior branches of the lumbar spinal nerves [31]. For many years, clinical importance of these structures was not adequately recognized. Hence, precise description of their anatomy was not present even in well-established anatomy atlases [19]. Bogduk et al. [7] were the first to provide a thorough analysis of posterior branches of lumbar spinal nerves anatomy in 1982.

The spinal nerve is divided into four distinct branches, after its exit from the respective intervertebral foramen; the communicating branch, the meningeal branch, the ventral ramus and the smaller dorsal ramus (DR) [31]. At levels L1–L4, DR is separated from the spinal nerve at an approximately right angle [19, 29]. They subsequently traverse the vertebral foramen, featuring then a dorsal and caudal course [7, 9, 30]. DR is from that point encountered at the orifice formed by the superior border of the adjacent transverse processes and the inferior border of the respective LFJ [19, 20]. This final aspect of DR
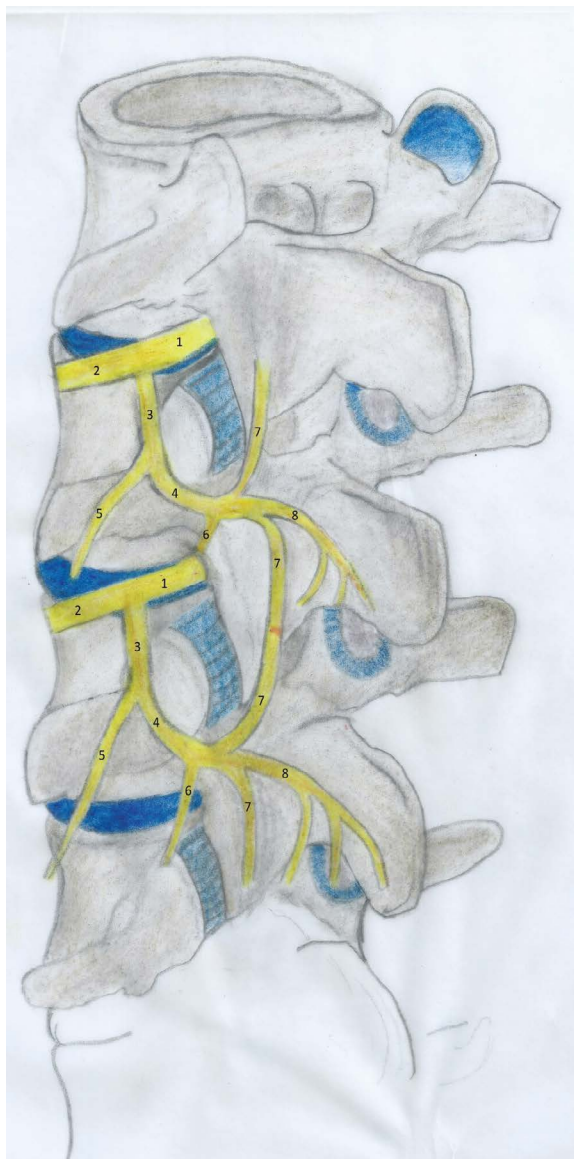
Figure 3. Schematic representation of lumbar dorsal ramus and its branches; 1 — lumbar spinal nerve; 2 — ventral ramus, 3 — dorsal ramus; 4 — medial branch of dorsal ramus; 5 — lateral branch of dorsal ramus; 6 — muscular branch of medial branch of dorsal ramus; 7 — articular branches of medial branch of dorsal ramus; 8 — cutaneous branches of medial branch of dorsal ramus.

is located at the medial portion of intertransverse musculature (Fig. 3) [31].

Dorsal ramus bifurcates, circa 5–10 mm distal to the abovementioned orifice, into a medial and a lateral branch, forming a 30-degree angle [19, 20]. This division is encountered at the superior edge of the underlying transverse process. There are multiple communicating branches between the adjacent lateral branches, medial branches and dorsal rami [31]. Nerve fibres composition for both branches is duplex, containing sensory as well as motor fibres. Ramifica-

tion of DR presents also a regional significance; lateral branch innervates tissues lateral to LFJs whereas medial provides innervations to the structures located medially to LFJs line [33] (Fig. 3).

Bogduk et al. [7] proposed that ramification of DR was triple, describing also a distinct intermediate branch in addition to medial and lateral. This thesis was later adopted from other authors as well. Middle or intermediate branch may co-exist with lateral branch in a short common trunk or separate directly from the DR. It is theorized that middle branch provides innervation to the longissimus lumbar muscle [19]. Furthermore, middle branch may also feature rich anastomoses with the other branches, thereby composing complex neural plexuses. Despite the published data about the anatomy of intermediate branch, dichotomy of DR into medial and lateral branches represents the majorly acceptable standard in the literature [31].

After its emergence, medial branch traverses the superior border of the underlying transverse process, proximal to its origin [27]. It then passes between the bases of SAP and adjacent transverse process, traversing the dorsal portion of intertransverse ligament. Medial branch is at this locus accompanied by the posterior branch of the lumbar artery, adhering to the adjacent periosteum via connective tissue [19]. Farther on, it features a medial course passing under the MAL into the fibro-osseous canal. Medial branches of L1–L4 dorsal rami are encountered at the posterolateral portion of this canal, featuring greater proximity to AP than the MP [11]. They subsequently follow a medial and caudal route towards the vertebral lamina, demonstrating thereafter a deep course into the adipose tissue of multifidus muscle [19]. Medial branch is there ramified into three distinct branches; muscular, articular and cutaneous branch, supplying LFJs, multifidus muscles and supra- and inter-spinous ligaments (Fig. 3) [7, 19, 31].

The anatomic course and distribution of medial branch may feature considerable variability, thus complicating the punctual description of LFJs innervation [19]. Bogduk et al. [7] stated in their paper that medial branch provides innervation to LFJs of respective level and one level caudally with descending branches. This statement was in general validated from the vast majority of subsequently published papers (Fig. 3) [11, 19, 29, 31]. There is, however, existing literature data supporting that LFJs innervation may be more

complex, with emerging branches of sympathetic trunk and adjacent spinal ganglion participating as well [19, 25, 34, 35].

In their cadaveric study, Shuang et al. [31] concluded that innervation of a particular LFJs is provided by medial branches of the two adjacent DR. Medial branches of lumbar DR demonstrate a terminal descending portion, which may extent to 1–3 intervertebral levels. Medial branches of cranial DR tend to finally exhibit a shorter descending course in contrast to caudal. Furthermore, it was elucidated that articular branches from medial branch are also derived prior to entrance in fibro-osseous canal. These branches provide regional innervation to lateral and inferior portion of LFJs, whereas the terminally separated articular branches supply superior and medial aspects of LFJs [31].

L5 spinal segment features special anatomic characteristics in terms of neural distribution. First, DR presents a longer course than ventral ramus, rising at the excavation between the superior surface of sacral ala and the base of S1 SAP [19, 26]. Perolat et al. [26] reviewed existing literature on FJ syndrome, quoting alongside data about LFJs anatomy. It was stated that L5 DR is bifurcated into a medial and an intermediate branch, with no presence of lateral branch [26]. However, this thesis is not universally accepted [31]. Medial branch of L5 DR subsequently runs caudally, giving rise to communicating branches to S1 DR [26].

CONCLUSIONS

Existing literature evidence indicates that LFJs represent complex structures in terms of anatomy, biomechanical sententiousness and functional importance. Despite the emerging interest on describing LFJs anatomy, a precise and universally accepted description of LFJs innervation remains absent. Future anatomic and radiologic studies with greater size of specimens may clarify this issue, contributing thus to better comprehension and optimisation of particular interventional procedures as LFJs denervation.

REFERENCES

1. Adams MA, Hutton WC. The mechanical function of the lumbar apophyseal joints. Spine (Phila Pa 1976). 1983; 8(3): 327–330, doi: 10.1097/00007632-198304000-00017, indexed in Pubmed: 6623200.

2. Ahmed AM, Duncan NA, Burke DL. The effect of facet geometry on the axial torque-rotation response of lumbar motion segments. Spine (Phila Pa 1976). 1990; 15(5): 391–401, doi: 10.1097/00007632-199005000-00010, indexed in Pubmed: 2363067.

3. Alonso F, Kirkpatrick CM, Jeong W, et al. Lumbar facet tropism: a comprehensive review. World Neurosurg. 2017; 102: 91–96, doi: 10.1016/j.wneu.2017.02.114, indexed in Pubmed: 28279769.

4. An SJ, Seo MiS, Choi SIl, et al. Facet joint hypertrophy is a misnomer: A retrospective study. Medicine (Baltimore). 2018; 97(24): e11090, doi: 10.1097/MD.0000000000011090, indexed in Pubmed: 29901623.

5. Ban E, Zhang S, Zarei V, et al. Collagen organization in facet capsular ligaments varies with spinal region and with ligament deformation. J Biomech Eng. 2017; 139(7), doi: 10.1115/1.4036019, indexed in Pubmed: 28241270.

6. Bogduk N. Clinical anatomy of the lumbar spine and sacrum. 3rd ed. Churchill Livingstone, Edinburgh 1997.

7. Bogduk N, Wilson AS, Tynan W. The human lumbar dorsal rami. J Anat. 1982; 134(Pt 2): 383–397, indexed in Pubmed: 7076562.

8. Chadha M, Sharma G, Arora SS, et al. Association of facet tropism with lumbar disc herniation. Eur Spine J. 2013; 22(5): 1045–1052, doi: 10.1007/s00586-012-2612-5, indexed in Pubmed: 23242621.

9. Cohen SP, Raja SN. Pathogenesis, diagnosis, and treatment of lumbar zygapophysial (facet) joint pain. Anesthesiology. 2007; 106(3): 591–614, doi: 10.1097/00000542-200703000-00024, indexed in Pubmed: 17325518.

10. Demir-Deviren S, Singh S, Hanelin J. Superior recess access of the lumbar facet joint. Clin Spine Surg. 2017; 30(3): E169–E172, doi: 10.1097/BSD.0000000000000271, indexed in Pubmed: 28323695.

11. Demondion X, Vidal C, Glaude E, et al. The posterior lumbar ramus: CT-anatomic correlation and propositions of new sites of infiltration. AJNR Am J Neuroradiol. 2005; 26(4): 706–710, indexed in Pubmed: 15814909.

12. Dupont G, Yilmaz E, Iwanaga J, et al. Ossification of the mamillo-accessory ligament: a review of the literature and clinical considerations. Anat Cell Biol. 2019; 52(2): 115–119, doi: 10.5115/acb.2019.52.2.115, indexed in Pubmed: 31338226.

13. Farfan HF, Sullivan JD. The relation of facet orientation to intervertebral disc failure. Can J Surg. 1967; 10(2): 179–185, indexed in Pubmed: 4225346.

14. Gao T, Lai Qi, Zhou S, et al. Correlation between facet tropism and lumbar degenerative disease: a retrospective analysis. BMC Musculoskelet Disord. 2017; 18(1): 483, doi: 10.1186/s12891-017-1849-x, indexed in Pubmed: 29166933.

15. Gellhorn AC, Katz JN, Suri P. Osteoarthritis of the spine: the facet joints. Nat Rev Rheumatol. 2013; 9(4): 216–224, doi: 10.1038/nrrheum.2012.199, indexed in Pubmed: 23147891.

16. Inoue N, Orías AA, Segami K. Biomechanics of the lumbar facet joint. Spine Surg Relat Res. 2020; 4(1): 1–7, doi: 10.22603/ssrr.2019-0017, indexed in Pubmed: 32039290.

17. Ishihara H, Matsui H, Osada R, et al. Facet joint asymmetry as a radiologic feature of lumbar intervertebral disc herniation in children and adolescents. Spine (Phila Pa 1976). 1997; 22(17): 2001–2004, doi: 10.1097/00007632-199709010-00012, indexed in Pubmed: 9306530.

18. Jiang X, Chen D, Li Z, et al. Correlation between lumbar spine facet joint orientation and intervertebral disk degeneration: a positional MRI analysis. J Neurol Surg A Cent Eur Neurosurg. 2019; 80(4): 255–261, doi: 10.1055/s-0039-1683450, indexed in Pubmed: 30934096.

19. Kozera K, Ciszek B. Posterior branches of lumbar spinal nerves - part I: anatomy and functional importance. Ortop Traumatol Rehabil. 2016; 18(1): 1–10, doi: 10.5604/15093492.1198827, indexed in Pubmed: 27053304.

20. Kozera K, Ciszek B, Szaro P. Posterior branches of lumbar spinal nerves. Part II: lumbar facet syndrome — pathomechanism, symptomatology and diagnostic work-up. Ortop Traumatol Rehabil. 2017; 19(2): 101–109, doi: 10.5604/15093492.1237716, indexed in Pubmed: 28508761.

21. Louis R. Spinal stability as defined by the three-column spine concept. Anat Clin. 1985; 7(1): 33–42, doi: 10.1007/BF01654627, indexed in Pubmed: 3994851.

22. Mahato NK. Facet dimensions, orientation, and symmetry at L5-S1 junction in lumbosacral transitional States. Spine (Phila Pa 1976). 2011; 36(9): E569–E573, doi: 10.1097/BRS.0b013e3181f6ecb2, indexed in Pubmed: 21245783.

23. Mohanty SP, Pai Kanhangad M, Kamath S, et al. Morphometric study of the orientation of lumbar zygapophyseal joints in a South Indian population. J Orthop Surg (Hong Kong). 2017; 25(3): 2309499017739483, doi: 10.1177/2309499017739483, indexed in Pubmed: 29121821.

24. O'Leary SA, Link JM, Klineberg EO, et al. Characterization of facet joint cartilage properties in the human and interspecies comparisons. Acta Biomater. 2017; 54: 367–376, doi: 10.1016/j.actbio.2017.03.017, indexed in Pubmed: 28300721.

25. Pedersen H, Blunck C, Gardner E. The anatomy of lumbosacral posterior rami and meningeal branches of spinal nerves (sinu-vertebral nerves). J Bone Joint Surg. 1956; 38(2): 377–391, doi: 10.2106/00004623-195638020-00015.

26. Perolat R, Kastler A, Nicot B, et al. Facet joint syndrome: from diagnosis to interventional management. Insights Imaging. 2018; 9(5): 773–789, doi: 10.1007/s13244-018-0638-x, indexed in Pubmed: 30090998.

27. Proietti L, Schirò GR, Sessa S, et al. The impact of sagittal balance on low back pain in patients treated with zygapophysial facet joint injection. Eur Spine J. 2014; 23 Suppl 6: 628–633, doi: 10.1007/s00586-014-3559-5, indexed in Pubmed: 25212449.

28. Putz R. The functional morphology of the superior articular processes of the lumbar vertebrae. J Anat. 1985; 143: 181–187, indexed in Pubmed: 3870725.

29. Saito T, Steinke H, Miyaki T, et al. The medial branch of the lateral branch of the posterior ramus of the spinal nerve.

Surg Radiol Anat. 2006; 28(3): 228–234, doi: 10.1007/s00276-006-0090-3, indexed in Pubmed: 16612554.

30. Saito T, Yoshimoto M, Yamamoto Y, et al. The medial branch of the lateral branch of the posterior ramus of the spinal nerve. Surg Radiol Anat. 2006; 28(3): 228–234, doi: 10.1007/s00276-006-0090-3, indexed in Pubmed: 16612554.

31. Shuang F, Hou SX, Zhu JL, et al. Clinical anatomy and measurement of the medial branch of the spinal dorsal ramus. Medicine (Baltimore). 2015; 94(52): e2367, doi: 10.1097/MD.0000000000002367, indexed in Pubmed: 26717379.

32. Song Q, Liu X, Chen DJ, et al. Evaluation of MRI and CT parameters to analyze the correlation between disc and facet joint degeneration in the lumbar three-joint complex. Medicine (Baltimore). 2019; 98(40): e17336, doi: 10.1097/MD.0000000000017336, indexed in Pubmed: 31577728.

33. Steinke H, Saito T, Miyaki T, et al. Anatomy of the human thoracolumbar Rami dorsales nervi spinalis. Ann Anat. 2009; 191(4): 408–416, doi: 10.1016/j.aanat.2009.04.002, indexed in Pubmed: 19570665.

34. Suseki K, Takahashi Y, Takahashi K, et al. Innervation of the lumbar facet joints. Origins and functions. Spine (Phila Pa 1976). 1997; 22(5): 477–485, doi: 10.1097/00007632-199703010-00003, indexed in Pubmed: 9076878.

35. Tessitore E, Molliqaj G, Schatlo B, et al. Clinical evaluation and surgical decision making for patients with lumbar discogenic pain and facet syndrome. Eur J Radiol. 2015; 84(5): 765–770, doi: 10.1016/j.ejrad.2014.03.016, indexed in Pubmed: 24801263.

36. Thorpe Lowis CG, Xu Z, Zhang M. Visualisation of facet joint recesses of the cadaveric spine: a micro-CT and sheet plastination study. BMJ Open Sport Exerc Med. 2018; 4(1): e000338, doi: 10.1136/bmjsem-2017-000338, indexed in Pubmed: 29527323.

37. Tulsi RS, Hermanis GM. A study of the angle of inclination and facet curvature of superior lumbar zygapophyseal facets. Spine (Phila Pa 1976). 1993; 18(10): 1311–1317, doi: 10.1097/00007632-199308000-00010, indexed in Pubmed: 8211363.

38. Twomey L, Taylor J. Age changes in lumbar intervertebral discs. Acta Orthop Scand. 1985; 56(6): 496–499, doi: 10.3109/17453678508993043, indexed in Pubmed: 4090952.

39. Varlotta GP, Lefkowitz TR, Schweitzer M, et al. The lumbar facet joint: a review of current knowledge: part 1: anatomy, biomechanics, and grading. Skeletal Radiol. 2011; 40(1): 13–23, doi: 10.1007/s00256-010-0983-4, indexed in Pubmed: 20625896.

40. Wang H, Zhang Z, Zhou Y. Irregular alteration of facet orientation in lumbar segments: possible role in pathology of lumbar disc herniation in adolescents. World Neurosurg. 2016; 86: 321–327, doi: 10.1016/j.wneu.2015.09.029, indexed in Pubmed: 26409076.

41. Yang KH, King AI. Mechanism of facet load transmission as a hypothesis for low-back pain. Spine (Phila Pa 1976). 1984; 9(6): 557–565, doi: 10.1097/00007632-198409000-00005, indexed in Pubmed: 6238423.

Ameliorating effect of selenium nanoparticles on cyclophosphamide-induced hippocampal neurotoxicity in male rats: light, electron microscopic and immunohistochemical study

H.M. Ibrahim[1] , M.A. Zommara[2], M.E. Elnaggar[1]

[1]Department of Anatomy and Embryology, Faculty of Medicine, Ain Shams University, Cairo, Egypt
[2]Department of Dairy Science, Faculty of Agriculture, Kaferelshikh University, Kaferelshikh, Egypt

Background: Cyclophosphamide (CPH) is a widely used chemotherapeutic drug that can affect the hippocampal neurocytes with a subsequent effect on memory and cognitive functions. Nanomedicine has the potential to overcome the current chemotherapeutic side effects, because of the unique nanoscale size and distinctive bioeffects of nanomaterials. So, the present study aims to investigate the potential ameliorative effect of the biologically synthesized nano-selenium (nano-Se) on CPH induced hippocampal neurotoxicity.

Materials and methods: Twenty four rats were randomly classified into four groups of 6 rats each: control group, nano-Se group (dose of 0.5 mg biological nano-Se/kg daily via oral gavage), CPH group (dose of 20 mg CPH/kg daily intraperitoneally), and CPH plus nano-Se group. After 4 weeks, the rats were sacrificed and the hippocampus was excised and processed. Sections were stained with haematoxylin and eosin stain and immunohistochemically stained for caspase-3 (apoptosis marker) and glial fibrillary acidic protein (astrocytic activity marker) (GFAP). Morphometric analysis and transmission electron microscopic (TEM) examination were also done.

Results: Control and nano-Se groups revealed no structural changes. By light microscopy, CPH group showed degeneration and necrosis of hippocampal neurocytes, significantly reduced thickness of the neurocyte cell layers, increased expression of GFAP and caspase-3 immunostains and significantly elevated apoptotic index. Moreover, neurocytes damage, mitochondrial cristeolysis, mild dilation of rough endoplasmic reticulum, and disrupted neurolemmal sheaths of nerve fibres were also demonstrated by TEM. Nano-Se cotreatment in the fourth group reversed all the aforementioned deleterious changes that induced by CPH in the hippocampal neurocytes.

Conclusions: Treatment with CPH caused damage to hippocampal neurocytes that can be reversed by biological nano-Se co-treatment. (Folia Morphol 2021; 80, 4: 806–819)

Key words: cyclophosphamide, hippocampus, neurotoxicity, nano-selenium

---

Address for correspondence: Dr. H.M. Ibrahim, Department of Anatomy and Embryology, Faculty of Medicine, Ain Shams University, Abbasia,
Postal code: 11591 Cairo, Egypt, tel: 00201099289523, e-mail: huseinmoh76@gmail.com

INTRODUCTION

Selenium (Se) is an indispensable trace element, needed for the maintenance of growth and health [47]. It plays a rule in illness prevention and fertility [9, 10]. Recently, with the progress of the nanotechnology field, nano-selenium (nano-Se) has gained widespread attention because the nanoparticles exhibit innovative properties such as a powerful adsorbing capacity, high surface activity, high catalytic ability, and less toxicity [46]. Some studies have also pointed out the possibility of use of nano-Se in the field of medical treatment as antimicrobial, anti-biofilm [45] and anticancer [57].

Nano-Se can be synthesized by chemical and biological methods. In chemical methods, the chemical stabilizers used may lead to environmental pollution [15]. On the contrary, biological synthesis is preferred as it is a nontoxic, clean, cost-effective, and more accessible approach. Moreover, nanoparticles produced by the biological methods have more novel properties [19, 36]. There are relatively few reports on the biologically synthesized nano-Se and it is still a big challenge for researchers to elucidate the potential health benefits of nano-Se [24].

Cyclophosphamide (CPH) is an anticancer agent, which is ordinarily used to treat numerous types of cancer [37]. Administration of CPH triggers oxidative stress in the brain [25] and massive cellular degeneration [39], consequently provoking apoptosis [32], and damage to cancer and healthy cells [49]. CPH uptake into healthy cells is higher than in cancer cells, rendering healthy cells more susceptible to damage [8]. The antineoplastic effects of CPH are associated with the production of acrolein which is the cause of the toxic side effects of CPH [28]. Acrolein diminishes cellular defence against oxidative stress, which can corrupt the blood-brain barrier [3, 50]. Moreover, CPH can alkylate DNA, inhibits the duplication of the genome in dividing cells, and arrests the cell cycle particularly at the S-phase [6, 51].

Treatment with CPH induces cognitive and psychological impairments especially the hippocampal-dependent memory task due to the negative impact of CPH on hippocampal neurogenesis [23, 43]. Neurogenesis continues in the hippocampus throughout adulthood [23]. The neurotoxic effects of CPH include not only neuronal damage but also disruption of the cholinergic pathways [2]. The aforementioned reports point out that there is a necessity to explore the possible therapeutic approaches to mitigate the neurotoxicity induced by cyclophosphamide on hip-
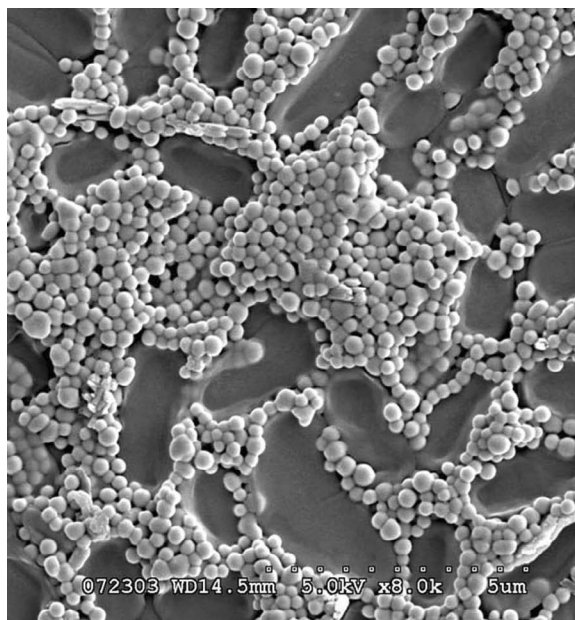
Figure 1. Scanning electron microscopic photograph of a yoghurt culture-nano-selenium suspension.

pocampal neurons. Therefore, the present study was conducted to investigate the potential ameliorative effect of the biologically synthesized nano-Se on CPH induced hippocampal neurotoxicity.

MATERIALS AND METHODS

Drugs

Cyclophosphamide (CPH). Cyclophosphamide monohydrate, trade name Endoxan, was manufactured by Baxter Oncology GmbH (Kantstrasse, Germany). It was available in the form of vials. Each vial contained 1 g CPH (dry powder). CPH was dissolved in saline to be intraperitoneally injected in rats.

Selenium nano-particles (nano-Se). Biologically synthesized nano-Se was prepared using yoghurt culture (*Lactobacillus delbrueckii subsp. bulgaricus* [*L. bulgaricus*, NCAIM B 02206] and *Streptococcus thermophilus* [*S. thermophiles*, CNCM I-1670] cultivated in MRS medium as described by Prokisch and Zommara, 2010 [41]. Nano-Se size ranged from 55 to 238 nm with an average of 122.6 ± 34.6 (SD) or 122.6 ± 8.6 (SE). Scanning electron microscopic (JSM-IT100, JEOL Co. Japan) photos of purified nano-Se were used for nano-Se size determination according to Nagy et al. [35] 2016 (Fig. 1).

Animals

Twenty four adult male albino rats with an average weight of 200–250 g were used in the current exper-

imental study. The animals were treated according to the guidelines of the Committee of Animal Research Ethics of the faculty of medicine, Ain-Shams University. The animals were housed in a convenient environment; 6 rats per cage, food, and water were freely allowed. All rats were exposed to 12 hours light-dark cycle, good ventilation, and suitable temperature 22–25°C.

Experimental design

Animals were divided into four groups:

— group I (control group): 6 rats received 0.1 mL of a saline intraperitoneal injection daily for 4 weeks;
— group II (nano-Se group): 6 rats received nano-Se (0.5 mg/kg body weight) by oral gavage daily for 4 weeks [16];
— group III (CPH group): 6 rats received a CPH (20 mg/kg body weight) intraperitoneal injection daily for 4 weeks [34];
— group IV (CPH plus nano-Se group): 6 rats received a CPH (20 mg/kg body weight) intraperitoneal injection daily and nano-Se (0.5 mg/kg body weight) by oral gavage daily for 4 weeks.

Light microscopic studies

At the end of the 4 weeks experimental period, rats were anaesthetised by ether, and then sacrificed also with a fatal dose of ether. For each animal, the brain was extracted. The cerebral hemispheres were separated into right and left halves. Then, the posterior portion of the brain containing the hippocampus was cut. The right hippocampus was put in 10% formal saline (5 days). Specimens were then dehydrated, cleared, and embedded in paraffin. Sagittal sections (5-μm) were cut and stained with haematoxylin and eosin (H&E) [4], and immunohistochemical staining for caspase-3 (apoptotic marker) and glial fibrillary acidic protein (GFAP) were also performed. GFAP was utilized to investigate the astrocytes distribution and their response to neurocyte damage [31].

Immunohistochemical staining

Tissue sections were deparaffinised, rehydrated and 10% hydrogen peroxide was added for endogenous peroxidase inhibition. Then, boiling with citrate buffer pH 6.0. For antigen retrieval was done. Sections were also incubated with the primary antibodies: anti-caspase-3 (BIOCYC GmbH, Germany), and anti-GFAP (Goat Polyclonal IgG, anti-rat antibody; Dako Cytomation, USA). Subsequently, incubation

with the secondary antibody, a biotinylated goat anti-rabbit immunoglobulin and a streptavidin–biotin complex was done. The site of the reaction was visualised by adding diaminobenzidine HCl, which was converted into a brown precipitate by peroxidase. Finally, haematoxylin was utilised for counterstaining [5].

Transmission electron microscopy

The left hippocampal formation was extracted immediately after sacrificing the animals; samples were cut into small pieces (1 × 1 × 1 mm). The pieces were thereafter fixed in formal glutaraldehyde 2.5% for 2 days. Then, postfixation with a 1% osmium tetroxide solution was performed. Washing four times with phosphate buffered saline and dehydration through graded ethanol was done followed by clearing in propylene. Finally, the specimens were embedded in epoxy resin. Semithin sections were cut (1 μm) and stained with toluidine blue and inspected by light microscope. Then, cutting the ultrathin sections (60 nm) and staining with uranyl acetate and lead citrate was done. The sections were examined using a transmission electron microscope (TEM) (Jeol 1200Ex, Japan) at the Electron Microscopy Centre, Faculty of Science Ain Shams University, Cairo, Egypt [42].

Morphometric and statistical analysis

The following data were measured:

— the thickness of the neurocyte cell layer, i.e. the pyramidal cell layer in CA1 and CA3 zones and the granular cell layer in dentate gyrus (DG). Vertical lines were drawn, by the software (Image Pro-Plus), from the uppermost pyramidal cell (or granule cell) to the lower most one detected. The lines were then measured;
— the area percentage of GFAP reaction, and the number of GFAP positive cells in CA1 in all groups. Briefly, the GFAP positive cells were marked by the software and the area percentage and the number of cells were counted at the high-power field (×400 magnification);
— the area percentage of caspase-3 reaction in CA1 in all groups. The caspase-3 positive cells were marked by the software and the area percentage was counted at the high-power field (×400 magnification). The number of caspase-3 positive cells (apoptotic cells) was expressed frequently in the previous studies by the apoptotic index (AI) [55].
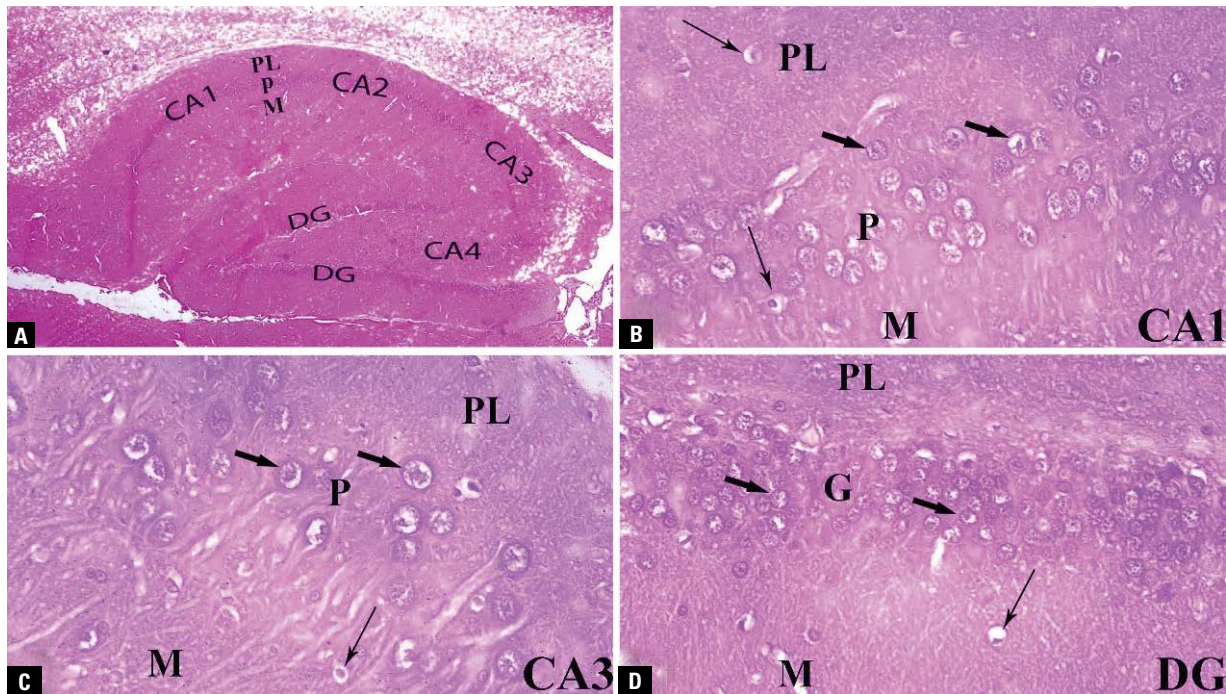
Figure 2. A. Hippocampus of control rat showing the dentate gyrus (DG) and the four regions of hippocampus CA1, CA2, CA3, and CA4; **B–D.** Showing that CA1, CA3 and DG are formed of 3 layers; PL — polymorphic layer; p — pyramidal cell layer, M — molecular cell layer. The pyramidal cell layer is replaced by granule cell layer (G) in DG. The thick arrows point to the pyramidal and granule cells and the thin arrows for the interneurons (H&E stain; A: ×40; B, C, D: ×400).

Five different captures in non-overlapping high-power fields (×400) were taken in the slides of each rat in all groups (the H&E stained slides and the immunostained slides). Then, the aforementioned parameters were measured by software. The AI represented the percentage of apoptotic cells in 1000 cells. Meanwhile, the AI was determined by counting at least 1000 cells per slide, subdivided into 10 fields chosen randomly. The counting process was done at 400 × magnification. AI = (number of caspase-3 positive cells/total number of calculated cells) ×100. Measurements were performed by an independent observer blinded to the specimens' details to achieve an unbiased evaluation. The morphometric analysis was performed on digital light microscopic images that had been captured by a digital camera Olympus (DP 20) on Olympus BX51 light microscope (Olympus, Hamburg, Germany). Image analysis procedures were carried out using the Image Pro-Plus Programme, Media cybernetics. Inc. (version 4.5.1.27).

All data were expressed as mean ± standard deviation and statistically analysed by IBM SPSS Statistics version 20 using one-way AVOVA analysis of variance, followed by Tukey test to compare statistical differences between all groups at p < 0.05.

Ethics approval and consent to participate

All the procedures of the experiment were carried out according to the guide rules of the Committee of the Animal Research Ethics, Faculty of Medicine, Ain Shams University.

RESULTS

Light microscopic results

Group (I and II: control and nano-Se groups). The microscopic sections of the control and nano-Se groups were nearly similar. In both groups, examination of H&E stained sections of the hippocampus revealed that it was formed of the hippocampal proper (proprius) and the DG. The hippocampus proper was composed of four zones (CA1, CA2, CA3, and CA4) of cornu ammonis. CA1 and CA2 were located dorsally while CA3 made the descending arch that ended at the beginning of the hilus of the DG. CA4 is situated inside the hilus of the DG. The DG appeared as a dark V-shaped structure, with its open part encircling the CA4 area of the hippocampus. Each area was formed of 3 layers: polymorphic, pyramidal, and molecular (Fig. 2A). The molecular and polymorphic layers contained few neurocytes (nerve cells), whereas the pyramidal layer was formed of numerous neurocytes
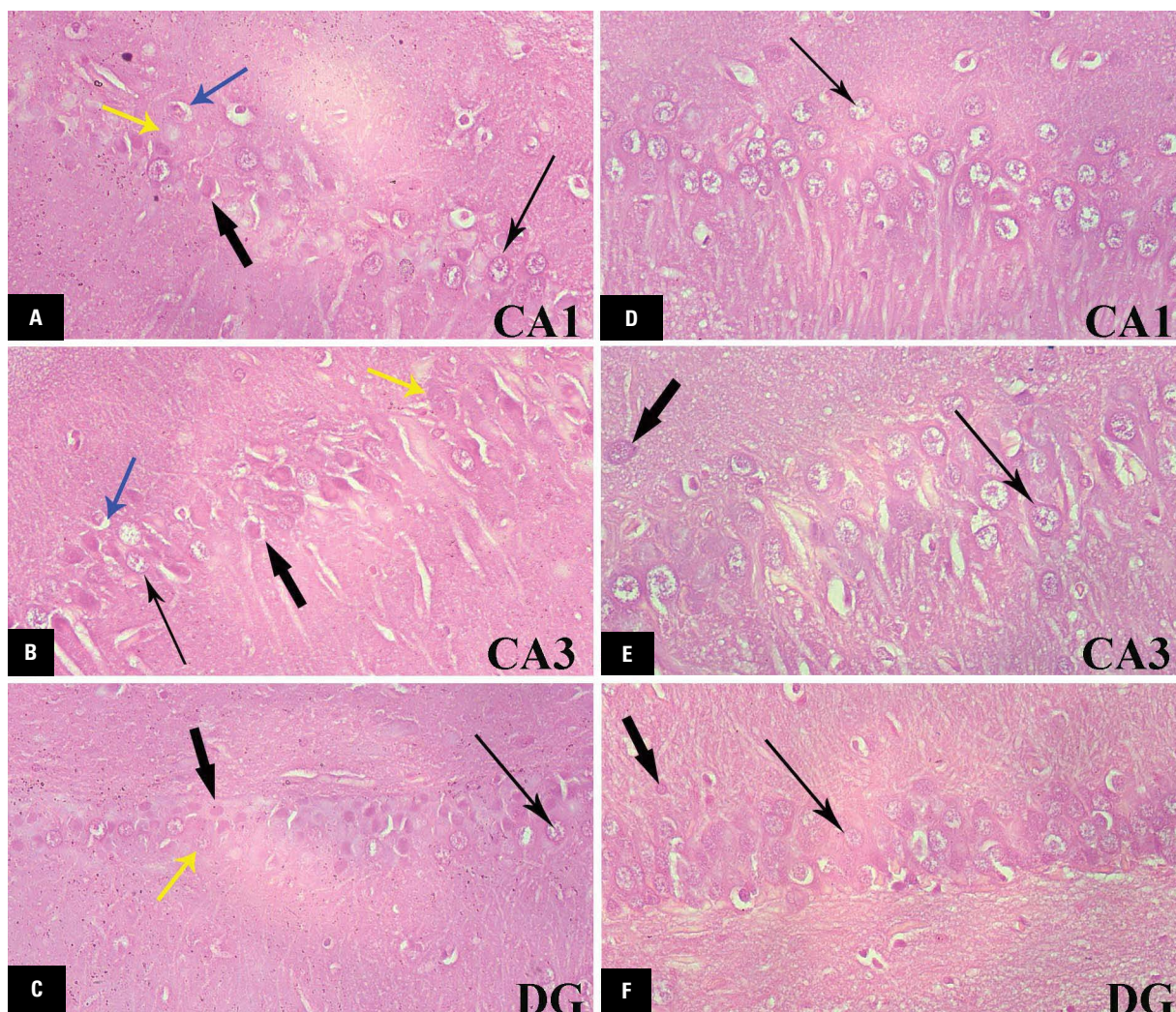
Figure 3. A–C. Sections from cyclophosphamide group showing the necrotic and degenerated neurocytes in all zones separated by few healthy cells; **D–F.** Sections in cyclophosphamide plus nano-selenium group showing that most of the neurocytes are healthy. Thick arrow — necrotic cell, thin arrow — healthy cell, yellow arrow — ghost like cell, blue arrow — cytoplasmic vacuolation in a degenerated cell (H&E stain ×400); DG — dentate gyrus.

(pyramidal cells) containing large vesicular nuclei with prominent nucleoli and pale basophilic cytoplasm. Glial cell interneurons were seen in all layers of the hippocampus. They had dark basophilic cytoplasm and deeply stained small rounded nuclei. The middle layer in the DG is called the granule cell layer instead of the pyramidal cell layer (Fig. 2B–D). The cellular structure of the various zones of the hippocampus proper is similar so figures of CA1 and CA3 were only included in the present study as examples to the different layers and to avoid repetition of unnecessary similar figures.

Group (III: CPH group). *Hippocampus proper:* The thickness of the pyramidal cell layer was apparently decreased. The pyramidal cells were disorganised and appeared either degenerated or necrotic. The cytoplasm of the degenerated cells was vacuolated with loss of cellular characteristics. The necrotic cells had shrunken deeply stained nuclei, i.e. pyknotic nuclei. Small perineural spaces were seen surrounding the necrotic pyramidal cells. Additionally, some cells had swollen karyolitic pale stained nuclei with pale faint cytoplasm giving the ghost-like appearance. Few cells were still healthy with vesicular nuclei in between the damaged cells (Figs. 3A, B).

Dentate gyrus: The granule cell layer was diminished in thickness and the majority of its cells had deeply stained shrunken pyknotic nuclei or ghost-like nuclei (Fig. 3C).

Morphometrically, the thickness of the pyramidal cell layer and the granule cell layer (neurocyte cell layers) was significantly decreased as compared to the

Table 1. Thickness of the pyramidal cell layer in CA1 and CA3 and the granular cell layer in dentate gyrus of the hippocampus in different groups (in μM)

	Control	Nano-Se	CPH	CPH + nano-Se
CA1	84.28 ± 7.41	87.48 ± 7.75	40.26 ± 4.11[a]	76.94 ± 7.18[b]
CA3	112.34 ± 5.50	116.56 ± 6.27	57.97 ± 5.46[a]	107.06 ± 8.00[b]
Dentate gyrus	69.61 ± 4.67	71.92 ± 4.06	40.31 ± 3.70[a]	63.91 ± 6.95[b]

Values are expressed as mean ± standard deviation. N = 6 for each group. One-way ANOVA; [a]significant vs. the control group; [b]significant vs. the CPH group; p < 0.05 was considered significant. CPH — cyclophosphamide; nano-Se — nano-selenium
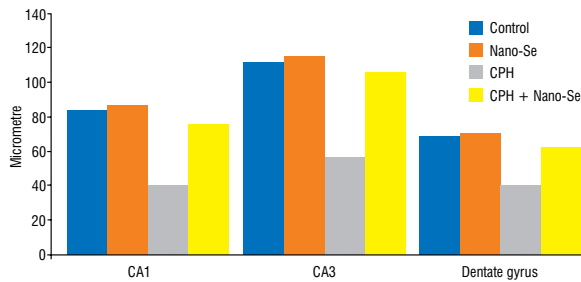
Figure 4. A histogram comparing the neurocyte cell layer thickness of the different groups; CPH — cyclophosphamide; nano-Se — nano-selenium.

control group (p < 0.05). So, the morphometric data were in harmony with the morphological observations (Table 1, Fig. 4).

Group (IV: CPH plus nano-Se group). Examination of H&E-stained sections in the hippocampus of rats treated with CPH plus nano-Se revealed that most of the pyramidal cells and granule cells appeared healthy with large rounded or oval vesicular nuclei. Few cells with shrunken pyknotic nuclei with dark cytoplasm could be also seen in between the healthy cells (Fig. 3D–F). The thickness of the pyramidal cell layer and the granule cell layer was significantly elevated as compared to CPH group by morphometric analysis (Table 1, Fig. 4).

Immunohistochemical results

Immunohistochemistry for GFAP. The control group and the nano-Se group (I and II groups) showed few positive brownish star-shaped GFAP immunoreactive cells. The immunoreactive cells were large
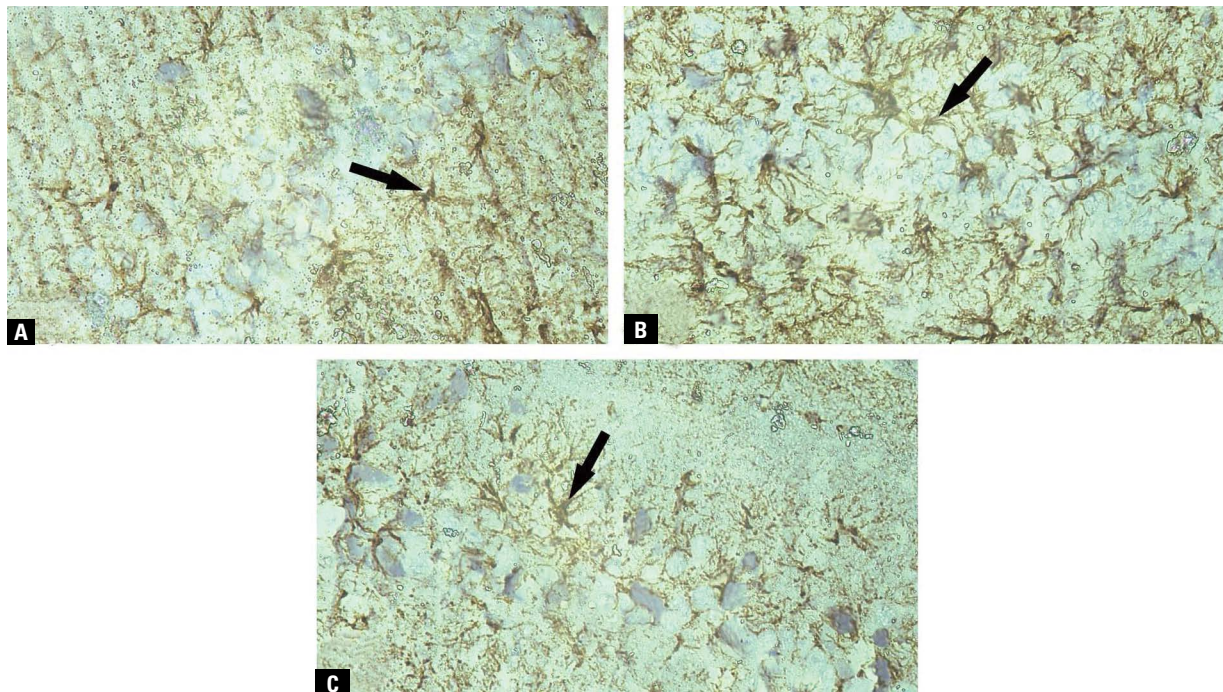
Figure 5. Sections in CA1; **A.** Few cells with positive reaction to glial fibrillary acidic protein (GFAP) in the control group; **B.** Many cells with positive reaction in cyclophosphamide (CPH) group; **C.** Few cells with positive reaction in CPH plus nano-selenium group (GFAP immune-stain ×400).

Table 2. The mean glial fibrillary acidic protein (GFAP) area percentage, number of GFAP positive cells, caspase-3 area percentage (%), and the apoptotic index (AI) in different groups

Groups	GFAP area %	Number of GFAP positive cells	Caspase-3 area %	AI
Control	2.99 ± 1.57	2.73 ± 1.44	1.44 ± 0.85	0.43 ± 0.25
Nano-Se	2.24 ± 1.53	1.73 ± 1.23	1.24 ± 0.92	0.32 ± 0.15
CPH	18.56 ± 10.25[a]	19.23 ± 6.60[a]	15.06 ± 6.12[a]	33.66 ± 5.14[a]
CPH + nano-Se	7.07 ± 2.96[b]	5.47 ± 2.11[b]	5.73 ± 1.61[b]	10.54 ± 2.58[b]

Values are expressed as mean ± standard deviation. N = 6 for each group. One-way ANOVA; [a]significant vs. the control group; [b]significant vs. the CPH group; $p < 0.05$ was considered significant. CPH — cyclophosphamide; nano-Se — nano-selenium
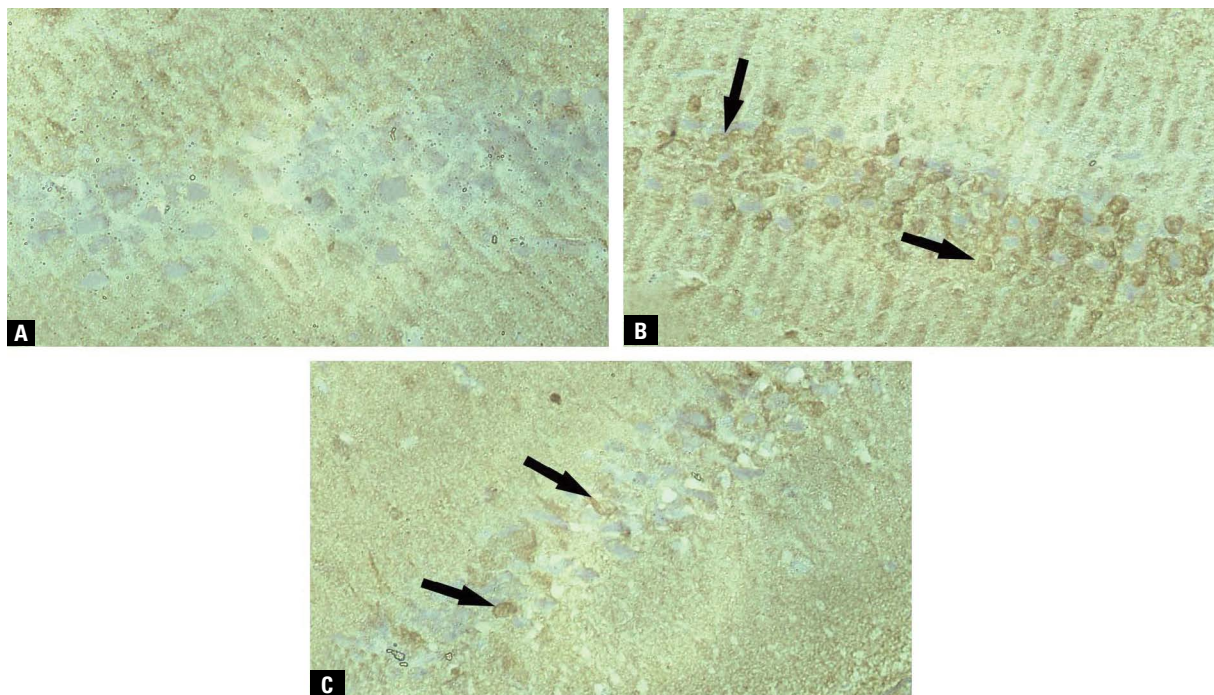
Figure 6. Sections in CA1; **A.** No positive reaction to caspase-3 in the control group; **B.** Many cells with positive reaction in cyclophosphamide (CPH) group; **C.** Few cells with positive reaction in CPH plus nano-selenium group (caspase-3 immune-stain ×400).

branched cells dispersed among various cell layers of the hippocampus. They were most probably activated astrocytes (Fig. 5A). The CPH group (group III) showed an apparent increase in the number and size of the star-shaped GFAP immunoreactive cells (Fig. 5B). The CPH plus nano-Se group (group IV) showed less number and size of the GFAP immunoreactive cells compared to the group of CPH treated rats (Fig. 5C). Morphometrically, the area percentage of the GFAP reaction and the mean number of immunoreactive cells were significantly increased in the CPH group as compared to the control group. Meanwhile, these measured parameters were significantly reduced in CPH plus nano-Se group as compared to the CPH group (Table 2, Fig. 7A).

Immunohistochemistry for caspase-3. Caspase-3 was rarely expressed in the neurocytes of the control and nano-Se groups (group I and II) (Fig. 6A). Enhanced staining of caspase-3 was observed in the neurocytes of the CPH group (group III) compared with the control group, indicating increased apoptosis (Fig. 6B). The CPH plus nano-Se group (group IV) showed decreased staining in comparison with the CPH group (Fig. 6C). Morphometrically, the area percentage of caspase-3 reaction, and the AI were significantly increased in the CPH group compared to the control group. Meanwhile, these measured parameters were significantly decreased in CPH plus nano-Se group as compared to the CPH group (Table 2, Fig. 7B).

A

B
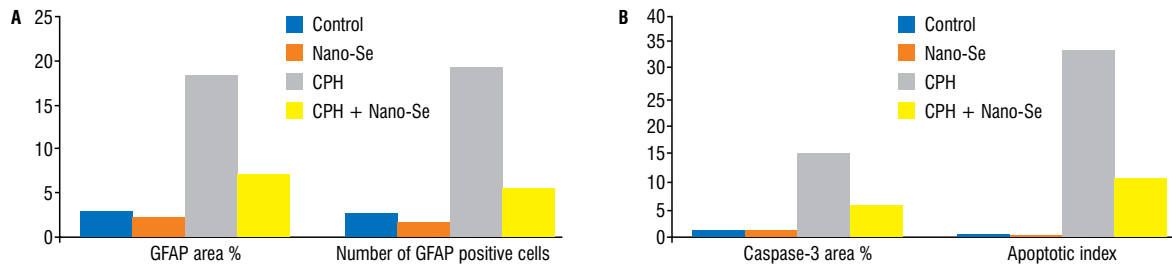
Figure 7. A histogram comparing; **A.** Glial fibrillary acidic protein (GFAP) area percentage and number of GFAP positive cells in the different groups; **B.** Caspase-3 area percentage and apoptotic index in the different groups; CPH — cyclophosphamide; nano-Se — nano-selenium.
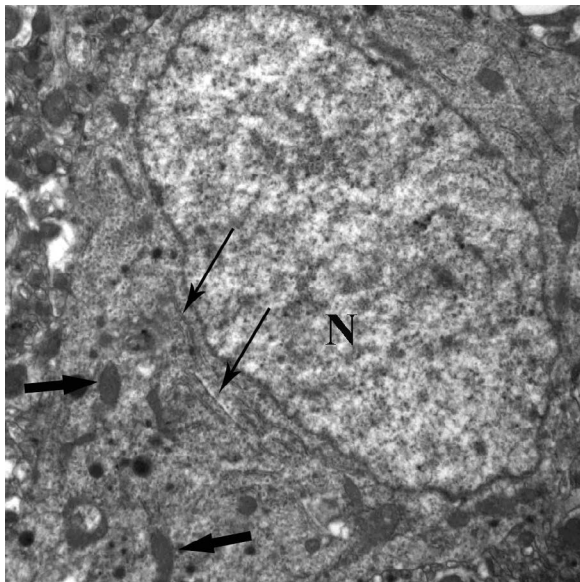
Figure 8. Transmission electron microscopic micrograph of a control neurocyte showing a large oval euchromatic nucleus (N), cisternae of rough endoplasmic reticulum (thin arrow), and intact mitochondria (thick arrow) ($\times$2500).

Transmission electron microscopic (TEM) results

Group (I and II: control and nano-Se groups). The neurocytes (nerve cells) of the control group showed large oval or rounded euchromatic nucleus with dispersed chromatin and a regular nuclear membrane. The cytoplasm contained multiple cisternae of rough endoplasmic reticulum, several free ribosomes, and intact mitochondria with prominent cristae (Fig. 8).

Group (III: CPH group). The nuclei of many cells had irregular outlines and condensed chromatin and some of them appeared shrunken and deeply stained, i.e. pyknotic (Fig. 9A, C). The nuclei of the degenerated cells appeared electro-lucent but their cytoplasm showed large vacuolation with remnants of the degenerated organelles (Fig. 9B). The mitochondrial cristae appeared damaged, i.e. cristeolysis

and the cisternae of the rough endoplasmic reticulum were slightly dilated (Fig. 9D). Some neurolemmal sheaths of the nerve fibres were disrupted (Fig. 9A, C).

Group (IV: CPH plus nano-Se group). The majority of cells had electro-lucent nuclei with nearly regular outlines and dispersed chromatin and their cytoplasm showed healthy mitochondria and a nearly normal rough endoplasmic reticulum. The neurolemmal sheaths of the nerve fibres appeared intact (Fig. 10A, B). Some cells had normal cytoplasmic organelles and electro-lucent chromatin, but their nuclei still had irregular outlines (Fig. 10C). While most of the cells appeared healthy, few cells still had deeply stained nuclei and/or cytoplasmic vacuolation (Fig. 10D).

DISCUSSION

Chemotherapeutic drugs as cyclophosphamide have been a cornerstone of cancer therapy. Extensive effort was done on the synthesis of more efficient and less toxic chemotherapeutic drugs, but less attention has been paid to factors that may decrease the harmful side effects created by the antineoplastic agents. Moreover, the clinical outcome of treatment with these agents is critically restricted, frequently due to their toxicity to normal tissues. Consequently, there was a need to develop adjuvant treatment to enhance the effectiveness and/or diminish the associated side effects. Nanoparticles have the potential to overcome the obstacles in the treatment of cancer by the traditional antineoplastic agents, due to the unique nano size and novel characteristics of nanomaterials [27, 59].

In the current study, H&E stained sections of the group of rats exposed to CPH showed either degeneration or necrosis of the neurocytes of the hippocampus, i.e. the pyramidal cells of the hippocampus proper and granule cells of the dentate
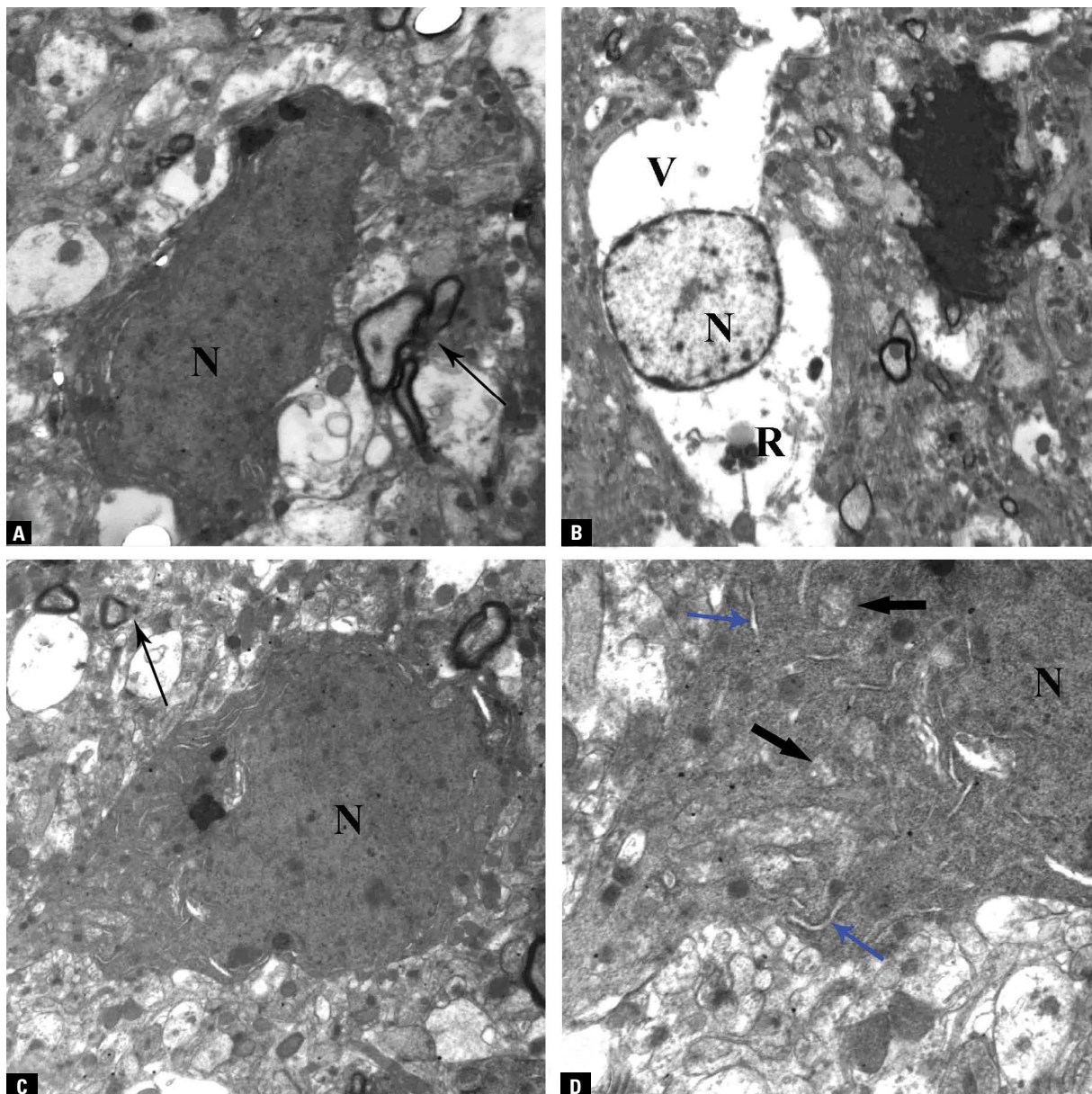
Figure 9. Transmission electron microscopic micrographs of neurocytes of the cyclophosphamide group; **A.** A nucleus (N) with irregular outline and condensed chromatin; **B.** A degenerated cell with electro lucent nucleus (N), vacuolated cytoplasm (V), and remnants of the degenerated organelles (R); **C.** A necrotic cell with a pyknotic nucleus (N); **D.** A higher magnification of panel C showing the cristeolysis of mitochondria (thick arrow) and the slightly dilated cisternae the rough endoplasmic reticulum (blue arrow). The disrupted neurolemmal sheaths (thin arrow) are seen in panels A and C (A, C: ×2500, B: ×1500, D: ×6000).

gyrus. The thickness of the pyramidal and granule cell layers was also significantly reduced. The results of the current study were similar to the observations of Shaibah et al., 2016 [44] who postulated that CPH caused highly significant dystrophic and apoptotic alterations in the neurocytes of the hippocampus with a marked reduction in the neurocyte cell layer thickness. On the contrary, Lyons et al., 2011 [30] pointed out that CPH did not affect the survival of the cells of the hippocampus in rats after a short-term treatment and it is less neurotoxic than other antineoplastic agents. Consequently, it is concluded that CPH could provoke neuronal damage in the hippocampus due to the long term and not in short term treatment.

The H&E stained sections of the rats treated with CPH plus nano-Se, in the present study, showed that most of the neurocytes were healthy in the hippocampus apart from few cells exhibited dystrophic changes. Additionally, the thickness of the pyramidal cell layer and granule cell layer was significantly increased
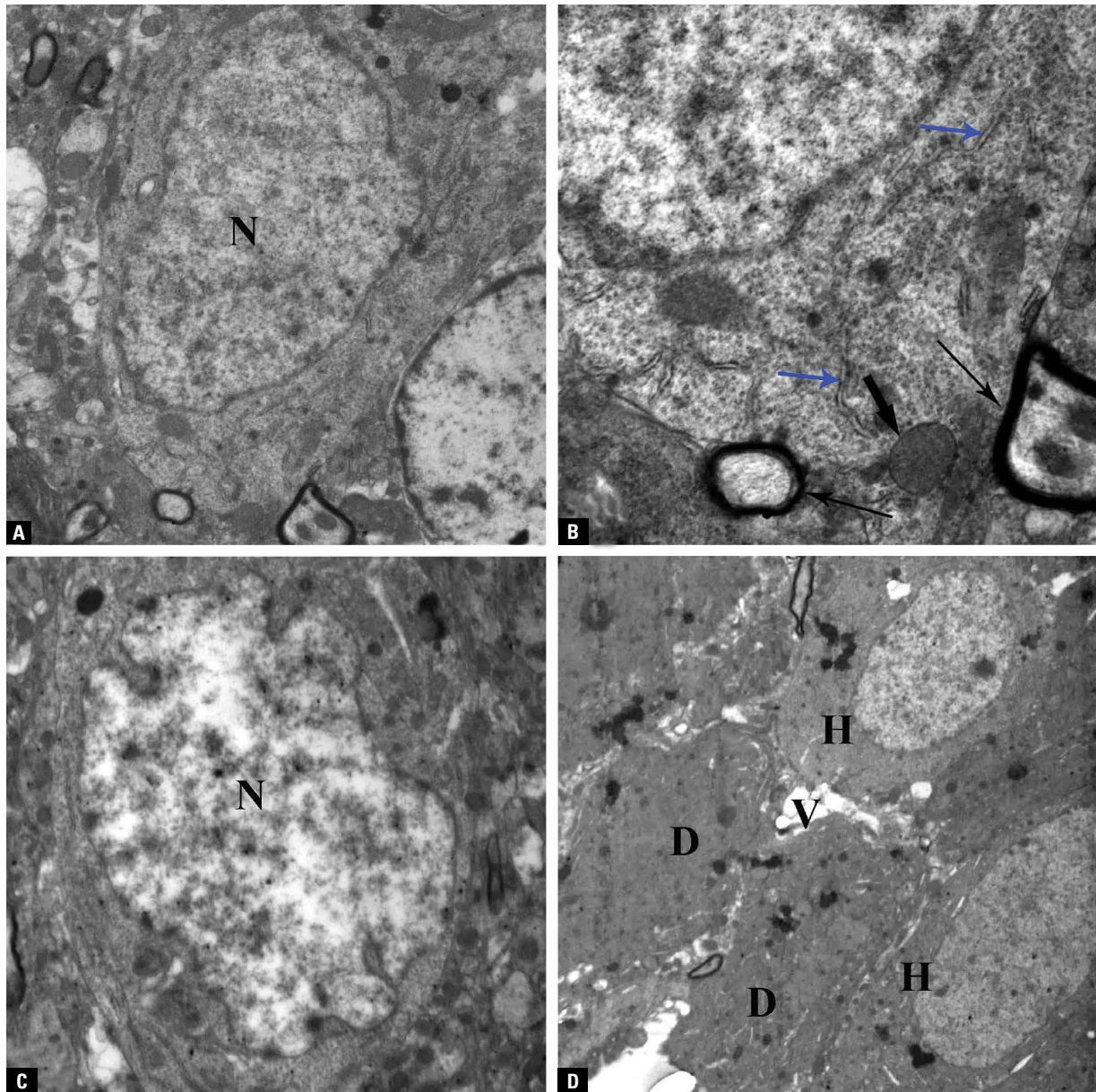
Figure 10. Transmission electron microscopic micrographs of neurocytes of the cyclophosphamide plus nano-selenium group; **A.** A cell with electro-lucent nucleus (N) with a nearly regular outline and dispersed chromatin; **B.** A higher magnification of panel A showing healthy mitochondria (thick arrow), nearly normal rough E (blue arrow), and intact neurolemmal sheaths (thin arrow); **C.** A cell with electro-lucent nucleus (N) with irregular outline; **D.** Healthy cells (H) and damaged cells (D) with deeply stained nuclei and cytoplasmic vacuolation (V) (A, C: ×2500, B: ×6000, D: ×1500).

as compared to the CPH group. These ameliorating results induced by nano-Se were in harmony with the previous studies insuring the ameliorating effect of nano-Se on the different tissues against the tissue deleterious effect of cyclophosphamide and the other injurious factors. In this context, Bhattacharjee et al., 2014 [7] reported that nano-Se alleviated degenerative changes in the liver induced by CPH. Moreover, Hamza et al., 2020 [17] reported that nano-Se could protect also against the hepatocellular

damage induced by acrylamide. Additionally, Dkhil et al., 2016 [13] stated that nano-Se prevented and minimised diabetes-induced spermatogenic cell loss in diabetic rats. Similarly, Abdel-Hakeem et al., 2020 [1] reported that nano-Se could mitigate the degeneration, necrosis, and inflammation of pancreatic acini and Langerhans cells caused by acute pancreatitis.

The protective effect of nano-Se on the hippocampus and the other tissues may be due to its antioxidant power against the oxidant damaging effect of

CPH as stated by the previous studies. Akomolafe et al., 2020 [2] postulated that CPH has a pro-oxidant character and its administration is associated with induction of oxidative stress by the generation of free radicals. Moreover, Valko et al., 2006 [52] reported that higher levels of malondialdehyde were noted in the brain of CPH treated mice. Malondialdehyde is an outcome of lipid peroxidation and has been recorded to cause neuronal damage [52]. On the other hand, nano-Se significantly inhibited CPH induced free radicals formation which may be due to its antioxidant property [7]. Nano Se played important roles in the enhancement of the antioxidant defence system and scavenging free radicals by increasing activities of both and glutathione S-transferase and glutathione peroxidase [20, 40, 58].

In the present study, the thickness of the neurocyte cell layers (pyramidal and granule layers) was significantly reduced in the group treated with CPH. This reduction occurred due to the decrease in the neurocyte population owing to the cellular damage (necrosis and/or apoptosis). Additionally, the reduction in the population of cells may be also due to the inhibition of hippocampal neurogenesis by CPH that was mentioned recently in numerous studies. The reduction in hippocampal neurogenesis by CPH could affect the hippocampal related cognitive functions and memory [12, 56]. Nano-Se, in the present study, prevented the decrease in the thickness of neurocyte cell layers in the group treated with CPH plus nano-Se. This may be due to the prevention of cellular degeneration, necrosis, and apoptosis by nano-Se. The positive impact of nano-Se on neurogenesis may be also assumed which could be an additional cause of increased neurocyte cell layers thickness.

Caspase-3 has been known as an essential therapeutic target in neurodegeneration owing to its involvement in neuroinflammation and apoptosis [21]. Immunohistochemical examination and morphometric analysis, in the current study, revealed that CPH injection significantly increased the area percentage of caspase-3 reaction and the AI which reflected the increase in the number of cells showing positive reactions to caspase-3 (an apoptosis marker). This result was in line with the observations of Shaibah et al., 2016 [44] who reported that immunohistochemical section of rats injected with CPH showed a large number of apoptotic neurons with a positive reaction for p53 (an apoptosis marker) and a less positive reaction for Bcl2 (anti-apoptotic marker).

The immunohistochemical results also revealed that nano-Se reduced the area percentage of caspase-3 reaction and the AI in the group exposed to CPH plus nano-Se. Our results were in harmony with that of Wang et al., 2019 [53] who studied the effect of nano-Se on cultured pancreatic cells. They stated that nano-Se completely inhibited the activation of caspase-3, -8, and -9 and consequently, suppressing apoptosis. On the contrary Huang et al., 2010 [18] proved that nano-Se provoked initiation of apoptosis through destabilization of the membrane potential of mitochondria and raised the expression of many pro-apoptotic caspases. These differences in results may due to the variations in doses and sizes of nano-Se utilised. As for nano-Se to produce apoptosis, it should reside within the cell at high concentrations. Moreover, the diversity in cell type upon which nano-Se acts, the variations in cellular redox status, and different durations of administration may be other causes [22].

Glial fibrillary acidic protein is a cellular protein that is found in various cell types of the brain particularly astrocytes [48]. GFAP is known to be essential for changing astrocyte shape and mobility by increasing the structural stability of the processes of astrocytes [29]. GFAP is also known as a specific marker for the maturity of astrocytes [14]. It was found that injury of the brain, whether because of chemical agents, diseases, or trauma led to astrogliosis. In astrogliosis, rapid synthesis of GFAP occurs and is detected by immunostaining with GFAP antibodies [26]. In the current study, CPH triggered the activation of astrocytes that was manifested in the form of increased expression of GFAP. This might be a compensatory mechanism for neuronal damage. Moreover, nano-Se significantly reduced the expression of GFAP which indicated that nano-Se could inhibit CPH induced neuronal damage and its concomitant astrogliosis.

So far, there was very limited data in the previous studies about the effect CPH on the ultrastructure of the hippocampus in adult rats. By TEM, the results of the present study revealed that CPH produced mild dilation of rough endoplasmic reticulum, mitochondrial cristeolysis, disrupted neurolemmal sheaths of nerve fibres, neuronal degeneration, and necrosis which was greatly reversed by nano-Se co-treatment. Our observations were in harmony with the developmental study of Xiao et al., 2007 [54] who reported that CPH decreased the growth and viability of neurons, destroyed

nuclear DNA, and provoked apoptotic morphological alterations in rat embryos. CPH may induce neuroinflammation and neurodegeneration due to enhancing nitric oxide synthesis and increasing arginase activity. Experimental studies have revealed that elevated arginase activity and changes in nitric oxide levels may contribute to neurodegeneration [11, 38]. Additionally, Mohammed and Safwat, 2013 [33] reported that the administration of nano-Se significantly decreased the nitric oxide concentration in brain tissue. So, the reduction in the nitric oxide level caused by nano-Se may be one of the causes of its neuroprotective effects.

CONCLUSIONS

Cyclophosphamide injection in rats triggered cellular degeneration, necrosis, and apoptosis of hippocampal neurocytes. Moreover, it caused mild dilation of rough endoplasmic reticulum, mitochondrial cristeolysis, and disrupted neurolemmal sheaths of nerve fibres at the ultrastructural level. Nano-Se co-treatment mitigated these deleterious changes induced by cyclophosphamide. So, nano-Se supplementation to the diet of patients treated with CPH may be useful. Further studies are required to elucidate the mechanism of action nano selenium as a protective factor against chemotherapeutic drugs as cyclophosphamide.

Funding

Conflict of interest: None declared

REFERENCES

1. Abdel-Hakeem EA, Abdel-Hamid HA, Abdel Hafez SM. The possible protective effect of Nano-Selenium on the endocrine and exocrine pancreatic functions in a rat model of acute pancreatitis. J Trace Elem Med Biol. 2020; 60: 126480, doi: 10.1016/j.jtemb.2020.126480, indexed in Pubmed: 32146341.
2. Akomolafe SF, Olasehinde TA, Oyeleye SI, et al. Curcumin administration mitigates cyclophosphamide-induced oxidative damage and restores alteration of enzymes associated with cognitive function in rats' brain. Neurotox Res. 2020; 38(1): 199–210, doi: 10.1007/s12640-020-00205-0, indexed in Pubmed: 32405958.
3. Arumugam N, Sivakumar V, Thanislass J, et al. Effects of acrolein on rat liver antioxidant defense system. Indian J Exp Biol. 1997; 35(12): 1373–1374, indexed in Pubmed: 9567773.
4. Bancroft J, Layton C, Suvarna S.K. Bancroft's Theory and Practice of Histological Techniques: Expert Consult: Online and Print, 7e; 2012.
5. Bancroft J, Stonard J. Classical histochemical methods. Bancroft's Theory and Practice of Histological Techniques. 2013: 563–575, doi: 10.1016/b978-0-7020-4226-3.00025-1.
6. Barton D, Loprinzi C. Novel approaches to preventing chemotherapy-induced cognitive dysfunction in breast cancer: the art of the possible. Clin Breast Cancer. 2002; 3 Suppl 3: S121–S127, doi: 10.3816/cbc.2002.s.023, indexed in Pubmed: 12533273.
7. Bhattacharjee A, Basu A, Ghosh P, et al. Protective effect of Selenium nanoparticle against cyclophosphamide induced hepatotoxicity and genotoxicity in Swiss albino mice. J Biomater Appl. 2014; 29(2): 303–317, doi: 10.1177/0885328214523323, indexed in Pubmed: 24522241.
8. Bohnenstengel F, Friedel G, Ritter CA, et al. Variability of cyclophosphamide uptake into human bronchial carcinoma: consequences for local bioactivation. Cancer Chemother Pharmacol. 2000; 45(1): 63–68, doi: 10.1007/PL00006745, indexed in Pubmed: 10647504.
9. Boostani A, Sadeghi AA, Mousavi SN, et al. Effects of organic, inorganic, and nano-Se on growth performance, antioxidant capacity, cellular and humoral immune responses in broiler chickens exposed to oxidative stress. Livestock Sci. 2015; 178: 330–336, doi: 10.1016/j.livsci.2015.05.004.
10. Cai SJ, Wu CX, Gong LM, et al. Effects of nano-selenium on performance, meat quality, immune function, oxidation resistance, and tissue selenium content in broilers. Poult Sci. 2012; 91(10): 2532–2539, doi: 10.3382/ps.2012-02160, indexed in Pubmed: 22991539.
11. Caldwell RB, Toque HA, Narayanan SP, et al. Arginase: an old enzyme with new tricks. Trends Pharmacol Sci. 2015; 36(6): 395–405, doi: 10.1016/j.tips.2015.03.006, indexed in Pubmed: 25930708.
12. Christie LA, Acharya MM, Parihar VK, et al. Impaired cognitive function and hippocampal neurogenesis following cancer chemotherapy. Clin Cancer Res. 2012; 18(7): 1954–1965, doi: 10.1158/1078-0432.CCR-11-2000, indexed in Pubmed: 22338017.
13. Dkhil MA, Zrieq R, Al-Quraishy S, et al. Selenium nanoparticles attenuate oxidative stress and testicular damage in streptozotocin-induced diabetic rats. Molecules. 2016; 21(11), doi: 10.3390/molecules21111517, indexed in Pubmed: 27869771.
14. Eng LF, Ghirnikar RS, Lee YL. Glial fibrillary acidic protein: GFAP-thirty-one years (1969-2000). Neurochem Res. 2000; 25(9-10): 1439–1451, doi: 10.1023/a:1007677003387, indexed in Pubmed: 11059815.
15. Goud KG, Veldurthi NK, Vithal M, et al. Characterization and evaluation of biological and photocatalytic activities of selenium nanoparticles synthesized using yeast fermented broth. Applied Nanomedicine. Published online. 2016.

16. Hamoud A. Possible role of selenium nano-particles on gentamicin-induced toxicity in rat testis: morphological and morphometric study. Egypt J Histol. 2019; 0(0): 0–0, doi: 10.21608/ejh.2019.9926.1093.

17. Hamza R, EL-Megharbel S, Altalhi T, et al. Hypolipidemic and hepatoprotective synergistic effects of selenium nanoparticles and vitamin. E against acrylamide-induced hepatic alterations in male albino mice. Applied Organometallic Chemistry. 2020; 34(3), doi: 10.1002/aoc.5458.

18. Huang G, Zhang Y, Zhang Q, et al. Vacuolization and apoptosis induced by nano-selenium in HeLa cell line. Science China Chemistry. 2010; 53(11): 2272–2278, doi: 10.1007/s11426-010-4116-7.

19. Kannan N, Subbalaxmi S. Biogenesis of nanoparticles: a current perspective. Reviews on Advanced Materials Science. Published online. 2011.

20. Khalaf AA, Ahmed W, Moselhy WA, et al. Protective effects of selenium and nano-selenium on bisphenol-induced reproductive toxicity in male rats. Hum Exp Toxicol. 2019; 38(4): 398–408, doi: 10.1177/0960327118816134, indexed in Pubmed: 30526071.

21. Khan S, Ahmad K, Alshammari EMA, et al. Implication of caspase-3 as a common therapeutic target for multineurodegenerative disorders and its inhibition using nonpeptidyl natural compounds. Biomed Res Int. 2015; 2015: 379817, doi: 10.1155/2015/379817, indexed in Pubmed: 26064904.

22. Khurana A, Tekula S, Saifi MA, et al. Therapeutic applications of selenium nanoparticles. Biomed Pharmacother. 2019; 111: 802–812, doi: 10.1016/j.biopha.2018.12.146, indexed in Pubmed: 30616079.

23. Kitamura Y, Kanemoto E, Sugimoto M, et al. Influence of nicotine on doxorubicin and cyclophosphamide combination treatment-induced spatial cognitive impairment and anxiety-like behavior in rats. Naunyn Schmiedebergs Arch Pharmacol. 2017; 390(4): 369–378, doi: 10.1007/s00210-016-1338-z, indexed in Pubmed: 28064347.

24. Kumar A, Prasad KS. Biogenic selenium nanoparticles for their therapeutic application. Asian J Pharmaceut Clin Res. 2019: 4–9, doi: 10.22159/ajpcr.2020.v13i1.35599.

25. Lal Bhatia A, Manda K, Patni S, et al. Prophylactic action of linseed (Linum usitatissimum) oil against cyclophosphamide-induced oxidative stress in mouse brain. J Med Food. 2006; 9(2): 261–264, doi: 10.1089/jmf.2006.9.261, indexed in Pubmed: 16822213.

26. Li DRi, Ishikawa T, Zhao D, et al. Histopathological changes of the hippocampus neurons in brain injury. Histol Histopathol. 2009; 24(9): 1113–1120, doi: 10.14670/HH-24.1113, indexed in Pubmed: 19609858.

27. Liang XJ, Chen C, Zhao Y, et al. Circumventing tumor resistance to chemotherapy by nanotechnology. Methods Mol Biol. 2010; 596: 467–488, doi: 10.1007/978-1-60761-416-6_21, indexed in Pubmed: 19949937.

28. Ludeman SM. The chemistry of the metabolites of cyclophosphamide. Curr Pharm Des. 1999; 5(8): 627–643, indexed in Pubmed: 10469895.

29. Lumpkins KM, Bochicchio GV, Keledjian K, et al. Glial fibrillary acidic protein is highly correlated with brain injury. J Trauma. 2008; 65(4): 778–782, doi: 10.1097/TA.0b013e318185db2d, indexed in Pubmed: 18849790.

30. Lyons L, Elbeltagy M, Bennett G, et al. The effects of cyclophosphamide on hippocampal cell proliferation and spatial working memory in rat. PLoS One. 2011; 6(6): e21445, doi: 10.1371/journal.pone.0021445, indexed in Pubmed: 21731752.

31. Martin PM, O'Callaghan JP. A direct comparison of GFAP immunocytochemistry and GFAP concentration in various regions of ethanol-fixed rat and mouse brain. J Neurosci Methods. 1995; 58(1-2): 181–192, doi: 10.1016/0165-0270(94)00175-g, indexed in Pubmed: 7475226.

32. Modica-Napolitano JS, Singh KK. Mitochondria as targets for detection and treatment of cancer. Expert Rev Mol Med. 2002; 4(9): 1–19, doi: 10.1017/S1462399402004453, indexed in Pubmed: 14987393.

33. Mohammed ET, Safwat GM. Assessment of the ameliorative role of selenium nanoparticles on the oxidative stress of acetaminophen in some tissues of male albino rats. Beni-Suef University J Basic Applied Sci. 2013; 2(2): 80–85, doi: 10.1016/j.bjbas.2013.01.003.

34. Morcos M. Histological and immunohistochemical study on the protective effects of cetrorelix against chemotherapy-induced ovarian damage. Egypt J Histol. 2012; 35(3): 587–597, doi: 10.1097/01.ehx.0000418132.61834.19.

35. Nagy G, Pinczes G, Pinter G, et al. In situ electron microscopy of lactomicroselenium particles in probiotic bacteria. Int J Mol Sci. 2016; 17(7), doi: 10.3390/ijms17071047, indexed in Pubmed: 27376279.

36. Narayanan KB, Sakthivel N. Biological synthesis of metal nanoparticles by microbes. Adv Colloid Interface Sci. 2010; 156(1-2): 1–13, doi: 10.1016/j.cis.2010.02.001, indexed in Pubmed: 20181326.

37. Oboh G, Ogunruku OO. Cyclophosphamide-induced oxidative stress in brain: protective effect of hot short pepper (Capsicum frutescens L. var. abbreviatum). Exp Toxicol Pathol. 2010; 62(3): 227–233, doi: 10.1016/j.etp.2009.03.011, indexed in Pubmed: 19447589.

38. Olasehinde TA, Olaniran AO, Okoh AI. Neuroprotective effects of some seaweeds against Zn - induced neuronal damage in HT-22 cells via modulation of redox imbalance, inhibition of apoptosis and acetylcholinesterase activity. Metab Brain Dis. 2019; 34(6): 1615–1627, doi: 10.1007/s11011-019-00469-2, indexed in Pubmed: 31346859.

39. Oraby HAS, Hassan AAM, Af N, et al. Effect of cyclophosphamide on transcription of SOD1mRNA and GPX1 mRNA in mice liver and brain tissues. Published online. 2010: 1736–1742.

40. Peng D, Zhang J, Liu Q, et al. Size effect of elemental selenium nanoparticles (Nano-Se) at supranutritional levels on selenium accumulation and glutathione S-transferase activity. J Inorg Biochem. 2007; 101(10): 1457–1463, doi: 10.1016/j.jinorgbio.2007.06.021, indexed in Pubmed: 17664013.

41. Prokisch J, Zommara MA. Process for producing elemental selenium nanospheres. 2010;(20100189634). http://www.freepatentsonline.com/y2010/0189634.html.

42. Salem M, Altayeb Z. Light and Electron Microscopic Study on the Possible Protective Effect of Nigella Sativa Oil on Cisplatin Hepatotoxicity in Albino Rats. Egypt J Histol. 2017; 40(1): 68–79, doi: 10.21608/ejh.2017.3698.

43. Seigers R, Loos M, Van Tellingen O, et al. Cognitive impact of cytotoxic agents in mice. Psychopharmacology (Berl). 2015; 232(1): 17–37, doi: 10.1007/s00213-014-3636-9, indexed in Pubmed: 24894481.

44. Shaibah HS, Elsify AEK, Medhat TM, et al. Histopatholog-ical and immunohistochemical study of the protective effect of triptorelin on the neurocytes of the hippocampus and the cerebral cortex of male albino rats after short-term exposure to cyclophosphamide. J Microsc Ultrastruct. 2016; 4(3): 123–132, doi: 10.1016/j.jmau.2015.12.002, indexed in Pubmed: 30023218.

45. Shakibaie M, Forootanfar H, Golkari Y, et al. Anti-biofilm activity of biogenic selenium nanoparticles and seleni-um dioxide against clinical isolates of Staphylococcus aureus, Pseudomonas aeruginosa, and Proteus mirabilis. J Trace Elem Med Biol. 2015; 29: 235–241, doi: 10.1016/j.jtemb.2014.07.020, indexed in Pubmed: 25175509.

46. Sheiha AM, Abdelnour SA, Abd El-Hack ME, et al. Effects of dietary biological or chemical-synthesized nano-sele-nium supplementation on growing rabbits exposed to thermal stress. Animals (Basel). 2020; 10(3), doi: 10.3390/ani10030430, indexed in Pubmed: 32143370.

47. Skalickova S, Milosavljevic V, Cihalova K, et al. Selenium nanoparticles as a nutritional supplement. Nutrition. 2017; 33: 83–90, doi: 10.1016/j.nut.2016.05.001, indexed in Pubmed: 27356860.

48. Sobaniec-Lotowska ME. Ultrastructure of Purkinje cell perikarya and their dendritic processes in the rat cere-bellar cortex in experimental encephalopathy induced by chronic application of valproate. Int J Exp Pathol. 2001; 82(6): 337–348, doi: 10.1046/j.1365-2613.2001.00206.x, indexed in Pubmed: 11846840.

49. Stankiewicz A, Skrzydlewska E, Makieła M. Effects of am-ifostine on liver oxidative stress caused by cyclophospha-mide administration to rats. Drug Metabol Drug Interact. 2002; 19(2): 67–82, doi: 10.1515/dmdi.2002.19.2.67, indexed in Pubmed: 12751907.

50. Subramaniam S, Subramaniam S, Shyamala Devi CS. Erythrocyte antioxidant enzyme activity in CMF treated breast cancer patients. Cancer Biochem Biophys. 1994; 14(3): 177–182, indexed in Pubmed: 7728738.

51. Ueno M, Katayama Ki, Yamauchi H, et al. Cell cycle progres-sion is required for nuclear migration of neural progenitor cells. Brain Res. 2006; 1088(1): 57–67, doi: 10.1016/j.brainres.2006.03.042, indexed in Pubmed: 16650835.

52. Valko M, Leibfritz D, Moncol J, et al. Free radicals and antiox-idants in normal physiological functions and human disease. Int J Biochem Cell Biol. 2007; 39(1): 44–84, doi: 10.1016/j.biocel.2006.07.001, indexed in Pubmed: 16978905.

53. Wang L, Li C, Huang Q, et al. Biofunctionalization of selenium nanoparticles with a polysaccharide from Rosa roxburghii fruit and their protective effect against HO-induced apoptosis in INS-1 cells. Food Funct. 2019; 10(2): 539–553, doi: 10.1039/c8fo01958d, indexed in Pubmed: 30662993.

54. Xiao R, Yu HL, Zhao HF, et al. Developmental neurotoxicity role of cyclophosphamide on post-neural tube closure of rodents in vitro and in vivo. Int J Dev Neurosci. 2007; 25(8): 531–537, doi: 10.1016/j.ijdevneu.2007.09.012, indexed in Pubmed: 18022788.

55. Xu C, Shu WQ, Qiu ZQ, et al. Protective effects of green tea polyphenols against subacute hepatotoxicity induced by microcystin-LR in mice. Environ Toxicol Pharmacol. 2007; 24(2): 140–148, doi: 10.1016/j.etap.2007.04.004, indexed in Pubmed: 21783802.

56. Yang M, Kim JS, Song MS, et al. Cyclophosphamide impairs hippocampus-dependent learning and memory in adult mice: Possible involvement of hippocampal neurogenesis in chemotherapy-induced memory deficits. Neurobi-ol Learn Mem. 2010; 93(4): 487–494, doi: 10.1016/j.nlm.2010.01.006, indexed in Pubmed: 20109567.

57. Yu Bo, Zhang Y, Zheng W, et al. Positive surface charge enhances selective cellular uptake and anticancer ef-ficacy of selenium nanoparticles. Inorg Chem. 2012; 51(16): 8956–8963, doi: 10.1021/ic301050v, indexed in Pubmed: 22873404.

58. Zhang J, Zhang SY, Xu JJ, et al. new method for the syn-thesis of selenium nanoparticles and the application to construction of H2O2 biosensor. Chinese Chemical Letters. Published online. 2004.

59. Zhao CY, Cheng R, Yang Z, et al. Nanotechnology for cancer therapy based on chemotherapy. Molecules. 2018; 23(4), doi: 10.3390/molecules23040826, indexed in Pubmed: 29617302.

VIA MEDICA

O R I G I N A L   A R T I C L E

Anatomical variations and morphometric properties of the circulus arteriosus cerebri in a cadaveric Malawian population

C. Nyasa[1], A. Mwakikunga[1, 2], L.H. Tembo[1, 2], C. Dzamalala[1], A.O. Ihunwo[2]

[1]Biomedical Sciences Department, Anatomy Division, College of Medicine, University of Malawi, Blantyre, Malawi
[2]School of Anatomical Sciences, Faculty of Health Sciences, University of the Witwatersrand, Parktown, Johannesburg, South Africa

Background: Knowledge of the anatomy of the circulus arteriosus cerebri (CAC) is important in understanding its role as an arterial anastomotic structure involved in collateral perfusion and equalisation of pressure, and may explain observed variations in neurovascular disease prevalences across populations. This study was aimed at understanding the anatomical configuration and morphometric properties of the CAC in Malawian population.

Materials and methods: Brains were collected from 24 recently-deceased black Malawian human cadavers during medico-legal autopsies. Photographs of the CACs were taken using a camera placed at a 30 cm height from the base of the brain. Whole-circle properties and segmental vessel parameters were analysed using the OSIRIS computer programme, paying attention to completeness, typicality, symmetry, and segmental vessel diameters and lengths.

Results: The complete-circle configuration was found in 69.57% of the CACs. Of these, 37.5% were typical, representing an overall typicality prevalence of 26.09%. Vessel asymmetry was observed in 30.43% of cases. There were 7 cases of vessel aplasia and 12 cases of vessel hypoplasia. The posterior communicating artery (PcoA) was the most variable (with 12 variations), widest (7.67 mm) and longest (27.7 mm) vessel while the anterior communicating artery (AcoA) was the shortest (0.78 mm). Both the AcoA and the PcoA were the narrowest vessels (0.67 mm) in this study. CAC variations in Malawian populations appeared to be similar to those observed in diverse populations.

Conclusions: Anatomical variations of the CAC exist in Malawian population and should be taken into consideration in clinical practice. (Folia Morphol 2021; 80, 4: 820–826)

Key words: anatomical configuration, neurovascular diseases, posterior communicating artery, anterior communicating artery, circle of Willis, hypoplasia, aplasia, vessel asymmetry, internal carotid artery

---

Address for correspondence: Dr. C. Nyasa, Biomedical Sciences Department, Anatomy Division, University of Malawi, Blantyre, Malawi,
tel: +265 88 433 1918, fax: 01 874 700, e-mail: cnyasa@medcol.mw

INTRODUCTION

The circulus arteriosus cerebri (CAC), also known as the circle of Willis, is a polygonal anastomotic system of arteries that constantly supplies blood to the brain. First described in the year 1658 and later detailed by Thomas Willis in the year 1664 [1], the CAC connects the four sources of brain vascular supply: 2 internal carotid arteries (ICA) and 2 vertebral arteries [19]. In a typical CAC, the ICA give rise to the anterior cerebral arteries (ACA) which are connected to each other by the anterior communicating artery (AcoA) while the vertebral arteries terminate by fusion into the basilar artery [21]. The basilar artery bifurcates to give rise to two posterior cerebral arteries (PCA). The PCA are connected to the ICA system by the posterior communicating arteries (PcoA) [1]. This anastomotic network forms an arterial ring at the base of the brain, which serves to provide collateral blood circulation to the brain through the major branches that arise from it and equalize the pressure. Anastomotic flow of blood in the proximal portions of the cerebral arterial tree is of great physiological importance, in as far as adequate brain perfusion is concerned. This is most evident in times of arterial incompetence such as during states of occlusive cerebrovascular conditions [21].

The clinical significance of the CAC needs no special emphasis. A number of studies have established the role of an anatomically complete circle of Willis in maintaining sufficient cerebral perfusion [19, 20]. Variations in the anatomy of the CAC have also been observed across population groups, ages and genders, some of which highly correlate with increased risk of neurosurgery complication and conditions such as migraine [1, 10], stroke [22, 24], and aneurysms [15, 23]. Evidence reveals existence of both typical and atypical CAC variants within populations [4]. A typical CAC exhibits a complete polygonal structure with all its component vessels intact and branching from usual locations. All CACs with missing (aplastic) or hypoplastic (string-like) component vessels are referred to as atypical.

The issue of segmental vessel aplasia or hypoplasia raises important questions on the systems' ability to maintain adequate cerebral perfusion in normal states and the relationship between these variations and the risks of neurovascular diseases. The number of working collaterals within a CAC has been associated with lower stroke incidence in 2-year follow up studies [6, 19]. Further, variations in anatomy of the CAC have, over the years, been used to explain, in part the observed difference in prevalence, incidence and geographical distribution of certain neurovascular diseases [2].

In literature, the CAC has been classified in at least three ways namely; whole circle classification [2, 5, 13, 20], classification by segmental vessels [3, 4, 18], and classification by configuration of the posterior circulation [24]. Unlike the other systems, whole circle classifications are particularly important in that they focus on both the completeness of the arterial ring and the calibre of its component vessels. In addition, whole circle studies enable comparison across populations. However, studies on whole-circle properties are sparse and when available direct comparison is often a challenge due to inconsistent study protocols, and unspecified methodologies by some researchers [4]. For instance, the definition of hypoplasia and methods of vessel measurement have varied greatly across studies.

The anatomy of the CAC has not been previously studied in Malawians and little is known on the distribution of neurovascular variations that exist in this population. Consequently, data on differences and similarities in anatomical configuration of the CAC between black Malawians and other diverse populations has not been established. This study aimed to understand and describe the anatomy of the CAC among indigenous Malawians and investigate variations in its anatomical configuration in comparison with other population groups. Knowledge of the morphological anatomy of the CAC among Malawians will help inform clinical practice, aid assessment of risks for public health interventions and offer convincing explanations on the prevalence of neuro-vascular diseases in Malawi.

MATERIALS AND METHODS

Sample collection

A total of 24 brains were studied from the recently deceased black Malawian cadavers aged 3–65 years who were candidates of autopsy for medical-legal reasons in the laboratories of the Anatomy Division, College of Medicine, University of Malawi. The brains were extracted from cranial cavities, washed with isotonic saline to remove blood around the region of interpeduncular fossa, and fixed with 10% formalin. Cases with remarkable alteration in brain arteries and gross pathological lesions such as crush injuries, macroscopically identified tumours and severe haemorrhage were excluded from the study.
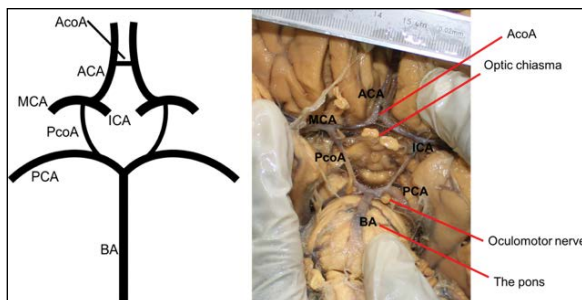
Figure 1. Schematic diagram and photograph of complete circulus arteriosus cerebri configurations showing major component vessels; AcoA — anterior communicating artery; ACA — anterior cerebral artery; MCA — middle cerebral artery; ICA — internal carotid artery; PcoA — posterior communicating artery; PCA — posterior cerebral artery; BA — basilar artery.

This study was conducted in accordance with the Government of Malawi Anatomy Act No. 14 of 1990 and was approved by the University of Malawi's College of Medicine Research and Ethics Committee (COMREC) with a clearance number P05/15/1729.

Photography and image analysis

Extracted brains were placed on a flat plane with a white background, ventral surface up. Images of the exposed base were taken with an 18.4 Megapixels camera (Canon EOS 600D, 2011 model, Cannon USA). Before photography, a metric calliper gauge was placed horizontally on the frontal lobes anterior to temporal poles and each image was taken perpendicularly from a 30 cm height in order to minimise errors that may arise due to variations in angles of view.

Photographs were initially studied under direct vision to define the completeness of the CACs, then with OSIRIS software package installed on a Microsoft Windows 10 computer to measure length and diameter of component vessels. OSIRIS is an open source extensible and portable programme for displaying, manipulating and analysing digital images. Designed in 1990 at the University Hospital of Geneva, the program is equipped with various image manipulation functions that allow a user to flip, zoom, pan and magnify images thereby allowing evaluation of distances and angles for research purposes [1]. The use of OSIRIS as a tool for studying morphometric anatomy of the CAC was described in previous works by Ansari et al. [1] and Eftekhar et al. [4], and needs not be repeated here.

Vessels studied included the AcoA, the precommunicating part of ACA (A1), the PcoA and the precommunicating part of PCA (P1) (Fig. 1). To be consistent with previous studies [1, 2, 12], a cut-off point of 1 mm was used to define vessel hypoplasia while asymmetry was defined as a vessel's diameter or length being less than half of that on the contralateral side within a CAC architecture. Data was processed in Microsoft Excel programme and CACs were schematised based on a scheme described by Riggs [20]. Descriptive statistics of component vessel properties and hypothesis tests were run in Stata version 14.

Table 1. Distribution of differences in whole circle properties

Property	Variant	Subvariant	Count (%)
Typicality	Typical		6 (26.09%)
	Atypical	Complete	10 (43.49%)
		Incomplete	7 (30.43%)
Symmetry	Symmetrical		16 (69.57%)
	Asymmetrical		7 (30.43%)

RESULTS

Data was processed at the level of the circle, where whole circle properties such as typicality, completeness and symmetry of the CAC were assessed, and at the level of individual segmental vessels, where vessel parameters such as length and diameter were analysed. One hundred and 58 segmental vessels from the 24 photographed arterial circles were measured and analysed in this study. There was one brain whose circle had completely lost posterior circulatory vessels (the P1 and PcoA). However, it was still included in the final analyses because its anterior circulation was intact. 69.57% of the CACs studied were complete, 37.5% of which exhibited the classical text-book (typical) configuration where all segmental vessels were intact and had diameters of at least 1 mm. This represented an overall typicality prevalence of 26.09% (Table 1). Asymmetry of vessels between opposite sides of the CAC was observed in 7 (30.43%) brains. Vessels involved in asymmetry included P1 (4), A1 (3) and PcoA (2). Two CACs had double asymmetry, one involving P1 and PcoA vessels, and the other involving A1 and PcoA vessels. Table 1 presents a summary on the distribution of whole-circle CAC characteristics.

Analysis at the level of segmental vessels revealed 19 separate cases of variations. There were 7 (29.17%) cases of vessel aplasia, 4 of which were observed on the right side of the CAC and 3 on the left. Cases of hypoplasia were seen in 5 instances on the right side
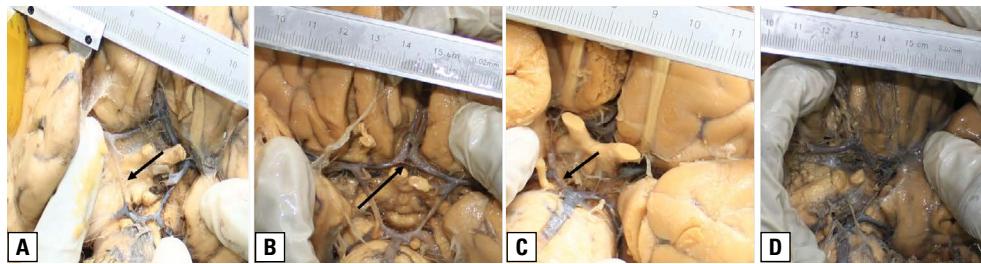
Figure 2. Some of the variations seen in this study; **A.** Circulus arteriosus cerebri with right unilateral posterior communicating artery hypoplasia (arrow); **B.** Circulus arteriosus cerebri with duplicated anterior communicating artery, the proximal of which was hypoplastic (arrow); **C.** Circulus arteriosus cerebri with unilateral P1 hypoplasia (arrow); **D.** Circulus arteriosus cerebri with right posterior communicating artery aplasia (missing).

of the CAC, 3 instances on the left and 3 instances in the AcoA, making a total of 12 (45.83%) cases.

Comparison between the posterior (P1 and PcoA) and anterior (A1, AcoA) circulatory routes of the CAC revealed existence of more variations in the posterior route. Eight cases of vessel hypoplasia and 7 cases of vessel aplasia were observed in the posterior circulation while only 4 cases of vessel hypoplasia were observed in the anterior. Most of the variations in the posterior circulation were associated with the PcoA. There was no case of aplasia in the anterior circulation.

Duplication of vessels, in this instance associated with the AcoA, was observed in 1 case (Fig. 2). There were only 2 candidates with more than one variation in the arterial circle (right PcoA hypoplasia with left PcoA aplasia; right PcoA and AcoA hypoplasia). The PcoA was the most variable vessel (with 12 variations) in this study, followed by the P1 (3 variations) and the AcoA (3 variations). The smallest diameter (0.67 mm) was observed both in AcoA and PcoA vessels. The AcoA was the shortest (0.78 mm) vessel while the PcoA was the widest (7.67 mm) and longest (27.7 mm) vessel. Hypoplasia was seen at least once in each vessel type (A1, P1, PcoA and AcoA) as shown in Table 2. A paired samples t-test revealed no statistically significant differences in length (p = 0.1256) and diameter (p = 0.9434) between first and second measurements that were collected in A1 vessel at an Alpha of 0.05. No aneurysms were observed in this study.

DISCUSSION

Whole circle properties: typicality and completeness

Our findings suggest that although anatomically complete arterial circles are common in most populations, circles exhibiting the classical or typical configuration are not. Despite the wide prevalence range (4.6% to 72.2%) reported in literature [3, 25], studies

Table 2. Variations in segmental vessels of the circulus arteriosus cerebri

Vessel segment	Parameter	Laterality	Count (n) or mean ± standard deviation
AcoA	Diameter		1.65 ± 0.64
	Length		2.92 ± 0.94
	Hypoplasia (n)		3
	Aplasia (n)		0
A1	Diameter		1.75 ± 0.45
	Length		12.54 ± 3.07
	Hypoplasia (n)	Unilateral	1 (left)
		Bilateral	0
	Aplasia (n)	Unilateral	0
		Bilateral	0
PcoA	Diameter		1.61 ± 1.05
	Length		12.95 ± 4.63
	Hypoplasia (n)	Unilateral	5 (4 right, 1 left)
		Bilateral	0
	Aplasia (n)	Unilateral	7 (3 right, 4 left)
		Bilateral	0
P1	Diameter		1.60 ± 1.05
	Length		5.87 ± 1.98
	Hypoplasia (n)	Unilateral	3 (1 right, 2 left)
		Bilateral	0
	Aplasia (n)	Unilateral	0
		Bilateral	0

Multiple variations: 2 (right PcoA hypoplasia and left PcoA aplasia, right PcoA and AcoA hypoplasia). Duplication of vessels: 1 (AcoA); AcoA — anterior communicating artery; PcoA — posterior communicating artery

that have reported typical CAC prevalences higher than 50% are rare. In the present study, the prevalence of typical CACs falls within the range and is consistent with studies conducted in other diverse populations [3, 25]. For instance, prevalences of 14.2%, 27%, 28%, and 48% were reported among Sri Lankans, Poles, Iranians and Indians, respectively [2–4, 10, 12]. Koker et al. [11],

reported a typical CAC prevalence of 8% in Turkish population while Americans registered 19% and 14.5% [20]. On the contrary, complete CACs are common in several populations. In the present study, 70.83% of the brains had complete CACs. Similarly, a 90% prevalence was reported among Iranians [4]. Regardless of typicality, Zulu and Buumba [25] found completeness in 90.2% of cases among 185 Zambian cadavers, while Gunnal et al. [8], found 1 typical CAC was in a sample of 150 adult brains 90 of which had complete CACs. However, due to lack of adequate information on sample selection, demographic distribution and methods of vessel measurement, the representativeness of the findings could not be commented on.

Typicality of the arterial circle is an attribute that depends on the proposed definition for hypoplasia. Across studies, researchers have defined hypoplastic vessels varyingly. This may have contributed to the wide disparity in the prevalence of CAC typicality in literature. For instance, some authors have previously presented whole circle properties of the CAC based on estimates without actually measuring component vessel parameters such as diameter and length. Others used terms such as 'string-like', 'minute' or 'threadlike' to describe the calibre of hypoplastic vessels [3]. Moreover, even among researchers who have measured component vessels directly, the definition of hypoplasia has not been uniform. Nagawa et al. [16], used a cut-off point of 0.5 mm in a study of Ugandan population while Iqbal used cut-off points of 0.5 mm in the AcoA alone and 1 mm in the rest of the vessels among Indians [10]. Meanwhile, Zulu and Buumba [25] did not exclude hypoplasia in the definition of typicality.

Hemodynamically-unfavourable CAC configurations were observed in this study. For instance, the case of unilateral PcoA and AcoA hypoplasia (Table 2) may affect collateral circulation of blood between the right and left arterial routes. Similarly, the case of PcoA aplasia with contralateral PcoA hypoplasia (Table 2) may affect collateral flow between the ICA and vertebral arteries systems. Both of these may be detrimental in times of cerebrovascular conditions especially where one route is affected (occluded or ruptured) and the other is required to provide backup in order to maintain adequate brain perfusion [3, 14]. Various configurations of atypical CAC have shown to exacerbate or increase the risk of neurovascular diseases [3, 19], and their presence within a population thus demands modification in routine clinical management [7]. For instance, knowing that a larger proportion of

the population exhibit CAC configurations that may inhibit communication between posterior and anterior circulatory routes or between the right and left ICAs (as may be the case in PcoA and AcoA aplasia) would mean that surgeons need to be cautious during neurovascular procedures, particularly those that involve temporary unilateral occlusion of cerebral arteries as would be the case during repair of intracranial aneurysms. Instances of bypassing or shunting effects, vascular inadequacy, recovery and lack of recovery after vascular occlusion procedures have previously been explained by variations in anatomy of cerebral arteries, particularly the CAC [1, 10].

Vessel asymmetry

Vessel asymmetry is a property that is scarcely reported among CAC studies. According to Ansari et al. [1], asymmetry is said to exist when the diameter of a component vessel is less than half of that of its contralateral counterpart. However, Pascalau et al. [19], used an extended definition incorporating both diameter and length. The present study used the latter.

A 30.43% prevalence of asymmetry was observed in the present study, with higher frequencies in the PcoA, followed by A1 and P1 vessels (Table 1). The patterns of asymmetry in the CAC architecture appear to be distributed similarly across populations. Gunnal et al. [8], reported higher frequency of asymmetry in PcoA (58%), A1 (31.33%) and P1 (22.66%) as compared to other vessels in Indian population, which is consistent with findings of the present study. Similar results were also observed among Turks in 2018 [19]. This seems to suggest that some variations in the anatomy of the CAC may, to some extent, be attributed to factors other than racial and geographical differences.

The issue of asymmetry causes variation in branching patterns of segmental vessels of the CAC where some segments arise from and terminate in unusual locations. This tends to position the arterial flow divider at points of bifurcation unfavourably, causing alterations in intravascular haemodynamics [10]. Using mathematical models approximating resistance to flow, vascular conductance and branching, Pascalau et al. [19] demonstrated that asymmetrical arteries offered higher resistance to blood flow and exhibited imbalanced bifurcation geometry to a higher extent than normal arteries. This has been proposed to be an independent risk factors for development of embolism and intracranial aneurysms due to higher

possibilities for increased wall sheer stress within such vessels which may over time accelerate atherogenesis and intimal degeneration [17]. Unsurprisingly, regions with greater likelihood of aneurysms development or rupture represent the most frequently reported sites for asymmetry [10, 19]. Moreover, A1 aplasia, PcoA hypoplasia and basilar artery asymmetrical fusion were independently associated with higher recurrence rate of saccular aneurysms following coil embolization in an 8 years cohort study [23].

Aplasia and hypoplasia

Consistent with other cadaveric studies [1, 12], the PcoA and AcoA were the narrowest vessels (0.67 mm in diameter) in the present study. Segmental vessels' diameter and length are independent factors that affect functionality of the CAC as an anastomotic structure. It has been established that volume of blood flow is directly proportional to arterial diameter and inversely proportional to arterial length [16]. Thus, shorter and wider segmental vessels are seen to favour haemodynamics of the CAC to a greater extent than longer and narrower (or hypoplastic). This is analogous to the way thicker and shorter wires favour flow of current in an electric circuit. Using mathematical models, Pascalau et al. [19], observed that hypoplastic arteries presented a higher resistance to flow than otherwise normal vessels. The PcoA has been the narrowest vessel in many studies [1, 12]. Moreover, in a normal CAC configuration, the PcoA are naturally the narrowest vessels and therefore a point of highest flow resistance in the entire CAC architecture. Due to the widely-established association between vessel hypoplasia and neurovascular diseases [10, 19, 23], this may partly explain the higher occurrence of abnormalities in the posterior half of the CAC as observed in literature.

Apart from hypoplasia, missing vessels (aplasia) also render the CAC unfavourable as a collateral channel for arterial supply to the brain. In literature, cases of complete absence of vessels are quite rare. Most variations have been associated with string-like appearance of vessels, accessory vessels and disparities at branching [3, 19]. De Silva et al. [3] found no aplasia among 225 Sri Lankan brains. In their study, circles were visualised under a dissecting stereomicroscope which may have improved the accuracy of vessel identification, enabling the researchers to measure even the very thin vessels that could otherwise be missed under naked vision. Gunnal et al. [8], found only 2.66%

aplasia cases in a sample of 150 formalin-fixed brains; however, the measurement tool was not specified. Using photography and picture manipulation computer software, the present study found aplasia in 29.17% and hypoplasia in 45.85% of the brains, reflecting fewer cases of aplasia than hypoplasia (Fig. 2). This is consistent with other cadaveric studies [1, 8, 12, 19].

In the present study, variations involving the posterior half (PcoA and P1) of the CAC were more frequent than those involving the anterior half (Table 2). This is a common finding among CAC studies across populations [8–10, 12, 19]. De Silva et al. [3] reported of these variations in 70% of 225 brains in 2009. Similarly, in a study of 100 Polish brains, Koziej et al. [12], found that 88% of the observed variations involved the PcoA alone. Using a similar method as used in the present study, Eftekhar et al. [4] found a total of 87% variations (60% PcoA hypoplasia, 10% PcoA aplasia, and 7% P1 hypoplasia) in the posterior half of the circle. These observations seem to suggest that the distribution of anatomical variations of the CAC may be uniform across populations.

CONCLUSIONS

The present study has provided data on whole-circle properties of the CAC among Malawians for the first time. Values of vessel diameter, vessel length as well as laterality have also been established. Variations in the anatomy of the CAC seem to exist in Malawian population and their distribution appears to be similar to those observed in other diverse populations. CAC configurations with the potential to favour atherogenesis, aneurysm formation and exacerbation of strokes have also been observed. These should be considered when performing various neurovascular procedures, particularly those that involve occlusion of main cerebral vessels in order to avoid unexpected complications. It is recommended based on this study, that such invasive neurovascular procedures be preceded by angiography and functional occlusion tests. Future studies should investigate the prevalence of neurovascular diseases, mechanisms of atherogenesis and aneurysm formation in Malawians.

Conflict of interest: None declared

REFERENCES

1. Ansari S, Dadmehr M, Eftekhar B, et al. A simple technique for morphological measurement of cerebral arterial circle variations using public domain software (Osiris). Anat Cell Biol. 2011; 44(4): 324–330, doi: 10.5115/acb.2011.44.4.324, indexed in Pubmed: 22254161.
2. De Silva KR, Silva R, Amaratunga D, et al. Types of the cerebral arterial circle (circle of Willis) in a Sri Lankan population. BMC Neurol. 2011; 11: 5, doi: 10.1186/1471-2377-11-5, indexed in Pubmed: 21241482.
3. De Silva KR, Silva R, Gunasekera WSL, et al. Prevalence of typical circle of Willis and the variation in the anterior communicating artery: A study of a Sri Lankan population. Ann Indian Acad Neurol. 2009; 12(3): 157–161, doi: 10.4103/0972-2327.56314, indexed in Pubmed: 20174495.
4. Eftekhar B, Dadmehr M, Ansari S, et al. Are the distributions of variations of circle of Willis different in different populations? Results of an anatomical study and review of literature. BMC Neurol. 2006; 6: 22, doi: 10.1186/1471-2377-6-22, indexed in Pubmed: 16796761.
5. El Kh, Azouzi M, Bellakhdar F, et al. Anatomical configuration of the circle of Willis in the adult studied by injection techniques. Apropos of 100 brains. Neurochirugie. 1985; 31(4): 287–293.
6. Eliasziw M, Henderson RD, Fox A, et al. Angiographically defined collateral circulation and risk of stroke in patients with severe carotid artery stenosis. Stroke. 2001; 31(1): 128–132, doi: 10.1161/01.str.31.1.128.
7. Gunnal SA, Farooqui MS, Wabale RN. Anatomical variability of the posterior communicating artery. Asian J Neurosurg. 2018; 13(2): 363–369, doi: 10.4103/ajns.AJNS_152_16, indexed in Pubmed: 29682035.
8. Gunnal SA, Farooqui MS, Wabale RN. Anatomical variations of the circulus arteriosus in cadaveric human brains. Neurol Res Int. 2014; 2014: 687281, doi: 10.1155/2014/687281, indexed in Pubmed: 24891951.
9. Hurst K, Musicki K, Molnár Z, et al. Cerebral cross-perfusion and the Circle of Willis: does physiology trump anatomy? J Vasc Diagnostics Interv. 2017; 5: 35–40, doi: 10.2147/jvd.s121839.
10. Iqbal S. A comprehensive study of the anatomical variations of the circle of willis in adult human brains. J Clin Diagn Res. 2013; 7(11): 2423–2427, doi: 10.7860/JCDR/2013/6580.3563, indexed in Pubmed: 24392362.
11. Koker M, Karatas A, Yilmaz H, Coban G, et al. The anatomy of circulus arteriosus cerebri (circle of willis): a study in turkish population. Turk Neurosurg. 2015; 26(1): 54–61, doi: 10.5137/1019-5149.JTN.13281-14.1, indexed in Pubmed: 26768869.
12. Koziej M, Klimek-Piotrowska W, Rybicka M, et al. A multitude of variations in the configuration of the circle of Willis: an autopsy study. Anat Sci Int. 2015; 91(4): 325–333, doi: 10.1007/s12565-015-0301-2, indexed in Pubmed: 26439730.
13. Lazorthes G, Gouaze A, Santini J, et al. The arterial circle of the brain (circulus arteriosus cerebri). Anat Clin. 1979; 1(3): 241–257.
14. Liebeskind D. Collateral circulation. Stroke. 2003; 34(9): 2279–2284, doi: 10.1161/01.str.0000086465.41263.06.
15. McCarthy P, Delassus P, Fahy P, et al. An experimental investigation of the hemodynamic variations due to aplastic vessels within three-dimensional phantom models of the circle of Willis. Ann Biomed Eng. 2013; 42(1): 123–138, doi: 10.1007/s10439-013-0905-4, indexed in Pubmed: 24018609.
16. Nagawa E, Mwaka E, Kalungi S. Bilateral hypoplasia of the posterior communicating artery: a morphological case report. Anat Physiol. 2017; 7(4): 276.
17. Nixon AM, Gunel M, Sumpio BE. The critical role of hemodynamics in the development of cerebral vascular disease. J Neurosurg. 2010; 112(6): 1240–1253, doi: 10.3171/2009.10.JNS09759, indexed in Pubmed: 19943737.
18. Ozaki T, Handa H, Tomimoto K, et al. Anatomical variations of the arterial system of the base of the brain. Nihon Geka Hokan (Arch Jap Chir). 1977; 46(1): 3–17, indexed in Pubmed: 561574.
19. Pascalau R, Padurean VA, Bartos D, et al. The geometry of the circle of willis anatomical variants as a potential cerebrovascular risk factor. Turk Neurosurg. 2019; 29(2): 151–158, doi: 10.5137/1019-5149.JTN.21835-17.3, indexed in Pubmed: 29484629.
20. Riggs H. Variation in form of circle of Willis. Arch Neurol. 1963; 8(1): 8, doi: 10.1001/archneur.1963.00460010024002.
21. Rosner J, Reddy V, Lui F. Neuroanatomy, Circle of Willis. [Updated 2020 Jul 31]. In: StatPearls [Internet]. Treasure Island (FL): StatPearls Publishing; 2020 Jan.
22. Siddiqi H, Ansar T, Fasih S. Variations in cerebral arterial circle of Willis in patients with hemorrhagic stroke: a computed tomography angiographic study. J Rawalpindi Med Coll. 2013; 17(2): 215–218.
23. Songsaeng D, Geibprasert S, Willinsky R, et al. Impact of anatomical variations of the circle of Willis on the incidence of aneurysms and their recurrence rate following endovascular treatment. Clin Radiol. 2010; 65(11): 895–901, doi: 10.1016/j.crad.2010.06.010, indexed in Pubmed: 20933644.
24. van Raamt AF, Mali WP, van Laar PJ, et al. The fetal variant of the circle of Willis and its influence on the cerebral collateral circulation. Cerebrovasc Dis. 2006; 22(4): 217–224, doi: 10.1159/000094007, indexed in Pubmed: 16788293.
25. Zulu H, Buumba PN. Anatomical Variations of the Circle of Willis as seen at the University Teaching Hospital, Lusaka, Zambia. J Prev Rehabil Med. 2017; 1(2): 61–66.

ORIGINAL ARTICLE

VIA MEDICA

Types of inferior mesenteric artery: a proposal for a new classification

A. Balcerzak[1], O. Kwaśniewska[1], M. Podgórski[3], Ł. Olewnik[1], M. Polguj[2]

[1]Department of Anatomical Dissection and Donation, Medical University of Lodz, Poland
[2]Department of Normal and Clinical Anatomy, Chair of Anatomy and Histology, Medical University of Lodz, Poland
[3]Polish Mother's Memorial *Hospital* Research Institute, *Lodz, Poland*

Background: The inferior mesenteric artery (IMA) is the third main branch of the abdominal aorta and arises at the level of L3, supplying the large intestine from the distal transverse colon to the upper part of the anal canal. The aim of this study was to characterise the course and morphology of the terminal branches of the IMA, and also creating a new IMA classification, which seems to be necessary for clinicians performing surgery in this area.

Materials and methods: The anatomical variations in the branching patterns of the IMA were examined in 40 cadavers fixed in a 10% formalin solution. Morphometric measurements were then obtained twice by two researchers.

Results: Due to the proposed classification system, type I characterised by a common trunk preceding bifurcation into sigmoidal branches and the superior rectal artery after giving left colic artery (LCA) occurred in 57.5% of cases, type II, trifurcation type, in 25%, type III with the superior rectal arteries originating firstly from the IMA in 5%, type IV with the ascending lumbar artery in 10% of cases and type V, a novelty, in 2.5%. The origin of IMA was observed at the level of L2/L3 in 22.5% of cases, at L3 in 25% of cases, at L3/L4 in 15% of cases, at L4 in 35% of cases and at the level of L5 in 2.5% of cases. More than one third (38.1%) of total cases with additional arteries and rapidly bifurcating branches occurred in types III, IV, and V. In women, only the IMA and LCA were significantly narrower than in men. Only the diameter of the IMA correlated with the diameter of the superior rectal artery.

Conclusions: The IMA is characterised by high morphological variability. The introduction of a new, structured, anatomical classification seems necessary for all clinicians. (Folia Morphol 2021; 80, 4: 827–838)

Key words: anatomical variations, inferior mesenteric artery, left colic artery, superior rectal artery, sigmoid branches, new classification, cadavers

INTRODUCTION

The inferior mesenteric artery (IMA) is the third main branch of the abdominal aorta and normally arises at the level of L3. It transports and supplies arterial blood to a significant portion of the gastrointestinal tract — the distal 1/3 of the transverse colon, splenic flexure, descending colon, sigmoid colon and rectum [14].

The most common branches of the IMA include: 1) the left colic, which is located retroperitoneally and supplies the descending colon; 2) the sigmoid branches, which supply the sigmoid colon; and 3) the superior rectal artery or arteries, which are the terminal branches of the IMA at the pelvic brim. Nonetheless, the IMA shows considerable anatomic variations. There have been reports of the left colic artery arising from the abdominal aorta, the IMA giving a branch to the left kidney or the left renal artery arising from the IMA and also a lot of other case reports, which describe numerous variations [1, 3, 7, 9, 12, 13, 15].

Familiarity with anatomical variations of the IMA is relevant to planning radiological and surgical procedures in the distal 1/3 part of the transverse colon, splenic flexure, descending colon, sigmoid colon, rectum and also in any deeply reaching interventions in the left iliac and hypogastrium region like radical resection with preservation of the left colic artery for rectal cancer or embolisation [24]. Embolisation is a remarkably versatile procedure used in nearly all vascular and nonvascular systems to treat a wide range of pathology. Embolisation is a minimally invasive surgical technique. The purpose is to close the lumen of the artery and prevent blood flow to an area of the body, which can effectively shrink a tumour or block an aneurysm.

The aim of our research is to determine variations of the branch origin from the IMA and its anatomical variations, including the occurrence of any additional arteries in the Caucasian population, which may be relevant to minimising complications after diagnostic tests and surgical procedures. A novelty in this work is a new, structured, anatomical classification that includes new types of IMA branches and multiple additional arteries, which are associated with more frequent selective endovascular application of chemotherapeutics to tumours of the transverse, descending or sigmoid colon, rectum, surgical removal of its parts and also selective embolisation. We hypothesize that the IMA is characterised by high morphological variability.

MATERIALS AND METHODS

Forty cadavers, including 21 male (M) and 19 female (F) cadavers, were studied. They were fixed in a 10% formalin solution. The specimens had no traces of surgical intervention in the abdominal area. The Local Bioethics Commission issued a consent for the study (consent no. RNN/93/16/KE).

The study was carried out with classical dissection techniques [17–20]. During the dissection, the IMA morphology, the point where it branched off the abdominal aorta in reference to the spine, the presence of additional arterial branches and of quickly-bifurcating arteries, i.e. those shorter than 2 cm, were evaluated.

The next stage consisted in morphometric measurements of the distance between the origin of IMA and first bifurcation, between the first bifurcation and the second, and between the common trunks from which the final branches originated. Each arterial diameter measurement was taken at the point of its origin from the appropriate artery.

The measurements were taken with an electronic calliper (Mitutoyo Corporation, Kawasaki-shi, Kanagawa, Japan). Each measurement was taken independently twice by two people with high experience in anatomical dissection, accurate within 0.1 mm as in many other studies [16, 17, 20].

Ethical approval and consent to participate

The anatomical protocol of the study was accepted by the Bioethics Committee of the Medical University of Lodz (resolution consent no. RNN/93/16/KE). The cadavers belong to the Department of Anatomical Dissection and Donation of the Medical University of Lodz, Poland.

Statistical analysis

The type of IMA was compared between sexes with the χ^2 test. The normality of the diameter distribution was checked with the Shapiro-Wilk test. As the data was not normally distributed in further comparisons, non-parametric tests were used (the Mann-Whitney, the Wilcoxon and the Kruskal-Wallis ANOVA with a dedicated post hoc test). Correlation was assessed with the Spearman's rank coefficient. Analysis was performed with the Statistica 13 software (StatSoft Polska, Krakow, Poland). A p-value lower than 0.05 was considered significant, and the results are presented as mean and standard deviation unless otherwise stated.

RESULTS

Evaluation of branching patterns of the IMA

Five main types of branching were distinguished based on the morphology of the IMA. Additionally, type I and type II were subdivided into subtype IA, subtype IB, subtype IC, subtype IIA and subtype IIB.
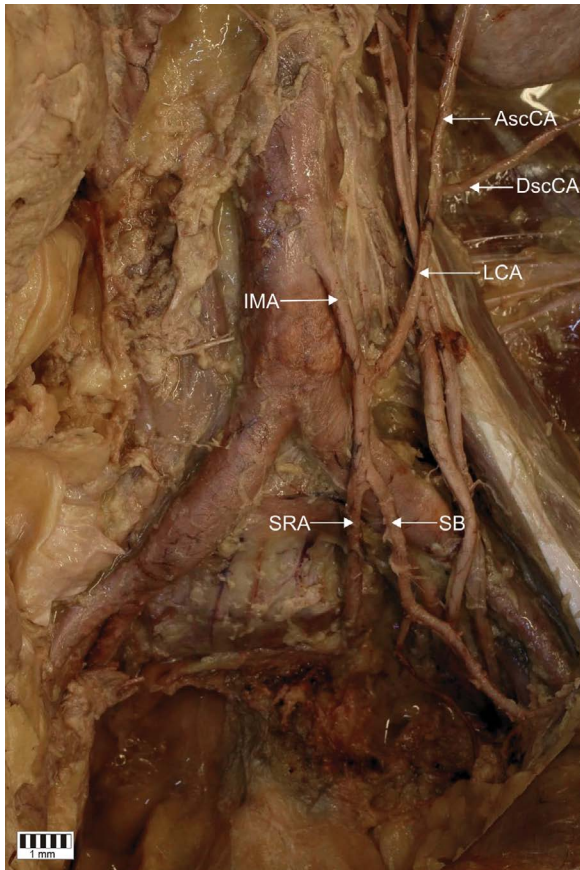
Figure 1. Inferior mesenteric artery (IMA) branching type IA. Independent origin of left colic artery (LCA), which further divides into ascending colic artery (AscCA) and descending colic artery (DscCA); SB — sigmoidal branch; SRA — superior rectal artery.
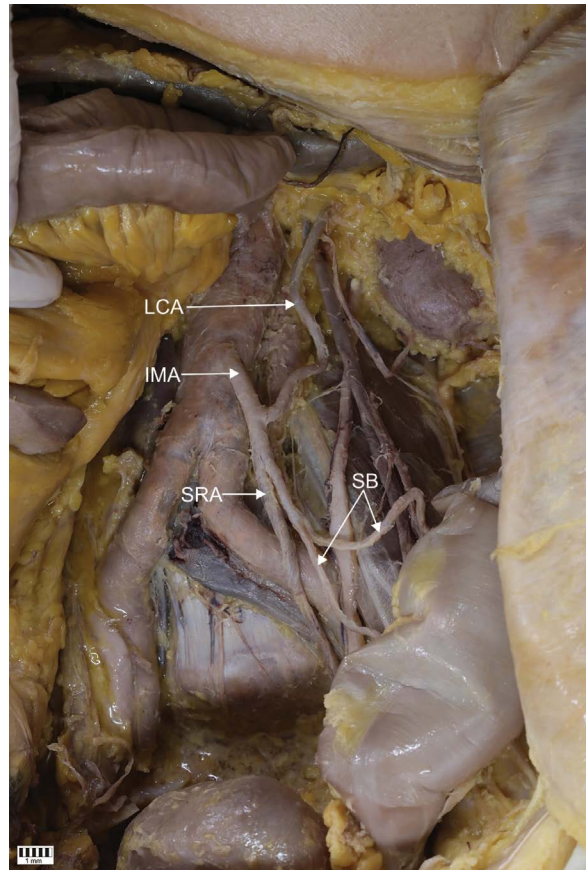
Figure 2. Inferior mesenteric artery (IMA) type IB. Independent origin of left colic artery (LCA), no bifurcation; SB — sigmoidal branches; SRA — superior rectal artery.

— Type I — exemplified by the presence of a common trunk which bifurcates into a sigmoidal branch and the superior rectal artery after giving the left colic artery (LCA) or ascending and descending left colic arteries, with the LCA itself being absent. Three subtypes were determined based on different originating and branching patterns of LCA. This type was present in 23 (57.5%) cases.

- Type IA — an independent origin of the LCA from the IMA; a common trunk preceding bifurcation into the ascending and descending left colic arteries. An independent origin of the sigmoid branch/branches and superior rectal artery. This subtype was present in 10 (25%) cases (Fig. 1).

- Type IB — an independent origin of the LCA from the IMA; no bifurcation observed. An independent origin of the sigmoid branch/branches and superior rectal artery (SRA). This subtype was observed in 8 (20%) cases (Fig. 2).

- Type IC — independent origins of the branches of LCA — ascending and descending left colic arteries; no common trunk preceding. An independent origin of the sigmoid branch/branches and superior rectal artery. This subtype was present in 5 (12.5%) cases (Fig. 3).

— Type II — trifurcation type — two subtypes were determined based on different originating and branching patterns of the LCA. This type was observed in 10 (25%) cases.

- Type IIA — the LCA; bifurcation into the left ascending colic artery (AscCA) and left descending colic artery (DscCA) preceded by the common trunk, sigmoid branch/branches and SRA originating from trifurcation of IMA. This subtype was observed in 8 (20%) cases (Fig. 4).

- Type IIB — the LCA; without bifurcation into the ascending and descending arteries, sigmoid branch/branches and the SRA originat-

829
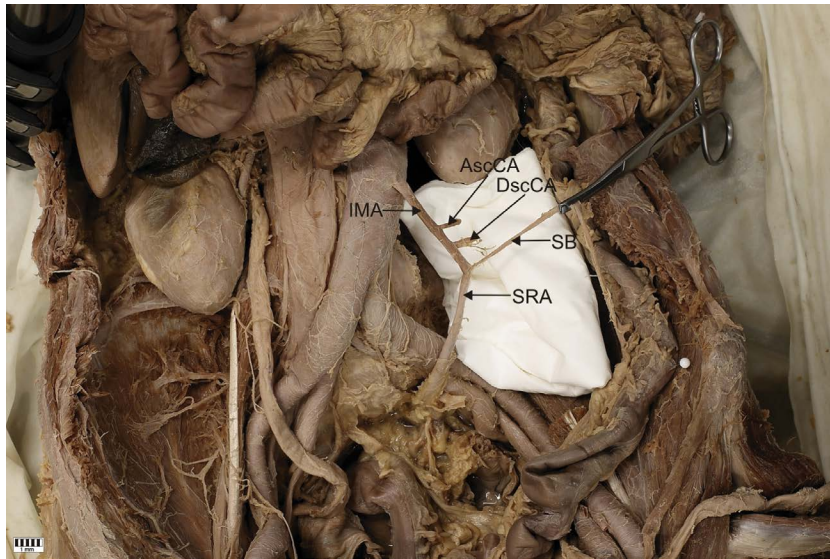
Figure 3. Inferior mesenteric artery (IMA) branching type IC. Lack of left colic artery, ascending colic artery (AscCA) and descending colic artery (DscCA) originating directly from IMA; SB — sigmoidal branch; SRA — superior rectal artery.
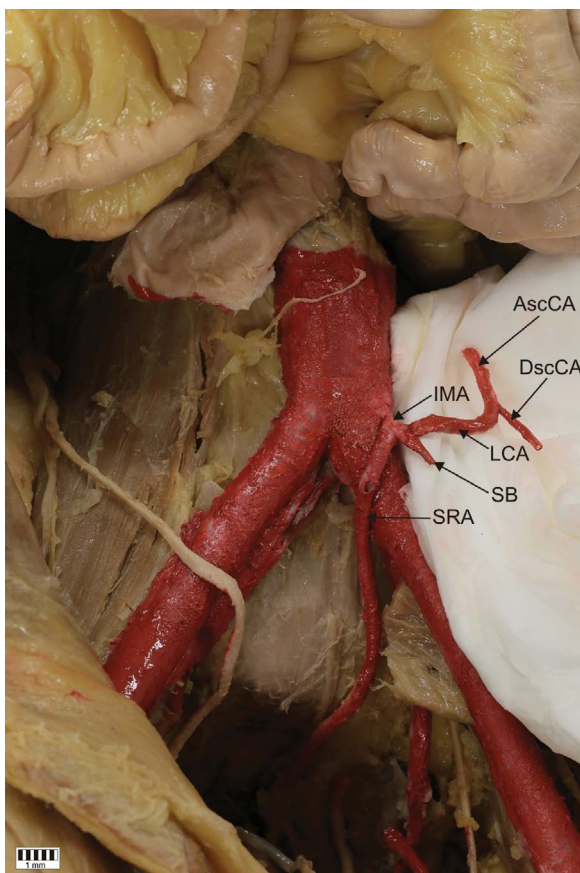
Figure 4. Inferior mesenteric artery (IMA) branching type IIA. Trifurcation type with left colic artery (LCA) branching off ascending colic artery (AscCA) and descending colic artery (DscCA); SB — sigmoidal branch; SRA — superior rectal artery.
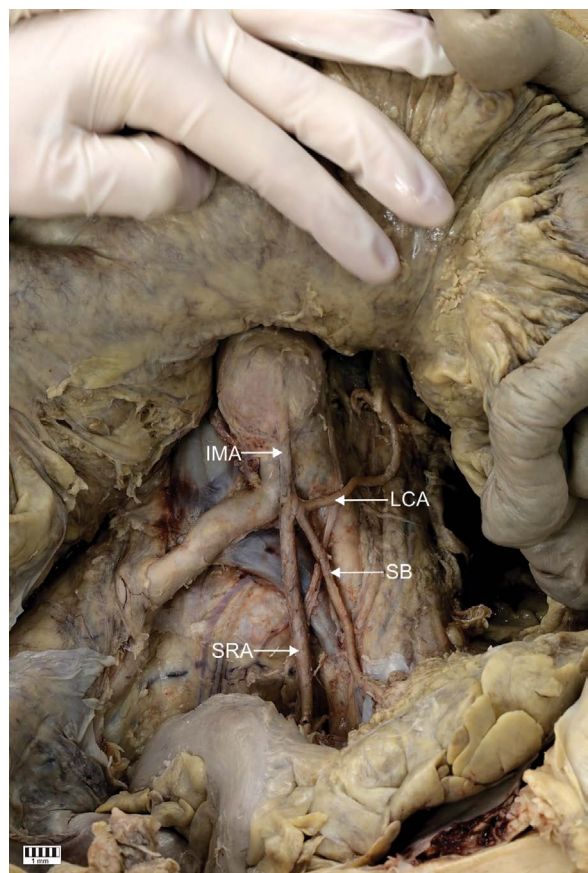
Figure 5. Inferior mesenteric artery (IMA) branching type IIB — trifurcation type with absence of left colic artery (LCA) bifurcation; SB — sigmoidal branch; SRA — superior rectal artery.
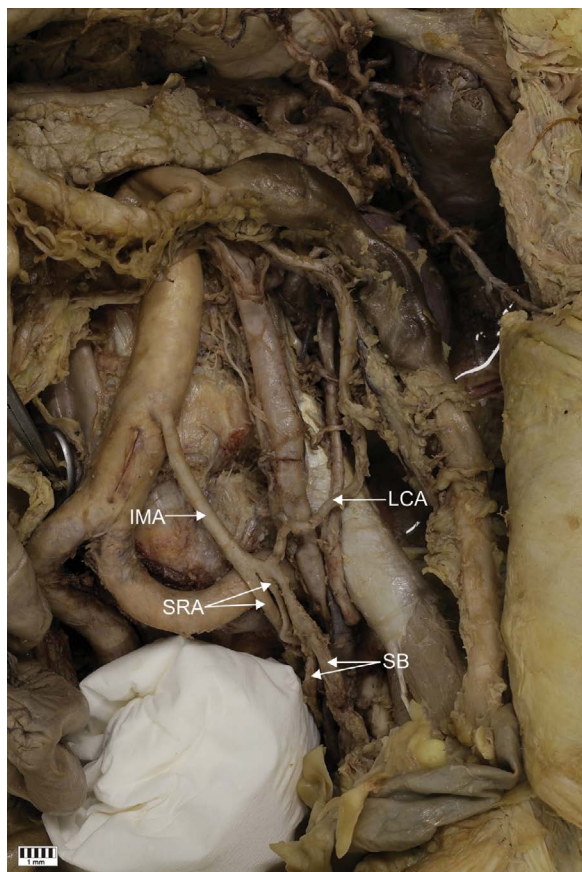
Figure 6. Inferior mesenteric artery (IMA) branching type III — superior rectal arteries (SRA) originating firstly; LCA — left colic artery; SB — sigmoidal branches.
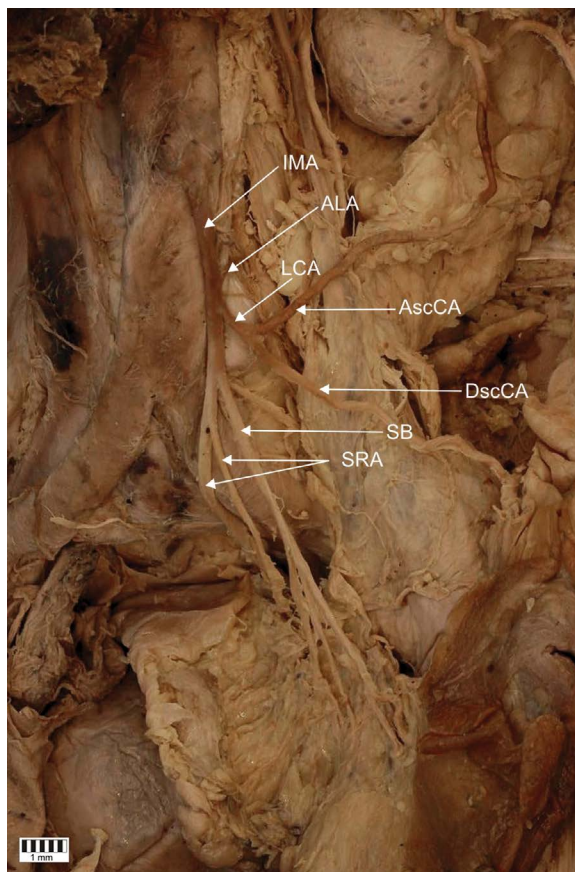
Figure 7. Inferior mesenteric artery (IMA) branching type IV — ascending lumbar artery (ALA) originating from IMA; LCA — left colic artery; AscCA — ascending colic artery; DscCA — descending colic artery; SB — sigmoidal branch; SRA — superior rectal arteries.

ing from trifurcation of IMA. This subtype was present in 2 (5%) cases (Fig. 5).

— Type III — the superior rectal artery (arteries) originating firstly from the IMA, the common trunk preceding bifurcation into the sigmoidal branch/branches (SB) and LCA. This type was present in 2 (5%) cases. In both of them, two SRAs were observed instead of a single one and, to our best knowledge, this branching pattern has not been previously observed in studies on IMA (Fig. 6).

— Type IV — the ascending lumbar artery originating independently from the IMA, the common trunk dividing into the LCA and main SB, second sigmoid branch and SRA originating independently from the IMA. To our knowledge, this type was observed in 4 (10%) cases. This branching pattern has not been previously classified by other authors (Fig. 7).

— Type V — the ascending LCA originating independently from the IMA. The first bifurcation of IMA divides it into the common superior rectal trunk and the common trunk branching off into

the descending LCA and the common trunk for sigmoidal branches (2). The ascending and descending left colic arteries create an anastomose, which has a further connection with the marginal artery of Drummond upwards, and with sigmoidal branches downwards. This type was present only in 1 (2.5%) case. To our best knowledge, this branching pattern has not been previously classified by other authors (Fig. 8).

Evaluation of the level of the IMA origin

The study revealed five different variations of the level of the IMA origin:

1. At the level of the intervertebral disc between the second and third lumbar vertebra — 22.5% (9/40) observed respectively:
   — in type I — 21.7% of cases (5/23);
   — in type II — 20% of cases (2/10);
   — in type III — 50% of cases (1/2);
   — in type IV — 25% of cases (1/4).
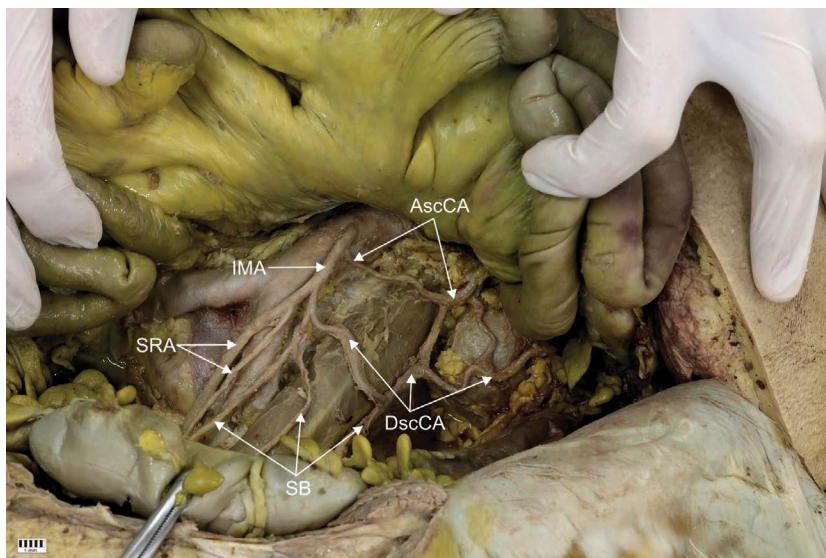
Figure 8. Inferior mesenteric artery (IMA) type V — rare case of IMA branching off ascending colic artery (AscCA) firstly, which further anastomose multiple times with descending colic artery (DscCA), DscCA and sigmoidal branch, which further divides, originating from IMA bifurcation; SRA — superior rectal arteries; SB — sigmoidal branches.

2. At the level of the third lumbar vertebra — 25% (10/40):
   — in type I — 26.1% of cases (6/23);
   — in type II — 30% of cases (3/10);
   — in type IV — 25% of cases (1/4).
3. At the level of the intervertebral disc between the third and fourth lumbar vertebra — 15% (6/40).
   — in type I — 13% of cases (3/23);
   — in type II — 10% of cases (1/10);
   — in type IV — 25% of cases (1/4).
4. At the level of the fourth lumbar vertebra — 35% (14/40).
   — in type I — 34.8% of cases (8/23);
   — in type II — 40% of cases (4/10);
   — in type III — 50% of cases (1/2);
   — in type V — 100% of cases (1/1).
5. At the level of the fifth lumbar vertebra — 2.5% (1/40), which, to our best knowledge, is a case that has never been reported before — observed in type I of the branching pattern.

Evaluation of the occurrence of additional SBs or SRAs

The study revealed:
1. The occurrence of more than one sigmoidal branch — observed in nine (22.5%) cases.
   — type I — in 3 cases, which is 33.3% (3/9);
   — type III — in 2 cases, which is 22.2% (2/9);
   — type IV — in 4 cases, which is 22.2% (4/9).

2. The occurrence of the quickly bifurcating sigmoidal branch — observed in 5 (12.5%) cases.
   — type I — in 3 cases, which is 60% (3/5);
   — type II — in 1 case, which is 20% (1/5);
   — type V — in 1 case, which is 20% (1/5).
3. The occurrence of more than one superior rectal artery — present in 6 (15%) cases.
   — type I — in 2 cases, which is 33.3% (2/6);
   — type IV — in 4 cases, which is 66.7% (4/6).
4. The occurrence of the quickly bifurcating superior rectal artery — present in 1 (2.5%) case.
   — type V.

Types III, IV and V constituted 66.7% of total cases, where more than one SB occurred; 20% of total cases, where the quickly bifurcating SB occurred; 66.7% of total cases, where more than one SRA occurred; and the only case with the occurrence of the quickly bifurcating superior rectal artery which formed type V.

Evaluation of differences in types of IMA branching between sexes

In Table 1, we presented the distribution of types in general and according to sex. There was no significant difference in types of IMA branching between females and males (p = 0.0853).

Evaluation of differences in arterial diameter between sexes

In women, only the IMA and LCA were significantly narrower than in men (Table 2).

Table 1. Types of the branching pattern according to sex

Type	Females	Males	Total
IA	4 (21.05)	6 (28.57)	10
IB	4 (21.05)	4 (19.05)	8
IC	3 (15.79)	2 (9.52)	5
IIA	1 (5.26)	7 (33.33)	8
IIB	2 (10.53)	0 (0.00)	2
III	2 (10.53)	0 (0.00)	2
IV	2 (10.53)	2 (9.52)	4
V	1 (5.26)	0 (0.00)	1

Table 2. Comparison of arterial diameter between sexes [mm]

Type	Females	Males	P
Inferior mesenteric artery	4.02 (0.56)	4.58 (0.93)	0.0292
Left colic artery	2.42 (0.56)	3.14 (0.83)	0.0060
Ascending colic artery	2.31 (0.52)	2.61 (0.75)	0.2930
Descending colic artery	2.09 (0.54)	1.97 (0.33)	0.5048
Main sigmoid artery	2.05 (0.65)	2.17 (0.83)	0.6130
Main superior rectal artery	2.85 (0.68)	3.17 (0.91)	0.2222

Evaluation of the relationship between the level of IMA arising from the aorta and type of its branching

The differences were not significant (Table 3).

Evaluation of the relationship between diameters of IMA branches and type of its branching

Diameters of evaluated arteries according to type of branching are presented in Table 4.

The average diameter of DscCA was different between types (p = 0.00042). This difference is caused by its significantly smaller diameter in type IA in comparison to type IC and type V.

The mean diameter of the main sigmoid artery was different between types (p = 0.0007). This difference is caused by a significantly smaller diameter in type IA than in type IB, IIA and V and a significantly smaller diameter in type IC in comparison to type IB and also a significantly smaller diameter in type III compared to types IB and V.

The average diameter of the main SRA was also different between the types (p = 0.0003). This difference is caused by its significantly smaller diameter in type IA in comparison to types IB, IIA, IIB and V and also a significantly smaller diameter in type IV in comparison to type IIA.

There was no significant difference in the diameter of the LCA (p = 0.0121) and AscCA (p = 0.0106).

The diameter of IMA was reduced after giving rise to the LCA (IMA before branching 4.39 ± 0.90 mm vs. IMA after branching 3.64 ± 0.77 mm, p = 0.0001).

Evaluation of the IMA diameter impact on other arteries

In the correlation analysis, only the diameter of IMA correlated with the diameter of the superior rectal artery (Table 5).

DISCUSSION

The key value of the present work is that it presents a systematic classification of IMA branching patterns and its origin based on anatomical dissection. It studies the occurrence of additional sigmoidal branches or superior rectal arteries and raises the question whether there are any branching patterns in which we can expect such variations. Furthermore, the research reveals a few cases, which to our best knowledge have not been presented before. It also raises the question of whether the IMA is character-

Table 3. The relationship between the level of inferior mesenteric artery arising from the aorta and type of its branching. Percentage for type is presented in parenthesis (p = 0.7818)

Type	L2/3	L3	L3/L4	L4	L5
IA	5 (50%)	4 (40%)	0 (0%)	1 (10%)	0 (0%)
IB	0 (0%)	2 (25%)	2 (25%)	3 (37.5%)	1 (12.5%)
IC	0 (0%)	0 (0%)	1 (20%)	4 (80%)	0 (0%)
IIA	2 (25%)	3 (37.5%)	1 (12.5%)	2 (25%)	0 (0%)
IIB	0 (0%)	0 (0%)	0 (0%)	2 (100%)	0 (0%)
III	1 (50%)	0 (0%)	0 (0%)	1 (50%)	0 (0%)
IV	1 (25%)	1 (25%)	2 (50%)	0 (0%)	0 (0%)
V	0 (0%)	0 (0%)	0 (0%)	1 (100%)	0 (0%)
Total	9	10	6	14	1

Table 4. Diameters of arteries according to the branching pattern [mm]

Type	Inferior mesenteric artery	Left colic artery	Ascending colic artery	Descending colic artery	Main sigmoid artery	Main superior rectal artery
IA	4.14 (0.64)	2.44 (0.56)	2.07 (0.51)	1.73 (0.35)	1.56 (0.25)	2.20 (0.22)
IB	4.80 (1.28)	3.50 (1.08)			2.68 (0.93)	3.47 (0.75)
IC	4.76 (1.03)		2.33 (0.27)	2.47 (0.19)	1.60 (0.34)	2.76 (0.56)
IIA	4.07 (0.52)	3.10 (0.42)	3.11 (0.63)	2.01 (0.27)	2.42 (0.28)	3.73 (0.69)
IIB	4.12 (0.06)	2.05 (0.22)			2.84 (0.54)	3.80 (0.71)
III	4.39 (0.09)	1.98 (0.05)			1.53 (0.50)	2.90 (0.02)
IV	3.84 (0.12)	2.60 (0.47)			1.91 (0.54)	2.47 (0.11)
V	3.85 (0.00)	2.79 (0.00)	2.65 (0.00)	2.64 (0.00)	3.79 (0.00)	4.17 (0.00)
P	0.3589	0.0121	0.0106	0.0042	0.0007	0.0003

Table 5. Correlations between the diameter of inferior mesenteric artery (IMA) and other arteries

Correlation of IMA diameter with	R	P
Left colic artery	0.3239	0.0577
Ascending colic artery	0.0249	0.9081
Descending colic artery	0.1334	0.5343
Main sigmoid artery	0.1682	0.2994
Main superior rectal artery	0.3542	0.0250

ised by high morphological variations such as the coeliac trunk.

Our proposed classification for the IMA is numbered from the most frequent to the least, and is divided according to morphology: although type III (5%) occurred less frequently than type IV (10%), the branching pattern of type III includes only arteries physiologically posing branches of IMA. In contrast, type IV consists of ascending lumbar artery, which is not a default branch of the IMA.

One of the first classifications was formulated by Testut and Latarjet [25] in the 20th century, and it covered two branching types — type I, separate LCA origin and type II, fan-shaped branching pattern [21]. Patroni et al. [21] used the Latarjete's classification to analyse 113 patients. The present research showed that type I occurred in 80 patients and type II in 33 patients (Table 5). In comparison to the Latarjete's classification, type I was found in 60% of cases and type II in 25% of cases in our study. A more extensive classification can be found in a study of 115 inferior mesenteric arteries performed by Zebrowski et al. in 1971 [28]. In the specimens they investigated, four forms of the IMA were observed:
— form 1 — the IMA divided into the LCA and common rectal-sigmoid trunk. Available database does not contain the results concerning the frequency of branching pattern types presented in their study;
— form 2 — the IMA divided into the superior rectal and colosigmoid trunk;
— form 3 — the IMA divided into two large arterial trunks: rectal-sigmoid and colosigmoid;
— form 4 — trifurcation type.

The research carried out by Zebrowski et al. [28] widely describes variations in the morphology of IMA and often suggests multiple anastomoses occurring between the majority of secondary branches, which is nowadays considered as a norm in the immediate vicinity of the wall of the large intestine and rectum. There is a strong connection between the classification proposed in 1971 and ours: type I from the present study and form I from the Zebrowski's research are almost the same. Similarly, form 3 (from the Zebrowski's research) and type IV described in our study with the inclusion of the ascending lumbar artery and also form 4 from the previous classification, is identical as our type II. However, the main difference between these classifications is that in our classification types are strictly based on the branching pattern of IMA and subtypes are distinguished based on the morphology of the biggest and in vast majority of cases first branch of the IMA — left colic artery — in contrast to the research done by Zebrowski et al. [28], where sigmoidal branches were used as a differentiating factor. We consider our idea as an innovation and improvement. One of relatively few IMA studies performed on foetuses has been conducted by Nuzhat [15]. A group of 100 cases was subjected to dissection to observe the origin and branching pattern of the IMA. The research has shown that the IMA branched off the abdominal aorta at the level of

L3 in 99 (99%) cases and only in 1 (1%) case at the level of L1. Out of 100 foetuses, 5 foetuses showed a variation — in 1 foetus, the LCA was arising from the abdominal aorta, and in 3 foetuses, the IMA was giving a branch to the left kidney. Ke et al. [11] also have done research on anatomical variations of the IMA and LCA. It was evaluated by three-dimensional (3D) computed tomography angiography (CTA) and performed on 188 patients with abdominal and pelvic contrast-enhanced CT scans, which were retrospectively enrolled and 3D-CTA was reconstructed [11]. However, the proposed classification is different from that by Zebrowski et al. [28]:

— type 1 — the LCA arose independently from the IMA;
— type 2 — the LCA and SB were given off at the same point;
— type 3 — the LCA and sigmoid arteries were branched from a common trunk from the IMA;
— type 4 — the LCA was lacking.

Similarly, as in our study, the LCA was used as a differential factor in describing various types of the branching pattern of IMA. However, there are some key differences. The research performed by Ke et al. [11] was focused on the LCA and sigmoid arteries — the classification does not mention any SRA and its position relative to a branching pattern, which can be seen as a significant feature in our type III, where superior rectal arteries are originating prior to other branches. Type 4 in Ke's study [11] may seem unspecified because the lack of LCA in type 4 can be interpreted as if there was no LCA and its branches and also as absence of LCA where its branches — Asc-CA and DscCA — are originating directly from IMA (type IC referring to our classification), which can be crucial in planning surgeries like rectal cancer surgery procedures. That research distinguishes only the situation where the level of IMA origin is below the upper border of L3 and cephalic to upper border of L3, while in our study we described precisely the number of vertebrae at which the origin of IMA was observed. Research results described by different authors are presented and compared in the Tables 6 and 7.

The unique origin points of IMA at the level of fifth lumbar vertebra (L5) to our best knowledge have not been reported before and figure as a novelty. Another issue our research is questioning is the evaluation of occurrence of additional sigmoidal branches or superior rectal arteries and their potential connection to the branching pattern.

Table 6. The differences between the types of different authors

Author	Type of examination	Number of cases	Type I (%)	Type IA (%)	Type IB (%)	Type IC (%)	Type II (%)	Type IIA (%)	Type IIB (%)	Type III (%)	Type IV (%)	Type V (%)	Absence of LCA
Patroni et al. [21]	CT	113	71	–	–	–	29	–	–	-	–	–	–
Zebrowski et al. [28]	AD	115	Occurred	–	–	–	Occurred	–	–	Occurred	–	–	–
Ke et al. [11]	CT	188	47.3	–	–	–	27.1	–	–	20.7	–	–	4.8
Balcerzak (present study)	AD	40	57.5	25	20	12.5	25	20	5	5	10	2.5	–

AD — anatomical dissection; CT — computed tomography; LCA — left colic artery

Table 7. Different origin points of inferior mesenteric artery in different studies

Author	L1 (%)	L2/L3 (%	L3 (%)	L3/L4 (%)	L4 (%)	L4/L5 (%)	L5 (%)
Zebrowski et al. [21]	–	3.5	67	20	7.8	1.7	–
Ke et al. [11]	88.3	88.3	88.3	11.7	11.7	11.7	11.7
Nuzhat (Foetuses) [15]	1	–	99	–	–	–	–
Balcerzak (present study)	–	22.5	25	15	35	–	2.5

The results presented in this study reveal that in every case where type IV or type V were observed, more than one sigmoidal branch and more than one superior rectal artery occurred. Furthermore, 57.1% (12/21) of discussed variations occurred in types III, IV, and V. That raises a question whether types IV and V can be characterised by multiple secondary branching bifurcations. In our opinion, further research is necessary to approve or deny this thesis. The same as for the coeliac trunk, the IMA is a major branch of the abdominal artery and has a vital function in supplying a significant part of the digestive system. However, is IMA characterised by high morphological variations such as the coeliac trunk? The answer to that question is not simple, as the coeliac trunk has been a subject of multiple studies since antiquity, where Galen was the first to describe the distribution of coeliac trunk branches. He concluded during his research that blood supplying the stomach, liver, and spleen comes from another source than the blood supplying the intestines [20]. According to Poynter [22], IMA has not been extensively studied before 1922 and the literature was not very extensive. The artery would appear to be rather stable and not subject to much variation. Cavasse (1856) [6] found an accessory hepatic artery as one of its branches and noted that it occasionally furnishes renal branches. Vicq D'Azyr [see 2] reported the absence of a connection between the middle colic and the left colic arteries. Poynter [22] observed a middle colic artery that arose as a large branch from the left colic near its origin [3]. With the passing of time and the increasing number of tests performed, the object of which was IMA, the number of occurring variations increased: duplication of this artery has been reported. The IMA may arise from the left common iliac artery. Its left colic branch may be absent. The IMA occasionally encroaches on the territory of the superior mesenteric artery, can be replaced by the superior mesenteric artery, or originates from it. In the place of a single inferior mesenteric trunk, two arteries originated from the aorta 2.6 cm apart, the inferior one located 3 cm superior to the bifurcation of the aorta. The superior of the two was directed superiorly and gave rise to two branches [3, 12, 15, 27].

Coeliac trunk is surely an artery that shows great variability in large numbers [20, 23, 26]; however, to answer the question whether IMA is characterised by as high morphological variations as the coeliac trunk, in our opinion, there is a need to further analyse and study the IMA branching patterns.

Laparoscopic surgery for colorectal cancer has recently gained wide clinical acceptance. However, due to the narrow view and lack of tactile sensation under laparoscopy, vascular bifurcation and variations could be misidentified and injured, which may cause severe complications, such as massive bleeding and bowel ischaemia [4]. Therefore, it is required to be preoperatively aware of the arterial branching or variations, which are very helpful for surgeons to make pre-operative strategies and perform safe and rapid vessel ligation and lymph node dissection.

Locating the origin of the IMA is also the first key step in rectal cancer surgery.

Many surgeons prefer to perform high ligation of the IMA during rectal cancer surgery to gain complete lymphadenectomy and better mesenteric mobilisation [5, 8].

Low ligation of IMA is recommended to protect blood supply of anastomosis during rectal cancer surgery. However, it increases the operational difficulty under laparoscopy because of the lympho-adipose tissue surrounding the IMA trunk and the highly variant pattern of IMA bifurcation, especially when some dense fibrous tissue surrounding IMA seems like vessel branch [10, 11].

If the branching pattern of the IMA trunk and additional secondary branches were preoperatively visualised, these surgical procedures would be much less challenging, but if the visualisation is not possible and surgeons during the procedure notice a branching pattern which can be often related to the occurrence of additional sigmoidal branches or superior rectal arteries, they can react properly, suspect a possible expanded branching connection and gain valuable knowledge resulting in successful operations without any complications.

Although the subject of this paper has previously been examined in previous studies, our findings highlight some previously unobserved variations. Furthermore, the present study collects, summarizes, and develops the classifications of previous authors, extends them with new types and subtypes, studies the relationships between the IMA branching pattern and the occurrence of additional secondary arterial branches, as well as between this pattern and its level of origin. Moreover, this study takes up the subject of IMA diversity, compares it to the coeliac trunk and provides a clear division between the IMA types and their nomenclature, which seems necessary for all clinicians.

Every research expanding our knowledge about the IMA as well as other major blood vessels is invaluable because it leads us to a better comprehension of how it originates, which are its branching patterns, and when we can suspect any additional branches or arteries and connections between these features, as they provide better outcomes of surgical procedures and increase the quality of life for our patients.

Limitations of the study

The present study does have some limitations. One of them is the heterogeneous nature of the classification which depends on several morphological details, such as a type of their arising. Due to the possible margin of error resulting from the potential presence of atherosclerotic lesions and related deformations, as well as changes in the direction of the aorta, our analysis of IMA origin points should be taken with caution. Finally, as this is only an anatomical study, a spectrum of variation could be presented; further studies should examine the potential value of angiography or magnetic resonance imaging for this purpose. Nonetheless, this study helps raise awareness of "what and where" to look for, and offers a uniform classification and terminology which can be used as a foundation for communication with surgeons, particularly those harvesting tendons for transplants. The small size of the research sample (n = 40) also presents a limitation; even so, this group is larger than used in anatomical studies. In addition, it should be noted that there are significant limitations in the availability of this type of material.

CONCLUSIONS

The presented classification is based on the major branch of IMA — left colic artery — as the most important differential factor and also on sigmoidal branches as well as the SRA. It consists of detailed specifications of most important bifurcations occurring during the course of IMA: type I in 57.5% of cases, followed by type II in 25% of cases, type III in 5% of cases, type IV in 10% of cases, and type V, as novelty, in 2.5% of cases.

The results revealed that there is a significant probability (38.1%) of the occurrence of additional sigmoidal branches or superior rectal arteries in types III, IV and V.

The study includes a few novelties, which, to our best knowledge, have not been presented before: the case of IMA branching pattern called in our classification as type V, which consists of the ascending lumbar artery, two cases of IMA branching pattern called in our classification as type III with two superior rectal arteries originating firstly from the IMA and the case of the unique origin point of IMA from the abdominal artery at the level of fifth lumbar vertebra (L5).

REFERENCES

1. Benton RS, Cotter WB. A hitherto undocumented variation of the inferior mesenteric artery in man. Anat Rec. 1963; 145: 171–173, doi: 10.1002/ar.1091450208, indexed in Pubmed: 13967564.
2. Bergman RA, Afifi AK, Miyauchi R. Anatomy Atlases, An anatomy digital library [WWW Document]. Illus. Encycl. Hum. Anat. Var. 2015.
3. Bergman R, Thompson S, Afifi A, Saadeh F. Compendium of human anatomic variation. Urban & Schwarzenberg, Baltimore 2018.
4. Bonnet S, Berger A, Hentati N, et al. High tie versus low tie vascular ligation of the inferior mesenteric artery in colorectal cancer surgery: impact on the gain in colon length and implications on the feasibility of anastomoses. Dis Colon Rectum. 2012; 55(5): 515–521, doi: 10.1097/DCR.0b013e318246f1a2, indexed in Pubmed: 22513429.
5. Boström P, Rutegård J, Haapamäki M, et al. Arterial ligation in anterior resection for rectal cancer: A validation study of the Swedish Colorectal Cancer Registry. Acta Oncol. 2014; 53(7): 892–897, doi: 10.3109/0284186X.2014.913101, indexed in Pubmed: 24954367.
6. Cavasse. Deux anomalies artérielles, cartiods et inferiuer diaphragmatiques. Bulletins et Mem. de la Société Anatomique de Paris. 1856; XXXI(3): 72–73.
7. Chiene. Complete obliteration of the cœliac and mesenteric arteries; the viscera receiving their supply through the extra-peritoneal system of vessels. Am J Med Sci. 1869;

57(113): 231–232, doi: 10.1097/00000441-186901000-00045.

8. Chin CC, Yeh CY, Tang R, et al. The oncologic benefit of high ligation of the inferior mesenteric artery in the surgical treatment of rectal or sigmoid colon cancer. Int J Colorectal Dis. 2008; 23(8): 783–788, doi: 10.1007/s00384-008-0465-5, indexed in Pubmed: 18438677.

9. Gwyn DG, Skilton JS. A rare variation of the inferior mesenteric artery in man. Anat Rec. 1966; 156(2): 235–237, doi: 10.1002/ar.1091560211, indexed in Pubmed: 5969677.

10. Horton KM, Fishman EK. CT angiography of the mesenteric circulation. Radiol Clin North Am. 2010; 48(2): 331–345, viii, doi: 10.1016/j.rcl.2010.02.004, indexed in Pubmed: 20609877.

11. Ke J, Cai J, Wen X, et al. Anatomic variations of inferior mesenteric artery and left colic artery evaluated by 3-dimensional CT angiography: Insights into rectal cancer surgery: a retrospective observational study. Int J Surg. 2017; 41: 106–111, doi: 10.1016/j.ijsu.2017.03.012, indexed in Pubmed: 28323157.

12. Kitamura S, Nishiguchi T, Sakai A, et al. Rare case of the inferior mesenteric artery arising from the superior mesenteric artery. Anat Rec. 1987; 217(1): 99–102, doi: 10.1002/ar.1092170113, indexed in Pubmed: 3454570.

13. Kostinovitch LI. A case of simultaneous occurrence of a number of variations of the visceral branches of the abdominal aorta. Anat Rec. 1937; 67(4): 399–403, doi: 10.1002/ar.1090670402.

14. Moore KL, Dalley AF. Clinical Oriented Anatomy, 4th ed. Lippincott Williams & Wilkins, Philadeplphia 1999.

15. Nuzhat A. Anatomy of inferior mesenteric artery in fetuses. Scientifica (Cairo). 2016; 2016: 5846578, doi: 10.1155/2016/5846578, indexed in Pubmed: 27313956.

16. Olewnik Ł. Fibularis tertius: anatomical study and review of the literature. Clin Anat. 2019; 32(8): 1082–1093, doi: 10.1002/ca.23449, indexed in Pubmed: 31408221.

17. Olewnik Ł, Łabętowicz P, Podgórski M, et al. Variations in terminal branches of the popliteal artery: cadaveric study. Surg Radiol Anat. 2019; 41(12): 1473–1482, doi: 10.1007/s00276-019-02262-3, indexed in Pubmed: 31134299.

18. Olewnik Ł, Waśniewska A, Polguj M, et al. Rare combined variations of renal, suprarenal, phrenic and accessory hepatic arteries. Surg Radiol Anat. 2018; 40(7): 743–748, doi: 10.1007/s00276-018-2026-0, indexed in Pubmed: 29667030.

19. Olewnik Ł, Wysiadecki G, Polguj M, et al. A rare anastomosis between the common hepatic artery and the superior mesenteric artery: a case report. Surg Radiol Anat. 2017; 39(10): 1175–1179, doi: 10.1007/s00276-017-1859-2, indexed in Pubmed: 28432408.

20. Olewnik Ł, Wysiadecki G, Polguj M, et al. Types of coeliac trunk branching including accessory hepatic arteries: a new point of view based on cadaveric study. Folia Morphol. 2017; 76(4): 660–667, doi: 10.5603/FM.a2017.0053, indexed in Pubmed: 28612916.

21. Patroni A, Bonnet S, Bourillon C, et al. Technical difficulties of left colic artery preservation during left colectomy for colon cancer. Surg Radiol Anat. 2016; 38(4): 477–484, doi: 10.1007/s00276-015-1583-8, indexed in Pubmed: 26526820.

22. Poynter CWM. Congenital anomalies of the arteries and veins of the human body with bibliography. University Studies of the University of Nebraska, 1922 22: 1–106.

23. Pinal-Garcia DF, Nuno-Guzman CM, Gonzalez-Gonzalez ME, et al. The celiac trunk and its anatomical variations: a cadaveric study. J Clin Med Res. 2018; 10(4): 321–329, doi: 10.14740/jocmr3356w, indexed in Pubmed: 29511421.

24. Samura M, Morikage N, Mizoguchi T, et al. Effectiveness of embolization of inferior mesenteric artery to prevent type II endoleak following endovascular aneurysm repair: a review of the literature. Ann Vasc Dis. 2018; 11(3): 259–264, doi: 10.3400/avd.ra.18-00064, indexed in Pubmed: 30402173.

25. Testut L, Latarjet A. Traité d'anatomie humaine. Doin & Cie, Paris 1949.

26. Torres K, Staśkiewicz G, Denisow M, et al. Anatomical variations of the coeliac trunk in the homogeneous Polish population. Folia Morphol. 2015; 74(1): 93–99, doi: 10.5603/FM.2014.0059, indexed in Pubmed: 25792402.

27. Yi SQ, Li J, Terayama H, et al. A rare case of inferior mesenteric artery arising from the superior mesenteric artery, with a review of the review of the literature. Surg Radiol Anat. 2008; 30(2): 159–165, doi: 10.1007/s00276-007-0298-x, indexed in Pubmed: 18189117.

28. Zebrowski W, Augustyniak E, Zajac S. Variation of origin and branches of the inferior mesenteric artery and its anastomoses. Folia Morphol. 1971: 510–517.

V M

VIA MEDICA

O R I G I N A L   A R T I C L E

The morphometric anatomy and clinical importance of the radial artery

W.A. Alasmari

Department of Anatomy, Faculty of Medicine, Umm Al-Qura University, Saudi Arabia

Background: The radial forearm flap (RFF), including the radial artery (RA) and venous components, is used for hand reconstruction surgery. Updating the knowledge of the vascular anatomy in the forearm and associated flaps, such as the RFF, is useful in bringing innovations into reconstructive surgery. This study aimed to describe the morphometric anatomy of the RA and the associated RFF in human cadavers.

Materials and methods: A total of 16 forearms from 8 human cadavers were dissected. The group consisted of 5 men and 3 women with a mean age at death of 59.05 ± 14.06 years. The inclusion criteria consisted of no history of trauma or surgery; thus, only apparently normal cadavers were included. The measurement of the following parameters was performed on these human cadavers: the mean diameter of the RA, the length of the RA, the average diameter of the cephalic vein, the length of the pedicle of the flap, and the average area of the radial forearm flap.

Results: In males, the mean diameter of the RA at the wrist was 2.58 ± 1.1 mm. In females, the mean diameter of the RA was 2.60 ± 0.99 mm, and the mean length of the RA was 20.55 ± 1.7 cm. The average diameter of the cephalic vein was 1.8 ± 0.8 mm. The length of the pedicle of the flap was 8.88 ± 1.6 cm. The average area of the RFF was 5 × 7 cm².

Conclusions: This study demonstrates the morphometric anatomy of the RA and lateral forearm radial artery flaps in human cadavers, which could be useful in improving the success rate during transradial coronary interventions and performing complex hand injuries. (Folia Morphol 2021; 80, 4: 839–844)

Key words: radial artery, radial forearm flap, vascular anatomy, forearm, radial artery graft

INTRODUCTION

The radial artery (RA) is the branch of the brachial artery that arises in the cubital fossa medial to the portion of the biceps tendon and runs in front of the radial neck. The RA passes through the lateral side of the forearm and traverses below the brachioradialis muscle. In its lower third portion, the RA is situated between the tendons of the brachioradialis and the flexor carpi radialis and is located anteriorly to the radius and pronator quadratus muscle [17]. The RA descends in the intermuscular septum that is located laterally. The intermuscular septum isolates the compartments that are responsible for the flexion and extension of the forearm. Due to this separation, the

RA is palpable towards its lower part. It enters the palm, where it is attached to the branch of the ulnar artery to form the deep palmar arch [17].

Due to its easy accessibility, the RA is useful in coronary procedures [8, 14]. It is used in coronary artery bypass grafting (CABG), forearm flaps, and renal dialysis by the creation of a fistula [14, 16]. The RA can be compressed easily to cause haemostasis and preliminary patient ambulation [8, 14]. The RA graft was introduced in the 1970s as one of the alternatives to be used for CABG but was not as prevalent due to complications [1].

The RA provides blood circulation to the forearm flap by perforating vessels, which used as radial forearm flaps (RFFs) on the microsurgery [5]. Since then, many alternatives to RFFs have been innovated [5]. The radial free forearm flap is widely used for substituting soft tissue in surgeries related to head and neck cancers [5]. Veins, including the cephalic vein, accompany the RA. The cephalic vein can be included in the flap, or it can be kept as it is for RA reconstruction after harvesting the flap. It has been reported on the use of the reverse-flow radial forearm island flap, including the RA and venous components, for hand reconstruction surgery [5]. Updating the knowledge of vascular anatomy in the forearm is useful bringing innovations into the design of the radial forearm flap [18].

There are variations in the anatomy of RA, which could be found at the origin of the RA or during its course. These variations could be obstacles to different interventions, for example, diagnostic, surgical, and therapeutic interventions [3, 14].

Therefore, the aim of this study was to perform a morphometric analysis of the RA/RFF in human cadavers by measuring the following parameters: the mean diameter of the RA at its beginning and its end, the length of the RA, the average diameter of the cephalic vein, the length of the pedicle of the flap, and the average area of the flap. Additionally, the application of the RA graft and RFF and clinical significance for CABG and reconstructive surgery are also discussed.

MATERIALS AND METHODS

This study was conducted in the Department of Anatomy, Faculty of Medicine at Umm Al-Qura University, Makkah, Saudi Arabia. Ethical approval was obtained from the biomedical ethics commit-

tee, Faculty of Medicine at Umm Al-Qura University, Makkah, Saudi Arabia. A total of 16 forearms from 8 human cadavers were considered for the dissection. The group consisted of 5 men and 3 women, who were used for the routine undergraduate teaching programme. The cadavers' mean age at death was 59.05 ± 14.06 years. Human cadavers with no history of trauma or surgery and without obvious vascular congenital anomalies or disease in the area under study were used; therefore, only apparently normal cadavers were included.

The surface anatomy of the structures, including the brachioradialis and flexor carpi radialis tendons in the distal part of the forearm, were documented, and the location of the RA was identified. The cephalic vein was located radially in the distal forearm.

The palmar side of the forearm was incised from wrist crease to elbow. The following parts were recognized: the flexor carpi radialis tendon, RA and its adjacent veins, palmaris longus muscle, and brachioradialis muscle. The superficial divisions of the RA and cephalic vein were identified. The external diameters of the RA and cephalic vein were observed using a digital Vernier calliper with an accuracy of ± 0.03 mm (General Tools Mfg. Co. LLC New York, NY 10013). The complete length of the RA and pedicles were measured using a metallic ruler.

The radial forearm flaps were designed, along with the template. The parts of the radial forearm flap design included the brachioradialis muscle, laterally located intermuscular septum, and cephalic vein. The medial and lateral fasciocutaneous parts of the flap, along with vessels, were raised from the distal-to-proximal side towards the lateral intermuscular septum [5].

The following parameters were estimated: the mean external diameter of the RA at its beginning and its end, the length of the RA, the average diameter of the cephalic vein, the length of the pedicle of the flap, and the average area of the radial forearm flap.

Statistical analysis

The data were statistically analysed for the means and the standard deviations.

RESULTS

Parameters associated with the RA and RFF are summarised in Table 1. The means of external diameter of RA represent the average of diameter at the

Table 1. Parameters associated with the radial artery (RA) and the radial forearm flap (RFF)

Parameter	Sex	Side or place	Mean ± standard deviation
Diameter of the RA [mm]	Male	Right	2.4 ± 0.2
		Left	2.1 ± 0.6
	Female	Right	2.5 ± 0.3
		Left	2.2 ± 0.5
Length of the RA [cm]	Both male and female	–	20.55 ± 1.7
	Male	–	21.6 ± 2.1
	Female	–	19.5 ± 1.8
Average diameter of the cephalic vein [mm]	–	–	1.8 ± 0.8
Length of the pedicle of the flap [cm]	–	–	8.88 ± 1.6
Average area of the RFF [cm²]	–	–	5 × 7

beginning and at the end of artery. In males, the mean diameter of the right RA was 2.4 ± 0.2 mm, the mean diameter of the left RA was 2.1 ± 0.6 mm. In females, the mean diameter of the right RA was 2.5 ± 0.3 mm, the mean diameter of the left RA was 2.2 ± 0.5 mm. The mean length of the RA was 20.55 ± 1.7 cm. The mean of RA length was 21.6 ± 2.1 cm in males and 19.5 ± 1.8 cm in females. The surgical anatomy of the RA and forearm flap is shown in Figure 1A and B. As shown in Figure 1, RA is a division of the brachial artery. It passes through the cubital fossa in front of the neck of the radius and then through the lateral side of the forearm, which traverses below the brachioradialis muscle. Surgically, this part is an area of caution, because the lateral antebrachial cutaneous nerve is located over the brachioradialis muscle, as shown in Figure 1A and B. In its lower third part, the RA is situated between the tendons of the brachioradialis and flexor carpi radialis (Fig. 1A, B) and passes anteriorly to the radius and pronator quadratus muscle (Fig. 2).

The anatomy of the RFF is shown in Figures 1 and 3. The RA supplies blood to the forearm flap. The length of the pedicle of the flap was 8.88 ± 1.6 cm. The average area of the RFF was 5 × 7 cm² (Table 1, Fig. 1A, B). The RFF is a fasciocutaneous type of flap, as septocutaneous perforators that arise from the RA supply the blood circulation. Branches of these cutaneous perforators supply blood to the skin of the lower forearm. The distant 1/3 part of the forearm is
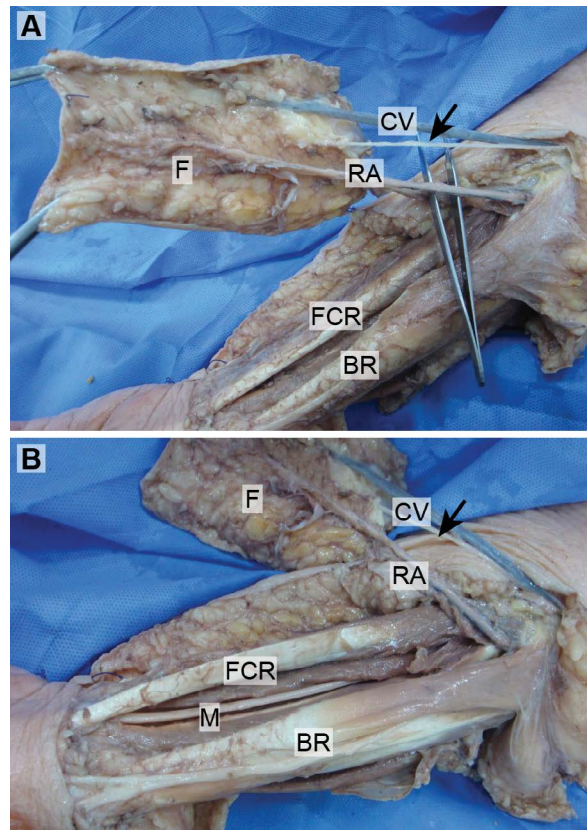
Figure 1. A, B. Surgical anatomy of the radial artery (RA) and the radial forearm flap (F). The forearm radial flap (F) with the cephalic vein (CV), RA, and lateral cutaneous nerve of the forearm (arrow); FCR — flexor carpi radialis; BR — brachioradialis; M — median nerve.
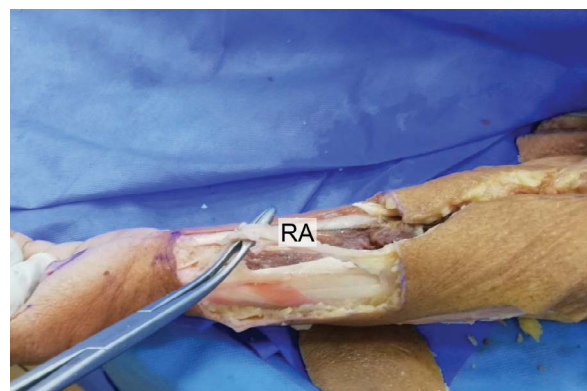
Figure 2. Anatomy of the radial artery (RA).

supplied by plenty of perforators of the RA. Perforators of the RA are shown in Figure 4.

Veins, including the subcutaneous cephalic vein, go along with the RA towards the radial side of the forearm (Fig. 1A, B). The average diameter of the cephalic vein was 1.8 ± 0.8 mm (Table 1).
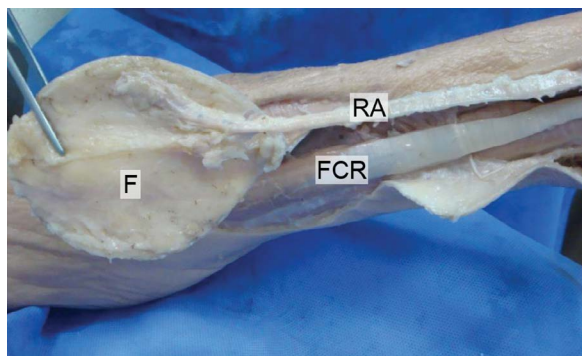
Figure 3. Anatomy of the radial artery (RA) and the dissected radial forearm flap (F); FCR — flexor carpi radialis.
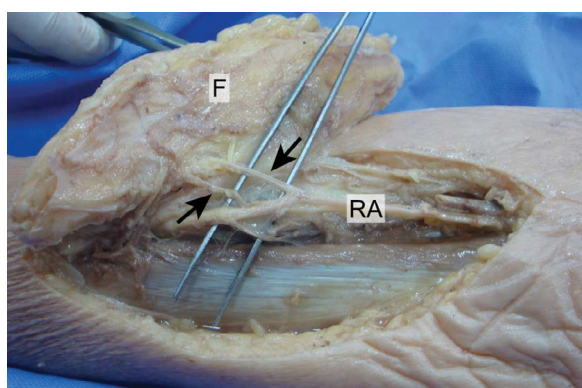
Figure 4. Perforators (arrows) of the radial artery (RA). F — raised skin flap.

DISCUSSION

Shima et al. (1996) [19] reported the mean diameter of the RA as 2.2 mm at the distal portions and 2.3 mm proximally in cadavers. Similarly, in the current study involving cadavers, in males, the mean diameter of the right RA was 2.4 ± 0.2 mm, the mean diameter of the left RA was 2.1 ± 0.6 mm, and the mean diameter of the RA at the wrist was 2.58 ± ± 1.1 mm. In females, the mean diameter of the right RA was 2.5 ± 0.3 mm, the mean diameter of the left RA was 2.2 ± 0.5 mm, and the mean diameter of the RA at the wrist was 2.60 ± 0.99 mm. However, in a study conducted by Nasr [14], the external diameter of the RA was 3.2–3.3 mm in men and women at 1 cm distal to its origin and 3.0–3.1 mm in men and women at 2 cm closer to the styloid process of the radius. A reason for these discrepancies could be related to the race of the cadavers used in the studies. The mean diameter of the RA seems to be different in live patients than that in cadavers based on various studies [2, 19, 24, 25]. Human cadavers are treated with formalin that may result in damage to tissues and differences in the diameters of the RA of living humans and cadavers. The internal diameter of the artery demonstrates the volume of blood flow to the tissue more significantly than the external diameter of the artery. It is important to know the RA diameter to improve the success rate during transradial coronary interventions. For coronary interventional procedures, using the RA appears to be a preferable option than transfemoral or transbrachial approaches due to easier haemostasis and unimportant veins or nerves around the RA and the presence of perforators [1–3, 5, 14, 16, 18, 19, 21, 24, 25].

In the present study, the mean length of the RA was 20.55 ± 1.7 cm. This finding was closer to that (20–24 cm) observed in previous studies conducted by Nasr [14] and Guo [9].

Radial artery grafts are more suitable for vessels with a higher degree of injury, such as CABG [7]. In a study conducted by Desai et al. (2004) [7] of 440 patients, RA grafts were related to fewer incidences of graft occlusion at one year compared to saphenous-vein grafts. Several studies have indicated that the RA is an advantageous option over the saphenous vein for grafting due to the following aspects: higher patency, easier harvest, lack of modification of blood circulation in the arm following removal of the graft, longer-lasting outcomes, fewer complications, and lesser impact on ischaemic reperfusion/ischaemia at rest and exercise in postoperative forearm blood flow at the donor site [1, 17]. However, harvesting the RA may rarely cause claudication of the hand, and patients should be informed about this possibility.

In a study conducted on a total of 34 cases of hand reconstruction surgery, the range of the flap (containing the skin island flap and adipofascial pedicle flap) was 9–18 cm, and the width and length of the adipofascial pedicle were 3–4 cm and 3–5 cm, respectively [5]. This was a study in relation to live human cases. However, in the present cadaveric study, the length of the pedicle of the flap was 8.88 cm, and the average area of the RFF was 5×7 cm². The RFF in the current study was centralized over the subcutaneous cephalic vein, which might be included in the flap, or it might be used for RA reconstruction after the flap is harvested. Moreover, throughout the elevation of the flap in this study, the lateral cutaneous nerve of the forearm was preserved in the flap to form a flap with sensations. This nerve is located in the plane superficial to the deep fascia. Generally, any portion

from the proximal to the distal section of the radial forearm can be used for the flap, as the RA supplies blood to the entire skin of the forearm and hand through perforators [5]. However, the distant 1/3 part of the forearm is supplied by plenty of perforators of the RA [5, 11, 12]. Kimura et al. (2017) [12] reported that the average number of cutaneous perforators for the RA was 9.03 ± 2.28 per forearm, and 2.29 cm was the mean distance between adjacent perforators of the RA. The number of perforators from the RA was greater than that from the ulnar artery. However, Hekner et al. (2016) [11] observed the distal segment of the forearm and found that the number of relevant perforators was not different between the radial and ulnar arteries.

The components of the fasciocutaneous flap are the underlying skin, fascia, and vascular pedicle. For many years, the RFF has been used commonly in plastic surgery [13]. It is used as a substitute for skin and the mucosa underneath. It is extremely pliable at the place where the skin is extremely damaged. Its skin islands, vascularized tendon, and bone (osteocutaneous flap) make it a multipurpose viable flap [5].

A free flap RFF is mainly used in head and neck surgery [20]. Fasciocutaneous RFF from the distal part is an appropriate option for hand reconstruction [5]. The reverse pedicle containing RFF is a widely recognized alternative option for treating dorsal hand wounds [23]. Primarily, a reverse pedicle containing RFF and rarely a free RFF is used for the reformation of the mutilated hand or complex hand injuries [4, 20, 22].

Sometimes, if the flap is elevated in the distal part of the limb, a large superficial vein causes venous congestion, excessive accumulation of blood that needs to be drained, and hampered function of the flap [6]. In such cases, ligation of the superficial vein at the distal part is helpful. Distally located forearm flaps, including the deeper important artery, have been widely used for hand and wrist reformation. A forearm flap with an intact deep important artery at the distal base is useful for hand and wrist rebuilding [5].

This reverse pedicled flap is useful, safe, and effective in hand rebuilding when it contains thin, easily transplantable, and realistic skin with optimum blood circulation. However, there are two major drawbacks of the reverse pedicled flap at the donor site. First, if the main artery is not used, then it affects the functionality of the flap. Second, a deformed scar is formed if a split skin graft is used during the closure of the flap [5]. In the reverse pedicle flap, it is impor-

tant to keep the RA intact, as it is a prominent artery in the distal part of the forearm, and this artery is an important source of blood circulation [5, 10, 15].

CONCLUSIONS

In summary, this study demonstrates the morphometric measurements of the RA/RFF in human cadavers. It is important to know the diameter, length, and other features of the RA to improve the success rate during transradial coronary interventions. The RA is an advantageous option versus the saphenous vein for CABG. A radial forearm flap is mainly used for the reformation of the mutilated hand or complex hand injuries. Therefore, updating knowledge of the vascular anatomy in the forearm and associated flaps, such as the RA/RFF, is useful for better diagnostic, therapeutic, and surgical interventions.

REFERENCES

1. Al-Sabti HA, Al Kindi A, Al-Rasadi K, et al. Saphenous vein graft vs. radial artery graft searching for the best second coronary artery bypass graft. J Saudi Heart Assoc. 2013; 25(4): 247–254, doi: 10.1016/j.jsha.2013.06.001, indexed in Pubmed: 24198449.
2. Ashraf T, Panhwar Z, Habib S, et al. Size of radial and ulnar artery in local population. J Pak Med Assoc. 2010; 60(10): 817–819, indexed in Pubmed: 21381609.
3. Bidarkotimath S, Avadhani R, Kumar A. An anatomical study of primary pattern of arteries of upper limb with relevance to their variations. J Health Allied Sci NU. 2020; 02(01): 08–14, doi: 10.1055/s-0040-1703547.
4. Chang J, Jones NF. The mutilated hand. 2005, doi: 10.1016/b978-1-56053-446-4.x5001-1.
5. Chang SM, Hou CL, Zhang F, et al. Distally based radial forearm flap with preservation of the radial artery: anatomic, experimental, and clinical studies. Microsurgery. 2003; 23(4): 328–337, doi: 10.1002/micr.10155, indexed in Pubmed: 12942523.
6. Chang SM, Hou CL. Role of large superficial veins in distally based flaps of the extremities. Plast Reconstr Surg. 2000; 106(1): 230–231, doi: 10.1097/00006534-200007000-00060, indexed in Pubmed: 10883652.
7. Desai ND, Miwa S, Kodama D, et al. A randomized comparison of radial-artery and saphenous-vein coronary bypass grafts. N Engl J Med. 2004; 351(22): 2302–2309, doi: 10.1056/NEJMoa040982, indexed in Pubmed: 15564545.
8. Franchi E, Marino P, Biondi-Zoccai GG, et al. Transradial versus transfemoral approach for percutaneous coronary proce-

dures. Curr Cardiol Rep. 2009; 11(5): 391–397, doi: 10.1007/s11886-009-0054-4, indexed in Pubmed: 19709500.

9. Guo W. Arterial grafting for coronary artery bypass surgery. Heidelberg, Springer, Berlin 2006.

10. Haerle M, Häfner HM, Dietz K, et al. Vascular dominance in the forearm. Plast Reconstr Surg. 2003; 111(6): 1891–1898, doi: 10.1097/01.PRS.0000057529.76413.D7, indexed in Pubmed: 12711949.

11. Hekner DD, Roeling TAP, Van Cann EM. Perforator anatomy of the radial forearm free flap versus the ulnar forearm free flap for head and neck reconstruction. Int J Oral Maxillofac Surg. 2016; 45(8): 955–959, doi: 10.1016/j.ijom.2016.03.003, indexed in Pubmed: 27012603.

12. Kimura T, Ebisudani S, Osugi I, et al. Anatomical Analysis of Cutaneous Perforator Distribution in the Forearm. Plast Reconstr Surg Glob Open. 2017; 5(10): e1550, doi: 10.1097/GOX.0000000000001550, indexed in Pubmed: 29184752.

13. Masquelet AC. Anatomy of the radial forearm flap. Anat Clin. 1984; 6(3): 171–176, doi: 10.1007/BF01784310, indexed in Pubmed: 6394038.

14. Nasr AY. The radial artery and its variations: anatomical study and clinical implications. Folia Morphol. 2012; 71(4): 252–262, indexed in Pubmed: 23197145.

15. Riekkinen H, Karkola K, Kankainen A. The radial artery is larger than the ulnar. Ann Thorac Surg. 2003; 75(3): 882–884, doi: 10.1016/s0003-4975(02)04557-5.

16. Rodríguez-Niedenführ M, Vázquez T, Nearn L, et al. Variations of the arterial pattern in the upper limb revisited: a morphological and statistical study, with a review of the literature. J Anat. 2001; 199(Pt 5): 547–566, doi: 10.1046/j.1469-7580.2001.19950547.x, indexed in Pubmed: 11760886.

17. Sajja LR, Mannam G, Pantula NR, et al. Role of radial artery graft in coronary artery bypass grafting. Ann Thorac Surg. 2005; 79(6): 2180–2188, doi: 10.1016/j.athoracsur.2004.07.049, indexed in Pubmed: 15919345.

18. Sham E, Masia JA, Reddy TJ. Vascular analysis of radial artery perforator flaps. Ann Maxillofac Surg. 2018; 8(1): 66–72, doi: 10.4103/ams.ams_1_18, indexed in Pubmed: 29963427.

19. Shima H, Ohno K, Michi Ki, et al. An anatomical study on the forearm vascular system. J Cranio-Maxillofac Surg. 1996; 24(5): 293–299, doi: 10.1016/s1010-5182(96)80062-x.

20. Soutar DS. In Flaps and Reconstructive Surgery. 2009. https://www.us.elsevierhealth.com/flaps-and-reconstructive-surgery-9780323243223.html.

21. Valsecchi O, Vassileva A, Musumeci G, et al. Failure of transradial approach during coronary interventions: anatomic considerations. Catheter Cardiovasc Interv. 2006; 67(6): 870–878, doi: 10.1002/ccd.20732, indexed in Pubmed: 16649233.

22. Wang SJ, Teknos TN, Chepeha DB. Complications in Head and Neck Surgery. 2009, doi: 10.1016/b978-1-4160-4220-4.x5001-9.

23. White CP, Steve AK, Buchel EW, et al. Reverse radial artery flap perforator anatomy and clinical applications. Ann Plast Surg. 2016; 77(3): 345–349, doi: 10.1097/SAP.0000000000000551, indexed in Pubmed: 26678105.

24. Yokoyama N, Takeshita S, Ochiai M, et al. Anatomic variations of the radial artery in patients undergoing transradial coronary intervention. Catheter Cardiovasc Interv. 2000; 49(4): 357–362, doi: 10.1002/(sici)1522-726x(200004)49:4<357::aid-ccd1>3.0.co;2-z, indexed in Pubmed: 10751755.

25. Yoo BS, Yoon J, Ko JY, et al. Anatomical consideration of the radial artery for transradial coronary procedures: arterial diameter, branching anomaly and vessel tortuosity. Int J Cardiol. 2005; 101(3): 421–427, doi: 10.1016/j.ijcard.2004.03.061, indexed in Pubmed: 15907410.

VIA MEDICA

ORIGINAL ARTICLE

Anatomical study of the common iliac arteries

E. Panagouli* , I. Antonopoulos* , V. Protogerou, T. Troupis

Department of Anatomy, Medical School, National and Kapodistrian University of Athens, Greece

Background: The common iliac arteries (CIA) are the two terminal branches of the abdominal aorta which supply the pelvis and the lower extremities. The present study aims to examine the morphometric features of the CIA in a cadaveric sample and possible correlations between lengths.

Materials and methods: Seventy-six formalin fixed cadavers of Greek origin were dissected in the Department of Anatomy, School of Medicine, National and Kapodistrian University of Athens. In each cadaver dissected, the abdominal aorta and the CIA were identified and their lengths were measured. Also the torso length was measured and the height of each cadaver. All the statistical analysis was done by SPSS 15.0.

Results: The mean length of the left CIA was 6.12 cm (SD: ± 1.791, SE: 0.205) and that of the right one was 6.03 cm (SD: ± 1.607, SE: 0.184). The lengths of the CIA differed between the sexes, but no statistically significant difference was observed. Statistically significant differences regarding the torso lengths and body heights were found between the sexes, as well as a statistically strong correlation between the lengths of the left and right CIA in the cadavers dissected.

Conclusions: The knowledge of the anatomy and morphology of the CIA is of great clinical significance, given that abnormal course, length or branching pattern of these vessels are not uncommon and their clinical impact may be great. Mostly interventional radiologists and vascular surgeons should be aware of this knowledge. (Folia Morphol 2021; 80, 4: 845–849)

Key words: anatomy, morphology, morphometry, abdominal aorta, cadaver, measurements

INTRODUCTION

The course of each common iliac artery (CIA) begins just after the termination of the aorta, usually at the level of the lower 3rd of the body of the 4th lumbar vertebra. Afterwards, each CIA follows an oblique descending trajectory outwards to the pelvic margin, where it is terminated at the level of the intervertebral disc between the sacrum and the 5th lumbar vertebra; at this point each CIA is divided into external and internal iliac artery (99% of the cases), whereas in 1% of the cases the CIAs may be totally absent and the internal and external iliac arteries arise directly from the abdominal aorta (AA) [9]. The right CIA is slightly longer than the left and in most of the cases it follows a more oblique trajectory across the L5 vertebral body. The right CIA comes laterally in relation to the inferior vena cava, the right common iliac vein (CIV) and the ipsilateral Psoas Magnus muscle, whereas the left CIA is related laterally only to the left Psoas Magnus muscle and

Address for correspondence: Dr. T. Troupis, Department of Anatomy, Medical School, University of Athens, Mikras Asias str. 75, 116 27 Athens, Greece, tel: +30 2107462388, fax: +30 2107462398, e-mail: ttroupis@med.uoa.gr

*The two first authors contributed equally to this manuscript.

medially to the ipsilateral CIV [7, 17, 18]. The two CIAs give off normally no lateral branches except from a few cases described in which the testicular arteries originated from the CIAs (< 1%) [9].

The point, at which each CIA bifurcates, varies, but in most of cases the left CIA divides in a lower level than the right CIA. Also, the length of these arteries is subject to a non-negligible variety [7, 17, 18]. Hence, aim of the present study is to find and present patterns of this variety as well as to examine the existence of statistically significant correlations between distances or sexes regarding measurements on the CIAs of a Greek population. The present paper constitutes a continuation of a previous study [14] with greater sample and a special focus on CIAs.

MATERIALS AND METHODS

Seventy-six adult cadavers of Caucasian (Greek) origin, of which 39 were males and 37 females, were dissected for educational and research purposes by the authors. The anatomical dissection took place at the Hall of Dissections of the Anatomy Department, Faculty of Medicine, National and Kapodistrian University of Athens. A 10% formalin solution was used for the embalming procedure. All the 76 cadavers derived from body donation with informed consent, written and signed by the donator himself [11]. Approval for the present research's protocol was obtained from the ethics committee of our institution. The age of the cadavers ranged between 39 and 98 years (average age 75.43 years, standard dimension [SD]: ± 11.23, standard error of mean [SE]: 1.288).

In every one cadaver, we identified and revealed the AA, as well as the right and left CIA according to the Clemente's Anatomy Dissector [1] and the length of both the right and left CIAs was measured from the level of the bifurcation of the abdominal aorta to the level at which each CIA was divided into external and internal iliac artery (Fig. 1). The torso length was also measured in all 76 cadavers of this study, from the level of the hyoid bone to the pubic symphysis, whereas the total height of the body was measured from the bregma to the medial process of the calcaneus (the bodies were in supine position). Additionally, the length between of the AA, from the origin of the coeliac artery to its bifurcation was also evaluated in order to perform correlations with the studies lengths.

The collected measurements were subjected in statistical analysis, in order to calculate the average, maximum and minimum value, SD, and SE and finally

the correlations between the discovered distances. For correlations we calculated the Pearson correlation coefficient (r) in each case and also examined the statistical significance of each resulting correlation (p < 0.05). All the statistical analysis was done by SPSS 15.0.

RESULTS

Both CIAs were observed in all the 76 cadavers (39 males and 37 females) without finding any anatomical variation.

The mean length of the left CIA was 6.12 cm (SD: ± 1.791, SE: 0.205), noticing a fairly wide range of values, with a minimum of 2.3 cm and a maximum of 13.9 cm (Table 1). The corresponding length in male cadavers was slightly longer, with a mean value of 6.37 cm (SD: ± 1.949, SE: 0.312) and a shorter range of values, from 4.1 cm to 13.9 cm (Table 1). On the contrary, in females the mean left CIA's length was 5.86 cm (SD: ± 1.534, SE: 0.262) and measurements ranged between 2.3 and 9.6 cm (Table 1). Nevertheless, no statistically significant difference between the two sexes was found (p = 0.222, p > 0.05).

The range of measurements on the length of the right CIA was shorter than the corresponding of the left CIA (min: 3.3 cm, max: 9.6 cm), and the mean length was 6.03 cm (SD: ± 1.607, SE: 0.184) (Table 1). The relationship of the CIA lengths observed between the sexes on the left side, was also found on the right side; the length of the right CIA was longer in male cadavers (mean: 6.10 cm, SD: ± 1.672, SE: 0.268) than in female ones (mean: 5.96 cm, SD: ± 1.555, SE: 0.256) (Table 1). Also in this category no statistically significant difference was found between males and females (p = 0.696, p < 0.05).

Additionally, no statistically significant difference was found between the lengths of the right and left CIAs (p = 0.746, p < 0.05), despite the small differences in measurements which were actually observed.

Regarding the torso length, the mean value was 62.27 cm (SD: ± 4.325, SE: 0.496) and the measurements ranged between 51.5 cm and 70.0 cm (Table 2). The torso length in males and females is presented in Table 2. Between the two sexes a statistically significant difference was found (p < 0.001).

The mean height of the cadavers dissected was 155.3 cm (SD: ± 10.124, SE: 1.161), with a minimum of 128.0 cm and a maximum of 174.5 cm (Table 2). Referring to the sexes, the height of men and women are shown in Table 2. Also, in this category, a sta-
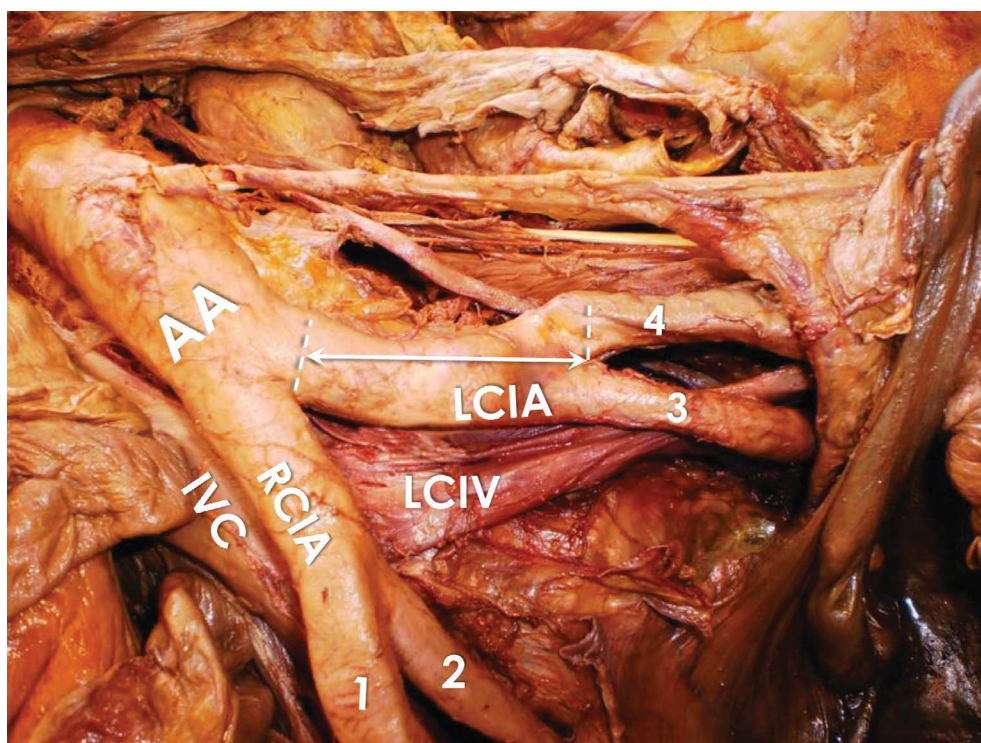
Figure 1. The length of both the right and left common iliac arteries (CIA) was measured from the level of the bifurcation of the abdominal aorta (AA) to the level at which each CIA was divided into external and internal iliac artery. The arrow points the measured length at left side – dashes are showing the level of the bifurcation of each artery; RCIA — right common iliac artery; LCIA — left common iliac artery; 1 — right external iliac artery; 2 — right internal iliac artery; 3 — left internal iliac artery; 4 — left external iliac artery; IVC — inferior vena cava; LCIV — left common iliac vein. Scale 1:1.2.

Table 1. Measurements of common iliac arteries (CIA)

CIA length (n = 76)	Mean	Minimum	Maximum	Standard deviation	Standard error
Left	6.12	2.3	13.9	± 1.791	0.205
Males (n = 39)	6.37	4.1	13.9	± 1.949	0.312
Females (n = 37)	5.86	2.3	9.6	± 1.534	0.262
Right	6.03	3.3	11.4	± 1.607	0.184
Males (n = 39)	6.10	3.4	11.4	± 1.672	0.268
Females (n = 37)	5.96	3.3	9.6	± 1.555	0.256

Table 2. Biometric features of the cadavers

Parameters (n = 76)	Mean	Minimum	Maximum	Standard deviation	Standard error
Age	75.43	39	98	± 11.23	1.288
Males (n = 39)	76.62	39	98	± 10.91	1.845
Females (n = 37)	74.27	52	92	± 10.97	1.804
Torso length [cm]	62.27	51.5	70.7	± 4.325	0.496
Males (n = 39)	64.78	59.5	70.7	± 3.249	0.520
Females (n = 37)	59.62	51.5	67	± 3.709	0.610
Height [cm]	155.3	128	174.5	± 10.124	1.161
Males (n = 39)	162.1	146	174.5	± 7.043	1.279
Females (n = 37)	148.1	128	162	± 7.571	1.245

tistically significant difference between males and females was found (p < 0.001).

Each of the measurements mentioned above was compared with each other and with the torso length, the height and the AA's length as well. The measured distances were also compared with each other both in the total of 76 cadavers and separately in the two sexes.

Between the lengths of the left and right CIAs resulted a strong correlation (r = 0.668, p < 0.001). Also, the length of the left CIA correlated negatively but not statistically significantly to the length of the AA (r = –0.222, p = 0.54), as well as the length of the right CIA did (r = –0.236, p = 0.40). No statistically significant correlations resulted between the torso length and the CIAs' length, or between the last and the height of the cadavers.

DISCUSSION

According to classical anatomical textbooks [7, 17, 18], the length of the left CIA is approximately 4 cm and that of the right one is 5 cm. In our previous study in a smaller sample, the recorded mean length was 5.9 ± 1.527 cm and 5.7 ± 1.427 cm in the left and right side, respectively [14]. Greater lengths were observed in the present study, with similar mean lengths (6.12 cm left and 6.10 cm right). Additionally, the lengths of both the CIAs appeared to have a wide range, especially in the left side, which was also a finding in our previous study [14]. Longer lengths were observed in the male cadavers; nevertheless, the difference was not statistically significant. The only statistically significant findings noticed, as expected, were the difference between the height and torso length among males and females. On the other hand, a strong correlation between the lengths of the left and right CIAs was found (observed also in our previous study [14]). The other correlations examined showed no statistical significance in our sample (76 adult cadavers), as well as differences in the resulting measurements. No anatomical variation was recorded.

According to the available literature, the course and the length of the CIAs present a significant variance with a resulting clinical impact in most cases. Fereydooni et al (2019) [5], described a rare case of a 20-year-old female patient with persistent bilateral leg swelling, caused by the compression of the left CIV that abnormally passed anterior to the contralateral CIA. Also abnormalities in dimensions and morphology in general of the CIAs seem to have

a clinical significance. Hypoplastic CIAs have been referred as a rare cause of absence of femoral pulse and reduced leg supply [20, 21] and absence or atresia of the right CIA has also been noted usually prohibiting catheter's guide advance through the artery, when femoral artery endovascular approach is being proceeded [3, 10].

One more clinical impact of the anatomical variations of the CIAs is the existence of fistulae between CIAs and veins of the pelvis and the abdominal cavity. Such a fistula may occur between the right CIA and the superior mesenteric vein leading to portal hypertension [13], or between the right CIA and the ipsilateral CIV that has been reported as a rare cause of pulmonary thromboembolism [19].

Regarding to the CIAs' bifurcation, Miller and Jamroz (2017) [12] reported a case in which the right CIA passed infra the inguinal ligament and behind the Psoas Magnus muscle and did not bifurcate to give off the right internal and external iliac arteries. Moreover, Rusu et al. (2017) [15] observed that the height of bifurcation in a male patient was bilaterally asymmetrical. More specifically, the right CIA bifurcated at the level of the middle tertiary of the L5 vertebral body and the left CIA at the level of the upper border of the L5 vertebra [15].

As for the morphological oriented measurements of the CIAs, Crisp et al. (2016) [2] measured the distance between the sacral suture and the CIAs in 11 patients that underwent sacrocolpopexy. According to the findings of this study, the mean distance between the sacral suture and the right CIA was 18 mm (SD: ± 5), whereas the distance between the right internal iliac artery and the sacral suture had a mean value of 10 mm (SD: ± 5). In addition, Deswal et al. (2014) [4] dissected 25 cadavers (16 males and 9 females) and measured the length of the CIAs, their diameter as well as the angle formed between the two CIAs. The mean length of the right CIA in men was 6.09 cm (SD: 1.889) and the contralateral corresponding was 5.776 cm (SD: 2.001). In contrast to our findings, the mean length of the CIA of the female cadavers in the aforementioned study was 4.865 cm (SD: 1.323) on the right side and 4.663 cm (SD: 1.265) on the left side. However, Deswal et al. [4] found no statistically significant difference except than that between the lengths of the two CIAs in males.

Knowledge of the clinical and surgical anatomy of the CIAs is of great significance not only for the differentiation and treatment of cases as those aforemen-

tioned, but also for approaching the most common clinical entity regarding the CIAs, the aneurysms. As known, aneurisms of the CIAs occur as a result of the expansion of a massive aneurysm of the AA. However, there have been reported cases of isolated CIA's aneurysm that extended from just distal to the AA's bifurcation to the CIA's bifurcation. In such cases the surgical intervention is the treatment of choice [6, 16].

CONCLUSIONS

Although there have been numerous morphological studies for other major arteries of the human and the pelvic vessels [8, 14], the corresponding literature for the CIAs is fairly poor, to the authors knowledge, despite the applications that morphometric features of the CIAs may have, mostly in vascular surgery and interventional radiology. Presumably, future studies with a larger sample may demonstrate the statistical significance of arterial length correlations attempted in the present study.

Acknowledgements

Conflict of interest: None declared

REFERENCES

1. Clemente C, Clemente C. Clemente's anatomy dissector. Lippincott Williams & Wilkins, Philadelphia, 2010: 131–160.
2. Crisp CC, Herfel CV, Pauls RN, et al. Critical anatomy relative to the sacral suture: a postoperative imaging study after robotic sacrocolpopexy. Female Pelvic Med Reconstr Surg. 2016; 22(1): 33–36, doi: 10.1097/SPV.0000000000000230, indexed in Pubmed: 26680566.
3. Dabydeen DA, Shabashov A, Shaffer K. Congenital absence of the right common iliac artery. Radiol Case Rep. 2008; 3(1): 47, doi: 10.2484/rcr.v3i1.47, indexed in Pubmed: 27303500.
4. Deswal A, Tamang BK, Bala A. Study of aortic common iliac bifurcation and its clinical significance. J Clin Diagn Res. 2014; 8(7): AC06–AC08, doi: 10.7860/JCDR/2014/8767.4559, indexed in Pubmed: 25177553.
5. Fereydooni A, Deyholos C, Nezami N, et al. Anomalous course of the left common iliac vein anterior to the right common iliac artery with resultant May-Thurner syndrome. J Vasc Surg Venous Lymphat Disord. 2019; 7(3): 450–451, doi: 10.1016/j.jvsv.2019.01.059, indexed in Pubmed: 31000065.
6. Goyal VD, Sood S, Gupta B. Isolated common iliac artery aneurysm: a rare entity. J Clin Diagn Res. 2014; 8(11): ND03–ND04, doi: 10.7860/JCDR/2014/9140.5106, indexed in Pubmed: 25584261.

7. Gray H, Carter H. Gray's Anatomy. 15th ed. Barnes & Noble, New York 2011: 536–537.
8. Hamabe A, Harino T, Ogino T, et al. Analysis of anatomical variations of intrapelvic vessels for advanced pelvic surgery. BMC Surg. 2020; 20(1): 47, doi: 10.1186/s12893-020-00711-0, indexed in Pubmed: 32178647.
9. Lippert H, Wacker F, Pabst R. Arterial Variations in Humans: Key Reference for Radiologists and Surgeons: Classifications and Frequency. Thieme; 2018.
10. Llauger J, Sabaté JM, Guardia E, et al. Congenital absence of the right common iliac artery: CT and angiographic demonstration. Eur J Radiol. 1995; 21(2): 128–130, doi: 10.1016/0720-048x(95)00701-q, indexed in Pubmed: 8850508.
11. McHanwell S, Brenner E, Chirculescu A. The legal and ethical framework governing Body Donation in Europe: a review of current practice and recommendations for good practice. Eur J Anat. 2008; 12: 1–24.
12. Miller JM, Jamroz BA. Undivided common iliac artery: unclear embryology. J Vasc Interv Radiol. 2017; 28(11): 1599, doi: 10.1016/j.jvir.2017.05.002, indexed in Pubmed: 29056192.
13. Qin J, Tang S, Jiang M, et al. Portal hypertension caused by right common iliac artery-superior mesenteric vein fistula. Jpn J Radiol. 2015; 33(5): 291–294, doi: 10.1007/s11604-015-0411-8, indexed in Pubmed: 25753263.
14. Panagouli E, Lolis E, Venieratos D. A morphometric study concerning the branching points of the main arteries in humans: relationships and correlations. Ann Anat. 2011; 193(2): 86–99, doi: 10.1016/j.aanat.2010.10.009, indexed in Pubmed: 21169000.
15. Rusu MC, Ilie AC, Brezean I. Human anatomic variations: common, external iliac, origin of the obturator, inferior epigastric and medial circumflex femoral arteries, and deep femoral artery course on the medial side of the femoral vessels. Surg Radiol Anat. 2017; 39(11): 1285–1288, doi: 10.1007/s00276-017-1863-6, indexed in Pubmed: 28451829.
16. Sandhu RS, Pipinos II. Isolated iliac artery aneurysms. Semin Vasc Surg. 2005; 18(4): 209–215, doi: 10.1053/j.semvascsurg.2005.09.007, indexed in Pubmed: 16360578.
17. Snell R. Clinical anatomy. Lippincott Williams & Wilkins, Philadelphia 2004: 63–64.
18. Standring S, Borley NR, Collins P, Crossman AR, Gatzoulis MA, Healy JC, Johnson D, Mahadevan V, Newell RLM, Wigley CB. Gray's anatomy. Theanatomical basis of clinical practice. Elsevier, Edinburgh 2008.
19. Takahashi F, Hiraiwa S, Takahashi G, et al. An autopsy case of paradoxical pulmonary thromboembolism by arteriovenous fistula from right common iliac artery to common iliac vein: a rare cause of pulmonary embolism. Am J Case Rep. 2018; 19: 1301–1305, doi: 10.12659/AJCR.910982, indexed in Pubmed: 30381754.
20. Tekgündüz KŞ, Ceviz N, Kantarcı M, et al. Rare cause of absence of femoral arterial pulse: bilateral common iliac artery hypoplasia. Pediatr Int. 2014; 56(6): 909–910, doi: 10.1111/ped.12343, indexed in Pubmed: 25521975.
21. Wallraff J, Roszel A. Hochgradige Hypoplasie der Arteria iliaca communis und der Arteria umbilicalis. Anat Anz. 1972; 132(1): 101–113.

VM VIA MEDICA

ORIGINAL ARTICLE

Telocyte and Cajal cell distribution in renal pelvis, ureteropelvic junction (UPJ), and proximal ureter in normal upper urinary tract and UPJ obstruction: reappraisal of the aetiology of UPJ obstruction

M. Wishahi[1], A.A. Mehena[1], H. Elganzoury[1], M.H. Badawy[1], E. Hafiz[2], T. El-Leithy[1]

[1]Department of Urology, Theodor Bilharz Research Institute, Cairo, Egypt
[2]Department of Pathology and Electron Microscopy, Theodor Bilharz Research Institute, Cairo, Egypt

Background: Telocytes and Cajal cells have been described in human urinary tract and reproductive system in women and men. Telocytes and Cajal cells have been differentiated from other interstitial cells and were described to be an element in smooth muscle conductivity. Previous studies examined the ureteropelvic junction (UPJ) segment in patients with UPJ obstruction (UPJO) and attributed the aetiology of UPJO to the low density or absence Cajal cells and telocytes. The present work aimed at the demonstration of the presence and the density of telocytes and Cajal cells in the upper urinary tract (UUT) in cases with normal UUT and UPJO. It included UPJ segment, renal pelvis, and proximal ureter. The morphological pattern of distribution of collagen in relation to smooth muscle was investigated in normal and obstructed UUT.

Materials and methods: The study was carried out on 12 surgical specimens, 5 of them represented the normal UUT and underwent nephrectomy for oncological reasons. Seven patients underwent dismembered pyeloplasty for UPJO. Surgical specimens included renal pelvis, UPJ segment, and proximal ureter. They were subjected to standard haematoxylin and eosin stain, Gomori's trichrome stain, immunohistochemistry with c-kit, and transmission electron microscopy.

Results: Telocytes and Cajal cells were demonstrated in the muscular layer of both normal UUT and UPJO with high density in the proximal ureter in normal UUT as well as in UPJO. The UPJ segment in normal UUT had moderate density of Cajal cells and telocytes while in UPJO the cells were scanty or absent. Renal pelvis in normal UUT showed excess density of cells while obstructed renal pelvis showed scanty Cajal cells and telocytes. Ultrastructural study showed the presence of Cajal cells, telocytes, stem cells, fibroblasts, smooth muscle cells, and collagen in different densities and distribution in normal and obstructed UUT.

Conclusions: Examination of the UPJ segment of UPJO revealed that Cajal cells and telocytes were scanty or absent, collagen to muscle ratio was high. The low density of Cajal cells and telocytes in the renal pelvis of the obstructed UUT, compared to the normal, points out to the role of the renal pelvis in the pathogenesis of UPJO. (Folia Morphol 2021; 80, 4: 850–856)

Key words: Cajal cells, telocytes, ureteropelvic junction, urinary tract, interstitial cells

---

Address for correspondence: Dr. M. Wishahi, Department of Urology, Theodor Bilharz Research Institute, El Nile Street, Embaba Giza-12411, P.O. Box 30, Cairo, Egypt, tel: +2 012 222 47437, e-mail: moh.weshahy@gmail.com

INTRODUCTION

The upper urinary tract is anatomically divided into renal pelvis, ureteropelvic junction (UPJ) and proximal ureter. The three parts have several cellular varieties: smooth muscle cells, blood vessels, and the interstitium of the connective tissues containing several types of interstitial cells: fibroblasts, mast cells, resident macrophages, stem cells, plasma cells, lymphocytes, granulocytes and monocytes, and, in addition, two unique types of interstitial cells: the interstitial like-cells of Cajal (Cajal cells), and telocytes. Telocytes and Cajal cells have been described to be responsible for the transmission of electric activity to smooth muscle cells and for their rhythmic contraction and relaxation. Cajal cells and telocytes were described in the urinary tract and their function is initiation of urine transport. Cajal in 1910 was the first to describe a distinct cell in the gut which was named on him later [1]. Cajal cells were described to be responsible for gut motility. Evidence suggests that Cajal cells' function is the generation of the electrical activities. They are unique cells that either have intrinsic pacemaker activity or are able to perform stimulus-induced pace-making; they act as networks for inhibitory and excitatory functions [9]. Cajal-cells were identified with immunohistochemistry (IHC) as c-kit positive-stained cells and were demonstrated in the human urinary tract [16], upper urinary tract [6, 8], ureter [3], urinary bladder [5], and urethra [14]. Interstitial cells of Cajal were demonstrated by transmission electron microscopy (TEM) studies. They are distinct from smooth muscle cells, fibroblasts, and monocytes, the surface membrane has abundant invaginations and prominent endoplasmic reticulum, and they are characterised by being uninucleate with thin cytoplasm and numerous mitochondria [4, 5, 7, 8, 11, 19, 20]. Low density or altered function of Cajal cells were attributes to the aetiology of UPJ obstruction [3, 4, 7, 15, 21]. Eken et al. [4] studied UPJ specimens from patients with UPJ obstruction and normal control, examining them with TEM, light microscopy, and IHC stain. They found out that the c-kit positive-stained cells were located near the circular muscle layer and were encountered more frequently in the control group. The ratio of areas with no cells in the UPJ obstruction group was significantly higher when compared to the control group. The working group of Popescu et al. [11, 12] in Romania in the year 2010 described cells which were semi-similar to Cajal cells and named them "telocytes". Telocytes were detected in the urinary system [22], kidney cortex [13], and urinary bladder [17]. Examination of tissue specimens with TEM would determine the presence of telocytes. The ultrastructural characteristics of the telocytes are their long cytoplasmic processes which are called "telopodes". The telopode is characterised by the alternation of thin tracts with dilations. The thin segments are called podomers and the dilated regions podoms. Podoms have a functional unit consisting of mitochondria, endoplasmic reticulum, and caveolae. The bodies of telocytes vary in shape: fusiform, pyriform, or triangular. The nucleus contains condensed heterochromatin; the surrounding cytoplasm is scarce and encompasses few organelles [2, 10, 17, 19]. Ultrastructural features characterising and differentiating telocytes and Cajal cells were described in detail by Vannuchi et al. [17–19]. Telocytes were attributed to the aetiology of UPJ obstruction [21]. We investigate the distribution of Cajal, telocytes, interstitial cells, and morphometric pattern of collagen to smooth muscles in normal UUT and UPJ obstruction by using haematoxylin and eosin stain, Gomori's modified Masson's trichrome stain for light microscopy, IHC and TEM.

MATERIALS AND METHODS

Patients

Twelve patients were included in the study. Of this total number, 5 patients, who had undergone nephrectomy for oncological reasons, represented the normal upper urinary tract without obstruction. Mean age was 52 ± 7 years (3 males and 2 females; age range was 44–57 years). They had renal cell carcinoma > 7 cm located in the periphery of the kidney, preoperative imaging studies showed normal pelvicalyceal system without obstruction. Seven patients, who had undergone Anderson-Hynes dismembered pyeloplasty for unilateral UPJ obstruction without crossing vessels, represented the UPJ obstruction. Mean age was 28 ± 10 years (5 male, 2 females; age range was 18–35 years). Imaging studies showed dilated pelvicalyceal system, obstructive pattern of the clearance curve and T1/2 greater than 20 min when evaluated with diuretic renogram, split renal function < 30%. The surgical specimens were composed of part of the dilated renal pelvis, the UPJ segment, and portion of the proximal ureter. The 12 surgical specimens were processed for histological, IHC, TEM studies. The institutional review board (IRB) approved the present study (Research Ethics Committee: TBRI-Protocol No: PT 536). The study was conducted in compliance with the relevant laws and

regulations, good clinical practice, and ethical principles as described in the World Medical Association's Declaration of Helsinki. Requiring patients to provide informed consents was waived by the IRB because of the retrospective feature of the present study.

Histopathology

Excised specimens from ureter, pelviureteric junction and renal pelvis were immediately fixed in a 10% formalin solution, processed in a tissue processor (Thermo Scientific STP 120 Spin, UK) and embedded in paraffin. Sections, 4 microns thick, were then stained with haematoxylin and eosin (H&E) stain to examine histopathologic changes. Gomori's modified Masson's trichrome stain was used to assess the fibrosis. The examined parts were the proximal ureter, UPJ segment, and renal pelvis. Standard H&E were primarily done to define the area in the segment to be compared in every studied part. The examination with Gomori's modified Masson's trichrome stain showed the distribution of collagen fibres in different segments of UUT in normal and obstructed cases.

Immunohistochemistry

Immunohistochemistry was performed on 5 microns thick sections of formalin-fixed and paraffin-embedded tissue samples. Sections were picked on charged glass slides and deparaffinised, hydrated, then treated for antigen retrieval at a high pH (pH 8) using an automated immunostainer (Dako, Denmark). Rabbit polyclonal anti-CD117 (c-kit) antibodies (CD 117, Cat. No. A4502, Dako, Denmark) at dilution 1:200 were used to label the Cajal cells. Goat anti-rabbit biotinylated immunoglobulins/HRP (Cat. No. P0448, Dako, Denmark) were used at dilution 1:300. Streptavidin–biotin–peroxidase complex and peroxidase-DAB (3,3'diaminobenzidine) (Dako, Denmark) detection method was preformed according to the manufacturer's instructions. Sections were counterstained with Mayer's haematoxylin. Positive and negative control slides were included in each run. As a negative control, a tissue section was processed as described but with the primary antibody omitted.

Transmission electron microscopy

Immediately following surgical excision, samples from the three (blinded) specimens were cut into 1 × 1 mm pieces, fixed in 2.5% glutaraldehyde in cacodylate buffer for 2 h at 4°C. The tissues were then washed in cacodylate-sucrose buffer and post-fixed for 1 h at 4°C in 2% osmium tetroxide. After dehydration in graded ethanol, the samples were impregnated in Epon 812 substitute (EMBed-812 Kit, Electron Microscopy Science, USA) at room temperature, and polymerised at 60°C for 48 h. Semi-thin sections were cut, stained with methylene blue-azure II, and examined by light microscopy to choose the region of interest for ultrathin sectioning. The ultrathin sections were then prepared using an Ultra cut R ultramicrotome (Leica, Vienna, Austria), double stained with uranyl acetate and lead citrate. Cellular ultrastructural morphological characterisation was examined at 80 kV with a Philips EM 208 S electron microscope (Philips Optics, Eindhoven, The Netherlands). Identification and differentiation of telocytes and Cajal was done according to the description of different authors.

RESULTS

Distribution of Cajal cells in normal upper urinary tract and in ureteropelvic junction obstruction (UPJO). The study was done on 5 normal upper urinary tracts and 7 cases with UPJO by IHC. Immunostaining with c-kit to demonstrate the distribution of Cajal cells showed that the distribution was different and specific to each segment in both normal and obstructed UUT. Cajal cells were demonstrated in the muscular layer of UUT in normal and UPJ obstruction. In normal UUT, high density was demonstrated in the proximal ureter, excess in renal pelvis, and moderate in the UPJ segment. In obstructed UUT, high density of Cajal cells was demonstrated in the proximal ureter, moderate density in renal pelvis, but in the UPJ segment the cells were scant or absent (Fig. 1).

Collagen to smooth muscle ratio in normal upper urinary tract and UPJO. The study by light microscopy using H&E and eosin stain as well as Gomori's modified Masson's trichrome stain showed that in normal UUT the collagen/muscle ratio was 2.3 for the proximal ureter, 1.5 for the UPJ segment, and 1 for the renal pelvis. The collagen/muscle ratio in UPJ obstruction showed that, compared to normal UUT, there was increased collagen in the UPJ segment, moderate collagen distribution in the renal pelvis, while the proximal ureter had an identical ratio (Fig. 1).

Telocytes, Cajal cells, smooth muscle cells, fibroblasts, collagen, and stem cells detection by TEM. Transmission electron microscopy examination demonstrated the presence of telocytes (Fig. 2), and Cajal cells (Fig. 3). Stem cells, fibroblasts, collagen

Proximal Ureter   UPJ   Renal Pelvis
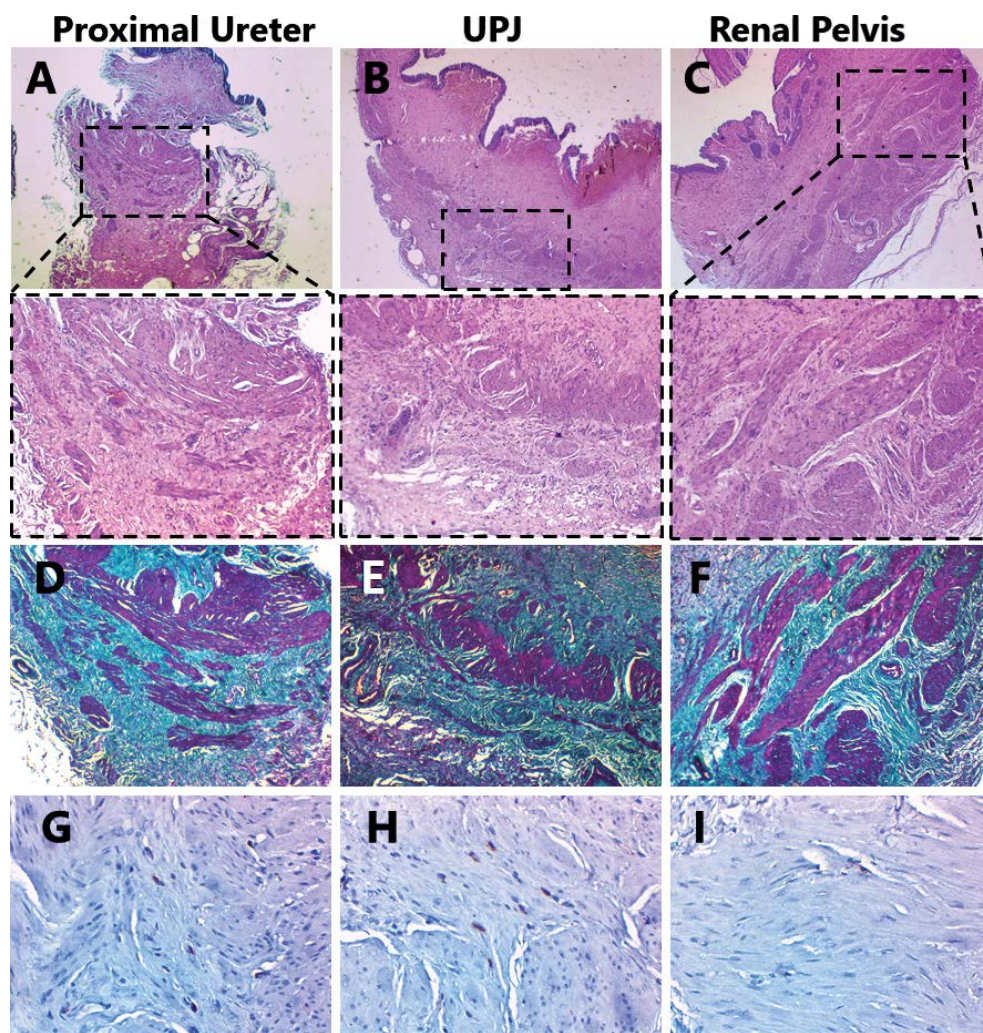
Figure 1. Morphological pattern of collagen to smooth muscles distribution in normal upper urinary tract, sections were stained with haematoxylin and eosin stain and Gomori's stain (**A–F**). Pattern of distribution of Cajal cells in normal upper urinary tract demonstrated with c-kit immunohistochemistry (**G–I**); **Left column** represents the proximal ureter, **middle column** represents ureteropelvic junction (UPJ) segment, **right column** represents renal pelvis. **Upper row:** Haematoxylin and eosin stained sections from muscularis propria with high insert box; proximal ureter (**A**), UPJ segment (**B**) and renal pelvis (**C**). Scale bar = 2 mm. **Middle row:** Gomori's trichrome stained sections showing smooth muscle bundles of the muscularis propria with collagen fibres. (collagen/muscle ratio of 2.3 for the proximal ureter (**D**) 1.5 for UPJ segment (**E**), and 1 for the renal pelvis (**F**). Scale bar = 2 mm. **Lower row:** Immunohistochemical staining with c-kit (CD 117) showing distribution of interstitial cells of Cajal in the upper urinary tract. The proximal ureter has the highest condensation of Cajal cells (**G**), the UPJ has a considerable density of Cajal cells (**H**), few cells are in the renal pelvis (**I**). Scale bar = 500 μm.

fibres, and myoblasts were demonstrated in all specimens of normal UUT and UPJO (Fig. 4). In the normal UUT, they were in excess in proximal ureter and renal pelvis, but moderately expressed in the UPJ segment. In UPJO, these interstitial cells were few in the renal pelvis, rare in the UPJ segment but in excess in the proximal ureter.

Correlation between density of Cajal cells and collagen/muscle ratio in normal UUT and UPJO. Distribution of interstitial cells in proximal ureter and renal pelvis in obstructed cases was similar to normal. Distribution of density of Cajal cells was correlated to the ratio of collagen to muscle fibres: the more muscle fibres in relation to collagen, the higher the density of Cajal cells. This finding was obvious in proximal ureter and renal pelvis in normal UUT. Diminished distribution of smooth muscle cells in the UPJ segment was associated with relative low density of Cajal cells and telocytes.

DISCUSSION

Cajal cells which are c-kit positive were demonstrated in this study in the muscular layer of normal UUT and in UPJO. Identification and characterisation
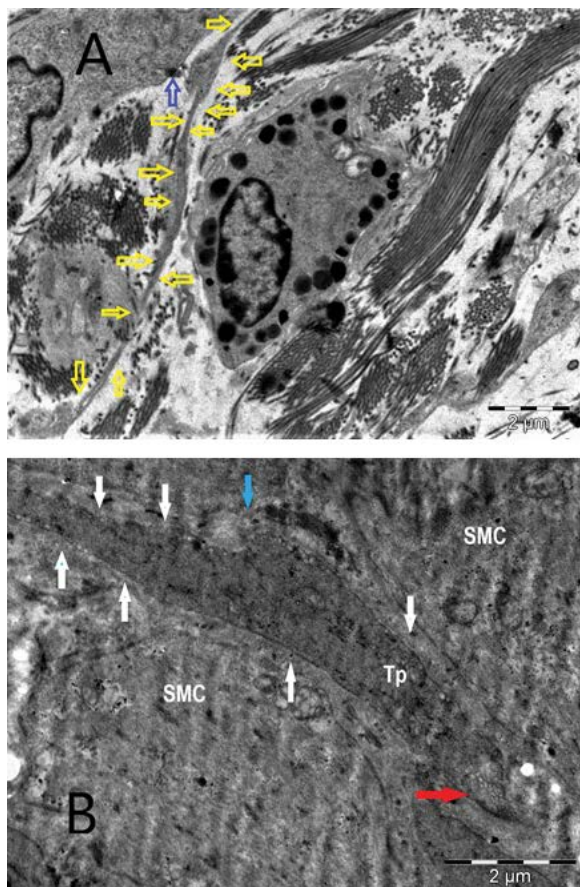
Figure 2. Transmission electron microscopy of the muscle layer of the ureteropelvic junction in normal upper urinary tract. **A.** Telocytes cytoplasmic process (telopode) (indicated with yellow arrows). The blue arrow indicates a contact between a telocyte and a myofibroblast. The telopode is characterised by a long slender cytoplasmic elongation that gets into contact with interstitial and smooth muscle cells; **B.** Telopode (Tp) is intervening between two smooth muscle cells (SMC; white arrow). The blue arrow indicates a group of caveolae, the white arrow is an attachment site between the telopode and smooth muscle cell (red arrow). Scale bar: A = 2 μm; B = 2 μm.

Figure 3. Transmission electron microscopy of muscle layer of the ureteropelvic junction in normal upper urinary tract. **A.** Interstitial cell of Cajal (ICC) is located between longitudinal and transverse muscle layer, it is characterised by notched nucleus and scant cytoplasm with cytoplasmic extension intervening between the smooth muscle cells (SMC). The segment shows properly arranged SMC, few collagen (C); **B.** Telocytes (TC), telopodes (Tp), and interstitial cells of Cajal (ICC) are existing in-between smooth muscle cells (SMC), there are scattered collagen fibres (C). Scale bar: A = 2 μm; B = 2 μm.

of these cells and their differentiation from other interstitial cells were in accordance with descriptions by previous studies on the upper urinary tract using IHC and TEM [3–9, 11, 20]. In our study, we showed that, in the normal UUT, Cajal cells were densely present in the proximal ureter, excessively in the renal pelvis, and moderately dense in the UPJ segment. In the UPJO, we demonstrated the presence of Cajal cells in the UPJ segment in few numbers, in moderate numbers in the renal pelvis, and in high numbers in the proximal ureter. Our results differ from previous studies [3, 4, 7, 15, 21] where only the UPJ segment was examined and changes in proximal ureter and renal pelvis were not considered. Eken et al. [4] searching for Cajal cells in the UPJ segment in UPJO in paediatric patients, found out that the Cajal

cells were either rare or absent. Our study confirmed their presence in the UPJ segment in UPJO, although not in the same density as in the normal UPJ segment. The difference in findings would be attributed to different age groups, as Eken et al. [4] studied the paediatric age group, while our study was applied to adults.

Examining the whole UUT in both normal and obstructed cases, we found that the three anatomical divisions express the same cells in different density, i.e. on cellular basis they are one unit. While in the past their division was based on shape and configuration, our concept is that the UUT is one entity and each part would play a role in the pathogenesis of UPJO.

Our study showed that the relationship between muscle density and collagen differed from one seg-
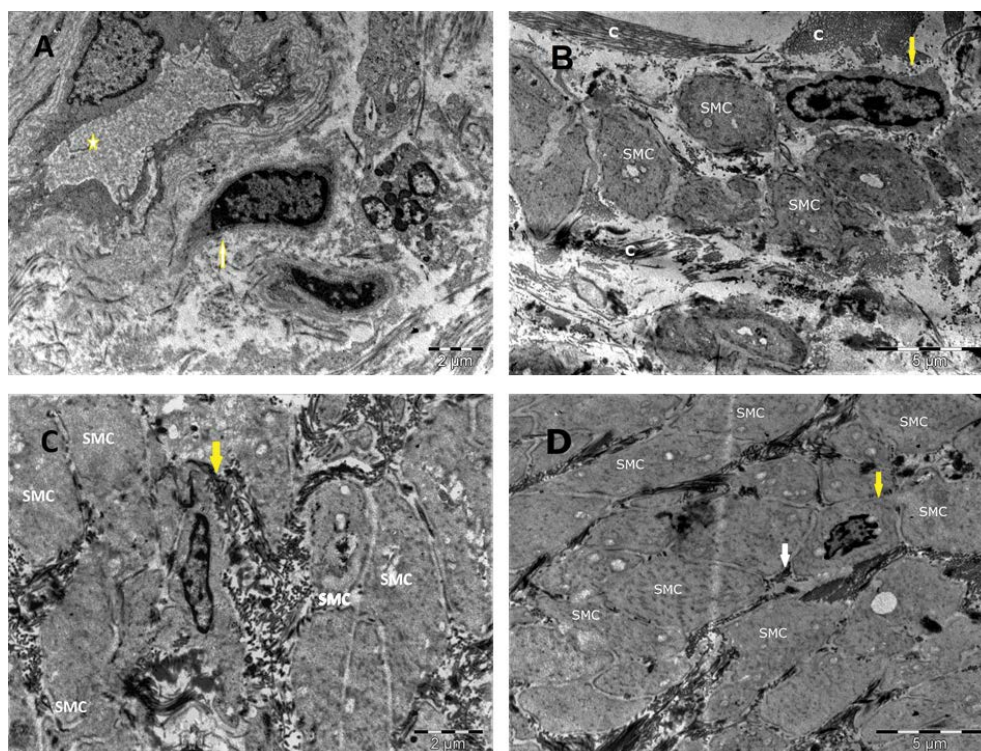
Figure 4. A. Dormant stem cell resident by the nearby capillary (arrow). It shows notched nucleus as well as rough endoplasmic reticulum alongside the nucleus. It also lacks the elongated processes of the telocytes, capillary vessel (asterisk). Scale bar $= 2\,\mu$m; **B.** Mesenchymal stem cells (yellow arrow), with scanty rim and obscured detailed cytoplasm, and polymorphic nuclei with deep notches. Scale bar $= 5\,\mu$m; **C.** Myofibroblast (yellow arrow) showing peripheral myofilaments with focal densities, and a dense basement membrane-like material. They are surrounded by matrix collagen fibres, smooth muscle cells (SMC) are in close cell-to-cell adhesion and few collagen (C) fibres intervening in the contact areas. Scale bar $= 2\,\mu$m; **D.** Myocyte (yellow arrow). The white arrow indicates collagen fibres of connective tissue, smooth muscles are in close contact to each other (SMC). Scale bar $= 5\,\mu$m.

ment to the other. In both normal and obstructed UUT, the muscle fibres were of higher concentration than the collagen in proximal ureter, renal pelvis, and UPJ segment, respectively.

Transmission electron microscopy of the normal UUT and UPJ obstruction showed the presence of telocytes in the proximal ureter, renal pelvis, and UPJ segment. Our work examined the three parts of UUT and confirmed the presence of telocytes. Previous reports by Zheng et al. [22], Qi et al. [13], Vannucchi et al. [17, 18], and Gevaert et al. [6] supported our findings. In our study on different parts of the UUT by TEM, we demonstrated the presence of stem cells, in addition to fibroblasts, myoblasts, telocytes, and Cajal cells. Previous studies on the interstitial cells of the UUT concentrated on one cell type, our study investigated all cell types and demonstrated their existence in normal and obstructed UUT.

CONCLUSIONS

Telocytes and Cajal cells were demonstrated with different density in the muscular layers of the UPJ segment, the renal pelvis, and the proximal ureter in normal and obstructed upper urinary tract secondary to UPJ obstruction. The low density of Cajal cells and increased collagen fibrils in the UPJ segment, in addition to the low density of Cajal cells in renal pelvis of UPJ obstruction, would be attributed to the aetiology of UPJ obstruction.

Conflict of interest: None declared

REFERENCES

1. Cajal SR. Histologie du système nerveux de l'homme et des vertébrés. Maloine (Paris). 1909; 2: 891–942, doi: 10.5962/bhl.title.48637.
2. Cretoiu SM, Popescu LM. Telocytes revisited. Biomol Concepts. 2014; 5(5): 353–369, doi: 10.1515/bmc-2014-0029, indexed in Pubmed: 25367617.
3. David SG, Cebrian C, Vaughan ED, et al. c-kit and ureteral peristalsis. J Urol. 2005; 173(1): 292–295, doi: 10.1097/01.ju.0000141594.99139.3d, indexed in Pubmed: 15592099.
4. Eken A, Erdogan S, Kuyucu Y, et al. Immunohistochemical and electron microscopic examination of Cajal cells in ureteropelvic junction obstruction. Can Urol Assoc J. 2013;

7(5-6): E311–E316, doi: 10.5489/cuaj.11293, indexed in Pubmed: 23069698.

5. Gevaert T, De Vos R, Everaerts W, et al. Characterization of upper lamina propria interstitial cells in bladders from patients with neurogenic detrusor overactivity and bladder pain syndrome. J Cell Mol Med. 2011; 15(12): 2586–2593, doi: 10.1111/j.1582-4934.2011.01262.x, indexed in Pubmed: 21251216.

6. Gevaert T, De Vos R, Van Der Aa F, et al. Identification of telocytes in the upper lamina propria of the human urinary tract. J Cell Mol Med. 2012; 16(9): 2085–2093, doi: 10.1111/j.1582-4934.2011.01504.x, indexed in Pubmed: 22151349.

7. Koleda P, Apoznanski W, Wozniak Z, et al. Changes in interstitial cell of Cajal-like cells density in congenital ureteropelvic junction obstruction. Int Urol Nephrol. 2012; 44(1): 7–12, doi: 10.1007/s11255-011-9970-5, indexed in Pubmed: 21547467.

8. Lang RJ, Klemm MF. Interstitial cell of Cajal-like cells in the upper urinary tract. J Cell Mol Med. 2005; 9(3): 543–556, doi: 10.1111/j.1582-4934.2005.tb00487.x, indexed in Pubmed: 16202204.

9. Maeda H, Yamagata A, Nishikawa S, et al. Requirement of c-kit for development of intestinal pacemaker system. Development. 1992; 116(2): 369–375, indexed in Pubmed: 1283735.

10. Petre N, Rusu MC, Pop F, et al. Telocytes of the mammary gland stroma. Folia Morphol. 2016; 75(2): 224–231, doi: 10.5603/FM.a2015.0123, indexed in Pubmed: 26711648.

11. Popescu LM, Ciontea SM, Cretoiu D. Interstitial Cajal-like cells in human uterus and fallopian tube. Ann N Y Acad Sci. 2007; 1101: 139–165, doi: 10.1196/annals.1389.022, indexed in Pubmed: 17360808.

12. Popescu LM, Faussone-Pellegrini MS. TELOCYTES — a case of serendipity: the winding way from Interstitial Cells of Cajal (ICC), via Interstitial Cajal-Like Cells (ICLC) to TELOCYTES. J Cell Mol Med. 2010; 14(4): 729–740, doi: 10.1111/j.1582-4934.2010.01059.x, indexed in Pubmed: 20367664.

13. Qi G, Lin M, Xu M, et al. Telocytes in the human kidney cortex. J Cell Mol Med. 2012; 16(12): 3116–3122, doi: 10.1111/j.1582-4934.2012.01582.x, indexed in Pubmed: 23241355.

14. Sergeant GP, Thornbury KD, McHale NG, et al. Interstitial cells of Cajal in the urethra. J Cell Mol Med. 2006; 10(2): 280–291, doi: 10.1111/j.1582-4934.2006.tb00399.x, indexed in Pubmed: 16796799.

15. Solari V, Piotrowska AP, Puri P. Altered expression of interstitial cells of Cajal in congenital ureteropelvic junction obstruction. J Urol. 2003; 170(6 Pt 1): 2420–2422, doi: 10.1097/01.ju.0000097401.03293.f0, indexed in Pubmed: 14634443.

16. van der Aa F, Roskams T, Blyweert W, et al. Identification of kit positive cells in the human urinary tract. J Urol. 2004; 171(6 Pt 1): 2492–2496, doi: 10.1097/01.ju.0000125097.25475.17, indexed in Pubmed: 15126883.

17. Vannucchi MG, Traini C, Guasti D, et al. Telocytes subtypes in human urinary bladder. J Cell Mol Med. 2014; 18(10): 2000–2008, doi: 10.1111/jcmm.12375, indexed in Pubmed: 25139461.

18. Vannucchi MG, Traini C. Interstitial cells of Cajal and telocytes in the gut: twins, related or simply neighbor cells? Biomol Concepts. 2016; 7(2): 93–102, doi: 10.1515/bmc-2015-0034, indexed in Pubmed: 26992201.

19. Vannucchi MG. The telocytes: ten years after their introduction in the scientific literature. An update on their morphology, distribution, and potential roles in the gut. Int J Mol Sci. 2020; 21(12), doi: 10.3390/ijms21124478, indexed in Pubmed: 32599706.

20. Yamataka A, Ohshiro K, Kobayashi H, et al. Abnormal distribution of intestinal pacemaker (C-KIT-positive) cells in an infant with chronic idiopathic intestinal pseudoobstruction. J Pediatr Surg. 1998; 33(6): 859–862, doi: 10.1016/s0022-3468(98)90660-1.

21. Yang X, Zhang Y, Hu J. The expression of Cajal cells at the obstruction site of congenital pelviureteric junction obstruction and quantitative image analysis. J Pediatr Surg. 2009; 44(12): 2339–2342, doi: 10.1016/j.jpedsurg.2009.07.061, indexed in Pubmed: 20006022.

22. Zheng Y, Zhu T, Lin M, et al. Telocytes in the urinary system. J Transl Med. 2012; 10: 188, doi: 10.1186/1479-5876-10-188, indexed in Pubmed: 22963412.

V M
VIA MEDICA

ORIGINAL ARTICLE

Heat shock protein 60 expression and localisation in different tissues and testis development of male cattle (cattle-yak and yak)

S. Zou[#], P. Liu[#], S. Yu, Y. Cui, J. He, S.Y. Afedo, H. Zhang, R. Niayale, K. Zhao

College of Veterinary Medicine, Gansu Agricultural University, Lanzhou, Gansu, China

Background: Heat shock protein 60 (Hsp60) play important roles in protecting testicular development and production of sperms. This study was conducted to investigate Hsp60 gene expression and localisation in testicular development to ascertain its influence on infertility and in different tissues of the male cattle-yak and yak. A total of 54 cattle (24 cattle-yak and 30 yak) were examined.

Materials and methods: Heat shock protein 60 mRNA of cattle-yak was cloned first and amino acid variations were found leading to differences at protein spatial structure compare with the yak. Real-time quantitative polymerase chain reaction analysis revealed that Hsp60 mRNAs expression were different in cattle-yak and yak.

Results: The results showed disparity in Hsp60 expression among different tissues and in different developmental stages of the testis. High Hsp60 expression was observed in juvenile and adult testicles. Moreover, Hsp60 expression in cattle-yak was significantly higher than yak (p < 0.01). The location of Hsp60 in tissue and testis was detected by immunohistochemistry and immunofluorescence. The results demonstrated that Hsp60 proteins located in epithelial cells, spermatocytes, sperm cells and mesenchymal cells.

Conclusions: The Hsp60 proteins are expressed in different tissues, and the highest expression level was observed in the testis of the cattle-yak, which suggests that infertility of cattle-yak have some correlation with up-regulation of Hsp60. (Folia Morphol 2021; 80, 4: 857–869)

Key words: yak, tissue, Hsp60, expression, localisation

INTRODUCTION

Cattle-yak (*Bos* cattle-yak) and yak (*Bos grunniens*) are important animals for local herdsmen of the Qinghai-Tibet Plateau in China. Cattle-yak as a hybrid, exhibits obvious heterosis of yak and cattle, such as tallness, robustness, fast growth speed, drought tolerance, and disease resistance [39]. Different organs play different roles in the metabolism of the body [3]. The testis is one most important male reproductive organs, and the heat shock protein 60 (Hsp60) location of its cell proliferation and development have significant importance [24]. Although infertility is a worldwide problem in male yak-cattle, the studies on causal mechanism are lacking.

Address for correspondence: Dr. Y. Cui, College of Veterinary Medicine, Gansu Agricultural University, Lanzhou 730070, Gansu, China,
e-mail: cuiyan369@sina.com

#The first two authors contributed equally to this manuscript.

Recent studies have shown that Hsp60 could protect spleen lymphocytes cells from damage, organ failure, spleen inflammatory diseases, and body shock [42]. Hsp60 not only participates directly or indirectly in endothelial dysfunction, atherosclerosis, cardiovascular diseases, and growth and development but also protects reproductive cell activity and regulates protein metabolism of organisms [2]. Previous studies have demonstrated that Hsp60 up-regulates in monocytic cells of the immune system, and tumour cells in stomach cancer, colon cancer, liver cancer, breast cancer, and lung cancer [17, 19]. Moreover, co-culturing of human myoblasts revealed that molecular patterns of Hsp60 induced interleukin-10 to protect THP-1 cells [38]. The level of expression of HSPs throughout the period of heat stress was highest in buffaloes, followed by bos indicus and taurus [18]. In addition, the HSPA2 expression levels significantly differed in the various tissues of yak, especially in the testes and breast, followed by the brain, kidney, heart, lung, and liver, and its weakest expression was found in the spleen [32]. In relation to these backdrops, this study was performed to investigate whether Hsp60 was differentially expressed in the various tissues of cattle-yak and yak.

The testes are most important male reproductive organs. When testicular tissue was exasperated by metals such as arsenic, copper and cadmium or a chemical (DEHP), mRNA and protein levels of Hsp60, Hsp70, and Hsp90 were up-regulated [8, 34]. Meanwhile, Hsp40, Hsp60, and Hsp70 expression increased respectively, when mice testis was buoyed up by high temperature [44]. Many factors are responsible for the infertility of male cattle-yak. These factors include testicular dysplasia, hindered spermatogenesis, metamorphosis phase, and sustentacular cells assisting the germ cell differentiation in the seminiferous tubule [23]. Thus, studies on the fertility of male cattle-yak and male yak have focused on distinguishing histologic structural development, the effects of genes expression, and the intensity of protein involved in the production and control of sperms [32].

Previous studies have shown that the cattle-yak infertility not only reflects histologically, but also manifestations of differential expression of related genes and proteins generated by sperms [33]. As creatures have low content of eight differential proteins containing triosephosphate isomerase, glycerol kinase, and HSP [36]. The Hsp60 high expression is used as a marker for semen quali-

ty, sperm concentration and functional capacity [7, 25]. In the sperm of human beings, the expression of HSPs in sperm cells are significantly higher than that of the primary spermatocyte, and diverse HSP chaperones are accessible for surface labelling on human sperm [27]. HSPs (Hsp60, Hsp70, Hsp90) are highly expressed in different physical, mechanical, and chemical stresses, an indication that these proteins might function in various processes such as mitochondrial function, gamete interaction, and receptor activity regulation [14, 35]. Research has shown that Hsp10 and Hsp60 were inducible and functional in testis development and migration process of Coilia nasus, suggesting their essential roles in these processes. The results also indicated that Hsp60 may be one indicator of properly working mitochondrial import and refolding in the fish testis [9]. However, the correlation between male sterility and Hsp60 of yak and cattle-yak is still unclear. Therefore, we determined the relationship between Hsp60, tissue specificities of cattle, and the regulation of testicular development and sperm production.

MATERIALS AND METHODS
Experimental animals

Cattle were sampled from a pasture in the Tibetan plateau in Qinghai, China [11]. A total of 54 healthy cattle (24 cattle-yak and 30 yaks) were used in this study (Table 1), All cattle were kept under the same natural conditions (altitude, approximately 2,300 m a.s.l.; temperature, 2~5°C; and oxygen content, 14.97%) [39]. Male cattle-yak without feeding value from herders were excluded, and no samples were taken from the senile group.

The cattle with conventional disease were considered healthy individuals. All experiments were performed in accordance with relevant guidelines and regulations. The euthanasia procedure was carried by atropine plus diazepam given intramuscularly as premedication for narcosis, and overdose intravenous injection of sodium pentobarbital sodium with IV administration when study was finished (Nembutal, l50 mg/kg; Abbot Labs, USA). The study was approved by the Animal Ethics Committee of Gansu Agricultural University, China (SYXK [Gan] 2015-0001).

Preparation of mRNA and proteins

Tissue samples were selected from 21 healthy cattle. Tissues were dissected, collected in frozen

Table 1. Specimens examined

Number of cattle-yaks and yak	Group	Age	Source	Application
6 + 6	Newborn	1~7 days	Xi'ning City Qinghai Province	Molecular biology Measurement
6 + 6	Calf	6~8 months		
6 + 6	Juvenile	1~1.5 years		
6 + 6	Adult	3~4 years		
0 + 6	Senile	8~10 years		

Table 2. Primer sequences of target and house-keeping genes

Primer name	Sequence (5'→3')	Tm (°C)	Note
Hsp60-1R	CGGAGTCGGGCGATTGT	59.5	RT-PCR
Hsp60-1F	CTCCAAATACTGCACCCCCA	60.6	1016bp
Hsp60-2R	TCTCATCTGGTGATAGCAAG	61.7	RT-PCR
Hsp60-2F	CCTTGTTTTGAATAGGTTGA	60.2	1293bp
β-actin-R	GCTCGGCTGTGGTGGTAAA	59.0	RT-qPCR
β-actin-F	AGGCTGTGCTGTCCCTGTATG	59.0	207bp
Hsp60-R	GCCAAAGGGAAGGACAGT	54.3	RT-qPCR
Hsp60-F	ATGACCGTGCGAGATAACG	54.6	204bp

liquid nitrogen, and then stored at −80°C before use. The RNA from the cattle tissues were isolated using a TRIzol kit (R1100, USA), and reverse-transcription polymerase chain reaction (RT-PCR) was performed to clone the cDNA.

Frozen samples were ground in liquid nitrogen and transferred to centrifuge tubes with RIPA/PMSF (Solarbio, China). After thoroughly blending and mixing, a pink colour was obtained. The sample tubes were incubated on a spiral oscillator for 2 h (200 r/h) on ice and centrifuged at 4°C for 10 min (12,000 r/h) to obtain the complete divided protein. The total protein concentration for each sample was measured. The total protein concentration was then adjusted to the same level, and 4× sample buffer at 100°C was added for 12 min to completely denature the proteins.

Molecular cloning of Hsp60

The degenerate primers used to amplify the Hsp60 sequence were based on the published partial sequence of Hsp60 mRNA in the National Centre for Biotechnology Information (NCBI) database (Accession No. NM-001012670.2). Primers for cloning the initial fragment of Hsp60 mRNA were designed according to the predicted conserved sequences in other

Bos cattle-yaks (Table 2). The amplified segments were inserted into the cloning vector pMD-18T and were transfected into *Escherichia coli* JM109 competent cells. The primers for 5' Hsp60 and 3' Hsp60 were designed using the sequencing data. Then, the segments from 5' to 3' Hsp60 from the first-strand cDNA were used for cloning and sequencing.

Analysis of Hsp60 protein

The open reading frames (ORF) in the complete mRNA sequence of HSP90 were identified using an ORF finder (http://www.ncbi.nlm.nih.gov/projects/gorf/orfig.cgi), and the nucleotide sequences were translated into amino acids using the Vector NTI 11 software [12]. The Hsp60 sequence was analysed using the ODC Hsp60 finder software, and the codon region and frameshifting site were identified [10].

Homology searches were performed using BLASTn and BLASTp in NCBI. The conserved domain. Search service was used to identify the conserved domains in the predicted protein sequences (http://www.ncbi.nlm.nih, https://web.expasy.org/protparam). The three-dimensional structure of the predicted protein was envisaged according to the methods described in the website (http://bioinf.cs.ucl.ac.uk/psipred/). The deduced amino acid sequence of HSP90 was aligned using the course line computer (CLC) main workbench software (http://www.clcbio.com) with known homologous proteins of the Hsp60 class obtained from the GenBank. A phylogenetic tree was constructed using the CLC main workbench software through the neighbour-joining method for the amino acid sequences of Hsp60 from the SwissProt databank/GenBank.

Expression of Hsp60 gene in different tissues

The distribution of Hsp60 in the tissues of cattle-yak and yaks were detected during the development of testicles and in the non-reproductive system (kidney, heart, cerebellum, liver, lung, and spleen). The expression levels of Hsp60 in the different tissues were detected using quantitative real-time PCR (Invitrogen, USA) with Hsp60 specific primers. Actin was used as a reference gene to normalise the amount and quality of each cDNA, because this gene is expressed constitutively in the different tissues [13].

Immunofluorescence and immunohistochemical assays

The different tissues of the cattle-yak and yak were fixed in 4% paraformaldehyde solution at room

temperature for hebdomad. Tissues were clipped and paraffin-embedded, and the sections were sliced (4 μm), dried, and stored.

Samples were dewaxed using dimethyl benzene and then dehydrated with an increasing alcohol gradient for immunohistochemical staining to investigate the Hsp60 expression levels. The endogenous peroxidase was eliminated with 3% deionised H_2O_2 (18––22 min), and the sections were rehydrated and sealed with goat serum (18–22 min). After overnight incubation at 4°C with primary rabbit anti-Hsp60 monoclonal antibodies (1:2500, Abcam, Hong Kong), the sections were then incubated with the secondary antibody. Then, the labelled samples were counterstained with 3,3'-diaminobenzidine, and the nuclei were observed [11]. Two antibodies showed different colours in immunofluorescence (BX53MTRF-S, OLYMPUS, Japan), and re-dyeing the nuclei was not necessary.

Measurement and statistical analyses

The intensity of immunofluorescence and immunohistochemical assays were measured using integrated optical density and Image-Pro plus 6.0. Data were analysed using SPSS 21.0. Spearman correlation of coefficients was analysed between β-actin and sample protein levels. Other data were analysed by one-way ANOVA and Duncan's post hoc test. P-values less than 0.05 between groups were considered statistically significant [12].

RESULTS

Analysis of physical and chemical properties of Hsp60

The cDNA sequence of Hsp60 was cloned and submitted to GenBank with accession number KF690729.

The nucleotide sequence and predicted amino acid sequence of Hsp60 were presented. Hsp60 nucleic acids were 2572 bp long. Results from the analysis of the contig showed that the predicted Hsp60 cDNA of 2572 bp contained an ORF of 1604 bp from 479 bp to 2083 bp. Analysis of the Hsp60 cDNA sequence in our study confirmed this conclusion. RT-PCR results show successful isolation of a cDNA fragment of 1604 bp from the cattle-yak total RNA of the heart. Finally, this confirmed cDNA sequence was deposited in the GenBank under accession number KF690729. To obtain the genomic DNA of Hsp60, the publicly available cow genome database at the NCBI Bovine Genome Resources (http://www.ncbi.nlm.nih.gov/projects/genome/guide/cow/) was screened using the Hsp60 cDNA sequence as

a query. A cow (*Bos taurus*) contig (GenBank Accession No. NM_001166608.1) which encompasses the entire Hsp60 gene was identified by BLASTGen analysis.

The basic physical and chemical properties of Hsp60 were analysed. The atomic number of the protein coding region was 26828. Hsp60 has a molecular formula of $C_{7704}H_{12838}N_{2572}O_{3228}S_{486}$, molecular weight of 56633.35 Da, and theoretical isoelectric point of 5.091. Hsp60 has a half-life of approximately 30 h, instability index of 34.82, fat soluble index of 29.70, and average hydrophobicity index of 0.725.

A molecular phylogenetic tree was constructed to analyse the evolutionary relationship of Hsp60 nucleotide sequences (Fig. 1). Analysis of the gene family tree showed that the cattle-yak HSP90 evolutionarily shared a higher sequence identity with *B. grunniens*, *Ovis aries*, *Bos taurus*, *Orcinus orca*, *Sus scrofa*, *Canis familiaris*, *Ceratotherium simum*, *Homo sapiens*, *Pan troglodytes*.

Analysis of structure specificity with proteins of Hsp60

The predicted amino acid sequence of Hsp60 was aligned with known *B. grunniens* sequences through BLASTp. The cattle-yak Hsp60 protein sequence shared a low percentage of similarity to other known Hsp60 protein sequences. This result indicated that the Hsp60 proteins were different from other members in the HSP family. The amino acid sequence of Hsp60 was approximately 99.87%, 98.54%, 97.39%, 95.62%, and 83.75% identical to those of HSPs from *B. grunniens*, *Ovis aries*, *B. taurus*, *Orcinus orca*, *Sus scrofa*, *Canis lupus.* The highest level of similarity appeared near the C-terminal, while the very low similarity was found in the N-terminal and in the middle of the amino acid sequence.

The cattle-yak Hsp60 protein sequence showed that mutational nucleotide caused the change of amino acids, such as the G into V, T into N, A into E, G into P and so on (Fig. 2). The most important result was the change in the protein spatial structure and differences in protein function, such as the H-key number (390), spiral number (25), link number (22) and corner number (54). In addition, compared with yak, the initiating terminal and terminal of the cattle-yak are longer.

Expression and distribution of Hsp60 in different tissue

The Hsp60 mRNA in tissues of cattle-yak and yak were investigated through RT-qPCR (Fig. 3-I), with the
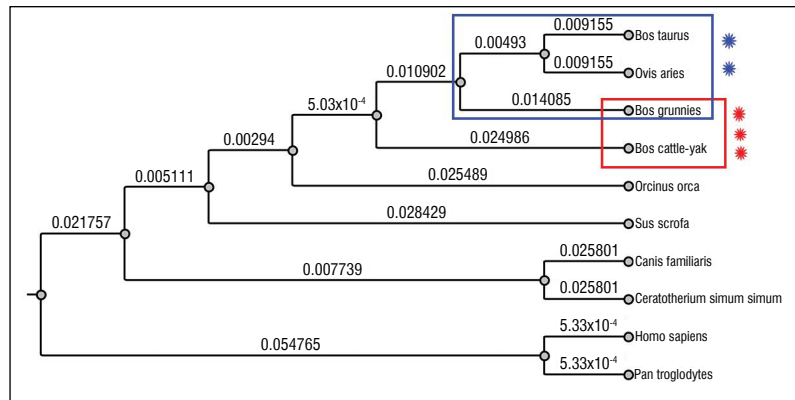
Figure 1. The heat shock protein 60 (Hsp60) phylogenetic tree of cattle-yak. The phylogenetic tree was constructed with course line computer main workbench software using the neighbour-joining method for the amino acid sequences of Hsp60 from the Swiss-Prot databank/GenBank.
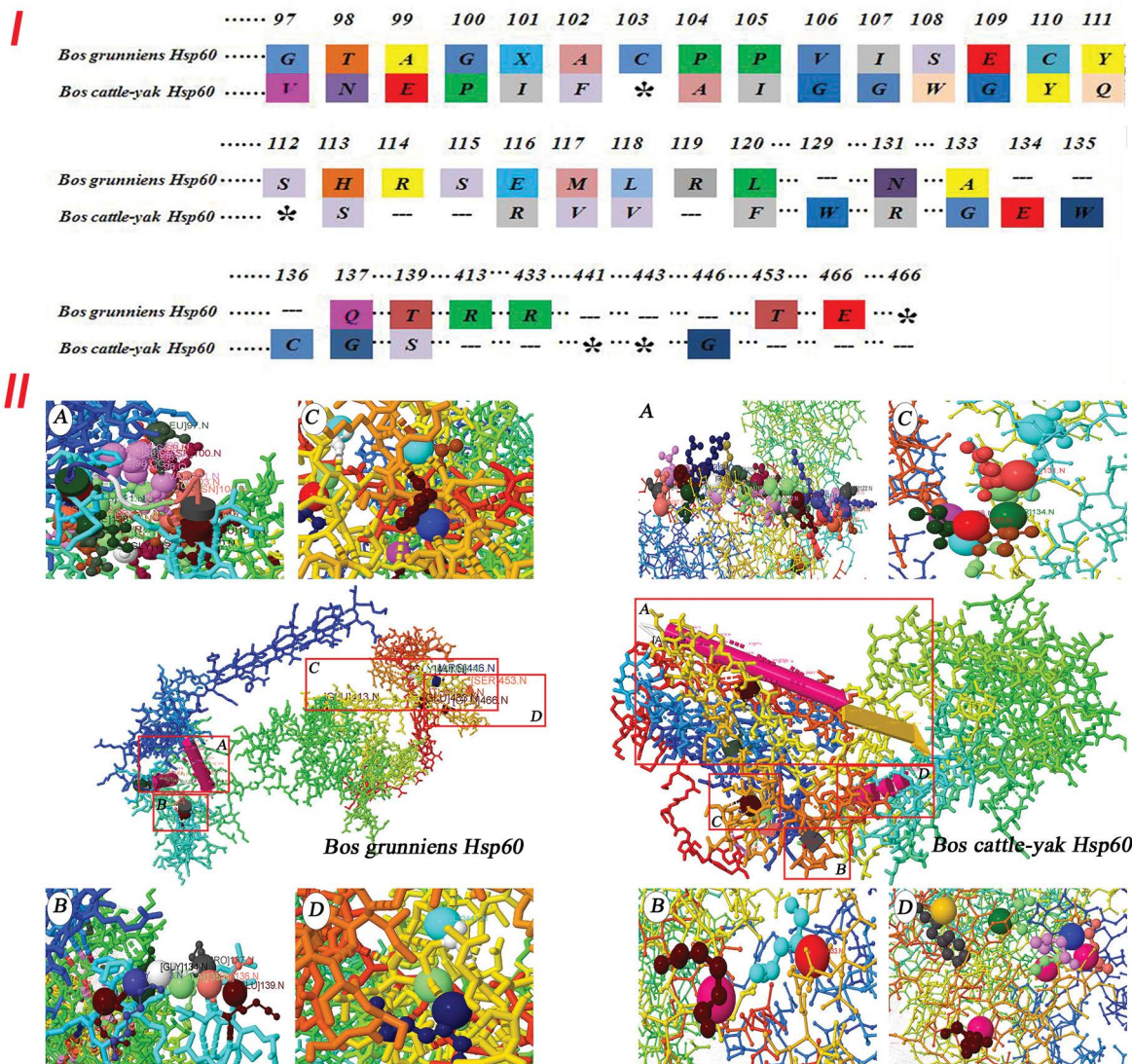
Figure 2. Analysis of heat shock protein 60 (Hsp60) protein structure of cattle-yak and yak; **I.** The Hsp60 amino acid sequence analysis that the sites and types of mutation in cattle-yak and yak; **II.** The Hsp60 protein structure of yak; **A.** The initiating terminal of the yak is mutation. as follows: 97~120 (G, T, A, G, X, A, C, P, P, V, I, S, E, C, Y, S, H, R, S, E, M, L, R, L); **B, C, D.** Mutation site and amino acids are as follows: 131(N), 133(A), 137(Q), 139(T), 413(R), 433(R), 453(T), 466(E); **III.** The Hsp60 protein structure of cattle-yak. 97~120 (V, N, E, P, I, F, *, A, I, G, G, W, G, Y, Q, *, S, R, V, V, F); **B, C, D.** Mutation site and amino acids are as follows: 129(W), 131(R), 133(G), 134(E), 135(W), 136(C), 137(G), 139(S), 441(*), 433(*), 446(G); Asterisk (*) is the unknown amino acids.
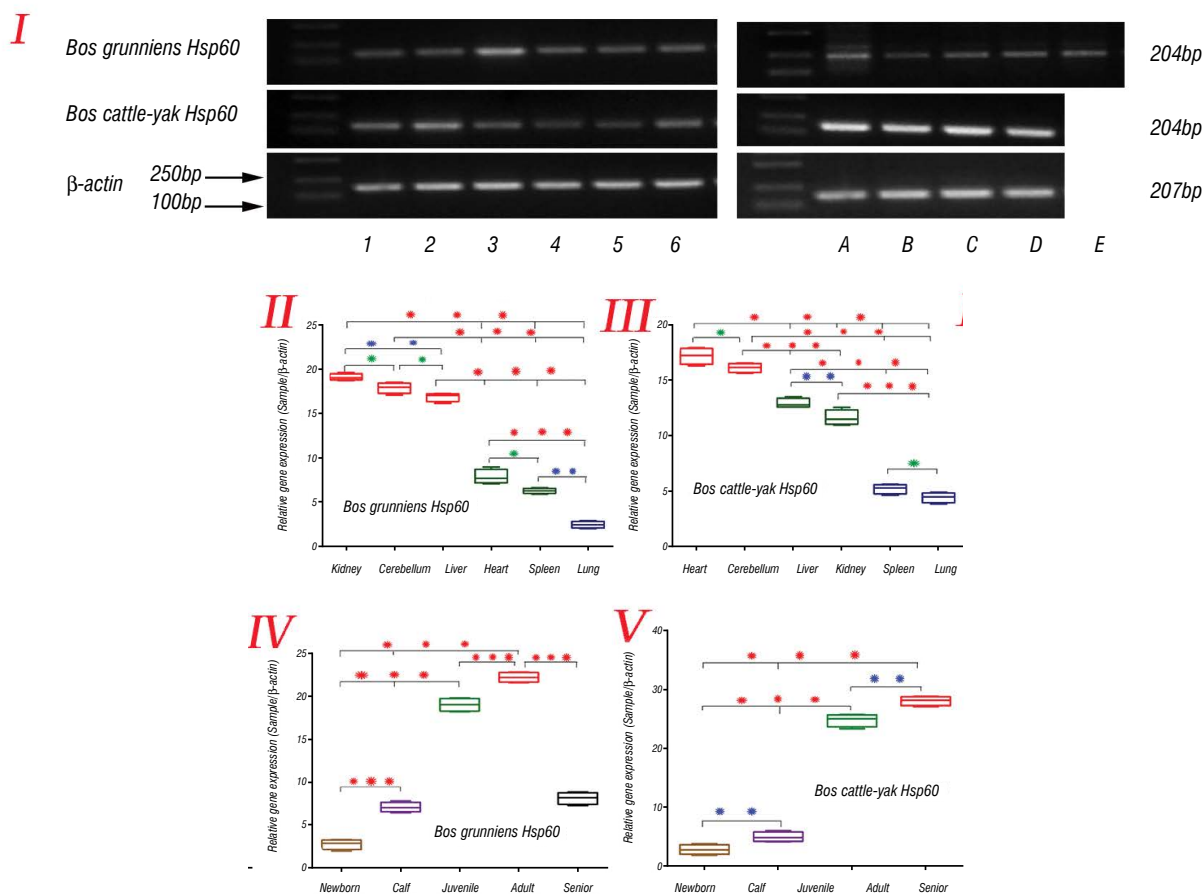
Figure 3. The heat shock protein 60 (Hsp60) gene expression in different tissues of cattle-yak and yak; **I.** The results of real time-polymerase chain reaction; 1 — kidney; 2 — cerebellum; 3 — liver; 4 — heart; 5 — spleen; 6 — lung; A — newborn; B — calf; C — juvenile; D — adult; E — senile; **II, III.** The gene expression levels of Hsp60 in different tissue of male yak and cattle-yak; **IV, V.** The gene expression levels of Hsp60 in testicular tissue of yak and cattle-yak. The columnar represent the expression trend of Hsp60 protein in different organizations and testis development stages. Different colours represent different expressions of Hsp60 in the organizations and testicular tissue of cattle-yak and yak. The asterisk represents the difference in positive expression. The more asterisks, the more significant the difference.

total RNA isolated from cattle-yak and yak tissues as templates. As shown in Fig. 3-II and 3-III, 6 tissues in cattle-yak and yak were examined. The expression of Hsp60 was widely distributed in all tissues. According to our data, Hsp60 expression was reduced in yak, with a trend from kidney, cerebellum, liver, heart, and spleen to the lungs. But Hsp60 expression increased in the cattle-yak, with a trend from heart, cerebellum, liver, kidney, and spleen to the lungs. There was significant difference about Hsp60 in these tissues, but interestingly the Hsp60 expression levels in yak were consistently higher than cattle-yak in almost all the tested tissues (p < 0.01). Although the expression of Hsp60 was higher in cerebellum and liver in yak and cattle-yak, the expression pattern in different tissues and levels were irregular. Taken together our data

suggest that Hsp60 expression in yak was consistently higher than cattle-yak in all the tested tissues (p < 0.01).

The Hsp60 was mainly observed in the kidney tubules, cardiac muscle cells, hepatocytes, Purkinje cells, red pulp, and cerebellar medulla (Fig. 4-I, 4-II and Fig. 5-I, 5-II). Position analysis indicated that Hsp60 protein was mainly concentrated in the connective tissue and epithelia. Thus, the proteins were mainly concentrated in the cell membrane and in the cytoplasm but not in the nucleus. Furthermore, Hsp60 protein expression was reduced in the yak, with a trend from kidney, cerebellum, liver, heart, and spleen to the lungs (p < 0.01), except in the kidney. But Hsp60 protein expression was same as gene expression of cattle-yak (Fig. 4-III and Fig. 5-III).
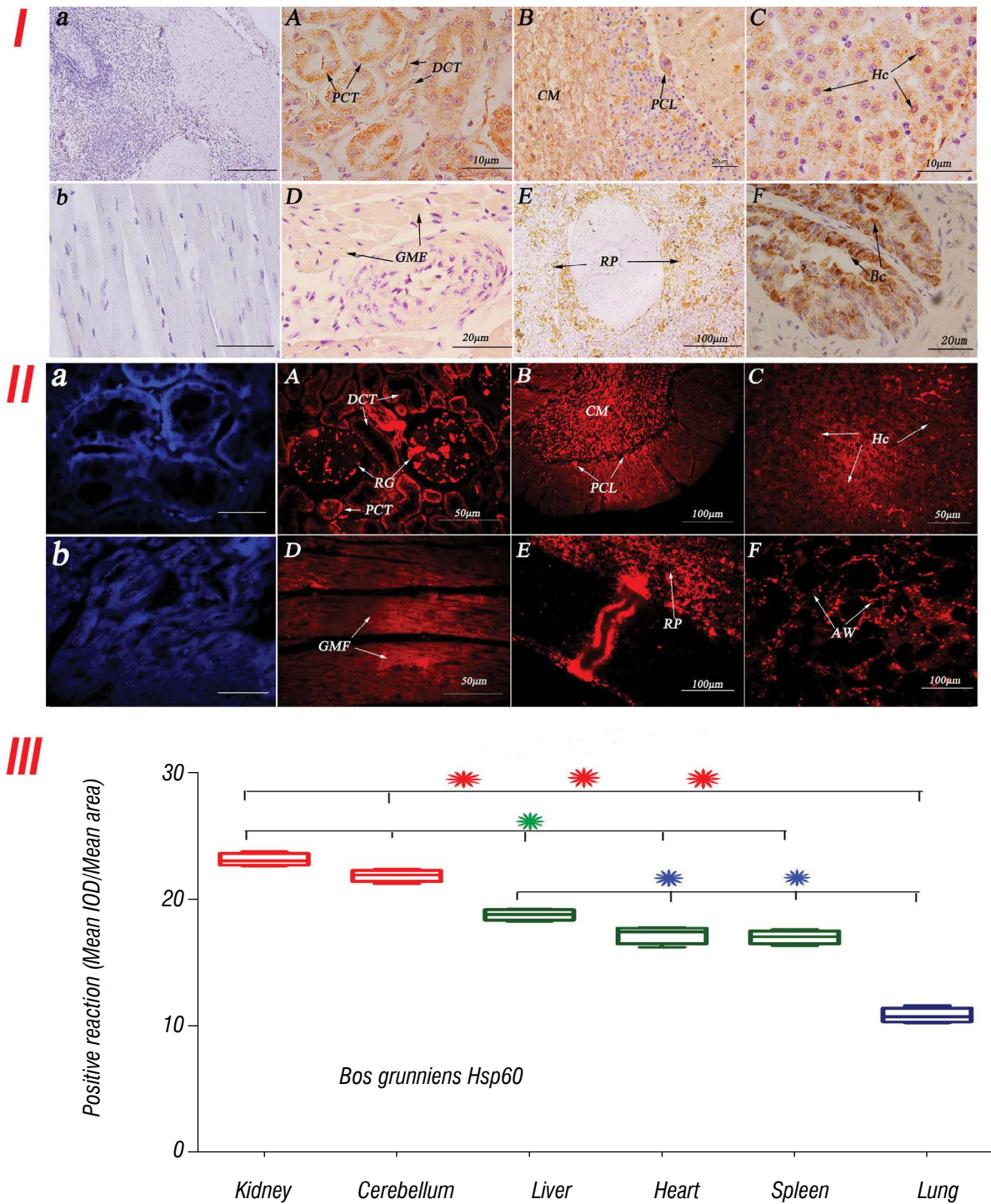
Figure 4. Immunohistochemistry and immunofluorescence localisation of heat shock protein 60 (Hsp60) in the different tissue of yak; **I, II: a, b.** The control sections collected from the different tissue of yak, without immunoreactions (negative control); **A.** Positive staining for Hsp60 was observed in the distal convoluted tubule and proximal convoluted tubule of kidney; **B.** Positive staining for Hsp60 was observed in the cerebellar medulla, granular layer and Purkinje cell layer of cerebellum; **C.** Positive staining for Hsp60 was observed in the hepatocytes of liver; **D.** Positive staining for Hsp60 was observed in the cardiac muscle fibres of heart; **E.** Positive staining for Hsp60 was observed in the red pulp of spleen; **F.** Positive staining for Hsp60 was observed in the terminal bronchioles of the lungs; **III.** The result of optical density analysis value. The columnar represent the expression trend of Hsp60 protein in different organizations; TB — terminal bronchiole; Hc — hepatocyte; CV — central vein; CMF — cardiac muscle fibres; DCT — distal convoluted tubule; PCL — Purkinje cell layer; RG — renal glomerulus; Bf — biofilm;Tc — trabecula; RP — red pulp; WP — white pulp; CM — cerebellar medulla; ML — molecular layer; GL — granular layer; PCT — proximal convoluted tubule; IOD — integral optical density. The main mode of positive expression was measured by image software. The asterisk represents the difference in positive expression. The more asterisks, the more significant the difference.

Figure 5. Immunohistochemistry and immunofluorescence localisation of heat shock protein 60 (Hsp60) in the different tissue of cattle-yak; **I, II: a, b.** The control sections collected from the different tissue of cattle-yak, without immunoreactions (negative control); **A.** Positive staining for Hsp60 was observed in the cardiac muscle fibres of heart; **B.** Positive staining for Hsp60 was observed in the cerebellar medulla, granular layer and Purkinje cell layer of cerebellum; **C.** Positive staining for Hsp60 was observed in the hepatocytes of liver; **D.** Positive staining for Hsp60 was observed in the distal convoluted tubule and proximal convoluted tubule of kidney; **E.** Positive staining for Hsp60 was observed in the red pulp of spleen; **F.** Positive staining for Hsp60 was observed in the terminal bronchioles of the lungs; **III.** The result of optical density analysis value. The columnar represent the expression trend of Hsp60 protein in different organizations; TB — terminal bronchiole; Hc — hepatocyte; CV — central vein; CMF — cardiac muscle fibres; DCT — distal convoluted tubule; PCL — Purkinje cell layer; RG — renal glomerulus; Bf — biofilm;Tc — trabecula; RP — red pulp; WP — white pulp; CM — cerebellar medulla; ML — molecular layer; GL — granular layer; PCT — proximal convoluted tubule; IOD — integral optical density. The main mode of positive expression was measured by image software. The asterisk represents the difference in positive expression. The more asterisks, the more significant the difference.

Figure 6. Immunohistochemistry and immunofluorescence localisation of heat shock protein 60 (Hsp60) in the testicular tissue of yak;
I, II: A, A1. Positive staining for Hsp60 was observed in the spermatogonium of the newborn testis; **B, B1.** Positive staining for Hsp60 was observed in mesenchymal, primary spermatocyte of the calf testis; **C, C1.** Positive staining for Hsp60 was observed in the primary spermatocyte and secondary spermatocyte of the juvenile testis; **D, D1.** Positive staining for Hsp60 was observed in the primary spermatocyte and spermoblast of adult testis; **E, E1.** Positive staining for Hsp60 was observed in the primary spermatocyte of senior testis; **III.** The result of optical density analysis value. The columnar represent the expression trend of Hsp60 protein in different age of testis tissues; PS — primary spermatocyte; SS — secondary spermatocyte; Sg — spermatogonium; Sb — spermoblast; S — sperm; SC — Sertoli cells; MC — mesenchymal cells; MC — myoid cells; ST — seminiferous tubule; IOD — integral optical density. The main mode of positive expression was measured by image software. The asterisk represents the difference in positive expression. The more asterisks, the more significant the difference.

Expression and distribution of Hsp60 at the different developmental stages of the testis

In addition to founding the differences in Hsp60 expression between cattle-yak and yak in the 6 tissues, the testicles were further examined. As shown in Figure 3-IV, Hsp60 gene expression levels showed significant differences in the cattle-yak and yak testicular tissues at different developmental stages (p < 0.01). In the yak, the expression of Hsp60 showed an obvious increasing trend from newborn to senior, with the highest expression in the adult and this tends to decrease. Whereas in cattle-yak, Hsp60 expression was highest in the adult than other. In short, Hsp60 expression in the cattle-yak remained higher during every development stage of the testis

(Fig. 3-V). It is worth noticing that Hsp60 expression in cattle-yak was significant higher than yak in every development stage of the testis.

The testicular seminiferous tubule of the newborn cattle-yak and yak was thin and sparse (Fig. 6-I, 6-II and Fig. 7-I, 7-II). The Hsp60 expression was strongest in the yak testis in primary spermatocyte, followed by that in the secondary spermatocyte. Sperm cells also had expression, contrary to the spermatogonium cells. We were interested in what was showed, as the organism developed, seminiferous tubules became closely packed, lumens became enlarged, and different amounts of sperm cells appeared during the development of sperms, with the largest count occurring during the adult stage. For the elderly yak,
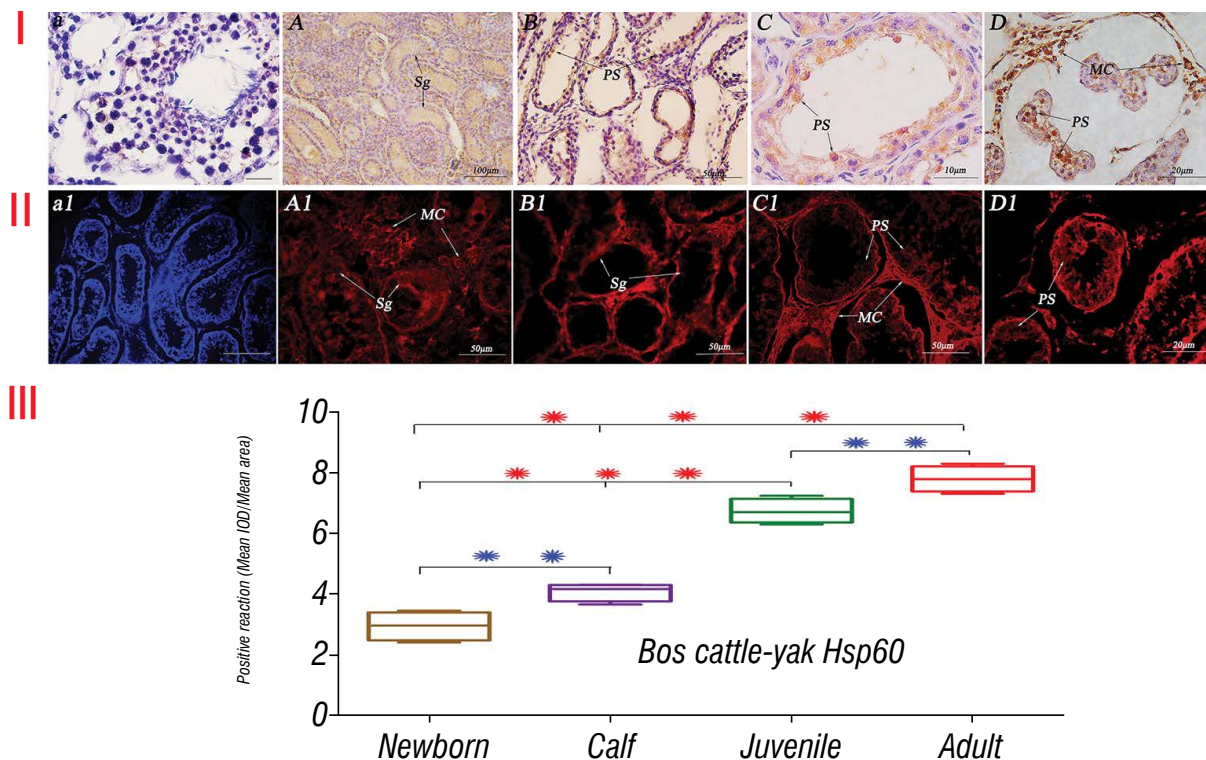
Figure 7. Immunohistochemistry and immunofluorescence localisation of heat shock protein 60 (Hsp60) in the testicular tissue of cattle-yak; **I, II: a, a1.** The control sections collected from the testicular tissue of adult yak, without immunoreactions (negative control); **A, A1.** Positive staining for Hsp60 was observed in the spermatogonium and mesenchymal of the newborn testis; **B, B1.** Positive staining for Hsp60 was observed in spermatogonium and primary spermatocyte of the calf testis; **C, C1.** Positive staining for Hsp60 was observed in the primary spermatocyte and mesenchymal of the juvenile testis; **D, D1.** Positive staining for Hsp60 was observed in the primary spermatocyte and mesenchymal of adult testis; **III.** The result of optical density analysis value. The columnar represent the expression trend of Hsp60 protein in different age of testis tissues. Abbreviated as shown in Figure 6. The asterisk represents the difference in positive expression. The more asterisks, the more significant the difference.

the amount of spermatogenic cells in the seminiferous tubule decreased significantly. As the cattle-yak aged, the number of spermatogenic cell at the different development stages decreased, and few sperm and sperm cells appeared. Hsp60 was highly expressed in all levels of spermatocyte in the cattle-yak testicular tissue, whereas the expression levels in the basement-membrane and myogenic cells were the lowest.

As shown in Figures 6-III and 7-III, protein expression levels of Hsp60 were detected in the testicular tissues at different developmental stages of yak and cattle-yak. In yak, the expression of Hsp60 showed obvious trend from newborn to senior, that expression increased to a higher level in the juveniles and then it tends to decrease, and at the same time, its expression was highest in the senior yaks. In the cattle-yak, the Hsp60 expression increased to highest in the adult. The results showed that the Hsp60 protein expression levels of cattle-yak were significantly higher than those of yak in almost all the developmental stages ($p < 0.01$).

DISCUSSION

For the first time, cDNA clones that encoded Hsp60 from cattle-yak were isolated, sequenced, and characterised. Previous studies have found that protein space structural differences led to functional differences [1]. Using reference sequence, our analytical results showed that three ORFs in Hsp60 illustrated frame-shifting property of the sequence. We also present evidence that the phylogenetic tree to cattle-yak Hsp60 associated with *Bos grunniens*, *Ovis aries* and *Bos taurus* were very high, and that cattle-yak evolution with the above animals had very close genetic relationship. In eukaryotic cells different HSP gene promoters upstream of TATA, heat shock element with size of approximately 20 bp was also necessary in the transcription of specific nucleotide sequence (C-GAA-TTC-G) [15, 29].

The amino acid sequences of the various protein spatial structures differed. Among the HSPs in cattle, Hsp70 was relatively more expressed followed by Hsp60 indicating the action of molecular chaperones to stabilise the native conformation of proteins [18]. Results (Fig. 2) showed cattle-yak amino acids multipoint mutation relative to yak. So, the molecular data show that Hsp60 gene could be used as a single nucleotide polymorphism marker to evaluate the loss of genetic diversity caused by hatchery selection or internal control gene in cattle-yak. Thus, we believed that the amino acid mutation is an important factor for functional differences of Hsp60.

The gene and protein expression of Hsp60 was significant not only in the different species but also in the different tissues of the same species. Interestingly, HSP60 and HSP10 were found to be the second most abundantly expressed HSPs. The relative mRNA abundance of HSF1 significantly increased ($p < 0.001$) in Murrah buffalo compared to Tharparkar and Sahiwal cattle during summer and winter [20]. In addition, the Hsp60 expression was high in under-cold stress and selenium deficient induced oxidative stress in the spleen and it also influenced immune function in chicks [16]. It was hard to believe these data also verified the controversies regarding the appropriate physiological function of different tissues. We found that gene and protein expression of Hsp60 was higher in the kidney, cerebellum, and liver of yak. However, Hsp60 had higher expression in the heart, cerebellum, and liver of cattle-yak. Studies have shown that under low-salinity (17 ppt) stress, RpHSP60 mRNA levels were significantly increased at 3, 72, and 96 h ($p < 0.05$). These results suggest that HSP60 of *R. philippinarum* may play important roles in responding to high-temperature and low salinity stresses [6]. In addition, when hepatic cells were exposed by enrofloxacin, Hsp60 mRNA levels significantly increased in hepatocyte of *Ctenopharyngodon idellus* [5]. So, considering the high expression in the kidney, cerebellum, and heart of yak and cattle-yak, we speculated that Hsp60 could protect cells and tissue from the environmental stimulus.

Previous studies demonstrated that Hsp60 can protect lung tissue from damage caused by bronchitis and cold air, and local response occurring at the level of the alveoli, bronchioles and respiratory bronchiole epithelial cells and smooth muscle cells [40]. Gene expression levels of Hsp27/40/60/70/90 were significant-

ly up-regulated when the treatment cytotoxicity in vitro spleen lymphocytes of chicken [45]. In addition, studies have shown that adenocarcinoma was characterised by the highest levels of Hsp10 and Hsp60 in epithelium and lamina propria [30]. Hsp60/70/90 possess the ability to modulate cellular anti-stress responses and play key roles in protecting organisms from high temperature and low salinity [4, 22]. This study demonstrated the localization of Hsp60 in the cell membrane and cytoplasm, not in the nuclei of organs. It is undeniable that, Hsp60 plays an active function in the tissue physiological adaptation in cattle-yak and yak.

Recent data have indicated that the expression level of Hsp60 has no apparent change during the developmental progress in rabbit testis, but high expression in cynomolgus monkeys The Hsp60 mRNA transcripts detected were highest during the developmental phase (in April), while the lowest levels were found in the resting phase (after spawning in late July) of fish testis [41, 43]. Interestingly, this result is largely consistent with our experimental result that Hsp60 expression level in the testicular tissue of cattle-yak increased gradually with age. Meanwhile, research shows that in situ and northern hybridizations significantly reduced levels of the Hsp60C transcripts in Hsp60C1 homozygous adult males (*Drosophila melanogaster*) [31]. In the human testis, Hsp60 expression in vitro was high than in vivo [21]. Encouragingly, Hsp60 expression in testicular tissue of cattle-yak was generally higher than yak, especially in the juvenile and adult. Thus, as in Figure 3, we speculated that the high expression of Hsp60 in the testicular tissue of male cattle that was activated offspring restore normal fertility of male cattle-yak.

Previous studies indicated that Hsp60 was detected in spermatogonia, premeiotic spermatocytes and germ cells of humans at different ages [28]. In the testis of immature rhesus, Hsp60 immunoreactivity was visible in spermatogonia and in Sertoli cells, whereas interstitial cells were negative [26]. In addition, Hsp60 immunoreactivity was detected in sperm midpiece of dog, cat, stallion and boar [37]. This study found that the Hsp60 detected in primary spermatocyte, secondary spermatocyte and sperm cell of yak and cattle-yak. Similarly, positive reactions have recently been described in Sertoli cells and spermatogonia, where it promotes testis development but may also underlie spermatogenesis [44]. Furthermore, the Hsp60 expression was low in early stages

of spermatogenesis and increased with the increase in age. Thus, high expression of Hsp60 caused the blockage of spermatocyte development. This study showed an important breakthrough in the study of male infertility.

CONCLUSIONS

The following conclusions can be drawn from this study. Changes in amino acids sequences were the main cause for protein functional differences of Hsp60. Hsp60 has an obvious differential expression in different organs and different ages of cattle-yak and yak. In addition, Hsp60 was mainly detected in epithelial of tissue, spermatocyte, sperm cells and mesenchymal cells in the testicles. Hsp60 showed the specific expression in yak and cattle-yak testicular tissue, and it has important correlation with cattle-yak infertility.

Funding

Conflict of interest: None declared

REFERENCES

1. Agarwal G, Garg V, Kudapa H, et al. Genome-wide dissection of AP2/ERF and HSP90 gene families in five legumes and expression profiles in chickpea and pigeonpea. Plant Biotechnol J. 2016; 14(7): 1563–1577, doi: 10.1111/pbi.12520, indexed in Pubmed: 26800652.
2. Bodolay E, Prohászka Z, Paragh G, et al. Increased levels of anti-heat-shock protein 60 (anti-Hsp60) indicate endothelial dysfunction, atherosclerosis and cardiovascular diseases in patients with mixed connective tissue disease. Immunol Res. 2014; 60(1): 50–59, doi: 10.1007/s12026-014-8552-x, indexed in Pubmed: 24838263.
3. Carper SW, Duffy JJ, Gerner EW. Heat shock proteins in thermotolerance and other cellular processes. Cancer Res. 1987; 47(20): 5249–5255, indexed in Pubmed: 3308075.
4. Cui Y, Liu Bo, Xie J, et al. The effect of hyperthermia on cell viability, oxidative damage, and heat shock protein expression in hepatic cells of grass carp (Ctenopharyngodon idellus). J Thermal Biol. 2013; 38(6): 355–361, doi: 10.1016/j.jtherbio.2013.04.007.
5. Cui Y, Liu Bo, Xie J, et al. Effect of enrofloxacin and emodin on heat-shock proteins' expression in hepatic cells of grass carp (Ctenopharyngodon idellus). Aquaculture International. 2013; 22(3): 1067–1077, doi: 10.1007/s10499-013-9727-5.
6. Ding J, Li J, Yang D, et al. Molecular characteristics of a novel HSP60 gene and its differential expression in Manila clams (Ruditapes philippinarum) under thermal and hypotonic stress. Cell Stress Chaperones. 2018; 23(2): 179–187, doi: 10.1007/s12192-017-0796-7, indexed in Pubmed: 29273967.
7. Eggert-Kruse W, Batschulat K, Demirakca T, et al. Male immunity to the chlamydial 60 kDa heat shock protein (HSP 60) - associated with semen quality? Andrologia. 2015; 47(1): 66–76, doi: 10.1111/and.12224, indexed in Pubmed: 24404853.
8. El-Fattah AA, Fahim AT, Sadik NA, et al. Resveratrol and curcumin ameliorate di-(2-ethylhexyl) phthalate induced testicular injury in rats. Gen Comp Endocrinol. 2016; 225: 45–54, doi: 10.1016/j.ygcen.2015.09.006, indexed in Pubmed: 26361869.
9. Fang DA, Zhou YF, Zhang MY, et al. Developmental Expression of HSP60 and HSP10 in the Coilia nasus Testis during Upstream Spawning Migration. Genes (Basel). 2017; 8(7), doi: 10.3390/genes8070189, indexed in Pubmed: 28754007.
10. Gandre S, Bercovich Z, Kahana C. Mitochondrial localization of antizyme is determined by context-dependent alternative utilization of two AUG initiation codons. Mitochondrion. 2003; 2(4): 245–256, doi: 10.1016/s1567-7249(02)00105-8.
11. Gu W, Yang L, Wang S, et al. Generation and application of a novel insp3r1mono-antibody from mouse. J Immun Immunochem. 2014; 36(5): 487–495, doi: 10.1080/15321819.2014.996817.
12. He Y, Yu S, Hu J, et al. Changes in the anatomic and microscopic structure and the expression of HIF-1 and VEGF of the yak heart with aging and hypoxia. PLoS One. 2016; 11(2): e0149947, doi: 10.1371/journal.pone.0149947, indexed in Pubmed: 26914488.
13. Hu R, Wang Z, Peng Q, et al. Effects of GHRP-2 and Cysteamine Administration on Growth Performance, Somatotropic Axis Hormone and Muscle Protein Deposition in Yaks (Bos grunniens) with Growth Retardation. PLoS One. 2016; 11(2): e0149461, doi: 10.1371/journal.pone.0149461, indexed in Pubmed: 26894743.
14. Huang X, Liu B, Huan P. The sperm proteome of the Pacific oyster Crassostrea gigas and immunolocalization of heat shock proteins[J]. Invert Reprod Develop. 2015; 59(3): 111–118.
15. Jenkins TG, Aston KI, Meyer TD, et al. Decreased fecundity and sperm DNA methylation patterns. Fertil Steril. 2016; 105(1): 51–7.e1, doi: 10.1016/j.fertnstert.2015.09.013, indexed in Pubmed: 26453269.
16. Khoso PA, Liu Ci, Liu C, et al. Selenium deficiency activates heat shock protein expression in chicken spleen and thymus. Biol Trace Elem Res. 2016; 173(2): 492–500, doi: 10.1007/s12011-016-0673-8, indexed in Pubmed: 27005933.
17. Kim BY, Son Y, Choi J, et al. 27-Hydroxycholesterol up-regulates the production of heat shock protein 60 of monocytic cells. J Steroid Biochem Mol Biol. 2017; 172: 29–35, doi: 10.1016/j.jsbmb.2017.04.015, indexed in Pubmed: 28549691.
18. Kishore A, Sodhi M, Kumari P, et al. Peripheral blood mononuclear cells: a potential cellular system to understand differential heat shock response across native cattle (Bos indicus), exotic cattle (Bos taurus), and riverine buffaloes (Bubalus bubalis) of India. Cell Stress Chaperones. 2014; 19(5): 613–621, doi: 10.1007/s12192-013-0486-z, indexed in Pubmed: 24363171.
19. Ko YG, Park HG, Yeom GT, et al. Proteomic analysis of cloned porcine conceptuses during the implantation

period. Biotechnol Lett. 2013; 35(12): 2021–2030, doi: 10.1007/s10529-013-1315-2, indexed in Pubmed: 23974496.

20. Kumar A, Ashraf S, Goud TS, et al. Expression profiling of major heat shock protein genes during different seasons in cattle (Bos indicus) and buffalo (Bubalus bubalis) under tropical climatic condition. J Therm Biol. 2015; 51: 55–64, doi: 10.1016/j.jtherbio.2015.03.006, indexed in Pubmed: 25965018.

21. Lachance C, Fortier M, Thimon V, et al. Localization of Hsp60 and Grp78 in the human testis, epididymis and mature spermatozoa. Int J Androl. 2010; 33(1): 33–44, doi: 10.1111/j.1365-2605.2008.00948.x, indexed in Pubmed: 19207617.

22. Liu P, Yu S, Cui Y, et al. Cloning of HSP90, expression and localization of HSP70/90 in different tissues including lactating/non-lactating yak (Bos grunniens) breast tissue. PLoS One. 2017; 12(7): e0179321, doi: 10.1371/journal.pone.0179321, indexed in Pubmed: 28715410.

23. Lu JY, Zi XD. Anatomical structure in testicular of F1 cattle-yak. Animal Husb Vet Med. 2014(12): 61–63.

24. Manjili MH, Henderson R, Wang XY. Development of a recombinant HSP110-HER-2/neu vaccine using the chaperoning properties of HSP110. Cancer Res. 2002; 62: 1737–1742.

25. Mazzoli S, Cai T, Addonisio P, et al. Chlamydia trachomatis infection is related to poor semen quality in young prostatitis patients. Eur Urol. 2010; 57(4): 708–714, doi: 10.1016/j.eururo.2009.05.015, indexed in Pubmed: 19482415.

26. Meinhardt A, Seitz J, Arslan M, et al. Hormonal regulation and germ cell-specific expression of heat shock protein 60 (hsp60) in the testis of macaque monkeys (Macaca mulatta and M. fascicularis). Int J Androl. 1998; 21(5): 301–307, doi: 10.1046/j.1365-2605.1998.00125.x, indexed in Pubmed: 9805247.

27. Naaby-Hansen S, Herr JC. Heat shock proteins on the human sperm surface. J Reprod Immunol. 2010; 84(1): 32–40, doi: 10.1016/j.jri.2009.09.006, indexed in Pubmed: 19962198.

28. Paranko J, Seitz J, Meinhardt A. Developmental expression of heat shock protein 60 (HSP60) in the rat testis and ovary. Differentiation. 1996; 60(3): 159–167, doi: 10.1046/j.1432-0436.1996.6030159.x, indexed in Pubmed: 8766595.

29. Pelham HR, Bienz M. A synthetic heat-shock promoter element confers heat-inducibility on the herpes simplex virus thymidine kinase gene. EMBO J. 1982; 1(11): 1473–1477, indexed in Pubmed: 6327271.

30. Rappa F, Pitruzzella A, Marino Gammazza A, et al. Quantitative patterns of Hsps in tubular adenoma compared with normal and tumor tissues reveal the value of Hsp10 and Hsp60 in early diagnosis of large bowel cancer. Cell Stress Chaperones. 2016; 21(5): 927–933, doi: 10.1007/s12192-016-0721-5, indexed in Pubmed: 27491302.

31. Sarkar S, Lakhotia SC. The Hsp60C gene in the 25F cytogenetic region in Drosophila melanogaster is essential for tracheal development and fertility. J Genet. 2005; 84(3): 265–281, doi: 10.1007/BF02715797, indexed in Pubmed: 16385159.

32. Shao LH, Zheng XW, Yi DX, et al. Comparative sequence and expression analysis of tapetum specific male sterility related genes in Medicago truncatula. Genet Mol Res.

2016; 15(2), doi: 10.4238/gmr.15028323, indexed in Pubmed: 27421020.

33. Shao Y, Zhao H, Wang Yu, et al. Arsenic and/or copper caused inflammatory response via activation of inducible nitric oxide synthase pathway and triggered heat shock protein responses in testis tissues of chicken. Environ Sci Pollut Res Int. 2018; 25(8): 7719–7729, doi: 10.1007/s11356-017-1042-7, indexed in Pubmed: 29288301.

34. Song Y, Zhang R, Wang H, et al. Protective effect of agaricus blazei polysaccharide against cadmium-induced damage on the testis of chicken. Biol Trace Elem Res. 2018; 184(2): 491–500, doi: 10.1007/s12011-017-1196-7, indexed in Pubmed: 29127548.

35. Spinaci M, Volpe S, Bernardini C, et al. Sperm sorting procedure induces a redistribution of Hsp70 but not Hsp60 and Hsp90 in boar spermatozoa. J Androl. 2006; 27(6): 899–907, doi: 10.2164/jandrol.106.001008, indexed in Pubmed: 16870948.

36. Tao SX, Guo J, Zhang XS, et al. Germ cell apoptosis induced by experimental cryptorchidism is mediated by multiple molecular pathways in Cynomolgus Macaque. Front Biosci. 2006; 11: 1077–1089, doi: 10.2741/1864, indexed in Pubmed: 16146798.

37. Volpe S, Galeati G, Bernardini C, et al. Comparative immunolocalization of heat shock proteins (Hsp)-60, -70, -90 in boar, stallion, dog and cat spermatozoa. Reprod Domest Anim. 2008; 43(4): 385–392, doi: 10.1111/j.1439-0531.2007.00918.x, indexed in Pubmed: 18226022.

38. Wang Bo, Zhang L, Cao H, et al. Myoblast transplantation improves cardiac function after myocardial infarction through attenuating inflammatory responses. Oncotarget. 2017; 8(40): 68780–68794, doi: 10.18632/oncotarget.18244, indexed in Pubmed: 28978156.

39. Wiener G, Jianlin H, Ruijun L. The yak. FAO Regional Office for Asia and the Pacific (2003).

40. Wood KL, Nunley DR, Moffatt-Bruce S, et al. The role of heat shock protein 27 in bronchiolitis obliterans syndrome after lung transplantation. J Heart Lung Transplant. 2010; 29(7): 786–791, doi: 10.1016/j.healun.2010.03.004, indexed in Pubmed: 20456980.

41. Wu Y, Pei Y, Qin Y. Developmental expression of heat shock proteins 60, 70, 90, and A2 in rabbit testis. Cell Tissue Res. 2011; 344(2): 355–363, doi: 10.1007/s00441-011-1151-4, indexed in Pubmed: 21538228.

42. Xie W, Lv Ai, Li R, et al. Agaricus blazei murill polysaccharides protect against cadmium-induced oxidative stress and inflammatory damage in chicken spleens. Biol Trace Elem Res. 2018; 184(1): 247–258, doi: 10.1007/s12011-017-1189-6, indexed in Pubmed: 29032405.

43. Zhang XS, Lue YH, Guo SH, et al. Expression of HSP105 and HSP60 during germ cell apoptosis in the heat-treated testes of adult cynomolgus monkeys (macaca fascicularis). Front Biosci. 2005; 10: 3110–3121, doi: 10.2741/1767, indexed in Pubmed: 15970565.

44. Zhao J, Zhang Y, Hao L, et al. Effects of a mild heat treatment on mouse testicular gene expression and sperm quality. Animal Cells Systems. 2010; 14(4): 267–274, doi: 10.1080/19768354.2010.525830.

45. Zhu Y, Lu X, Wu Di, et al. The effect of manganese-induced cytotoxicity on mRNA expressions of HSP27, HSP40, HSP60, HSP70 and HSP90 in chicken spleen lymphocytes in vitro. Biol Trace Elem Res. 2013; 156(1-3): 144–152, doi: 10.1007/s12011-013-9817-2, indexed in Pubmed: 24081778.

V M
VIA MEDICA

ORIGINAL ARTICLE

Concomitant administration of sitagliptin and rutin improves the adverse hepatic alterations in streptozotocin-induced diabetes mellitus in albino rats: an overview of the role of alpha smooth muscle actin

R.A. Attia, S. Abdel Fattah, M.M. Nasralla

Department of Anatomy and Embryology, Faculty of Medicine, Cairo University, Cairo, Egypt

Background: Diabetes mellitus (DM), one of the commonest worldwide metabolic conditions, is believed to be associated with an imbalance between oxidants and antioxidants. Sitagliptin is an oral anti-hyperglycaemic drug that blocks dipeptidyl peptidase 4 (DPP4). Rutin is a polyphenolic natural flavonoid which has antioxidant and anti-proliferative activity. The aim of the present work is to elucidate the concomitant effect of sitagliptin and rutin on the deleterious alterations in the liver of experimentally induced diabetes in rats.

Materials and methods: Fifty adult male albino rats, weighing 170–200 g were used. Rats were randomly divided into five groups (n = 10): group 1 (control group), the other four groups (groups II, III, IV and V) received a single i.p. injection of streptozotocin, 65 mg/kg body weight to induce diabetes; group II (diabetic), group III (diabetic and rutin administered), group IV (diabetic and sitagliptin administered), and group V (diabetic with sitagliptin and rutin concomitantly administered). Haematoxylin and eosin, Masson trichrome, periodic acid Schiff, immune-histochemistry: α-smooth muscle actin (α-SMA), histomorphometric analysis, liver enzymes and oxidants/anti-oxidants; malondialdehyde/glutathione and were done.

Results: Distorted hepatic architecture, dilatation, congestion of sinusoids and central veins as well as cytoplasmic vacuolations were remarkable changes in the diabetic group. There was extravasation of blood, diffuse fibrous tissue formation, increase in the mean values of liver enzymes, oxidative markers and α-SMA expression in the same group. The aforementioned changes were ameliorated in groups III and IV. Concomitant administration of sitagliptin and rutin resulted in marked enhancement of these hepatic alterations.

Conclusions: Combination of sitagliptin and rutin has an ameliorating effect on the hepatic deterioration induced by diabetes, which is better than either sitagliptin or rutin alone. (Folia Morphol 2021; 80, 4: 870–880)

Key words: streptozotocin, liver, diabetes, alpha smooth muscle actin, sitagliptin, rutin

---

Address for correspondence: S. Abdel Fattah, MD, Department of Anatomy and Embryology, Faculty of Medicine, Cairo University, Cairo, Egypt, e-mail: dr_shery.fattah@yahoo.com

INTRODUCTION

Diabetes mellitus (DM) is a metabolic syndrome categorized by elevated blood glucose levels and typical symptoms; polydipsia, polyuria and polyphagia [26]. Abnormal function of chief body organs comprising the liver can be a consequence of the upsurge of blood glucose levels [31]. The pivotal role of reactive oxygen species in the progress and exacerbation of DM has been discussed for several epochs [18, 25]. Lipid peroxidation disturbs all lipid-encompassing structures in cells, resulting in cytopathological consequences [29].

Rutin is a flavonoid compound that exists in various plants and possesses several pharmacological functions: blood glucose reducer, insulin release regulator, and dyslipidaemic modifier. Moreover, it owns anti-inflammatory and anti-tumour properties as well as attenuates the damage caused by reactive oxygen species (ROS) [13, 15, 27, 33].

Many studies have revealed that rutin has a robust therapeutic influence on liver injury triggered by different reasons for instance: biliary obstruction and high fatty diet. Nevertheless, the mechanism of rutin in DM-induced liver injury was not very distinct [24, 34]. Some researchers suggest that the safety of rutin in diabetic liver can be attributed to its anti-inflammatory properties, impeding lipogenesis [16].

Sitagliptin is an antidiabetic prescription drug taken orally that blocks dipeptidyl peptidase 4 (DPP4). Suppression of DPP4 increases insulin sensitivity and hence, lowers blood glucose concentrations [32]. Sitagliptin definitely has been approved by the Food and Drug Administration, Health Canada, as well as the European Commission for the treatment of diabetes. It can be used alone or with either metformin or glitazone [2, 4].

The objective of this study was to elucidate the effects of the combination of sitagliptin and rutin on the pathological alterations in the liver in experimentally induced diabetes in rats.

MATERIALS AND METHODS

Chemicals

Streptozotocin (STZ) (trade name Zanosar) was purchased from Sigma Chemical Company, St. Louis Missouri, USA, in the form of 1 g vials. The drug was dissolved in 0.1 M sodium citrate (pH adjusted to 4.5).

Sitagliptin (in the form of Januvia 100 tablet). Each tablet was ground and dissolved in 10 mL solution of 0.5% carboxymethyl cellulose, and afterwards shaken to obtain a suspension form (10 mg/mL).

Rutin was purchased from Sigma Chemical Company, St. Louis, Missouri, USA, in the form of powder and dissolved in saline.

Experimental animals

Fifty adult male Sprague-Dawley albino rats, weighing 170–200 g were used. They were kept in the animal house of Kasr Al-Aini Faculty of Medicine, Cairo University, Egypt. The rats had free access to standard rat chow and water. They were maintained according to the standard guidelines of the Institutional Animal Care and Use Committee, subsequent to the Institutional Review Board approval. The rats were permitted to accustom for 2 weeks prior to the experiment.

The rats were randomly divided into five groups (n = 10).

Group 1 (control) received an intraperitoneal (i.p.) injection of 0.1 mol/L sodium citrate buffer (pH 4.5).

The other four groups (groups II, III, IV, V) received a single i.p. injection of STZ, 65 mg/kg body weight [10], freshly dissolved in 0.1 M citrate buffer (pH 4.5). Diabetes mellitus was verified by measuring blood glucose levels (after overnight fast) with the use of glucose oxidase reagent strips (Lif3 scan, Milpitas, CA, USA). Rats with blood sugar level > 250 mg/dL were used as the diabetic group. In order to monitor blood glucose levels, blood glucose was tested every week for 4 weeks.

Group II (diabetic): diabetic rats received no treatment during the course of the study.

Group III (diabetic + rutin): diabetic rat received rutin at a dose of 10 mg/kg/day dissolved in saline orally for 4 weeks [34].

Group IV (diabetic + sitagliptin): diabetic rats received oral sitagliptin at a dose of 100 mg/kg/day sitagliptin via gastric gavage for 4 weeks [28].

Group V (diabetic + rutin+ sitagliptin): diabetic group receiving oral sitagliptin at a dose of 100 mg/ /kg/day concomitantly with rutin at a dose of 10 mg/ /kg/day orally via gastric gavage for 4 weeks.

All animals were clinically monitored and weighed on a weekly basis. After 4 weeks a blood sample was withdrawn from the tail vein, using a fine heparinized capillary tube, for the assessment of liver function. Formerly, the rats of each group were sacrificed with an overdose of intraperitoneal phenobarbital sodium (40 mg/kg). The rats were dissected. The liver of each animal was excised and prepared for light microscopic study.

Liver specimens were fixed in 10% formalin dehydrated in ethyl alcohol, cleared in xylol and embedded in paraffin wax. Sections of 5 μm thickness were cut and mounted on glass slides. Other sections were mounted on positive charged slides for immunohistochemistry. These sections were subjected to the following.

Light microscopic study
— Haematoxylin and eosin (H&E) stain to study the changes in histopathological architecture.
— Masson's trichrome stain to demonstrate collagen fibres.

Histochemical study
Periodic acid Schiff (PAS) reaction to demonstrate the glycogen. The paraffin sections were dewaxed, rehydrated and then oxidized in 1% of periodic acid (5 min). Formerly, they were wash away with distilled water, pickled with Schiff's reagent for 15 min, rinsed in tap water for 5–10 min, counterstained in haematoxylin, discerned in 1% acid-alcohol, cleansed in tap water, dehydrated in ascending degrees of alcohol, cleared in xylene, and mounted in Canada balsam. Glycogen and other reactive carbohydrates appeared magenta.

Immunohistochemical staining
Alpha smooth muscle actin (α-SMA) to evaluate the fibrosis processes [5]. The segments from each paraffin block were incubated with primary antibody α-SMA antibody [(ab7817) 1:100]. Next, the sections were incubated with Goat anti-Rabbit IgG H&L (HRP) (ab205718) for 20 min at 37°C. Each phase was tailed by satisfactorily wash with phosphate buffered saline (PBS).

Morphometric study
Using Leica image analysis computer system (software Qwin 500, Switzerland), the following parameters were assessed:
— area percentage of collagen fibres in Masson's trichrome;
— mean optical density of PAS reaction in PAS;
— area percentage of immune reaction of α-SMA.

Stained sections were inspected by magnification ×400 and measured within a field of standard measuring frame. This was completed in 10 non overlapping microscopic fields of each specimen and their mean values were acquired.

Biochemical study
Liver function assay. Retro-orbital blood samples were extracted from each rat for valuation of liver enzymes. Alkaline phosphatase (ALP), aspartate aminotransferase (AST) and alanine aminotransferase (ALT) enzymes levels were assessed using specific kits provided by Bio-diagnostic Company (Bio-diagnostic eka@lycos.com and info@bio-diagnostic.com). These measurements were done in the Biochemistry Department, Faculty of Medicine, Cairo University, Egypt.

Assays of oxidative/antioxidative markers. We measured malondialdehyde (MDA) using a commercial kit (Biodiagnostic, Cairo, Egypt), according to the manufacturer's instructions. Concisely, roughly 10–20 mg liver tissue was homogenised in 1 mL PBS, pH 7.0, utilising a micropestle in a micro tube. At that point, 20% (w/v) trichloroacetic acid was supplemented to the homogenate to precipitate the protein, and centrifuged at 12,000 g for 15 min. Afterwards, 0.8% thiobarbituric acid solution was added to the liver homogenate to precipitate the protein. After boiling for 10 min in a water bath, the absorbance was measured at 405 nm using a spectrophotometer. The concentration of MDA was calculated per milligram protein using a standard curve. The standard curve was prepared as follows. We dissolved 25 μL 1,1,3,3-tetraethoxypropane (TEP) in 100 mL water to attain a 1 mM stock solution. We organized a working standard by hydrolysis of 1 mL TEP stock solution in 50 mL 1% sulfuric acid and incubation for 2 h at room temperature. The resultant MDA 20 nmol/mL standard was diluted with 1% sulfuric acid to yield the final concentrations of 10.5, 2.5, 1.25 and 0.625 nmol/mL to prepare a standard curve for estimating total MDA. Then, 0.250 mL standard were mixed with 25 μL DNPH solution and incubated for 10 min. A 20 μL volume of the reaction mixture was injected directly onto HPLC system.

Glutathione (GSH) the antioxidant stress marker was measured using a commercial kit to detect glutathione (Biodiagnostic, Cairo, Egypt), according to the producer's instructions. The measurement was based on reduction of 5,5-dithiobis-2 nitrobenzoic acid, with reduced glutathione to create yellow compound. The reduced chromogen was directly proportional to GSH levels, and the ultimate reaction product was assayed spectrophotometrically by quantifying its absorbance at 405 nm.
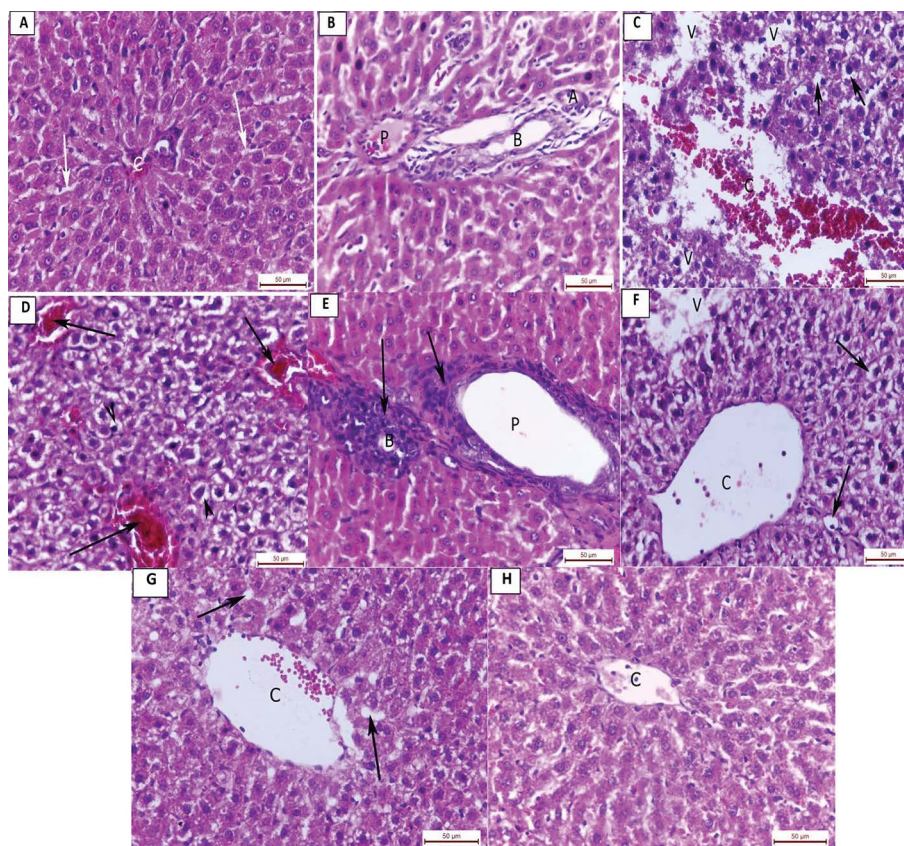
Figure 1. A photomicrograph of sections of liver. A, B (control); **A.** Hepatic lobules and central vein (C); **B.** The portal triad consisting of branch of portal vein (P), bile ductule (B) and branch of hepatic artery (A); C, D, E (diabetic); **C.** Loss of hepatic architecture with marked dilatation of central vein (C), cytoplasmic vacuolations in the hepatocytes (arrows) and vacuoles (V) in between the hepatocyte; **D.** Dilatation of blood sinusoids (arrows) and degeneration of hepatocyte (arrow head); **E.** Marked congestion of portal vein (P) with mononuclear cell infiltration (arrows); **F** (diabetic and rutin-treated): Marked dilatation of central vein (C) and vacuolated areas (V); **G** (diabetic and sitagliptin-treated): Dilatation of central vein with minimal vacuolation (arrows); **H** (diabetic + rutin- + sitagliptin-treated): Minimal dilatations of central vein (H&E ×400).

Statistical analysis

The statistical package for the social science (SPSS) was used for data analysis. The data obtained from image analyser were summarised as means and standard deviations and compared using one-way analysis of variance (ANOVA). P values < 0.05 were considered statistically significant, while p < 0.01 was considered statistically highly significant.

RESULTS

Light microscopic study

Haematoxylin and eosin results. Liver sections obtained from rats of the control group showed classic hepatic lobules consisting of intersecting plates of liver cells (hepatocyte) radiating outwards from a central vein to the periphery of the lobules. Narrow blood sinusoids were seen intervening between cords of hepatocyte (Fig. 1A). The portal area at the periphery of the lobules was seen formed of the bile duc-

tule, a branch of portal vein with thin wall and wide lumen and branch of hepatic artery which appeared narrower in lumen and thicker in wall (Fig. 1B). The diabetic group (group II) revealed distortion of the parenchymal architecture. The hepatocytes exhibited marked pathologic affection where the cytoplasm displayed marked degree of cytoplasmic vacuolations. The central vein was dilated and congested. There was marked congestion of portal vein with mononuclear cell infiltration in the portal area (Fig. 1C–E). The liver in H&E sections in the diabetic and rutin-treated group (group III) revealed dilatation of central vein with vacuolated areas of degenerated hepatocytes (Fig. 1F). The diabetic and sitagliptin-treated group (group IV) exposed dilatation of central vein with small vacuolated areas between the hepatocytes (Fig. 1G). Concomitant administration of rutin and sitagliptin (group V) resulted in an apparently normal hepatic architecture as that of the control group apart from
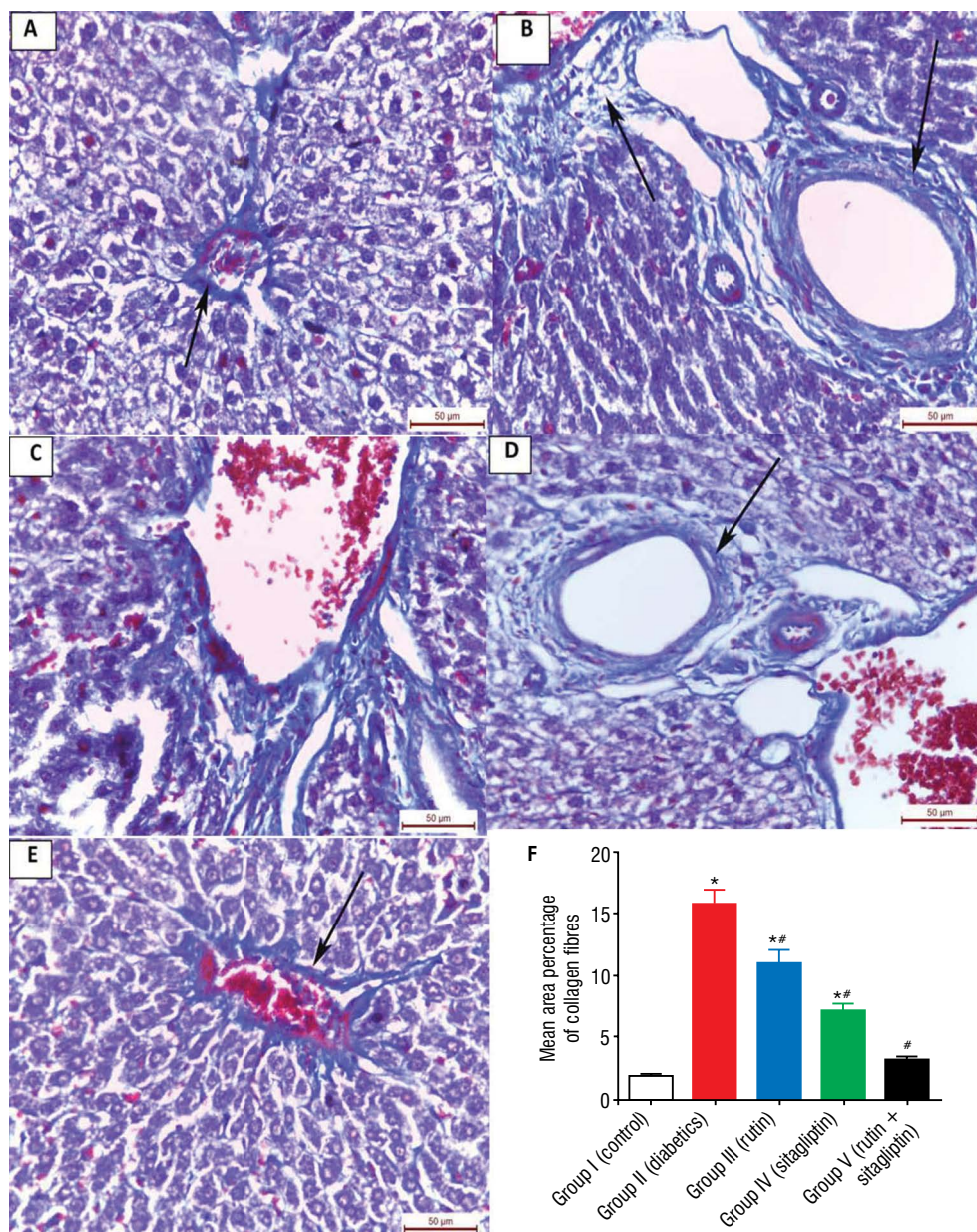
Figure 2. Photomicrographs of sections of liver. **A** (control): Minimal amount of collagen deposition (arrow) around the central vein; **B** (diabetic): Increased collagen fibres deposition (arrows) in the portal area. Note the marked engorged portal vein (P); **C** (diabetic and rutin-treated): Increased collagen fibres deposition (arrows); **D** (diabetic and sitagliptin-treated): Moderate collagen fibres deposition (arrows); **E** (diabetic + rutin- + sitagliptin-treated): Minimal collagen fibres deposition (arrows); **F.** Area percentage of collagen content in liver following administration of rutin and/or sitagliptin to diabetic rats; *Significantly different from control at p < 0.05; #Noticeably different from diabetic p < 0.05 (Masson's trichrome ×400).

mild affections. Most hepatocytes were apparently normal with eosinophilic cytoplasm and rounded nuclei. There was mild dilatation of central vein (Fig. 1H).

Masson's trichrome results. Histological examination of sections of the liver from rats of group I showed minimal amount of collagen fibres in the form of a thin layer of collagen fibres around the central vein and hepatic sinusoids (Fig. 2A). Group II exhibited an increase in the amount of dense collagen fibres around the portal tract and the blood sinusoids (Fig. 2B) and in between hepatocytes (Fig. 2B). Meanwhile, group III and IV displayed moderate increase in the amount of dense collagen fibres around the portal tract and the blood sinusoids (Fig. 2C, D). On the other hand, group V showed mild increase in the amount of collagen fibres around the central vein and in the portal tract (Fig. 2E).
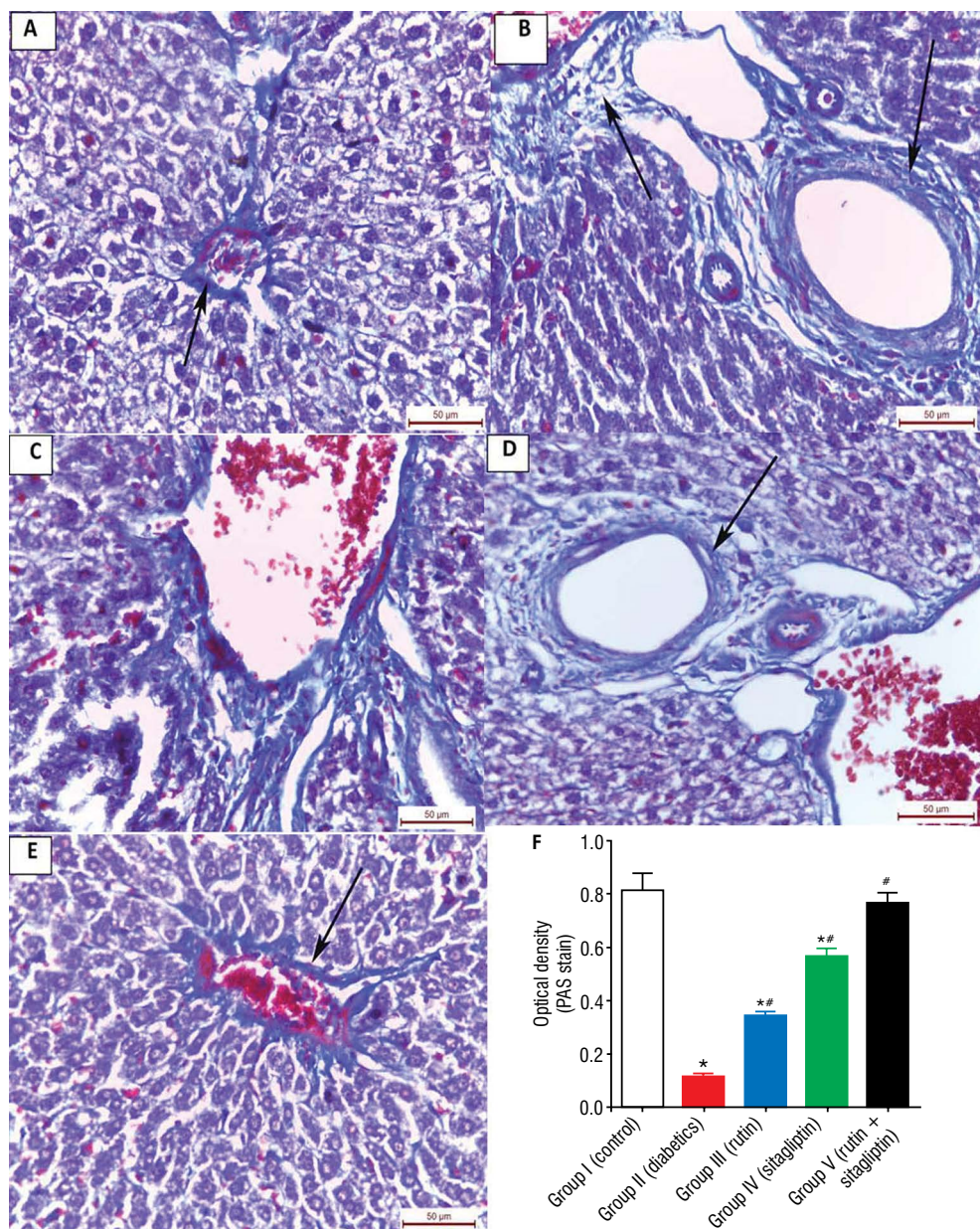
Figure 3. Photomicrographs of sections of liver. **A** (control): Strong positive PAS reaction of the hepatocyte around the central vein (C); **B** (diabetic): Weak positive PAS reaction of the hepatocyte; **C** (diabetic and rutin-treated): Moderate positive PAS reaction of the hepatocyte; **D** (diabetic and sitagliptin-treated): Moderate positive PAS reaction of the hepatocyte; **E** (diabetic + rutin- + sitagliptin-treated): Strong positive PAS reaction of the hepatocyte around the central vein (C); **F.** Optical density in liver following administration of rutin and/or sitagliptin to diabetic rat; *Significantly different from control at $p < 0.05$; #Noticeably different from diabetic $p < 0.05$ (PAS ×400).

Histochemical study

PAS reaction results. In the control group the hepatocytic cytoplasm contained considerable amounts of glycogen and displayed strong positive PAS reaction in the form of small red granules filling the cytoplasm (Fig. 3A), while group III exposed very faint weak positive PAS reaction (Fig. 3B). Group IV displayed weak positive and group IV showed moderate positive PAS reaction (Fig. 3D). However, group V revealed strong positive PAS reaction in the cytoplasm of hepatocyte (Fig. 3E).

Immune-histochemical results

Examination of the liver sections of group I revealed negative immunoreactivity of α-SMA in the hepatocyte. There was localised immunoreactivity around the central vein (Fig. 4A). Group II and III showed strong positive immune-reactivity
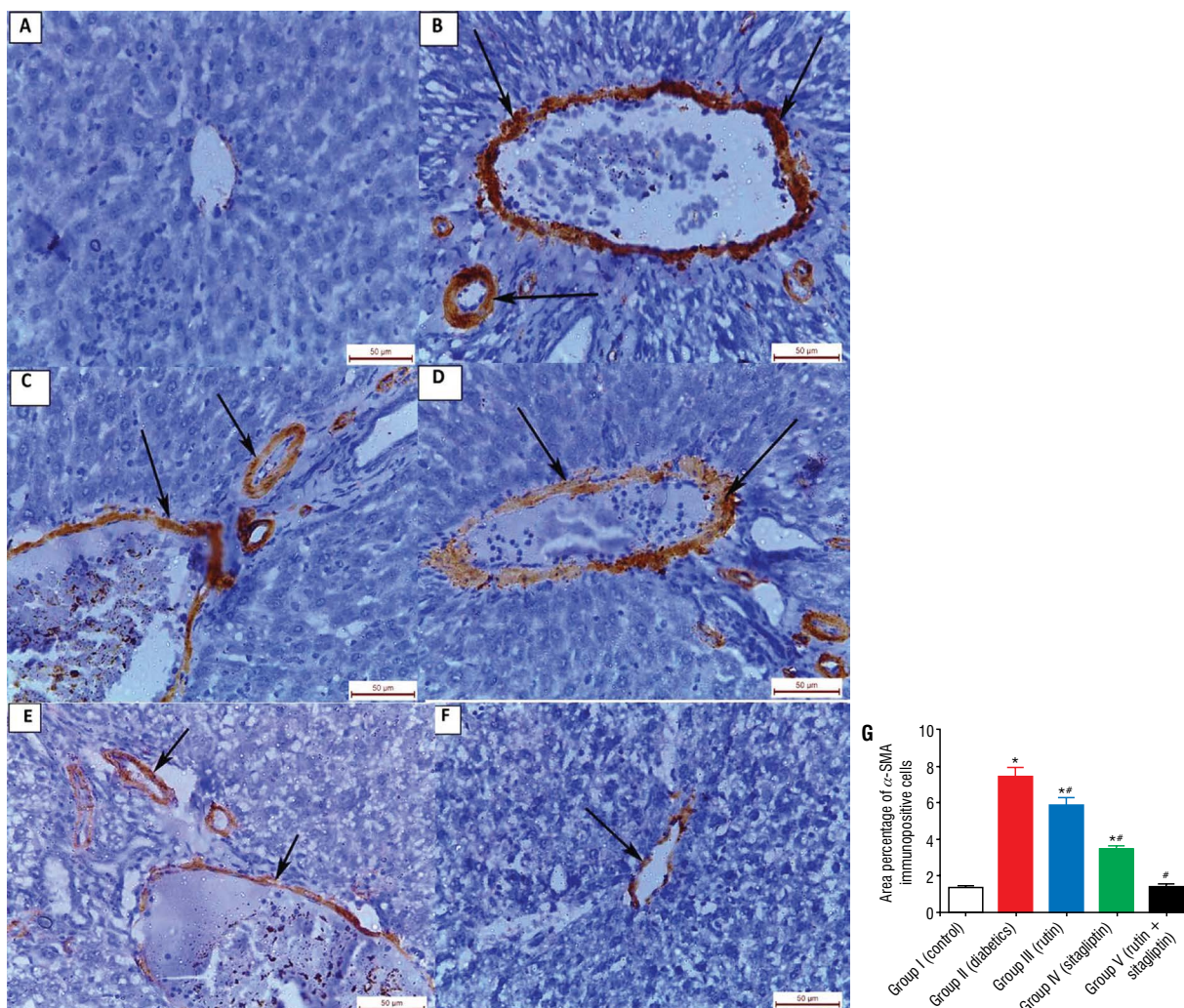
Figure 4. Photomicrographs of sections of liver. **A** (control): Localised positive immune-reactivity around central vein (arrows) and negative immune-reactivity in other parts; **B, C** (diabetic): Strong positive immune-reactivity; **D** (diabetic and rutin-treated group): Positive immune-reactivity; **E** (diabetic and sitagliptin-treated): Moderate positive immunoreactivity; **F** (diabetic + rutin- + sitagliptin-treated): Weak positive immunoreactivity (arrows); **G.** Area percentage of alpha smooth muscle actin (α-SMA) in liver following administration of rutin and/or sitagliptin to diabetic rats; *Significantly different from control at $p < 0.05$; #Noticeably different from diabetic $p < 0.05$ (α-SMA $\times 400$).

(Fig. 4B, C). Group IV exposed moderate positive PAS reaction and moderate positive immunoreactivity (Fig. 4D). Nevertheless, group V showed minimal positive immune-reactivity (Fig. 4E).

Morphometric results

Statistical study of the mean area percentage of collagen fibres. The mean area percentage of the collagen fibres of group II, III and IV showed highly significant increase in its value compared with the corresponding control group. However, the mean value of the above mentioned parameter of group V was non-significant compared with the corresponding control group. The mean value of the area percentage of

the collagen fibres of group II, III and IV increased significantly in comparison with group V (Table 1, Fig. 2F).

Statistical study of the mean optical density of PAS reaction. A significant increase in the optical density was found in group II and III in comparison with the corresponding control group. On the other hand, a significant decrease in the optical density was found in group IV and V in comparison with the group II (Table 1, Fig. 3F).

Statistical study of the area percentage of immune reaction of α-SMA. The mean area percentage of α-SMA immune-positive cells showed no significant difference among the control group and group V. While diabetic group (group II) resulted in significant

Table 1. Area percentage of collagen fibres, optical density and area percentage of alpha smooth muscle actin (α-SMA) immune-reaction in different experimental groups

Groups	Area % of collagen fibres	Optical density	Area % of α-SMA
Group I (control)	1.89 ± 0.16	0.812 ± 0.065	1.36 ± 0.12
Group II (diabetics)	15.74[a] ± 1.17	0.113[a] ± 0.011	7.45[a] ± 0.47
Group III (rutin)	10.99[a, b] ± 1.06	0.339[a, b] ± 0.016	5.86[a, b] ± 0.43
Group IV (sitagliptin)	7.19[a, b] ± 0.49	0.565[a, b] ± 0.031	3.44[a, b] ± 0.21
Group V (rutin + sitagliptin)	3.19[b] ± 0.21	0.765[b] ± 0.041	1.44[b] ± 0.11

Data is shown as mean ± standard error of the mean, n = 10. Multiple comparisons were made using ANOVA one-way test followed by Tukey-Kramer as a post-hoc test. [a]Certainly different from control $p < 0.05$; [b]Significantly different from diabetic $p < 0.05$

Table 2. Mean values of liver enzymes in different experimental groups

Groups	AST [IU/L]	ALT [IU/L]	ALP [IU/L]
Group I (control)	89.24 ± 4.1	36.18 ± 2.3	71.22 ± 6.2
Group II (diabetics)	152.16[a] ± 8.2	74.14[a] ± 3.4	162.32[a] ± 8.4
Group III (rutin)	125.99[a,b] ± 1.06	59.39[a,b] ± 0.016	115.86[a,b] ± 0.43
Group IV (sitagliptin)	112.15[a,b] ± 0.49	51.55[a,b] ± 0.031	89.44[a,b] ± 0.21
Group V (rutin + sitagliptin)	94.12[b] ± 4.1	40.18[b] ± 2.6	78.28[b] ± 9.2

Data is shown as mean ± standard deviation, n = 10. Multiple comparisons were made using ANOVA one-way test followed by Tukey-Kramer as a post-hoc test. [a]Certainly different from control $p < 0.05$; [b]Significantly different from diabetic $p < 0.05$; AST — aspartate aminotransferase; ALT — alanine aminotransferase; ALP — alkaline phosphatase

increase) in the mean area percentage of the α-SMA immunoreactivity as compared with groups I and V (Table 1, Fig. 4G).

Biochemical assay

Liver enzymes

Biochemical assay of the liver enzymes of the diabetic group revealed a marked increase in AST mean value which was statistically significant compared with the mean values of group I and groups IV and V. Meanwhile, treatment with sitagliptin and rutin in group V displayed a decrement in AST mean value which was statistically non-significant compared with the corresponding values in the control group.

Group II (diabetic group) showed marked increases in ALT mean value, which was statistically significant compared with the mean values of the control group and sitagliptin- and rutin-treated groups. Meanwhile, treatment with sitagliptin and rutin in group V showed reduction in ALT mean value which was insignificant in relation with the control group.

The diabetic group showed a marked increase in ALP mean value which was statistically significant compared with the mean value of the control, and

sitagliptin- and rutin-treated groups. On the other hand, treatment with sitagliptin and rutin in group III showed a reduction in ALP mean value which was statistically significant compared with diabetic group and non-significant compared with the value in the control group (Table 2).

Assay of oxidant and antioxidant markers

Malondialdehyde. The liver homogenates of diabetic group demonstrated a marked upsurge in MDA mean value which was statistically significant compared with the mean value of the control group. Meanwhile, treatment with sitagliptin and rutin showed a reduction in MDA mean value compared with the same values in group II, and was statistically non-significant compared with the values in the control group (Table 3).

Glutathione. The liver homogenates of group II demonstrated a marked decrease in GSH mean value which was statistically significant compared with the mean value of the control group. On the other hand, treatment with sitagliptin and rutin demonstrated an increase in the mean value, which was statistically non-significant compared with the value of the control group (Table 3).

Table 3. Mean values of oxidative/antioxidative markers in different experimental groups

Groups	Malondialdehyde [nmol/g protein]	Glutathione [μmol/g protein]
Group I (control)	18.62 ± 2.4	0.28 ± 0.02
Group II (diabetics)	42.18[a] ± 3.6	0.12[a] ± 0.02
Group III (rutin)	30.99[a,b] ± 1.06	0.19[a,b] ± 0.016
Group IV (sitagliptin)	26.14[a,b] ± 0.49	0.20[a,b] ± 0.031
Group V (rutin + sitagliptin)	20.16[b] ± 1.8	0.22[b] ± 0.01

Data is shown as mean ± standard deviation, n = 10. Multiple comparisons were made using ANOVA one-way test followed by Tukey-Kramer as a post-hoc test. [a]Certainly different from control $p < 0.05$; [b]Significantly different from diabetic $p < 0.05$

DISCUSSION

In the present study, manifestations of the pathological effects of diabetes on the liver were observed. These histopathological effects include distorted hepatic architecture, dilatation and congestion of central veins, and hepatocytic degeneration in the form of cytoplasmic vacuolation. These alterations in the liver were attributed to cellular necrosis and inflammation, which might be a result of amplified mitochondrial oxidative stress. The later stress could be a consequence of triglyceride metabolism and the establishment of free radicals in peroxisomes [17, 22]. The cytoplasmic vacuolation of hepatocytes is due to deprivation of the ATP energy stocks, which is a prerequisite for sustaining ionic and fluid homeostasis [30]. The aforementioned mechanism results in reduced activity of the energy-dependent sodium pump plasma membrane. The failure of this active transportation system grounds sodium to cross the threshold and accumulate within the cells and potassium to blowout followed by gain of water, triggering cellular swelling [23]. In addition, high deliberations release of ROS caused by suppressed oxidative phosphorylation predictably contribute to depletion of ATP [28].

Histomorphometric studies exhibited diminished PAS reaction (glycogen content) in the hepatocytes of the STZ-treated animals. Glycogen dislodgment in the cytoplasm of the hepatocytes might be due to the accumulation of lipid droplets [6].

In the present study, fibrosis is an obvious manifestation in the diabetic group in the form of increased collagen fibres around central vein and portal area and increased expression of α-SMA. Beta-oxidation of fatty might occur due to inadequate insulin, and this leads to accumulation of hydrogen peroxide in

tissues [8, 12, 21]. The existence of collagen in the presinusoidal spaces may impede blood supply to liver cells and reduce metabolic exchange, probably leading to hepatocellular dysfunction and necrosis [11]. The deposition of collagen in the liver can be accredited to hepatic stellate cells (HSCs) that are involved in pathogenesis by liver damage-dependent activation. Activated HSCs differentiate into myofibroblasts [7]. Myofibroblasts blasts exhibit a synthesis profile that lead to increase in their deposition in the extracellular matrix. This process helps them to proliferate, alters their morphology, and increases contractility by activating fibre formation of smooth muscle actin. Then, this contributes to the constriction of sinusoidal blood flow and increases collagen fibres synthesis and release.

In the existing research, tests for liver function were conducted to observe the effects of STZ-induced diabetes on the liver at 4 weeks after STZ treatment. Compared with control rats, levels of AST, ALT, and ALP were increased in diabetic rats. AST and ALT are both enzymes that are established principally in liver mitochondria [32]. If there is liver impairment the enzymes are released into the bloodstream after death of the liver cells [14]. Peculiarly, high levels of AST and ALT are pivotal indicators of hepatic injury [29].

The present work revealed increment in MDA and decreased GSH in liver homogenates of diabetic rats. Recent studies have shown that the cause of DM advance and its complications is lipid peroxidase which leads to ROS formation [19]. An increase in ROS generation and a decrease in antioxidant system activity result in an imbalance that leads to oxidative hassle [20]. The high blood glucose levels in diabetes lead to oxidative stress and diminish the capacity of endogenous antioxidants. This is due to the production of many reducing sugars over both the glycolytic and polyol pathways [20].

In experimentally induced diabetic rats treated with oral intake of rutin (group III) or sitagliptin (group IV), microscopic examination of the liver disclosed variable microscopic changes in the form of dilated congested central veins and cellular infiltrations at the region of portal tract and some vacuolated areas. The allocations of collagenous fibres were slightly decreased compared with the control group.

In the current study co-administration of sitagliptin and rutin in group V significantly improved the histological picture of the liver and the severity of

liver damage was lower as compared with the group treated with either sitagliptin or rutin alone.

Sitagliptin is an oral anti-diabetes drug known as an inhibitor of DPP4 used to treat type II DM [3]. DPP4 inhibition was proposed to reduce hepatic lipogenesis by several mechanisms: down-regulating the gene expression of sterol regulatory factor binding protein-1c (SREBP-1c), constraining fatty acid synthase, lowering the serum levels of very low density lipoprotein and low density lipoprotein cholesterol, subsequently decreasing hepatic lipid accumulation and steatosis [24]. In addition, DPP4 inhibition enhanced glycaemic regulation; moreover, it modifies cholesterol synthesis, lipoproteins [9] and liver function enzymes (ALT, AST, ALP). Hence, all the previous mechanisms lead to amelioration of hepatic histopathological features in clinical trials of patients with type 2 diabetes [33].

Previous studies have shown that rutin has a significant outcome on blood glucose control, and also has a very significant effect on the safety of liver cells [1, 6, 7]. DM-related hepatic cellular damage is strictly interrelated to free-radical burden; therefore, rutin's antioxidant activity can shield the liver cells [15, 34].

CONCLUSION AND RECOMMENDATIONS

Concomitant administration of sitagliptin and rutin has an outstanding ameliorating role on diabetes-induced hepatic histopathological and biochemical alterations. This is better than either rutin or sitagliptin alone. Therefore, the use of both sitagliptin and rutin give outstanding results in liver protection against diabetic changes. It is recommended to use rutin on higher doses to test its effect on diabetes-induced and other hepatic injuries.

Conflict of interest: None declared

REFERENCES

1. Ahmed OM, Moneim AA, Yazid IA, et al. Antihyperglycemic, antihyperlipidemic and antioxidant effects and the probable mechanisms of action of Ruta graveolens infusion and rutin in nicotinamide-streptozotocin-induced diabetic rats. Diabetol Croat. 2010; 39(1): 15–35.
2. Ahrén B. Clinical results of treating type 2 diabetic patients with sitagliptin, vildagliptin or saxagliptin: diabetes control and potential adverse events. Best Pract Res Clin Endocrinol Metab. 2009; 23(4): 487–498, doi: 10.1016/j.beem.2009.03.003, indexed in Pubmed: 19748066.
3. Amori RE, Lau J, Pittas AG. Efficacy and safety of incretin therapy in type 2 diabetes: systematic review and meta-analysis. JAMA. 2007; 298(2): 194–206, doi: 10.1001/jama.298.2.194, indexed in Pubmed: 17622601.
4. Aschner P, Kipnes MS, Lunceford JK, et al. Sitagliptin Study 021 Group. Effect of the dipeptidyl peptidase-4 inhibitor sitagliptin as monotherapy on glycemic control in patients with type 2 diabetes. Diabetes Care. 2006; 29(12): 2632–2637, doi: 10.2337/dc06-0703, indexed in Pubmed: 17130196.
5. Bancroft JD, Gamble M. Theory and Practice of Histological Techniques. 7th ed. Staining methods. Churchill Livingstone,, Edinburgh, London, Madrid, Melbourne, New York and Tokyo 2008.
6. Bertolani C, Marra F. The role of adipokines in liver fibrosis. Pathophysiology. 2008; 15(2): 91–101, doi: 10.1016/j.pathophys.2008.05.001, indexed in Pubmed: 18602801.
7. Geerts A. History, heterogeneity, developmental biology, and functions of quiescent hepatic stellate cells. Semin Liver Dis. 2001; 21(3): 311–335, doi: 10.1055/s-2001-17550, indexed in Pubmed: 11586463.
8. Giacco F, Brownlee M. Oxidative stress and diabetic complications. Circ Res. 2010; 107(9): 1058–1070, doi: 10.1161/CIRCRESAHA.110.223545, indexed in Pubmed: 21030723.
9. Giampietro O, Giampietro C, Bartola LD, et al. Sitagliptin as add-on therapy in insulin deficiency: biomarkers of therapeutic efficacy respond differently in type 1 and type 2 diabetes. Drug Des Devel Ther. 2013; 7: 99–104, doi: 10.2147/DDDT.S38346, indexed in Pubmed: 23439744.
10. Haidara MA, Ibrahim MI, Sit EI, et al. Effect of a-tocopherol on glucose uptake and contractility in rat skeletal muscles. Med Sci Monv. 2003; 9(5): 214–217.
11. Horn T, Junge J, Christoffersen P. Early alcoholic liver injury: changes of the Disse space in acinar zone 3. Liver. 1985; 5(6): 301–310, doi: 10.1111/j.1600-0676.1985.tb00253.x, indexed in Pubmed: 4088004.
12. Hramiak IM, Finegoodk DT, Adams PC. Factors affecting glucose tolerance in hereditary hemochromatosis. Clin Invest Med. 1997; 20: 110–118.
13. Hsu CY, Shih HY, Chia YC, et al. Rutin potentiates insulin receptor kinase to enhance insulin-dependent glucose transporter 4 translocation. Mol Nutr Food Res. 2014; 58(6): 1168–1176, doi: 10.1002/mnfr.201300691, indexed in Pubmed: 24668568.
14. Jeschke MG. The hepatic response to thermal injury: is the liver important for postburn outcomes? Mol Med. 2009; 15(9-10): 337–351, doi: 10.2119/molmed.2009.00005, indexed in Pubmed: 19603107.
15. Júnior II, Barbosa Hd, Carvalho DCR, et al. Brazilian attenuated hyperglycemia, dyslipidemia, and prooxidant status in alloxan-induced diabetic rats. Scientific World J. 2017; 2017: 5275813, doi: 10.1155/2017/5275813, indexed in Pubmed: 28567440.
16. Liu Q, Pan R, Ding L, et al. Rutin exhibits hepatoprotective effects in a mouse model of non-alcoholic fatty liver disease by reducing hepatic lipid levels and mitigating lipid-induced oxidative injuries. Int Immunopharmacol. 2017; 49: 132–141, doi: 10.1016/j.intimp.2017.05.026, indexed in Pubmed: 28577437.
17. Manaras K, Jongdee N, Uraporn V, et al. Effect of glabridin on collagen deposition in liver and amelioration of hepatocyte destruction in diabetes rats. Exp Ther Med. 2019; 18(2): 1164–1174, doi: 10.3892/etm.2019.7664, indexed in Pubmed: 31316610.

18. Maritim AC, Sanders RA, Watkins JB. Diabetes, oxidative stress, and antioxidants: a review. J Biochem Mol Toxicol. 2003; 17(1): 24–38, doi: 10.1002/jbt.10058, indexed in Pubmed: 12616644.

19. Masarone M, Rosato V, Dallio M, et al. Role of oxidative stress in pathophysiology of nonalcoholic fatty liver disease. Oxid Med Cell Longev. 2018; 2018: 9547613, doi: 10.1155/2018/9547613, indexed in Pubmed: 29991976.

20. Meng XM, Chung ACK, Lan HY. Role of the TGF-β/BMP-7/ Smad pathways in renal diseases. Clin Sci (Lond). 2013; 124(4): 243–254, doi: 10.1042/CS20120252, indexed in Pubmed: 23126427.

21. Moustafa Hassan I, El-Gharabawy G, Moustafa AG. The effect of Sitagliptin (Januvia) on the liver of adult Albino rats in cases of experimental diabetes mellitus(Microscopic and laboratory studies). Egyptian J Hosp Med. 2012; 47(1): 260–278, doi: 10.21608/ejhm.2012.16296.

22. Nakashima O, Kurogi M, Yamaguchi R, et al. Unique hypervascular nodules in alcoholic liver cirrhosis: identical to focal nodular hyperplasia-like nodules? J Hepatol. 2004; 41(6): 992–998, doi: 10.1016/j.jhep.2004.08.014, indexed in Pubmed: 15582133.

23. Newmeyer DD, Ferguson-Miller S. Mitochondria: releasing power for life and unleashing the machineries of death. Cell. 2003; 112(4): 481–490, doi: 10.1016/s0092-8674(03)00116-8, indexed in Pubmed: 12600312.

24. Pan PH, Lin SY, Wang YY, et al. Protective effects of rutin on liver injury induced by biliary obstruction in rats. Free Radic Biol Med. 2014; 73: 106–116, doi: 10.1016/j.freeradbiomed.2014.05.001, indexed in Pubmed: 24815012.

25. Rahimi R, Nikfar S, Larijani B, et al. A review on the role of antioxidants in the management of diabetes and its complications. Biomed Pharmacother. 2005; 59(7): 365–373, doi: 10.1016/j.biopha.2005.07.002, indexed in Pubmed: 16081237.

26. Rother KI. Diabetes treatment — bridging the divide. N Engl J Med. 2007; 356(15): 1499–1501, doi: 10.1056/NEJMp078030, indexed in Pubmed: 17429082.

27. Soares JM, Pereira Leal AE, Silva JC, et al. Influence of flavonoids on mechanism of modulation of insulin secretion. Pharmacogn Mag. 2017; 13(52): 639–646, doi: 10.4103/pm.pm_87_17, indexed in Pubmed: 29200726.

28. Tian S, Bilin Xu, Taolei C, et al. Sitagliptin reduces insulin resistance and improves rat liver steatosis via the SIRT1/ /AMPKα pathway. Exp Ther Med. 2018; 16(4): 3121–3128, doi: 10.3892/etm.2018.6554, indexed in Pubmed: 30214535.

29. Uchida K. Future of toxicology: lipid peroxidation in the future: from biomarker to etiology. Chem Res Toxicol. 2007; 20(1): 3–5, doi: 10.1021/tx600304n, indexed in Pubmed: 17226920.

30. Vanlangenakker N, Vanden Berghe T, Krysko DV, et al. Molecular mechanisms and pathophysiology of necrotic cell death. Curr Mol Med. 2008; 8(3): 207–220, doi: 10.2174/156652408784221306, indexed in Pubmed: 18473820.

31. Wada J, Makino H. Inflammation and the pathogenesis of diabetic nephropathy. Clin Sci (Lond). 2013; 124(3): 139–152, doi: 10.1042/CS20120198, indexed in Pubmed: 23075333.

32. Yilmaz Y, Senates E, Yesil A, et al. Not only type 2 diabetes but also prediabetes is associated with portal inflammation and fibrosis in patients with non-alcoholic fatty liver disease. J Diabetes Complications. 2014; 28(3): 328–331, doi: 10.1016/j.jdiacomp.2014.01.013, indexed in Pubmed: 24602757.

33. Yoo H, Ku SK, Baek YD, et al. Anti-inflammatory effects of rutin on HMGB1-induced inflammatory responses in vitro and in vivo. Inflamm Res. 2014; 63(3): 197–206, doi: 10.1007/s00011-013-0689-x, indexed in Pubmed: 24292859.

34. Zargar S, Wani TA, Alamro AA, et al. Amelioration of thioacetamide-induced liver toxicity in Wistar rats by rutin. Int J Immunopathol Pharmacol. 2017; 30(3): 207–214, doi: 10.1177/0394632017714175, indexed in Pubmed: 28590141.

The morphology of the afferent and efferent domain of the sheep glomerulus

K. Aycan[iD], T. Ulcay[iD], B. Kamaşak[iD]

Department of Anatomy, Faculty of Medicine, Kırşehir Ahi Evran University, Kırşehir, Turkey

Background: It is important to know the morphology of the glomerulus in order to explain kidney infiltration. The present study aims to research the morphology of afferent and efferent domains of sheep kidney glomeruli.

Materials and methods: In this study, 2000 glomeruli from 20 kidneys of Akkaraman sheep were examined using the polyester resin method.

Results: It was found that the glomeruli of sheep kidney usually had an afferent arteriole as well as an efferent arteriole. Besides, it was also found that five glomeruli had two efferent arterioles. It is known that the afferent domain constitutes the largest part of the glomerulus. In two of the glomeruli that we examined, the afferent domain formed the 1/2 of the glomeruli wherein the other two glomeruli afferent domain formed the 3/4.

Conclusions: It is known that there are many anastomoses between the afferent and efferent domain of capillaries. However, it is not well-explained how anastomosis is created between the afferent and efferent domains. In our study, it was identified that those anastomoses were not inside the lobes but between the surrounding capillaries. (Folia Morphol 2021; 80, 4: 881–887)

Key words: morphology, sheep glomerulus, afferent arteriole, efferent arteriole

INTRODUCTION

Kidney is a significant organ which controls homeostasis, water volume and electrolytes in blood, and blood pressure. The foremost function of the kidney is urine filtration. Histologically, the kidney is formed of peripherally situated cortex and a centrally located medulla. The cortex is very rich in nephrons that are considered the main functional unit consisting of the renal corpuscle and renal tubules. On histological specimens, the renal corpuscle looks like a small rounded structure that has a centrally located glomerulus surrounded peripherally by Bowman's capsule. The glomerulus is a collection of capillaries lined and united by a delicate mesangial matrix, while the Bowman's capsule consists of two epithelium layers: visceral (envelops glomerulus) and parietal [12].

It is essential to know the morphology of the glomerulus in order to explain kidney infiltration. In 1666, Malpighi first described the glomeruli and demonstrated their continuity with the renal vasculature [see 20]. About 175 years later, Bowman elucidated in detail the capillary architecture of glomerulus and the continuity between its surrounding capsule and the proximal tubule [3, see 20]. The renal corpucle consist of a tuft of interconnected capillaries and an enclosing capsule named after Bowman. The term "glomerulus" is commonly used refer to glomerular capillary tuft and Bowman's capsule, although the

term "renal corpucle" is more accurate in a strick ball of capillaries. Providing structural support for the capillary tuft is a central region termed the mesangium, which contains cells and their surrounding matrix material. The capillaries are a thin layer of endotelial cells, contain a basement membran, and are covered by epitelial cells that form the visceral layer of Bowman's capsule. The parietal epithelium is continous with the visceral epithelium at the vascular pole where the afferent arteriole enters the glomerulus and the efferent arteriol exits [13, 20].

The human glomerulus average diameter is 200 μm; juxtaglomedullary glomeruli are 20–50% greater than superficial glomeruli in mammals [13, 20].

Afferent arteriole capillaries entering the Bowman's capsule form the afferent domain via heading towards the urinary pole. These capillaries bend into the urinary pole in a U shape to form an efferent domain. Capillaries of efferent domain merge and form efferent arteriole. Efferent arteriole leaves the glomerulus at the blood vascular pole [10, 23].

The glomerular tuft, originating from afferent arteriole that enters at the vascular pole, separates into lobules. Each lobule has an afferent and efferent domain. The afferent domain of lobules constitutes most of the glomerular tuft. In human and some animals, the glomerular tuft is split into three to eight lobules [11, 20, 23].

The efferent domain is located in the middle of the afferent domain [5, 23]. Glomeruli have an afferent domain and efferent arteriole. In some animals, glomeruli have two afferent or four efferent arterioles [5, 10, 14, 15].

The diameter of the efferent arteriole is smaller than the diameter of the afferent arteriole [5, 7, 10, 16].

There are a few studies investigating sheep kidney glomerulus. These studies did not show the morphology of sheep glomerulus clearly [1, 4, 16]. It is known that there are anastomoses between the capillaries of the afferent and efferent domains. However, it has not been explained how these anastomoses are formed [6, 10, 11, 17]. The present study aims to research the morphology of afferent and efferent domains of sheep kidney glomeruli.

MATERIALS AND METHODS

Twenty sheep kidneys from 10 Akkaraman sheep (12–20 months old and 35–45 kg) were used in this study. Ten mililitres physiological saline containing 2% heparin was injected into the renal arteries after
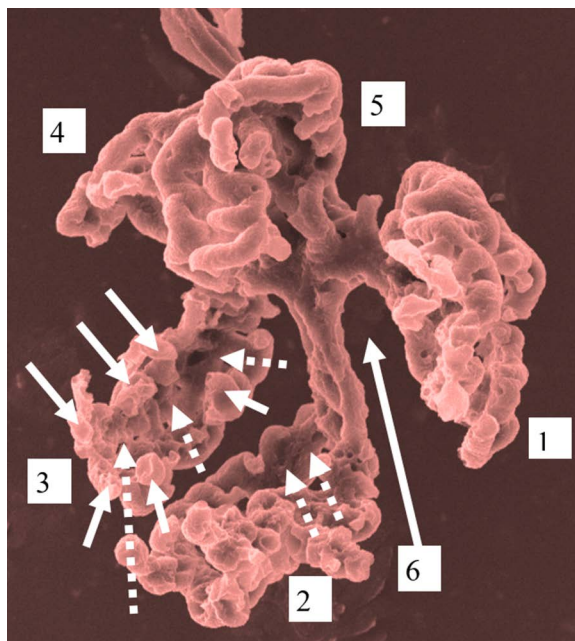
Figure 1. Afferent domain of the sheep. Lobe of the glomerulus (1–5), capillary anastomoses between afferent and efferent domain (white arrow), no capillary anastomoses on the internal surface of the glomerular lobe (dotted arrow), and exit pole of the efferent arteriole (6). Magnification ×423.

cleaning the tissues surrounding the kidney. In order to show the glomeruli, 15 mL of the polyester resin solution was injected into renal arteries with a 120--mmHg pressure. Twenty-four hours passed for the solidification of the polyester solution. The kidneys were put into a 37% HCL solution for 24 hours. Kidney tissues that were dissolved were washed under tap water and air-dried. With the use of a stereomicroscope, glomeruli with afferent and efferent domains were dissected with a forceps from the blood vessels of the kidneys (2000 glomeruli were analysed on average) [2, 16, 22]. Isolated glomeruli were placed on metal plates, and then they were covered with gold in a vacuum evaporator (Polaron 7650 Mini Sputter Coater). They were studied with a scanning electron microscope (LEO 440).

RESULTS

In this study, the afferent and efferent domains of sheep glomeruli were investigated using the polyester resin method. The morphology of sheep kidney glomeruli was shown well with this method.

All of the sheep glomeruli studied had an afferent and efferent arteriole (Figs. 1–7). Glomeruli of sheep kidneys usually had five lobules (Figs. 1, 7).
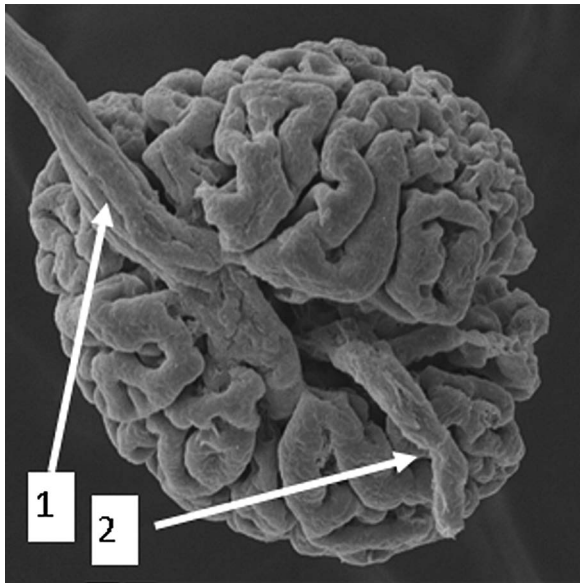
Figure 2. Glomerulus of the sheep. Afferent arteriole (1), efferent arteriole (2). External view shows gyri of the cerebrum. Magnification ×515.
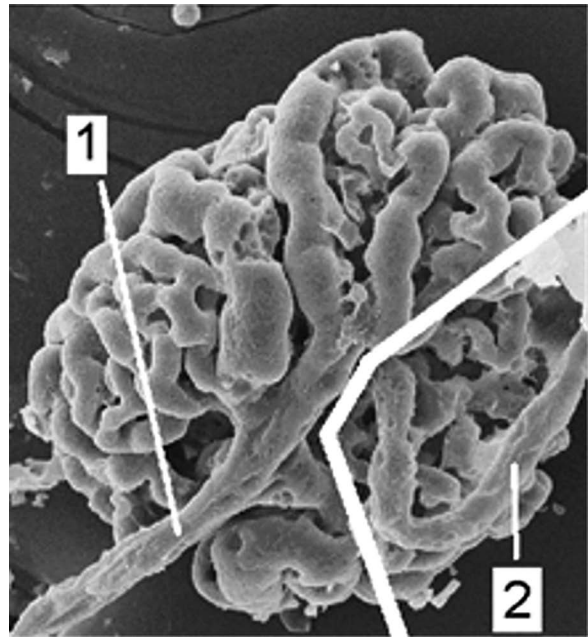
Figure 4. Afferent domain covers 3/4 of the glomerular tuft; 1 — afferent arteriole (domain); 2 — efferent arteriole (domain). Magnification ×436.
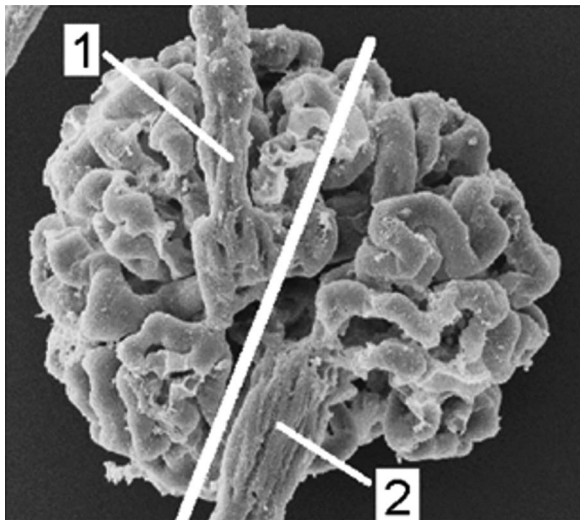
Figure 3. Afferent and efferent domain covers 1/2 of the glomerular tuft; 1 — afferent arteriole; 2 — efferent arteriole. Magnification ×41.
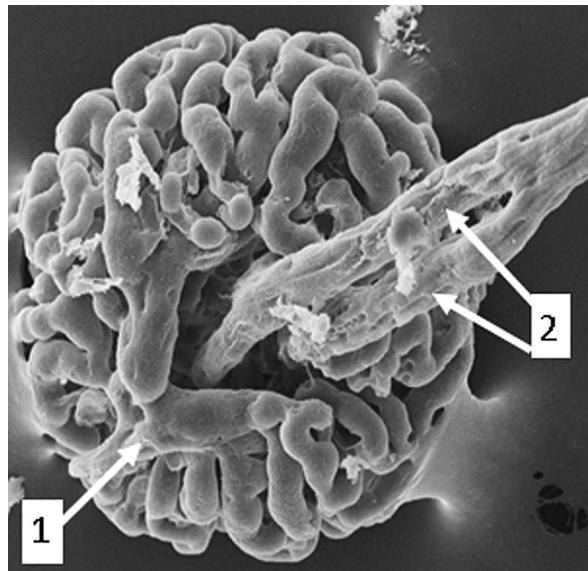
Figure 5. Two roots of the efferent arteriole are merged out of the glomerulus; 1 — afferent arteriole; 2 — efferent arteriole. Magnification ×370.

Branches of afferent arterioles formed a ring-like cavity in the blood vascular pole of the glomerulus. Efferent arterioles that were formed by merged capillaries of the efferent domain came through this cavity (Figs. 1, 2, 5, 8).

The capillaries of the efferent arteriole joined at the vascular pole to form an efferent arteriole. Sometimes in the case of a failure of this joining, the glomerulus might have two efferent arterioles. In this study, five glomeruli having two efferent arterioles (5/2000) were observed (Figs. 5, 6) Although the afferent domain constituted most of the glomerular tuft, it was identified that the afferent domain formed 3/4 of the glomerulus in two cases and 1/2 of the glomerulus in two other cases (Figs. 3, 4).

883
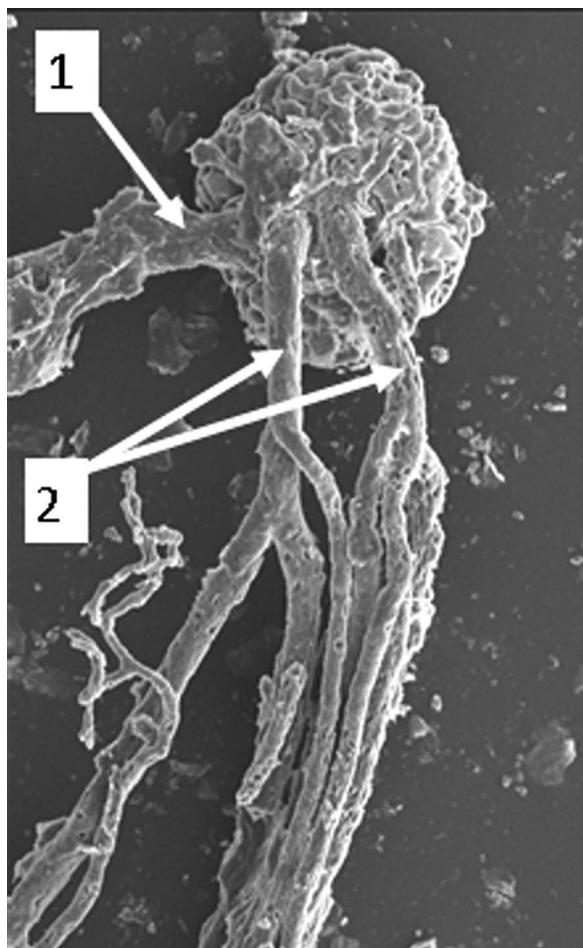
Figure 6. Five sheep glomeruli have two efferent arterioles; 1 — afferent arteriole; 2 — efferent arteriole. Magnification ×50.

The outer surface of each lobule of sheep glomerulus was convex, whereas the inner surface was concave. The efferent domain resided in the flat inner surface of the lobule (Figs. 2, 5). Anastomoses that were between the afferent domain arterioles showed protrusions that were similar to the gyri of the brain. Some of these structures resembled the letters U, O, S, J, and H. There were holes inside the cavities between those protrusions (Figs. 9, 10).

Anastomoses that were located between the capillaries of the afferent and efferent domains existed around the lobule. There were no capillary anastomoses inside the lobule (Figs. 1, 8).

The average diameter of all glomerular capillary tufts was 139.5 μm, the average value for afferent arterioles was 12.08 μm, and the same value for efferent arteriole was 11.18 μm. The diameter of the afferent arterioles was greater than the diameter of the efferent arterioles.
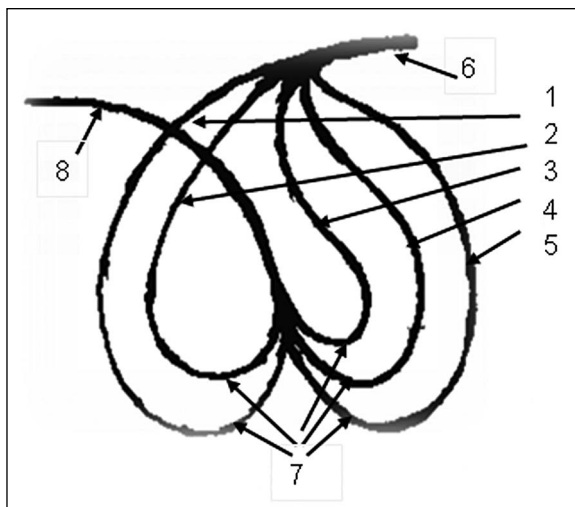
Figure 7. Schematic view of the glomerular lobe; 1, 2, 3, 4, 5 — afferent domain and afferent arteriole divided in five lobes; 6 — afferent arteriole; 7 — efferent domain; 8 — efferent arteriole.
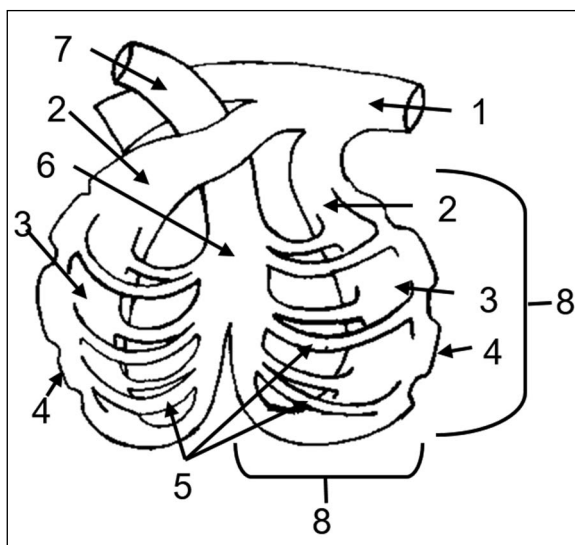
Figure 8. Schematic view of a lobe of glomerular microvasculature; 1 — afferent arteriole; 2 — afferent domain; 3 — internal surface of the glomerular lobule (hollow in shape) (there is no capillary anastomoses between afferent and efferent arterioles in here); 4 — capillary enlargement of the afferent domain in gyrus shape; 5 — capillary anastomoses between afferent and efferent domain; 6 — efferent domain; 7 — efferent arteriole; 8 — one lobe of glomerulus.

DISCUSSION

Knowledge of glomerulus morphology is of great importance in explaining kidney infiltration. Therefore, the afferent and efferent domains of the glomerular tuft have been studied with different methods for years [5–8, 10, 11, 15, 17, 18, 23]. The renal glomeruli
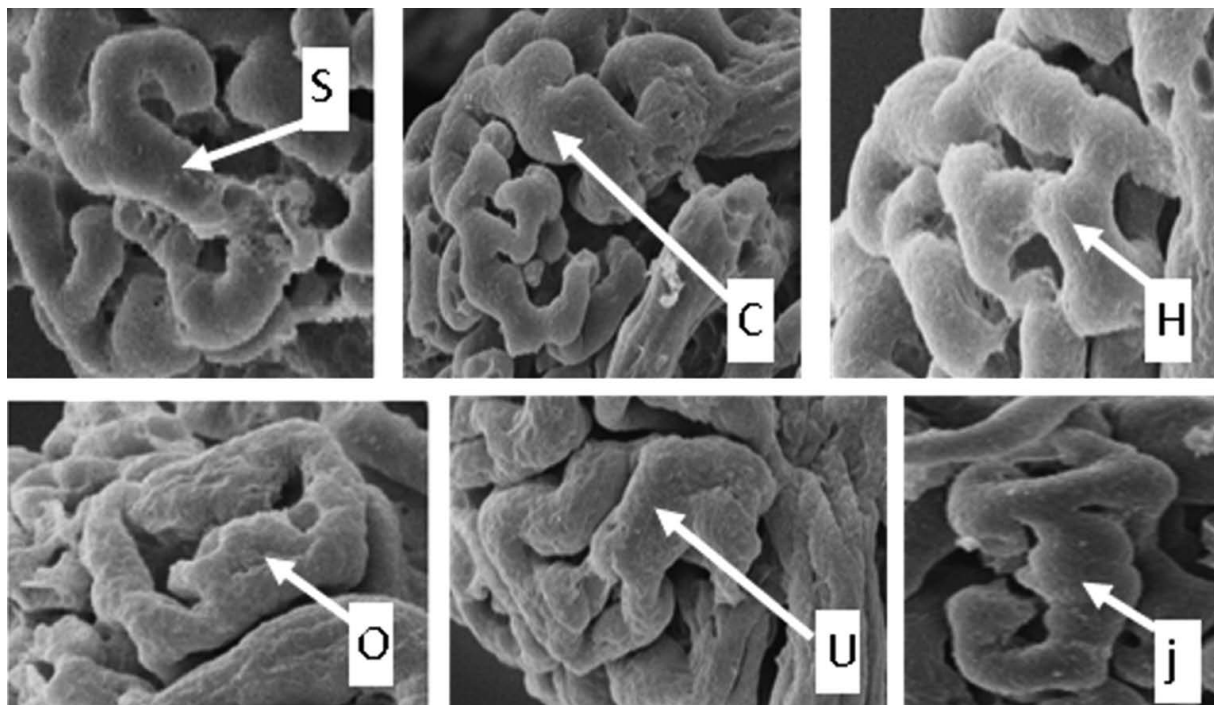
Figure 9. Capillary enlargement of the of external surface of afferent domain (S, C, H, O, U, and J shape).
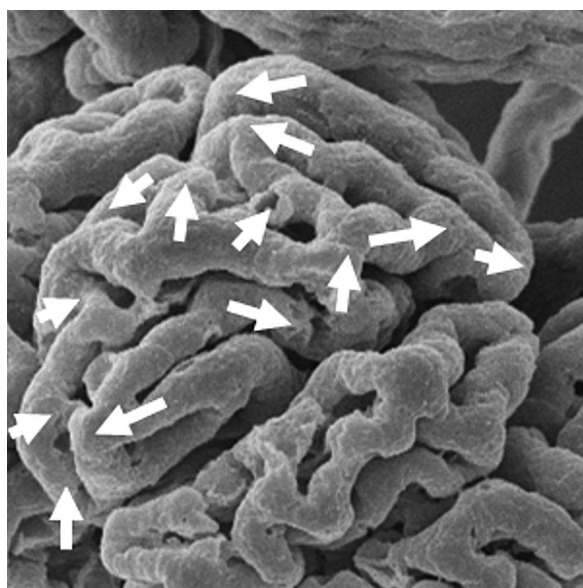
Figure 10. Capillary anastomoses in one lobule of the afferent domain (white arrow).

of the sheep have not been explained yet by corrosion casting method. The glomerulus is located in the cortex of the kidney. The cortex is composed of three parts: outer, middle, and inner cortex. In this study, the middle and outer cortex of 2000 sheep kidney glomeruli were examined [9]. It is known that afferent arterioles originate from interlobular arteries [1]; the sheep glomerulus afferent arterioles also originated from interlobular arteries in our study. In our study, afferent arteriole separated into five branches that entered the Bowman's capsule. Every branch of afferent arterioles constitute a lobule of glomerulus. Glomeruli of sheep kidneys usually have five lobules (Figs. 1, 7). Every lobule has an afferent domain and efferent domain. Every efferent domain capillary is merged with each other to constitute efferent arteriole. Capillaries of every lobule anastomose with each other; this capillary do not anastomose with the other capillary of the lobule.

Recent studies indicate that mouse, rabbit, dog, sheep, and human glomeruli have two to eight lobules [11, 20, 23]. In our study, it was observed that sheep glomeruli had five lobules (Figs. 1, 7). Human glomerulus in health and disease comprises seven lobule-like structures with numerous anastomoses, but there are no direct anastomoses between the afferent and efferent arterioles [4]. In our study, Akkaraman sheep glomerulus comprised five lobules. Every lobuls has afferent and efferent domain. This domain of lobule do not anastomose with other lobules. There are direct anastomoses between this domain's arterioles.

885

Recent studies and our study showed that the afferent domain composed most of each lobule or outer surface of the glomerular tuft. The efferent domain resides in the middle of the afferent domain [23]. Although the same cases were observed in our study, it also indicated that the afferent domain formed 3/4 of the glomerular tuft, whereas in the other two cases the afferent domain constituted 1/2 of the glomerular tuft (Figs. 3, 4).

Various studies show that each glomerulus has one afferent arteriole. It was found in our study that all sheep glomeruli had one afferent arteriole. However, some investigations shows that there are two or four afferent arterioles in a glomerulus. One of these feeds two lobules, whereas the other one feeds three lobules [5, 10, 15].

It is known that the efferent domains merge and form an efferent arteriole in the glomerulus. Sometimes when the merging fails, two or four efferent arterioles exist [5, 10, 18, 22]. Five glomeruli were identified in our study having two efferent arterioles (Figs. 5, 6).

Our investigations found sheep glomeruli average diameter to be 139.5 μm. The lomerulus average diameter was 200 μm. Juxtaglomedullary glomeruli are 20–50% greater than superficial glomeruli in mammals; others have found no significant size difference between these glomerular population in the normal human adult kidney [13, 20].

The calibres of the afferent and efferent arterioles of the glomeruli appear in the casts to be about the same. In the human juxtaglomedullary glomeruli the afferent and efferent arterioles are of equal calibre, while in the cortical glomeruli the efferent arterioles are much narrower than the afferent [21]. In the fowl, arterioles of both cortical and juxtaglomedullary glomeruli appear to be equal in diameter [19].

As in recent animal research, the diameter of the efferent arteriole is smaller than the diameter of the afferent arteriole [5, 7, 10, 16]. In the sheep, the diameter of the afferent arteriole was greater than that of the efferent arteriole [1]. In our study afferent arteriole diameter was 12.08 μm, efferent arteriole dimeter was 11.18 μm. The smaller diameter of efferent arteriole has great importance in infiltration [16].

The total length of the capillaries in a single glomerulus is 0.95 cm. The total surface area of all glomerular capillaries is 6,000 cm^2 [4]. We have not measured the total length or total surface area of the capillaries in a single glomerulus.

Protrusions like the gyri of the brain were observed on the outer surface of afferent domain capillaries in our research (Fig. 9). It is understood that those protrusions are the anastomoses located between the capillaries. These structures that are formed by afferent domain resemble letters U, O, S, J, and H (Figs. 9, 10). This suggests that these protrusions have an essential role in infiltration.

CONCLUSIONS

The morphology of sheep kidney glomeruli is well shown with corrosion method. The afferent arteriole separated into five branches enter the Bowman's capsule in sheep glomeruli. Every branch of afferent arterioles constitutes a lobule of glomerulus. Glomeruli of sheep kidneys usually have five lobules. Every lobule has an afferent domain and efferent domain. Every efferent domain capillary is merged with each other to constitute efferent arteriole. Capillaries of every lobule anastomose with each other; this capillary do not anastomose with the other capillary of lobule. Anastomoses that are located between the capillaries of the afferent and efferent domains exist around the lobule. There are no capillary anastomoses inside the lobule. There are holes inside the cavities of lobule.

The efferent domain resides in the flat inner surface of the lobule. The capillaries of the efferent arteriole join at the vascular pole to form an efferent arteriole. All of the sheep glomeruli have an afferent and efferent arteriole. Sometimes sheep glomerulus might have two efferent arterioles.

The diameter of the afferent arterioles is greater than the diameter of the efferent arterioles. Anastomoses that are between the afferent domain arterioles show protrusions that are similar to the gyri of the brain. Some of these structures resemble the letters U, O, S, J, and H.

It is believed that the present study has a vital role in revealing the morphology of human or mammal glomeruli.

Conflict of interest: None declared

REFERENCES

1. Anderson B, Anderson W, Seguin R. Renal microvasculature of the black bear (*Ursus americanus*). Cells Tissues Organs. 1988; 132(2): 124–131, doi: 10.1159/000146563.
2. Aycan K, Bilge A. Plastik enjeksiyon ve korrozyon metodu ile vasküler sistem anatomisinin Araştırılması. Erciyes Üniv Tıp Fak Dergisi. 1984; 6: 545–552.

3.   Bellomo G. A short history of 'glomerulus'. Clin Kidney J. 2013; 6(2): 250–251, doi: 10.1093/ckj/sft022, indexed in Pubmed: 26019863.

4.   Bohle A, Aeikens B, Eenboom A, et al. Human glomerular structure under normal conditions and in isolated glomerular disease. Kidney Int Suppl. 1998; 67: S186–S188, doi: 10.1046/j.1523-1755.1998.06742.x, indexed in Pubmed: 9736285.

5.   Brown JA. Renal microvasculature of the rainbow trout, Salmo gairdneri: scanning electron microscopy of corrosion casts of glomeruli. Anat Rec. 1985; 213(4): 505–513, doi: 10.1002/ar.1092130405, indexed in Pubmed: 4083531.

6.   Casellas D, Mimran A. Aglomerular pathways in intrarenal microvasculature of aged rats. Am J Anat. 1979; 156(2): 293–299, doi: 10.1002/aja.1001560209, indexed in Pubmed: 506956.

7.   Casotti G, Braun EJ. Structure of the glomerular capillaries of the domestic chicken and desert quail. J Morphol. 1995; 224(1): 57–63, doi: 10.1002/jmor.1052240107, indexed in Pubmed: 7723047.

8.   Elger M, Sakai T, Kriz W. The vascular pole of the renal glomerulus of rat. Adv Anat Embryol Cell Biol. 1998; 139: 1–98, doi: 10.1007/978-3-642-80449-6, indexed in Pubmed: 9386305.

9.   Evan AP, Dail WG. Efferent arterioles in the cortex of the rat kidney. Anat Rec. 1977; 187(2): 135–145, doi: 10.1002/ar.1091870202, indexed in Pubmed: 848773.

10. Frank M, Kriz W. Scanning electron microscopy studies of the vascular pole of the rat glomerulus. Anat Rec. 1982; 204(2): 149–152, doi: 10.1002/ar.1092040208, indexed in Pubmed: 7181131.

11. Kazimierczak J. A study of scanning (SEM) and transmission (TEM) electron microscopy of the glomerular capillaries in developing rat kidney. Cell Tissue Res. 1980; 212(2): 241–255, doi: 10.1007/BF00233959, indexed in Pubmed: 7428030.

12. Kotyk T, Dey N, Ashour AS, et al. Measurement of glomerulus diameter and Bowman's space width of renal albino rats. Comput Methods Programs Biomed. 2016; 126: 143–153, doi: 10.1016/j.cmpb.2015.10.023, indexed in Pubmed: 26796351.

13. Mills SE. Histology for patologists. Fourth edition. Wolters Kluwer/Liicott/Philadelphia, PA: Liincott Williams and Wilkins., Philadelphia-London 2012: 928–938.

14. Murakami T. Double afferent arterioles of the rat renal glomerulus as studied by the injection replica scanning electron microscopic method. Arch Histol Jpn. 1976; 39(5): 327–332, doi: 10.1679/aohc1950.39.327, indexed in Pubmed: 1021016.

15. Murakami T, Kikuta A, Akita S, et al. Multiple efferent arterioles of the human kidney glomerulus as observed by scanning electron microscopy of vascular casts. Arch Histol Jpn. 1985; 48(4): 443–447, doi: 10.1679/aohc.48.443, indexed in Pubmed: 4084007.

16. Oguz O, Dere F, Yücel AH, et al. Examination of microvascular structures of midcortical region in sheep kidneys: a three dimensional approach. Acta Med Okayama. 1991; 45(2): 77–80, doi: 10.18926/AMO/32185, indexed in Pubmed: 1867114.

17. Oguz O, Dere F, Yücel AH, et al. Scanning electron microscopic (SEM) examination of structures which supply subcapsular and midcortical region postglomerular microcirculation in sheep kidney. Acta Morphol Hung. 1992; 40(1-4): 195–202, indexed in Pubmed: 1365763.

18. Rovenská E. Two types of capillaries in the rat renal glomerulus. Acta Anat (Basel). 1983; 115(1): 31–39, indexed in Pubmed: 6829268.

19. Siller WG, Hindle RM. The arterial blood supply to the kidney of the fowl. J Anat. 1969; 104(Pt 1): 117–135, indexed in Pubmed: 5761744.

20. Sternberg SS. Histology for pathologists. 2nd ed. Lippincott-Raven Publishers, Philadelphia 1997.

21. Trueta J, Barclay AE, Daniel PM. Studies of the Renal Circulation. Blackwell Scientific Publications, Oxford 1947.

22. Tsikaras PD, Hytiroglou PM, Lazos LM. The use of unsaturated polyester resin solutions in preparing casts of the renal vessels. Bull Assoc Anat (Nancy). 1985; 69(204): 71–78, indexed in Pubmed: 3833313.

23. Winkler D, Elger M, Sakai T, et al. Branching and confluence pattern of glomerular arterioles in the rat. Kidney Int Suppl. 1991; 32: S2–S8, indexed in Pubmed: 1881043.

VIA MEDICA

ORIGINAL ARTICLE

Liver anatomy, intrahepatic vascular and biliary branching system of the mole rat (*Spalax leucodon*)

I. Nešić[1], N. Krstić[2], N. Djelić[3], M. Zdravković[4], B. Tošković[4], M. Djordjević[1], M. Blagojević[1]

[1]Department of Anatomy, Faculty of Veterinary Medicine, University of Belgrade, Serbia
[2]Department of Radiology and Radiation Hygiene, Faculty of Veterinary Medicine, University of Belgrade, Serbia
[3]Department of Biology, Faculty of Veterinary Medicine, University of Belgrade, Serbia
[4]Faculty of Medicine, University of Belgrade, Medical Centre Bežanijska Kosa, Belgrade, Serbia

Background: There are many studies on the morphology of the liver and its blood vessels in experimental animals, but such studies are lacking in the mole rat (Spalax leucodon). The aim of this paper was a detailed basic study on the topography, morphology, vascular and biliary branching systems of the liver in the mole rat.

Materials and methods: Coloured gelatine and mixture of coloured lead oxide and linseed oil were injection contrast masses used to obtain vascular and biliary branching pattern in the liver. It was revealed that the liver of the mole rat had five lobes (left, quadrate, right medial, right lateral and caudate lobes).

Results: The left, undivided lobe was the largest lobe of the liver. The quadrate lobe was divided into two components by a deep notch. The gallbladder, of cylindrical shape, was present and attached to the quadrate lobe. The common bile duct was formed by the union of the left and right hepatic ducts. The pancreatic duct joined the common bile duct before it entered the duodenum. In the present study, only the right medial lobe and quadrate lobe always showed a single lobar artery, portal and hepatic veins. The left lobe showed four lobar arteries, portal and hepatic veins. The caudate lobe with its two processes and the right lateral and medial lobes had different arterial and portal blood supply as well as hepatic and biliary drainage of these lobes. The intrahepatic branches of the proper hepatic artery ran parallel to the branches of the common portal vein in the same lobes of the liver.

Conclusions: The results of this study are significant for comparative studies among different species of rodents and other experimental animals. Morphology, vasculature and biliary tract of the liver in the mole rat were similar to that of other experimental animals and identified differences may be related to the adaptation to the mode of life and diet of this rodent. (Folia Morphol 2021; 80, 4: 888–894)

Key words: liver, a. hepatica propria, v. portae, vv. hepaticae, bile ducts

INTRODUCTION

The mole rat (*Spalax leucodon*) is a rodent belonging to the Muroidea superfamily and the Spalacidae family. *Spalax leucodon* is the only species of mole rats found in Serbia in the area of Vojvodina province [6]. They live under the ground in branched tunnels they dig using their powerful front teeth. Mole rats are truly blind. Their small eyes are completely covered by a layer of skin [8]. Because of its specific way of life the mole rat was used as experimental animals in studies of biology, immunology, microbiology, physiology and they are interesting also for anatomical studies of morphology and vascularisation of their organs. Available literature offers very little information on the morphology of the organs of this rodent.

The liver lobes, their number and nomenclature, as well as their biliary and vascular system are still the subject of investigation, in several species of the experimental animals, such as the rat [3, 5, 19, 24], rabbit [12, 13, 16, 18, 19], guinea pig [19–21], nutria [12], chinchilla [9, 19], pig [11], and dog [4, 22]. The only description of the liver in the mole rat was found of Tammam et al. [23], mentioning the nomenclature of the liver lobes, histological structure of the liver as well as the presence of a gallbladder.

Within the rodent species, the mole rat has been less used as an experimental animal in the detailed study of the liver in terms of its lobes, biliary ducts and blood vessels. For this reason, we undertook a detailed basic study on the topography, morphology and vascularisation of the liver in the mole rat.

MATERIALS AND METHODS

The investigation was carried out on 7 adult mole rats of both sexes (3 females and 4 males) which weighed between 180 and 240 g. The mole rats were trapped in Serbia, in the area of south Banat (Deliblato Sands). All animals were found to be clinically healthy.

Being an endangered species, the mole rat is protected by law in the Republic of Serbia. For this reason, the Ministry of Environmental Protection of the Republic of Serbia issued an approval for obtaining the animals from their natural habitats (No. 353--01-1185/2011-03) and the Ethics Committee of the Faculty of Veterinary Medicine in Belgrade issued an approval for conducting this research.

Prior to sacrifice, the animals were sedated with xylazine (Rompur®, Bayer, Mississauga/Ontario, Canada) in a dose of 0.1 mL/kg intramuscular, and then euthanized with ketamine (Ketamidor 10%, Richter

Pharma AG, Wels, Austria) in a dose of 0.1 mL/kg intramuscular. The topographical position and morphology of livers were studied in the sacrificed animals and preparations preserved in 3% formaldehyde solution. The biliary system and pancreatic ducts, as well as arterial and venous system of the liver were investigated in injected preparations and roentgenograms. In order to obtain preparations with arterial vascularisation of the liver, after bleeding out stained gelatin was injected into the abdominal aorta. After 24 h the arterial blood vessels were prepared and photographed with a digital camera. A mixture of red-coloured lead oxide and linseed oil was used for roentgenograms. This mixture was injected into the portal system through the portal vein (PV) before its entry into the liver, and into the liver veins through the caudal vena cava previously tied cranially to the diaphragm. This mixture also was injected into the biliary system through the gallbladder, and into the system of pancreatic ducts through the duodenum, which, in both cases, had been tied off previously. The injected pancreatic ducts, venous blood vessels and biliary system of the liver were X-rayed.

Latin terms were used in accordance with Nomina Anatomica Veterinaria, 2017 [7].

RESULTS

The liver of the mole rat was located in the intrathoracic part of the abdominal cavity, with the exception of ventral part of the left hepatic lobe which was located on the ventral abdominal wall in the *regio xiphoidea*, somewhat left to the median plane. On the right of the intrathoracic part of the abdominal cavity the liver was situated between the diaphragm, descending duodenum, jejunum and right kidney, and on the left between the diaphragm, stomach, jejunum and dorsal end of the spleen.

The parietal surface of the liver was strongly convex and it was in contact with diaphragm.

Liver lobes

Deep fissures divided the liver into five lobes as follow: left, quadrate, right medial, right lateral and caudate lobes.

The left lobe (LS, *lobus hepatis sinister*) (Fig. 1A, B-1) was the largest and undivided lobe of the liver. It was positioned in the left intrathoracic part of the abdominal cavity with the exception of a small ventral part of this lobe which rests upon the ventral
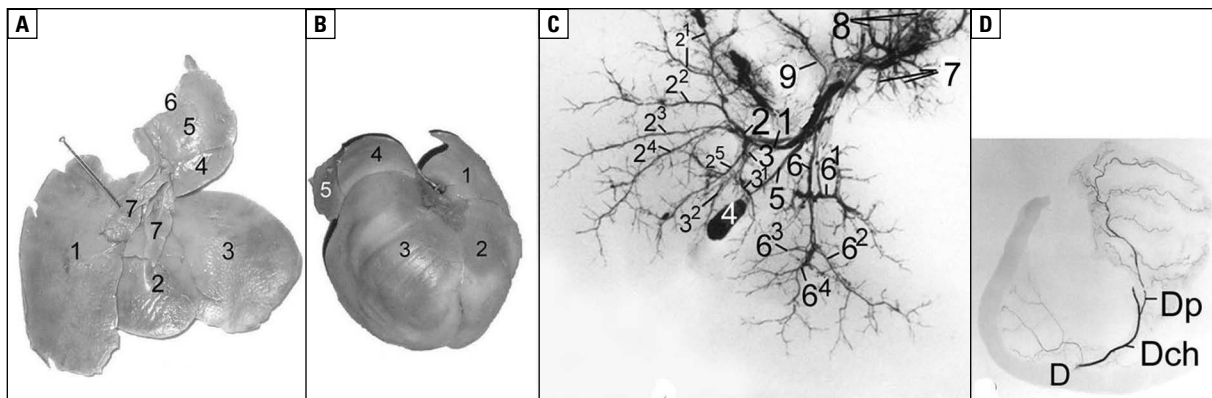
Figure 1. Visceral (**A**), parietal surface of the liver (**B**), bile ducts (**C**) and the common bile duct (**D**) of the liver in the mole rat; A and B: 1 — lobus hepatis sinister; 2 — lobus quadratus; 3 — lobus hepatis dexter medialis; 4 — lobus hepatis dexter lateralis; 5 — processus caudatus; 6 — impressio renalis; 7 — processus papillaris; C: 1 — d. lobi sinistri et lobi quadrati; 2 — d. lobi sinistri; 2^{1-5} — rr. lobi sinistri; 3 — d. lobi quadrati; 3^{1-2} — rr. lobi quadrati; 4 — vesica fellea; 5 — d. cysticus; 6 — d. lobi dextri medialis; 6^{1-4} — rr. lobi dextri medialis; 7 — rr. lobi dextri lateralis; 8 — rr. processi caudati; 9 — d. processi papillaris; D: D — duodenum; Dp — d. pancreaticus; Dch — d. choledochus.

abdominal wall, in the *regio xiphoidea*. The stomach overlapped almost the whole visceral surface of the left lobe with the exception of a small ventral portion of that lobe, resting on the jejunum. The left lobe of the liver was covered on the parietal surface by the quadrate lobe.

The quadrate lobe (LQ, *lobus quadratus*) (Fig. 1A, B-2) was situated on the left in the intrathoracic part of the abdominal cavity. It was separated from the left and right medial liver lobes by deep notches. The quadrate lobe was divided into two components by a deep notch. Its visceral surface rested upon the parietal surface of the left lobe and these lobes partly overlapped each other (Fig. 1B-1, 1B-2). The quadrate lobe was attached to the gallbladder.

The right lobe (RL, *lobus hepatis dexter*) was positioned completely in the right intrathoracic part of the abdominal cavity. It was divided into medial (RML) and lateral (RLL) lobes by a deep fissure. The RML (Fig. 1A, B-3) was the second largest lobe of the liver. On the parietal surface from the medial border of the RML, the falciforme ligament appeared as a thin fold that connected the liver to the diaphragm. Parietal surface of the right lateral lobe was partially overlapped by visceral surface of the right medial lobe (Fig. 1B-4, 1B-3).

The caudate lobe (CL, *lobus caudatus*) was situated dorsal to the portal fissure and it was divided into a caudate and a papillary process.

The caudate process (CP, *processus caudatus*) (Fig. 1A, B-5) was almost overlapped by the visceral surface of the right lateral lobe. Its caudodorsal edge showed very marked imprint for the right kidney (Fig. 1A-6).

The papillary process (PP, *processus papillaris*) (Fig. 1A-7) was divided by a deep fissure into two narrow and long portions.

The gallbladder (GB, *vesica fellea*) (Fig. 1C-4) lay in a slight depression on the quadrate lobe. It was cylindrical shaped and it did not reach the ventral border of the liver.

The cystic duct (CD, *ductus cysticus*) (Fig. 1C-5) was a short duct, 9 to 10 mm long. It joined the left hepatic duct. The left hepatic duct drained the left and quadrate lobe by one bile duct (Fig. 1C-1). The right hepatic duct was formed by the confluence of the ducts that drained the caudate process of the caudate lobe with the duct that drained the right lateral lobe, than from the duct that drained papillary process of the caudate lobe and the last duct drained the right medial lobe.

The common bile duct (CBD, *ductus choledochus*) (Fig. 1D-Dch) was formed by the union of the right and left hepatic ducts. It entered the duodenum 6.5 to 7 mm caudal of the pylorus. A single pancreatic ducts joined lobar and lobular ducts of the pancreas and joined the common bile duct before it entered the duodenum.

The proper hepatic artery (*a. hepatica propria*)

The liver of the mole rat was supplied with blood by the proper hepatic artery (PHA), a branch of the hepatic artery (HA, *a. hepatica*). At the porta hepatis, the PHA (Fig. 2A-I) bifurcated into the right (Fig. 2A-II) and left (Fig. 2A-III) branches. The right branch of PHA first gave off the common branch to the right lateral lobe and caudate process of the caudate lobe
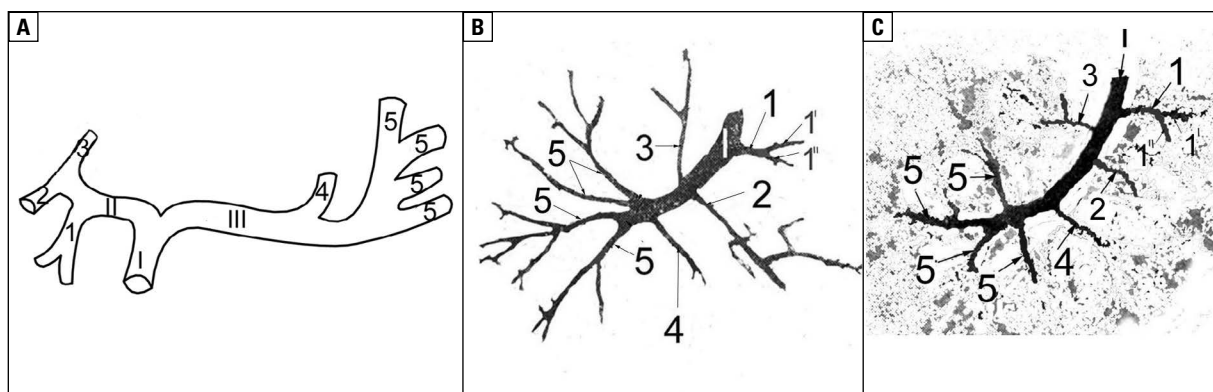
Figure 2. Schematic representation of the intrahepatic branches of the proper hepatic artery (**A**), radiograph of intrahepatic branches of the portal vein (**B**) and hepatic veins (**C**) in the mole rat; A: I — a. hepatica propria; II — r. dexter; III — r. sinister; 1 — r. lobi dextri lateralis et processi caudati; 2 — r. lobi dextri medialis; 3 — r. processi papillaris; 4 — r. lobi quadrati; 5,5,5,5 — rr. lobi sinistri; B: I — v. portae; 1 — r. lobi dextri lateralis et processi caudati; 2 — r. lobi dextri medialis; 3 — r. processi papillaris; 4 — r. lobi quadrati; 5,5,5,5 — rr. lobi sinistri; C: I — v. cava caudalis; 1 — v. hepatica lobi dextri lateralis et processi caudati; 2 — v. hepatica lobi dextri medialis; 3 — v. hepatica processi papillaris; 4 — v. hepatica lobi quadrati; 5 — v. hepatica lobi sinistri.

(Fig. 2A-1), then the branch to the right medial lobe (Fig. 2A-2) and last branch to the papillary process of the caudate lobe (Fig. 2A-3). The left branch of PHA first gave off the branch that supplied the quadrate lobe (Fig. 2A-4) and then it branched into four larger arterial branches that supplied the left lobe (Fig. 2A-5).

The portal vein (*v. portae*)

The first portal branch of the common portal vein (CPV) (Fig. 2B-I) was very short and it immediately was divided into two branches, one to the caudate process of the caudate lobe and one to the right lateral lobe (Fig. 2B-1). From its ventral wall, CPV gave off two separated branches to the right medial (Fig. 2B-2) and quadrate lobe (Fig. 2B-4). From the dorsal wall, CPV gave off a portal branch to the papillary process of the caudate lobe that ramified into both portion of the papillary process (Fig. 2B-3). Between the left and quadrate lobes the CPV divided into four final branches (Fig. 2B-5) supplying the dorsal, middle and ventral portion of the left lobe.

The hepatic veins (*vv. hepaticae*)

Eight large hepatic veins (HVs) drained the blood from the lobes of the liver into the caudal vena cava (Fig. 2C-I) during its passage through the liver. The caudate processes of the caudate lobe and right lateral lobe were drained by two separated HVs united by a common HV (Fig. 2C-1) that opened into the caudal vena cava. The right medial lobe (Fig. 2C-2), papillary process of the caudate lobe (Fig. 2C-3) and quadrate lobe (Fig. 2C-4), were drained by three separated HVs that opened into the caudal vena cava separately. The left lobe was drained into the caudal vena cava by four HVs (Fig. 2C-5).

DISCUSSION

Knowledge of the nomenclature of liver lobes was of great importance for understanding the vascular and biliary branching pattern in the liver of experimental animals.

There has been no study in the literature describing the liver and intrahepatic vascular and biliary system of the mole rat. Only topographical position and names of the liver lobes were mentioned by Tammam et al. [23] in mole rats. For this reason, our study is the first study on the topography, morphology, intrahepatic ramification of the artery, veins and bile ducts of mole rats (*Spalax leucodon*) described and illustrated in detail.

A comparable topography of the liver of rats, rabbits, guinea pigs and chinchillas was described by Stan [19]. The livers of those animals were positioned almost in intrathoracic part of the abdominal cavity. Tammam et al. [23], in the study on the histological structure of the digestive tract of mole rats, including the liver, mentioned that the liver of this rodent was located in the intrathoracic part of the abdominal cavity. However, our study suggested the presence a small ventral portion of the left lobe located on the ventral abdominal wall in the *regio xiphoidea*, which was not described in mole rats by Tammam et al. [23]. This portion of left lobe is an accessible

place for puncture of the liver and further laboratory analysis of this organ.

The liver of mole rats was lobulated as found in experimental small mammals [5, 9, 12, 18, 21] and some domestic mammals, such as pigs and dogs [11, 22]. Stan [19] compared the division of the liver into lobes among rabbits, guinea pigs and chinchillas, and showed that six liver lobes in guinea pigs (left lateral and medial lobes, quadrate lobe, right medial and lateral lobes and caudate lobe) corresponded to that in nutria liver [12]. The same number of lobes was described by Osman et al. [11] in pigs and by Swielim [22] in dogs. In rabbits the right lobe was single [13, 18, 19]. The quadrate lobe recognised by Stamatova-Yovcheva et al. [18] in rabbits, Stan et al. [21] in guinea pigs and Osman et al. [11] in pigs was very small and was not observed on the diaphragmatic surface of the liver in these animals.

The basic nomenclature of the rat liver lobes was not uniform. Kogure et al. [3], Martins and Neuhaus [5] and Quesenberry [14] described four lobes of the liver in rats (left lateral, middle, caudate and right lobes) and Vdoviaková et al. [24] merged the left lateral lobe with the middle lobe into one lobe, thus the rat liver was divided into the left lateral and medial lobes, right medial and lateral lobes and caudate lobe divided into two portions. The middle lobe of rats, described by Martins and Neuhaus [5] divided into the left medial and right medial lobes, was not detected in our study.

Tammam et al. [23] in the study on morphology of the liver in mole rats did not explain according to which nomenclature the liver was divided into: left, right, right central, spigelian and caudate lobes. In our study, the division of the liver into left, quadrate, right medial, right lateral and caudate lobes was adopted according to Nomina Anatomica Veterinaria 2017 [7].

The presence of the GB in small mammals was variable and its morphology was mainly dependent upon diet [10]. The most species of the experimental animals, except rats, had a well-developed GB, located in the shallow depression on the quadrate or the right medial lobes [18–20]. The presence of a gallbladder on the right medial lobe of the liver described by Tammam et al. [23] in mole rats was not confirmed in our study in which the GB was attached to the quadrate lobe.

Among laboratory animals, rats are the most frequently used as animal models in biomedical research.

Detailed knowledge of the intrahepatic vascular and biliary anatomy and also their variations are of the great importance for experimental hepatobiliary surgery and transplantation of the liver [15]. Previous anatomical studies described vascular and biliary anatomy of the liver in rats [3, 5, 15, 24] and the obtained data were compared with those of humans.

In the literature there have been no studies describing the vascular and biliary branching pattern in the liver of mole rats.

The liver of different species of experimental animals was supplied by the PHA or HA and their division into the right and left branches was described by Martins and Neuhaus [5] and Vdoviaková et al. [24] in rats, Stamatova-Yovcheva et al. [17] in rabbits and Osman et al. [11] in pigs. Stamatova-Yovcheva et al. [17] asserted that in rabbits PHA first supplied the caudate lobe and its continuation was HA that bifurcated into the right and left branches. In rats [5, 24] and rabbits [17] the caudate and right (lateral and medial) lobes were supplied by branches from the right branch of HA. The same lobes supplied by r. dexter lateralis and medialis were described by Osman et al. [11] in pigs and by Swielim [22] in dogs. The left lateral, left medial and quadrate lobes were supplied by branches from the left branch of PHA in rats [24] and branches of HA in rabbits [17].

The presence of the PV in the porta (PH, *porta hepatis*) and its division into two main branches, right and left, was described by Sänger et al. [15], Vdoviaková et al. [24] in rats, Stamatova-Yovcheva et al. [17] in rabbits and Mari and Acocella [4] in dogs. However, Osman et al. [11] mentioned that in pigs, PV was divided into R. dexter dorsalis, R. dexter ventralis and left branch. The division of the PV into the main branches was not detected in our study.

Kogure et al. [3] and Martins and Neuhaus [5] recorded that in rats each liver lobe had their own lobar portal branch. In studies on rabbits, Stamatova-Yovcheva et al. [17] showed that the right portal branch supplied only right lobe. Similar results were obtained by Vdoviaková et al. [24] in rats where right portal branch supplied the caudate, right lateral and right medial lobes. The same lobes in pigs were supplied by r. dexter lateralis, as described by Osman et al. [11]. All of the above authors agreed that the left lobes and quadrate lobe of the liver in rats, rabbits, and pigs were supplied by branches from the left branch of PV.

Numerous authors have studied hepatic venous system of the liver of mammals [4, 5, 11, 16, 17]. It has been reported that both portion of the caudate lobe in rats [5, 24] was drained into the caudal vena cava (CVC) by one HV. Similar results were reported in rabbits by Stamatova-Yovcheva et al. [17]. However, in dogs, the caudate lobe was drained by two HVs, as described by Mari and Acocella [4], of which the vein from the caudate process entered directly and the vein from the papillary process indirectly through the main lobar vein, into the CVC.

In rats, both portions of the right lobe were drained into the CVC by one HV [5, 15]. Such results were found by Mari and Acocella [4] in dogs. The undivided right lobe of rabbits described by Seo et al. [16] was drained into CVC by two separated veins. In the present study both processes of the caudate lobe and both lobes of the right lobe had a different vascular blood supply.

The quadrate lobe was drained indirectly through the middle HV into the CVC, as described in rabbits by Seo et al. [16], and through the main HV, as reported in dogs by Mari and Acocella [4]. In the present study the quadrate lobe was drained into CVC by one HV.

The left lateral lobe in rats [3, 5, 15], rabbits [17] and dogs [4] was drained into CVC by one HV. Also, in rabbits and dogs the left medial lobe had one HV.

In the present study four HVs drained blood from the left lobe.

The extrahepatic biliary tract of the experimental animals has been the subject of research by numerous authors, and studies on their intrahepatic bile branching system have been scarce. At the literature, there was no study on the biliary system of mole rats. The presence of the CBD, common hepatic duct (CHD) and CD in experimental animals were described by many authors [5, 17, 20]. The formation of the CBD by the union of the right and left hepatic ducts revealed in our study was also reported in guinea pigs by Stan [20]. However, the union of the right and left hepatic ducts resulting in a CHD has been described in rabbits by Seo et al. [16] and Stamatova-Yovcheva et al. [17]. The results observed in chinchillas by Nowak et al. [9] have shown that two to three cystic ducts formed a network joined with the hepatic duct system into complex system of bile ducts.

The presence of CBD formed by the union of the CD and CHD was reported in pigs by Osman et al. [11]. Rats have neither a GB nor a CD. In rats, all lobar bile ducts fused into the CHD, so that on its course

to the duodenum it was completely imbedded in the pancreas [5]. The CBD and the pancreatic duct opened into the duodenum separately in guinea pigs, rats and chinchillas [1, 5, 9].

The presence of the right and left hepatic ducts in experimental mammals was described by numerous authors [11, 17, 24].

The presence of the right hepatic duct to drain right and caudate lobes was described by Stamatova-Yovcheva et al. [17] in rabbits and by Vdoviacová et al. [24] in rats. Similar results were obtained by Stan [20] in guinea pigs. Osman et al. [11] in pigs and Coq [2] in dogs mentioned that the right hepatic duct was formed by the confluence of ducts from the caudate process and the right lateral and right medial lobes. The left hepatic duct draining the left (lateral and medial) and quadrate lobes were noted by Stan [20] in guinea pigs, Vdoviacová et al. [24] in rats and Stamatova-Yovcheva et al. [17] in rabbits.

CONCLUSIONS

The macroscopic anatomy of the liver and its vascular and biliary system of mole rats was similar to that of other experimental animals, and identified differences may be related to the adaptation to the mode of life and nature of diet in this rodent.

Conflict of interest: None declared

REFERENCES

1. Cai WQ, Gabella G. Innervation of the gall bladder and biliary pathways in the guinea-pig. J Anat. 1983; 136(Pt 1): 97–109, indexed in Pubmed: 6833124.
2. Coq P. La segmentation hepatique des carnivores. Rec Med Vet. 1965; 141: 234–268.
3. Kogure K, Ishizaki M, Nemoto M, et al. A comparative study of the anatomy of rat and human livers. J Hepatobiliary Pancreat Surg. 1999; 6(2): 171–175, doi: 10.1007/s005340050101, indexed in Pubmed: 10398905.
4. Mari L, Acocella F. Vascular anatomy of canine hepatic venous system: A basic for liver surgery. Anat Histol Embryol. 2015; 44: 212–224.
5. Martins PN, Neuhaus P. Surgical anatomy of the liver, hepatic vasculature and bile ducts in the rat. Liver Int. 2007; 27(3): 384–392, doi: 10.1111/j.1478-3231.2006.01414.x, indexed in Pubmed: 17355461.
6. Méhley L. Species generis Spalax, a földi kutyák fajai. Szarmazès ès rendszertani takinètben. A Madyar Tudomanyos Akademia, Kiadasa, Budapest 1969.
7. Nomina Anatomica Veterinaria, sixth edition. Prepared by the International Committee on Veterinary Gross Anatomical Nomenclature (I.C.V.G.A.N.). Editorial Committee Hannover, Ghent, Columbia, MO (U.S.A.), Rio de Janeiro 2017.

8. Nowak RM. Walker's Mammals of the World. The Johns Hopkins University Press, Baltimore, USA; London, United Kingdom 1999.

9. Nowak E, Kuchinka J, Szczurkowski A, et al. Extrahepatic biliary tract in chinchilla (Chinchilla laniger, Molina). Anat Histol Embryol. 2015; 44(3): 236–240, doi: 10.1111/ahe.12137, indexed in Pubmed: 25091180.

10. Oldham-Ott C, Gilloteaux J. Comparative morphology of the gallbladder and biliary tract in vertebrates: Variation in structure, homology in function and gallstones. Microsc Res Tech. 1997; 38(6): 571–597, doi: 10.1002/(sici)1097-0029(19970915)38:6<571::aid-jemt3>3.0.co;2-i.

11. Osman F, Wally Y, El-Nady F, et al. Gross anatomical studies on the portal vein, hepatic artery and bile duct in the liver of the pig. J Vet Anat. 2008; 1(1): 59–72, doi: 10.21608/jva.2008.45456.

12. Pérez W, Lima M. Anatomical Description of the Liver, Hepatic Ligaments and Omenta in the Coypu (Myocastor coypus). Int J Morphol. 2007; 25(1), doi: 10.4067/s0717-95022007000100007.

13. Pérez W, Möller R, Martin E. Peritoneal folds of the rabbit (Oryctolagus cuniculus). Anat Histol Embryol. 2005; 34(3): 167–170, doi: 10.1111/j.1439-0264.2005.00587.x, indexed in Pubmed: 15929731.

14. Quesenberry K. Ferrets, rabbits and rodents: Clinical Medicine and Surgery. 3th ed. Elsevier, St. Louis, Missouri, USA 2012.

15. Sänger C, Schenk A, Schwen LO, et al. Intrahepatic vascular anatomy in rats and mice — variations and surgical implications. PLoS One. 2015; 10(11): e0141798, doi: 10.1371/journal.pone.0141798, indexed in Pubmed: 26618494.

16. Seo TS, Oh JH, Lee DH, et al. Radiologic anatomy of the rabbit liver on hepatic venography, arteriography, portography, and cholangiography. Invest Radiol. 2001; 36(3): 186–192, doi: 10.1097/00004424-200103000-00008, indexed in Pubmed: 11228583.

17. Stamatova-Yovcheva K, Dimitrov R, Dilek GO. Radiographic study of the topography of the hepatic vasculature and bile ducts of the rabbit. Bulg J Agric Sci. 2018; 24(3): 497–502.

18. Stamatova-Yovcheva K, Dimitrov R, Kostov D, et al. Anatomical macromorphological features of the liver in domestic rabbit (Oryctolagus cuniculus). J Sci. 2012; 10: 85–90.

19. Stan F. Comparative study of the liver anatomy in the rat, rabbit, guinea pig and chinchilla. Bulletin UASVM Veterinary Medicine. 2018; 75(1): 33, doi: 10.15835/buasvmcn-vm:002717.

20. Stan F. Macroscopic anatomy of the gallbladder and extrahepatic biliary tract in the guinea pig (Cavia porcellus). Scientific Works. Series C. Veterinary Medicine. 2017; 43(2): 25–29.

21. Stan F, Martonos C, Dezdrobitu C, et al. Detailed morphological description of the liver and hepatic ligaments in the guinea pig (Cavia porcelus). Scientific Works. Series C. Veterinary Medicine. 2017; 43(1): 35–41.

22. Swielim GEA. Intrahepatic distribution of the portal vein and hepatic vessels in the dog. A lex. J Vet Sci. 1989; 5(2): 33–45, doi: 10.21608/jva.2008.45456.

23. Tammam O, Emara S, Sedera DA. Some histological studies on the digestive system of the spalax leucodon (lesser blind mole rat) inhabit the egyptian north coast. J Environ Studies Res. 2017; 6((E2)): 124–135, doi: 10.21608/jesr.2017.57278.

24. Vdoviaková K, Vdoviaková K, Petrovová E, et al. Importance Rat Liver Morphology and Vasculature in Surgical Research. Med Sci Monit. 2016; 22: 4716–4728, doi: 10.12659/msm.899129, indexed in Pubmed: 27911356.

VIA MEDICA

ORIGINAL ARTICLE

Quantitative anatomy of primary ossification centres of the lateral and basilar parts of the occipital bone in the human foetus

M. Grzonkowska[ID], M. Baumgart[ID], M. Badura, M. Wiśniewski[ID], J. Lisiecki, M. Szpinda

Department of Normal Anatomy, the Ludwik Rydygier Collegium Medicum in Bydgoszcz,
the Nicolaus Copernicus University in Torun, Poland

Background: Computed tomography (CT)-based quantitative analysis of primary ossification centres in the cranium has not been carried out to date due to the limited availability of the foetal human material. Detailed morphometric data about the development of primary ossification centres in human foetuses may be useful in the early detection of developmental defects. Understanding the growth and development of the occipital bone is crucial in assessing the normal and pathological development of the cranial base, and the cranium as a whole.
Materials and methods: The study material comprised 37 human foetuses (16 males and 21 females) aged 18–30 weeks of gestation. Using CT, digital image analysis software, three-dimensional reconstruction and statistical methods, the size of the primary ossification centres of the lateral and basilar parts of the occipital bone was evaluated.
Results: The morphometric characteristics of primary ossification centres of the lateral and basilar parts of the occipital bone display neither sex nor laterality differences. These ossification centres grow linearly with respect to their sagittal and transverse diameters, projection surface area and volume.
Conclusions: The obtained morphometric data of primary ossification centres in the lateral and basilar parts of the occipital bone may be considered as norma- tive for their respective prenatal weeks and may contribute to the estimation of gestational ages and the diagnostics of congenital defects. (Folia Morphol 2021; 80, 4: 895–903)

Key words: occipital bone, bone development, osteogenesis, foetal development

INTRODUCTION

The development and ossification of the cranium is divisible into a slower and relatively stable growth of the cranial base and a considerably faster growth of the calvaria. The growth and formation of the cranial base has a major impact on the development of the brain and the final appearance of the facial skeleton. Ossification within the cranial base starts with the occipital bone and progresses anteriorly, delimiting the calvaria from the facial skeleton [9].

The occipital bone is made up of five components positioned around the foramen magnum, i.e. the

basilar part anteriorly, the two lateral parts on both sides, and the lower or supraoccipital and the upper or interparietal parts of the squamous part posteriorly [2, 10]. The basilar, lateral and supraoccipital parts of the occipital bone surround the foramen magnum and ossify in an endochondral manner, while the interparietal part presents intramembranous ossification. The basilar part of the occipital bone develops from two parachordal or basioccipital cartilages that are derivatives of the middles of all occipital somites [1–4]. The lateral parts of the occipital bone develop from two exoccipital cartilages, while the inferior part of the squamous part of occipital bone develops from two supraoccipital cartilages.

The ossification of the occipital bone begins as early as at 8 weeks of gestational age in the following order: lower part of its squamous part, upper part of its squamous part, and finally its lateral parts. At 11 weeks of gestational age, ossification also includes the basilar part of the occipital bone [8].

In the newborn, the occipital bone consists of four independent parts. Fusion of the squamous part with the lateral parts occurs between 1 and 4 years of age, while fusion of the basilar part with the lateral parts progresses between 3 and 6 years of age [2].

The timing of ossification of particular cranial bones is relatively well-known. However, no morphometric data concerning primary ossification centres of the occipital bone has been reported owing to the limited availability of the foetal material [8].

The present paper is the first report in the professional literature to focus on the morphometric analysis of the primary ossification centres in the lateral and basilar parts of the occipital bone in human foetuses with the use of computed tomography (CT) imaging.

Detailed morphometric data on the development of ossification centres in human foetuses may be useful in the early detection of developmental defects. Understanding the growth and development of the occipital bone is crucial in assessing the normal and abnormal development of the cranial base. Abnormalities of the occipital bone development may involve stenosis of the foramen magnum in thanatoforic dysplasia, malformations in anencephaly, or shallowing of the posterior cranial fossa typical of Chiari malformation [7].

In the present study we aimed:
— to determine normative values for linear, planar and volumetric parameters of the primary ossification centres of the lateral and basilar parts of the occipital bone in human foetuses;
— to examine possible sex differences for all analysed parameters;
— to compute growth dynamics for the analysed parameters, expressed by best-matched mathematical models.

MATERIALS AND METHODS

The study material comprised 37 human foetuses (16 males and 21 females) aged 18 to 30 weeks of gestation, originating from spontaneous miscarriages and preterm deliveries. The foetuses were collected before the year 2000 and still remain part of the foetal collection of the Department of Normal Anatomy. The experiment was approved by the Bioethics Committee of the Ludwik Rydygier Collegium Medicum in Bydgoszcz (KB 275/2011). The inclusion criteria of the foetuses were based on the evaluation of their explicit morphology and statistical cards with the course of pregnancy. Since on macroscopic examination, neither internal nor external conspicuous morphological malformations were found, all included specimens were identified as normal. Of note, the foetuses did not display any developmental abnormalities of the musculoskeletal system. Foetal ages were determined based on the crown–rump length (CRL) and the known date of the beginning of the last maternal menstrual period. Furthermore, the investigated foetuses could not suffer from growth retardation, as the correlation between the gestational age based on the CRL and that calculated by the last menstruation reached $R = 0.98$ ($p < 0.001$). Table 1 lists the characteristics of the study group, including the age, number and sex of the foetuses.

Using the Siemens–Biograph 128 mCT scanner (Siemens Healthcare GmbH, Erlangen, Germany) located in the Department of Positron Emission Tomography and Molecular Imaging (Oncology Centre, the Ludwik Rydygier Collegium Medicum in Bydgoszcz, the Nicolaus Copernicus University Bydgoszcz, Poland), scans of foetuses in DICOM format were acquired at 0.4 mm intervals (Fig. 1). The grey scale of the obtained CT images expressed in Hounsfield units (HU) varied from -275 to -134 for minimum, and from $+1165$ to $+1558$ for maximum. Therefore, the window width (WW) varied from 1.404 to 1.692, and the window level (WL) varied from $+463$ to $+712$. The specifics of the imaging protocol were as

Table 1. Age, number and sex of the foetuses studied

Gestational age	Crown-rump length [mm] of foetuses				Number	Sex	
	Mean	**SD**	**Minimum**	**Maximum**		**Male**	**Female**
18	133.33	5.77	130.00	140.00	3	1	2
19	146.50	2.89	143.00	150.00	4	2	2
20	161.00	2.71	159.00	165.00	4	2	2
21	173.67	2.31	171.00	175.00	3	2	1
22	184.67	1.53	183.00	186.00	3	1	2
23	198.67	2.89	197.00	202.00	3	1	2
24	208.00	3.56	205.00	213.00	4	1	3
25	214.00		214.00	214.00	1	0	1
26	229.00	5.66	225.00	233.00	2	1	1
27	240.33	1.15	239.00	241.00	3	3	0
28	249.50	0.71	249.00	250.00	2	0	2
29	253.00	0.00	253.00	253.00	2	0	2
30	262.67	0.58	262.00	263.00	3	2	1
Total					37	16	21

SD — standard deviation
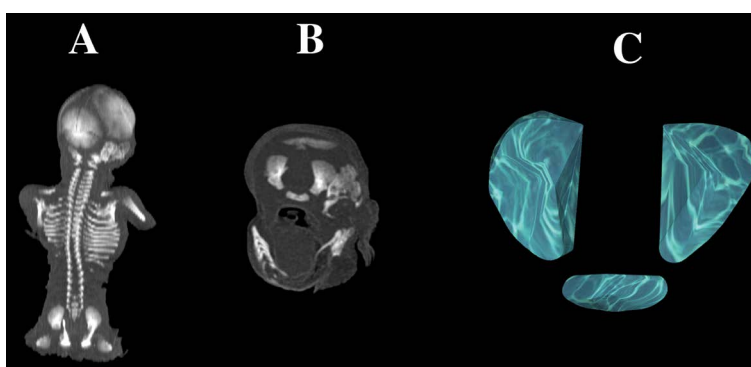
Figure 1. A female human foetus aged 21 weeks in the frontal projection (**A**), its skeletal reconstruction in the frontal projection (**B**), three--dimensional reconstruction of ossification centres of the lateral and basilar parts of the occipital bone (**C**) using Osirix 3.9 MD.

follows: mAs — 60, kV — 80, pitch — 0.35, field of view — 180, rotation time — 0.5 s, while those of the CT data were: slice thickness — 0.4 mm, image increment — 0.6 mm, and kernel — B45 f-medium. Measurements for either lateral part and the basilar part of the occipital bone were conducted in a specific order (Fig. 2). In each foetus, assessment of the linear parameters, projection surface area and volume of primary ossification centres of the lateral and basilar parts of the occipital bone was carried out. Despite the cartilaginous stage of development, a morpho-metric analysis regarding their sagittal diameter and volume was feasible, as outlines of the entire bone were already evidently visible [3, 4].

Measurements of primary ossification centres of the lateral (right and left) and basilar parts of the occipital bone included:
— their sagittal diameter in the lateral (right and left) parts, based on the determined distance between proximal and distal borderlines in the frontal plane (Fig. 2);
— their transverse diameter in the lateral (right and left) parts, based on the determined distance between medial and lateral borderlines in the frontal plane (Fig. 2);
— their transverse diameter in the basilar part, based on the determined distance between medial and lateral borderlines in the frontal plane;

— their sagittal diameter in the basilar part, based on the determined distance between proximal and distal borderlines in the frontal plane (Fig. 2);
— projection surface area in the lateral (right and left) parts, based on the outlined area occupied by the ossification centre in the frontal plane (Fig. 2);
— projection surface area in the basilar part, based on the outlined area occupied by the ossification centre in the frontal plane (Fig. 2);
— volume, calculated using advanced diagnostic imaging tools for three-dimensional reconstruction, taking into account position and the absorption of radiation by bony tissue (Fig. 1C).

Statistical analysis

In the present study the Statistica 12.5 and PQStat 1.6.2. programmes were used to analyse all numerical data. Distribution of variables was checked using the Shapiro–Wilk (W) test, while homogeneity of variance was checked using Fisher's test. To compare the means, Student's t test for dependent (left–right) and independent (male–female) variables was used. Afterwards, one-way analysis of variance and Tukey's test were used for post-hoc analysis. If no similarity of variance occurred, the non-parametric Kruskal-Wallis test was used. The characterisation of developmental dynamics of the analysed parameters was based on linear and curvilinear regression analysis. The match between the estimated curves and measurement results was evaluated on the basis of the coefficient of determination (R^2). Differences were considered statistically significant at $p < 0.05$. The relationship between variables was also estimated with the Pearson correlation coefficient (r).

In an attempt to minimise measurement and observer bias, all measurements were completed by one experienced researcher (M.B.) specialising in image interpretation. Each measurement was reiterated 3 times under the same conditions but at different times, and then averaged. As shown in Table 2, the intra-class correlation coefficients calculated on the basis of an observer were statistically significant ($p < 0.01$) and of excellent reproducibility.

RESULTS

The mean values and standard deviations of the analysed parameters of primary ossification centre of the lateral parts of the occipital bone are shown in Tables 3 and 4, while those referring to the basilar part of the occipital bone are shown in Table 5.
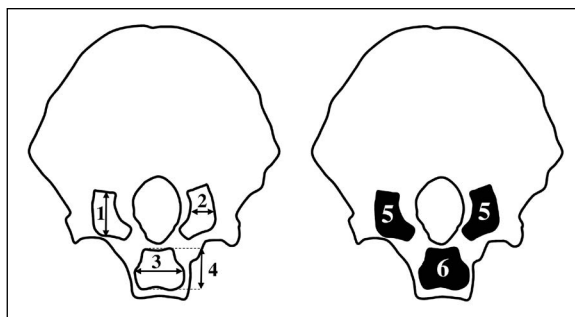
Figure 2. A measurement scheme of ossification centres of the lateral and basilar parts of the occipital bone: 1 — sagittal diameter of the lateral part; 2 — transverse diameter of the lateral part; 3 — transverse diameter of the basilar part; 4 — sagittal diameter of the basilar part; 5 — projection surface area of the lateral part; 6 — projection surface area of the basilar part.

Table 2. Intra-class correlation coefficients (ICC) values for inter-observer recurrence

Parameter	ICC
Right sagittal diameter of the lateral part	0.996*
Left sagittal diameter of the lateral part	0.995*
Right transverse diameter of the lateral part	0.997*
Left transverse diameter of the lateral part	0.998*
Transverse diameter of the basilar part	0.999*
Sagittal diameter of the basilar part	0.996*
Projection surface area of the right lateral part	0.998*
Projection surface area of the left lateral part	0.997*
Projection surface area of the basilar part	0.999*
Volume surface area of the right lateral part	0.997*
Volume surface area of the left lateral part	0.997*
Volume surface area of the basilar part	0.998*

ICC marked with asterisk (*) are statistically significant at $p < 0.0001$

The statistical analysis revealed neither significant sex nor laterality differences, which allowed us to compute one growth curve for each analysed parameter. The developmental dynamics of the sagittal and transverse diameters, projection surface area and volume of the lateral (right and left) parts followed proportionately in reference to gestational age expressed in weeks.

The mean sagittal diameter of the ossification centre of the lateral part of the occipital bone in the gestational age range of 18–30 weeks was between 8.37 ± 0.17 mm and 18.74 ± 1.06 mm on the right, and between 8.49 ± 1.05 mm and 15.36 ± 1.08 mm on the left, demonstrating a proportionate growth: $y = -3.714 + 0.681 \times age \pm 1.346$ ($R^2 = 0.79$).

Table 3. Right and left sagittal and transverse diameters of the lateral part of the occipital ossification centre

N	Lateral part of the occipital ossification centre							
	Sagittal diameter [mm]				Transverse diameter [mm]			
	Right		Left		Right		Left	
	Mean	SD	Mean	SD	Mean	SD	Mean	SD
3	8.37	0.17	8.49	1.05	5.13	0.19	5.00	0.23
4	8.97	0.32	9.66	0.21	5.50	0.19	5.44	0.24
4	9.95	1.29	10.19	0.34	6.03	0.17	6.02	0.18
3	8.62	1.52	11.00	0.22	6.48	0.08	6.48	0.08
3	9.00	0.31	11.65	0.27	6.77	0.12	6.78	0.13
3	11.90	2.14	12.19	0.30	6.99	0.02	7.01	0.00
4	13.93	2.06	12.77	0.27	7.17	0.01	7.17	0.01
1	14.26		13.24		7.41		7.41	
2	13.37	1.32	13.59	0.02	7.49	0.05	7.32	0.18
3	15.72	1.82	13.85	0.08	7.85	0.20	7.51	0.19
2	14.35	0.45	14.00	0.01	8.11	0.04	7.75	0.03
2	17.39	1.56	14.24	0.20	8.38	0.04	8.02	0.04
3	18.74	1.06	15.36	1.08	8.98	0.29	8.87	0.29

SD — standard deviation

Table 4. Projection surface area and volume of the lateral part of the occipital ossification centre

Gestational age [weeks]	N	Lateral part of the occipital ossification centre							
		Projection surface area [mm²]				Volume [mm³]			
		Right		Left		Right		Left	
		Mean	SD	Mean	SD	Mean	SD	Mean	SD
18	3	27.95	4.20	24.04	1.28	33.82	5.08	29.09	1.55
19	4	33.52	1.60	27.65	1.90	40.56	1.93	33.45	2.29
20	4	39.11	2.30	33.59	4.76	47.32	2.78	40.64	5.76
21	3	46.02	1.75	34.84	11.02	55.69	2.12	42.15	3.33
22	3	51.91	2.19	34.12	1.78	62.81	2.65	41.29	2.16
23	3	55.89	1.46	49.17	1.81	67.62	1.76	59.49	1.50
24	4	59.79	1.33	55.94	2.31	72.35	1.60	67.68	1.06
25	1	63.73		75.77		77.11		91.68	
26	2	65.95	0.47	64.35	6.97	79.80	0.57	77.86	0.54
27	3	71.43	2.49	76.28	2.85	86.43	3.02	92.30	3.54
28	2	75.58	0.36	83.34	0.98	91.45	0.43	100.84	1.02
29	2	78.99	1.00	91.02	1.07	95.58	1.21	110.14	1.49
30	3	92.00	3.15	94.39	6.21	111.32	11.08	114.22	9.93

SD — standard deviation

The mean transverse diameter of the ossification centre of the lateral part of the occipital bone in the gestational age range of 18–30 weeks increased from 5.13 ± 0.19 mm to 8.98 ± 0.29 mm on the right, and from 5.00 ± 0.23 mm to 8.87 ± 0.29 mm on the left, following the linear function: $y = 0.412 + 0.278 \times age \pm 0.269$ ($R^2 = 0.94$) (Figs. 3A, B).

The mean projection surface area of the ossification centre of the lateral part of the occipital bone ranged from 27.95 ± 4.20 mm² at 18 weeks of gestation to

Table 5. Sagittal and transverse diameters, projection surface area and volume of the basilar part of the occipital ossification centre

Gestational age [weeks]	N	Basilar part of the occipital ossification centre							
		Sagittal diameter [mm]		Transverse diameter [mm]		Projection surface area [mm²]		Volume [mm³]	
		Mean	SD	Mean	SD	Mean	SD	Mean	SD
18	3	5.76	0.08	5.06	0.08	22.71	0.63	29.52	0.82
19	4	5.94	0.13	5.24	0.13	24.29	1.17	31.57	1.52
20	4	6.21	0.10	5.51	0.10	26.67	0.90	34.67	1.17
21	3	6.49	0.14	5.79	0.14	29.29	1.36	38.08	1.77
22	3	6.71	0.06	6.01	0.06	31.49	0.56	40.94	0.73
23	3	6.86	0.03	6.16	0.03	33.00	0.31	42.89	0.40
24	4	6.93	0.04	6.23	0.04	33.65	0.42	43.75	0.55
25	1	6.98		6.28		34.19		44.45	
26	2	7.10	0.02	6.40	0.02	35.39	0.22	46.01	0.29
27	3	7.19	0.01	6.49	0.01	36.40	0.11	47.32	0.14
28	2	7.21	0.01	6.51	0.01	36.56	0.08	47.52	0.10
29	2	7.32	0.07	6.62	0.07	37.80	0.77	49.14	1.00
30	3	7.65	0.20	6.95	0.20	41.45	2.32	53.89	3.02

SD — standard deviation
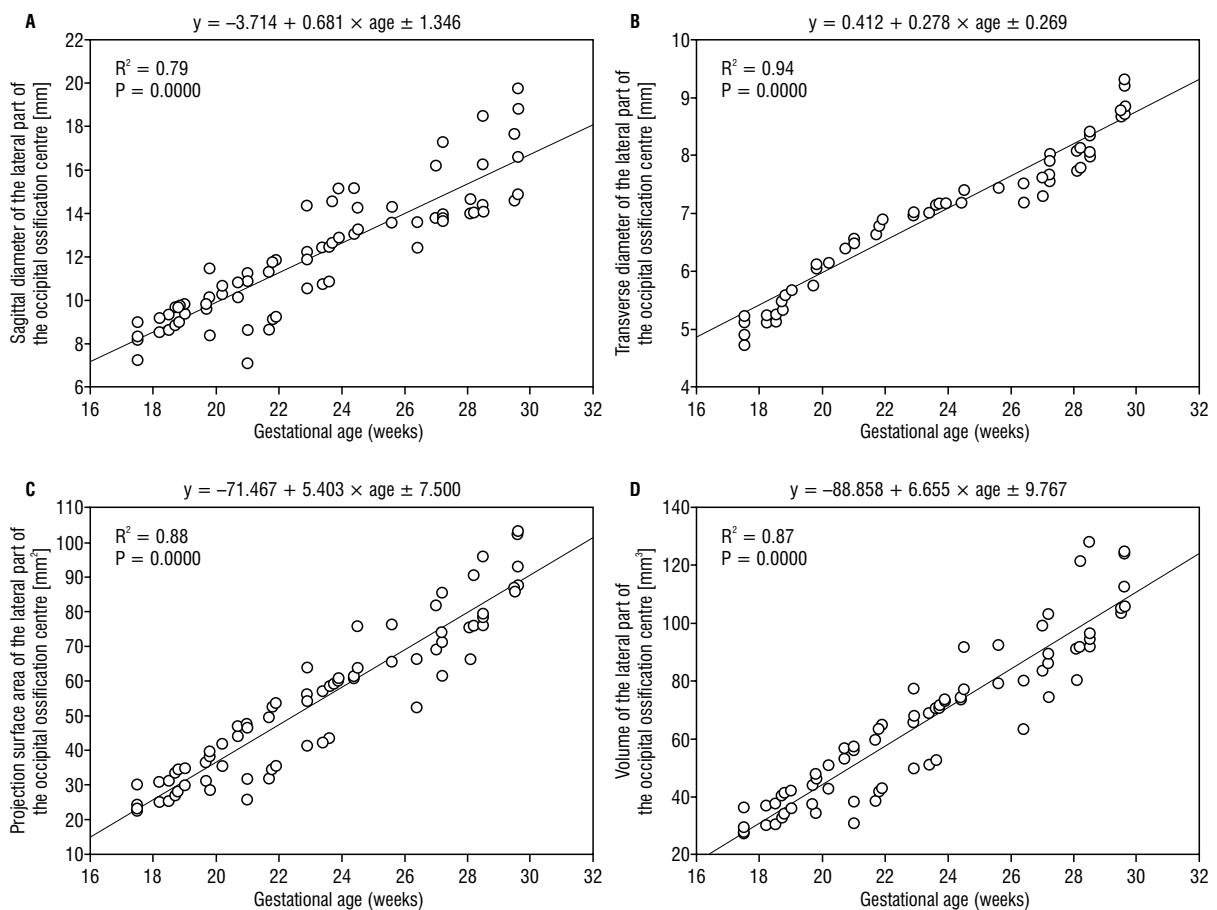
Figure 3. Regression lines for sagittal diameter (**A**), transverse diameter (**B**), projection surface area (**C**) and volume (**D**) of ossification centres of the lateral parts of the occipital bone.
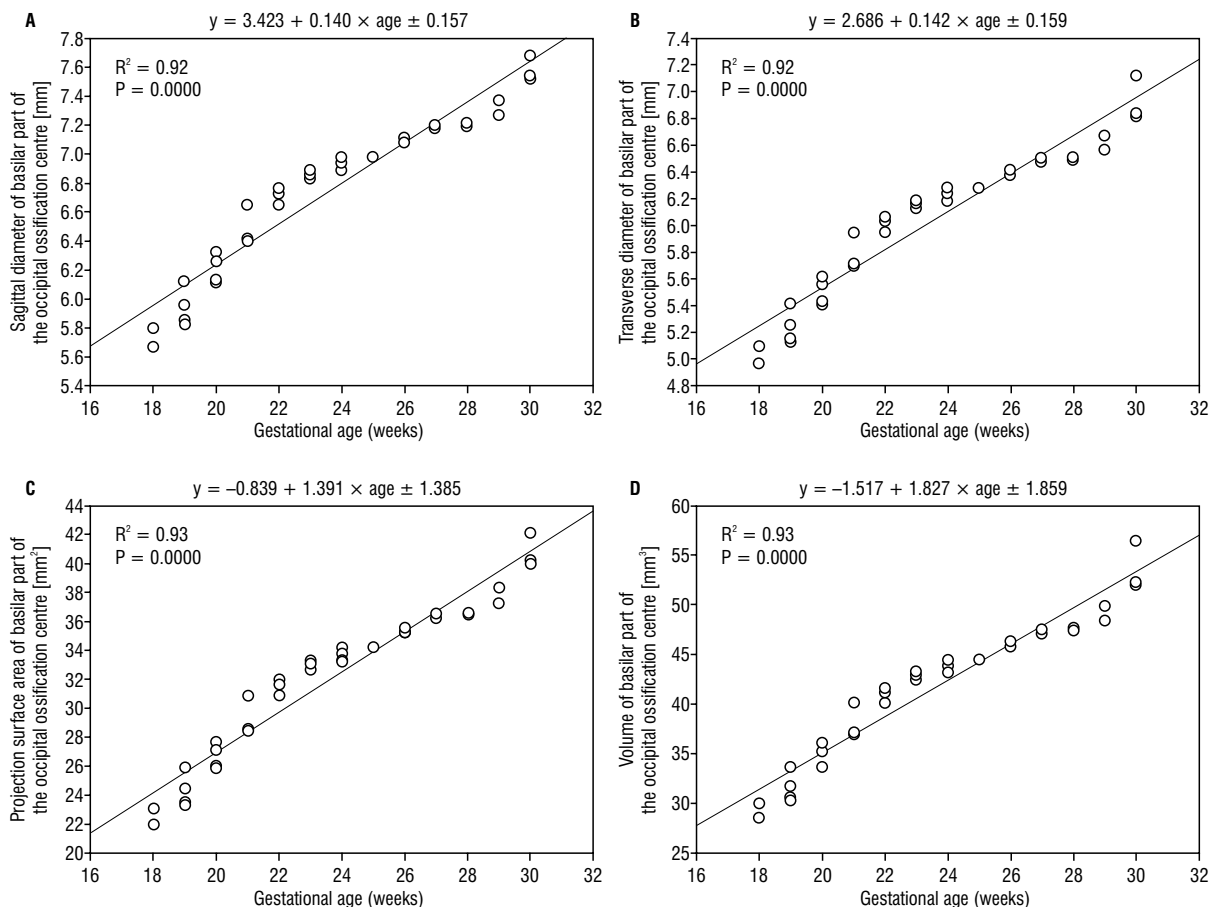
Figure 4. Regression lines for sagittal diameter (**A**), transverse diameter (**B**), projection surface area (**C**) and volume (**D**) of ossification centre of the basilar part of the occipital bone.

92.00 ± 3.15 mm^2 at 30 weeks of gestation on the right, and from 24.04 ± 1.28 mm^2 to 94.39 ± 6.21 mm^2, respectively, on the left, following the function: $y = -71.467 + 5.403 \times age \pm 7.500$ ($R^2 = 0.88$) (Fig. 3C).

The mean volume of the ossification centre of the lateral part of the occipital bone in the gestational age range of 18–30 weeks was between 33.82 ± 5.08 mm^3 and 111.32 ± 11.08 mm^3 on the right, and between 29.09 ± 1.55 mm^3 and 114.22 ± 9.93 mm^3 on the left, in accordance with the function: $y = -88.858 + 6.655 \times age \pm 9.767$ ($R^2 = 0.87$) (Fig. 3D).

The mean sagittal diameter of the ossification centre of the basilar part of the occipital bone in the gestational age range of 18–30 weeks was between 5.76 ± 0.08 mm and 7.65 ± 0.20 mm, demonstrating a proportionate growth: $y = 3.423 + 0.140 \times age \pm 0.157$ ($R^2 = 0.92$) (Fig. 4A).

The mean transverse diameter of the ossification centre of the basilar part of the occipital bone in

the gestational age range of 18–30 weeks revealed an increase from 5.06 ± 0.08 to 6.95 ± 0.20 mm, demonstrating a proportionate growth: $y = 2.686 + 0.142 \times age \pm 0.159$ ($R^2 = 0.92$) (Fig. 4B).

The mean projection surface area of the ossification centre of the basilar part of the occipital bone ranged from 22.71 ± 0.63 mm^2 at 18 weeks to 41.45 ± 2.32 mm^2 at 30 weeks of gestational age, according to the function: $y = -0.839 + 1.391 \times age \pm 1.385$ ($R^2 = 0.93$) (Fig. 4C).

The mean volume of the ossification centre of the basilar part of the occipital bone in the gestational age range of 18–30 grew from 29.52 ± 0.82 mm^3 to 53.89 ± 3.02 mm^3, following the linear model: $y = -1.517 + 1.827 \times age \pm 1.859$ ($R^2 = 0.93$) (Fig. 4D).

DISCUSSION

Zhang et al. [13] measured the basilar part of the occipital bone in 22 human foetuses aged 15 to 20 weeks of gestation and observed two patterns

of its ossification in foetuses with a CRL between 115 and 142 mm. In the first pattern found in 7 foetuses, the medial ossification centres of the basilar part of the occipital bone fused into one at an early stage of development. In the second pattern found in 6 foetuses, two medial ossification centres of the basilar part remained separate. The authors measured the length and width of the ossification centres of the basilar part of occipital bone. In foetuses with a CRL corresponding to the period between 17 and 20 weeks of gestational age, the length of the basilar part of the occipital bone was greater than its width. However, between 15 and 17 weeks of gestational age, the width of the basilar part increased faster than its length. The authors concluded that the developmental patterns depend on the developmental stage. The length of the ossification centres in foetuses aged 15 to 20 weeks of gestation ranged from 5.54 ± 0.07 mm to 7.83 ± 0.45 mm, while their width ranged from 3.58 ± 0.16 to 5.73 ± 0.69 mm.

With the use of a digital calliper Badiu et al. [1] measured the vertical and transverse diameters of the basilar and lateral parts of the occipital bone in 19 human foetuses aged 16 to 34 weeks of gestation. They found the vertical diameter of the basilar and lateral parts to increase from 5.54 to 11.14 mm and from 5.92 to 20.89 mm, respectively. The transverse diameter of the basilar and lateral parts increased from 3.96 to 12.24 mm and from 2.88 to 12.03 mm, respectively.

The present paper is the first to report morphometric parameters of ossification centres of the lateral and basilar parts of the occipital bone in human foetuses based on computed tomography with their growth models.

The size of the ossification centres in the lateral and basilar parts of the occipital bone followed linear functions of gestational age: $y = -3.714 + 0.681 \times age \pm 1.346$ for sagittal diameter in the lateral parts, $y = 0.412 + 0.278 \times age \pm 0.269$ for transverse diameter in the lateral parts, $y = -71.467 + 5.403 \times age \pm 7.500$ for projection surface area in the lateral parts, $y = -88.858 + 6.655 \times age \pm 9.767$ for volume in the lateral parts, $y = 3.423 + 0.140 \times age \pm 0.157$ for sagittal diameter in the basilar part, $y = 2.686 + 0.142 \times age \pm 0.159$ for transverse diameter in the basilar part, $y = -0.839 + 1.391 \times age \pm 1.385$ for projection surface area in the basilar part, and $y = -1.517 + 1.827 \times age \pm 1.859$ for volume in the basilar part.

In our previous study [6] about the development of the ossification centre of the squamous part of occipital bone in human foetuses, the growth dynamics of the vertical diameter followed the linear functions: $y = -6.462 + 1.109 \times age \pm 0.636$ on the right, and $y = -9.395 + 1.243 \times age \pm 0.577$ on the left. The transverse diameters of the supraoccipital and interparietal parts as well as projection surface area of the occipital squama ossification centre increased in relation to gestational age expressed in weeks, following the logarithmic functions: $y = -98.232 + 39.663 \times ln(age) \pm 0.721$, $y = -79.903 + 32.107 \times ln(age) \pm 0.974$, $y = -3062.89 + 1108.98 \times ln(age) \pm 29.476$, respectively. The volume of the occipital squama ossification centre increased in accordance with the quadratic function: $y = -330.105 + 1.554 \times age^2 \pm 32.559$.

Furthermore, in our study [5] of the development of the frontal squama ossification centre in human foetuses, the growth dynamics of its vertical diameter, projection surface area and volume followed the quadratic functions: $y = 13.756 + 0.021 \times age^2 \pm 0.024$, $y = 38.285 + 0.889 \times age^2 \pm 0.034$, and $y = -90.020 + 1.375 \times age^2 \pm 11.441$, respectively. However, its transverse diameter increased proportionately to gestational age, as $y = 0.956 + 0.956 \times age \pm 0.823$.

Regrettably, a lack of reports concerning ossification centres of the lateral and basilar parts of the occipital bone in the medical literature precludes a more detailed discussion on this topic.

Understanding the development of the occipital bone in human foetuses is indispensable for the detection of anomalies of the craniovertebral junction and fractures of the cranial base [10]. The cranial base supports the brain, and many congenital anomalies of the brain correspond to anomalies of the cranial base during development, such as basilar invagination, platybasia, or Chiari malformation [13]. One of such congenital bone defects is atlantooccipital assimilation, a disorder consisting of the presence of bone fusion between the first cervical vertebra and the occipital bone. This fusion is usually incomplete and refers only to the anterior atlantal arch and the anterior edge of the foramen magnum. Atlantooccipital assimilation is often linked to developmental anomalies of the first and second pharyngeal arches. This defect is accompanied by hypoplasia of the occipital bone, reduced clivus length, lack or abnormal formation

of the atlantooccipital joint, dislocation of the atlantoaxial joint and platybasia. Clinical signs may include an abnormally short neck, reduced cervical spine mobility, abnormal head posture, headache, pain in the neck and upper limbs, scapular elevation, weakness, numbness, dysphagia, dysarthria and torticollis. This anomaly may result in the formation of Chiari syndrome, which represents a group of various developmental disorders whose common feature is reduction of the posterior part of the cranial cavity which does not include the cerebellum or the lower part of the brainstem. Atlantooccipital assimilation may also result in compression or even complete closure of the vertebral artery by the bone canal, leading to dizziness, convulsions, mental disorders or fainting [11, 12].

Another anomaly of the occipital bone is basilar impression — invagination of the edges of the foramen magnum into the cranial cavity, resulting in a reduction of the capacity of the posterior cranial fossa. This invagination often co-exists with syndromes such as Klippel-Feil or Chiari, as well as atlantoaxial dislocations. This defect usually leads to serious neurological disorders and may result in the compression of spinal nerve roots, the spinal cord and brainstem, vascular or respiratory disorders [12].

The main limitation of this study was a relatively narrow gestational age group, ranging from 18 to 30 weeks, and a small number of cases, including 37 human foetuses.

CONCLUSIONS

The morphometric characteristics of primary ossification centres of the lateral and basilar parts of the occipital bone display neither sex nor laterality differences.

These primary ossification centres grow linearly with respect to their sagittal and transverse diameters, projection surface area, and volume.

The obtained morphometric data of primary ossification centres in the lateral and basilar parts of the occipital bone may be considered as normative for their respective prenatal weeks and may contribute to the estimation of gestational ages and the diagnostics of congenital defects.

Conflict of interest: None declared

REFERENCES

1. Badiu GA, Tarţa-Arsene E, Ispas AT, et al. Estimation of the age from fetal occipital bone. Rev Rom Anat Funcţ Clin Macro Microsc Antropol. 2019; 18(3): 165–168.
2. Bernard S, Loukas M, Rizk E, et al. The human occipital bone: review and update on its embryology and molecular development. Childs Nerv Syst. 2015; 31(12): 2217–2223, doi: 10.1007/s00381-015-2870-8, indexed in Pubmed: 26280629.
3. Chano T, Matsumoto K, Ishizawa M, et al. Analysis of the presence of osteocalcin, S-100 protein, and proliferating cell nuclear antigen in cells of various types of osteosarcomas. Eur J Histochem. 1996; 40(3): 189–198, indexed in Pubmed: 8922947.
4. Duarte WR, Shibata T, Takenaga K, et al. S100A4: a novel negative regulator of mineralization and osteoblast differentiation. J Bone Miner Res. 2003; 18(3): 493–501, doi: 10.1359/jbmr.2003.18.3.493, indexed in Pubmed: 12619934.
5. Grzonkowska M, Baumgart M, Badura M, et al. Morphometric study of the primary ossification center of the frontal squama in the human fetus. Surg Radiol Anat. 2020; 42(7): 733–740, doi: 10.1007/s00276-020-02425-7, indexed in Pubmed: 32025797.
6. Grzonkowska M, Baumgart M, Badura M, et al. Quantitative anatomy of the fused ossification center of the occipital squama in the human fetus. PLoS One. 2021; 16(2): e0247601, doi: 10.1371/journal.pone.0247601, indexed in Pubmed: 33621236.
7. Lee SK, Kim YS, Jo YA, et al. Prenatal development of cranial base in normal Korean fetuses. Anat Rec. 1996; 246(4): 524–534, doi: 10.1002/(SICI)1097-0185(199612)246:4<524::AID-AR11>3.0.CO;2-Q, indexed in Pubmed: 8955791.
8. Morimoto N, Ogihara N, Katayama K, et al. Three-dimensional ontogenetic shape changes in the human cranium during the fetal period. J Anat. 2008; 212(5): 627–635, doi: 10.1111/j.1469-7580.2008.00884.x, indexed in Pubmed: 18430090.
9. Nemzek WR, Brodie HA, Hecht ST, et al. MR, CT, and plain film imaging of the developing skull base in fetal specimens. Am J Neuroradiol. 2000; 21(9): 1699–1706, indexed in Pubmed: 11039353.
10. Shapiro R, Robinson F. Embryogenesis of the human occipital bone. Am J Roentgenol. 1976; 126(5): 1063–1068, doi: 10.2214/ajr.126.5.1063, indexed in Pubmed: 178231.
11. Skrzat J, Mróz I, Jaworek JK, et al. A case of occipitalization in the human skull. Folia Morphol. 2010; 69(3): 134–137, indexed in Pubmed: 21154282.
12. Wysocki J, Bubrowski M, Szymański I. Developmental anomalies of the atlantooccipital region and their meaning for disturbances of hearing and balance (in Polish). Otorynolaryngologia. 2003; 2(2): 65–71.
13. Zhang Q, Wang H, Udagawa J, et al. Morphological and morphometric study on sphenoid and basioccipital ossification in normal human fetuses. Congenit Anom (Kyoto). 2011; 51(3): 138–148, doi: 10.1111/j.1741-4520.2011.00322.x, indexed in Pubmed: 21848997.

ORIGINAL ARTICLE

Development and growth of the foot lumbricalis muscle: a histological study using human foetuses

Z.-W. Jin[1], S. Hayashi[2], K.H. Cho[3], G. Murakami[4], J. Wilting[5], J.F. Rodríguez-Vázquez[6]

[1]Department of Anatomy, Wuxi School of Medicine, Jiangnan University, Wuxi, Jiangsu, China
[2]Department of Anatomy, Division of Basic Medicine, Tokai University School of Medicine, Isehara, Japan
[3]Department of Neurology, Wonkwang University School of Medicine and Hospital, Institute of Wonkwang Medical Science, Iksan, Republic of Korea
[4]Division of Internal Medicine, Cupid Clinic, Iwamizawa, Japan
[5]Department of Anatomy, School of Medicine, Georg-August-Universität Göttingen, Germany
[6]Department of Anatomy and Embryology, School of Medicine, Complutense University, Madrid, Spain

Background: Our group has shown early development of the hand lumbricalis and hypothesized that, at midterm, the lumbricalis (LU) bundles flexor tendons to provide a configuration of "one tendon per one finger" (Cho K.H. Folia Morphol. 2012; 71, 3: 154–163). However, the study concentrated on the hand and contained no sections of near-term foetuses.

Materials and methods: The present examination of paraffin-embedded tangential sections along the planta from 25 embryos and foetuses at 6–40 weeks (15–320 mm crown-rump length) demonstrated that, at 8 weeks, the initial foot LU appeared in the proximal side of the common tendinous plate of all five deep tendons.

Results: After midterm, a drastic three-phase change occurred at the muscle origin: 1) the LU originated from each of the flexor digitorum longus tendon (FDLT), but abundant tenocyte candidates separated the muscle fibre from the tendon collagen bundle; 2) the LU arose from the covering fascia depending on increased thickness of the muscle; and 3) the LU muscle fibres intermingled with tendon collagen bundles and partly surrounded the tendon. Simultaneously, a dividing site of the FDLT migrated distally to accelerate the changes at the LU origin. These phases did not always correspond to the size of foetus after 30 weeks.

Conclusions: Consequently, in contrast to the hand LU, the delayed changes in the foot were characterised by involvement of the LU origin into a single common part of the FDLT. The quadratus plantae muscle fibres did not attach to the LU at any phase, and connected with the fourth and fifth toe tendons. (Folia Morphol 2021; 80, 4: 904–915)

Key words: flexor digitorum longus muscle, flexor halluces longus muscle, quadratus plantae muscle

INTRODUCTION

The lumbricalis (LU) in the foot seems to be considered a small muscle, the function of which is limited because minute control is unnecessary at the phalangeal joints of the toe and because the muscle often shows variations, including absence [17, 18]. Indeed, previous studies of finger tendons did not consider LU attachment [3, 8]. However, Cho et al. [6] paid special attention to early development of the hand LU and hypothesized that, at midterm, the LU rearranges the deep flexor tendons to provide a configuration of "one tendon per one finger". This hypothetical contribution of the LU onto tendon splitting from the common tendinous plate seems to be consistent with the fact that, in adults, crisscrossing of the deep tendon fibres frequently occurs at the LU muscle origin [13]. Although Cho et al. [6] tried to compare between the hand and foot, their study contained few observations of the foot and no demonstration of the near-term morphology. Near-term foetuses were likely to carry morphologies that were the same as or similar to that in children.

Dylevsky [8] reported, in contrast to superficial flexure tendons, that a single common tendon is transiently built by the union of tendons from the flexor digitorum profundus and flexor pollicis longus in human foetus hands. His reported "united tendon" was most likely to correspond to a "common tendinous plate" described by Cho et al. [6]. The common tendinous plate is seen much later than the finger separation with apoptosis. People may consider that a splitting of the common plate occurs by mechanical stress from the muscle movements of each finger. Further, the finger movement is likely to accelerate the tendon splitting. Therefore, how and when the common tendinous plate disappears is an interesting viewpoint in the human foetal anatomy. However, independent movement of a single finger (e.g., such as that of a pianist) seems to be unnecessary for the foetus foot. Cho et al. [6] failed to find the plate in the foot at midterm, possibly because almost all of their observations were based on transverse sections. Rather than transverse sections, sectional planes tangential to the hand palm or foot planta aspect provide a much better understanding of the anatomy of the LU and flexor tendons.

In contrast to the flexor digitorum profundus tendons in the hand palm, the flexor digitorum longus tendon (FDLT) is one tendon at the posterior half of the planta and divides into four tendons at the mid-planta near the metatarsal joints. However, there seemed to be no information regarding the topographical relation of the LU origin with the dividing site of the FDLT. We do not know whether the LU plays a role in the re-arrangement of FDLT at or after division. Likewise, morphology near term is also interesting because toe movements in utero may accelerate tendon division. Consequently, using tangential sections, the aim of this study was to clarify the foetal morphology of the LU muscle origins with special reference to the topographical relation to the four growing deep tendons.

MATERIALS AND METHODS

The study was performed in accordance with the provisions of the Declaration of Helsinki 1995 (as revised in 2013). We examined the paraffin-embedded histology of 28 embryos and foetuses at 6–15 weeks of estimated gestational age (crown-rump length [CRL] 15–118 mm): 7 embryos and early foetuses at 6–8 weeks (CRL 15–31 mm), 6 foetuses at 12–15 weeks (CRL 70–118 mm), and 15 foetuses at 31–40 weeks (CRL 260–320 mm).

Five embryonic and three foetal specimens belonged to the Blechschmidt collection at the Medical Museum of Georg-August-Universität Göttingen. Although the sectional plane was sagittal to the head and trunk, we found five specimens containing a tangentially-cut foot. Most sections were stained with haematoxylin and eosin (HE), and a small amount were stained with azan or Masson trichrome. The use of this collection did not require specific approval of the Institute. The other 20 foetuses were a part of the large collection kept at the Department of Anatomy and Embryology, School of Medicine, Universidad Complutense, Madrid; the foetuses were the result of miscarriages and ectopic pregnancies at the Department of Obstetrics of the University. All sections were tangential along the plantar or palmar aspect and they were stained with HE. The use of the Spanish specimens was approved by the Complutense University Ethics Committee (B08/374).

RESULTS

Observations of embryos and early and midterm foetuses

At 6 weeks, the lumbricalis did not yet appear (Fig. 1). Rather than along the superficial side, the flexor digitorum brevis tendon lied between the FDLT: thus, the superficial and deep tendons appeared to be intercalated (Fig. 1A–C). A single FDLT ran distally along a long course in almost two-thirds of the planta. In the
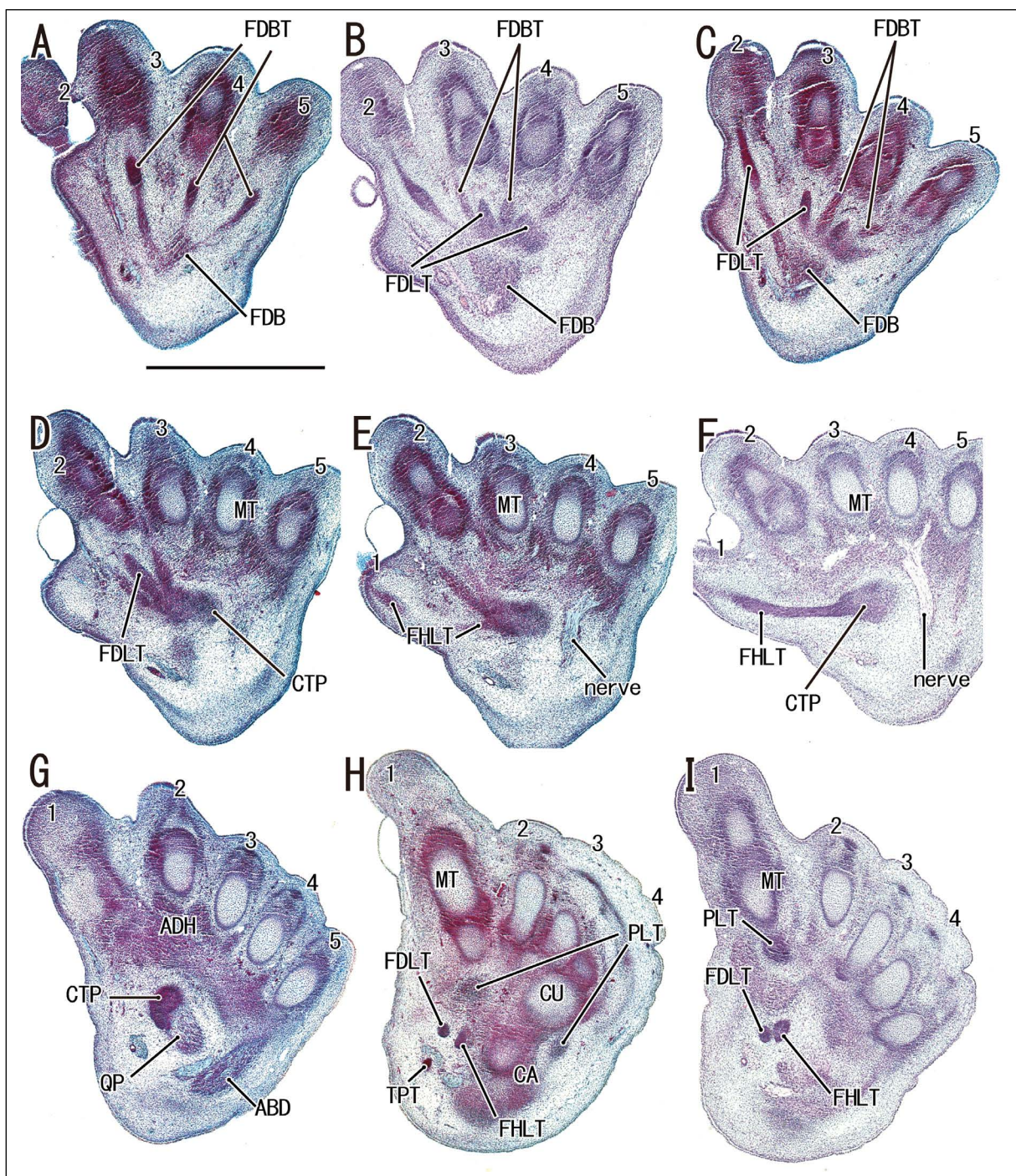
Figure 1. A–F. Early development of the flexor tendons in the foot planta. Crown-rump length 15 mm. Tangential sections along the planta. Haematoxylin and eosin staining. Panel A displays the most superficial plane near the skin, while panel I exhibits the deepest plane in the figure. In panels A–C, the flexor digitorum brevis tendon (FDBT) appears to interdigitate with the flexor digitorum longus tendon (FDLT). In panels D–F, the flexor halluces longus tendon (FHLT) joins the FDLT to provide a common tendinous plate (CTP). The quadratus plantae (QP) inserts to the posterior margin of the common plate (panel G). All panels were prepared at the same magnification (scale bar in panel A, 1 mm). Either the lumbricalis or interosseous is not yet developed; ABD — abductor digiti minimi; ADH — adductor hallucis; CA — calcaneus; CU — cuboid; FDB — flexor digitorum brevis; MT — metatarsal bone; PLT — peroneus longus tendon; TPT — tibialis posterior tendon.

deep and distal side of the muscle belly of the flexor digitorum brevis, the FDLT joined the flexor halluces longus tendon to provide a common tendinous plate (Fig. 1D–F). The quadratus plantae inserted to the deep and posterior part of the common plate (Fig. 1G). At 7–8 weeks, however, the flexor digitorum brevis
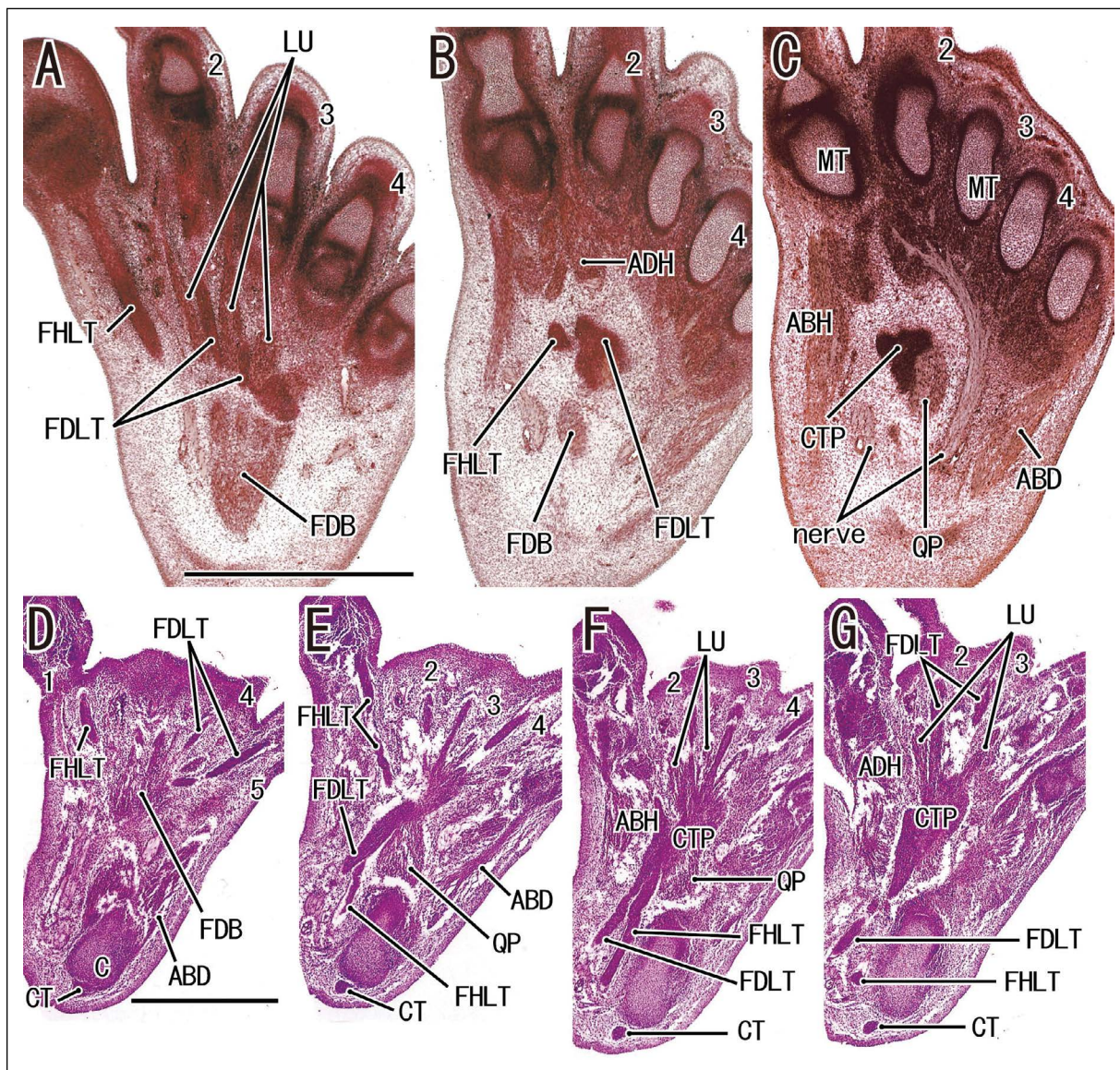
Figure 2. A–G. Early development of the foot lumbricalis; **A–C.** Crown-rump length (CRL) 30.5 mm; **D–G.** CRL 28 mm. Tangential sections along the planta. Haematoxylin and eosin staining. Panels A and D display the most superficial plane near the skin in each specimen. In panels A and F, the initial lumbricalis (LU) is lying between the flexor digitorum longus tendons (FDLT, numbers indicate the corresponding finger). In panels B, C, F and G, the flexor halluces longus tendon (FHLT) joins the FDLT to provide a common tendinous plate (CTP). The quadratus plantae (QP) inserts to the common plate (panels C, F). Panels A–C or D–G were prepared at the same magnification (scale bars in panels A and D, 1 mm); ABD — abductor digiti minimi; ABH — abductor hallucis; ADH — adductor hallucis; C — calcaneus; CT — calcaneus tendon; FDB — flexor digitorum brevis; MT — metatarsal bone.

tendon was laid over and along the superficial aspect of the FDLT. The initial LU appeared between the FDLT (Fig. 2). Thus, it was located in the deep side of the superficial tendons. Notably, the common tendinous plate appeared not to attach to the initial lumbricalis, but it extended in a layer deeper than the LU (Fig. 2A, B). However, after enlargement of the common tendinous plate, the lumbricalis proximal end appeared to attach to the plate (Fig. 2F, G).

We failed to obtain complete tangential sections at midterm, but the sectional plane was much or less tilted (Fig. 3). Moreover, abortion manipulation might provide abundant red blood cells scattering in and between muscles. A common tendinous plate had already disappeared between the FDLT and flexor hallucis longus tendon. The foot lumbricalis did not originate from the common plate, but from the FDLT itself (Fig. 3D–F).

Observations of near-term foetuses

At the beginning of this study, we were confused regarding the variations in shape, location, and origin of the LU in near-term foetuses because multiple

907
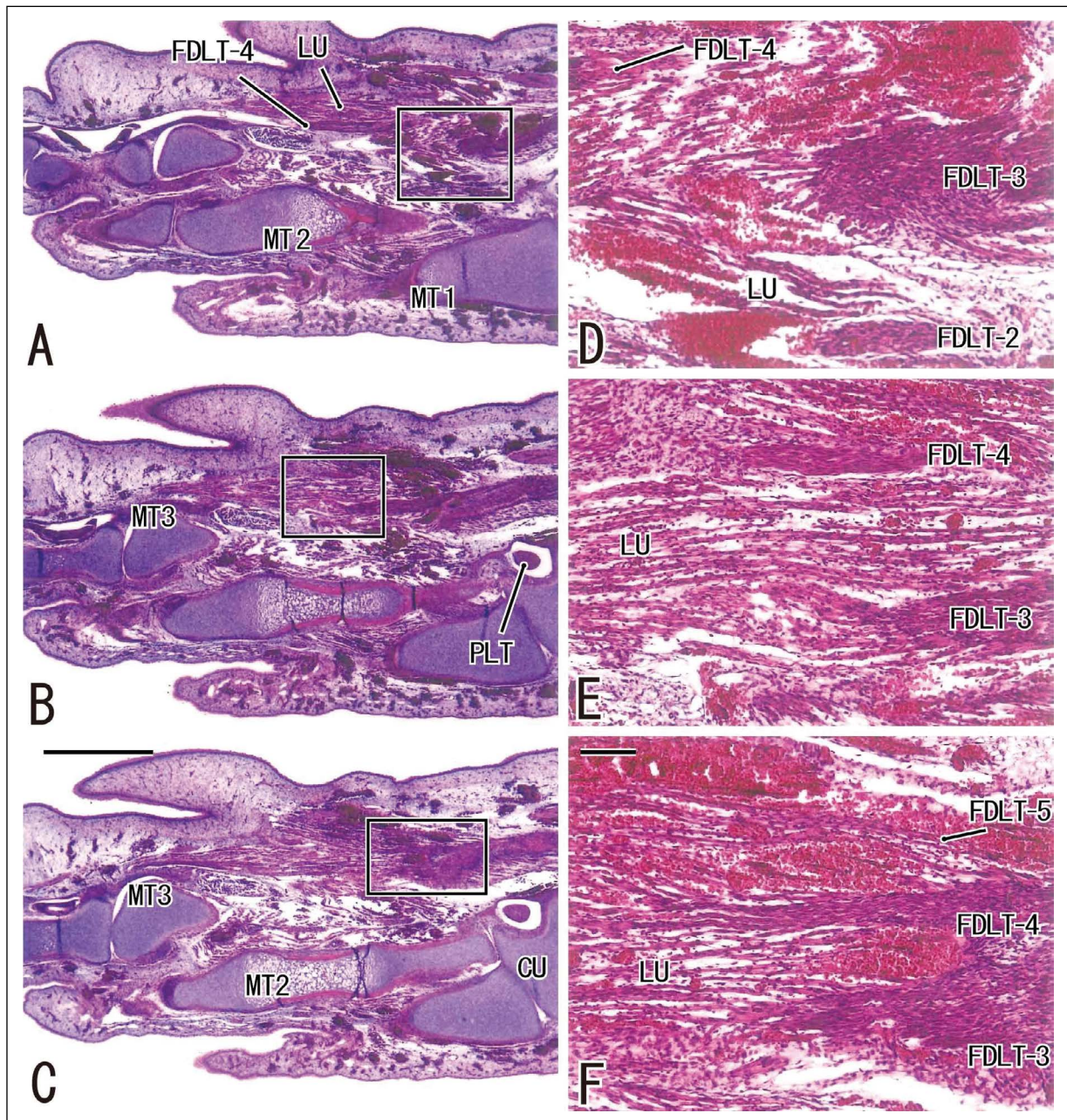
Figure 3. A–F. Foot lumbricalis at midterm. Crown-rump length 118 mm. Tilted tangential sections along the planta. Haematoxylin and eosin staining. Panel A displays the most superficial plane near the skin in the figure. Panels D–F are higher-magnification views of squares in panels A–C, respectively. The lumbricalis (LU) originate from the flexor digitorum longus tendon (FDLT): the third toe tendon (panel E) and the third-fifth tendons (panel F). Abortion manipulation might result in abundant red blood cells that scatter in and between the muscles. Panels A–B (or D–F) were prepared at the same magnification (scale bar: 1 mm in panel A; 0.1 mm in panel F); CU — cuboid; MT — metatarsal bone; PLT — peroneus longus tendon.

stages appeared to be mixed in a single section. After 30 weeks, the LU morphology as well as the growth was different between specimens irrespective of the age or size. Below, we describe the most likely sequence of the morphological changes.

First, the LU muscle origin from the FDLT appeared to be established in the distal side of the dividing site of the tendon (Fig. 4A–F). The muscle fibre did not connect to the tendon collagen bundle; however, there was a narrow interface tissue containing abundant cells presumed tenocytes (Fig. 5A–C). Second, the LU grew to provide a thick muscle belly at the posterior or proximal half and was covered by fascia (Fig. 6A–C). Because of the thick muscle belly, the LU
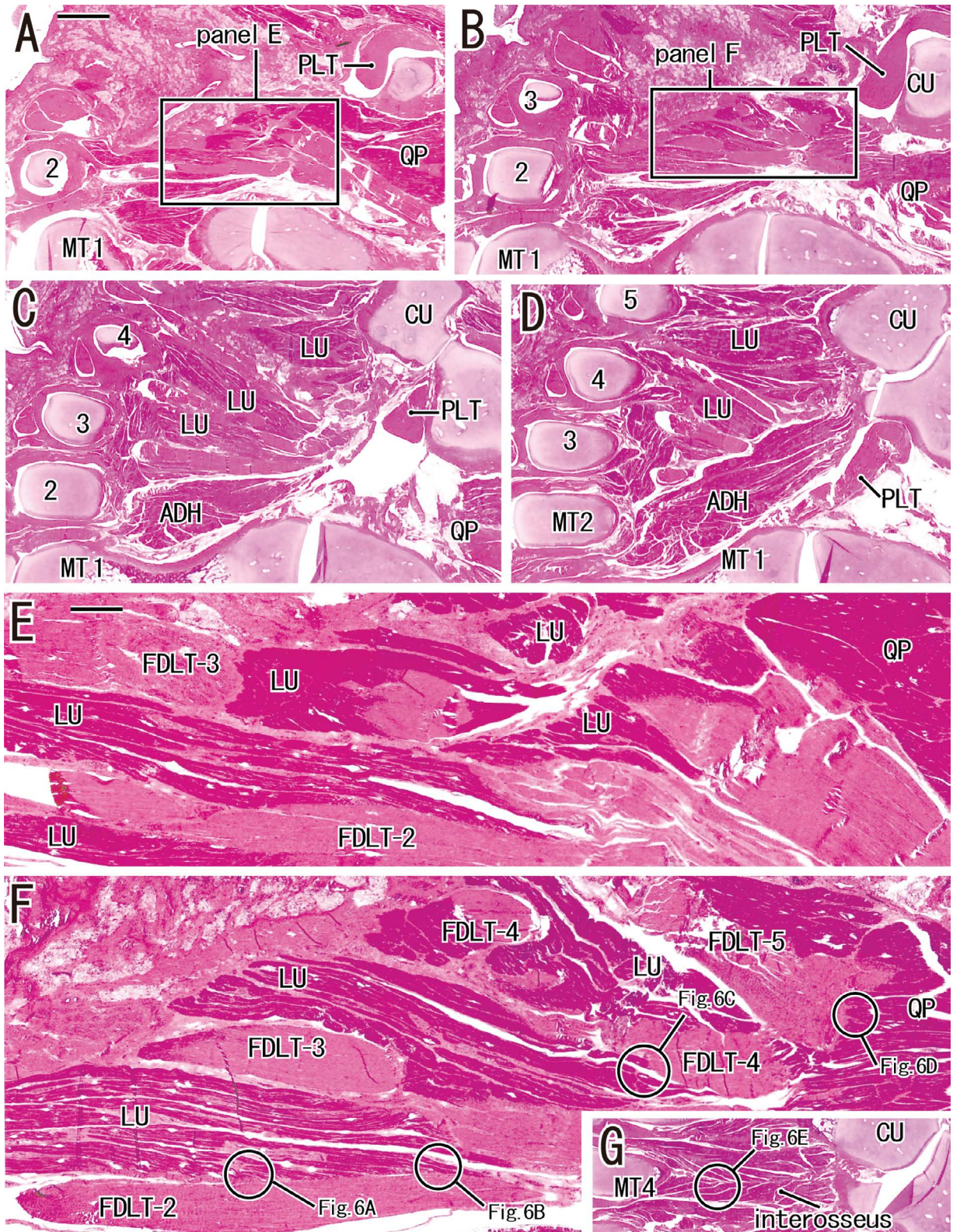
Figure 4. A–F. Foot lumbricalis origins from deep tendons near term. Crown-rump length 328 mm. Tangential sections along the planta. Haematoxylin and eosin staining. Panel A displays the most superficial plane near the skin in the figure. Panels E and F are higher magnification views of squares in panels A and B, respectively. Panel G, showing the interosseous muscle between the third and fourth toes, corresponds to a plane deeper than panel F. The lumbricalis (LU) is surrounded by the flexor digitorum longus tendons (FDLT), but due to a slightly wavy course of the tendons, the muscle origin appears to be irregularly intermingled with deep tendons (panels E, F). Higher magnification views of the lumbricalis origin from the deep tendon are shown in Figure 6. Panels A–D (or E and F) were prepared at the same magnification (scale bars: 10 mm in panel A; 1 mm in panel E); CU — cuboid; MT — metatarsal bone; PLT — peroneus longus tendon; QP — quadratus plantae.
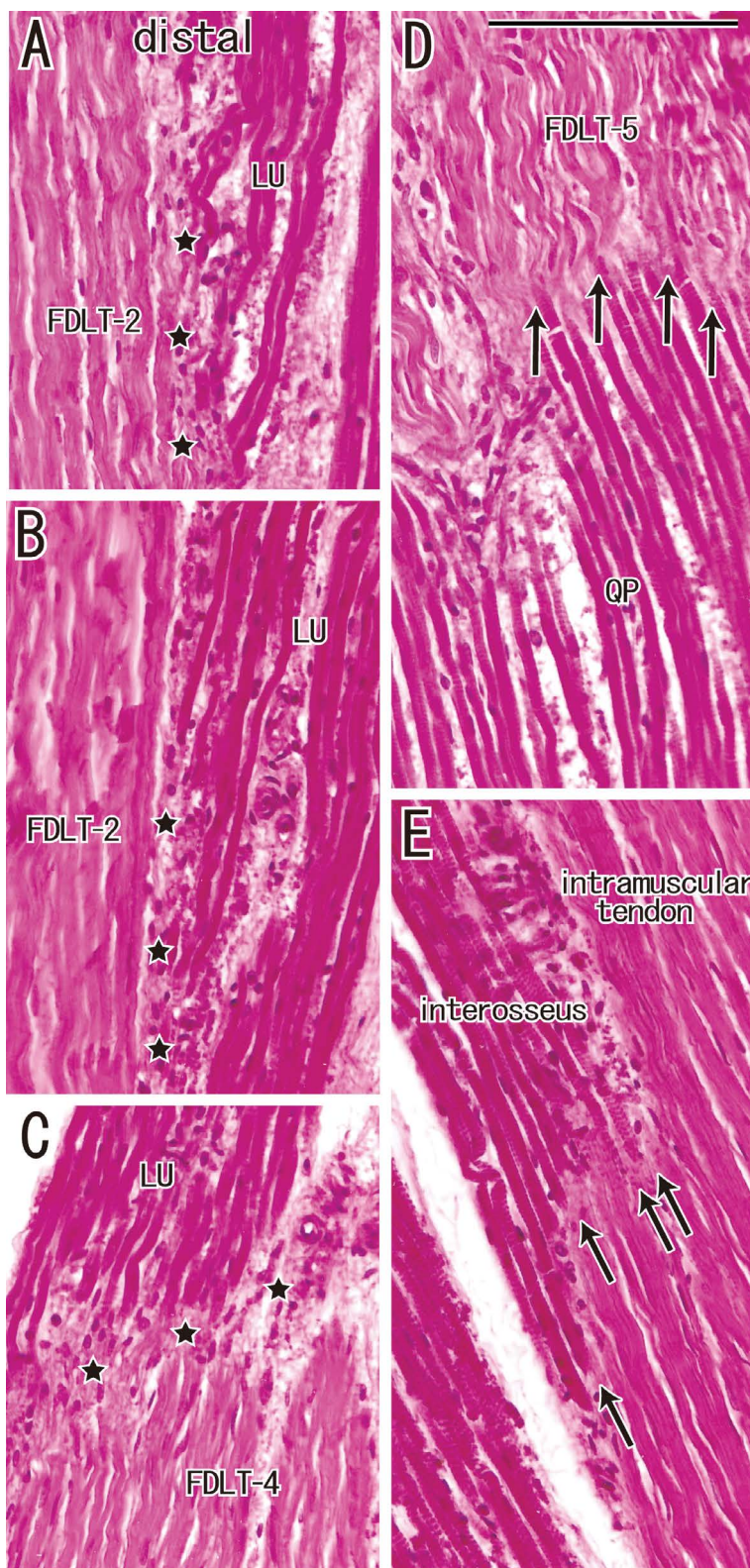
Figure 5. A–E. Histology of the lumbricalis origin: a difference from other muscle origins (higher magnification views of Fig. 4). The upper side of each panel corresponds to the distal side of the specimen. Panels A–C, corresponding to circles in Figure 4F, display foot lumbaricalis origins (LU). Panel D (corresponding to a circle in Fig. 4F) and panel E (a circle in Fig. 4G) exhibit the quadratus plantae insertion (QP) and the plantar interosseous origin, respectively. Along the flexor digitorum longus tendons (FDLT), muscle fibres of the foot lumbricalis attach to relatively loose connective tissue containing abundant tenocyte candidates (stars in panels A–C). Muscle fibres of the QP and interosseous are connected to a collagen fibre bundle of tendons (arrows in panels D, E). All panels were prepared at the same magnification (scale bar in panel D, 0.1 mm).
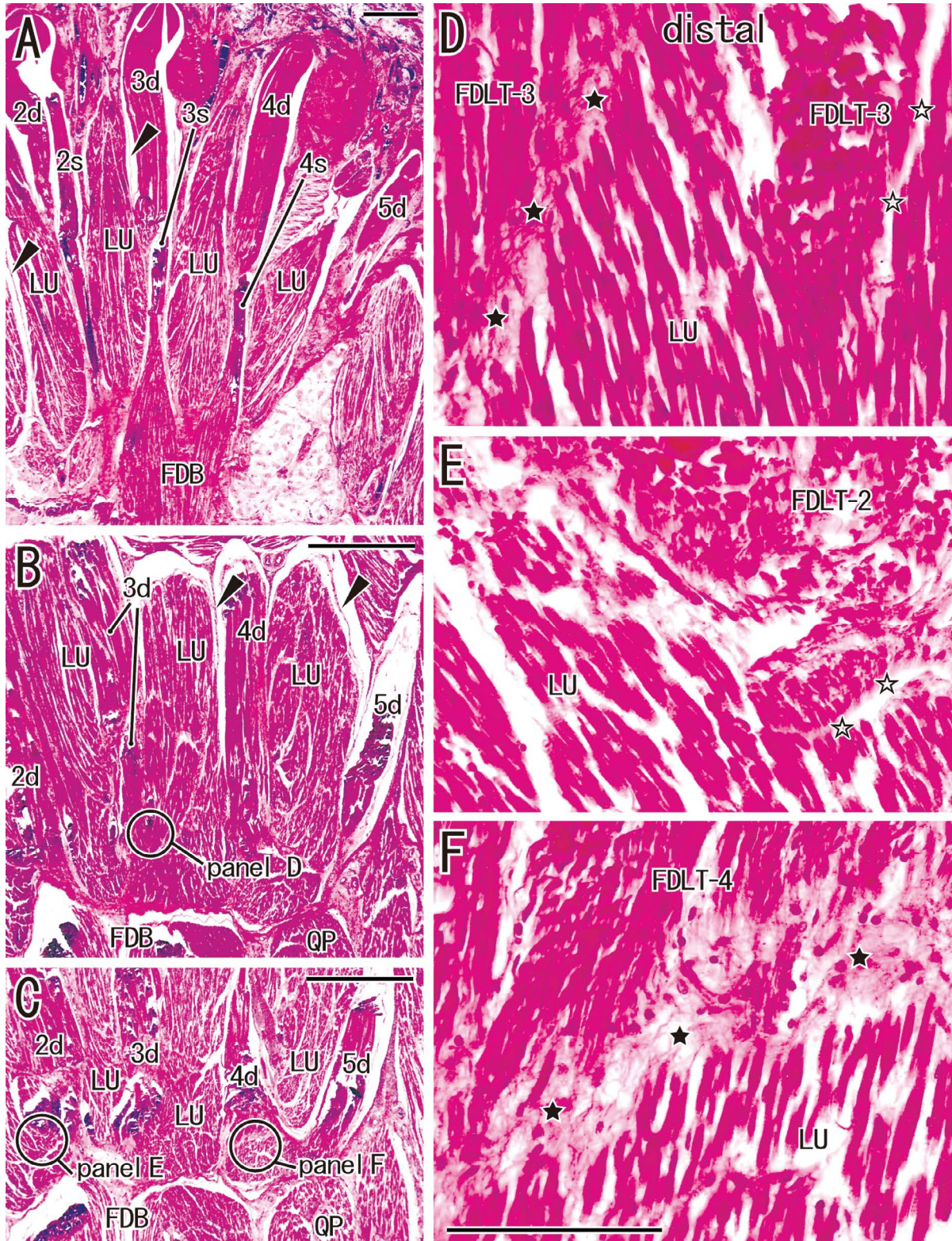
Figure 6. A–F. Increased thickness of the lumbricalis and a start of the intermingling with deep tendons. Crown-rump length 295 mm. Tangential sections of a specimen without a direct origin of the lumbricalis (LU) from deep tendons. The proximal part of the LU is thick between superficial tendons 2s–4s in panel A. In deeper planes (panels B and C), the LU is surrounded by or intermingled with deep tendons 2d–5d. Each of the LU muscles is surrounded by fascia (arrowheads in panels A and B). Panels D–F are higher-magnification views of circles in panels B and C. Because the flexor digitorum longus tendon (FDLT) is partly surrounded by the LU, in panels D and F, the LU muscle fibres are seen in the proximal side of the tendon. There is fibrous tissue (fascia; black stars in panels D, F) or a narrow space (open stars in panels D, E) between the FDLT and LU. Panels D–F were prepared at the same magnification (scale bar: 1 mm in panels A–C; 0.1 mm in panel F); FDB — flexor digitorum brevis; QP — quadratus plantae.
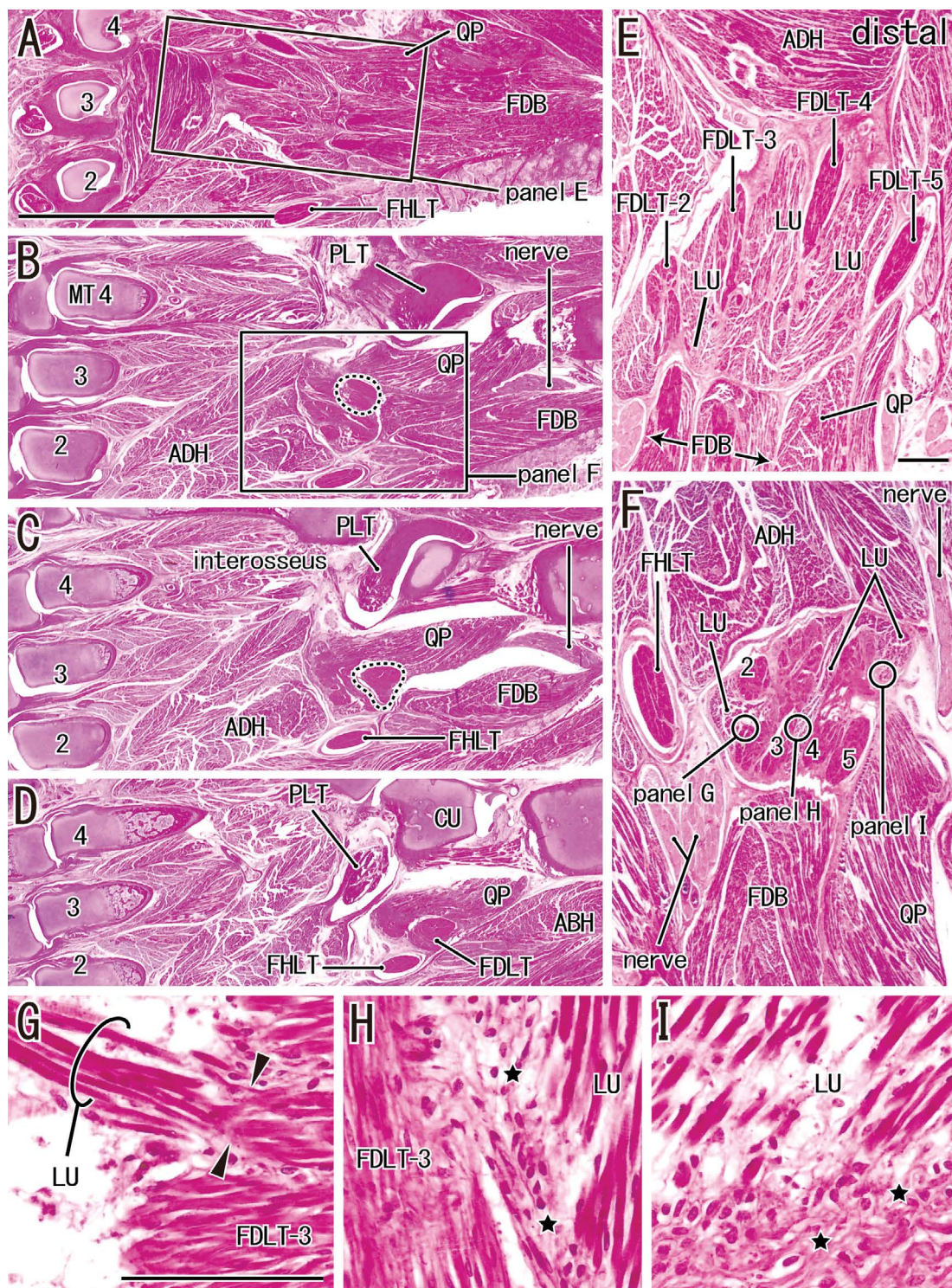
Figure 7. A–I. Intermingling between the lumbricalis and tendon near and at the division of the flexor digitorum longus near term. Crown-
-rump length 274 mm. Tangential sections deeper than the flexor digitorum brevis tendons. Haematoxylin and eosin staining. Panel A displays
the most superficial plane near the skin in the figure. Panels E and F are higher magnification views of squares in panels A and B, respectively.
Panels G–I are higher magnification views of three circles in panel F. The lumbricalis (LU) is surrounded by and intermingled with the flexor
digitorum longus tendons (FDLT; panels E, F). A major part of the FDLT, encircled by a dotted line in panels B and C, continues to the FDLT in
panel D: it is composed of the fourth and fifth deep tendons. Another part the tendons, largely from the second and third tendons, receives
the quadratus plantae (QP; panels C, D). The QP is separated from the LU by fibrous tissue (panels E, F). Panel G exhibits a rare connection
(arrowheads) between the LU and a deep tendon. Panels H and I show an interface tissue (stars) between the LU and tendon. Panels A–D,
panels E and F or panels G–I were prepared at the same magnification, respectively (scale bar: 5 mm in panel A; 1 mm in panel E; 0.1 mm in
panel G); ABH — abductor hallucis; ADH — adductor halluces; CU — cuboid; FHLT — flexor hallucis longus tendon; MT — metatarsal bone;
PLT — peroneus longus tendon.

extended superficially, as opposed to at the level of the deep tendons. Thus, in superficial sections, the LU appeared to be surrounded by the flexor digitorum brevis tendons rather than FDLT (Fig. 6A). Third, the proximal end of the LU became intermingled with collagen bundles of deep tendons at and near the dividing site of the FDLT, and they together provided a musculotendinous complex (Figs. 6C; 7). The proximal parts of the LU were divided by tendons into several clusters. Thus, some of the muscle clusters were located in the "proximal or posterior" side of the tendon. Therein, in contrast to the initial origin from the tendon, the LU distal end controversially appeared to "insert" into the FDLT (Fig. 6D–F). The intermingling and dividing process made parts of the LU surround deep tendons. Conversely, we rarely found a close relation between the muscle fibre and tendon (Fig. 7G); it was also rare to find a loose interface tissue between the LU and the tendon (Fig. 7H, I). In accordance with those changes, the dividing site of the FDLT appeared to migrate distally when compared with the peroneus longus tendon that transversed the foot medially in the deep side of the FDLT (Fig. 4B vs. Fig. 7B).

In the deep side of the LU, the interosseous contained a thin intramuscular tendon to provide a bipennatus appearance (Figs 4G; 7C). The quadratus plantae did not attach to the LU (Figs. 6C; 7C). In contrast to the LU origin from deep tendons, the nearby muscle origin or insertion was composed of a direct connection between a collagen fibre bundle and a muscle fibre (Fig. 5D, E). At the dividing site of the FDLT, the laterally-located elements (the fourth and fifth tendons) received the quadratus plantae, while the medially-located elements (the second and third tendons) tended to continue posteriorly to a single tendon of the flexor digitorum longus (Fig. 7A–D).

DISCUSSION AND CONCLUSIONS

The most striking observation in this study seemed to be the great variation in LU morphologies in near-term foetuses. In contrast to a rather stable morphology in early and midterm foetuses, at and near the muscle origin near term, we found four evidences: phase 1) the LU origin was interposed by abundant cells presumed tenocytes; phase 2) the growing LU expanding the origin to the covering fascia; phase 3) the muscle proximal end intermingling with deep tendons to provide a musculotendinous complex; and phase 4) several proximal muscle clusters divided by ten-
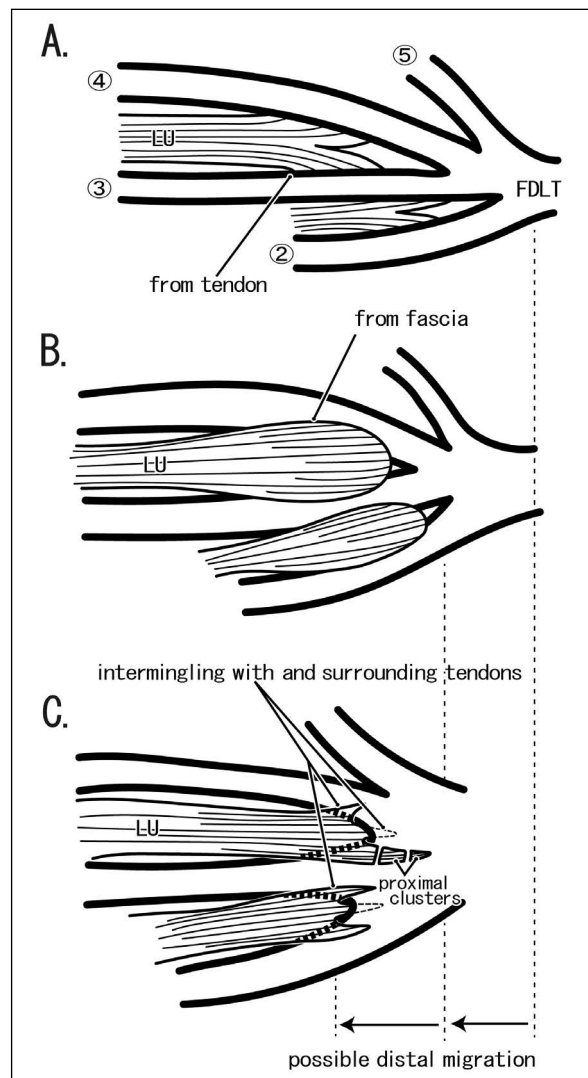
Figure 8. A–C. A hypothetical change in the lumbricalis origin from deep flexor tendons. The flexor digitorum longus tendon (FDLT) is numbered as ②, ③, ④, and ⑤. In the early phase (panel **A**), the lumbricalis (LU) originates from each division of the FDLT. In the mid-phase (panel **B**), the LU appears to arise from the covering fascia depending on increased thickness of the muscle. In the late phase (panel **C**), the LU muscle fibres intermingle with and partly surround the tendon. As these changes advance, a dividing site of the FDLT migrates distally to accelerate the involvement of the lumbricalis into tendons. The LU is not drawn between the fourth and fifth toes.

dons. These morphologies were not simple variations, but were most likely sequential changes or growth (early-, mid- and late-phases in Fig. 8). Except for phase 1, the other phases were not described in the hand, possibly because of no observations of near-term specimens [6]. Although a morphometric analysis was not performed, a distal migration of the dividing site of the FDLT was likely and it seemed to accelerate the intermingling (phase 3) and dividing (phase 4) of the proximal part of

the LU. The distal migration of the tendon dividing site might be an analogy of the recession of flexor muscle bellies onto the foream, although the direction was reversed between the hand and foot [14]. A mixture of the LU and tendon might be limited between the first and second toes, resulting in a higher incidence (around 10%) of second LU absence in the foot [17, 18].

Cho et al. [6] considered that, based on observations of cross sections from midterm foetuses, the common tendinous plate is absent between the FDLT and flexor hallucis tendon. Actually, present observations also ensure the absence at midterm. However, their tangential sections were very limited in number. The present tangential sections demonstrated the foot common plate in embryos and early foetuses. Therefore, the union of all five tendons was a process common between the hand and foot. After (and independent of) programmed cell death for sculpturing the fingers/toes, the common plate seemed to appear to unite flexure tendons. A tendon to the thumb or first toe is separated from the others until midterm. However, in contrast to the hand, strict correspondence between the LU and deep tendon became lost in the near-term foot. Perhaps, the hand of near-term foetuses might also carry a morphology or variation similar to the foot LU. As shown in the quadratus plantae and interosseous, to maintain the initial muscle morphology throughout prenatal life, a definite connection seemed to be necessary between the muscle fibre and a tendon collagen bundle without an interface tissue. Leijnse [13] considered that, in the hand, tendon splitting occurs due to finger movements in utero. Limited, independent movement of the toes might make a difference in the LU between the hand and foot, although we do not have ultrasound information of living foetuses.

In the extremities, a muscle belly develops in accordance with its tendon at the same time [4, 7, 15, 20]. Foetal development of the muscle-tendon interface has been one of the leading topics in anatomical research [1, 2, 22]. In contrast to the concept of the definite connection between the muscle and tendon, our group has demonstrated a delayed morphological change at the origin or insertion of human foetus striated muscles at multiple sites [5, 9, 11, 12, 16, 21]. Because an anchoring of striated muscle fibre to a collagen bundle requires a large molecular complex including dystrophin, desmin, nitric oxide synthase, and other proteins, a destruction and rebuilding of the complex seemed to be unlikely in foetal development, especially in the very late stage between 30 and 40 weeks [10, 19]. Therefore, the aforementioned delayed change in the origin and insertion seemed to occur in the "collagen side" of the enthesis, i.e., the muscle fibre attachment moves from a collagen bundle of the tendon, via that of the fascia to the musculotendinous complex at the division of the FDLP.

Acknowledgements

Conflict of interest: None declared

REFERENCES

1. Abe S, Rhee Sk, Osonoi M, et al. Expression of intermediate filaments at muscle insertions in human fetuses. J Anat. 2010; 217(2): 167–173, doi: 10.1111/j.1469-7580.2010.01246.x, indexed in Pubmed: 20500537.
2. Benjamin M, Ralphs JR. The cell and developmental biology of tendons and ligaments. Int Rev Cytol. 2000; 196: 85–130, doi: 10.1016/s0074-7696(00)96003-0, indexed in Pubmed: 10730214.
3. Chaplin DM, Greenlee TK. The development of human digital tendons. J Anat. 1975; 120(Pt 2): 253–274, indexed in Pubmed: 1201962.
4. Charvet B, Ruggiero F, Le Guellec D. The development of the myotendinous junction. A review. Muscles Ligaments Tendons J. 2012; 2(2): 53–63, indexed in Pubmed: 23738275.
5. Cho KH, Jin ZW, Abe H, et al. Tensor fasciae latae muscle in human embryos and foetuses with special reference to its contribution to the development of the iliotibial tract. Folia Morphol. 2018; 77(4): 703–710, doi: 10.5603/FM.a2018.0015, indexed in Pubmed: 29500891.
6. Cho KH, Kim JH, Ha YS, et al. Development of the deep flexor tendons and lumbricalis muscle in the hand and foot: a histological study using human mid-term foetuses. Folia Morphol. 2012; 71(3): 154–163, indexed in Pubmed: 22936550.
7. Deries M, Schweitzer R, Duxson MJ. Developmental fate of the mammalian myotome. Dev Dyn. 2010; 239(11): 2898–2910, doi: 10.1002/dvdy.22425, indexed in Pubmed: 20865781.
8. Dylevsky I. Tendons of the m. flexor digitorum superficialis et profundus in the ontogenesis of the human hand. Folia Morphol. 1968; 16: 124–130.
9. Hayashi S, Hirouchi H, Murakami G, et al. Transient connection or origin of the inferior pharyngeal constrictor during fetal development: A study using human fetal sagittal sections. Ann Anat. 2020; 228: 151438, doi: 10.1016/j.aanat.2019.151438, indexed in Pubmed: 31726208.

10. Heydemann A, McNally E. NO more muscle fatigue. J Clin Invest. 2009; 119(3): 448–450, doi: 10.1172/jci38618, indexed in Pubmed: 19306501.

11. Jin ZW, Abe H, Jin Y, et al. Positional changes in tendon insertions from bone to fascia: development of the pes anserinus and semimembranosus muscle insertion in human foetuses. Folia Morphol. 2016; 75(4): 503–511, doi: 10.5603/FM.a2016.0020, indexed in Pubmed: 27830876.

12. Jin ZW, Jin Y, Yamamoto M, et al. Oblique cord (chorda obliqua) of the forearm and muscle-associated fibrous tissues at and around the elbow joint: a study of human foetal specimens. Folia Morphol. 2016; 75(4): 493–502, doi: 10.5603/FM.a2016.0019, indexed in Pubmed: 27830875.

13. Leijnse JN. A generic morphological model of the anatomic variability in the m. flexor digitorum profundus, m. flexor pollicis longus and mm. lumbricales complex. Acta Anat (Basel). 1997; 160(1): 62–74, doi: 10.1159/000147997, indexed in Pubmed: 9643660.

14. Lewis WH. The development of the muscular system. In: Keibel F, Mall FP (eds.). Manual of human embryology. Lippincott, Philadelphia 1910: 454–522.

15. Murchison ND, Price BA, Conner DA, et al. Regulation of tendon differentiation by scleraxis distinguishes force-transmitting tendons from muscle-anchoring tendons. Development. 2007; 134(14): 2697–2708, doi: 10.1242/dev.001933, indexed in Pubmed: 17567668.

16. Naito M, Suzuki R, Abe H, et al. Fetal development of the human obturator internus muscle with special reference to the tendon and pulley. Anat Rec (Hoboken). 2015; 298(7): 1282–1293, doi: 10.1002/ar.23121, indexed in Pubmed: 25683268.

17. Onari T. On the foot short muscles with the so-called double innervation (In Japanese with an English abstract.). Nihon Univ J Med. 1960; 19: 1411–1430.

18. Oukouchi H, Murakami T, Kikuta A. Insertions of the lumbrical and interosseous muscles in the human foot. Okajimas Folia Anat Jpn. 1992; 69(2-3): 77–83, doi: 10.2535/ofaj1936.69.2-3_77, indexed in Pubmed: 1436952.

19. Percival JM, Anderson KNE, Huang P, et al. Golgi and sarcolemmal neuronal NOS differentially regulate contraction-induced fatigue and vasoconstriction in exercising mouse skeletal muscle. J Clin Invest. 2010; 120(3): 816–826, doi: 10.1172/JCI40736, indexed in Pubmed: 20124730.

20. Pryce BA, Watson SS, Murchison ND, et al. Recruitment and maintenance of tendon progenitors by TGF-beta signaling are essential for tendon formation. Development. 2009; 136(8): 1351–1361, doi: 10.1242/dev.027342, indexed in Pubmed: 19304887.

21. Shiraishi Y, Jin ZW, Mitomo K, et al. Foetal development of the human gluteus maximus muscle with special reference to its fascial insertion. Folia Morphol. 2018; 77(1): 144–150, doi: 10.5603/FM.a2017.0060, indexed in Pubmed: 28653302.

22. Shukunami C, Takimoto A, Nishizaki Y, et al. Scleraxis is a transcriptional activator that regulates the expression of Tenomodulin, a marker of mature tenocytes and ligamentocytes. Sci Rep. 2018; 8(1): 3155, doi: 10.1038/s41598-018-21194-3, indexed in Pubmed: 29453333.

VM VIA MEDICA

ORIGINAL ARTICLE

Investigation the anterior mandibular lingual concavity by using cone-beam computed tomography

M. Çitir[1] , K. Gunduz[2] , P. Kasap[3]

[1]Department of Dentomaxillofacial Radiology, Faculty of Dentistry, University of Gaziosmanpasa, Tokat, Turkey
[2]Department of Dentomaxillofacial Radiology, Faculty of Dentistry, University of Ondokuz, Mayis, Samsun, Turkey
[3]Department of Statistics, Faculty of Science and Literature, University of Ondokuz, Mayis, Samsun, Turkey

Background: In the presence of lingual concavity in the mandible, the cortical perforation and consequently the life-threatening intraoral haemorrhages obstructing the upper respiratory tract may be seen during the surgical intervention. The present study was aimed to determine the prevalence of lingual concavity in the interforaminal region and its relationship with gender and dentate status.

Materials and methods: The images of 106 patients who underwent cone-beam computed tomography (CBCT) between 2016 and 2017 in Department of Dental and Maxillofacial Radiology Department of Faculty of Dentistry of Ondokuz Mayıs University were retrospectively examined. The images were obtained using a Galileos device (98 kVp, 15–30 mA). The bone height and width in interforaminal region and the frequency of lingual concavity were analysed.

Results: Of patients involved in the present study, 42.5% were male and 57.5% were female After the examinations performed, the bone was morphologically classified into four classes as type I lingual concavity, type II inclined to lingual, type III enlarging towards labiolingual and type IV buccal concavity. Type III (77.9%) was the most common type in the anterior region, followed by type II (16.5%), type I (4.7%) and type IV (0.9%). The lingual concavity angle was 76.5 ± 3.69° and the concavity depth was 2.09 ± 0.34 mm.

Conclusions: The lingual concavity can be detected by using the cross-sectional CBCT images and the complications related with lingual cortical perforation can be prevented. (Folia Morphol 2021; 80, 4: 916–922)

Key words: anterior, concavity, cone-beam computed tomography, dental implant, mandible

INTRODUCTION

The use of removable dentures in the mandible with total or partial edentulous provides not sufficient comfort, function and aesthetics for the patient. The mandibular two-implant-retained overdenture prosthetic, in case of insufficient stability and retention of complete denture has become a standard treatment protocol [40]. The interforaminal region is considered a reliable area for placing dental implants in the mandible. In this region, there are important

---

Address for correspondence: M. Çitir, DDS, Gaziosmanpasa University, Faculty of Dentistry, Department of Dentomaxillofacial Radiology, Tokat, Turkey,
tel: 03562124222-7913, e-mail: mesudectr@hotmail.com

neurovascular structures such as lingual foramen, incisive canal, mental foramen, and anterior loop. The sublingual branch of lingual artery, the submental branch of facial artery, and the incisive branch of inferior alveolar artery anastomosis in the anterior mandible [15, 17, 19]. This rich vascular plexus courses nearby the lingual cortex in interforaminal region. The perforation in lingual cortex and consequently a vascular damage may develop in this region during dental implant placement or other surgical interventions, especially in presence of concavity. The severe haemorrhage, upper respiratory tract obstruction and haematoma on the mouth floor may develop as a result of the vascular damage [7, 15, 16, 31, 32]. Up to 24% of haemorrhage complications have been reported after implant placement [11]. Although the minimal perforation developing in lingual cortex has been previously considered to be benign, it has been observed that the haematoma developing on the mouth floor may reach severe levels. Moreover, mycotic pseudoaneurysms, which result in rupture of the internal carotid artery and lingual arteries, are also very rare complications [1, 12]. Severe bleeding can occur during the procedure, minutes or 6–7 hours later [19, 28, 39, 42].

The clinical palpation of alveolar crest offers limited information in the presence of concavity [5, 41]. In examination with intraoral film and panoramic radiography, however, the buccolingual dimension cannot be assessed. It is necessary to use the cross-sectional imaging methods such as cone-beam computed tomography (CBCT) in order to obtain detailed information about the volume and morphology of bone and relationship of tooth root with neurovascular structures [15, 17, 24].

The present study aimed to determine the prevalence of lingual concavity in interforaminal region and to detect relationship of concavity with gender and dentate status.

MATERIALS AND METHODS

The approval for the present study was obtained from the Clinical Research Ethics Committee of Ondokuz Mayıs University (B.30.2.ODM.0.20.08/795-900). In this study, the images of 106 patients who underwent CBCT for dental implant or having loss of teeth in mandible between 2016 and 2017 in Department of Dental and Maxillofacial Radiology Department of Faculty of Dentistry of Ondokuz Mayıs University were retrospectively examined. The images containing

pathological formations such as cyst, tumour etc. in interforaminal region were not included in analyses. All the CBCT images were obtained from Galileos (Sirona Dental Systems, Bensheim, Germany) device with parameters of 98 kVp, 15–30 mA, 15 × 15 mm image area, 2–5 s irradiation and 14 s scanning. The synchronous reconstruction was performed by using SIRONA Sidexis XG 2.61 viewer software with isotropic voxels having 12-bit grey-scale depth and 0.25 mm3 size. All the examinations and measurements were performed using 27″ LCD monitor (3.7 MP, 68 cm, 2560 × 1440 resolution) (the Radi-Force MX270W, Eizo Nanao Corporation, Ishikawa, Japan) under low level of illumination. In cross-sectional images, the height, width and morphology of the bone were evaluated in the anterior region of the mandible. To standardise the measurements, the region 4–6 mm anterior of the mental foramen was examined. The bone in the anterior region was classified as type I lingual concavity, type II inclined to lingual, type III enlarging towards labiolingual and type IV buccal concavity (Fig. 1). The parallel lines were drawn tangentially to the most buccal and most lingual point of the cortical bone. The distance between parallel lines was determined as the maximum bone width. The distance between the tip of alveolar crest and the cortical border of mandibular inferior was recorded as the maximum bone height. The horizontal distance at the deepest point of concavity was noted as concavity depth. The angle between mandibular inferior cortical border and lingual cortex (for type I and type II, the most lingual point was referenced) was determined as lingual slope angle. The slope angle of the lingual concavity was determined as the lingual concavity angle (for type I) (Fig. 2).

This cross-sectional study was reviewed and approved by the Ethics Committee for Human Research of the University of 19 Mayıs. (B.30.2.ODM. 0.20.08/795-900) mention under heading of ethical approval.

All procedures followed were in accordance with the ethical standards of the responsible committee on human experimentation (institutional and national) and with the Helsinki Declaration of 1975, as revised in 2008.

Statistical analyses

The data obtained from the examined images were analysed using SPSS 20.0 (Statistical Package for Social Sciences) for Windows. Data were presented as mean ± standard deviation and frequency. The
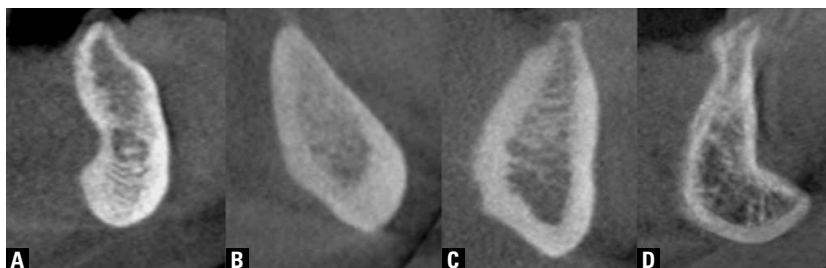
Figure 1. Cross-sectional cone-beam computed tomography images representing the mandible shapes; **A.** Type I lingual concavity; **B.** Type II inclined to lingual; **C.** Type III enlarging towards labiolingual; **D.** Type IV buccal concavity.
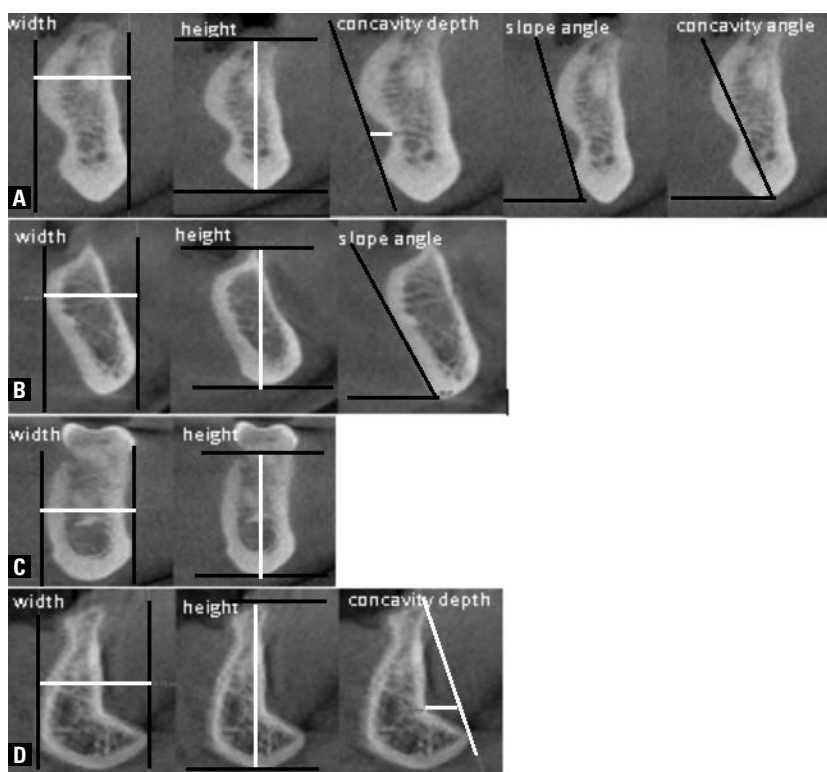
Figure 2. A–D. Schematic representation of the cone-beam computed tomography images for the measurement of bone type I, II, III and IV, recpectively.

relationship between bone types and age, gender, and dentate status was analysed using the χ^2 test. The paired sample t-test was used for determining the relationship between height and width of bone and age/gender. The p value 0.05 was considered to be statistically significant.

RESULTS

Of the patients, 45 (42.45%) were male and 61 (57.55%) were female. The mean age of the patients was 55.7 ± 10.31 years (range, 23–77). In interforaminal region, 37 of the patients were edentulous, 58 were partially edentulous, and 11 were dentate.

The shape of the anterior mandible was classified into four types, as shown in Figure 1. Of the patients, 4.7% had type I, 16.5% had type II, 77.9% had type III and 0.9% had type IV bone morphology. Type III was the most common type in both gender and dentate status. Type I was more common in females and type II was more common in males (Table 1). There was a significant relationship between the bone type and gender (p = 0.005). Type I was more common in dentate patients and type II was more common in edentulous patients. There was a significant relationship between the bone type and dentate status (p = 0.000; Table 1).

Table 1. Distribution of bone types by gender and dentate status

	Male	Female	Dentate	Edentulous
Type I	1.11%	7.38%	5.34%	3.7%
Type II	24.44%	10.65%	4.58%	35.8%
Type III	73.55%	81.15%	88.56%	60.5%
Type IV	0.9%	0.82%	1.52%	–
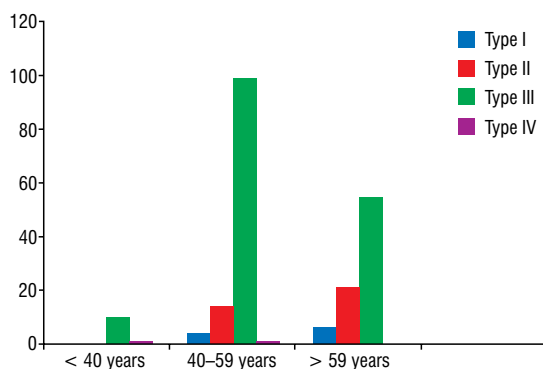
Figure 3. Distribution of bone types by age.

Patients were divided into three groups as < 40, 40–59 and > 59 according to age. Type I and II were most frequently > 59 years, type III was the 40–59 age. There was a significant relationship between the bone type and age (p = 0.019; Fig. 3).

The maximum bone height in male and female ranged from 18.65 to 37.32 mm and from 13.29 to 32.92 mm, respectively. The maximum bone width in male and female ranged from 9.33 to 16.31 mm and 8.60 to 18.47 mm, respectively. The bone height and width in male was significantly greater than in female (p < 0.05; Table 2). The bone height in dentate patients was significantly greater than in edentulous patients (p < 0.05; Table 2).

Type I and type IV concavity depth were 2.09 ± ± 0.34 mm and 4.02 ± 1.28 mm, respectively. In type I, the lingual slope angle was 70.59 ± 4.10º and the lingual concavity angle was 76.5 ± 3.69º. In type II, the lingual slope angle was 66.02 ± 6.58º.

DISCUSSION

The objective of this study is to explain the size and morphology of the mandible in order to guide the surgical interventions by using CBCT data of 106 patients. The interforaminal region is considered as a safe region for placing a dental implant in the mandible. However there are important neurovascular structures and blood vessels, considered to be 1–2 mm in diameter in the region. From these vessels, approximately half a litre of blood can be drained in 30 min [5]. Severe postoperative complications were also reported for this region [6, 9, 28, 34, 39].

Although the life-threatening complications were not frequently seen, they should be taken into consideration before the surgical interventions planned for this region [5, 6, 8, 9, 21, 24, 34]. Therefore in surgical procedures such as implant placement, the surgeon should have extensive knowledge of the shape and size of the bone.

The panoramic radiography can be utilized for the preliminary examination in order to obtain information about the bone height and, to a certain extent, the horizontal distance. However, the two-dimensional information provided has specific disadvantages such as distortion and magnification in images [5, 6, 8, 9, 21, 23, 24, 34, 41]. In studies comparing the computed tomography (CT) and panoramic radiography, the bone height was statistically significantly greater in panoramic radiography [2, 13, 20, 38]. These studies emphasize the importance of three-dimensional imaging methods in accurately measuring

Table 2. Measurements of mandibular dimension and lingual-buccal concavity

	Maximum bone width [mm]	Maximum bone height [mm]	Lingual slope angle [°]	Lingual concavity angle [°]	Concavity depth [mm]
Type I	11.2 ± 1.55	25.6 ± 3.49	70.59 ± 4.10	76.5 ± 3.69	2.09 ± 0.34
Type II	13.6 ± 1.42	23.5 ± 4.74	66.02 ± 6.58		
Type III	12 ± 1.57	27.3 ± 3.98			
Type IV	17.19 ± 1.28	31.89 ± 0.37			4.02 ± 1.28
Female	11.72 ± 1.57	26.02 ± 3.77	67.26 ± 7.29	75.98 ± 3.19	2.86 ± 0.47
Male	12.99 ± 1.70	28.19 ± 4.86	66.54 ± 4.75	81.9	6.61 ± 1.81
Dentate	12.06 ± 1.79	28.85 ± 3.40	70.36 ± 3.8	77.88 ± 3.43	3.82 ± 1.77
Edentulous	12.59 ± 1.60	23.86 ± 4.05	65.37 ± 6.29	73.53 ± 0.5	2.54 ± 0.14

the vertical dimension. In many studies, CT or CBCT evaluation has been suggested before implant placement in the interforaminal region [24, 27, 36]. Also in a study comparing CT and CBCT, reported that the error rate in CT (6.6%, 8.8%) was higher than CBCT (2.3%, 4.7%) [37]. Therefore, evaluation with CBCT can be more reliable.

Quirynen et al. [33] and Watanabe et al. [41] investigated the anterior mandible using CT. Quirynen et al. [33] reported, type III was the most common (69.5%), followed type II (28.1%). They [33] stated that lingual concavity prevalence is 2.4%. Watanabe et al. [41] reported the prevalence of lingual concavity 8% and buccal concavity 74%. In this study, lingual concavity is more common (4.7%) than Quirynen et al. [33], the buccal concavity was less (0.9%) than Watanabe et al. [41].

Nickenig et al. [29] evaluated the bone morphology in the mandibular canine-1 premolar region with CBCT and found a lingual concavity in 14.4%. They [29] stated that the lingual concavity was less frequently in the edentulous mandible. In our study, Nickenig et al. [29] unlike, 70% of the patients with lingual concavity were dentate. However, in some studies declared that the dentate status and bone morphology are not related [18, 22]. The differences between the lingual and buccal concavity prevalence values reported in different studies can be explained with the racial and class differences and dentate status.

The risk of lingual perforation is high when placing the implant in case of lingual concavity (type I). Also, if a large diameter (5 mm) implants are placed where bone volume is not sufficient, the risk increases more [21, 30]. Therefore, narrow diameter implants, such as 3 mm, is recommended to prevent perforation in the lingual concavity [21, 29]. If an implant of less than 3 mm diameter is used, the implant length must be longer to increase the load resistance. However, long implants may increase the possibility of reaching the artery and most cases of haemorrhage have been reported in cases using ≥ 15 mm implant [15, 19, 25, 39]. For this reason, Givol et al. [10] suggested short implants (14 mm or less) in the mandibular canine region.

There is also a risk of lingual perforation in type II bone morphology and depends on the degree of lingual slope. In cases with buccal concavity perforation may develop while implant placement, as in lingual concavity.

Previous studies reported the prevalence of lingual concavity in the posterior mandible ranged from 32.5% to 80%, higher than the anterior region [3, 5, 14, 26, 30]. Moreover, the risk of lingual perforation also varies in anterior and posterior region. The branches of major arteries in the anterior mandible (submental and sublingual arteries) might be closer to the mouth floor. Since there are no important vital structures in the posterior (submandibular gland and lymph node), immediate severe bleeding and nerve damage are not expected there is a perforation above the mylohyoid ridge [4]. Due to this anatomical difference between the anterior and posterior mandible, the determination of lingual concavity in the anterior is more important. Already severe bleeding has been reported more frequently in the anterior region [17, 35].

Nickenig et al. [29] detected minimal bone width in lingual concavity (type I, 7.6 mm). Similarly, the minimum bone width values were observed in lingual concavity (11.2 mm). Quirynen et al. [33] and Nickenig et al. [29] reported the lowest bone height in type of bone enlarging to labiolingual direction (type III, 26.8 mm and 26.9 mm, respectively). On the contrary with these results, the minimum bone height was observed in type of bones inclined to lingual (type II, 23.5 mm).

The lingual concavity depth was reported 6 mm by Quirynen et al. [33] and 0.8 mm by Nickenig et al. [29]. In our study, this value was 2.09 mm. In cases where the depth of the concavity was more than 2 mm, a high amount of lingual perforation has been reported [29].

In Quirynen et al. [33] and Nickenig et al. [29] study, lingual concavity angle was 84.4º and 84.4º, respectively. However, the angle was lower in this study (76.5º). When the relationship of lingual concavity angle with gender is evaluated, Herranz-Aparicio et al. [14] found higher values in females (+5º); in contrast, Chan et al. [5] detected higher values in males (+3º). We measured higher values in males (+6º), similar to Chan et al. [5].

Quirynen et al. [33] reported the lingual slope angle in type II as 67.6º. Our results were very close to those reported by Quirynen et al. [33] (66.02º). The degree of slope guides the osteotomy before implant placement. Therefore in type II, the risk of perforation is related to the lingual slope angle and when the lingual slope decreases (the smaller slope angle), the risk of perforation increases [33].

CONCLUSIONS

Buccal and lingual concavity may be seen in the interforaminal area. Detecting the concavity in this region is very important to prevent the perforation occurring during the surgical interventions and the consequent neurovascular damage and infection. Considering the risks, CBCT should be used in addition to panoramic radiography in cases of lingual or buccal concavity and lingual inclination.

Conflict of interest: None declared

REFERENCES

1. Badloo K, Levi E, Downie L, et al. Mycotic pseudoaneurysm of the lingual artery: a rare complication of parapharyngeal abscess. J Paediatr Child Health. 2012; 48(11): 1045–1046, doi: 10.1111/j.1440-1754.2012.02599.x, indexed in Pubmed: 23126396.
2. Bolin A, Eliasson S, von Beetzen M, et al. Radiographic evaluation of mandibular posterior implant sites: correlation between panoramic and tomographic determinations. Clin Oral Implants Res. 1996; 7(4): 354–359, doi: 10.1034/j.1600-0501.1996.070408.x, indexed in Pubmed: 9151602.
3. Braut V, Bornstein MM, Lauber R, et al. Bone dimensions in the posterior mandible: a retrospective radiographic study using cone beam computed tomography. Part 1 — analysis of dentate sites. Int J Periodontics Restorative Dent. 2012; 32(2): 175–184, indexed in Pubmed: 22292147.
4. Chan HL, Benavides E, Yeh CY, et al. Risk assessment of lingual plate perforation in posterior mandibular region: a virtual implant placement study using cone-beam computed tomography. J Periodontol. 2011; 82(1): 129–135, doi: 10.1902/jop.2010.100313, indexed in Pubmed: 20653440.
5. Chan HL, Brooks SL, Fu JH, et al. Cross-sectional analysis of the mandibular lingual concavity using cone beam computed tomography. Clin Oral Implants Res. 2011; 22(2): 201–206, doi: 10.1111/j.1600-0501.2010.02018.x, indexed in Pubmed: 21044167.
6. Darriba M, Mendonça-Caridad J. Profuse bleeding and life-threatening airway obstruction after placement of mandibular dental implants. J Oral Maxillofacial Surg. 1997; 55(11): 1328–1330, doi: 10.1016/s0278-2391(97)90195-6.
7. Felisati G, Saibene AM, Di Pasquale D, et al. How the simplest dental implant procedure can trigger an extremely serious complication. BMJ Case Rep. 2012; 2012, doi: 10.1136/bcr-2012-007373, indexed in Pubmed: 23192578.
8. Flanagan D. Important arterial supply of the mandible, control of an arterial hemorrhage, and report of a hemorrhagic incident. J Oral Implantol. 2003; 29(4): 165–173, doi: 10.1563/1548-1336(2003)029<0165:iasotm>2.3.co;2.
9. Frenken JW, Zijderveld SA, van den Bergh JPA, et al. [Haematoma of the floor of the mouth following implant surgery]. Ned Tijdschr Tandheelkd. 2010; 117(1): 17–21, doi: 10.5177/ntvt2010.01.08146, indexed in Pubmed: 20180345.
10. Givol N, Chaushu G, Halamish-Shani T, et al. Emergency tracheostomy following life-threatening hemorrhage in the floor of the mouth during immediate implant placement in the mandibular canine region. J Periodontol. 2000; 71(12): 1893–1895, doi: 10.1902/jop.2000.71.12.1893, indexed in Pubmed: 11156047.
11. Goodacre C, Bernal G, Rungcharassaeng K, et al. Clinical complications with implants and implant prostheses. J Prosthetic Dentistry. 2003; 90(2): 121–132, doi: 10.1016/s0022-3913(03)00212-9.
12. Greenstein G, Cavallaro J, Romanos G, et al. Clinical recommendations for avoiding and managing surgical complications associated with implant dentistry: a review. J Periodontol. 2008; 79(8): 1317–1329, doi: 10.1902/jop.2008.070067, indexed in Pubmed: 18672980.
13. Hanazawa T, Sano T, Seki K, et al. Radiologic measurements of the mandible: a comparison between CT-reformatted and conventional tomographic images. Clin Oral Implants Res. 2004; 15(2): 226–232, doi: 10.1111/j.1600-0501.2004.00991.x, indexed in Pubmed: 15008935.
14. Herranz-Aparicio J, Marques J, Almendros-Marqués N, et al. Retrospective study of the bone morphology in the posterior mandibular region. Evaluation of the prevalence and the degree of lingual concavity and their possible complications. Med Oral Patol Oral Cir Bucal. 2016; 21(6): e731–e736, doi: 10.4317/medoral.21256, indexed in Pubmed: 27694785.
15. Hofschneider U, Tepper G, Gahleitner A, et al. Assessment of the blood supply to the mental region for reduction of bleeding complications during implant surgery in the interforaminal region. Int J Oral Maxillofac Implants. 1999; 14(3): 379–383, indexed in Pubmed: 10379111.
16. Hwang HD, Kim JW, Kim YS, et al. Angiographic embolization for hemorrhage control after dental implantation. J Korean Assoc Oral Maxillofac Surg. 2013; 39(1): 27–30, doi: 10.5125/jkaoms.2013.39.1.27, indexed in Pubmed: 24471014.
17. Kalpidis CDR, Setayesh RM. Hemorrhaging associated with endosseous implant placement in the anterior mandible: a review of the literature. J Periodontol. 2004; 75(5): 631–645, doi: 10.1902/jop.2004.75.5.631, indexed in Pubmed: 15212344.
18. Kamburoğlu K, Acar B, Yüksel S, et al. CBCT quantitative evaluation of mandibular lingual concavities in dental implant patients. Surg Radiol Anat. 2015; 37(10): 1209–1215, doi: 10.1007/s00276-015-1493-9, indexed in Pubmed: 25994600.
19. Krenkel C, Holzner K, Poisel S. [Hematoma of the mouth floor following oral surgery and its anatomical characteristics]. Dtsch Z Mund Kiefer Gesichtschir. 1985; 9(6): 448–451, indexed in Pubmed: 3879682.
20. Lam EW, Ruprecht A, Yang J. Comparison of two-dimensional orthoradially reformatted computed tomography and panoramic radiography for dental implant treatment planning. J Prosthet Dent. 1995; 74(1): 42–46, doi: 10.1016/s0022-3913(05)80227-6, indexed in Pubmed: 7674189.
21. Leong DJM, Chan HL, Yeh CY, et al. Risk of lingual plate perforation during implant placement in the posterior mandible: a human cadaver study. Implant Dent. 2011; 20(5): 360–363, doi: 10.1097/ID.0b013e3182263555, indexed in Pubmed: 21811168.

22. Locks BJ, Claudino M, Azevedo-Alani L, et al. Evaluation of the bone anatomy of the anterior region of the mandible using cone beam computed tomography. Rev Odontol UNESP. 2018; 47(2): 69–73, doi: 10.1590/1807-2577.10517.

23. Lofthag-Hansen S, Gröndahl K, Ekestubbe A. Cone-beam CT for preoperative implant planning in the posterior mandible: visibility of anatomic landmarks. Clin Implant Dent Relat Res. 2009; 11(3): 246–255, doi: 10.1111/j.1708-8208.2008.00114.x, indexed in Pubmed: 18783419.

24. Longoni S, Sartori M, Braun M, et al. Lingual vascular canals of the mandible: the risk of bleeding complications during implant procedures. Implant Dent. 2007; 16(2): 131–138, doi: 10.1097/ID.0b013e31805009d5, indexed in Pubmed: 17563503.

25. Loukas M, Kinsella CR, Kapos T, et al. Anatomical variation in arterial supply of the mandible with special regard to implant placement. Int J Oral Maxillofac Surg. 2008; 37(4): 367–371, doi: 10.1016/j.ijom.2007.11.007, indexed in Pubmed: 18262766.

26. Magat G. Radiomorphometric analysis of edentulous posterior mandibular ridges in the first molar region: a cone-beam computed tomography study. J Periodontal Implant Sci. 2020; 50(1): 28–37, doi: 10.5051/jpis.2020.50.1.28, indexed in Pubmed: 32128271.

27. Miller RJ, Edwards WC, Boudet C, et al. Maxillofacial anatomy: the mandibular symphysis. J Oral Implantol. 2011; 37(6): 745–753, doi: 10.1563/AAID-JOI-D-10-00136, indexed in Pubmed: 20932161.

28. Mordenfeld A, Andersson L, Bergström B. Hemorrhage in the floor of the mouth during implant placement in the edentulous mandible: a case report. Int J Oral Maxillofac Implants. 1997; 12(4): 558–561, indexed in Pubmed: 9274086.

29. Nickenig HJ, Wichmann M, Eitner S, et al. Lingual concavities in the mandible: a morphological study using cross-sectional analysis determined by CBCT. J Cranio-maxillofac Surg. 2015; 43(2): 254–259, doi: 10.1016/j.jcms.2014.11.018, indexed in Pubmed: 25547216.

30. Parnia F, Fard EM, Mahboub F, et al. Tomographic volume evaluation of submandibular fossa in patients requiring dental implants. Oral Surg Oral Med Oral Pathol Oral Radiol Endod. 2010; 109(1): e32–e36, doi: 10.1016/j.tripleo.2009.08.035, indexed in Pubmed: 20123366.

31. Peñarrocha-Diago M, Balaguer-Martí JC, Peñarrocha-Oltra D, et al. Floor of the mouth hemorrhage subsequent to dental implant placement in the anterior mandible. Clin Cosmet Investig Dent. 2019; 11: 235–242, doi: 10.2147/CCIDE.S207120, indexed in Pubmed: 31496828.

32. Pigadas N, Simoes P, Tuffin JR. Massive sublingual haematoma following osseo-integrated implant placement in the anterior mandible. Br Dent J. 2009; 206(2): 67–68, doi: 10.1038/sj.bdj.2009.2, indexed in Pubmed: 19165260.

33. Quirynen M, Mraiwa N, van Steenberghe D, et al. Morphology and dimensions of the mandibular jaw bone in the interforaminal region in patients requiring implants in the distal areas. Clin Oral Implants Res. 2003; 14(3): 280–285, doi: 10.1034/j.1600-0501.2003.140305.x, indexed in Pubmed: 12755778.

34. Ratschew C, Czernicky W, Watzek G. Lebensbedrohliche Blutung nach Implantation im Unterkiefer. Dtsch Zahnärztl Z. 1994; 49: 65–67.

35. Romanos GE, Gupta B, Crespi R. Endosseous arteries in the anterior mandible: literature review. Int J Oral Maxillofac Implants. 2012; 27(1): 90–94, indexed in Pubmed: 22299084.

36. Sammartino G, Prados-Frutos JC, Riccitiello F, et al. The relevance of the use of radiographic planning in order to avoid complications in mandibular implantology: a retrospective study. Biomed Res Int. 2016; 2016: 8175284, doi: 10.1155/2016/8175284, indexed in Pubmed: 27294136.

37. Suomalainen A, Vehmas T, Kortesniemi M, et al. Accuracy of linear measurements using dental cone beam and conventional multislice computed tomography. Dentomaxillofac Radiol. 2008; 37(1): 10–17, doi: 10.1259/dmfr/14140281, indexed in Pubmed: 18195249.

38. Tal H, Moses O. A comparison of panoramic radiography with computed tomography in the planning of implant surgery. Dentomaxillofac Radiol. 1991; 20(1): 40–42, doi: 10.1259/dmfr.20.1.1884852, indexed in Pubmed: 1884852.

39. Ten Bruggencate CM, Krekeler G, Kraaijehagen HA, et al. Hemorrhage of the floor of the mouth resulting from lingual perforation during implant placement: a clinical report. Int J Oral Maxillofac Implants. 1993; 8: 329–334, indexed in Pubmed: 8225469.

40. Thomason JM, Feine J, Exley C, et al. Mandibular two implant-supported overdentures as the first choice standard of care for edentulous patients--the York Consensus Statement. Br Dent J. 2009; 207(4): 185–186, doi: 10.1038/sj.bdj.2009.728, indexed in Pubmed: 19696851.

41. Watanabe H, Mohammad Abdul M, Kurabayashi T, et al. Mandible size and morphology determined with CT on a premise of dental implant operation. Surg Radiol Anat. 2010; 32(4): 343–349, doi: 10.1007/s00276-009-0570-3, indexed in Pubmed: 19812884.

42. Woo BM, Al-Bustani S, Ueeck BA. Floor of mouth haemorrhage and life-threatening airway obstruction during immediate implant placement in the anterior mandible. Int J Oral Maxillofac Surg. 2006; 35(10): 961–964, doi: 10.1016/j.ijom.2006.03.020, indexed in Pubmed: 16829038.

VIA MEDICA

O R I G I N A L   A R T I C L E

Anatomic characteristics and dimensions of the nasopalatine canal: a radiographic study using cone-beam computed tomography

C. Görürgöz[1] , B. Öztaş[2]

[1]Department of Dentomaxillofacial Radiology, Bursa Uludağ University, Faculty of Dentistry, Bursa, Turkey
[2]Department of Dentomaxillofacial Radiology, Ankara University, Faculty of Dentistry, Ankara, Turkey

Background: Description of the nasopalatine canal (NPC) is important for planning surgical treatment and comprehension of the morphology and pathogenesis of lesions that occur in the anterior maxilla. The goal of this study was to analyse the dimensions and anatomic characteristics of the NPC on cone-beam computed tomography (CBCT) scans, to determine the incidence of anatomical variation; and to assess the correlations of these variables with age, gender, and dental status.
Materials and methods: A total of 320 individual CBCT images were included. Reformatted sagittal, coronal and axial slices were evaluated. Sagittal images were used for measurements of the NPC and to classified shape and direction-course of the NPC. Coronal images were used to analyse the NPC division levels and axial images were used to detect the number of palatal and nasal opening.
Results: The mean NPC length was 11.45 ± 2.50 mm; statistically significant differences were detected between males and females (p < 0.05). Mean naso-palatine angle was 76.26 ± 8.12°; significant differences were detected in sagittal and coronal classifications. The most common canal was: funnel-shaped (29%), slanted-curved direction-course (53.1%), middle third division level (43.1%), and one incisive foramen with two Stenson's foramina (1–2) (77.2%).
Conclusions: The current study ensures new findings on the literature concerning the description of the anatomical structure of the canal. Also, the study highlights a significant variability in the anatomy and morphology of the NPC. Therefore, three-dimensional analysis of this structure is important for facilitating surgical management and preventing possible complications in this area. (Folia Morphol 2021; 80, 4: 923–934)

Key words: anatomy, cone-beam computed tomography, maxilla, nasopalatine canal, radiology

INTRODUCTION

The nasopalatine canal (NPC) is an important pathway between the nasal fossa and the palate, hence its name. It is also called the incisive canal since the NPC is located palatal to the central inci-

sors [29]. In 1683, Stenson [24] made a complete description of the NPC for the first time. The NPC usually courses in the midline of the palate and behind the roots of central incisors. The opening of the NPC in the mouth is underneath the incisive

Address for correspondence: Dr. C. Görürgöz, Bursa Uludağ University, Faculty of Dentistry, Dentomaxillofacial Radiology Department, 16059 Bursa, Turkey,
tel: +90 224 294 00 53-71, fax: +90 224 294 00 78, e-mail: cansugorurgoz@uludag.edu.tr

papilla as incisive foramen (IF) and this canal ends in the nasal cavity through the nasal foramen as the Stensen's foramina (SF) [12, 19]. The NPC contains the nasopalatine nerve and vessels, branches of the maxillary nerve, the maxillary artery [17] along with connective tissue, fat and minor salivary glands [13, 14].

Evaluation of morphological features and the morphometry of the NPC is especially important for preventing possible complications and planning many surgical treatments in the maxilla like apical surgery of central teeth, removal of the incisive duct cyst, dental implants, surgically-assisted rapid palatal expansion, dentoalveolar fractures, LeFort I osteotomy operations [9].

In recent years, some studies were published about the radiological morphology of the NPC on cone-beam computed tomography (CBCT) images, which are revealing considerable variation in the morphological characteristics of the canal [1, 5–7, 10, 21, 26]. The present study aimed to a comprehensive evaluation of the radiological features of the canal in all three planes for relation to age, gender and dental status using CBCT imaging and to create our relevant data on morphological characteristics of NPC which have received less attention or have not been defined still.

MATERIALS AND METHODS

The study sample consisted of CBCT images of 1,651 patients who referred to the Dentistry Faculty's Department of Dentomaxillofacial Radiology, between November 2016 and December 2017. CBCT examination of cases with several dentomaxillofacial problems such as impacted teeth, oral pathologies, orthognathic surgery, dental implants were retrospectively evaluated. Three hundred-twenty CBCT images were selected randomly. The protocol of the study was approved by local the Ethics Board of the Institution (Decision Number: 02/03. Clinical Trials Identifier: 36290600/08).

The inclusion criteria were: age ≥ 15 years individuals; CBCT images with sufficient diagnostic quality and imaging area. Patients with evidence of bone disease, dental trauma history, congenital abnormality, presence of impacted teeth, radiolucent or radiopaque pathologies, residual roots or dental implants, suspected NPC pathology (cyst), bone grafts and fixed orthodontic expansion devices were excluded from the final sample.

CBCT imaging

All CBCT scans were made in compliance with a standardised scanning protocol. CBCT images were obtained with Planmeca ProMax 3D Max (Helsinki, Finland with following parameters; 96 kVp, 5.6–8 mA, 9–12 s scan time, field of view (50 × 55 mm, 100 × × 55 mm, 100 × 90 mm, 130 × 55 mm, 130 × × 90 mm, 230 × 160 mm) and with two different voxel sizes (200 μm, 400 μm). All data were reconstructed at 0.5 mm slice interval and thickness.

CBCT evaluations

All the measurements and analysis were carried out by same oral radiologist on CBCT images, using Romexis 3.7 software programmes (Planmeca Oy, Helsinki, Finland) on a 21.3-inch flat-panel monitor (NEC MultiSync, Munchen, Germany) with 2048 × × 2560 pixel resolution, in a darkroom. The examiner could adjust the brightness and contrast of the images with the image-processing tool in the software to ensure ideal visual conditions for an accurate diagnosis. Before the evaluation, the three dimensions were calibrated and the three planes (sagittal, horizontal, and coronal) defined in each image.

Measurements to detecting the dimensions of the NPC

The following morphometric parameters, the width of the SF, IF and the length of the NPC were performed considering the protocol of Bornstein et al. [5]. The dimensions of the NPC (in mm) and the canal angulation (in degrees) were estimated in the reformatted sagittal CBCT scans (Fig. 1): (1) The width (mm) of the SF. If the canal had two or more nasal foramina, all visible SFs were added together; (2) The width (mm) of the IF. If the canal had two or more palatal foramina, all visible IFs were added together; (3) The length (mm) of the NPC. The length of the NPC was defined as the distance from mid-point of IF to the mid-point of SF; (4) The nasopalatine angle was defined as the intersection of the long axis of the canal and the palatal plane.

Classifications of the variants in three planes

In sagittal plane, the shapes of the canal were evaluated and classified into nine groups by adding two different types to the classification of Sekerci et al. [21]. In the literature, the type 4 canal shape which was only described in the study of Friedrich et al. [8] was added to the classification as "kink
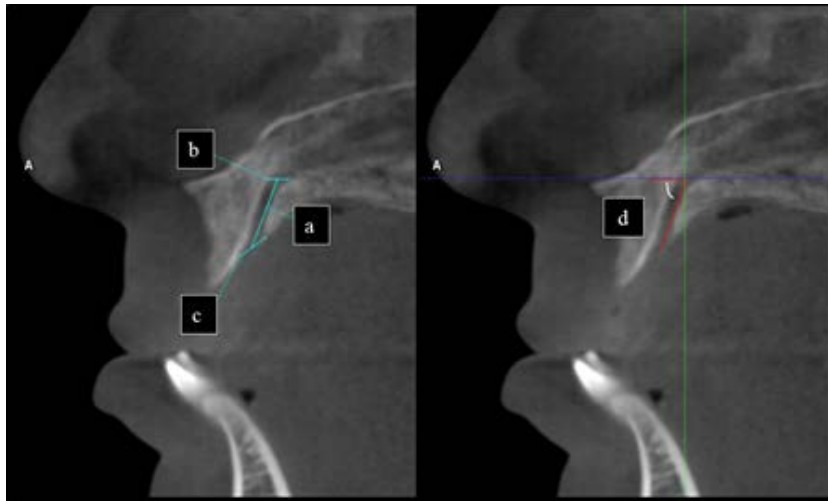
Figure 1. Measurements of anatomical structures in sagittal sections from cone-beam computed tomography image: the length of the nasopalatine canal (a); the diameter of the Stensen's foramina (b); the diameter of the incisive foramen (c); nasopalatine angle (d).
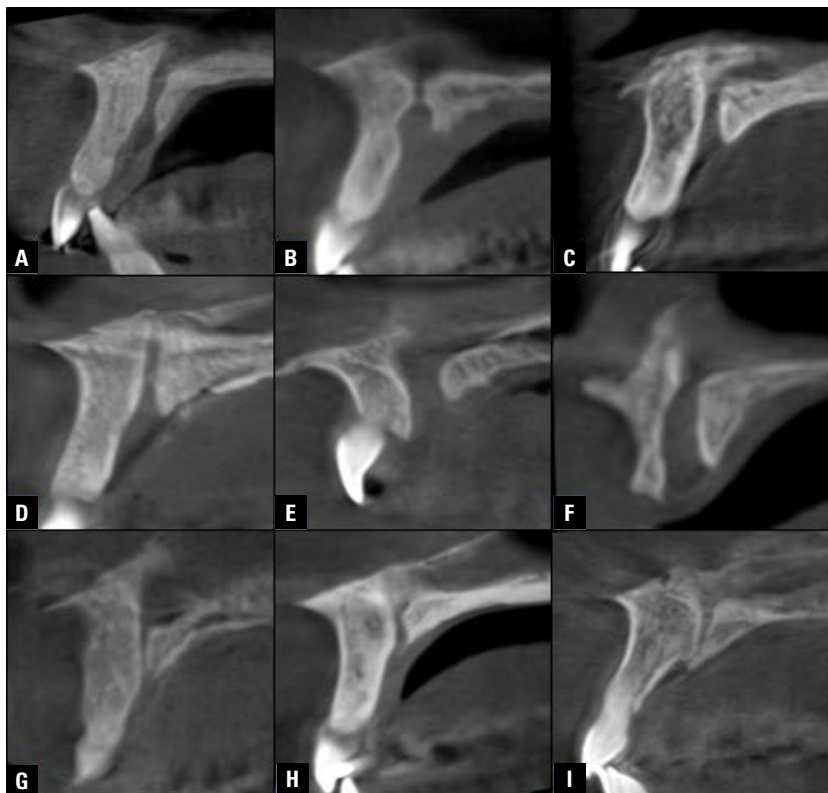
Figure 2. The nasopalatine canal shape classification in sagittal sections of cone-beam computed tomography images; **A.** Hourglass; **B.** Spindle; **C.** Cone; **D.** Funnel; **E.** Cylindrical; **F.** Banana; **G.** Tree branch; **H.** Kink; **I.** Other.

shape". In this group, this kinking was observed in the nasal or palatal third of the canal. The inverted cone shape is included in the cone group and the inverted funnel shape is included in the funnel group. The canal shapes that could not be included in these eight groups were classified under the title of "other". A total of nine groups were created: (1) hourglass, (2) spindle, (3) cone, (4) funnel, (5) banana, (6) cylindrical, (7) tree branch like, (8) kink, (9) other (Fig. 2). The NPC was also assessed concerning the classification of Song et al. [23] for its sagittal direction-course: (1) vertical-straight, (2) vertical-curved, (3) slanted-straight, (4) slanted-curved (Fig. 3).
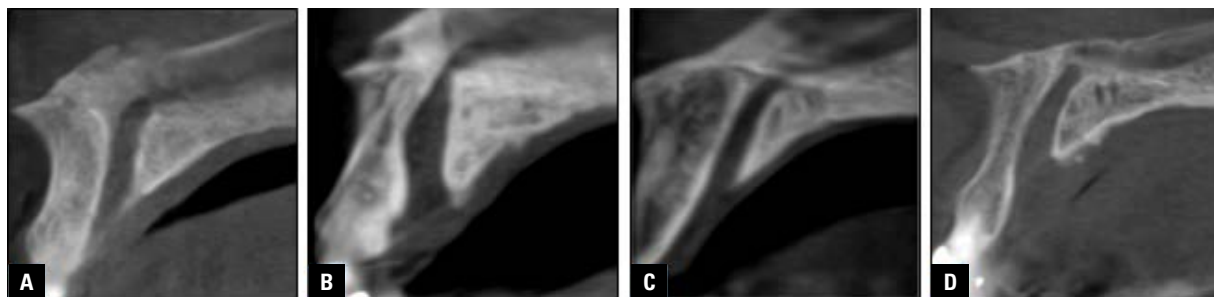
Figure 3. Direction-course of nasopalatine canal in sagittal slice; **A.** Vertical-straight canal; **B.** Vertical-curved canal; **C.** Slanted-straight canal; **D.** Slanted-curved canal.
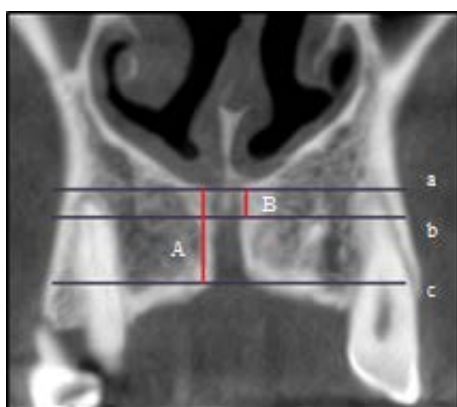
Figure 4. Cone-beam computed tomography frontal reconstruction showing the level of division of the nasopalatine canal (NPC), which is the ratio between the NPC coronal division length (B) and NPC coronal length (A); a — NPC nasal level; b — division plane level; c — NPC palate level.

In coronal plane, the NPC division levels were examined in the coronal slices based on the coronal ratio, that is the ratio of the canal length above the division to the entire length of the canal in the coronal plane (Fig. 4). The anatomic variants of the canal were classified into four groups [27]: (1) no division; (2) a division of the NPC in the upper-third level (coronal ratio < 0.33); (3) a division of the NPC in the middle-third level (coronal ratio of 0.66–0.33); (4) a division of the NPC in the lower-third level (coronal ratio of 1–0.65) (Fig. 5).

In axial plane, the variants of the canal were classified concerning the number of IFs (Fig. 6) and SF (Fig. 7). The axial groups were: 1–1, 1–2, 1–3, 1–4, 2–2, 3–2.

In addition, four groups were established according to dental status: group A — both central incisors present; group B — total edentulous individuals; group C — no central incisors present; group D — one central incisor present.

Finally, after an interval of 4 weeks, 20% of the 320 cases were selected randomly and measurements repeated by the same researcher to assess intra-observer variability.

Statistical analysis

Data analysis was performed using the IBM SPSS Statistics 21.0 (Statistical Package for Social Sciences) programme. The Shapiro-Wilk test was applied for evaluating compliance with the normal distribution of the data. The Student t-test and Kruskal–Wallis H test were performed for the comparison of two independent groups and three or more than groups, respectively. In addition, categorical variables were analysed using the χ^2 test. The association between morphometric parameters and age was evaluated using the Spearman correlation coefficient. The p value of less than 0.05 was considered significant.

RESULTS

The descriptive retrospective study subject comprised of 189 (59%) females and 131 (41%) males with an average age of 42.4 ± 16.2 (standard deviation [SD]) years (range 15–85 years).

The analysis of the sizes of the canal found out a mean width of the SF of 2.51 ± 1.28 mm and a wider IF with a diameter of 5.29 ± 1.37 mm. The mean length of the canal was 11.45 ± 2.50 mm and mean nasopalatine angle was 76.26 ± 8.12°. The gender of the evaluated groups had a statistically significant effect on the length of the NPC and the width of IF, with the mean values tending to be greater for male subjects (p < 0.001). Males presented a wider SF diameter (mean 2.60 mm) and nasopalatine angle (mean 77.11°) than females (mean 2.45 mm, mean 75.68°, respectively) although no significant differences were found (p > 0.05) (Table 1).
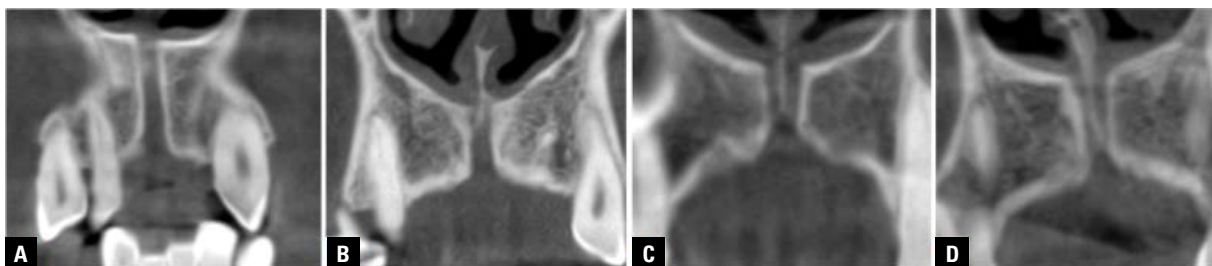
Figure 5. Division of the nasopalatine canal in coronal slice; **A.** No division; **B.** Upper-third level; **C.** Middle-third level; **D.** Lower-third level.

Figure 6. Axial images from cone-beam computed tomography scanner showing number of incisive foramina (IF); **A.** One IF; **B.** Two IFs; **C.** Three IFs (arrows).
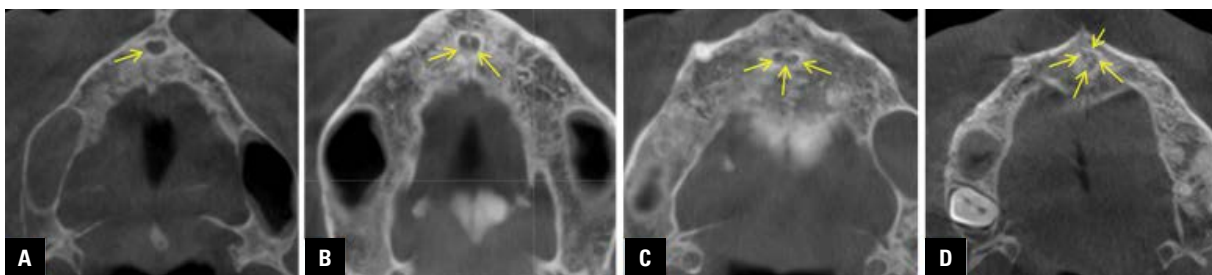
Figure 7. Axial images from cone-beam computed tomography scanner showing number of Stensen's foramina (SFs); **A.** One SF; **B.** Two SFs; **C.** Three SFs; **D.** Four SFs (arrows).

In sagittal plane, the most prevalent canal shape was found to be 93 (29.1%) funnel-shaped, followed by hourglass-shaped in 52 (16.3%) cases. Since the NPC shape (3.1%) of 10 cases could not be included in this classification, they were examined under the title of "other". With respect to the sagittal shapes of canals, there was no significant difference between female and male (p > 0.05). The prevalences of NPC shapes according to sex are shown in Table 2.

In terms of the sagittal direction-course of NPC, the most common type was slanted-curved in 170 (53.1%) cases, followed by vertical-curved in 67 (20.9%) cases, slanted-straight in 48 (15%) cases, and vertical-straight in 35 (10.9%) cases (Table 2). The slanted type was detected more frequently (218, 68.12%) than the vertical type (102, 31.88%). The sagittal direction and course of the canal revealed no significant difference between genders (p = 0.685) (Table 2).

The NPC length results for kink-shaped and cone-shaped groups were significantly lower than other groups (p < 0.05). The width of the SF in the funnel-shaped was significantly narrow than the other groups (p < 0.05). No statistically significant correlations were detected with respect to the sagittal shape of the canal and the diameter of the IF and nasopalatine angle (Table 3).

Table 1. Analysis effect of gender on the dimensions (in mm) of the nasopalatine canal, using reformatted sagittal slices from cone-beam computed tomography images

	Male				Female				Total				P
	Min	Max	Mean	SD	Min	Max	Mean	SD	Min	Max	Mean	SD	
a	6.28	19.22	12.46	2.46	5.20	18.22	10.74	2.27	5.20	19.92	11.45	2.5	0,0001*
b	0.40	7.11	2.6	1.39	0.4	8	2.45	1.19	0.40	8	2.51	1.28	0,306
c	1.72	9.4	5.63	1.35	1.56	10.47	5.06	1.34	1.56	10.47	5.29	1.37	0,0001*
d	60.26	104.58	77.11	8.03	58.52	99.92	75.68	8.16	58.52	104.58	76.26	8.12	0,121

*Statistically significant differences (p < 0.05), min — minimum; max — maximum; SD — standard deviation. Measurements a–d correspond to distances shown in Figure 1

Table 2. Nasopalatine canal shape distributions by gender

Nasopalatine canal classifications		Male		Female		Total		P
		N	%	N	%	N	%	
Sagittal variation/sagittal shape	Hourglass	24	18.3	28	14.8	52	16.3	0.704
	Spindle	3	2.3	9	4.8	12	3.8	
	Cone	13	9.9	23	12.2	36	11.6	
	Funnel	38	29.	55	29.1	93	29.1	
	Banana	10	7.6	17	9	27	8.4	
	Cylindrical	19	14.5	30	15.9	49	15.3	
	Tree branch like	10	7.6	7	3.7	17	5.3	
	Kinking shape	11	8.4	13	6.9	24	6	
	Other	3	2.3	7	3.7	10	3.1	
Sagittal direction-course	Vertical-straight	21	11.1	14	10.7	35	10.9	0.685
	Vertical-curved	39	20.6	28	21.4	67	20.9	
	Slanted-straight	32	16.9	16	12.2	48	15	
	Slanted-curved	97	51.3	73	55.7	170	53.1	

*Statistically significant differences (p < 0.05), N — number of subjects

The NPC length was significantly higher in the slanted-curved canal groups than other groups (p = 0.005). The SF diameter values were significantly higher in the vertical-straight canal group than other groups (p = 0.015). The IF diameters were significantly lower in the vertical-curved canal groups compared to the slanted-curved and the vertical-straight canal groups (p = 0.042). The nasopalatine angle was significantly wider in the vertical type than the slanted type (p < 0.05) (Table 4).

In coronal plane, the division of the canal was assessed. The middle-third level was the most frequent with 138 (43.1%) cases, followed by the upper-third level in 90 (28.1%) cases, and the lower-third level in 54 (16.9%) cases. In 38 cases, no divisions were observed during the course of the NPC. No significant difference was found between the presence of division in the NPC and gender (p > 0.05) but, there was a statistically significant relationship between division level of the canal and gender (p = 0.006). The NPC division in the middle-third level was the most common in males, while in females the most prevalent division levels of NPC were detected as upper-third and lower-third level. However, the same could not be detected for age groups. Also, the effect of the division in the canal on the measurements in the NPC was presented in Table 5.

In axial plane, the prevalences of incisive foramina were the following: 98.4% of the individuals had single IF, while 1.3% had double IFs and only 1 case had triple IFs. Results for the number of foramina of Stenson: the most common opening was double SFs with 252 (78.8%) individuals, single SF was observed in 41 (12.8%) individuals, triple SFs in 23 (7.2%) individuals, and quadruple SFs in 4 (1.3%) individuals. Also, the most prevalent axial group was "1–2" in 247 (77.2%) cases, meanwhile "3–2" axial group was observed in only 1 (0.3%) case (Table 6).

The findings regarding total distribution of dental status are shown in Table 7. With respect to the existence of central incisors, there was no significant difference

Table 3. Effect of sagittal shape of the canal on nasopalatine canal dimensions

Parameters	Sagittal shape	N	Mean	SD	H	P
Nasopalatine canal length [mm]	Hourglass	52	11.38	2.35	25.4	0.001*
	Spindle	12	11.20	2.56		
	Cone	36	10.69	2.05		
	Funnel	93	12.22	2.53		
	Banana	27	11.20	2.54		
	Cylindrical	49	10.83	2.35		
	Tree branch like	17	11.75	2.37		
	Kinking shape	24	10.47	2.88		
	Other	10	13.19	1.91		
Foramina of Stenson diameter [mm]	Hourglass	52	3.03	1.14	65.6	0.0001*
	Spindle	12	2.30	1		
	Cone	36	2.23	1.02		
	Funnel	93	1.81	1.06		
	Banana	27	2.95	1.51		
	Cylindrical	49	3.08	1.21		
	Tree branch like	17	2.36	1.49		
	Kinking shape	24	3.15	1.18		
	Other	10	2.19	1.14		
Incisive foramina diameter [mm]	Hourglass	52	5.56	1.29	8.1	0.424
	Spindle	12	5.52	1.42		
	Cone	36	5.54	1.11		
	Funnel	93	5.25	1.44		
	Banana	27	4.99	1.43		
	Cylindrical	49	5.13	1.38		
	Tree branch like	17	5.07	1.44		
	Kinking shape	24	5.09	1.29		
	Other	10	5.54	1.94		
Nasopalatine angle [°]	Hourglass	52	76.03	7.78	6.6	0.576
	Spindle	12	78.03	10.58		
	Cone	36	77.11	7.26		
	Funnel	93	75.65	7.72		
	Banana	27	78.90	9.25		
	Cylindrical	49	76.47	9.19		
	Tree branch like	17	77.15	8.59		
	Kinking shape	24	74.40	6.95		
	Other	10	72.79	6.11		

*Statistically significant differences (p < 0.05), SD — standard deviation; N — number of subjects

between genders. However, statistically, a significant correlation was found among age and presence of central incisors. The age of Group B was older than the other groups (p = 0.001). Also, dental status had no statistically important influence on the variations and morphometric measurements of the NPC (p > 0.05).

Statistically, no significant correlation was detected among age and length of the NPC, SF width, and the nasopalatine angle (p = 0.23, p = 0.114, p = 0.098, respectively) (Table 8). However, there is a weak, positive and statistically significant relationship between age and the width of IF was detected.

Table 4. Effect of sagittal direction-course of the nasopalatine canal dimensions, nasopalatine angle and nasopalatine canal length

Parameters	Sagittal direction-course	N	Mean	SD	H	P
Nasopalatine canal length [mm]	Vertical-straight	35	11.12	2.50	12.6	0.005*
	Vertica-curved	67	10.89	2.35		
	Slanted-straight	48	10.74	2.22		
	Slanted-curved	170	11.93	2.54		
Foramina of Stenson diameter [mm]	Vertical-straight	35	3.14	1.38	10.4	0.015*
	Vertical-curved	67	2.39	1.42		
	Slanted-straight	48	2.50	1.14		
	Slanted-curved	170	2.43	1.20		
Incisive foramina diameter [mm]	Vertical-straight	35	5.38	1.09	8.2	0.042*
	Vertical-curved	67	4.97	1.61		
	Slanted-straight	48	5.11	1.49		
	Slanted-curved	170	5.45	1.27		
Nasopalatine angle [°]	Vertical-straight	35	85.58	4.92	203.1	0.0001*
	Vertical-curved	67	85.10	3.80		
	Slanted-straight	48	72.44	4.84		
	Slanted-curved	170	71.94	5.98		

*Statistically significant differences (p < 0.05), SD — standard deviation; N — number of subjects

Table 5. Effect of the division of the canal on nasopalatine canal dimensions

Parameters	Division	N	Mean	SD	H	P
Nasopalatine canal length [mm]	No division	38	11.70	2.55	20.4	0.0001*
	Upper third level	90	11.71	2.62		
	Middle third level	138	11.73	2.29		
	Lower third level	54	10.11	2.39		
Foramina of Stenson diameter [mm]	No division	38	2.07	1.31	10.2	0.016*
	Upper third level	90	2.33	1.18		
	Middle third level	138	2.62	1.28		
	Lower third level	54	2.81	1.31		
Incisive foramina diameter [mm]	No division	38	5.44	1.23	7.8	0.049*
	Upper third level	90	5.19	1.44		
	Middle third level	138	5.47	1.24		
	Lower third level	54	4.90	1.60		
Nasopalatine angle [°]	No division	38	73.69	8.44	3.9	0.272
	Upper third level	90	76.67	8.11		
	Middle third level	138	76.43	7.61		
	Lower third level	54	76.98	9.05		

*Statistically significant differences (p < 0.05), SD — standard deviation; N — number of subjects

Intraobserver consistency

The Cohen's kappa, weighted kappa statistic, and intra-class correlation (ICC) were performed to evaluate the observer's agreement. An excellent agreement was indicated between the first and second measurements and figural analysis: ICC = 0.790 (p < 0.001) for diameter SF; ICC = 0.877 (p < 0.001) for diameter IF, and ICC = 0.944 (p < 0.001) for length of NPC; κw = 0.963 (p < 0.001) for shape of the NPC.

Table 6. The distribution of the nasopalatine canal morphology

		Male		Female		Total		P
		N	%	N	%	N	%	
Number of Stensen's foramina	1	13	9.9	28	14.8	41	12.8	0.457
	2	104	79.4	148	78.3	252	78.8	
	3	12	9.2	11	5.8	23	7.2	
	4	2	1.5	2	1.1	4	1.3	
Number of incisive foramen	1	130	99.2	185	97.9	315	98.4	0.792
	2	1	0.8	3	1.6	4	1.3	
	3	0	0.0	1	0.5	1	0.3	
Axial group	1–1	13	9.9	28	14.8	41	12.8	0.604
	1–2	103	78.6	144	76.2	247	77.2	
	1–3	12	9.2	11	5.8	23	7.2	
	1–4	2	1.5	2	1.1	4	1.3	
	2–2	1	0.8	3	1.6	4	1.3	
	3–2	0	0.0	1	0.5	1	0.3	

*Statistically significant differences (p < 0.05), N — number of subjects

Table 7. Results of dimensional comparison of nasopalatine canal measurements according to edentulous status

Edentulous status	N	Mean length of nasopalatine canal ± SD [mm]	Mean diameter of Stensen's foramina ± SD [mm]	Mean diameter of incisive foramen ± SD [mm]	Mean nasopalatine angle ± SD [º]	P
Group A	251	11.47 ± 2.46	2.55 ± 1.29	5.24 ± 1.33	76.12 ± 8.38	0.666
Group B	25	11.63 ± 2.40	2.13 ± 1.00	5.76 ± 1.53	78.03 ± 7.85	0.701
Group C	26	10.95 ± 2.65	2.53 ± 1.51	5.63 ± 1.30	75.58 ± 6.41	0.055
Group D	18	11.59 ± 3.05	2.41 ± 0.98	4.91 ± 1.76	76.79 ± 7.30	0.602

*Statistically significant differences (p < 0.05), SD — standard deviation; N — number of subjects

Table 8. Correlation between nasopalatine canal measurements and patient age

Correlation coefficients	Nasopalatine canal length	Foramina of Stenson diameter	Incisive foramen diameter	Nasopalatine angle
Age				
r	0.067	−0.089	0.158**	−0.093
p	0.23	0.114	0.005	0.098

r < 0.01 is statistically significant, p < 0.05 is statistically significant

DISCUSSION

Radiologic imaging is an important diagnostic instrument for surgical procedures and post-operative assessment in today's surgical approach. Description of the variations, particularly involving neurovascular anatomy, plays a significant role in surgical process. The neurovascular content in the premaxilla increases the risk of complications in this region [21].

Conventional imaging methods do not have adequate confidence in the assessment of neurovascular structures in bone [3, 25]. Various imaging techniques were used in other presented studies about the NPC.

CT images [14, 16, 17], micro-CT scans [23] or magnetic resonance imaging [12] have been used in the previously to evaluate the macro and micro-anatomy of the premaxilla and also the neurovascular bundle of the NPC. In the current study, the NPC was analysed with CBCT for three-dimensional evaluation. More recently, CBCT has been accepted as an alternative imaging modality for assessment of the neurovascular content and bone in the anterior maxillary region compared using by CT due to higher spatial resolution, substantially lower radiation dose, low cost, easy access and increased use [15].

931

Measurements

In some studies, the IF was estimated by a line parallel to the transverse plane [17]. The authors suggest that using this technique would have resulted in a shorter NPC length than its exact size and the narrower width for IF. So, in the current research in which dimensional assessments of the canal were performed using the Bornstein et al. [5] method, the average length of the NPC was found to be 11.45 mm. In the literature, the mean length of NPC has been reported to be between 8.1 mm and 16.33 mm [16, 28]. Bornstein et al. [5], Ozcakir-Tomruk et al. [18], Tözüm et al. [28], and Sekerci et al. [21] indicated similar mean values at 10.99 mm, 10.87 mm, 10.86 mm, and 10.8 mm, respectively, but Mraiwa et al. [17] and Liang et al. [14] reported a lower canal lengths.

No significant correlation was observed between patient ages and length of the canal. Therefore it can be speculated that NPC length differences among studies are not owing to the mean age of the samples, but may result from the method used, scanning techniques, ethnic differences or variations in gender distribution of the samples [18]. Furthermore, Bajoria et al. [4], although they found statistically significant results (p = 0.0001) in different age groups with length of NPC, they stated that this difference might be due to dental status rather than age-related changes. Mardinger et al. [16] have concluded that the canal was not a static formation that tended to expanded in all dimensions after tooth extractions and aging. Thus, the edentulous group might be older than the dentate group, so the morphological differences according to the dental status related to not only teeth existence but also age-related changes in bone quantity and quality.

In terms of dental status, our findings were unlike other researches that noted significantly longer canal length in the dentulous group [6, 14, 18]. In the current study, NPC length was shortest in group B (total edentulous individuals) which was not statistically significant. In addition, statistically significant differences were not observed between the width of the IF and SF according to the dental status. These results are consistent with the conclusions of Liang et al. [14] and Tözüm et al. [28].

It is generally believed that the diameter of the IF is less than 6 mm and when it exceeds 10 mm pathological risks should be considered [17]. In this study, the IF stayed under this cut-off value (mean 5.29 mm), but the width between 1.56 to 10.47 mm, even no presence of NPC pathology.

Although there was the difference between one of the reference points used by these researchers [14] and our study (while our reference plane was the nasal floor, some of them used the horizontal plane of the palate), both planes are parallel and comparisons can be made. In the present study, no correlation was found between the length of NPC and the nasopalatine angle.

The variations of the NPC

In this study, all three planes were taken into consideration to make a detailed anatomical analysis.

In sagittal plane. In the literature, studies about the variations of the shape of the canal have been reported, but standard classification was not found. Fernandez-Alonso et al. [7] and Gönül et al. [9] classified the shape of the canal in four groups (hourglass, cylindrical, funnel, banana) in sagittal planes, but Liang et al. [14] divided into only two groups: conical and cylindrical. Sekerci et al. [21], Etoz and Şişman [6] and Hakbilen and Magat [11] evaluated the shape of the canal in six groups (hourglass, cone, funnel, cylinder, banana and tree branches) in their studies. However, these classifications were inadequate to fully evaluate the shape of the NPC. All canal shapes defined in the literature were analysed and a new classification was made. It was detected that, while the funnel shapes (29.1%) and hourglass shapes (16.3%) were found at the highest rate, the rate of the spindle shapes and "other" groups were seen at the lowest rated, respectively 3.8%, 3.1%. These results are consistent with most studies in the literature [4, 6, 11, 20, 21, 26]. However, the results are different from studies presented by Tözüm et al. [28], Hakbilen and Magat [11] and Gönül et al. [9]. We suggest that these variations may come out from racial characteristics, the number of samples and distinctions between classifications.

Our results for sagittal direction-course are contrary to Song et al. [23] who found the majority of the vertical type of the canal, but in this study, slanted ones were more frequent than vertical types. Also, the present results for the straight canal versus curved canal types were different from these researchers. It can be owing to the less sample number in their study [23].

Which was analysed in only one study previously, we presented differences in the NPC angle with re-

spect to the direction and course [7]. In the present study, it is shown that the angle results of the vertical types were greater than those of the slanted types. This finding is consistent with the results of Fernandez-Alonso et al. [7].

The shape, direction and course of the canal with the NPC angle should be considered for the location and angulation of dental implants [7]. Liang et al. [14] point out that the contact of dental implants with neural tissue may affect the osseointegration of the implant.

In coronal plane. Since the shape of the canal may change due to the divisions within the canal between the coronal sections, only the presence and level of the division were evaluated in this plane, unlike previous studies [5–9, 18, 21].

In the literature, only 3 studies are examining the division classification of the NPC [20, 26, 27]. Thakur et al. [26] and Safi et al. [20] mentioned the division at the middle third as the most frequent form, respectively 51%, 51.5% were found in the upper third. These findings were compatible with the present study.

While not analysed by previous studies, divisions within the canal affect the diameters and length of the canal. Regarding coronal slice, the NPC length and width of IF were significantly lower in the lower-third level group than other groups (p < 0.05). However, the width of SF was greater in the lower-third level group. In addition, no significant difference was found between division groups and the NPC angle (p > 0.05).

In axial plane. In the literature, NPC was classified according to the numbers in the axial plane on CBCT images. Most variations of the NPC reported at the level of the nasal floor. Some of the studies classified nasopalatine foramina in four groups [6, 8, 14, 26, 27] while some of them evaluated in three groups [4, 21] on the axial section. However, they did not give any information about the number of incisive foramina. Also, Sicher [22] found that nasal opening might be present from a single foramen and up to six separate foramina. Besides, in contrast to common belief, Al-Amery et al. [1] and Song et al. [23] evaluated the NPC at the middle portion to the level of the nasal opening. In this study, the number of openings of the canal in the nasal and palatal level detected and these levels were evaluated together for established the axial classification.

In terms of axial classification, the most often axial group in the current study was "1–2" (in 77.2% of individuals). The result was consistent with the literature [8, 9]. However, Liang et al. [14] reported that "1–1" to be the most frequent group (44%), followed by "1–2" (39%).

In this study, no significant difference was found in the morphology of the canal between the dental groups. It may result from the interindividual variations and non-homogenous distribution of dental groups. Also, the rate of resorption can change inter-individual and even in the same individual at different times [2]. The time span since tooth loss and factors (anatomic, metabolic, functional, and prosthetic factors) which affect the rate of resorption should be taken into consideration in future studies.

CONCLUSIONS

Rehabilitation of the anterior maxilla is with high clinical relevance in relation to function and aesthetic. New findings are reported in this study, about the classification of the canal shape and differences in morphometric measurements with respect to the level of the division. The present results emphasized the variability of the NPC in terms of several parameters; therefore, the authors recommend an improved understanding of this anatomic structure and using cross-sectional imaging for better surgical results and to reduce surgical complications.

Conflict of interest: None declared

REFERENCES

1. Al-Amery SM, Nambiar P, Jamaludin M, et al. Cone beam computed tomography assessment of the maxillary incisive canal and foramen: considerations of anatomical variations when placing immediate implants. PLoS One. 2015; 10(2): e0117251, doi: 10.1371/journal.pone.0117251, indexed in Pubmed: 25679505.
2. Asaumi R, Kawai T, Sato I, et al. Three-dimensional observations of the incisive canal and the surrounding bone using cone-beam computed tomography. Oral Radiology. 2010; 26(1): 20–28, doi: 10.1007/s11282-010-0039-4.
3. Bahşi I, Orhan M, Kervancıoğlu P, et al. Anatomical evaluation of nasopalatine canal on cone beam computed tomography images. Folia Morphol. 2019; 78(1): 153––162, doi: 10.5603/FM.a2018.0062, indexed in Pubmed: 30009362.
4. Bajoria A, Kochar T, Sangamesh NC, et al. Nasopalatine canal revisited: an insight to anterior maxillary implants.

Open J Stomatol. 2018; 08(01): 1–15, doi: 10.4236/ojst.2018.81001.

5. Bornstein MM, Balsiger R, Sendi P, et al. Morphology of the nasopalatine canal and dental implant surgery: a radiographic analysis of 100 consecutive patients using limited cone-beam computed tomography. Clin Oral Implants Res. 2011; 22(3): 295–301, doi: 10.1111/j.1600-0501.2010.02010.x, indexed in Pubmed: 21039896.

6. Etoz M, Sisman Y. Evaluation of the nasopalatine canal and variations with cone-beam computed tomography. Surg Radiol Anat. 2014; 36(8): 805–812, doi: 10.1007/s00276-014-1259-9, indexed in Pubmed: 24488202.

7. Fernández-Alonso A, Suárez-Quintanilla JA, Muinelo-Lorenzo J, et al. Three-dimensional study of nasopalatine canal morphology: a descriptive retrospective analysis using cone-beam computed tomography. Surg Radiol Anat. 2014; 36(9): 895–905, doi: 10.1007/s00276-014-1297-3, indexed in Pubmed: 24752396.

8. Friedrich RE, Laumann F, Zrnc T, et al. The nasopalatine canal in adults on cone beam computed tomograms: a clinical study and review of the literature. In Vivo. 2015; 29(4): 467–486, indexed in Pubmed: 26130792.

9. Gönül Y, Bucak A, Atalay Y, et al. MDCT evaluation of nasopalatine canal morphometry and variations: An analysis of 100 patients. Diagn Interv Imaging. 2016; 97(11): 1165–1172, doi: 10.1016/j.diii.2015.11.012, indexed in Pubmed: 26797526.

10. Güncü GN, Yıldırım YD, Yılmaz HG, et al. Is there a gender difference in anatomic features of incisive canal and maxillary environmental bone? Clin Oral Implants Res. 2013; 24(9): 1023–1026, doi: 10.1111/j.1600-0501.2012.02493.x, indexed in Pubmed: 22587805.

11. Hakbilen S, Magat G. Evaluation of anatomical and morphological characteristics of the nasopalatine canal in a Turkish population by cone beam computed tomography. Folia Morphol. 2018; 77(3): 527–535, doi: 10.5603/FM.a2018.0013, indexed in Pubmed: 29399754.

12. Jacobs R, Lambrichts I, Liang X, et al. Neurovascularization of the anterior jaw bones revisited using high-resolution magnetic resonance imaging. Oral Surg Oral Med Oral Pathol Oral Radiol Endod. 2007; 103(5): 683–693, doi: 10.1016/j.tripleo.2006.11.014, indexed in Pubmed: 17320428.

13. Keith DA. Phenomenon of mucous retention in the incisive canal. J Oral Surg. 1979; 37(11): 832–834, indexed in Pubmed: 290778.

14. Liang X, Jacobs R, Martens W, et al. Macro- and micro-anatomical, histological and computed tomography scan characterization of the nasopalatine canal. J Clin Periodontol. 2009; 36(7): 598–603, doi: 10.1111/j.1600-051X.2009.01429.x, indexed in Pubmed: 19538333.

15. Librizzi ZT, Tadinada AS, Valiyaparambil JV, et al. Cone-beam computed tomography to detect erosions of the temporomandibular joint: Effect of field of view and voxel size on diagnostic efficacy and effective dose. Am J Orthod Dentofacial Orthop. 2011; 140(1): e25–e30, doi: 10.1016/j.ajodo.2011.03.012, indexed in Pubmed: 21724068.

16. Mardinger O, Namani-Sadan N, Chaushu G, et al. Morphologic changes of the nasopalatine canal related to dental implantation: a radiologic study in different de-grees of absorbed maxillae. J Periodontol. 2008; 79(9): 1659–1662, doi: 10.1902/jop.2008.080043, indexed in Pubmed: 18771366.

17. Mraiwa N, Jacobs R, Van Cleynenbreugel J, et al. The nasopalatine canal revisited using 2D and 3D CT imaging. Dentomaxillofac Radiol. 2004; 33(6): 396–402, doi: 10.1259/dmfr/53801969, indexed in Pubmed: 15665234.

18. Özçakır-Tomruk C, Dölekoğlu S, Özkurt-Kayahan Z, et al. Evaluation of morphology of the nasopalatine canal using cone-beam computed tomography in a subgroup of Turkish adult population. Surg Radiol Anat. 2016; 38(1): 65–70, doi: 10.1007/s00276-015-1520-x, indexed in Pubmed: 26228382.

19. Radlanski RJ, Emmerich S, Renz H. Prenatal morphogenesis of the human incisive canal. Anat Embryol. 2004; 208(4): 265–271, doi: 10.1007/s00429-004-0389-y, indexed in Pubmed: 15293047.

20. Safi Y, Moshfeghi M, Rahimian S, et al. Assessment of nasopalatine canal anatomic variations using cone beam computed tomography in a group of Iranian population. Iran J Radiol. 2016; 14(1), doi: 10.5812/iranjradiol.37028.

21. Sekerci AE, Buyuk SK, Cantekin K. Cone-beam computed tomographic analysis of the morphological characterization of the nasopalatine canal in a pediatric population. Surg Radiol Anat. 2014; 36(9): 925–932, doi: 10.1007/s00276-014-1271-0, indexed in Pubmed: 24590491.

22. Sicher H. Anatomy and oral pathology. Oral Surgery, Oral Medicine, Oral Pathology. 1962; 15(10): 1264–1269, doi: 10.1016/0030-4220(62)90163-9.

23. Song WC, Jo DI, Lee JY, et al. Microanatomy of the incisive canal using three-dimensional reconstruction of microCT images: an ex vivo study. Oral Surg Oral Med Oral Pathol Oral Radiol Endod. 2009; 108(4): 583–590, doi: 10.1016/j.tripleo.2009.06.036, indexed in Pubmed: 19778745.

24. Stenson N. Stenonis De muscuhs et glandulis. Lugdunum Batavorum (Leyden) -de narium vasis; in Mangeti. Bibl Anatom Genev 1685; 11: 763.

25. Temmerman A, Hertelé S, Teughels W, et al. Are panoramic images reliable in planning sinus augmentation procedures? Clin Oral Implants Res. 2011; 22(2): 189–194, doi: 10.1111/j.1600-0501.2010.02000.x, indexed in Pubmed: 20868452.

26. Thakur AR, Burde K, Guttal K, et al. Anatomy and morphology of the nasopalatine canal using cone-beam computed tomography. Imaging Sci Dent. 2013; 43(4): 273–281, doi: 10.5624/isd.2013.43.4.273, indexed in Pubmed: 24380067.

27. Tlili N, Abdallah S, Amor F, et al. Anatomo-radiological assessment of incisive canal using cone beam computed tomographs. Int J Anat Res. 2017; 5(3.3): 4333–4342, doi: 10.16965/ijar.2017.328.

28. Tözüm TF, Güncü GN, Yıldırım YD, et al. Evaluation of maxillary incisive canal characteristics related to dental implant treatment with computerized tomography: a clinical multicenter study. J Periodontol. 2012; 83(3): 337–343, doi: 10.1902/jop.2011.110326, indexed in Pubmed: 21910596.

29. von Arx T, Lozanoff S. Clinical oral anatomy: a comprehensive review for dental practitioners and researchers. Springer 2016.

V M
VIA MEDICA

ORIGINAL ARTICLE

Extensive pneumatisation of the sphenoid bone: anatomical investigation of the recesses of the sphenoid sinuses and their clinical importance

J. Jaworek-Troć[1, 2], J.A. Walocha[1], M. Loukas[3], R.S. Tubbs[4], J. Iwanaga[4], J. Zawiliński[1],
K. Brzegowy[1], J.J. Zarzecki[5], A. Curlej-Wądrzyk[6], E. Kucharska[7], F. Burdan[8], P. Janda[1],
M.P. Zarzecki[1]

[1]Department of Anatomy, Jagiellonian University Medical College, Krakow, Poland
[2]Department of Radiology, Jagiellonian University Medical College, Krakow, Poland
[3]Department of Anatomical Sciences, St. George's University, Grenada
[4]Department of Neurosurgery, Tulane University School of Medicine, New Orleans, United States
[5]Medical University of Silesia, Katowice, Poland
[6]Department of Integrated Dentistry, Dental Institute, Jagiellonian University Medical College, Krakow, Poland
[7]Department of Gerontology, Geriatrics and Social Work, Jesuit University Ignatianum, Krakow, Poland
[8]Human Anatomy Department, Medical University, Lublin, Poland

Background: There is a great variance between the extents of pneumatisation of the sphenoid sinuses that can reach beyond the body of the sphenoid bone. The purpose of this study was to find the prevalence of the recesses of the sphenoid sinuses in Polish adult population.

Materials and methods: Two hundred ninety-six computed tomography (CT) scans of patients who did not present any pathology in the sphenoid sinuses were evaluated in this retrospective analysis. Spiral CT scanner (Siemens Somatom Sensation 16) was used to glean the medical images. Standard scan procedure was applied, with Siemens CARE Dose 4D option enabled. No contrast medium was administered.

Results: In the majority of the patients (93.92%), the pneumatisation of the sphenoid sinuses expanded beyond the body of the sphenoid bone; hence, there were recesses of the sinuses present. The most common variant was the presence of two recesses — 12.84% of cases. The prevalence of all the 17 recesses was only 0.34%. Amongst the uneven recesses present, the sphenoidal rostrum's recess (61.15% of the patients) and the inferior clinoid recess (56.42%) were the most common. Amongst the even recesses present, the lateral recess was prevalent in the majority (65.88%), whereas the posterior clinoid process' recess was the least common (9.8%).

Conclusions: Presence of the recesses might facilitate access to the cranial fossae; hence, comprehensive evaluation of the sphenoid sinuses is of immense importance in order to avoid unnecessary drills through the hard bone, which could potentially damage the nearby neurovascular structures. (Folia Morphol 2021; 80, 4: 935–946)

Key words: sphenoid sinus, recess, anatomy, otorhinolaryngology, neurosurgery

Address for correspondence: Dr. M.P. Zarzecki, MD, Department of Anatomy, Jagiellonian University Medical College, ul. Kopernika 12, 31–034 Kraków, Poland, tel/fax: +48 12 422 95 11, e-mail: michal.zarzecki@uj.edu.pl

INTRODUCTION

The body of the sphenoid bone contains pneumatic spaces filled with air, lined with mucous membrane, known as the sphenoid sinuses. Usually denoted as right and left, separated by the main septum, they are known to have a vastly varied morphology. Some of the most notable discrepancies between them include: their dimensions, relation to the surrounding neurovascular structures, the number of septa present, and the degree to which they are aerated (pneumatised) [20–23]. Henceforth, it is extremely difficult to assign one variation as a "normal anatomical variant" of the sphenoid sinuses due to the scarcity of unequivocal patterns found [21].

Previous studies reported that the sphenoid sinuses begin to develop approximately around the 3rd–4th month of gestation, as a result of bilateral intussusception of the nasal mucosa in the direction of the sphenoid bone [13, 52]. It is possible to find the yet not pneumatised sinuses in the newborn which at that period of their development form small cavities within the sphenoid body [9]. This primary process of aeration is a form of continuation of the sphenoethmoidal recess [30]. The proper pneumatisation of the sphenoid sinuses commences postnatally (around the age of 3–4), but the exact moment of termination of this process is not known (approximately 12–16 years of age), usually with completely aerated sinuses in the third decade of life [55]. This secondary process of aeration involves the growth of connective tissue into the viscerocranium [30].

However, quite often the pneumatisation of the sphenoid sinuses reaches beyond the body of the sphenoid bone, forming recesses. It might involve other parts of the sphenoid bone (e.g. lesser and greater wings, pterygoid process) and/or neighbouring bones (e.g. vomer, palatine bones) [21]. As such they become a matter of clinical importance during invasive procedures carried out within the lumen of the sinuses. For example, presence of the anterior clinoid process pneumatisation (the posterolateral recess) might lead to pneumocephalus or rhinorrhoea [51], but its presence is also useful while accessing aneurysms of the paraclinoid and supraclinoid parts of the internal carotid artery or central nervous system tumours in that region [2].

Preoperative comprehensive evaluation of the sphenoid sinus and its neighbouring neurovascular structures is of immense importance in order to perform a safe procedure and diminish the risk of

iatrogenic complications [1, 14, 15, 25, 27, 28, 34, 35, 37, 40, 48]. Computed tomography (CT) scan is regarded as one of the most accurate methods of gleaning the medical images of the paranasal sinuses, as it allows pinpointing a clear-cut representation of the osseous structures and identify anatomical variations. Most certainly it provides more accurate information regarding the variant morphology of the sphenoid sinuses than the data provided from cadaveric dissections [6].

Endoscopic approaches are said to be the golden standard for the treatment of cerebrospinal fluid (CSF) leakage [3] and facilitate access to various pathologies found "between the frontal sinus and the upper border of lower 1/3 of the clivus (dens) in the sagittal plane or those between the 2 orbits superiorly and jugular foramens inferiorly in the paramedian plane" [50]. The minimally invasive endoscopic techniques allowed medical professionals to decrease the number of classical extensive surgical interventions performed in this region.

The primary aim of this study was to present the up-to-date prevalence of the recesses of the sphenoid sinuses in Polish adult patients by the means of CT imaging in order to aid physicians in carrying out invasive endoscopic procedures in that region. The secondary outcome of the study was the subgroup analysis of females and males so as to evaluate whether there are any statistically significant differences between the presence of the particular recesses and gender. To the best knowledge of the authors this is the first study that has comprehensively taken into the account the possible impact of patients' sex upon the prevalence of all the possible sphenoid sinus' recesses.

MATERIALS AND METHODS

The researchers had access to a total of 359 medical images of patients referred to the Department of Medical Imaging of the University Hospital in Krakow to undergo a CT scan. In order to participate in this study, the patients had to be over eighteen years old and present no pathologies in the sphenoid sinuses. Patients, who had suffered from a head trauma or had undergone nasal, orbital or cranial basis surgery prior to the research, were not included in the following analysis (63 patients). A total of 296 patients (147 females, 149 males) fulfilled the inclusion criteria and were hence included in this retrospective analysis.

Standard procedure was applied with Siemens CARE Dose 4D option enabled while obtaining the

CT scans via spiral CT scanner Siemens Somatom Sensation 16. Contrast medium was not administered to any of the patients. Multiplans reconstruction tool was used in order to reconstruct the images in the coronal and sagittal planes, after the CT images in the axial planes were gleaned in the first instance. Diagnostic station Siemens Volume Wizard was used to evaluate the medical imaging data. Seven researchers evaluated the obtained data (J.J.T., J.A.W., M.L., J.Z., K.B., J.J.Z., M.P.Z.).

The analysis of the obtained images involved the presence of the sphenoid sinuses' recesses (depending on the direction of the pneumatisation), as adapted from the classification of the previous authors [8, 10, 38]:

1. The median pneumatisation:
   — in the anterior direction:
   • the sphenoidal rostrum's recess (in the direction of the sphenoidal rostrum),
   • the septal recess (in the direction of the main septum of the sphenoid sinuses),
   • the vomeral recess (in the direction of the vomer);
   — in the posterior direction:
   • the superior clinoid recess (in the dorsal direction of the sella turcica; for this recess, presence of the pneumatisation of the posterior clinoid process was also taken into account),
   • the inferior clinoid recess (in the direction of Blumenbach's clivus).
2. The lateral pneumatisation:
   — the anterolateral recess (in the direction of the lesser wing of the sphenoid bone, superior to the optic canal);
   — the posterolateral recess (in the direction of the lesser wing of the sphenoid bone, comprising the anterior clinoid processes);
   — the lateral recess (in the direction of the greater wing of the sphenoid bone if the pneumatisation crossed the conventional line between the foramen rotundum and the pterygoid/Vidian canal);
   — the pterygoid recess (in the direction of the pterygoid process of the sphenoid bone);
   — the palatine recess (in the direction of the palatine bone).

Ethical approval

All procedures performed in studies involving human participants were in accordance with the ethical standards of the institutional and/or national research committee and with the 1964 Helsinki declaration and its later amendments or comparable ethical standards. For this type of study formal consent is not required.

Statistical analysis

Statistical analysis in this study was conducted with STATISTICA version 13.3 by TIBCO Software Inc®. Chi^2 test, Mann-Whitney's test and Fisher's exact test were used to detect between-gender differences in prevalences of specific recesses. A statistically significant value of $p < 0.05$ was chosen for all the results.

RESULTS

In the majority of the patients included in the study (278 — 136 females, 142 males), the pneumatisation of the sphenoid sinuses reached beyond the body of the sphenoid bone, hence there were recesses of the sinuses present. Only in 18 patients (11 females, 7 males) the recesses did not develop. Presence of two recesses was the most common variant — found in 38 patients (15 females, 23 males); sporadically there were more than ten recesses present, whereas presence of all the 17 recesses was noted only in one patient. The distributions of the prevalence of the recesses differed significantly between males and females ($p = 0.012$, Mann-Whitney's test). The total number of all of the recesses found is collected in Table 1.

Amongst the uneven recesses, the sphenoidal rostrum's recess was prevalent the most often (in 181 patients — 80 females, 101 males), but the inferior clinoid recess was also present in the majority of patients (167 — 71 females, 96 males). The pneumatisation of the main septum was the least common (noted only in 26 patients — 8 females, 18 males). Amongst the even recesses, the lateral recess was prevalent the most often (in 195 patients — 97 females, 98 males), whereas the rarest variant was the presence of the posterior clinoid process' recess (only in 29 patients — 4 females, 25 males).

There was a statistically significant difference between the proportions of females and males with the presence of the sphenoidal rostrum's recess ($p = 0.018$, χ^2 test), the septal recess ($p = 0.045$, χ^2 test), the inferior clinoid recess ($p = 0.005$, χ^2 test), and the superior clinoid recess ($p = 0.045$, χ^2 test). No statistically significant difference was found between the proportion of females and males with the presence of the vomeral recess ($p = 0.639$, χ^2 test) (Table 2).

Table 1. The prevalence of the sphenoid sinuses' recesses — the number of the recesses

The number of the recesses	F	F%	M	M%	F + M	F + M%
0	11	7.48%	7	4.7%	18	6.08%
1	12	8.16%	11	7.38%	23	7.77%
2	15	10.2%	23	15.44%	38	12.84%
3	21	14.29%	7	4.7%	28	9.46%
4	17	11.56%	12	8.05%	29	9.8%
5	10	6.8%	8	5.37%	18	6.08%
6	17	11.56%	11	7.38%	28	9.46%
7	9	6.12%	12	8.05%	21	7.09%
8	12	8.16%	17	11.41%	29	9.8%
9	14	9.52%	11	7.38%	25	8.45%
10	4	2.72%	9	6.04%	13	4.39%
11	2	1.36%	7	4.7%	9	3.04%
12	1	0.68%	8	5.37%	9	3.04%
13	1	0.68%	2	1.34%	3	1.01%
14	1	0.68%	3	2.01%	4	1.35%
15	0	0%	0	0%	0	0%
16	0	0%	0	0%	0	0%
17	0	0%	1	0.67%	1	0.34%

F — females; F% — the percentage of females; M — males; M% — the percentage of males

Table 2. The prevalence of the uneven recesses in the sphenoid sinuses — the types of the recesses

	F	F%	M	M%	F + M	F + M%
Sphenoidal rostrum's	80	54.42%	101	67.79%	181	61.15%
Septal	8	5.44%	18	12.08%	26	8.78%
Vomeral	39	26.53%	36	24.16%	75	25.34%
Inferior clinoid	71	48.3%	96	64.43%	167	56.42%
Superior clinoid	42	28.57%	59	39.6%	101	34.12%

F — females; F% — the percentage of females; M — males; M% — the percentage of males

Table 3. The prevalence of the even sphenoid sinuses' recesses — the types of the recesses

	F	F%	M	M%	F + M	F + M%
Post. clin. proc.	4	2.72%	25	16.78%	29	9.8%
Anterolateral	29	19.73%	52	34.9%	81	27.36%
Posterolateral	40	27.21%	55	36.91%	95	32.09%
Lateral	97	65.99%	98	65.77%	195	65.88%
Pterygoid	59	40.14%	67	44.97%	126	42.57%
Palatine	72	48.98%	70	46.98%	142	47.97%

Post. clin. proc. — posterior clinoid process' recess; F — females; F% — the percentage of females; M — males, M% — the percentage of females

There was a statistically significant difference between the proportions of females and males with the presence of the posterior clinoid process' recess (p < 0.001, χ^2 test), and the anterolateral recess (p = 0.003, χ^2 test). Notwithstanding, no statistically significant difference was found between the proportion of females and males with the presence of the posterolateral recess (p = 0.074, χ^2 test), the lateral recess (p = 0.969, χ test), the pterygoid recess (p = 0.401, χ^2 test), and the palatine recess (p = 0.731, χ^2 test) (Table 3).

A statistically significant difference was found between the proportions of females and males with the presence of the posterior clinoid process' recess (PCP) bilaterally (R+L) (p = 0.011, χ^2 test), the PCP unilaterally (R/L) (p = 0.002, χ^2 test), the anterolateral recess (A-L) R+L (p < 0.001, χ^2 test), the posterolateral recess (P-L) R/L (p < 0.001, χ^2 test), the P-L R/L (p = 0.034, χ^2 test), and the lateral recess (La) R/L (p = 0.003, χ^2 test). Nonetheless, no statistically significant differences were found between the proportions of females and males with the presence of the A-L R/L (p = 0.173, Fischer's exact test), the P-L R+L (p = 0.910, χ^2 test), the La R+L (p = 0.621, χ^2 test), the pterygoid recess (P) R+L (p = 0.182, χ^2 test), the P R/L (p = 0.728, χ^2 test), the palatine recess (Pl) R+L (p = 0.938, χ^2 test), and the Pl R/L (p = 0.719, χ^2 test) (Table 4).

There was a statistically significant difference found between the proportions of males and females with PCP R+L present (p = 0.011, χ^2 test), PCP R (p = 0.033, χ^2 test), and A-L R+L (p < 0.001, χ^2 test). In the remaining variants, no statistically significant difference was noted between genders in the prevalences of the respective recesses: PCP (left unilateral location — L) (p = 0.067, Fischer's exact test), A-L (right unilateral location — R) (p = 0.506, χ^2 test), A-L L (p = 0.229, χ^2 test), P-L R+L (p = 0.910, χ^2 test), P-L R (p = 0.051, χ^2 test), P-L L (p = 0.393, χ^2 test), La R+L (p = 0.621, χ^2 test), La R (p = 0.518, χ^2 test), La L (p = 0.265, χ^2 test), P R+L (p = 0.182, χ^2 test), P R (p = 0.846, χ^2 test), P L (p = 0.574, χ^2 test), Pl R+L (p = 0.939, χ^2 test), Pl R (p = 0.789, χ^2 test), Pl L (p = 0.821, χ^2 test) (Tables 5 and 6, Figs. 1–11).

DISCUSSION

In the majority of patients (93.92%), the pneumatisation of the sphenoid sinuses reached beyond the body of the sphenoid bone. The most common variant was the presence of two recesses — found

Table 4. The prevalence of the even sphenoid sinuses' recesses, taking into the account the unilateral and bilateral location — the types and location of the recesses

	F	F%	M	M%	F + M	F + M%
PCP R+L	1	0.68%	9	6.04%	10	3.38%
PCP R/L	3	2.04%	16	10.74%	19	6.42%
A-L R+L	15	10.2%	44	29.53%	59	19.93%
A-L R/L	14	9.52%	8	5.37%	22	7.43%
P-L R+L	22	14.97%	23	15.44%	45	15.2%
P-L R/L	18	12.24%	32	21.48%	50	16.89%
La R+L	58	39.46%	63	42.28%	121	40.88%
La R/L	39	26.53%	35	23.49%	74	25%
P R+L	28	19.05%	38	25.5%	66	22.3%
P R/L	31	21.09%	29	19.46%	60	20.27%
Pl R+L	45	30.61%	45	30.2%	90	30.41%
Pl R/L	27	18.37%	25	16.78%	52	17.57%

R+L — bilateral location; R/L — unilateral location; PCP — posterior clinoid process' recess; A-L — the anterolateral recess; P-L — the posterolateral recess; La — the lateral recess; P — the pterygoid recess; Pl — the palatine recess; F — females; F% — the percentage of females; M — males; M% — the percentage of males

Table 5. The prevalence of the even sphenoid sinuses' recesses, taking into the account the unilateral and bilateral location, as well as the right and left sides (for unilateral locations) — the types and the location of the recesses

	F	F%	M	M%	F + M	F + M%
PCP R+L	1	0.68%	9	6.04%	10	3.38%
PCP R	2	1.36%	9	6.04%	11	3.72%
PCP L	1	0.68%	7	4.7%	8	2.7%
A-L R+L	15	10.2%	44	29.53%	59	19.93%
A-L R	6	4.08%	4	2.68%	10	3.38%
A-L L	8	5.44%	4	2.68%	12	4.05%
P-L R+L	22	14.97%	23	15.44%	45	15.2%
P-L R	9	6.12%	19	12.75%	28	9.46%
P-L L	9	6.12%	13	8.72%	22	7.43%
La R+L	58	39.46%	63	42.28%	121	40.88%
La R	9	6.12%	12	8.05%	21	7.09%
La L	30	20.41%	23	15.44%	53	17.91%
P R+L	28	19.05%	38	25.5%	66	22.3%
P R	10	6.8%	11	7.38%	21	7.09%
P L	21	14.29%	18	12.08%	39	13.18%
Pl R+L	45	30.61%	45	30.2%	90	30.41%
Pl R	10	6.8%	9	6.04%	19	6.42%
Pl L	17	11.56%	16	10.74%	33	11.15%

R+L — bilateral location; R — right side location; L — left side location; PCP — the posterior clinoid process' recess; A-L — the anterolateral recess; P-L — the posterolateral recess; La — the lateral recess; P — the pterygoid recess; Pl — the palatine recess; F — females; F% — the percentage of females; M — males; M% — the percentage of males

Table 6. The prevalence of the even and uneven sphenoid sinuses' recesses, cumulative data

	F	F%	M	M%	F + M	F + M%
Sphenoidal rostrum's	80	54.42%	101	67.79%	181	61.15%
Septal	8	5.44%	18	12.08%	26	8.78%
Vomeral	39	26.53%	36	24.16%	75	25.34%
Inferior clinoid	71	48.3%	96	64.43%	167	56.42%
Superior clinoid	42	28.57%	59	39.6%	101	34.12%
Pos. clin. proc.	4	2.72%	25	16.78%	29	9.8%
Anterolateral	29	19.73%	52	34.9%	81	27.36%
Posterolateral	40	27.21%	55	36.91%	95	32.09%
Lateral	97	65.99%	98	65.77%	195	65.88%
Pterygoid	59	40.14%	67	44.97%	126	42.57%
Palatine	72	48.98%	70	46.98%	142	47.97%

Post. clin. proc. — posterior clinoid process' recess; F — females; F% — the percentage of females; M — males; M% — the percentage of males
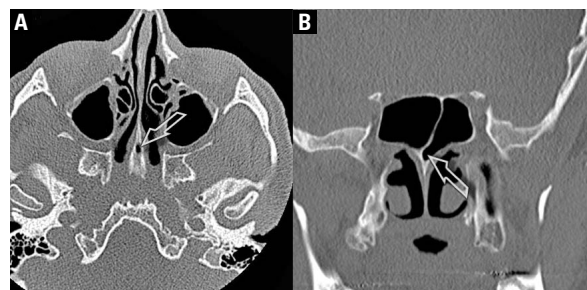

Figure 1. A computed tomography scan of the paranasal sinuses, the sphenoidal rostrum's recess; **A.** Axial plane; **B.** Coronal plane.

in 12.84% of the case, sporadically there were more than ten recesses present, whereas the presence of all the 17 recesses was noticed only in 0.34% of the patients (0.67% males).

Amongst the uneven recesses, the most common was the sphenoidal rostrum's recess (61.15%), but the inferior clinoid recess was also prevalent very often (56.42%). The rarest variant found was the pneumatisation of the main septum (8.78%). Amongst the even recesses, the lateral recess was present in the majority of the patients (65.88%), whereas the rarest was the posterior clinoid process' recess, found only in 9.8% of the patients. Table 7 presents the comparison between the results presented in this research and the previous studies [2, 4, 7, 8, 10–13, 16–19, 24, 27, 31–33, 36, 39, 45, 46, 49, 56].
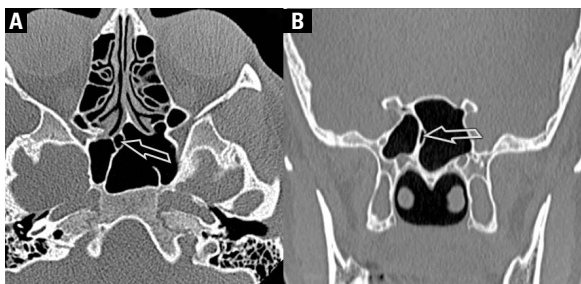
Figure 2. A computed tomography scan of the paranasal sinuses, the septal recess; **A.** Axial plane; **B.** Coronal plane.
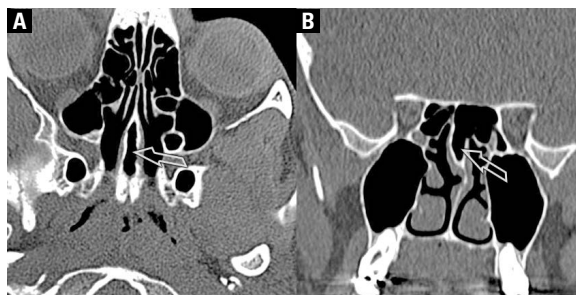

Figure 3. A computed tomography scan of the paranasal sinuses, the vomeral recess; **A.** Axial plane; **B.** Coronal plane.
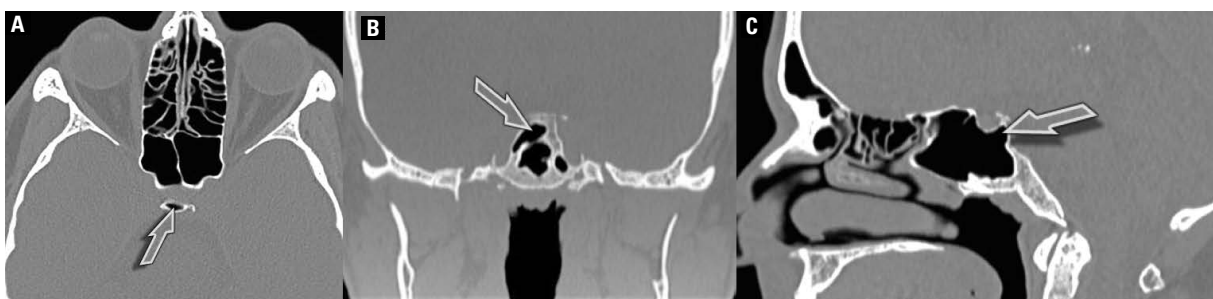

Figure 4. A computed tomography scan of the paranasal sinuses, the superior clinoid recess; **A.** Axial plane; **B.** Coronal plane; **C.** Sagittal plane.
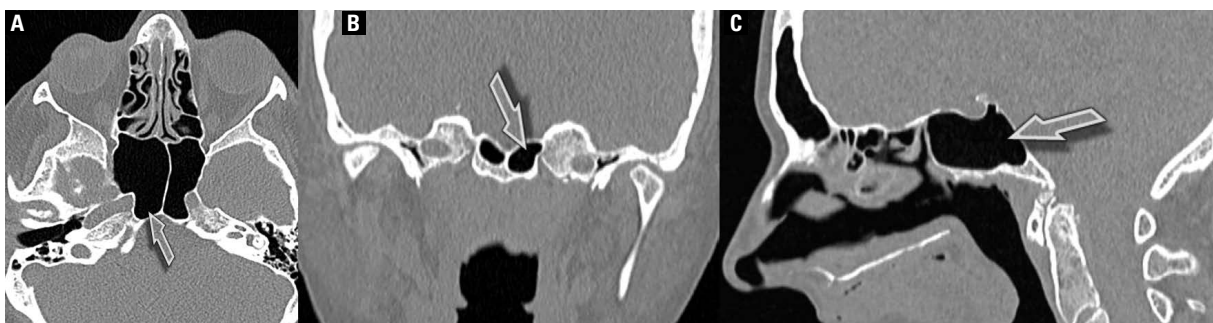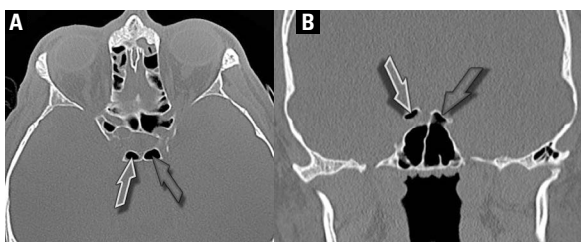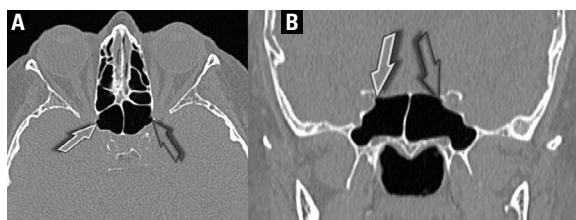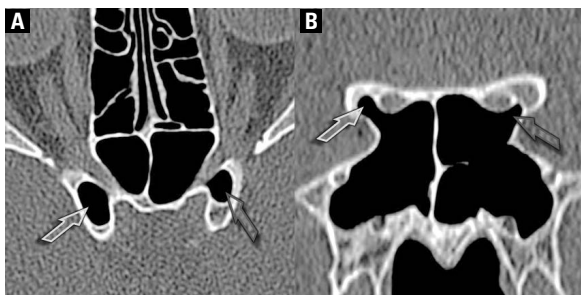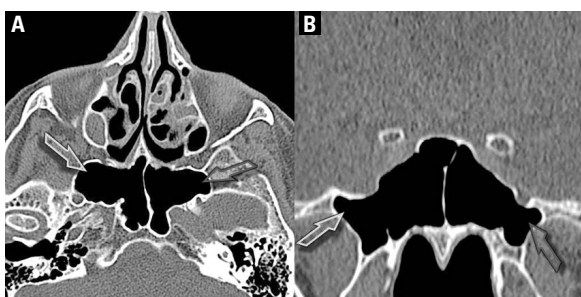

Figure 5. A computed tomography scan of the paranasal sinuses, the inferior clinoid recess; **A.** Axial plane; **B.** Coronal plane; **C.** Sagittal plane.

Figure 6. A computed tomography scan of the paranasal sinuses, the superior clinoid recess. Bilateral pneumatisation of the posterior clinoid process; **A.** Axial plane; **B.** Coronal plane.

Figure 7. A computed tomography scan of the paranasal sinuses, the bilateral anterolateral recess; **A.** Axial plane; **B.** Coronal plane.

Figure 8. A computed tomography scan of the paranasal sinuses, the bilateral posterolateral recess; **A.** Axial plane; **B.** Coronal plane.

Figure 9. A computed tomography scan of the paranasal sinuses, the bilateral lateral recess; **A.** Axial plane; **B.** Coronal plane.
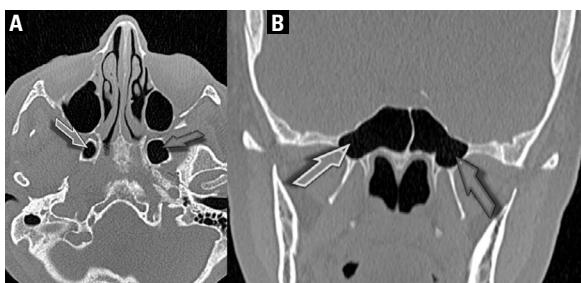

Figure 10. A computed tomography scan of the paranasal sinuses, the bilateral pterygoid recess; **A.** Axial plane; **B.** Coronal plane.
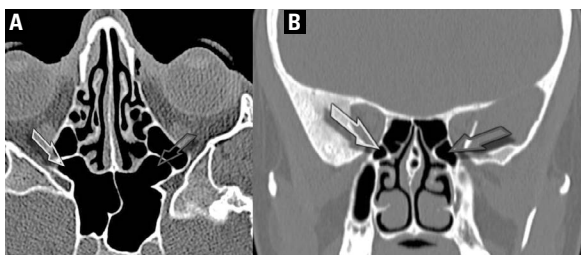

Figure 11. A computed tomography scan of the paranasal sinuses, the bilateral palatine recess; **A.** Axial plane; **B.** Coronal plane.

Lower prevalence of the superior clinoid recess was given by Hamid et al. [16] (13.51%), but higher for the anterolateral recess (described as the pneu-

matisation of the sphenoidal plane) (36.49%). It may be associated with the patient inclusion criteria (all the patients had a pituitary adenoma) and the ethnic group studied (the Egyptians). Lupascu et al. [33] provided a similar data for the presence of the pterygoid recess (evaluating it as 33%), but the prevalence of the posterolateral recess in their research is worth noting — only 10%. There is a discrepancy between the age criterions — their lower boundary was 15 years of age, whereas in the present study the lower boundary was 18 years of age.

Awadalla et al. [4] provided a different set of results. In the research group A (anatomical study of 25 skulls), they found the following frequencies of the sinuses' pneumatisation: the sphenoid body type (36%), the lateral type including the distinction between the greater wing type (12%), the pterygoid process type (16%), the clival recess (12%), the dorsal type (4%), the subdorsal type (4%) and the lesser wing type (12%). In the group B (radiological study: CT/magnetic resonance imaging [MRI] scans of 364 patients), Awadalla et al. [4] provided only the pneumatisation of the sphenoid body type (20%) and the lateral types: the greater wing type (5%) and the pterygoid process type (4%). Additionally, they found the prevalence of the full bilateral lateral pneumatisation (the bilateral pneumatisation of the greater wing and the pterygoid process) at 3.6% [4]. The dissimilar results may possibly be put down to the ethnicity of the patients (the Egyptians), the study method with which the sphenoid sinuses were researched (anatomical study of the skulls or MRI scans), the number of the skulls evaluated in the group A (25; from this group only skulls with the sellar type of pneumatisation were chosen and evaluated — 22 skulls) and the evaluation criteria of the types of pneumatisation (not reported in the work).

Definitely lower prevalence of the pneumatisation of the anterior clinoid process (the posterolateral recess) was noted by Abuzayed et al. [2], who estimated it as 9.6% (2.1% on the right side, 1.7% on the left side, 5.7% bilateral). The aforementioned scientists divided the degree of pneumatisation into three types: the type I — less than 50% of the recesses was pneumatised (6.6%), the type II — more than 50% of the recesses was pneumatised, but they were not completely pneumatised (3.5%) and the type III — the completely pneumatised recesses (2.5%) [2].

Cope stated that the lumen of the sphenoid sinuses extends more often outside the body of the sphe-

Table 7. The prevalence [%] of the sphenoid sinuses' recesses — the types of the recesses

Author (material and methods)	NR	SR	Sep	V	SC	PCP	IC	A-L	P-L	La	P	Pl
Ota et al. (72 CT scans)	–	–	–	–	–	–	–	–	27.7	–	–	–
Heskova et al. (34 CT scans)	–	–	–	–	–	–	–	–	26.5	–	–	–
Lakshmi et al. (114 CT scans)	–	–	–	–	–	–	–	–	23.6	–	–	–
Kazkayasi et al. (267 CT scans)	–	–	–	–	–	–	–	–	17.2	–	39.7	–
Lewin et al. (72 CT scans)	–	–	–	–	–	–	–	–	–	56.94	–	–
Tomovic et al. (170 HRCT)	–	–	–	–	–	–	–	–	20	72.4	–	–
Kajoak et al. (201 CT scans)	–	–	–	–	–	–	–	–	13.9	34.8	40.3	–
Hamid et al. (296 CT and MRI scans)	–	–	–	–	13.51	–	–	36.49	–	–	–	–
Lupascu et al. (200 CT scans)	–	–	–	–	–	–	–	–	10	–	33	–
Citardi et al. (64 CT scans of the skulls)	–	–	–	–	–	–	–	–	23	–	38	–
Hewaidi and Omami (300 CT scans)	–	–	–	–	–	–	–	–	15.3	20	29	–
Awadalla gr. A (25 skulls, dissection study)	36	–	–	–	8	–	12	–	12	12	16	–
Awadalla gr. B (364 CT and/or MRI scans)	20	–	–	–	–	–	–	–	–	5/3.6	4/3.6	–
Earwaker (800 CT scans)	–	9.75	15.25	7.5	4.86	–	8.63	4.86	14	30	14.25	–
Abuzayed et al. (648 CT scans)	–	–	–	–	–	–	–	–	9.6	–	–	–
Li et al. (350 CT scans)	–	–	–	–	–	–	–	–	10	–	–	–
Cope (–)	?	–	–	–	–	–	?	5	5	24.66	–	–
Elwany et al. 1983 (100 X-rays, 100 skulls X-rayed, 50 skulls — dissection study)	–	–	–	–	–	a	6	–	a	b	b	–
Elwany et al. 1999 (93 skulls, endoscopic and dissection study)	–	–	–	–	–	5.9	–	–	–	31.7	15.5	–
ELKammash et al. (182 CT and MRI scans)	–	–	–	–	–	–	21.1	6.4	7	5.1	18	–
Stokovic et al. (51 skulls in CBCT)	–	–	–	–	9	–	18	62	–	12	17	–
Tan and Ong (48 skulls, endoscopic and dissection study)	77.5	77.5	77.5	77.5	77.5	77.5	77.5	77.5	77.5	77.5	77.5	77.5
Idowu et al. (60 CT scans)	–	–	–	–	–	–	–	–	–	0	–	–
Yune et al. (–)	?	?	?	?	?	?	?	?	?	?	?	?
Jaworek-Troć et al. (296 CT scans)	6.08	61.15	8.78	25.34	34.12	9.8	56.42	27.36	32.09	65.88	42.57	47.97

? — the authors were aware of this variant but did not provide numerical values; [a]The summarised prevalence of the clinoid processes recesses (21%); [b]The summarised prevalence of the lateral and the pterygoid recesses (15%); NR — no recesses; SR — the sphenoidal rostrum's recess; Sep — the septal recess; V — the vomeral recess; SC — the superior clinoid recess; PCP — the posterior clinoid process' recess; IC — the inferior clinoid recess; A-L — the anterolateral recess; P-L — the posterolateral recess; La — the lateral recess; P — the pterygoid recess; Pl — the palatine recess; CT — computed tomography; CBCT — cone-beam computed tomography; HRCT — high resolution computed tomography; MRI — magnetic resonance imaging

Table 8. The prevalence [%] of the sphenoid sinuses' recesses — the number of the recesses

Author (material and methods)	0	1	2	3	4	5	6	7	8	9	10	11	12	13	14	15	16	17
Earwaker (800 CT scans)	–	17.13	11.86	8.13	2.36	2.63	2.86	1.13	1.36	0.5	0.86	0.86	0.86	0.86	–	–	–	–
Jaworek-Troć et al. (296 CT scans)	6.08	7.77	12.84	9.46	9.8	6.08	9.46	7.09	9.8	8.45	4.39	3.04	3.04	1.01	1.35	0	0	0.34

CT — computed tomography

noid bone anteriorly, posteriorly or laterally than it is confined to the body of the sphenoid [8]. He found the lateral recess (extending towards the greater wing of the sphenoid bone) in 24.66% (292 sinuses studied), but in a few instances (no specific number specified) the pneumatisation reached the pterygoid process of the sphenoid bone [8]. Furthermore, the author mentioned the presence of the very rare posterior recess (in the direction of the Blumenbach's clivus) [8].

Idowu et al. [19] noted a completely different set of results — they did not find any lateral recesses after studying 60 CT scans of their patients. The dissimilarity between the data may be associated with the small research group and the Nigerian population studied. Yune et al. [56] noticed that the pneumatisation of the sphenoid sinuses varies from the minimal to relatively big (reaching the anterior or the posterior clinoid processes, the lesser or greater wings of the sphenoid bone or the pterygoid process), but they did not provide the prevalence of the recesses.

Earwaker [10] in the researched material from 800 patients (CT scans of the paranasal sinuses) provided similar frequencies for the two and three recesses present in 1 patient (11.86% and 8.13% respectively). Notwithstanding, other results differ from the data found in the present study — the aforementioned researcher reported a higher presence of a single recess in one patient (17.13%), but lower prevalence for multiple recesses in 1 patient. The author did not provide the number of the patients in whose sphenoid sinuses there were no recesses present nor there were more than 13 recesses noted (Table 8) [10].

The vomeral recess, when present, poses a risk of a constricted access towards the sphenoidal sinus, as depending on its size it is possible that it would narrow the sphenoethmoidal recess and hinder the way towards the ostium of the sphenoid sinus [5]. Similarly, the septal recess might impede the entrance to the sphenoid sinus via its ostium. In this study, the vomeral recess was present in 25.34%, whereas the septal recess in 8.78% of the patients.

The posterolateral recess (that comprises the anterior clinoid process) might be a useful variation aiding surgeons during the anterior clinoidectomy by pointing a safe limit during the drilling, if present [2]. As a medical professional reaches these air-filled cells, it warrants a more careful continuation of the surgery due to the closeness of nearby neurovascular structures with vigilance whilst removing the rest of this thin cortical bone [2]. In the proximity of the anterior clinoid process there can be found the following anatomical structures: the oculomotor nerve, the trochlear nerve, the ophthalmic nerve, and the clinoidal segment of the internal carotid artery. We would like to acknowledge Abuzayed et al. [2] in saying that the greater the aeration of the anterior clinoid process, the bigger the safe margin for controlled drilling, but the presence of the posterolateral recess necessitates its later closure after the procedure to diminish the risk of rhinorrhoea and

CSF leakage from that region. Notwithstanding, it can also be an unusual site of development of mucocoele that might compress the nearby neurovascular structures, causing frontal or orbital headaches or signs and symptoms assigned to cranial nerves II to VI [47]. Henceforth it is crucial not to cause the rupture the mucous membrane covering the lumen of the posterolateral recess, so as to diminish the risk of mucocoele [2]. In this study, the posterolateral recess was present in 32.09%, predominantly bilaterally (15.2% of the patients studied).

Presence of the lateral recess of the sphenoid sinuses noted preoperatively can be of immense importance, as it facilitates access to the lateral lesions of the cavernous sinus [29]. The size of the access point to the middle cranial fossa through the lateral recess has the following boundaries: inferiorly the Vidian nerve, superiorly the maxillary nerve, and posteriorly the terminal petrous and adjacent segments of the internal carotid artery [53]. Notwithstanding, a surgeon has to drill through the bone of the sphenoid in the proximity of the internal carotid artery when this recess is absent, a difficult task with the narrow endoscopic surgical field [29] that might result in iatrogenic injury to the artery. Moreover, it is probable that an infection of the sphenoid sinus might spread to the cavernous sinus [26], especially when the bone separating them is thinned by the presence of the lateral recess. Furthermore, the lateral recess of the sphenoid sinus is a known point of origin of the CSF leakage, most often of spontaneous nature [54]. Shetty et al. [42] in their retrospective analysis of spontaneous sphenoid CSF leaks have found extensive lateral pneumatisation of the sphenoid sinus in 90% of their patients compared to 23% controls. Moreover there are reports noting temporal lobe meningocoeles that herniated through the lateral recess into the sphenoid sinus [41]. Trans-sphenoidal approach towards the lateral recess might be attained with the help of angled endoscopes [50]. In this study, the lateral recess was present in 65.88% of the patients, predominantly bilaterally (40.88%).

The inferior clinoid recess might aid in approaching the posterior cranial fossa, especially since the extensive pneumatisation thinners the clivus, making it easier to create the clival window [53]. As a result of the clival aeration, a surgeon can gain access to the space between the dorsum sellae and foramen magnum [53], possibly allowing for biopsy of brainstem lesions or approaching the surrounding CSF

cisterns. The inferior clinoid recess was present in 56.42% of the patients studied.

In orthodontics, lateral cephalometric radiographic assessment is a crucial step whilst planning treatment. Sinha et al. [43] have suggested a possible correlation between the dimensions of the sella turcica and its skeletal pattern. Presence of the recesses of the sphenoid sinus might modify the shape and dimensions of the sella, hence their prevalence and impact could be the future direction of research in this area.

The extensive pneumatisation brings the lumen of the sphenoid sinus closer to crucial neurovascular structures, e.g. the maxillary nerve or the Vidian nerve, but fortunately intraoperative fluoroscopic imaging or navigational devices are utilised to curtail the risk of iatrogenic damage to these structures [6]. Some of the most modern techniques of analysing anatomical structures prior to a surgery involve the use of the virtual dissection tables (VDT). Stecco et al. [44] reported that the VDTs helped with stating a more confident diagnosis of perplexing Le Fort fractures (the pterygoid process of the sphenoid bone is involved in all of the types of these fractures), compared to the single use of the standard Picture Archiving and Communication System. Preoperational planning of a trans-sphenoidal surgery with the help of VDT might possibly further assist surgeons in preparation for the procedure in the nearby future, thus enabling better outcomes and quality of the surgery.

CONCLUSIONS

In the majority of the patients, the pneumatisation of the sphenoid sinuses reached beyond the body of the sphenoid bone, hence there were recesses of the sinuses present. The most common were two recesses of the sphenoid sinuses. The lateral, sphenoidal rostrums and inferior clinoid recesses where the most prevalent types (65.88%, 61.15% and 56.42%, respectively). Comprehensive preoperational CT evaluation of the sphenoid sinuses should most certainly involve the analysis of presence of the recesses in every case, as they might facilitate access to the cranial fossae that could potentially be less traumatic than drilling through the hard cortical bone of the sphenoid.

Acknowledgements

Conflict of interest: None declared

REFERENCES

1. Abdullah B, Arasaratnam S, Kumar G, et al. The Sphenoid Sinuses: Computed Tomographic Assessment of Septation, Relationship to the Internal Carotid Arteries, and Sidewall Thickness in the Malaysian Population. Hong Kong J Radiol. 2001; 4(3): 185–188.
2. Abuzayed B, Tanriover N, Biceroglu H, et al. Pneumatization degree of the anterior clinoid process: a new classification. Neurosurg Rev. 2010; 33(3): 367–374, doi: 10.1007/s10143-010-0255-8, indexed in Pubmed: 20333429.
3. Alexander NS, Chaaban MR, Riley KO, et al. Treatment strategies for lateral sphenoid sinus recess cerebrospinal fluid leaks. Arch Otolaryngol Head Neck Surg. 2012; 138(5): 471–478, doi: 10.1001/archoto.2012.614, indexed in Pubmed: 22652945.
4. Awadalla AM, Hussein Y, ELKammash TH. Anatomical and Radiological Parameters of the Sphenoid Sinus among Egyptians and its Impact on Sellar Region. Egypt J Neurosurg. 2015; 30(1): 1–12.
5. Beale TJ, Madani G, Morley SJ. Imaging of the paranasal sinuses and nasal cavity: normal anatomy and clinically relevant anatomical variants. Semin Ultrasound CT MR. 2009; 30(1): 2–16, doi: 10.1053/j.sult.2008.10.011, indexed in Pubmed: 19388234.
6. Chougule MS, Dixit D. A cross-sectional study of sphenoid sinus through gross and endoscopic dissection in north karnataka, India. J Clin Diagn Res. 2014; 8(4): AC01––AC05, doi: 10.7860/JCDR/2014/7947.4243, indexed in Pubmed: 24959426.
7. Citardi MJ, Gallivan RP, Batra PS, et al. Quantitative computer-aided computed tomography analysis of sphenoid sinus anatomical relationships. Am J Rhinol. 2004; 18(3): 173–178, indexed in Pubmed: 15283492.
8. Cope VZ. The internal structure of the sphenoidal sinus. J Anat. 1917; 51(Pt 2): 127–136, indexed in Pubmed: 17103809.
9. Degirmenci B, Haktanir A, Acar M, et al. Agenesis of sphenoid sinus: three cases. Surg Radiol Anat. 2005; 27(4): 351–353, doi: 10.1007/s00276-005-0336-5, indexed in Pubmed: 16200385.
10. Earwaker J. Anatomic variants in sinonasal CT. Radiographics. 1993; 13(2): 381–415, doi: 10.1148/radiographics.13.2.8460226, indexed in Pubmed: 8460226.
11. ELKammash T, Enaba M, Awadalla A. Variability in sphenoid sinus pneumatization and its impact upon reduction of complications following sellar region surgeries. Egypt J Radiol Nucl Med. 2014; 45(3): 705–714, doi: 10.1016/j.ejrnm.2014.04.020.
12. Elwany S, Elsaeid I, Thabet H. Endoscopic anatomy of the sphenoid sinus. J Laryngol Otol. 1999; 113(2): 122–126, doi: 10.1017/s0022215100143361, indexed in Pubmed: 10396560.
13. Elwany S, Yacout YM, Talaat M, et al. Surgical anatomy of the sphenoid sinus. J Laryngol Otol. 1983; 97(3): 227–241, doi: 10.1017/s0022215100094056, indexed in Pubmed: 6833847.
14. Eryilmaz A, Ozeri C, Bayiz U, et al. Functional endoscopic sinus surgery (FESS). Turk J Med Res. 1993; 11(5): 221–223.
15. Haetinger RG, Navarro JAC, Liberti EA. Basilar expansion of the human sphenoidal sinus: an integrated anatomical and computerized tomography study. Eur Radiol. 2006; 16(9):

2092–2099, doi: 10.1007/s00330-006-0208-3, indexed in Pubmed: 16642328.

16. Hamid O, El Fiky L, Hassan O, et al. Anatomic variations of the sphenoid sinus and their impact on trans-sphenoid pituitary surgery. Skull Base. 2008; 18(1): 9–15, doi: 10.1055/s-2007-992764, indexed in Pubmed: 18592020.

17. Heskova G, Mellova Y, Holomanova A, et al. Assessment of the relation of the optic nerve to the posterior ethmoid and sphenoid sinuses by computed tomography. Biomed Pap Med Fac Univ Palacky Olomouc Czech Repub. 2009; 153(2): 149–152, doi: 10.5507/bp.2009.025, indexed in Pubmed: 19771141.

18. Hewaidi Gh, Omami Gm. Anatomic variation of sphenoid sinus and related structures in libyan population: CT scan study. Libyan J Med. 2008; 3(3): 128–133, doi: 10.4176/080307, indexed in Pubmed: 21499453.

19. Idowu OE, Balogun BO, Okoli CA. Dimensions, septation, and pattern of pneumatization of the sphenoidal sinus. Folia Morphol. 2009; 68(4): 228–232, indexed in Pubmed: 19950072.

20. Jaworek-Troć J, Iwanaga J, Chrzan R, et al. Anatomical variations of the main septum of the sphenoidal sinus and its importance during transsphenoidal approaches to the sella turcica. Transl Res Anat. 2020; 21: 100079, doi: 10.1016/j.tria.2020.100079.

21. Jaworek-Troć J, Zarzecki M, Bonczar A, et al. Sphenoid bone and its sinus - anatomo-clinical review of the literature including application to FESS. Folia Med Cracov. 2019; 59(2): 45–59, indexed in Pubmed: 31659348.

22. Jaworek-Troć J, Zarzecki M, Mróz I, et al. The total number of septa and antra in the sphenoid sinuses — evaluation before the FESS. Folia Med Cracov. 2018; 58(3): 67–81, doi: 10.24425/fmc.2018.125073, indexed in Pubmed: 30521512.

23. Jaworek-Troć J, Zarzecki M, Zamojska I, et al. The dimensions of the sphenoid sinuses: evaluation before the functional endoscopic sinus surgery. Folia Morphol. 2021; 80(2): 275–282, doi: 10.5603/FM.a2020.0059, indexed in Pubmed: 32488857.

24. Kajoak SA, Ayad CE, Najmeldeen M, et al. Computerized tomography morphometric analysis of the sphenoid sinus and related structures in sudanese population. Glo/ Adv Res J Med Med Sci. 2014; 3(7): 160–167.

25. Kantarci M, Karasen RM, Alper F, et al. Remarkable anatomic variations in paranasal sinus region and their clinical importance. Eur J Radiol. 2004; 50(3): 296–302, doi: 10.1016/j.ejrad.2003.08.012, indexed in Pubmed: 15145491.

26. Kayalioglu G, Erturk M, Varol T. Variations in sphenoid sinus anatomy with special emphasis on pneumatization and endoscopic anatomic distances. Neurosciences (Riyadh). 2005; 10(1): 79–84, indexed in Pubmed: 22473192.

27. Kazkayasi M, Karadeniz Y, Arikan OK. Anatomic variations of the sphenoid sinus on computed tomography. Rhinology. 2005; 43(2): 109–114, indexed in Pubmed: 16008065.

28. Keast A, Yelavich S, Dawes P, et al. Anatomical variations of the paranasal sinuses in Polynesian and New Zealand European computerized tomography scans. Otolaryngol Head Neck Surg. 2008; 139(2): 216–221, doi: 10.1016/j.otohns.2008.05.014, indexed in Pubmed: 18656718.

29. Kikuchi R, Toda M, Tomita T, et al. Analysis of sphenoid sinus lateral pneumatization for endonasal endoscopic surgery. Surg Neurol Int. 2015; 6: 166, doi: 10.4103/2152-7806.168313, indexed in Pubmed: 26962467.

30. Krzeski A, Osuch-Wójcikiewicz E, Szwedowicz P, et al. Chirurgia endoskopowa w leczeniu guzów jam nosa i zatok przynosowych. Mag ORL. 2004; 3(3): 79–84.

31. Lewin JS, Curtin HD, Eelkema E, et al. Benign expansile lesions of the sphenoid sinus: differentiation from normal asymmetry of the lateral recesses. Am J Neuroradiol. 1999; 20(3): 461–466, indexed in Pubmed: 10219412.

32. Li Y, Sun J, Zhu X, et al. Study of the relationship between sphenoid sinus volume and protrusions in the sphenoid sinus. Forensic Med Anat Res. 2014; 02(01): 2–7, doi: 10.4236/fmar.2014.21002.

33. Lupascu M, Comsa G, Zainea V. Anatomical variations of the sphenoid sinus: a study of 200 cases. ARS Medica Tomitana. 2014; 20(2): 57–62, doi: 10.2478/arsm-2014-0011.

34. Mafee MF, Chow JM, Meyers R. Functional endoscopic sinus surgery: anatomy, CT screening, indications, and complications. Am J Roentgenol. 1993; 160(4): 735–744, doi: 10.2214/ajr.160.4.8456654, indexed in Pubmed: 8456654.

35. Mutlu C, Unlu HH, Goktan C, et al. Radiologic anatomy of the sphenoid sinus for intranasal surgery. Rhinology. 2001; 39(3): 128–132, indexed in Pubmed: 11721501.

36. Ota N, Tanikawa R, Miyazaki T, et al. Surgical microanatomy of the anterior clinoid process for paraclinoid aneurysm surgery and efficient modification of extradural anterior clinoidectomy. World Neurosurg. 2015; 83(4): 635–643, doi: 10.1016/j.wneu.2014.12.014, indexed in Pubmed: 25527880.

37. Sabaté J, Carmona A, Catalina-Herrera CJ, et al. Anatomical variations in the human paranasal sinus region studied by CT. J Anat. 2000; 197 (Pt 2): 221–227, doi: 10.1046/j.1469-7580.2000.19720221.x, indexed in Pubmed: 11005714.

38. Peele JC. Unusual anatomical variations of the sphenoid sinuses. Laryngoscope. 1957; 67(3): 208–237, doi: 10.1288/00005537-195703000-00004, indexed in Pubmed: 13417674.

39. Santhana Lakshmi R, Gugapriya S, Vinay Kumar NT, et al. Positional variation of optic nerve in relation to sphenoid sinuses and its association with pneumatisation of anterior clinoid process: a radiological study. J Evid Based Med Healthc. 2015; 2(32): 4719–4728, doi: 10.18410/jebmh/2015/663.

40. Sareen D, Agarwal AK, Kaul JM, et al. Study of sphenoid sinus anatomy in relation to endoscopic surgery. Int J Morphol. 2005; 23(3), doi: 10.4067/s0717-95022005000300012.

41. Schlosser RJ, Bolger WE. Significance of empty sella in cerebrospinal fluid leaks. Otolaryngol Head Neck Surg. 2003; 128(1): 32–38, doi: 10.1067/mhn.2003.43, indexed in Pubmed: 12574756.

42. Shetty PG, Shroff MM, Fatterpekar GM, et al. A retrospective analysis of spontaneous sphenoid sinus fistula: MR and CT findings. Am J Neuroradiol. 2000; 21(2): 337–342, indexed in Pubmed: 10696020.

43. Sinha S, Shetty A, Nayak K. The morphology of Sella Turcica in individuals with different skeletal malocclusions: a cephalometric study. Trans Res Anat. 2020; 18: 100054, doi: 10.1016/j.tria.2019.100054.

44. Stecco A, Boccafoschi F, Falaschi Z, et al. Virtual dissection table in diagnosis and classification of Le Fort fractures: A retrospective study of feasibility. Trans Res Anat. 2020; 18: 100060, doi: 10.1016/j.tria.2019.100060.

945

45. Štoković N, Trkulja V, Dumić-Čule I, et al. Sphenoid sinus types, dimensions and relationship with surrounding structures. Ann Anat. 2016; 203: 69–76, doi: 10.1016/j. aanat.2015.02.013, indexed in Pubmed: 25843780.

46. Tan HKK, Ong YK. Sphenoid sinus: an anatomic and endoscopic study in Asian cadavers. Clin Anat. 2007; 20(7): 745–750, doi: 10.1002/ca.20507, indexed in Pubmed: 17583590.

47. Tchoyoson Li, Dillon WP, McDermott MW. Mucocele involving the anterior clinoid process: MR and CT findings. Am J Neuroradiol. 1999; 20(2): 287–290.

48. Terra ER, Guedes FR, Manzi FR, et al. Pneumatization of the sphenoid sinus. Dentomaxillofac Radiol. 2006; 35(1): 47–49, doi: 10.1259/dmfr/55048928, indexed in Pubmed: 16421265.

49. Tomovic S, Esmaeili A, Chan NJ, et al. High-resolution computed tomography analysis of variations of the sphenoid sinus. J Neurol Surg B Skull Base. 2013; 74(2): 82–90, doi: 10.1055/s-0033-1333619, indexed in Pubmed: 24436893.

50. Ulu MO, Aydin S, Kayhan A, et al. Surgical management of sphenoid sinus lateral recess cerebrospinal fluid leaks: a single neurosurgical center analysis of endoscopic endonasal minimal transpterygoid approach. World Neurosurg. 2018; 118: e473–e482, doi: 10.1016/j. wneu.2018.06.219, indexed in Pubmed: 29981913.

51. Unal B, Bademci G, Bilgili YK, et al. Risky anatomic variations of sphenoid sinus for surgery. Surg Radiol Anat. 2006; 28(2): 195–201, doi: 10.1007/s00276-005-0073-9, indexed in Pubmed: 16429266.

52. Vidić B. The postnatal development of the sphenoidal sinus and its spread into the dorsum sellae and posterior clinoid processes. Am J Roentgenol Radium Ther Nucl Med. 1968; 104(1): 177–183, doi: 10.2214/ajr.104.1.177, indexed in Pubmed: 5672763.

53. Wang J, Bidari S, Inoue K, et al. Extensions of the sphenoid sinus: a new classification. Neurosurgery. 2010; 66(4): 797–816, doi: 10.1227/01.NEU.0000367619.24800.B1, indexed in Pubmed: 20305499.

54. Woodworth BA, Prince A, Chiu AG, et al. Spontaneous CSF leaks: a paradigm for definitive repair and management of intracranial hypertension. Otolaryngol Head Neck Surg. 2008; 138(6): 715–720, doi: 10.1016/j. otohns.2008.02.010, indexed in Pubmed: 18503841.

55. Yonetsu K, Watanabe M, Nakamura T. Age-related expansion and reduction in aeration of the sphenoid sinus: volume assessment by helical CT scanning. Am J Neuroradiol. 2000; 21(1): 179–182, indexed in Pubmed: 10669247.

56. Yune HY, Holden RW, Smith JA. Normal variations and lesions of the sphenoid sinus. Am J Roentgenol Radium Ther Nucl Med. 1975; 124(1): 129–138, doi: 10.2214/ajr.124.1.129, indexed in Pubmed: 167598.

ORIGINAL ARTICLE

VIA MEDICA

Agenesis of the sphenoid sinus and a single sphenoid sinus: a computed tomography anatomical evaluation

J. Jaworek-Troć[1, 2], J.A. Walocha[1], M. Lipski[1], S. Popovchenko[1], K. Shafarenko[1],
T. Gładysz[3], P. Depukat[1], J.J. Zarzecki[4], R. Chrzan[2], A. Urbanik[2], M.P. Zarzecki[1]

[1]Department of Anatomy, Jagiellonian University Medical College, Krakow, Poland
[2]Department of Radiology, Jagiellonian University Medical College, Krakow, Poland
[3]Department of Dental Surgery, Institute of Dentistry, Jagiellonian University Medical College, Krakow, Poland
[4]Medical University of Silesia, Katowice, Poland

Background: Sphenoid sinuses are pneumatic spaces within the body of the sphenoid bone. Their development begins in the prenatal life and continues until the adulthood. Agenesis of the sphenoid sinuses is a situation in which they are undeveloped. On the other hand, a single sphenoid sinus lacks the presence of the main septum, leading to the formation of a single antrum. Contemporary use of transnasal transsphenoidal approaches for the pituitary surgery, as well as functional endoscopic sinus surgery urges medical professionals to be well acquainted with the aforementioned variant.
Materials and methods: Paranasal sinuses of 300 patients (150 females, 150 males) were evaluated using computed tomography, without the use of contrast medium. Inclusion criteria involved absence of any identifiable pathology within the sphenoid sinuses and age over 18 years. Subgroup analysis involved probing for potential sources of heterogeneity, namely gender.
Results: In the whole research material of 300 patients, agenesis of the sphenoid sinuses was noted in 1% of the patients. No statistically significant differences were noted between the absence of the sphenoid sinuses and gender (p = 0.999). A single sphenoid sinus was found in 0.33% of the patients. There were no statistically significant differences found between the presence of fully developed sphenoid sinuses and gender (p = 0.498).
Conclusions: Both agenesis of the sphenoid sinuses and a single sphenoid sinus are rare anatomical variants. Adequate planning for transsphenoidal surgeries with preoperative medical imaging is of essence in order to perform a safe and quality procedure. (Folia Morphol 2021; 80, 4: 947–953)

Key words: agenesis, sphenoid sinus, computed tomography, anatomy

INTRODUCTION

Undoubtedly sphenoid sinuses are an anatomical entity with one of the most variant anatomy, con- cerning namely its septation, proximity to the nearby crucial neurovascular structures, pneumatisation patterns and others [19–27, 34]. Notwithstanding, there

is still a constant need for new reports regarding their variations due to the fact that they are of immense importance namely in functional endoscopic sinus surgery and transnasal transsphenoidal approaches for the pituitary surgery and medical professionals are still poorly acquainted with some of the anatomical features (e.g. the exact parasympathetic pathway of the ethmoid and sphenoid sinuses) [8].

Bilateral intussusception of the nasal mucosa posteriorly, in the direction of the sphenoid bone, is said to be the initial process of sphenoid sinus development, occurring around the 3rd–4th month of gestation [14, 35]. They resemble recesses (i.e. sphenopalatine recesses) and correspond to the later sphenoid sinus' ostia. The sphenoid sinuses can be noted in the neonates, having approximately 2 mm in dimension [9]. Nonetheless, their pneumatisation is initiated in the postnatal life, roughly around the 3rd–4th year, and terminates following the puberty, around the 12th–16th year of life [36].

The presphenoidal area is the primary site of pneumatisation of the sphenoid sinuses that in due time extends towards the anterior wall of the clivus, at the basisphenoidal area [9]. When a person reaches puberty, their sphenoid sinuses are said to be fully and properly developed; however, the process of pneumatisation might advance outside the body of the sphenoid thus creating recesses of the sphenoid sinus in some individuals [3]. In their recent study, Jaworek-Troć et al. [21] have found that only in 18/296 patients studied via the computed tomography (CT) there were no recesses present. It is said that the pneumatisation of the sphenoid sinuses terminates in the third decade of life of a human, what might be related to the potential aeration of the sphenoid bone even more posteriorly, towards the basis of the occipital bone that coincides with ossification of the spheno-occipital synchondrosis (approximately at the 20th year of age) [36]. Agenesis of the sphenoid sinuses is a situation in which the said anatomical entities do not develop in an individual.

The aim for the current study was to evaluate the prevalence of the agenesis of sphenoid sinuses, as well as single sphenoid sinuses, among Polish adult population and to probe for potential heterogeneity of the results in terms of gender.

MATERIALS AND METHODS

A total of 300 patients (150 females, 150 males) were included in this retrospective analysis of CT evaluation of paranasal sinuses, conducted at the Department of Medical Imaging, University Hospital in Krakow, Poland. Only patients over 18 years of age with no identifiable pathology in the sphenoid sinuses were deemed eligible for this study. Any head trauma or a surgical intervention in the nasal, orbital or cranial basis region excluded patients from the research group.

A spiral CT scanner (Siemens Somatom Sensation 16) was utilised in a standard procedure, in the option Siemens CARE Dose 4D, in order to obtain images of the paranasal sinuses. No contrast medium was administered to any of the patients. Images in the frontal and sagittal planes were obtained with the secondary reconstruction tool (multiplans reconstruction) from the images in the transverse plane. The medical images were processed with the help of Siemens Volume Wizard diagnostic station.

Ethical approval

All procedures performed in studies involving human participants were in accordance with the ethical standards of the institutional and/or national research committee and with the 1964 Helsinki declaration and its later amendments or comparable ethical standards. For this type of study, formal consent is not required.

Statistical analysis

STATISTICA version 13.3 by TIBCO Software Inc.® was used for the statistical analysis in the current study. Fisher's exact test applied whilst probing for potential differences between the agenesis of the sphenoid sinuses and gender. Value of $p < 0.05$ was regarded as statistically significant.

RESULTS

The agenesis of the sphenoid sinuses was noted in 3 patients (2 females, 1 male) in the total research group of 300 patients (150 females, 150 males).

No statistically significant differences were found between the agenesis of the sphenoid sinuses and gender ($p = 0.999$, Fisher's exact test). Henceforth, the proportion of developed sphenoid sinuses and their agenesis is approximately similar in both sexes. The prevalence of fully developed sphenoid sinuses was approximately 99% for both the female and male research groups (Figs. 1–3, Table 1).

A single sphenoid sinus (with no visible main septum dividing the sinus into two antra) was found only

Figure 1. A computed tomography scan of the paranasal sinuses, three sequential images in the transverse plane, taken in a single patient, showing agenesis of the sphenoid sinuses.

Figure 2. A computed tomography scan of the paranasal sinuses, an image in the sagittal plane. The arrow shows no pneumatisation of the body of the sphenoid bone — agenesis of the sphenoid sinuses.

Figure 3. A computed tomography scan of the paranasal sinuses, an image in the frontal plane. The arrow shows no pneumatisation of the body of the sphenoid bone — agenesis of the sphenoid sinuses.

Table 1. Prevalence of the agenesis of the sphenoid sinuses

	F	F%	M	M%	F + M	F + M%
Agenetic SS	2	1.33%	1	0.67%	3	1%
Developed SS	148	**98.67%**	149	**99.33%**	297	**99%**

Agenetic SS — agenesis of the sphenoid sinuses; Developed SS — fully developed sphenoid sinuses; F — number of females; F% — the percentage of females; M — number of males; M% — the percentage of males

in 1 female patient (0.33% of all the patients). Fully developed sphenoid sinuses (i.e. having at least two antra) were noted in 296 (99.68%) patients. No statistically significant differences were found between the presence of a single sphenoid sinus or at least two sinuses and gender (p = 0.498, Fisher's exact test) (Figs. 4, 5).

DISCUSSION

In the current study, agenesis of the sphenoid sinus was found in 3 (1%) patients in the whole research material of 300 patients.

Earwaker [11] has estimated the frequency of prevalence of undeveloped sphenoid sinuses as 1.625% (13/800) in his CT study of paranasal sinuses, but the research group studied comprised also children (the age range of the patients studied was 12–81). Lower prevalence of the sphenoid sinus agenesis was found by Cakur et al. [7] who estimated it to be approximately 0.26%. The population studied involved patients of Turkish origins.

Different results were obtained by Aydinlioglu and Erdem [5] who did not find any cases of sphenoid sinus agenesis in their research group of 1526 patients (conducted on the CT scans). The said differ-
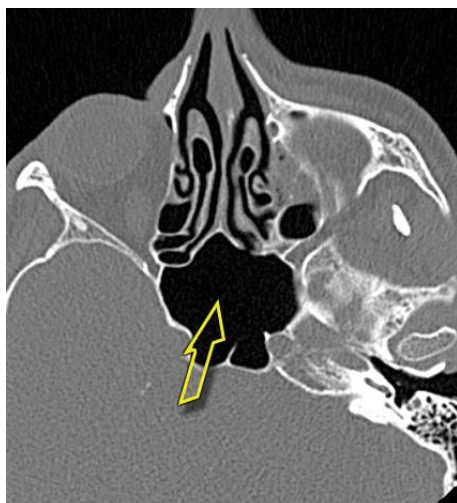
Figure 4. A computed tomography scan of the paranasal sinuses, an image in the transverse plane. A single sphenoid sinus — the main septum is absent.
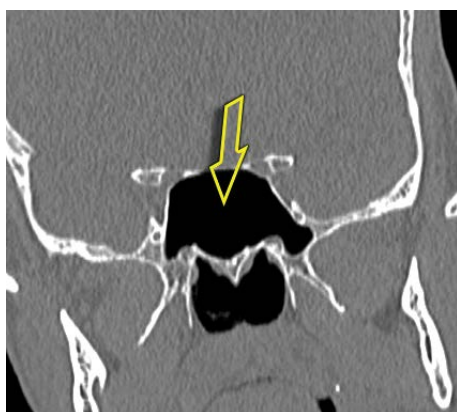

Figure 5. A computed tomography scan of the paranasal sinuses, an image in the frontal plane. A single sphenoid sinus — the main septum is absent.

Table 2. Prevalence of the agenesis of the sphenoid sinuses in the available literature

Authors (materials and methods)	Agenesis of the sphenoid sinuses
Earwaker (800 CT scans)	1.625%
Cakur et al. (384 DVCT scans)	0.26%
Aydinlioglu and Erdem (1526 CT scans)	0%
Yune et al. (–)	?
Anik et al. (–)	?
Haktanir et al. (–)	?
Degirmenci et al. (–)	?
Jaworek-Troć et al. (300 CT scans)	1%

? — the authors were aware of the said variant, but did not provide a specific numerical value; CT — computed tomography; DVCT — dental volumetric computed tomography

ences might possibly be put down to the population studied — the patients originated from Turkey. Yune et al. [37], Anik et al. [2], Haktanir et al. [16] and Degirmenci et al. [9] state that the sphenoid sinus agenesis is a rare finding, but provide no specific details on the matter (Table 2).

The present research did not find any statistically significant differences between gender and agenesis of the sphenoid sinuses (p = 0.999). Furthermore, this aspect was not previously investigated by other authors who have identified the aforementioned variant [7, 11]. Nonetheless, the presence of this variant is rare (1% in the current study) what might account for the lack of the observed differences that ought to be better addressed in studies involving bigger number of patients (counting possibly in thousands).

As shown in the present study, the sphenoid sinus is typically divided by at least one septum into 2 or more antra, whilst the presence of a single developed sphenoid sinus (with the main septum absent) was noted in 0.33% of all the patients.

Similar prevalence of a single sphenoid sinus was stated by Aydinlioglu and Erdem [5] — 0.13% (2/1526); however, one of their patients was under 18 years of age (they were 16 years old). Seddighi et al. [29] (in their research group of 64 CT and magnetic resonance imaging [MRI scans]), Abdullah et al. [1] (70 CT scans), and Tan and Ong [33] (cadaveric and endoscopic study of 48 human skulls) did not find a single case of absence of the main septum, which might possibly be put down to the limited number of the sinuses studied. Likewise, Hammer and Radberg [18] state the presence of at least one septum in 100%, which might be related to the diagnostic method used (120 skulls evaluated in X-ray and CT and 103 X-ray images). Battal et al. [6] found the frequency of the absence of the main septum of around 1.3%, but the study group included patients with the conchal (foetal) type of pneumatisation (3 patients), as well as 1 patient in whom not a single septum was noted.

Slightly higher prevalence of a single sphenoid sinus was noted by Dündar et al. [10] — 2.2% (5/218) and Kapur et al. [28] — 2%. Hamid et al. [17] state even higher frequency of the said variant — 10.8% (32/296). The aforementioned differences might possibly be attributed to the research group studied (all the patients suffered from pituitary adenoma), as

Table 3. Prevalence of a single sphenoid sinus

Author (materials and methods)	Single sphenoid sinus: no main septum present
Aydinlioglu and Erdem (1526 CT)	0.13%
Seddighi et al. (64 CT and MRI)	0%
Abdullah et al. (70 CT)	0%
Tan and Ong (48 skulls, endoscopic and cadaveric study)	0%
Hammer and Radberg (120 skull X-ray and CT images and 103 X-ray images)	0%
Battal et al. (314 angio-CT)	1.3%
Dündar et al. (218 CT)	2.2%
Kapur et al. (200 CT)	2%
Hamid et al. (296 CT and MRI)	10.8%
Awadalla et al. (Gr. A: 25 skulls, cadaveric study)	16%
Awadalla et al. (Gr. B: 364 CT and/or MRI)	13%
ELKammash et al. (182 CT and MRI)	13.2%
Jaworek-Troć et al. (300 CT)	0.33%

CT — computed tomography; MRI — magnetic resonance imaging

well as the ethnicity of the patients (all patients were of Egyptian origin). Yet higher results were found by Awadalla et al. [4], noted for the two different study groups: group A — cadaveric evaluation of 25 skulls (the main septum was absent in 16%) and group B — radiologic evaluation (CT and/or MRI) of 364 patients (the main septum was absent in 13%). The said results pertain to the people of Egyptian origin and are akin to the one provided by Hamid et al. [17] for the same ethnic group. Moreover, ELKammash et al. [13] also studied the same population (182 CT and MRI scans in the Egyptians) and determined the main septum to be absent in 13.2% (Table 3).

Similarly to the agenesis of the sphenoid sinuses, there were no statistically significant differences between gender and prevalence of a single sphenoid sinus found in the present study ($p = 0.498$). Battal et al. [6] did not find any statistically significant differences between the numbers of septa and gender overall; however, they did not specify it for the single sphenoid sinus variant only. Likewise, it is possible that studies conducted on a larger sample of patients (counting in thousands) could potentially point towards the sex predilection of the said variant, as its prevalence is rare (0.33% in the current study).

Undoubtedly, adequate level of pneumatisation of the sphenoid sinuses is crucial in order to perform the transnasal transsphenoidal approach for the pituitary

surgery. Should agenesis of the sinuses or the conchal (foetal) type of aeration be present, the said surgical approach might prove troublesome and posing a higher risk to the patient, as it would require drilling through the bone, potentially leading to iatrogenic injuries to the nearby neurovascular structures [5]. Nonetheless, extensive pneumatisation of the sphenoid sinuses could also make the procedure prone to iatrogenic complications, but definitely facilitates surgical access [21]. There are reports in the available literature of agenesis and/or hypoplasia of a few paranasal sinuses in a single patient [15, 16, 30]; however, those are single cases and more large-scale studies ought to be performed in order to confirm or reject their potential association. Virtual dissection tables might become the future of anatomic evaluation of more complex variants [32], but conventional methods of imaging of the sphenoidal region still finds its use in orthodontics [31].

Aydinlioglu et al. [5] performed a study in 1,526 patients, presenting with a headache or undergoing diagnostic tests for possible sinusitis. We would like to acknowledge the aforementioned authors in saying that due to the agenesis of sphenoid sinuses being a rare variant, attributing its presence to extensive experience of symptoms (such as headache, infections) is yet to be determined on a larger and more varied group of patients [5].

In 2 out of 3 cases reported by Degirmenci et al. [9], sinusitis of different paranasal sinuses was found in addition to the agenesis of the sphenoid sinuses. It raises a question to the level of insufficiency of the ostiomeatal complex caused by the absence of sphenoid sinuses, and the subject definitely requires further research.

Eggesbø et al. [12] concluded that for the cystic fibrosis patients the pneumatisation of the sphenoid sinuses does not reach beyond the presphenoidal area, and medical professionals who have found the aeration in the basisphenoidal area ought to reconsider the diagnosis of cystic fibrosis. Nonetheless, the said authors did not find any agenesis of the sphenoid sinuses neither in the study group, nor the controls [12]. Sharma et al. [30] report a case with a bilateral agenesis of both frontal and sphenoid sinuses in a patient with Kartagener's syndrome. Whilst there is still need for more studies regarding this topic across various populations, this concept raises an interesting question whether the agenesis of the sphenoid sinuses and / or their hypoplasia is a result of the defected

cilia; hence, possibly patients with other ciliary defects ought to be included in future study groups.

CONCLUSIONS

The absence of the sphenoid sinuses is a relatively rare variant, found in approximately 1%. A single sphenoid sinus, with the main septum absent, was noted only in 0.33% of the patients. Acquaintance with those variants (however rare) is of dire importance to medical professionals performing transsphenoidal surgical procedures. Nonetheless, there is still need for new reliable, large-scale studies that would attempt to correlate the agenesis of the sphenoid sinuses with potential clinical symptoms, as well as look into the potential cause and effect of ciliary defects.

REFERENCES

1. Abdullah BJ, Arasaratnam A, Kumar G, et al. The sphenoid sinuses: computed tomographic assessment of septation, relationship to the internal carotid arteries and sidewall thickness in the Malaysian population. Hong Kong J Radiol. 2001; 4: 185–188.
2. Anik I, Anik Y, Koc K, et al. Agenesis of sphenoid sinuses. Clin Anat. 2005; 18(3): 217–219, doi: 10.1002/ca.20096, indexed in Pubmed: 15768410.
3. Antoniades K, Vahtsevanos K, Psimopoulou M, et al. Agenesis of sphenoid sinus. Case report. ORL J Otorhinolaryngol Relat Spec. 1996; 58(6): 347–349, doi: 10.1159/000276868, indexed in Pubmed: 8958546.
4. Awadalla AM, Hussein Y, ElKammash TH. Anatomical and radiological parameters of the sphenoidal sinus among Egyptians and its impact on sellar region surgery. Egypt J Neurosurg. 2015; 30(1): 1–12.
5. Aydinlioğlu A, Erdem S. Maxillary and sphenoid sinus aplasia in Turkish individuals: a retrospective review using computed tomography. Clin Anat. 2004; 17(8): 618–622, doi: 10.1002/ca.20026, indexed in Pubmed: 15495178.
6. Battal B, Akay S, Karaman B, et al. The Relationship between the Variations of Sphenoid Sinus and Nasal Septum. Gulhane Med J. 2014; 56(4): 232, doi: 10.5455/gulhane.173275.
7. Cakur B, Sümbüllü MA, Yılmaz AB. A retrospective analysis of sphenoid sinus hypoplasia and agenesis using dental volumetric CT in Turkish individuals. Diagn Interv Radiol. 2011; 17(3): 205–208, doi: 10.4261/1305-3825.DIR.3304-10.1, indexed in Pubmed: 20698004.
8. Carvey M, Baek W, Hage R. Bridging the divide: the widening gap between basic science and clinical research.

Transl Res Anat. 2021; 24: 100117, doi: 10.1016/j.tria.2021.100117.
9. Degirmenci B, Haktanir A, Acar M, et al. Agenesis of sphenoid sinus: three cases. Surg Radiol Anat. 2005; 27(4): 351–353, doi: 10.1007/s00276-005-0336-5, indexed in Pubmed: 16200385.
10. Dündar R, Kulduk E, Soy FK, et al. Radiological evaluation of septal bone variations in the sphenoid sinus. J Med Updates. 2014; 4(1): 6–10, doi: 10.2399/jmu.2014001002.
11. Earwaker J. Anatomic variants in sinonasal CT. Radiographics. 1993; 13(2): 381–415, doi: 10.1148/radiographics.13.2.8460226, indexed in Pubmed: 8460226.
12. Eggesbø HB, Eken T, Eiklid K, et al. Hypoplasia of the sphenoid sinuses as a diagnostic tool in cystic fibrosis. Acta Radiol. 1999; 40(5): 479–485, doi: 10.3109/02841859909175571, indexed in Pubmed: 10485235.
13. ELKammash T, Enaba M, Awadalla A. Variability in sphenoid sinus pneumatization and its impact upon reduction of complications following sellar region surgeries. Egypt J Radiol Nuclear Med. 2014; 45(3): 705–714, doi: 10.1016/j.ejrnm.2014.04.020.
14. Elwany S, Yacout YM, Talaat M, et al. Surgical anatomy of the sphenoid sinus. J Laryngol Otol. 1983; 97(3): 227–241, doi: 10.1017/s0022215100094056, indexed in Pubmed: 6833847.
15. Güven DG, Yilmaz S, Ulus S, et al. Combined aplasia of sphenoid, frontal, and maxillary sinuses accompanied by ethmoid sinus hypoplasia. J Craniofac Surg. 2010; 21(5): 1431–1433, doi: 10.1097/SCS.0b013e3181ecc2d9, indexed in Pubmed: 20856033.
16. Haktanir A, Acar M, Yucel A, et al. Combined sphenoid and frontal sinus aplasia accompanied by bilateral maxillary and ethmoid sinus hypoplasia. Br J Radiol. 2005; 78(935): 1053–1056, doi: 10.1259/bjr/38163950, indexed in Pubmed: 16249610.
17. Hamid O, El Fiky L, Hassan O, et al. Anatomic Variations of the Sphenoid Sinus and Their Impact on Trans-sphenoid Pituitary Surgery. Skull Base. 2008; 18(1): 9–15, doi: 10.1055/s-2007-992764, indexed in Pubmed: 18592020.
18. Hammer G, Radberg C. The sphenoidal sinus: an anatomical and roentgenologic study with reference to transsphenoid hypophysectomy. Acta Radiol. 2013; 56(6): 401–422, doi: 10.1177/028418516105600601.
19. Jaworek-Troć J, Iwanaga J, Chrzan R, et al. Anatomical variations of the main septum of the sphenoidal sinus and its importance during transsphenoidal approaches to the sella turcica. Transl Res Anat. 2020; 21: 100079, doi: 10.1016/j.tria.2020.100079.
20. Jaworek-Troć J, Walocha JA, Chrzan R, et al. Protrusion of the carotid canal into the sphenoid sinuses: evaluation before endonasal endoscopic sinus surgery. Folia Morphol. 2021; 80(3): 642–649, doi: 10.5603/FM.a2020.0086, indexed in Pubmed: 32789847.
21. Jaworek-Troć J, Walocha JA, Loukas M, et al. Extensive pneumatisation of the sphenoid bone — anatomical investigation of the recesses of the sphenoid sinuses and their clinical importance. Folia Morphol. 2020 [Epub ahead of print], doi: 10.5603/FM.a2020.0120, indexed in Pubmed: 33084012.
22. Jaworek-Troć J, Walocha JA, Skrzat J, et al. A computed tomography comprehensive evaluation of the ostium of the

sphenoid sinus and its clinical significance. Folia Morphol. 2021 [Epub ahead of print], doi: 10.5603/FM.a2021.0063, indexed in Pubmed: 34219216.

23. Jaworek-Troć J, Zarzecki M, Bonczar A, et al. Sphenoid bone and its sinus - anatomo-clinical review of the literature including application to FESS. Folia Med Cracov. 2019; 59(2): 45–59, indexed in Pubmed: 31659348.

24. Jaworek-Troć J, Zarzecki M, Lusina D, et al. Incorporation of the sphenoid sinuses' septum / septa in the carotid canal: evaluation before the FESS. Folia Med Cracov. 2020; 60(4): 65–78, indexed in Pubmed: 33821852.

25. Jaworek-Troć J, Zarzecki M, Mróz I, et al. The total number of septa and antra in the sphenoid sinuses - evaluation before the FESS. Folia Med Cracov. 2018; 58(3): 67–81, doi: 10.24425/fmc.2018.125073, indexed in Pubmed: 30521512.

26. Jaworek-Troć J, Zarzecki M, Zamojska I, et al. The height and type of the main septum in the sphenoid sinuses: evaluation before the fess. Folia Med Crac. 2020; 60(3): 65–74, doi: 10.24425/fmc.2020.135796, indexed in Pubmed: 33582746.

27. Jaworek-Troć J, Zarzecki M, Zamojska I, et al. The dimensions of the sphenoid sinuses: evaluation before the functional endoscopic sinus surgery. Folia Morphol. 2021; 80(2): 275–282, doi: 10.5603/FM.a2020.0059, indexed in Pubmed: 32488857.

28. Kapur E, Kapidžić A, Kulenović A, et al. Septation of the sphenoid sinus and its clinical significance. Int J Coll Res Int Med Public Health. 2012; 4(10): 1793–1802.

29. Seddighi A, Seddighi AS, Mellati O, et al. Sphenoid sinus: anatomic variations and their importance in trans-sphenoid surgery. Int Clin Neurosci J. 2014; 1(1): 31–34.

30. Sharma S, Durgaprasad BK, Vijayalakshmi P. A case of Kartagener's syndrome with combined aplasia of frontal and sphenoid sinuses and hypoplasia of maxillary and ethmoid sinuses. J Family Community Med. 2021; 28(2): 129–132, doi: 10.4103/jfcm.JFCM_304_20, indexed in Pubmed: 34194278.

31. Sinha S, Shetty A, Nayak K. The morphology of Sella Turcica in individuals with different skeletal malocclusions: a cephalometric study. Transl Res Anat. 2020; 18: 100054, doi: 10.1016/j.tria.2019.100054.

32. Stecco A, Boccafoschi F, Falaschi Z, et al. Virtual dissection table in diagnosis and classification of Le Fort fractures: A retrospective study of feasibility. Transl Res Anat. 2020; 18: 100060, doi: 10.1016/j.tria.2019.100060.

33. Tan HKK, Ong YK. Sphenoid sinus: an anatomic and endoscopic study in Asian cadavers. Clin Anat. 2007; 20(7): 745–750, doi: 10.1002/ca.20507, indexed in Pubmed: 17583590.

34. Tesfaye S, Hamba N, Gerbi A, et al. Radio-anatomic variability in sphenoid sinus pneumatization with its relationship to adjacent anatomical structures and their impact upon reduction of complications following endonasal transsphenoidal surgeries. Transl Res Anat. 2021; 24: 100126, doi: 10.1016/j.tria.2021.100126.

35. Vidić B. The postnatal development of the sphenoidal sinus and its spread into the dorsum sellae and posterior clinoid processes. Am J Roentgenol Radium Ther Nucl Med. 1968; 104(1): 177–183, doi: 10.2214/ajr.104.1.177, indexed in Pubmed: 5672763.

36. Yonetsu K, Watanabe M, Nakamura T. Age-related expansion and reduction in aeration of the sphenoid sinus: volume assessment by helical CT scanning. Am J Neuroradiol. 2000; 21(1): 179–182, indexed in Pubmed: 10669247.

37. Yune HY, Holden RW, Smith JA. Normal variations and lesions of the sphenoid sinus. Am J Roentgenol Radium Ther Nucl Med. 1975; 124(1): 129–138, doi: 10.2214/ajr.124.1.129, indexed in Pubmed: 167598.

VIA MEDICA

O R I G I N A L   A R T I C L E

New accessory palatine canals and foramina in cone-beam computed tomography

H.A.M. Marzook[1] , A.A. Elgendy[2], F.A. Darweesh[3]

[1]Oral and Maxillofacial Surgery Department, Faculty of Dentistry, Mansoura University, Mansoura, Egypt
[2]Endodontics, Head of Conservative Dentistry Department, Faculty of Dentistry, Zagazig University, Zagazig, Egypt
[3]Oral Biology Department, Faculty of Dentistry, Zagazig University, Zagazig, Egypt

Background: Palatal surgeries are associated with many complications. Accessory foramina may be a cause of concern. The present study was conducted to assess the presence and to evaluate the anatomical characteristics of accessory palatine foramina (APF) and related bony canals in cone beam computed tomography (CBCT) scans.

Materials and methods: The incidence, location, and types of foramina on the palate were evaluated in 170 CBCT scans. Readings from coronal, sagittal, and axial planes were recorded using a computer programme and evaluated.

Results: Other than nasopalatine, greater and lesser palatine foramina, 278 foramina were seen in the palate in different locations. New APF were found posteriorly in 14.71% of the studied scans with wide anatomical variations. Unusual foraminal canals were seen crossing the antral floor laterally. The anterior APF were seen in 73.53% of scans while bilateral APF were found in 43.53% of cases.

Conclusions: Accessory palatine foramina and related canals are frequently seen in CBCT with many anatomical variations. New unusual connecting canals are found passing through the antral floor from palatine foramina to the lateral antral wall. These anatomical structures should be considered in preoperative planning for local analgesia and surgical interventions in the palate. (Folia Morphol 2021; 80, 4: 954–962)

Key words: cone-beam computed tomography, anatomical landmarks, new palatine foramina, nasopalatine foramen, palate, canalis sinuosus

INTRODUCTION

Palatal surgical interventions are associated with different complications. Complications include intraoperative bleeding, wound dehiscence, and nerve injury [6, 8, 13, 33]. To avoid these complications, total knowledge of bony neurovascular anatomical variations is recommended [2, 38]. Cone-beam computed tomography (CBCT) was found to play an important role in studying anatomical variations of the jaws [27]. The palatine foramina and canals were previously studied by many researchers [21, 35].

The maxillary nerve is a completely sensory nerve that supplies the maxillary teeth and related soft tissues of the hard and soft palate, nose, upper lip, maxillary sinus, as well as many adjoining structures [37]. The anatomical variations may be a cause of anaesthesia failure or surgical complications.

Table 1. Distribution of anterior and posterior accessory palatine foramina (APF) in the cone-beam computed tomography scans

No.	Studied structure	No. of readings	No. of patients	Bilateral cases	Per cent
1	Anterior APF	234	125	65	73.53%
2	Posterior APF	44	25	9	14.71%

Many studies investigated neurovascular structures in the anterior maxilla which may show different variations. Greater palatine canal and nasopalatine canal are among those structures [21, 28, 34–37]. Variants such as accessory canal of canalis sinuosus was studied by many investigators. It could be seen as a unilateral or bilateral canal with a palatal foramen located opposite anterior teeth. Nerves and blood vessels running through these canals often considered as extensions of the infraorbital nerve and its branches. Accessory canals of canalis sinuosus were previously considered a rare anatomical variant but many of these structures were recorded in recent reports [22, 24, 26, 32, 41].

In the posterior part of the hard palate, the anatomical features of the greater palatine and lesser palatine canals and foramina were studied [18, 28, 34, 36]. The greater palatine nerve canal is located bilaterally. Its shape, location, and size have been assessed by many research studies [10, 16]. Reports concerning anatomical variants such as accessory canals in the posterior palatal bone are lacking. CBCT analysis for accessory palatine foramina (APF), however, has not been widely studied or used in clinical dental practice yet. Therefore, it is important to evaluate the anatomical features of APF and related canals in CBCT. This study was undertaken to assess the presence and to evaluate the anatomical characteristics of APF and the related channels using CBCT.

MATERIALS AND METHODS

The protocol of the present study was approved by the Research Ethics Committee of Mansoura Faculty of Dentistry (code 03100918). Palatal bone was studied in 170 patients (108 female and 62 male) for any additional foramina and canals other than nasopalatine, greater palatine and lesser palatine. Readings from a computer programme (Planmeca Romexis Viewer 5.4.1.R, Planmeca Co., Italy) were recorded by two investigators. CBCT coronal, axial, and sagittal slices from 170 scans were studied to evaluate the occurrence, location, and direction of accessory canals. The recorded foramina were classified according to their location into anterior and posterior accessory palatal foramina. Anterior foramina are those located in front of upper first premolars; however, the others were considered posterior. The mean age of enrolled cases was 35.33 years. Scans with large pathological bony lesions or fractures in the palatal region were excluded. The course and relations of additional canals were studied. Only after studying their related bony canals, APF were considered branched from canalis sinuosus. Agreement between the two investigators is essential for considering recorded foramina. Data were collected for the location, incidence, and course of the anterior and posterior APF and their canals, and evaluated.

RESULTS

A total of 278 additional foramina of the palate other than nasopalatine, greater palatine, and lesser palatine were seen and recorded from the different planes of 170 CBCT scans. The additional foramina were divided into anterior and posterior accessory palatine foraminal groups (Table 1). Nasopalatine foramen was seen in the midline in all scans with different morphological variations. One hundred and thirty-three (78.24%) patients showed at least one more additional foramen.

A new type of palatine foramina was detected in the posterior region of the palate in 25 CBCT scans with abnormal directions of their associated bony canals (Fig. 1). These canals were found to extend upward to the medial antral wall and nasal cavity and to follow a lateral course in the floor of the sinus. Posterior accessory palatine foraminal canals were found to exhibit multidirectional course in many cases (Fig. 2). Different positions of posterior APF in the palate were seen (Fig. 3). Multiple posterior additional palatine canal was detected in 12 cases either unilateral or bilateral. Some posterior accessory foramina were found to be passing anteriorly and originating from canalis sinuosus (Fig. 4).

There was a prevalence of the anterior accessory foramina, with significant differences in their positions and anatomical features. Lateral incisor and cuspid region foramina were also seen. In many instances accessory anterior foramina were found to be connected to canalis sinuosus branch of infraorbital
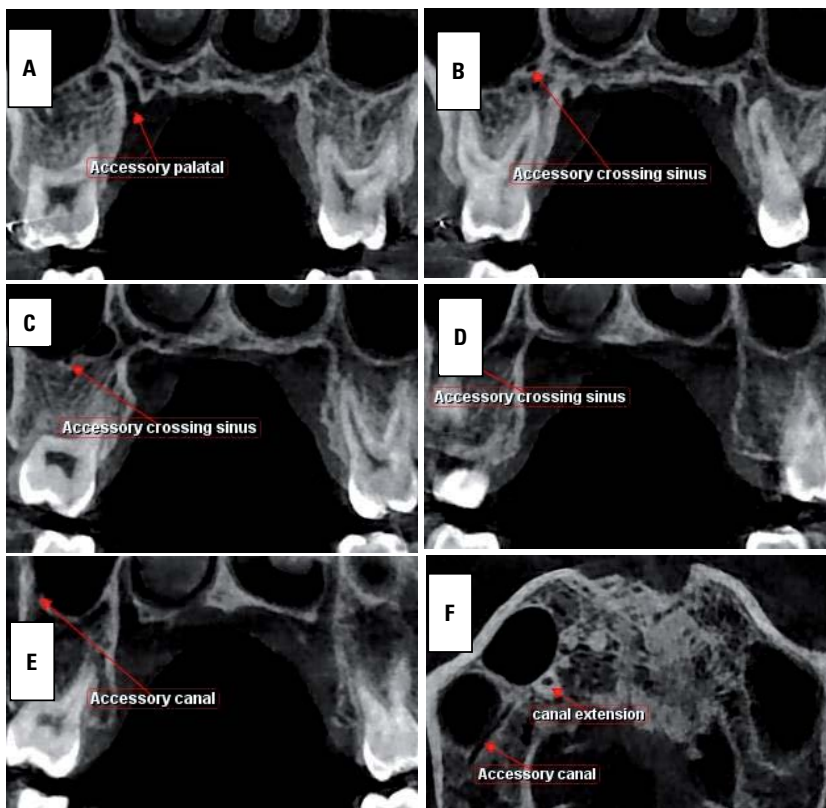
Figure 1. New posterior accessory palatine foramen canal shown in coronal sections passing from palate to maxillary sinus (**A**); through sinus floor (**B**), to the middle of the floor (**C**), then to the lateral antral wall (**D**), upward posteriorly (**E**), and in axial section with lateral, posterior, and upward direction (**F**).

Figure 2. Variants of the new posterior accessory palatine foramina and their canals shown in axial sections directed anteriorly first (**A**), or passing directly from palate to maxillary, and in coronal sections ascending upward (**B**), laterally to medial sinus wall (**C**), or directly through palate to nasal cavity (**D**).

nerve (Fig. 5) and were directed upward anteriorly. Anterior accessory foramina originating from canalis sinuosus were found to be present in 125 (73.53%) patients. Different locations of APF in the anterior region were found. Many of the anterior accessory palatine canals were connected to nasopalatine canal and some were found to be related to the supply of upper anterior teeth (Fig. 6). Bilateral occurrence was found in 65 patients. More than two unilateral or bilateral APF could be detected in 88 scans (Fig. 2).
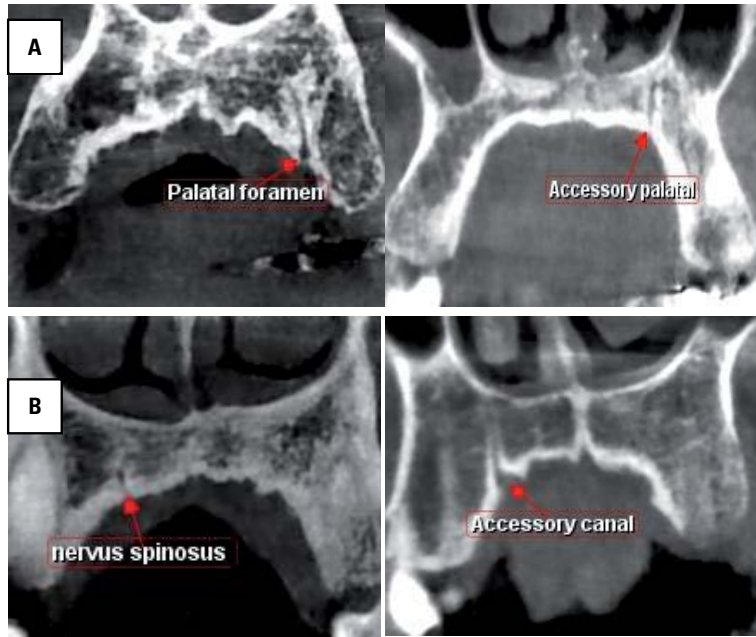
Figure 3. Different positions of posterior accessory palatine foramina in relation to alveolar ridge in coronal sections: **A.** Near the ridge in most of the cases; **B.** Away from ridge.
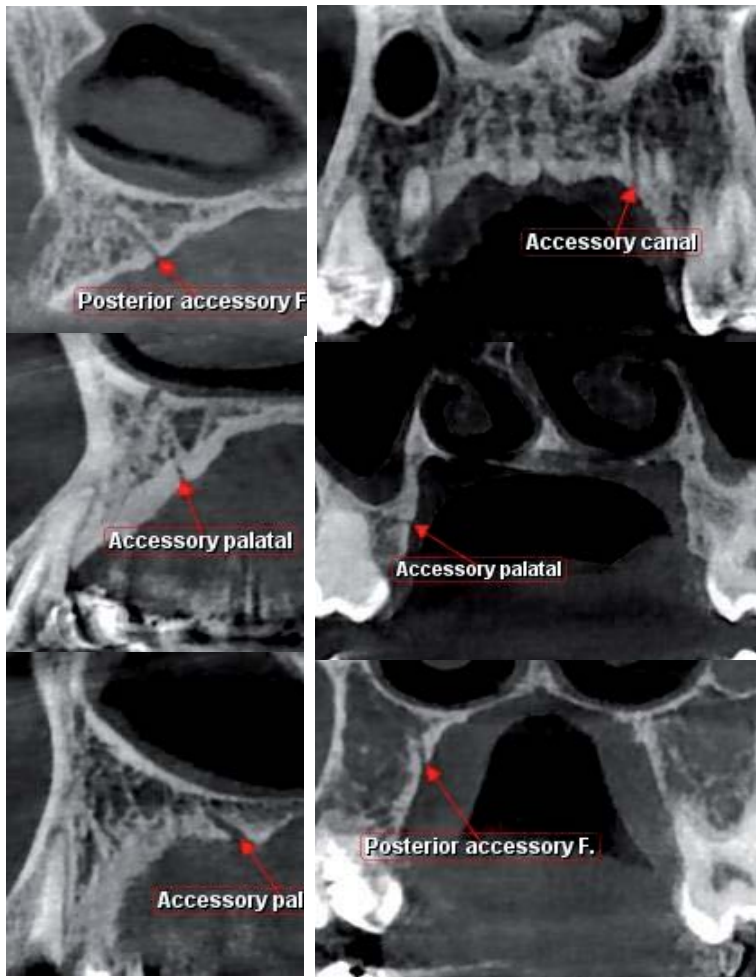
Figure 4. Posterior accessory foramina originating from canalis sinuosus.

957
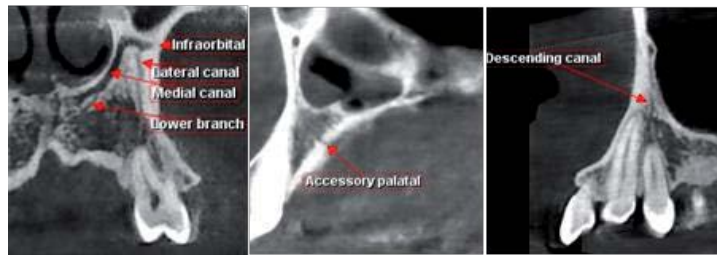
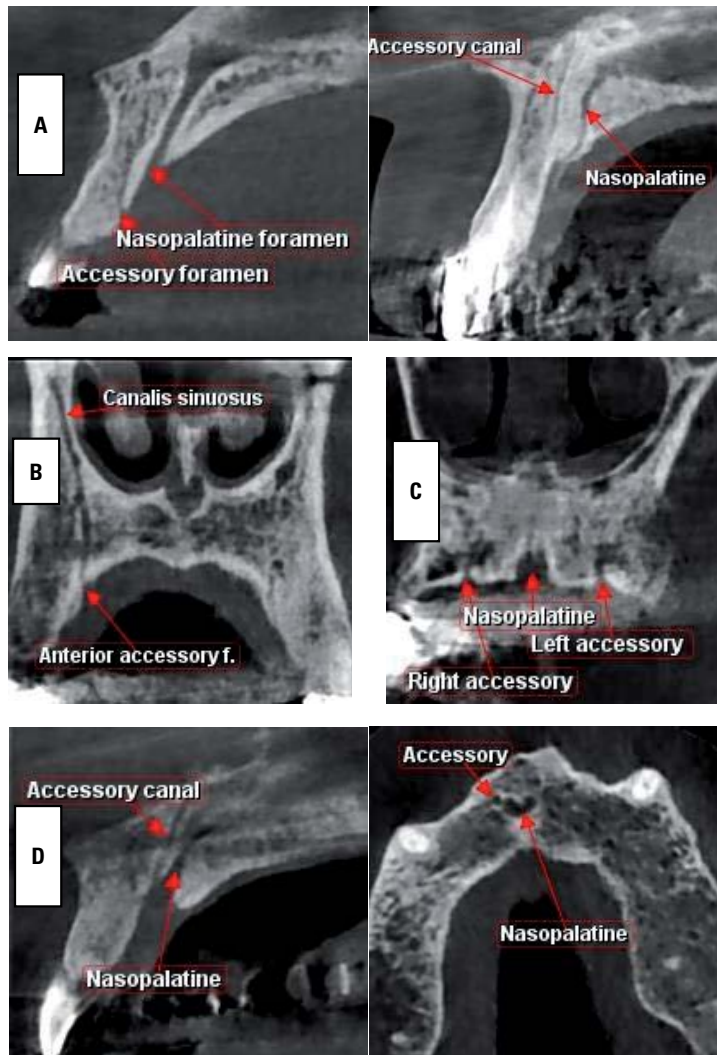**Figure 5.** Branching of canalis sinuosus in the upper jaw.

Figure 6. Different relations of accessory anterior palatine canals to nasopalatine canal: **A.** Anterior; **B.** Posterior; **C.** Lateral; **D.** Opening into nasopalatine foramen.

Additional palatine foramina could not be related to canalis sinuosus in 26 scans (Fig. 3). Variations in size of APF could be seen in many cases (Fig. 4). Additional foramina were found in different coronal (Fig. 5), axial (Fig. 6), and sagittal planes (Fig. 7).

DISCUSSION

Complications occurring during surgical treatment of palatal conditions had been reported. Identification of the location of neurovascular anatomical structures is essential for the avoidance of complications such as haemorrhage and neurosensory impairment
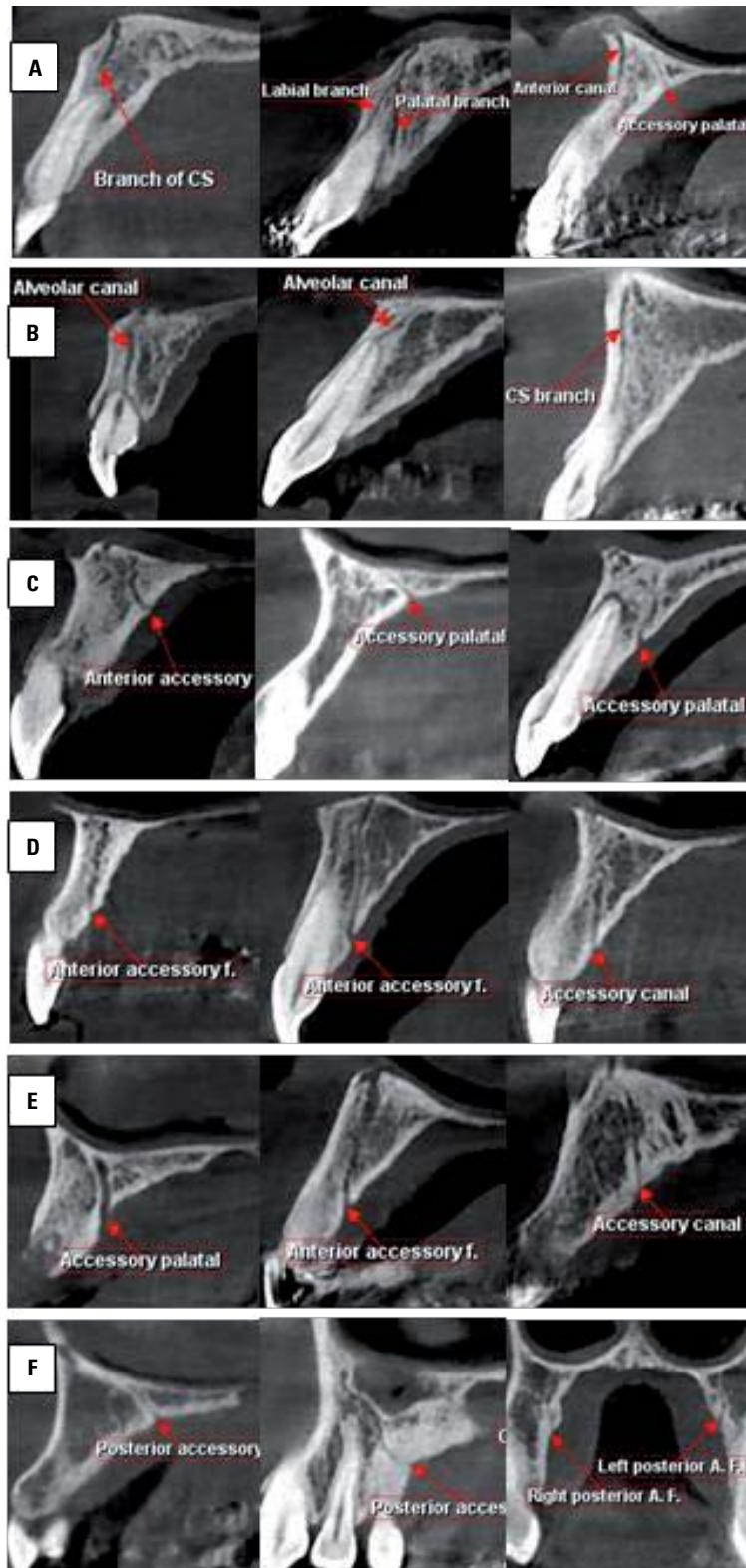
Figure 7. Variation of branching of canalis sinuosus: **A.** Labial and palatal bony plates branches; **B.** Dental branches; **C.** High anterior accessory palatine branches; **D.** Low anterior accessory palatine; **E.** Wide or branched; **F.** Posterior palatine branching unilateral and bilateral.

[1, 2, 6–8, 13, 33, 38]. Osseous neurovascular structures include the nasopalatine, greater and lesser palatine foramina and their canals [10, 21, 31]. In this study, these structures were found in all cases (100%). These findings are in agreement with several previous research results [9, 31]. There was a high incidence of APF in our adult Egyptian sample. There was a prevalence of the anterior accessory foramina, with many differences in their locations and anatomical features. In most instances, these additional foramina were related to canalis sinuosus. These results are consistent with what had been found in previous studies [11, 17, 39, 40].

More studies are needed to investigate the abnormal lateral origin of the unusual new type of posterior palatine foramina. The possibility of being derived from the posterior superior alveolar nerve may result in a change of the common belief that greater palatine nerve block is sufficient for anaesthesia of palatal gingiva opposing upper posterior teeth. This result may be supported by the findings of previous reports of occurrence of palatal anaesthesia after a single buccal infiltration [3, 5, 20]. On the contrary, it may also put a question mark upon the accuracy of studies investigating the palatal effect of some local anaesthetic solutions proposed to penetrate the alveolar bone after buccal infiltration [23, 25, 29]. Studies searching for the occurrence or the anatomical features of posterior APF and canals are lacking. Failure of greater palatine anaesthesia might be attributed to the presence of this extra abnormal innervation in some patients.

There is no clear evidence in previous studies that multidirectional posterior APF canals are present in humans. Most studies investigated the anatomic features of the greater palatine canal or the opening direction, dimensions, and shape of the greater palatine foramen [34, 36, 37]. Multiple APF were considered previously as double or triple greater or lesser palatine foramina [4, 9]. Our results disagree with these considerations as the lateral extensions of foraminal canals cross the antral floor laterally. This result may also support the recommendations of previous reports concerning the necessity of preoperative planning [15, 19].

The findings of the present study proved that there is a connection between many of the anterior accessory palatine canals and nasopalatine canal. Some of these canals were related to the supply of upper anterior teeth. These results are in accordance with some reports indicating this supply [15, 19]. The presence of anastomosis between different bony canals forming sometimes a plexus or a network of channels in the anterior part of the maxilla may add to the complexity of some periapical surgeries. This may also explain postoperative bleeding or sensory disturbances after endodontic surgery or palatal mucosal grafting in some cases [12].

In our study, cases showed variations of intra-bony canals. Many studies postulated the possibility of the presence of bony nutrient canals and this should be put in consideration [14, 30]. Most recent studies do not clearly demonstrate this.

In this work, there was a high incidence for the APF in comparison to previous studies [26, 32, 38]. A new type of APF was discovered in the posterior region of the palate with abnormal extension of its canal to the floor of maxillary sinus. Any graft or implant placement in this area of the palate should not be done without a thorough CBCT investigation of the area. There was a great variability in the occurrence of palatine foramina and their bony canals anatomy and location in our sample. Considering narrow canals and using recent technology may be the cause of this high occurrence. Thorough preoperative CBCT examination is mandatory to preserve these neurovascular variants in any surgical treatment.

CONCLUSIONS

Accessory palatine foramina and their related bony canals are present frequently in the palate with high anatomical variability. In the anterior region of the palate, the incidence of anterior accessory foramina was the higher. Posterior APF were also frequently seen with wide morphological variations. These findings should be taken into consideration in preoperative planning for any surgical intervention in the palate to avoid complications. A thorough CBCT examination of the anterior and posterior palatal areas is highly advocated prior to surgery in these regions. In this study, accessory palatine canals were evaluated only on CBCT images, and the contents of the canals were not confirmed. More cadaveric and clinical studies exploring the histological and anatomical contents are essential to validate the current findings.

REFERENCES

1. Allareddy V, Vincent SD, Hellstein JW, et al. Incidental findings on cone beam computed tomography images. Int J Dent. 2012; 2012: 871532, doi: 10.1155/2012/871532, indexed in Pubmed: 23304148.

2. Arruda JA, Silva P, Silva L, et al. Dental implant in the canalis sinuosus: a case report and review of the literature. Case Rep Dent. 2017; 2017: 4810123, doi: 10.1155/2017/4810123, indexed in Pubmed: 28928992.

3. Ashwath B, Subramoniam S, Vijayalakshmi R, et al. Anesthetic efficacy of 4% articaine and 2% lignocaine in achieving palatal anesthesia following a single buccal infiltration during periodontal therapy: A randomized double-blind split-mouth study. J Anaesthesiol Clin Pharmacol. 2018; 34(1): 107–110, doi: 10.4103/joacp.JOACP_200_15, indexed in Pubmed: 29643633.

4. Badshah M, Soames R, Khan MJ, et al. Morphology of the human hard palate: a study on dry skulls. Italian J Anat Embryol. 2018; 123(1): 55–63, doi: 10.13128/IJAE-23011.

5. Bataineh AB, Al-Sabri GA. Extraction of maxillary teeth using articaine without a palatal injection: a comparison between the anterior and posterior regions of the maxilla. J Oral Maxillofac Surg. 2017; 75(1): 87–91, doi: 10.1016/j.joms.2016.06.192, indexed in Pubmed: 27528103.

6. Bouloux GF, Bays RA. Neurosensory recovery after ligation of the descending palatine neurovascular bundle during Le Fort I osteotomy. J Oral Maxillofac Surg. 2000; 58(8): 841–5; discussion 846, doi: 10.1053/joms.2000.8196, indexed in Pubmed: 10935581.

7. Bouloux GF, Perciaccante VJ. Massive hemorrhage during oral and maxillofacial surgery: ligation of the external carotid artery or embolization? J Oral Maxillofac Surg. 2009; 67(7): 1547–1551, doi: 10.1016/j.joms.2009.03.014, indexed in Pubmed: 19531434.

8. Buff LR, Bürklin T, Eickholz P, et al. Does harvesting connective tissue grafts from the palate cause persistent sensory dysfunction? A pilot study. Quintessence Int. 2009; 40(6): 479–489, indexed in Pubmed: 19587889.

9. Cagimni P, Govsa F, Ozer MA, et al. Computerized analysis of the greater palatine foramen to gain the palatine neurovascular bundle during palatal surgery. Surg Radiol Anat. 2017; 39(2): 177–184, doi: 10.1007/s00276-016-1691-0, indexed in Pubmed: 27177906.

10. Chrcanovic BR, Custódio ALN. Anatomical variation in the position of the greater palatine foramen. J Oral Sci. 2010; 52(1): 109–113, doi: 10.2334/josnusd.52.109, indexed in Pubmed: 20339241.

11. de Oliveira-Santos C, Rubira-Bullen IRF, Monteiro SAC, et al. Neurovascular anatomical variations in the anterior palate observed on CBCT images. Clin Oral Implants Res. 2013; 24(9): 1044–1048, doi: 10.1111/j.1600-0501.2012.02497.x, indexed in Pubmed: 22587228.

12. Dridi SM, Chousterman M, Danan M, et al. Haemorrhagic risk when harvesting palatal connective tissue grafts: a reality? PERIO. 2008; 5: 231–240.

13. Filippi A, Pohl Y, Tekin U. Sensory disorders after separation of the nasopalatine nerve during removal of palatal displaced canines: prospective investigation. Br J Oral Maxillofac Surg. 1999; 37(2): 134–136, doi: 10.1054/bjom.1997.0092, indexed in Pubmed: 10371320.

14. Goodman-Topper ED, Chosack A. Radiographic appearance of nutrient canals in the region of the erupting permanent maxillary cuspid. Oral Surg Oral Med Oral Pathol. 1989; 67(5): 606–610, doi: 10.1016/0030-4220(89)90281-8, indexed in Pubmed: 2717159.

15. Gurler G, Delilbasi C, Ogut EE, et al. Evaluation of the morphology of the canalis sinuosus using cone-beam computed tomography in patients with maxillary impacted canines. Imaging Sci Dent. 2017; 47(2): 69–74, doi: 10.5624/isd.2017.47.2.69, indexed in Pubmed: 28680842.

16. Hafeez NS, Ganapathy S, Sondekoppam R, et al. Anatomical variations of the greater palatine nerve in the greater palatine canal. J Can Dent Assoc. 2015; 81: f14, indexed in Pubmed: 26214834.

17. Hu KS, Kwak HH, Song WC, et al. Branching patterns of the infraorbital nerve and topography within the infraorbital space. J Craniofac Surg. 2006; 17(6): 1111–1115, doi: 10.1097/01.scs.0000236436.97720.5f, indexed in Pubmed: 17119413.

18. Iwanaga J, Kido J, Lipski M, et al. Anatomical study of the palatine aponeurosis: application to posterior palatal seal of the complete maxillary denture. Surg Radiol Anat. 2018; 40(2): 179–183, doi: 10.1007/s00276-017-1911-2, indexed in Pubmed: 28823003.

19. Jung J, Yim JH, Kwon YD, et al. A radiographic study of the position and prevalence of the maxillary arterial endosseous anastomosis using cone beam computed tomography. Int J Oral Maxillofac Implants. 2011; 26(6): 1273–1278, indexed in Pubmed: 22167433.

20. Kolli NK, Nirmala SV, Nuvvula S. The effectiveness of articaine and lidocaine single buccal infiltration versus conventional buccal and palatal injection using lidocaine during primary maxillary molar extraction: a randomized control trial. Anesth Essays Res. 2017; 11(1): 160–164, doi: 10.4103/0259-1162.186589, indexed in Pubmed: 28298777.

21. Liang X, Jacobs R, Martens W, et al. Macro- and micro-anatomical, histological and computed tomography scan characterization of the nasopalatine canal. J Clin Periodontol. 2009; 36(7): 598–603, doi: 10.1111/j.1600-051X.2009.01429.x, indexed in Pubmed: 19538333.

22. Machado Vd, Chrcanovic BR, Felippe MB, et al. Assessment of accessory canals of the canalis sinuosus: a study of 1000 cone beam computed tomography examinations. Int J Oral Maxillofac Surg. 2016; 45(12): 1586–1591, doi: 10.1016/j.ijom.2016.09.007, indexed in Pubmed: 27720336.

23. Majid OW, Ahmed AM. The anesthetic efficacy of articaine and lidocaine in equivalent doses as buccal and non-palatal infiltration for maxillary molar extraction: a randomized, double-blinded, placebo-controlled clinical trial. J Oral Maxillofac Surg. 2018; 76(4): 737–743, doi: 10.1016/j.joms.2017.11.028, indexed in Pubmed: 29257943.

24. Manhães Júnior LR, Villaça-Carvalho MF, Moraes ME, et al. Location and classification of Canalis sinuosus for cone beam computed tomography: avoiding misdiagnosis. Braz Oral Res. 2016; 30(1): e49, doi: 10.1590/1807-3107BOR-2016.vol30.0049, indexed in Pubmed: 27119586.

25. Mittal M, Sharma S, Kumar A, et al. Comparison of anesthetic efficacy of articaine and lidocaine during primary maxillary molar extractions in children. Pediatr Dent. 2015; 37(7): 520–524, indexed in Pubmed: 26883609.

26. Neves FS, Crusoé-Souza M, Franco LC, et al. Canalis sinuosus: a rare anatomical variation. Surg Radiol Anat. 2012; 34(6): 563–566, doi: 10.1007/s00276-011-0907-6, indexed in Pubmed: 22134775.

27. Orhan K, Gorurgoz C, Akyol M, et al. An anatomical variant: evaluation of accessory canals of the canalis sinuosus using cone beam computed tomography. Folia Morphol. 2018; 77(3): 551–557, doi: 10.5603/FM.a2018.0003, indexed in Pubmed: 29345719.

28. Ortug A, Uzel M. Greater palatine foramen: assessment with palatal index, shape, number and gender. Folia Morphol. 2019; 78(2): 371–377, doi: 10.5603/FM.a2018.0088, indexed in Pubmed: 30234897.

29. Ozeç I, Taşdemir U, Gümüş C, et al. Is it possible to anesthetize palatal tissues with buccal 4% articaine injection? J Oral Maxillofac Surg. 2010; 68(5): 1032–1037, doi: 10.1016/j.joms.2009.12.023, indexed in Pubmed: 20223573.

30. Patel JR, Wuehrmann AH. A radiographic study of nutrient canals. Oral Surg Oral Med Oral Pathol. 1976; 42(5): 693–701, doi: 10.1016/0030-4220(76)90220-6, indexed in Pubmed: 1068424.

31. Piagkou M, Xanthos T, Anagnostopoulou S, et al. Anatomical variation and morphology in the position of the palatine foramina in adult human skulls from Greece. J Craniomaxillofac Surg. 2012; 40(7): e206–e210, doi: 10.1016/j.jcms.2011.10.011, indexed in Pubmed: 22055651.

32. Shelley AM, Rushton VE, Horner K. Canalis sinuosus mimicking a periapical inflammatory lesion. Br Dent J. 1999; 186(8): 378–379, doi: 10.1038/sj.bdj.4800116, indexed in Pubmed: 10365458.

33. Tavelli L, Barootchi S, Ravidà A, et al. What is the safety zone for palatal soft tissue graft harvesting based on the locations of the greater palatine artery and foramen? A systematic review. J Oral Maxillofac Surg. 2019; 77(2): 271.e1–271.e9, doi: 10.1016/j.joms.2018.10.002, indexed in Pubmed: 30395825.

34. Tomaszewska IM, Tomaszewski KA, Kmiotek EK, et al. Anatomical landmarks for the localization of the greater palatine foramen: a study of 1200 head CTs, 150 dry skulls, systematic review of literature and meta-analysis. J Anat. 2014; 225(4): 419–435, doi: 10.1111/joa.12221, indexed in Pubmed: 25131842.

35. Tomaszewska IM, Frączek P, Gomulska M, et al. Sex determination based on the analysis of a contemporary Polish population's palatine bones: a computed tomography study of 1,200 patients. Folia Morphol. 2014; 73(4): 462–468, doi: 10.5603/FM.2014.0069, indexed in Pubmed: 25448904.

36. Tomaszewska IM, Kmiotek EK, Pena IZ, et al. Computed tomography morphometric analysis of the greater palatine canal: a study of 1,500 head CT scans and a systematic review of literature. Anat Sci Int. 2015; 90(4): 287–297, doi: 10.1007/s12565-014-0263-9, indexed in Pubmed: 25467526.

37. Tomaszewska IM, Zwinczewska H, Gładysz T, et al. Anatomy and clinical significance of the maxillary nerve: a literature review. Folia Morphol. 2015; 74(2): 150–156, doi: 10.5603/FM.2015.0025, indexed in Pubmed: 26050800.

38. Torres MG, de Faro Valverde L, Vidal MT, et al. Branch of the canalis sinuosus: a rare anatomical variation: a case report. Surg Radiol Anat. 2015; 37(7): 879–881, doi: 10.1007/s00276-015-1432-9, indexed in Pubmed: 25616849.

39. von Arx T, Lozanoff S. Anterior superior alveolar nerve (ASAN). Swiss Dent J. 2015; 125(11): 1202–1209, indexed in Pubmed: 26631255.

40. von Arx T, Lozanoff S, Sendi P, et al. Assessment of bone channels other than the nasopalatine canal in the anterior maxilla using limited cone beam computed tomography. Surg Radiol Anat. 2013; 35(9): 783–790, doi: 10.1007/s00276-013-1110-8, indexed in Pubmed: 23539212.

41. Wanzeler AM, Marinho CG, Alves Junior SM, et al. Anatomical study of the canalis sinuosus in 100 cone beam computed tomography examinations. Oral Maxillofac Surg. 2015; 19(1): 49–53, doi: 10.1007/s10006-014-0450-9, indexed in Pubmed: 24752931.

ORIGINAL ARTICLE

Morphologic and morphometric characteristics of the adductor minimus in Korean: its topographic relationship with respect to neighbouring anatomical structure and clinical significance

S.C. Kwak[1, 2] *, H.-S. Won[1, 2] *, Y.-D. Kim[2, 3] , W.K. Kim[4], Y.S. Nam[5]

[1]Department of Anatomy, Wonkwang University School of Medicine, Iksan, Republic of Korea
[2]Jesaeng-Euise Clinical Anatomy Centre, Wonkwang University School of Medicine, Iksan, Republic of Korea
[3]Department of Anaesthesiology and Pain Medicine, Wonkwang University School of Medicine,
Wonkwang University Hospital, Iksan, Republic of Korea
[4]Department of Anatomy and Cell Biology, College of Medicine, Hanyang University, Seoul, Republic of Korea
[5]Department of Anatomy and Catholic Institute for Applied Anatomy, College of Medicine, The Catholic University
of Korea, Seoul, Republic of Korea

Background: The aim of this study was to clarify the morphologic and morphometric characteristics of the adductor minimus (AMi) and to observe its topographic relationships relative to the adjacent anatomical structures.

Materials and methods: This study investigated 54 thighs of 27 Korean cadavers.

Results: The AMi was a small and flat muscle observed in 94.4% of the specimens. It originated from the inferior ramus of the pubis as the upper part of the adductor magnus (AMa), and inserted from the lesser trochanter to the upper part of the linea aspera. The AMi was completely separate from the AMa in 63.0% of the specimens. The medial circumflex femoral artery was always found at the superior border of the AMi, while the first and second perforating arteries were found inferior to the muscle in 55.6% and 37.0% of specimens, respectively. A supernumerary muscle was found with the AMi in 42.6% of the specimens, and it originated from the inferior ramus of the pubis and inserted into the posterior side of the lesser trochanter. The obturator externus and AMi were found superoposterior and inferior to the supernumerary muscle, respectively, while the posterior branch of the obturator nerve passed underneath it.

Conclusions: The results of this study may provide physicians with the accurate anatomical knowledge that they require for managing groin pain and applying a regional nerve block with ultrasound guidance in this adductor region. (Folia Morphol 2021; 80, 4: 963–971)

Key words: adductor magnus, cadaver, obturator nerve block, ultrasound, variation

---

Address for correspondence: Y.S. Nam, PhD, Department of Anatomy, Catholic Institute for Applied Anatomy, College of Medicine, The Catholic University of Korea, 222, Banpo-daero, Seocho-gu, Seoul, 06591, Republic of Korea, tel: +82-2-22587441, fax: +82-2-5377081, e-mail: boffin@catholic.ac.kr

*S.C. Kwak and H.-S. Won are co-first authors and contribute equally to this work.

INTRODUCTION

The obturator nerve arises from the anterior rami of spinal nerves L2 to L4 in the lumbar plexus, and descends to the thigh via the obturator canal. This nerve divides into two main branches near the canal: an anterior branch and a posterior branch. The anterior branch runs anterior to the obturator externus and descends in front of the adductor brevis, behind the pectineus and adductor longus. The posterior branch pierces the obturator externus anteriorly, and passes between the adductor brevis and magnus (AMa) [8]. Various abnormal conditions such as tumour, hernia, and aneurysm could cause an entrapment syndrome at any point along the entire course of the obturator nerve [5]. The chief complaints of patients with such entrapment of the obturator nerve are numbness and sensory loss of the medial thigh, sometimes involving the calf. Weakness of leg adduction can also occur, as well as pain in the groin and medial thigh [5, 49]. Such pain is reportedly worsened by extension or rotation of the lower leg that stretches the nerve [11].

For both diagnosis and treatment when managing this symptom, obturator nerve block (ONB) has been commonly adapted to each branch under guidance provided by real-time ultrasound (US) imaging [12, 43, 47, 52].The block for the anterior branch is induced by injecting a local anaesthetic between the pectineus and adductor brevis [12, 43], while the posterior branch is blocked by injecting between the adductor brevis and AMa [47]. During this procedure, the existence of the adductor minimus (AMi) or supernumerary muscle (SM) needs to be considered for avoiding confusion about the final position of the tip of the injection needle, especially for inexperienced operators. Thus, an accurate knowledge of the muscle layers in the target region is essential to successfully achieving nerve blocks.

This study was designed to clarify the topographic relationships among the AMi, SM, and adjacent structures such as arteries, bone, and other muscles in the adductor region, with the aim of facilitating the diagnosis and treatment using ONB.

MATERIALS AND METHODS

Fifty-four thighs of 27 embalmed Korean adult cadavers (20 males, 7 females; mean age at death, 71.6 years; age range at death, 48–87 years) were investigated for this study. All of the cadavers used in this study had been legally donated to the Catholic University of Korea, and all of the research procedures were performed in accordance with the Helsinki Declaration. None of the cadavers showed any evidence of gross pathologies, previous surgical procedures, or traumatic lesions to the thigh region. This study was not subject to a review by the institutional review board (IRB) because of a cadaveric study that did not any personal identifiable information, which was confirmed by the IRB of the Catholic University of Korea (No. CHRPP CR-08).

All muscles of the thigh were exposed after removing the skin, subcutaneous tissue, and fascia lata. The sartorius and adductor longus were cut to check for the presence of the AMi and SM. If they were found, the target muscles and adjacent anatomical structures were carefully dissected without changing their locations. Chi-square test was used to compare the incidence of a SM between two genders and between both sides, with a statistical significance level of $p < 0.05$.

RESULTS

The AMi formed the upper part of the AMa, and its muscle fibres ran more horizontally than those of the AMa (Fig. 1). This muscle originated from the inferior pubic ramus, and inserted between the lesser trochanter and the upper part of the linea aspera, corresponding to the proximal one-fourth of the distance from the lesser trochanter to the adductor tubercle (Fig. 2). The portions where the muscle attached to the pubic ramus and femur were 3.2 ± 0.7 cm and 7.7 ± 2.0 cm long (mean ± standard deviation), respectively. The AMi was observed in 94.4% of the specimens. This muscle was completely separate from the AMa in 63.0% of the specimens, and could be distinguished but not as a separate muscle in 31.5% of them (Table 1). In the former cases, the inferior part of the muscle partly overlapped the AMa (by 2.8 ± ± 1.9 cm) at its insertion portion (Figs. 2C; 3). In the latter cases, the insertion portions of both muscles were continuously connected with each other.

The medial circumflex femoral artery was always found at the superior border of the AMi. The inferior border of the muscle was bounded by three kinds of the arteries (Fig. 4): the first perforating artery (55.6% of the specimens), the second perforating artery (37.0%), and the muscular branch of the deep femoral artery (7.4%).

A triangular shaped SM was observed in 42.6% of the specimens, which was located posterior to the
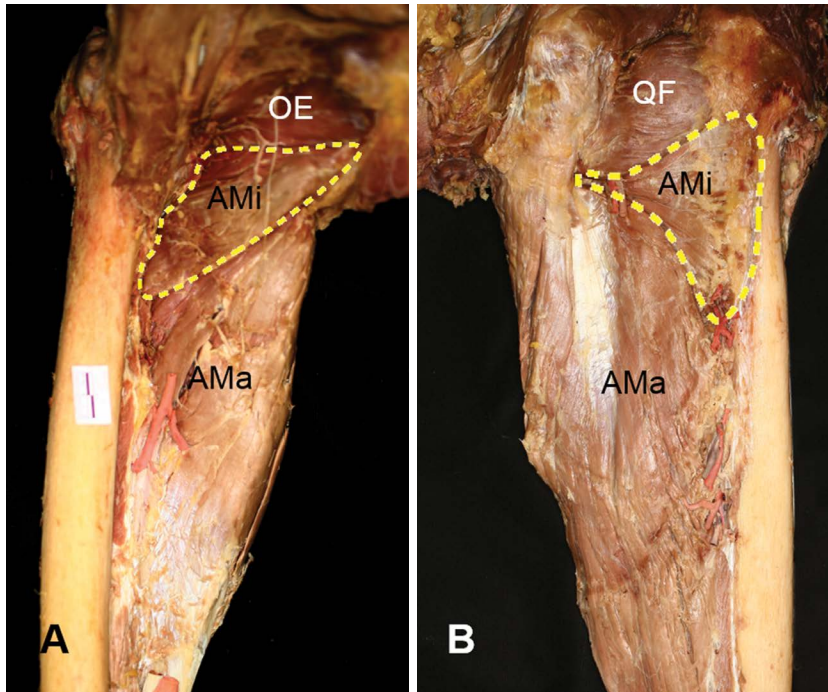
Figure 1. Anterior (**A**) and posterior (**B**) views of the adductor minimus. All muscles in the thigh except the obturator externus (OE), quadratus femoris (QF), adductor minimus (AMi), and adductor magnus (AMa) were removed. Dashed lines indicate the boundaries of the adductor minimus.
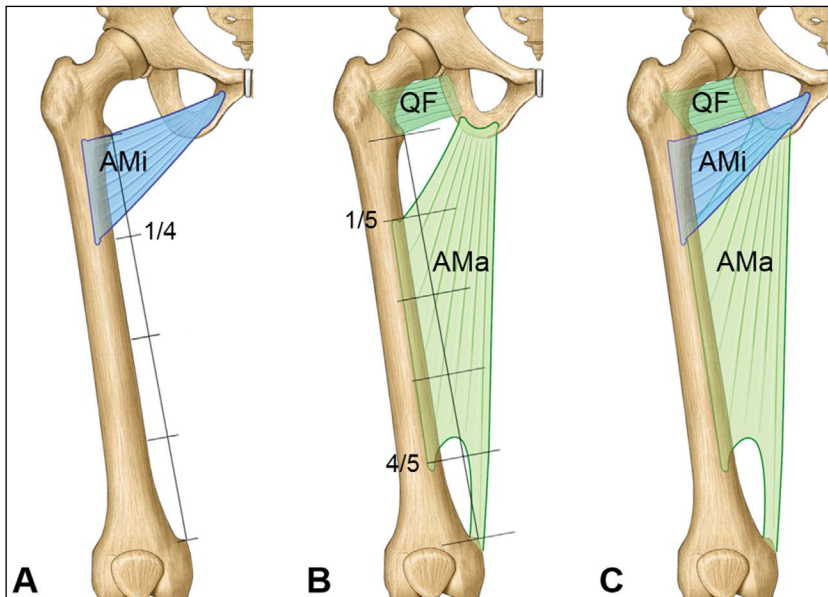

Figure 2. Schematic drawings of the topographic relationships among the adductor minimus (AMi), adductor magnus (AMa), and quadratus femoris (QF); **A.** The adductor minimus is attached to the proximal one-fourth of the distance from the lesser trochanter to the adductor tubercle; **B.** The adductor magnus is attached to the distal four-fifths of this distance; **C.** The adductor minimus is inferior to the QF and superior to the adductor magnus, and some parts of the adductor minimus an adductor magnus overlap.

adductor brevis, superior to the AMi, inferoanterior to the obturator externus, and anterior to the posterior branch of the obturator nerve (Fig. 5). The incidence of a SM did not differ between males and females, and between the right and left sides (Table 2). This muscle originated from the inferior pubic ramus and inserted into the posterior side of the lesser trochanter.
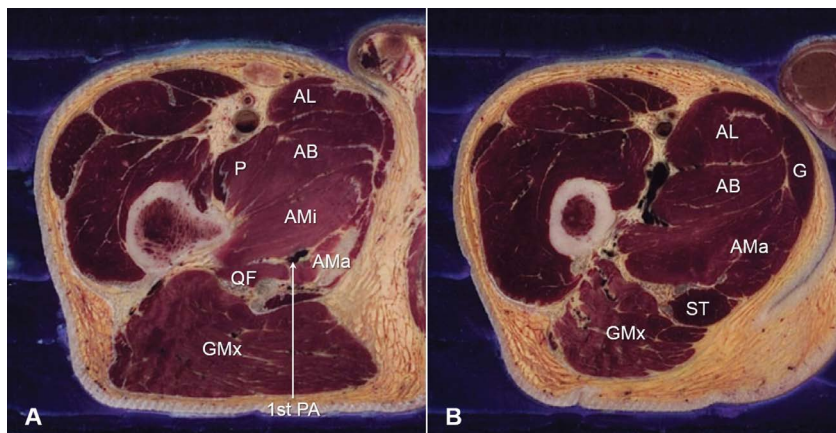
Figure 3. Cross-section images showing the adductor minimus (AMi) obtained from the Visible Human Korean project; **A.** The adductor minimus overlaps the adductor magnus (AMa) at the proximal one-fourth of the thigh. The adductor minimus can be distinguished from the adductor magnus by the first perforating artery (1st PA); **B.** The adductor minimus disappears below the 1st PA, with only the adductor magnus being visible; AL — adductor longus; AB — adductor brevis; P — pectineus; GMx — gluteus maximus; G — gracilis; ST — semitendinosus.
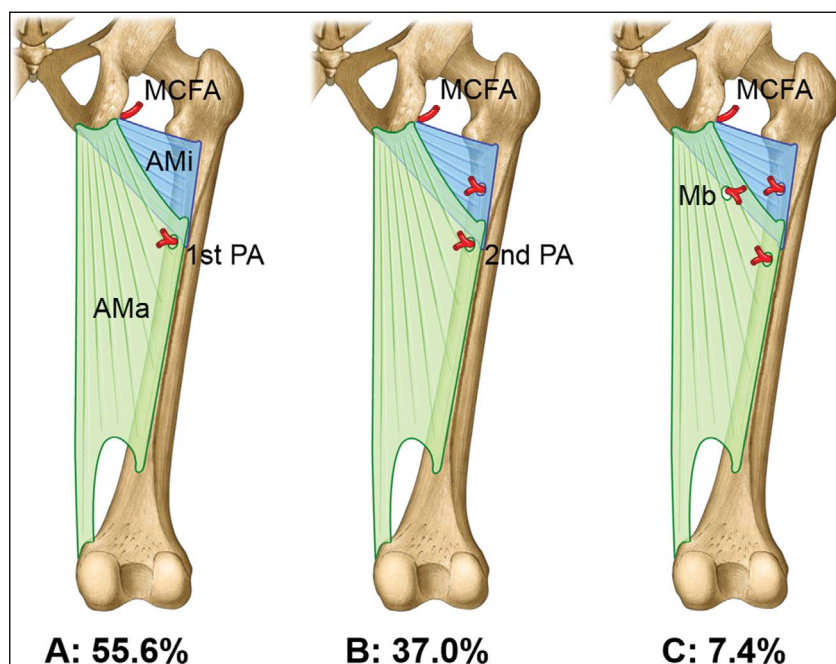

Figure 4. Structures that can help to distinguish the superior and inferior borders of the adductor minimus (AMi), and their prevalence rates; **A.** The medial circumflex femoral artery (MCFA) and the first perforating artery (1st PA); **B.** The MCFA and the second perforating artery (2nd PA); **C.** The MCFA and the muscular branch of deep femoral artery (Mb); AMa — abductor magnus.

DISCUSSION

Since ONB was first introduced by Labat and Mayo in 1922, it has been adapted for the management of various conditions [16]. This type of nerve block can prevent abnormal contraction of the thigh muscles during the ablation of bladder tumours [34], relax adductor muscle spasm secondary to paraplegia [23], and provide postoperative pain management [20]. Moreover, it can be applied to manage acute or chronic pain in the groin and thigh, since the obturator nerve is at risk of entrapment, compression, and damage at many sites related to surgery and trauma [22]. US-guided ONB has recently been regarded as the optimal technique. This type of block is safe, cost-effective, and makes it possible to observe the position of the injection needle in real time, which
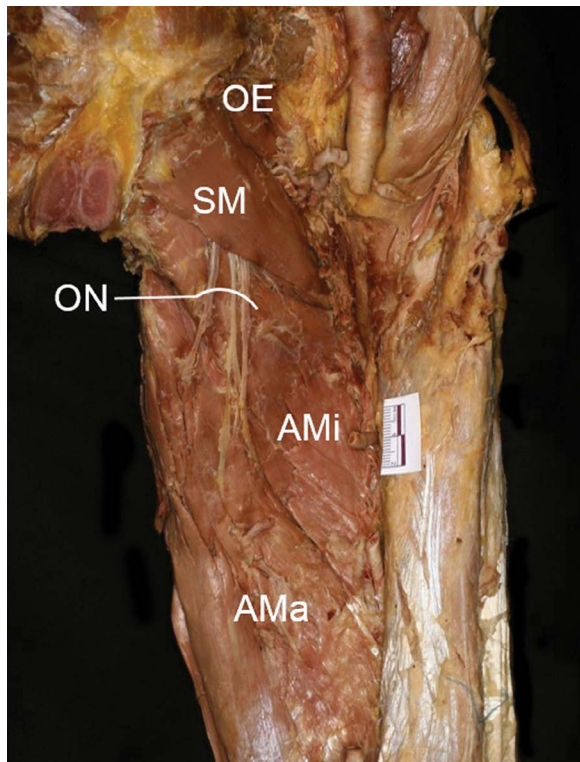
Figure 5. Anterior view of a supernumerary muscle (SM). The adductor longus and adductor brevis were removed to expose the SM and adjacent muscles. The SM is superior to the adductor minimus (AMi) and inferoanterior to the obturator externus (OE). The posterior branch of the obturator nerve (ON) passes behind the SM; AMa — abductor magnus.

Table 1. Different types of the adductor minimus and their frequencies in the present study

	Males, %	Females, %	Total, %
Separate	50 (n = 27)	13 (n = 7)	63 (n = 34)
Distinguishable	20.4 (n = 11)	11.1 (n = 6)	31.5 (n = 17)
Absent	3.75 (n = 2)	1.9 (n = 1)	5.6 (n = 3)
Total	74.1 (n = 40)	25.9 (n = 14)	100 (n = 54)

Table 2. Frequency of the supernumerary muscle in males and females and on the left and right sides in the present study

	Males, %	Females, %	Right, %	Left, %
Present	42.5 (n=17)	42.9 (n=6)	55.6 (n=15)	29.6 (n=8)
Absent	57.5 (n=23)	57.1 (n=8)	44.4 (n=12)	70.4 (n=19)
Total	100 (n=40)	100 (n=14)	100 (n=27)	100 (n=27)

Table 3. Frequency of the adductor minimus in different studies

Study	Population	Specimens	Per cent
Mori (1964)	Japanese	50	92%
Tubbs et al. (2011)	American	40	52.5%
Gusmão et al. (2014)	Brazilian	40	32%
This study (2020)	Korean	54	94.4%

can reduce the amount of local anaesthetic that needs to be administered, the risk of systemic toxicity, and the block onset delay [3, 48].

Numerous studies have attempted to provide exact information about the structures in US images through cadaver dissections in this region [4, 35, 53]. Nonetheless, US-guided ONB is not always successful [25, 43]. The likelihood of success can be influenced by various factors including the physician's experience, the patient's condition, and the performance of the US imaging system, similarly to the situation for other types of block [17]. Anatomical features such as the presence of unexpected muscles or the accessory obturator nerve in this region might also affect the likelihood of success [42].

There are two kinds of muscles being able to confuse physicians in the adductor region through reviews of the previous literatures: the AMi and SM. The AMi is small, flat, and can be distinguished at the posterior part of the adductor brevis and the upper part of the AMa [50]. This muscle originates

predominantly from the inferior ramus of the pubis [50] or the ischiopubic ramus [15] and inserts into the femur, and is innervated by the obturator nerve. The descriptions of the origin and insertion of the muscle are broadly consistent in the anatomical literature, whereas those related to distinguishing the muscle have been inconsistent: some authors have regarded this muscle as the upper part of the AMa [9, 26, 39, 41], while others have suggested that it is independent of adjacent muscles [6, 10, 36]. Some textbooks do not even mention this muscle at all [2, 27, 37]. The AMi is normally present in apes such as gorillas and chimpanzees [30], while its incidence in humans has been reported as 32% to 92% of the specimens according to the different populations [15, 28, 50] (Table 3). The present study found that its incidence was 94.4% in Korean cadavers, which was similar to that in the previous study using same race [28]. In the human embryo, the AMa arises as two distinct parts that subsequently fuse to form the muscle in the adult. This means that the AMi could appear to be present when two distinct parts of the AMa do not fuse completely [30]. In addition, the function of

Table 4. Frequency of the supernumerary muscle in different studies

Study	Population	Specimens	Per cent
Abe (1964)	Japanese	98	11.2%
Nakamura et al. (1992)	Japanese	100	33%
Yatsunami et al. (2004)	Japanese	73	23.3%
This study (2020)	Korean	54	42.6%

the AMi has been reported that it is not totally same with that of the AMa by a previous electromyographic study [7]. Both of these muscles show the highest activities during the maximal resisted extension of the hip joint, and have also the moderate activities during maximal hip adduction. However, the AMi is more active than the AMa during external rotation of hip joint. The AMi has also been suggested that it could be used as a landmark for identifying the posterior extent of the medial femoral circumflex artery and the first perforating artery for vascular anastomosis or for avoiding vascular structures [50]. In the present study, the medial circumflex femoral artery was always found at the superior border of the AMi, whereas the first perforating artery was only found at the inferior border of the muscle in 55.6% of the specimens. Thus, other arteries should also be considered when identifying the inferior border of the muscle, such as the second perforating artery and the muscular branch of the deep femoral artery, which were found in 37% and 7.4% of the present cases, respectively (Fig. 4).

A SM can be found between the adductor brevis and AMi, which has been reported as an anomalous muscle belonging to the adductor brevis [1] or the obturator externus [51]. This muscle is innervated by the posterior branch of the obturator nerve [29, 51], and its reported incidence has ranged from 11.2% to 33% in Japanese adults [1, 29, 51] (Table 4). Nakamura et al. [29] found that this muscle arose from the inferior ramus of the pubis and attached to the aponeurosis of AMi in 51.5% of their specimens, to the upper part of the pectineal line (27.3%), or to the posterior side of the base of the lesser trochanter (21.2%). In the present study, this muscle was observed posterior to the adductor brevis, superior to the AMi, and inferoanterior to the obturator externus. Its incidence was 42.6%, which is higher than in previous studies. Moreover, in all cases this muscle originated from the inferior pubic ramus, and inserted simply into the posterior side of the lesser

trochanter. Peiris et al. [32] insisted that the greater cross-sectional area of hip adductors could be related to the better function and quality of life in patients with hip osteoarthritis. The SM located between the adductor brevis and AMi in the present cases might affect this kind of cross-sectional area, which will need to be revealed through the other study.

Various SMs are frequently found in the upper and lower limbs, thoracic wall, neck, face, and eye, which include three-headed biceps brachii [40], pronator teres accessories [21], adductor accessories [13], pectoralis quartus [46], supernumerary digastric muscle [44], gracillimus orbitis muscle [19], and supernumerary extraocular muscle [33], with their embryologic origins also being hypothesized. The limbs first develop as the upper and lower limb buds, which are formed at levels C4–T2 and L2–S2, respectively [38]. Further development of the limb buds occurs via a series of stages including outgrowth, rotation, and the regional singular growth of structures [31]. The limb musculature develops from the paraxial mesoderm, and in the 7th week of development appears as the condensation of mesenchyme near the base of the limb buds [38]. The elongation of the limb buds results in the muscle tissue splitting into flexor and extensor components, which then fuse and form a single muscle mass [14]. In humans, the embryologic development of the adductor group of the thigh is first evident in the proximal region of an 11-mm-long embryo (approximately at a gestational age of early during week 6), with the separation into independent masses for the different muscles of the group. These separate muscles are evident once the embryo length reaches 14 mm (late during week 6), and at 20 mm long (week 7) the muscles of the adductor compartment are clearly discernible [18]. The lower limb rotates 90° medially between the 6th and 8th weeks of gestation [38]. While the limb musculature is differentiating, some muscle cells undergo apoptosis that determines the normal shape or the variations in the growing muscles and muscular compartments [24]. The SM in the present study was found in the medial thigh and located posterior to the adductor brevis, superior to the AMi, and inferoanterior to the obturator externus. Although the exact mechanisms of the formation of this muscle remain to be revealed, they might originate from the persistence of cells not undergoing the process of cell death [45] or abnormal 90° medial rotation of the lower limb bud [31].
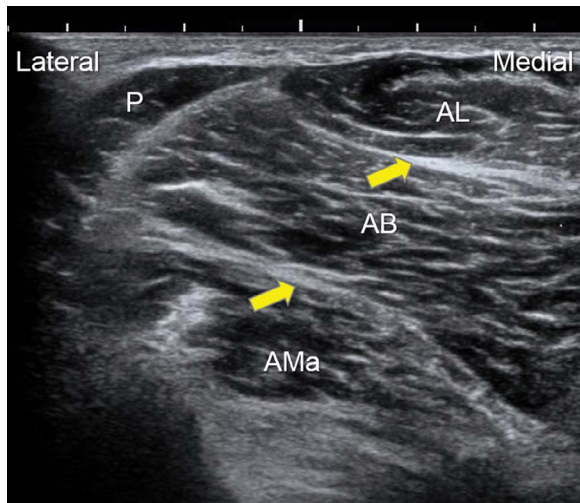
Figure 6. A patient ultrasound image (Linear probe 12–5 Hz, Samsung HS 60, Samsung Medison, Korea) showing the interfascial plane between the adductor longus (AL) and adductor brevis (AB) and between the adductor magnus (AMa) and AB. Arrows indicate the injection points for the anterior and posterior divisions of the obturator nerve (ON); P — pectineus.
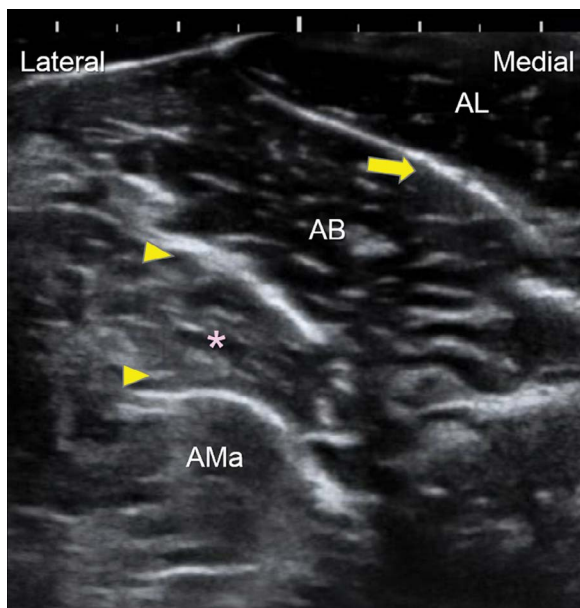

Figure 7. A patient ultrasound image (Linear probe 12–5 Hz, Samsung HS 60, Samsung Medison, Korea) showing a case that might confuse the physician during ultrasound-guided obturator nerve block. The arrow indicates the injection point for the anterior division of the obturator nerve. Arrowheads indicate structures mimicking the posterior division of the obturator nerve. The asterisk indicates either an adductor minimus or a supernumerary muscle; AL — adductor longus; AB — adductor brevis; AMa — adductor magnus.

Regarding clinical practice, the techniques used by physicians performing US-guided ONB can be classified into distal or proximal approaches based on the position of the US transducer. A common method for US-guided ONB involves the distal approach, in which the anterior and posterior divisions of the obturator nerve are blocked separately by two injections of local anaesthetic directed toward the interfascial planes [12]. The adductor brevis is located between the anterior and posterior divisions of the obturator nerve in the thigh, and these two divisions of the nerve are thin and flat as the fascicles disperse to the muscle groups [47]. The interfascial plane for the adductor muscle group could be identified based on two hyperechoic lines superficial and deep to the adductor brevis muscle in the present US images (Fig. 6), whereas the presence of the obturator nerve could not be confirmed. Thus, when performing a US-guided ONB it is recommended that the physician employs an interfascial injection to block each branch of the obturator nerve [43]. However, these interfascial planes sometimes can be confused (Fig. 6), especially in patients who are morbidly obese or who have structural abnormalities related to trauma or surgery, which could lead to an incomplete block. In addition, the existence of the AMi or SM can also result in physicians performing misguided injections because they cannot decide about the exact presence or location of a facial plane for ONB (Fig. 7). In this condition, US-guided ONB with nerve stimulation is recommended for ensuring a successful procedure.

CONCLUSIONS

This is the first study to reveal the existence frequencies of the AMi and SM in the Korean population, and also to address clinical considerations with respect to the layering of these muscles. The authors expect that these results will help physicians to decide about the ideal injection point in US-guided ONB. However, this study had the limitations that it was not possible to accurately determine the procedure success rate or the optimal amount of local anaesthetic for US-guided ONB in the target area, because it had an observational design and involved fixed cadavers. Future studies should investigate fresh cadavers using dye injection based on this study, and perform clinical trials in living patients referring to those results.

Acknowledgements

Conflict of interest: None declared

REFERENCES

1. Abe K. [Variation of m.adductor brevis]. Kaibogaku Zasshi. 1964; 39: 232–234, indexed in Pubmed: 14199759.
2. Agur AMR, Lee MJ. Grant's Atlas of Anatomy. 10th ed. Lippincott Williams & Wilkins, Philadelphia 1999.
3. Akkaya T, Ozturk E, Comert A, et al. Ultrasound-guided obturator nerve block: a sonoanatomic study of a new methodologic approach. Anesth Analg. 2009; 108(3): 1037–1041, doi: 10.1213/ane.0b013e3181966f03, indexed in Pubmed: 19224822.
4. Anagnostopoulou S, Kostopanagiotou G, Paraskeuopoulos T, et al. Anatomic variations of the obturator nerve in the inguinal region: implications in conventional and ultrasound regional anesthesia techniques. Reg Anesth Pain Med. 2009; 34(1): 33–39, doi: 10.1097/AAP.0b013e3181933b51, indexed in Pubmed: 19258986.
5. Anderson-Jones SR. Lower Extremity. In: Trescot AM (ed.). Peripheral Nerve Entrapments: Clinical Diagnosis and Management. Springer, Switzerland 2016: 615–881.
6. Anson BJ. An Atlas of Human Anatomy. 2nd ed. WB Saunders, Philadelphia 1963.
7. Benn ML, Pizzari T, Rath L, et al. Adductor magnus: An EMG investigation into proximal and distal portions and direction specific action. Clin Anat. 2018; 31(4): 535–543, doi: 10.1002/ca.23068, indexed in Pubmed: 29520841.
8. Berry MM, Standring SM, Bannister LH. Nervous System. In: Williams PL (ed.). Gray's Anatomy. 38th ed. Churchill Livingstone, New York 1995: 901–1397.
9. Bouchet A, Cuilleret J. Anatomie: Topographique Descriptive et Functionnelle. 2nd ed. Simep, Paris 1990.
10. Brizon J, Castaing J. Les Feuillets D'anatomie: Muscles Du Membre Inférieur. 2nd ed. Maloine, Paris 1997.
11. Busis NA. Femoral and obturator neuropathies. Neurol Clin. 1999; 17(3): 633–653, doi: 10.1016/s0733-8619(05)70156-0.
12. Fujiwara Y, Sato Y, Kitayama M, et al. Obturator nerve block using ultrasound guidance. Anesth Analg. 2007; 105(3): 888–889, doi: 10.1213/01.ane.0000268517.37921.ef, indexed in Pubmed: 17717272.
13. Goel S, Arora J, Mehta V, et al. Adductor accessorius: an unusual supernumerary adductor muscle of thigh. Clin Ter. 2015; 166(3): 114–117, doi: 10.7417/CT.2015.1840, indexed in Pubmed: 26152618.
14. Grigoriță L, Gug C, Vaida MA, et al. An unusual case of unilateral supernumerary extensor carpi radialis muscle. Folia Morphol. 2019; 78(4): 888–892, doi: 10.5603/FM.a2019.0037, indexed in Pubmed: 30949998.
15. Gusmão L, Lima JB, Santos ML, et al. Músculo Aductor Mínimo en Individuos Brasileños. Int J Morphol. 2014; 32(2): 440–443, doi: 10.4067/s0717-95022014000200010.
16. Hadzic A. Textbook of Regional Anesthesia and Acute Pain Management. 2nd ed. McGraw-Hill Education, New York 2017.
17. Huang J, Li J, Wang H. The principles and procedures of ultrasound-guided anesthesia techniques. Cureus. 2018; 10(7): e2980, doi: 10.7759/cureus.2980, indexed in Pubmed: 30237941.
18. Jeno SH, Schindler GS. Anatomy, bony pelvis and lower limb, thigh adductor magnus muscles. StatPearls Publishing, Treasure Island 2018.
19. Jordan DR, Stoica B. The gracillimus orbitis muscle. Ophthalmic Plast Reconstr Surg. 2017; 33(5): e120–e122, doi: 10.1097/IOP.0000000000000842, indexed in Pubmed: 27930425.
20. Kamenetsky E, Nader A, Kendall MC. Use of peripheral nerve blocks with sedation for total knee arthroplasty in a patient with contraindication for general anesthesia. Case Rep Anesthesiol. 2015; 2015: 950872, doi: 10.1155/2015/950872, indexed in Pubmed: 26587290.
21. Kumari S, Chauhan P, Kathole M, et al. Pronator teres accessorius: a new variant in flexor antebrachial musculature. Morphologie. 2018; 102(336): 21–24, doi: 10.1016/j.morpho.2017.07.174, indexed in Pubmed: 28927574.
22. Kumka M. Critical sites of entrapment of the posterior division of the obturator nerve: anatomical considerations. J Can Chiropr Assoc. 2010; 54(1): 33–42, indexed in Pubmed: 20195424.
23. Kwon T, Kim H, Moon J, et al. Ultrasound guided both obturator nerve block for patient with adductor thigh muscle spasm: a case report-. Korean J Pain. 2009; 22(1): 78, doi: 10.3344/kjp.2009.22.1.78.
24. Larsen WJ. Anatomy: development, function, clinical correlations. WB Saunders, Philadelphia 2002.
25. Lee SH, Jeong CW, Lee HJ, et al. Ultrasound guided obturator nerve block: a single interfascial injection technique. J Anesth. 2011; 25(6): 923–926, doi: 10.1007/s00540-011-1228-y, indexed in Pubmed: 21918855.
26. McMinn RMH, Hutchings RT, Pegington J, Abrahams PA. Colour Atlas of Human Anatomy. 3rd ed. Wolfe Publishing, London 1993.
27. Moore KL, Dalley AF, Agur AMR. Clinically Oriented Anatomy. 7th ed. Lippincott Williams & Wilkins, Philadelphia 2014.
28. Mori M. Statistics on the musculature of the Japanese. Okajimas Folia Anat Jpn. 1964; 40: 195–300, doi: 10.2535/ofaj1936.40.3_195, indexed in Pubmed: 14213705.
29. Nakamura E, Masumi S, Miura M, et al. A supernumerary muscle between the adductors brevis and minimus in humans. Okajimas Folia Anat Jpn. 1992; 69(2-3): 89–98, doi: 10.2535/ofaj1936.69.2-3_89, indexed in Pubmed: 1436954.
30. Ochiltree AB. Some muscular anomalies in the lower limb. J Anat Physiol. 1912; 47(Pt 1): 31–34, indexed in Pubmed: 17232941.
31. Paraskevas GK, Raikos A, Ioannidis O. Supernumerary semitendinosus muscle: A rare case presentation and its

clinical significance. Clin Anat. 2010; 23(8): 909–910, doi: 10.1002/ca.21029, indexed in Pubmed: 20830796.

32. Peiris WL, Cicuttini FM, Constantinou M, et al. Association between hip muscle cross-sectional area and hip pain and function in individuals with mild-to-moderate hip osteoarthritis: a cross-sectional study. BMC Musculoskelet Disord. 2020; 21(1): 316, doi: 10.1186/s12891-020-03348-5, indexed in Pubmed: 32438921.

33. Peragallo JH, Hudgins PA. Strabismus from supernumerary extraocular muscle restriction. Neurology. 2016; 87(18): 1958–1959, doi: 10.1212/WNL.0000000000003292, indexed in Pubmed: 27799476.

34. Pladzyk K, Jureczko L, Lazowski T. Over 500 obturator nerve blocks in the lithotomy position during transurethral resection of bladder tumor. Cent European J Urol. 2012; 65(2): 67–70, doi: 10.5173/ceju.2012.02.art2, indexed in Pubmed: 24578931.

35. Rha DW, Lee SH, Lee HJ, et al. Ultrasound-guided injection of the adductorlongus and pectineus in a cadaver model. Pain Physician. 2015; 18(6): E1111–E1117, doi: 10.36076/ppj.2015/18/e1111.

36. Rohen JW, Yokochi C, Lütjen-Drecoll E. Color Atlas of Anatomy: A Photographic Study of the Human Body. 6th ed. Lippincott Williams & Wilkins, Philadelphia 2006.

37. Romanes GJ. Cunningham's Textbook of Anatomy. 12th ed. Oxford University Press, Oxford 1981.

38. Sadler TW. Langman's Medical Embryology. 14th ed. Lippincott Williams & Wilkins, Philadelphia 2019.

39. Salmons S. Muscle. In: Williams PL (ed.). Gray's Anatomy. Churchill Livingstone, New York 1995: 737–900.

40. Saluja S, Das SS, Kumar D, et al. Bilateral three-headed biceps brachii muscle and its clinical implications. Int J Appl Basic Med Res. 2017; 7(4): 266–268, doi: 10.4103/ijabmr.IJABMR_339_16, indexed in Pubmed: 29308368.

41. Schüenke M, Schulte E, Schumacher U, Ross LM, Lamperti ED, Voll M. Atlas of Anatomy: General Anatomy and Musculoskeletal System. Thieme, Stuttgart 2006.

42. Sim IW, Webb T. Anatomy and anaesthesia of the lumbar somatic plexus. Anaesth Intensive Care. 2004; 32(2): 178–187, doi: 10.1177/0310057X0403200204, indexed in Pubmed: 15957714.

43. Sinha SK, Abrams JH, Houle TT, et al. Ultrasound-guided obturator nerve block: an interfascial injection approach without nerve stimulation. Reg Anesth Pain Med. 2009;

34(3): 261–264, doi: 10.1097/AAP.0b013e3181a32c4d, indexed in Pubmed: 19587627.

44. Šink Ž, Umek N, Cvetko E. Cross-over type of supernumerary digastric muscle. Folia Morphol. 2019; 78(3): 647–650, doi: 10.5603/FM.a2018.0112, indexed in Pubmed: 30536357.

45. Smith J, Pourcho AM, Kakar S. Sonographic appearance of the extensor carpi radialis intermedius tendon. PM R. 2015; 7(7): 789–791, doi: 10.1016/j.pmrj.2015.04.005, indexed in Pubmed: 25857593.

46. Song H, Kim J, Yoon SP. Coexistence of a pectoralis quartus muscle, a supernumerary head of biceps brachii muscle and an accessory head of flexor digitorum profundus muscle. Folia Morphol. 2019; 78(1): 204–207, doi: 10.5603/FM.a2018.0048, indexed in Pubmed: 29802720.

47. Soong J, Schafhalter-Zoppoth I, Gray AT. Sonographic imaging of the obturator nerve for regional block. Reg Anesth Pain Med. 2007; 32(2): 146–151, doi: 10.1016/j.rapm.2006.10.012, indexed in Pubmed: 17350526.

48. Suk JIm, Walker FO, Cartwright MS. Ultrasonography of peripheral nerves. Curr Neurol Neurosci Rep. 2013; 13(2): 328, doi: 10.1007/s11910-012-0328-x, indexed in Pubmed: 23314937.

49. Tipton JS. Obturator neuropathy. Curr Rev Musculoskelet Med. 2008; 1(3-4): 234–237, doi: 10.1007/s12178-008-9030-7, indexed in Pubmed: 19468309.

50. Tubbs RS, Griessenauer CJ, Marshall T, et al. The adductor minimus muscle revisited. Surg Radiol Anat. 2011; 33(5): 429–432, doi: 10.1007/s00276-010-0741-2, indexed in Pubmed: 21052670.

51. Yatsunami M, Tai T, Irie Y, et al. A morphological study on the human obturator externus muscle with reference to anomalous muscle and anomalous fasciculus originating from the obturator externus muscle. Okajimas Folia Anat Jpn. 2004; 80(5-6): 103–114, doi: 10.2535/ofaj.80.103, indexed in Pubmed: 15134328.

52. Yoshida T, Nakamoto T, Kamibayashi T. Ultrasound-Guided obturator nerve block: a focused review on anatomy and updated techniques. Biomed Res Int. 2017; 2017: 7023750, doi: 10.1155/2017/7023750, indexed in Pubmed: 28280738.

53. Yoshida T, Onishi T, Furutani K, et al. A new ultrasound-guided pubic approach for proximal obturator nerve block: clinical study and cadaver evaluation. Anaesthesia. 2016; 71(3): 291–297, doi: 10.1111/anae.13336, indexed in Pubmed: 26620274.

VIA MEDICA

ORIGINAL ARTICLE

Remodelling compartment in root cementum

J.F. Brochado Martins[1], C.F.D. Rodrigues[2], P. Diogo[3], S. Paulo[3], P.J. Palma[3],
F.F. do Vale[4]

[1]Hard Tissues Laboratory, Faculty of Medicine, University of Coimbra, Portugal
[2]Internal Medicine Department II, Hospital Infante D. Pedro, Centro Hospitalar do Baixo Vouga, Aveiro, Portugal
[3]Institute of Endodontics, Faculty of Medicine, University of Coimbra, Portugal
[4]Institute of Orthodontics, Faculty of Medicine, University of Coimbra, Portugal

Background: Bone remodelling represents the most remarkable bone response to mechanical stress and mineral homeostasis. It is the consequence of complex highly orchestrated and tightly regulated cellular processes taking place in a specialised entity — the bone remodelling compartment (BRC).
Materials and methods: Cementum is an understudied tissue that requires more research to understand its biology, pathology, and potential for regeneration. Although analogue to bone in structure and composition distinct structural and functional differences were ascribed to each of these mineralised tissues. The precise role of cementocytes in cementum turnover is unclear but they may work the same way as osteocytes in bone remodelling, regulating the full process.
Results: Although cementum is not liable to regular physiological remodelling as bone is, pathological cases triggered by orthodontic forces or large periapical periodontitis, those lesions can acutely induce cementum remodelling. Nevertheless, the cellular mechanisms behind this particular remodelling process are yet to be identified, as its eventual involvement of specialised anatomic structures as the BRC.
Conclusions: Hypothesizing that similar cellular mechanisms underlie bone and cementum remodelling, the present work shows, for the first time, the histological evidence of a specialized remodelling compartment in dental hard tissues. (Folia Morphol 2021; 80, 4: 972–979)

Key words: bone remodelling compartment, bone, cementum, cementocytes, root resorption

INTRODUCTION

The importance of a specified structure overlying the bone-remodelling unit named bone-remodelling compartment (BRC) has been underlined by several authors [1, 7, 11, 15, 25]. This structure unit is formed by a canopy of bone lining cells, under which the remodelling process takes place isolated from the remaining intact tissues [4, 7, 11, 15, 25]. The specific and non-random localisation of blood capillaries and sinusoids close to the BRC ensures a fast access and targeted delivery of systemic regulators to the remodelling compartment, enabling guidance of osteoclasts and osteoblasts progenitors to critical points on the bone surface [1, 7, 18]. By secreting critical factors and expressing specific receptors, canopy cells along with osteocytes are the main orchestrators of

the overall remodelling process, being the canopy an important reservoir of osteoblast progenitors during remodelling [14].

Bone resorption and formation is synchronized by direct cell contact between osteoblasts and osteoclasts and a variety of secreted factors [28]. It has also been established that the tight equilibrium between these two cellular populations is fundamentally maintained by a triad of elements composed by osteoprotegerin (OPG), the receptor activator of NF-κβ (RANK) and the RANK ligand (RANKL) [3, 18, 20, 31]. However, osteocytes prevailed as the main orchestrators of the overall remodelling process, as they are the only cells with the lacuno-canalicular network, endowed with the capability to detect load changes, and consequently activate cellular signalling cascades aimed at either bone reabsorption or remodelling [25, 32]. In fact, several studies had demonstrated that osteocytes are the major source of RANKL in the bone tissue, and not the osteoblasts [2, 22, 29].

Osteocytes act as mechanosensing cells and initiate the remodelling process predominantly when microfractures and loading are involved [5, 26, 35]. In these situations, osteocytes' physiology is profoundly altered and apoptosis is triggered [13, 35, 37]. As a consequence, osteoclastogenesis and bone reabsorption prevail, thus driving deep changes in bone tissue architecture [8, 17]. It is reasonable to conclude that the osteocyte acts as the leading mechanosensor in bone, which has also been recently confirmed by targeted ablation of osteocytes in a mouse model [32].

Cementum prevails as the least-known mineralised tissue and is often referred to as a bone-like tissue. It is, however, avascular and non-innervated, it lacks marrow and the typical lamellar organization of the bone, and it does not undergo dynamic remodelling or increased thickness throughout life [38]. On contrary, both cementocytes and osteocytes are sensitive to mechanical features, mainly pressure and trauma [9, 23]. Finally, cementocytes express RANKL and sclerostin, thus underlying their particular importance on triggering cementum resorption, remodelling and repair, which eventually occurs in a similar way as bone remodelling [10, 19, 34]. Although cementum is not exposed to regular physiologic remodelling, recent evidence showed that cementum resorption might be triggered under specific circumstances as, for example, orthodontic forces or large apical periodontitis lesions.

The purpose of this work was to evaluate the effect of a distraction protocol on bone remodelling and root surface of the anchoring teeth.

The results hereby presented describe the identification of a specialised remodelling structure, which we refer to as the cementum remodelling compartment (CRC). It is associated with cementum at the dental root surfaces, and this work provides a description on its light microscopic morphology and cellular phenotype in comparison to the BRC.

MATERIALS AND METHODS

Animals

Four skeletal mature conditioned male Beagle dogs, 1 year old and weighing 15 to 18 kg, were selected for the study. Animals were kept in adequate standard structures, precisely identified and with the appropriate conditions of light and temperature. The water, administered *ad libitum* to the animals, was originated from the municipal supply network. Food was provided once daily, as commercial dry feed (Canine Adult Lamg & Rice, Chicken Advanced Fitness, Hills™) with concentrations of contaminants analysed and monitored by the manufacturer. After surgical intervention and during latency and mandibular stretching phases, the dry feed was softened in warm water (ratio 1:3). From the consolidation period until euthanasia, the softened food was mixed with water in a ratio 1:1. All animal procedures were conducted according to the European Union Directive 2010/63/EU for animal experiments and reviewed and approved by DGAV (no 0420/000/000/2012) and the animal facility ethics committee.

Anaesthesia protocol

Dogs were anesthetised by intravenous administration of 0.2 mg/kg diazepam (Diazepam Labesfal, Portugal) and 2 mg/kg propofol (Propofol Lipuro 2%, Braun Medical, Portugal), and maintained alive with inhalation of oxygen and 1–2% isoflurane (Isoflo, Esteve Farma, Portugal).

Experimental group

Three animals underwent mandibular distraction following bilateral midbody osteotomy (between the third and fourth premolar), to preserve the integrity of the mandibular nerve and lingual periosteum. After ensuring bone mobility, tooth distractor was placed in each hemimandible, using the third and the fourth premolars as anchorage teeth for the distraction ap-

paratus. The 6 hemimandibles were subjected to a repeated daily activation of 1 mm, with moderate to severe pressure applied to the anchorage teeth for 10 days (10 mm in total), followed by a consolidation period of 12 weeks.

Control group

Two hemimandibles underwent no treatment. The animal was kept under the same conditions as its experimental counterparts, for the same period of time.

Euthanasia protocol

Animals were euthanized by anaesthetic overdose (pentobarbital 100 mg/kg intravenously, Pentotal, Abbot, Portugal), followed by bilateral perfusion with 10% phosphate buffered formalin (PRS Panreac, Spain).

Histological analysis

Histological processing was carried out at the Hard Tissues Laboratory of the Faculty of Medicine of the University of Coimbra. Half of the samples were prepared for histological evaluation in non-decalcified material and the other half for decalcified material. Mandibular blocks were dissected. Half of the samples from the anchorage teeth were processed and embedded in methylmethacrylate, sectioned and ground to a thickness of 20 µm on Exact Cutting-Grinding System (Exakt® Apparatebau, GmbH & CO, Norderstedt, Hamburg, Germany). Mandibular blocks were dissected, post-fixed with 10% phosphate buffered formalin and subsequently decalcified with Morse's solution for 8 weeks. The specimens were then trimmed and embedded in paraffin wax, and 30 serially sections with 6 µm each were subsequently prepared. Toluidine blue, haematoxylin-eosin and Masson trichromic were used to stain the specimens for bone tissue, periodontal tissue and the radicular structure. Histological assessment was performed under a light microscope (Nikon® SMZ 1500, Tokyo, Japan), attached to digital cameras (Optronics® DEI 750D CE, Goleta, California, USA and Nikon® Digital Camera DXM-1200 C, Tokyo, Japan) connected to a computer (Intel® Pentium™ III and Intel®Core™ 2 Duo Core™) with an image software analysis programme (Nikon® ACT-1C, Tokyo, Japan) for the evaluation of the bone tissue and root surfaces. One observer blinded to all group's allocation examined all specimens. The images were prepared and edited with Adobe Illustrator CC 2017, Adobe Systems.
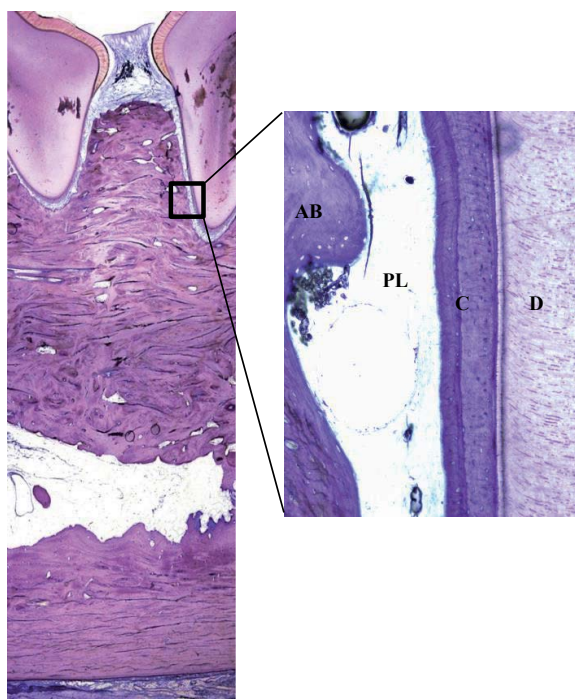

Figure 1. Histologic section of a hemimandible attained from the control group dog depicting normal bone tissue architecture (toluidine blue, ×7.5 in the original). Higher magnification of the periodontal apparatus (×100) showing the alveolar bone (AB), the space of the periodontal ligament (PL), cementum (C) and dentin (D).

RESULTS

Following the experimental protocol, dogs were euthanized and the mandibles collected and processed for histological analysis. Not surprisingly, hemimandibles from the control group displayed normal radicular architecture and bone histology (Fig. 1).

In the experimental group, however, although the distraction protocol did not induce alterations in either the routine or the alimentary habits of the animals, bone remodelling was observed inside the BRC in both groups (Figs. 2, 3). The first evidence of bone reabsorption was indicated by the detachment of the bone lining cells from the bone surface, and the invasion of clastic cells to attach to the denuded bone matrix surface (Fig. 2.1). Reversal cells were subsequently recruited to the BRC and repopulated the bone surface, and osteoblasts were embedded by mineralized bone matrix (Fig. 2.2, black arrow). Figure 2.3 displays what is believed to be a pericyte (red arrow) lying just above the canopy. During bone formation phase, osteoblasts (OsB) populated the bone surface, layering osteoid, while flattened cells with thin and flat nucleus bordering the marrow side and forming the canopy of the BRC (Fig. 3).
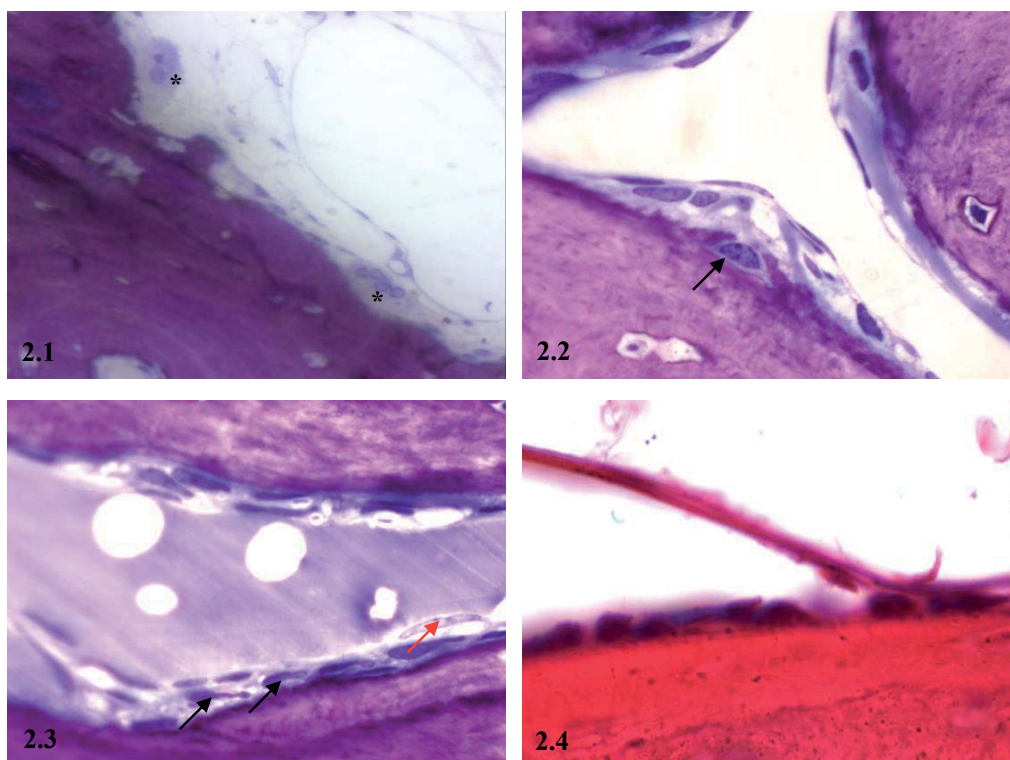
Figure 2. The bone remodelling compartment; **2.1.** Microphotography of a bone remodelling compartment, in resorption phase, observed in the compact bone tissue. Howship lacuna and several osteoclasts (*) are observed on the bone surface, in close proximity to a blood vessel (toluidine blue, ×400 in the original); **2.2.** Reversal phase. It is also observed of a blood vessel in close proximity to bone remodelling compartment (BRC) as well as an osteoblast being embedded by the extracellular matrix (black arrow) (toluidine blue, ×400 in the original); **2.3.** Reversal phase of bone remodelling compartment, in compact bone tissue containing in its interior a great density of elongated cells, the reversal cells (black arrows). Note the presence a pericyte (red arrow) (toluidine blue, ×400 in the original); **2.4.** Morphological appearance of the initial formation of the BRC canopy in a trabecula of alveolar woven bone (haematoxylin-eosin, ×1000 in the original).

Remodelling was also observed in discreet zones along the dental root (Fig. 4). Surprisingly, however, it also implicated the formation of a special remodelling compartment, delineated by a canopy of flat cells in close proximity to the blood vessels (Fig. 4.1). In fact, a Howship lacuna reaching dentine was observed, along with a layer of flattened cells (Fig. 4.1, black arrow) that formed the equivalent to the canopy. Even though no clastic cells were identified, the ones close to the cementum and dentin surfaces displayed characteristics of reversal cells, and they also repopulated the resorption area during the formation phase. Because it was difficult to distinguish the canopy from the endothelial cells, a complete remodelling compartment could not be perfectly delineated. However, a singular cell-rich space between the mineralised tissues and a blood vessel was evident, resembling the remodelling progression in the characteristic cutting cones of the compact bone tissue (Fig. 4.2). Moreover, by morphologic comparison to the bone tissue, the cell population adjacent to the dentin and cementum surface most probably represented the beginning of the reversal phase (Fig. 4.2). Finally, the tissue apposition phase was also recognised in the cement remodelling process by the identification of a remodelling compartment next to a newly formed cementum area, covered by cementoid tissue and cementoblasts (Figs. 4.3, 4.4). Figure 4.3 illustrates in detail canopy cells and a layer of cuboid cementoblasts, morphologically similar to osteoblasts, adjacently placed to a region of non-mineralised cement. It also identifies a band of mineralized matrix of cementum repairing an area of resorbed dentin matrix, as well as a region of dentin portraying its typical tubular structure.

DISCUSSION

The present work provides evidence of organized cementum remodelling taking place inside specific structures along the dental root of distracted tooth, similarly to bone remodelling inside BRCs. These structures, named CRCs, are formed to enclose local factors and potentiate the remodelling process. They are also
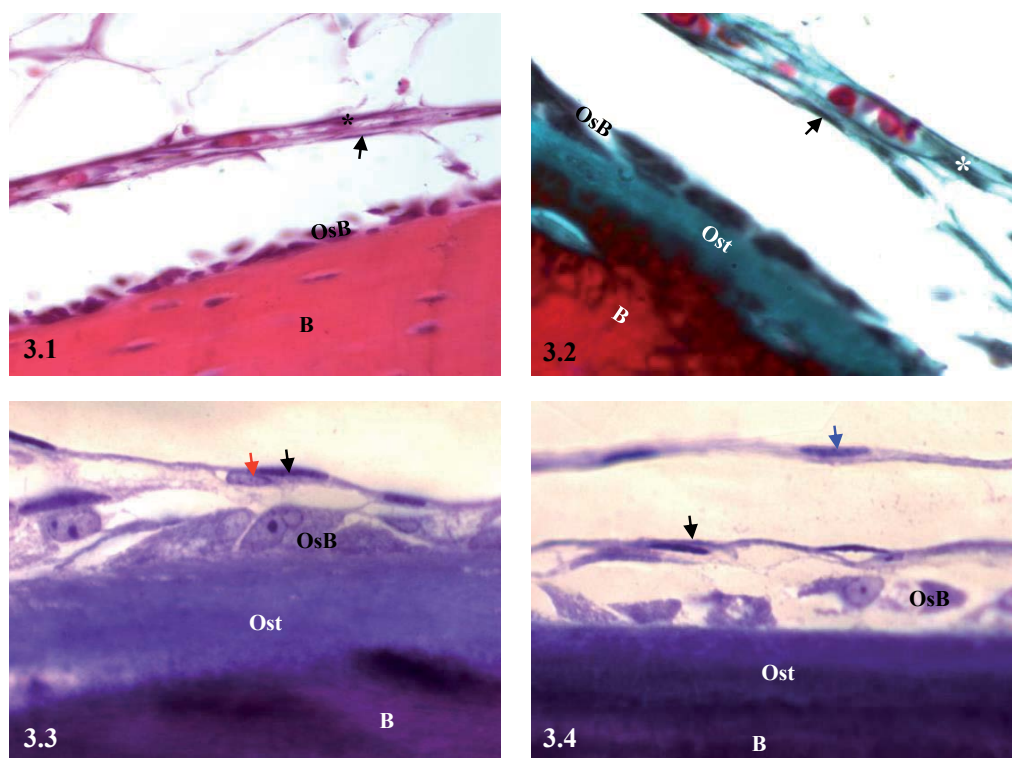
975

Figure 3. Osteo-angiogenic platform; **3.1.** Histologic section of the capillary network located next to the canopy of a bone remodelling compartment (BRC), running along in a parallel direction in almost all its extension. Close proximity between endothelial cells (*) and lining cells (black arrow); B — bone; OsB — osteoblasts (haematoxylin-eosin, ×200 in the original); **3.2.** Histological section of a capillary following a parallel path to the canopy of a BRC, in formative phase. Close proximity between endothelial cells (*) and lining cells (black arrow); B — bone; OsB — osteoblasts; Ost — osteoid; black arrow — canopy (Masson's trichromic, ×400 in the original); **3.3.** Microphotograph of a blood capillary following in close proximity the remodelling compartment. Cell intimately adjacent to the endothelial wall (black arrow) is seen as a pericyte (red arrow) (toluidine blue, ×1000 in the original); **3.4.** Histological aspect of the constitution of a BRC in bone formation phase, located on the surface of a trabecula. Osteoblasts (OsB), coating cells that form the canopy (black arrow), the proximity of a blood vessel (blue arrow) that runs parallel path to the canopy; B — bone; OsB — osteoblasts; Ost — osteoid (toluidine blue, ×1000 in the original).

delineated by a flattened canopy of cells, and always localise in close proximity to blood vessels, thus allowing the trade of cells and/or systemic factors from the bloodstream.

Cementum is a highly responsive mineralized tissue, and its biological activity is of extreme importance to maintain the integrity of the root, namely its adequate position. It shares morphological, functional and biochemical similarities with the bone tissue; however, cementum is avascular and consequently depicts higher levels of hypoxia [34, 39]. There are two main types of cementum fibres, acellular extrinsic fibres (AEFCs) and cellular intrinsic cementum fibres (CIFCs). According to Schroeder [30], AEFCs are mostly involved in tooth support, and thus are the ones recruited following tooth distraction; while CIFCs, on the other hand, appear to be more associated with tooth adaptation, i.e. the reshaping of the root surface during tooth' movement. CIFCs are also recruited as reparative cementum to fulfil the resorbed

root surfaces [30]. The results attained in the present work come to support others in the literature postulating that given the similarities between the bone and cementum, it is reasonable to hypothesise that cementocytes may play a central regulatory role in the homeostasis and remodelling of cementum, not only following extrinsic stimulation, but also during the normal orthodontic movement and endodontic infections [12, 27, 30, 38, 39].

Cementum remodelling, as the bone, also depends upon a mechanic stimulus to be transmitted to the mineralised tissue matrix, and the consequent triggering of the reabsorption-formation cascade. In agreement, the application of a severe pressure to the anchored teeth of the animals in this study, triggered a radicular cementum remodelling, along with alveolar bone remodelling and redistribution of the principal fibres, thus driving dental repositioning. In fact, even though cementum is more resistance to resorption than bone, when orthodontic forces are
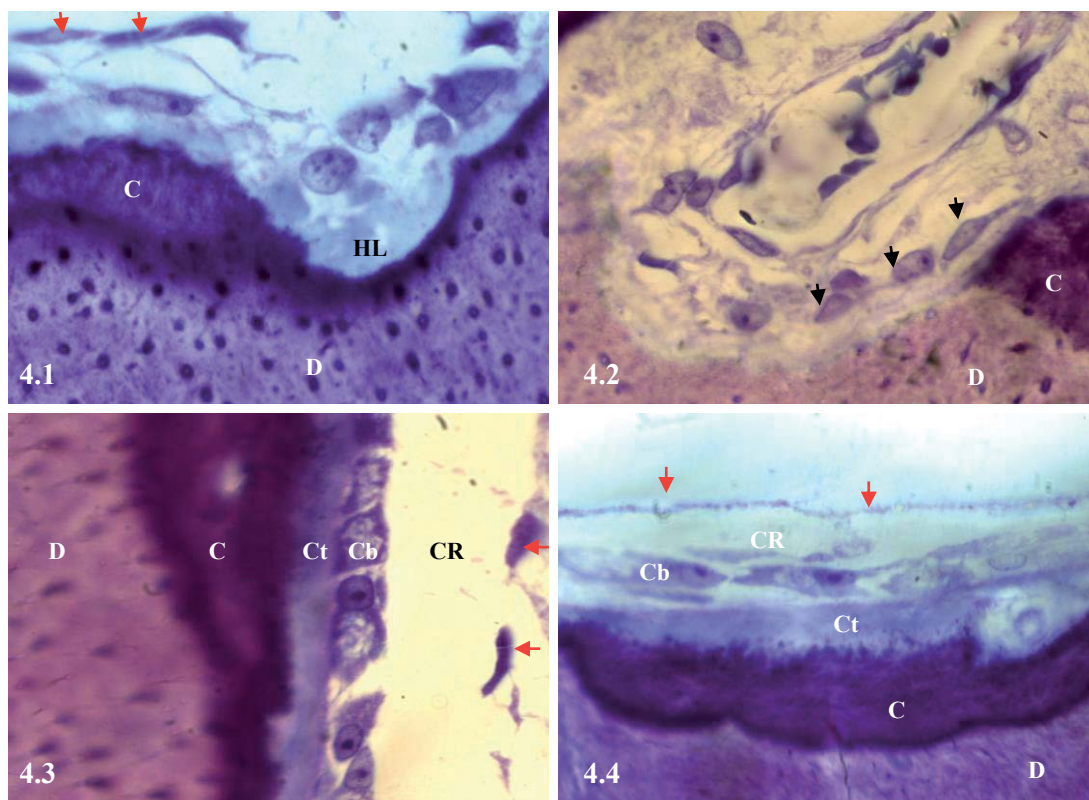
Figure 4. Dental hard tissue remodelling compartment; **4.1.** Resorption phase observed in the cement reaching the dentin, showing Howship lacunae (HL) even without the presence of odontoclasts. It is possible to observe some canopy cells (red arrows); D — dentin; C — cement (toluidine blue, ×400 in the original); **4.2.** Dentine resorption area aspect (D) with the reversal cells (black arrows) close to resorption areas. It is obvious the resemblance to a cutting cone observed in compact bone tissue including the presence of a central blood vessel (toluidine blue, ×1000 in the original); **4.3.** Appearance of a remodelling compartment in the formation phase located in the cementum adjacent to the dentin showing a cementum area (C) covered by cementoid (Ct) and cementoblasts (Cb), remodelling compartment (CR) and the canopy (red arrows) (toluidine blue, ×400 in the original); **4.4.** Analogous image to the previous, showing a dentine area (D), mineralised cementum (C), cementoid (Ct), a cementoblasts layer (Cb), a space corresponding to the remodelling compartment (CR) and the canopy (red arrows) (toluidine blue, ×1000 in the original).

applied, they not only disrupt cementum's structure, but proceed invading the root dentin [12]. Studies in orthodontic patients to whom extrinsic forces were applied, showed that the application of an external pressure to the dental root activated cementoblasts, and consequently drove the removal of the cementum from the root surface, followed by a cementoblast-mediated restoration [16, 21, 33, 38].

Root repair is constant during orthodontic tooth movement, and permanent total root loss only occurs if the tooth structure is not fully repaired [6]. Using a mice endodontic infection model, Rossi et al. [27] proved that in healthier mature teeth, cementocytes and osteocytes did not express RANKL. In response to infection, however, RANKL was strongly expressed by cementocytes and its expression increased along the lesion and time progression, an effect that was not observed in osteocytes [27]. The detection of a CRC

emphasizes the fact that hard tissues remodelling is a demanding and controlled process that might not occur with external interferences; thus, a remodelling compartment is created to allow local regulation of the process. Simultaneously, the canopy may act as a diffusion barrier for cytokines, growth factors and chemoattractants, thus allowing systemic factors to act over the cells inside the remodelling compartment [20, 24]. Moreover, its presence seems to have a crucial impact on the overall remodelling cycle success, as highlighted by several studies on diverse pathologic situations where the absence of BRC canopies beyond eroded surfaces was correlated with a greater amount of arrested reversal surfaces and a reduced amount of bone formation, thus reflecting both disrupted and arrested remodelling cycles [36]. Besides, the absence of BRC canopies above formative surfaces leads to a shift in the osteoblastic phenotype, which

causes an arrest or even the non-progression of the formative phase. Altogether, these facts suggest that BRC canopies had a critical role for longevity, function and the control and coordination of the underlying cells activity [36], and the same may be envisioned for the CRC. In agreement, remodelling areas with fragmented canopies were also observed in the animals under study, and were also associated to the interruption or arrest of the formative or inversion phases, driving cementolytic lesions that the authors hypothesise that may also occur in humans.

Limitations of this study

Limitations of this study include the fact that it is merely an observational study meant to report the existence and identification of the CRC. To determine the cellular ultrastructure as well as the nature and function of each type of cells involved, immunohistochemistry and electron microscopy would be needed. Additionally, more studies are needed to clarify the interactions of the multiple signal transduction pathways. It is also likely that the future holds the discovery of novel molecules that will lead to further insights into the mechanisms responsible for cementum formation and resorption.

CONCLUSIONS

This is the first study to identify and histologically describe a histologic remodelling structure in dental mineralised tissues, which the authors named CRC. The existence of such a remodelling compartment in cementum, and the fact that it shares so many defining characteristics with the BRC, may hide the existence of a common underlying cellular mechanism that regulates remodelling of the hard tissues. Understanding physiology underlying the dynamics of cementum modelling and remodelling will be essential for the comprehension of its kinetics in orthodontics and trauma.

Acknowledgements

Conflict of interest: None declared

REFERENCES

1. Andersen TL, Sondergaard TE, Skorzynska KE, et al. A physical mechanism for coupling bone resorption and formation in adult human bone. Am J Pathol. 2009; 174(1): 239–247, doi: 10.2353/ajpath.2009.080627, indexed in Pubmed: 19095960.

2. Bellido T. Osteocyte-driven bone remodeling. Calcif Tissue Int. 2014; 94(1): 25–34, doi: 10.1007/s00223-013-9774-y, indexed in Pubmed: 24002178.

3. Boyce BF, Xing L. Functions of RANKL/RANK/OPG in bone modeling and remodeling. Arch Biochem Biophys. 2008; 473(2): 139–146, doi: 10.1016/j.abb.2008.03.018, indexed in Pubmed: 18395508.

4. Feng Xu, Teitelbaum SL. Osteoclasts: New Insights. Bone Res. 2013; 1(1): 11–26, doi: 10.4248/BR201301003, indexed in Pubmed: 26273491.

5. Goulet GC, Cooper DML, Coombe D, et al. Influence of cortical canal architecture on lacunocanalicular pore pressure and fluid flow. Comput Methods Biomech Biomed Engin. 2008; 11(4): 379–387, doi: 10.1080/10255840701814105, indexed in Pubmed: 18568832.

6. Hartsfield JK. Pathways in external apical root resorption associated with orthodontia. Orthod Craniofac Res. 2009; 12(3): 236–242, doi: 10.1111/j.1601-6343.2009.01458.x, indexed in Pubmed: 19627526.

7. Hauge EM, Qvesel D, Eriksen EF, et al. Cancellous bone remodeling occurs in specialized compartments lined by cells expressing osteoblastic markers. J Bone Miner Res. 2001; 16(9): 1575–1582, doi: 10.1359/jbmr.2001.16.9.1575, indexed in Pubmed: 11547826.

8. Henriksen K, Neutzsky-Wulff AV, Bonewald LF, et al. Local communication on and within bone controls bone remodeling. Bone. 2009; 44(6): 1026–1033, doi: 10.1016/j.bone.2009.03.671, indexed in Pubmed: 19345750.

9. Huang L, Meng Y, Ren A, et al. Response of cementoblast-like cells to mechanical tensile or compressive stress at physiological levels in vitro. Mol Biol Rep. 2009; 36(7): 1741–1748, doi: 10.1007/s11033-008-9376-3, indexed in Pubmed: 18850302.

10. Jäger A, Götz W, Lossdörfer S, et al. Localization of SOST/sclerostin in cementocytes in vivo and in mineralizing periodontal ligament cells in vitro. J Periodontal Res. 2010; 45(2): 246–254, doi: 10.1111/j.1600-0765.2009.01227.x, indexed in Pubmed: 19778325.

11. Jensen PR, Andersen TL, Søe K, et al. Premature loss of bone remodeling compartment canopies is associated with deficient bone formation: a study of healthy individuals and patients with Cushing's syndrome. J Bone Miner Res. 2012; 27(4): 770–780, doi: 10.1002/jbmr.1490, indexed in Pubmed: 22162180.

12. Krishnan V, Davidovitch Z. Cellular, molecular, and tissue-level reactions to orthodontic force. Am J Orthod Dentofacial Orthop. 2006; 129(4): 469.e1–469.32, doi: 10.1016/j.ajodo.2005.10.007, indexed in Pubmed: 16627171.

13. Krishnan V, Davidovitch Z. On a path to unfolding the biological mechanisms of orthodontic tooth movement. J Dent Res. 2009; 88(7): 597–608, doi: 10.1177/0022034509338914, indexed in Pubmed: 19641146.

14. Kristensen HB, Andersen TL, Marcussen N, et al. Osteoblast recruitment routes in human cancellous bone remodeling. Am J Pathol. 2014; 184(3): 778–789, doi: 10.1016/j.ajpath.2013.11.022, indexed in Pubmed: 24412092.

15. Kristensen HB, Andersen TL, Marcussen N, et al. Increased presence of capillaries next to remodeling sites in adult human cancellous bone. J Bone Miner Res. 2013; 28(3): 574–585, doi: 10.1002/jbmr.1760, indexed in Pubmed: 22991221.

16. Kumasako-Haga T, Konoo T, Yamaguchi K, et al. Effect of 8-hour intermittent orthodontic force on osteoclasts

and root resorption. Am J Orthod Dentofacial Orthop. 2009; 135(3): 278.e1–8; discussion 278, doi: 10.1016/j.ajodo.2008.11.007, indexed in Pubmed: 19268821.

17. Kurata K, Heino TJ, Higaki H, et al. Bone marrow cell differentiation induced by mechanically damaged osteocytes in 3D gel-embedded culture. J Bone Miner Res. 2006; 21(4): 616–625, doi: 10.1359/jbmr.060106, indexed in Pubmed: 16598382.

18. Lafage-Proust MH, Roche B, Langer M, et al. Assessment of bone vascularization and its role in bone remodeling. Bonekey Rep. 2015; 4: 662, doi: 10.1038/bonekey.2015.29, indexed in Pubmed: 25861447.

19. Lehnen SD, Götz W, Baxmann M, et al. Immunohistochemical evidence for sclerostin during cementogenesis in mice. Ann Anat. 2012; 194(5): 415–421, doi: 10.1016/j.aanat.2012.02.014, indexed in Pubmed: 22560000.

20. Martin T, Gooi JH, Sims NA. Molecular mechanisms in coupling of bone formation to resorption. Crit Rev Eukaryot Gene Expr. 2009; 19(1): 73–88, doi: 10.1615/critreveukargeneexpr.v19.i1.40, indexed in Pubmed: 19191758.

21. Mullally NN. Cementoblastic Response to High vs. Low Level of Mechanical Force in Vitro. [dissertation]. Marquette University. 2010. Paper 41.

22. Nakashima T, Hayashi M, Fukunaga T, et al. Evidence for osteocyte regulation of bone homeostasis through RANKL expression. Nat Med. 2011; 17(10): 1231–1234, doi: 10.1038/nm.2452, indexed in Pubmed: 21909105.

23. Nanci A, Ten Cate AR. Ten Cate´s - Oral Histology - Development, Structure, and Function. Sixth Ed. Mosby, St. Louis 2013.

24. Owen R, Reilly GC. models of bone remodelling and associated disorders. Front Bioeng Biotechnol. 2018; 6: 134, doi: 10.3389/fbioe.2018.00134, indexed in Pubmed: 30364287.

25. Parfitt AM. The bone remodeling compartment: a circulatory function for bone lining cells. J Bone Miner Res. 2001; 16(9): 1583–1585, doi: 10.1359/jbmr.2001.16.9.1583, indexed in Pubmed: 11547827.

26. Proff P, Römer P. The molecular mechanism behind bone remodelling: a review. Clin Oral Investig. 2009; 13(4): 355–362, doi: 10.1007/s00784-009-0268-2, indexed in Pubmed: 19319579.

27. Rossi AD, Fukada SY, De Rossi M, et al. Cementocytes express receptor activator of the Nuclear factor kappa-B ligand in Response to endodontic infection in mice. J Endod. 2016; 42(8): 1251–1257, doi: 10.1016/j.joen.2016.05.009, indexed in Pubmed: 27342005.

28. Sanchez-Fernandez MA, Gallois A, Riedl T, et al. Osteoclasts control osteoblast chemotaxis via PDGF-BB/PDGF receptor beta signaling. PLoS One. 2008; 3(10): e3537, doi: 10.1371/journal.pone.0003537, indexed in Pubmed: 18953417.

29. Sapir-Koren R, Livshits G. Osteocyte control of bone remodeling: is sclerostin a key molecular coordinator of the balanced bone resorption-formation cycles? Osteoporos Int. 2014; 25(12): 2685–2700, doi: 10.1007/s00198-014-2808-0, indexed in Pubmed: 25030653.

30. Schroeder H. Biological problems of regenerative cementogenesis: synthesis and attachment of collagenous matrices on growing and established root surfaces. Int Rev Cytol. 1992: 1–59, doi: 10.1016/s0074-7696(08)62074-4.

31. Sims NA, Gooi JH. Bone remodeling: multiple cellular interactions required for coupling of bone formation and resorption. Semin Cell Dev Biol. 2008; 19(5): 444–451, doi: 10.1016/j.semcdb.2008.07.016, indexed in Pubmed: 18718546.

32. Tatsumi S, Ishii K, Amizuka N, et al. Targeted ablation of osteocytes induces osteoporosis with defective mechanotransduction. Cell Metab. 2007; 5(6): 464–475, doi: 10.1016/j.cmet.2007.05.001, indexed in Pubmed: 17550781.

33. Tyrovola JB, Spyropoulos MN, Makou M, et al. Root resorption and the OPG/RANKL/RANK system: a mini review. J Oral Sci. 2008; 50(4): 367–376, doi: 10.2334/josnusd.50.367, indexed in Pubmed: 19106463.

34. van Bezooijen RL, Bronckers AL, Gortzak RA, et al. Sclerostin in mineralized matrices and van Buchem disease. J Dent Res. 2009; 88(6): 569–574, doi: 10.1177/0022034509338340, indexed in Pubmed: 19587164.

35. Verborgt O, Gibson GJ, Schaffler MB. Loss of osteocyte integrity in association with microdamage and bone remodeling after fatigue in vivo. J Bone Miner Res. 2000; 15(1): 60–67, doi: 10.1359/jbmr.2000.15.1.60, indexed in Pubmed: 10646115.

36. Wesseling-Perry K. The BRC canopy: an important player in bone remodeling. Am J Pathol. 2014; 184(4): 924–926, doi: 10.1016/j.ajpath.2014.01.004, indexed in Pubmed: 24561288.

37. Xing L, Boyce BF. Regulation of apoptosis in osteoclasts and osteoblastic cells. Biochem Biophys Res Commun. 2005; 328(3): 709–720, doi: 10.1016/j.bbrc.2004.11.072, indexed in Pubmed: 15694405.

38. Yamamoto T, Hasegawa T, Yamamoto T, et al. Histology of human cementum: Its structure, function, and development. Jpn Dent Sci Rev. 2016; 52(3): 63–74, doi: 10.1016/j.jdsr.2016.04.002, indexed in Pubmed: 28408958.

39. Zhao N, Foster BL, Bonewald LF. The cementocyte: an osteocyte relative? J Dent Res. 2016; 95(7): 734–741, doi: 10.1177/0022034516641898, indexed in Pubmed: 27029548.

ORIGINAL ARTICLE

Parietal foramen: incidence and topography

J. Naidoo, J.S. Luckrajh, L. Lazarus

Department of Clinical Anatomy, School of Laboratory Medicine and Medical Sciences, College of Health Sciences, University of KwaZulu-Natal, Westville Campus, Durban, South Africa

Background: The parietal foramen (PF) is a small inconsistent aperture located at the border of the middle 1/3 and posterior 1/3 of the parietal bone near the sagittal suture and is considered an emissary foramen. Cranial emissary foramina are of utmost importance due to the structures that traverse the foramen. Variations in these foramina are common. Knowledge of the PF is important when performing neurosurgical procedures as the emissary vessels are at risk.

Materials and methods: The present study used 100 dry adult calvaria to determine the frequency of PF, the diameter of the PF, as well as topography of the PF (using the sagittal suture as an anatomical landmark).

Results: A total of 32% of calvaria had PF present bilaterally; whilst 35% of calvaria had unilateral PF. The study also reports 5% calvaria in which PF were present on the sagittal suture. The mean diameter recorded was 1.55 mm (0.74–3.08 mm), and the mean distance between the lateral margin of the PF and the sagittal suture was 9.02 mm (4.44–18.20 mm).

Conclusions: Knowledge of the incidence and topography of the PF may aid neurosurgeons in creating and adjusting techniques and procedures in order to mitigate the risk of injury to emissary veins and other structures emerging from the PF. (Folia Morphol 2021; 80, 4: 980–984)

Key words: parietal foramen, emissary foramen, osteology, incidence, topography, diameter, sagittal suture

INTRODUCTION

The parietal foramen (PF) is a small inconsistent opening located near the sagittal suture in the posterior part of the parietal bone [13]. This area is described as the obelion due to the representation of the Greek symbol obelos (%) which depicts the PF on either side of the sagittal suture [7, 8].

When present, the PF transmits an emissary vein and is therefore considered one of the emissary foramina of the cranium [7]. Emissary veins drain the neurocranium as well as cephalic structures, and the parietal emissary veins connect the scalp veins with the superior sagittal sinus [8, 14]. Emissary foramina also share an important relationship with the diploic veins of the skull, which may act as a pathway for the spread of infections from the extracranial veins to the intracranial sinuses [16].

No satisfactory explanation regarding the function of the PF has been reported, besides the transmission of vessels; therefore, the function of the PF remains unclear and under investigation [1, 14]. Due to advancements in radiological techniques, information pertaining to skull foraminal size and symmetry has become increasingly important in the diagnosis of pathological conditions surrounding these foramina [2, 16].

Address for correspondence: Dr. L. Lazarus, Department of Clinical Anatomy, School of Laboratory Medicine and Medical Sciences, College of Health Sciences, University of KwaZulu-Natal, Westville Campus, Durban, South Africa, e-mail: ramsaroopl@ukzn.ac.za

Table 1. Incidence of the presence of the parietal foramen

Author (year) [REF.]	Country	Sample size (n)	Incidence (%)
Boyd (1930) [4]	Scotland	1500	60
Berry and Berry (1967) [3]	Egypt	250	44.2
	Nigeria	56	59.2
	Palestine (Lachish)	54	35.2
	Palestine (Modern)	18	22.2
	India	53	50
	Burma	51	50
	North America	50	62
	Peru	53	53
Keskil et al. (2003) [9]	Turkey	200	63
Wysocki et al. (2006) [18]	Poland	100	60
Yoshioko et al. (2006) [20]	USA	20	50
Mann et al. (2009) [11]	Japan	137	80.3
Debbarma et al. (2015) [6]	India	40	43.8
Gangmei et al. (2018) [7]	India	48	77.1
Weighted mean	–	–	**58.5**
Present study (2019)	**South Africa**	**100**	**68**

Knowledge of the PF is imperative to neurosurgical perspectives since the emissary veins may be ruptured during surgery [14, 16]. Bleeding from emissary veins may then result in the formation of a postoperative epidural haematoma [12].

The aim of the study was to investigate the anatomy of the PF with the objective of recording incidence, diameter, and topography of the PF in relation to the sagittal suture.

MATERIALS AND METHODS

A total of 100 adult calvaria were obtained from the Department of Clinical Anatomy, University of KwaZulu-Natal, South Africa. These calvaria were analysed to record the incidence and diameter of the PF. Furthermore, the distance of the PF from the sagittal suture was taken as a horizontal line from the midpoint of the sagittal suture to the lateral margin of the PF. Institutional ethical clearance was obtained from the Biomedical Research Ethics Committee (BE124/19).

A digital calliper (Linear Tools 2012, 0–150 mm, LIN 86500963) was employed to take measurements; these measurements were taken 3 times to ensure accuracy.

Exclusion criteria include: calvaria in which the parietal bone was damaged, and the distance of the foramina could not be recorded due to feint sagittal suture were excluded from the study.

Inclusion criteria include: calvaria without damage to the parietal bone and visible sagittal sutures were included in the study.

RESULTS

Incidence

The PF was found to be present in 68% of calvaria (Table 1) and 32% of calvaria displayed a bilateral presence of the PF. A total of 35% of calvaria had PF present unilaterally (right: 17%, left: 18%). The present study also reports 5% of calvaria which had PF present on the sagittal suture (Table 2).

Topography

The distance between the midpoint of the sagittal suture and the lateral margin of the PF, in the present study, was found to range between 4.44–18.20 mm, with a mean distance of 9.02 mm (Table 3).

Diameter

The present study recorded a mean diameter of 1.55 mm, with a range of 0.74–3.08 mm (Table 4).

DISCUSSION AND CONCLUSIONS

The PF are generally found bilaterally at the junction of the middle 1/3 and posterior 1/3 of the parietal bone near the sagittal suture [7, 14, 19]. Margins of the PF are sharply defined enabling the radiologist to

Table 2. Incidence of the topographical location of the parietal foramen

Author (year) [REF.]	Country	Sample size (n)	Present bilaterally (%)	Present unilaterally (%)	Present on sagittal suture (%)	Absent bilaterally (%)
Boyd (1930) [4]	Scotland	1500	19.9	25.9	–	39.6
Berge and Bergman (2001) [2]	USA	100	40	30	–	20
Keskil et al. (2003) [9]	Turkey	200	27	31	5	–
Yoshioko et al. (2006) [20]	USA	20	40	20	5	40
Mann et al. (2009) [11]	Japan	137	45.3	34.3	0.7	19.7
Singh and Raibagkar (2011) [17]	India	103	51	29	–	20
Debbarma et al. (2015) [6]	India	40	30	13.75	–	42.50
Murlimanju et al. (2015) [14]	India	58	55.20	32.70	3.40	12.10
Gangmei et al. (2018) [7]	India	48	62.50	29.20	–	8.30
Weighted mean	–	–	**41.2**	**29.9**	**3.4**	**20.5**
Present study (2019)	**South Africa**	**100**	**32**	**35**	**5**	**32**

Table 3. Topography of the parietal foramen from the sagittal suture

Author (year) [REF.]	Country	Sample size	Distance from sagittal suture [mm]	
			Range	Mean
Yoshioko et al. (2006) [20]	USA	20	3.00–12.00	8.00
Pereira et al. (2013) [15]	Brazil	31	–	7.9
Murlimanju et al. (2015) [14]	India	58	0.50–15.00	6.70
Halagatti and Sagar (2018) [8]	India	215	–	6.60
Shantharam and Manjunath (2018) [16]	India	78	–	7.34
Weighted mean	–	–	–	**6.9**
Present study (2019)	**South Africa**	**100**	**4.44–18.20**	**9.02**

Table 4. Size of the parietal foramen

Author (year) [REF.]	Country	Sample size	Diameter [mm]	
			Range	Mean
Berge and Bergman (2001) [2]	USA	100	–	0.67
Yoshioko et al. (2006) [20]	USA	20	0.40–4.30	1.80
Collipal et al. (2009) [5]	Chile	39	0.37–2.65	–
Mann et al. (2009) [11]	Japan	110	1.80–2.00	–
Singh and Raibagkar (2011) [17]	India	103	–	0.91
Shantharam and Manjunath (2018) [16]	India	78	0.86–5.57	–
Weighted mean	–	–	–	**0.88**
Present study (2019)	**South Africa**	**100**	**0.74–3.08**	**1.55**

differentiate between these foramina and other burr holes, caused by neurosurgical procedures, which are larger in size than that of the PF [14, 16].

Calvaria are formed by intramembranous ossification with the parietal bone forming via two ossification centres, located on either side of the midline, which eventually fuse [1, 19]. The formation of the PF, occurring initially as a single defect, is due to the prolonged ossification of the posterior parietal region of the skull leading to a 'V-shaped' notch known as the third fontanelle, or pars obelica [1, 7]. Thus, the defect persists as a small or oval foramen and the formation of the unilateral or bilateral foramina occurs as the third fontanelle closes [1, 14].
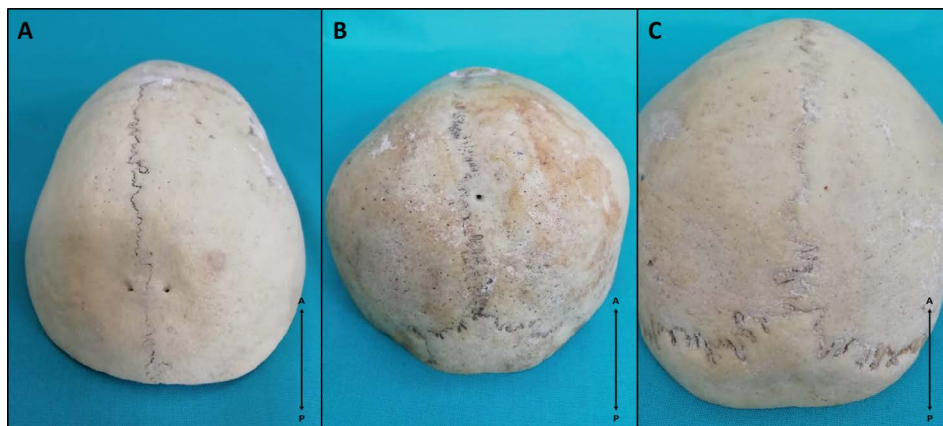
Figure 1. Calvaria depicting incidence of parietal foramen (PF); **A.** PF present bilaterally; **B.** PF present unilaterally; **C.** PF absent bilaterally.
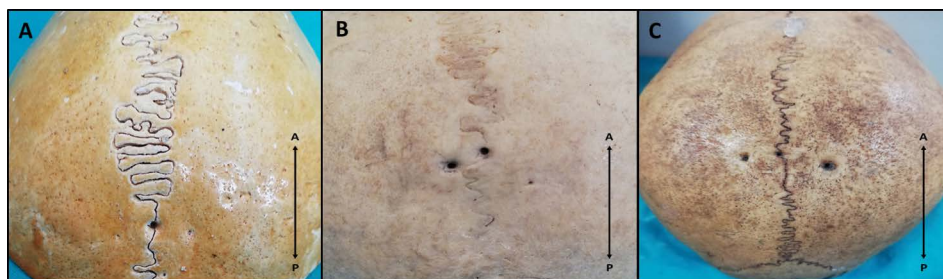

Figure 2. Calvaria depicting presence of median parietal foramen (PF); **A.** Median PF; **B.** Median PF with unilateral PF; **C.** Median PF with bilateral PF.

The identification of emissary foramina, such as the PF, is imperative for the understanding of regional vessels and to distinguish between these foramina and variant anatomy [14]. The present study recorded the incidence of PF in 68% of cases which concurs with the literature reviewed, which recorded a weighted mean incidence of 58.5% (Table 1). Makandar et al. [10] stated that the incidence of the PF is a standard phenomenon — this statement concurs with the high incidence found in the present study.

This study reports a 32% occurrence of bilateral PF which is similar to the findings of Debbarma et al. [6] (30%); however, this finding is lower than those of Murlimanju et al. [14] (55.2%) and Gangmei et al. [7] (62.5%) (Fig. 1A, Table 2). The weighted mean incidence of bilateral PF in the literature is 41.2% (Table 2).

A review of the literature revealed a weighted mean incidence of unilateral PF as 29.9% (Table 2). This finding correlates with that of the present study which recorded unilateral PF in 35% (right: 17%, left: 18%) of cases (Fig. 1B, Table 2). The finding of the present study correlates closely with that of Berge and Bergman [2] (30%) and Murlimanju et al. [14]

(32.7%) which were conducted in American and Indian populations, respectively (Table 2).

Parietal foramen located on the sagittal suture has been termed median PF [7]. The present study revealed a 5% incidence of the median PF (Table 2), of which 1% had only the median foramen present (Fig. 2A), 2% had the median foramen present along with a unilateral PF (Fig. 2B), and 2% had the median foramen present with bilateral PF (Fig. 2C). This type of foramen was reported by Keskil et al. [9] (5%) and Mann et al. [11] (0.7%) which were conducted in Turkish and Japanese populations, respectively (Table 2). The weighted mean incidence of the median PF in the literature is 3.4% (Table 2).

Determining the topography of the foramen in relation to the sagittal suture is clinically important for neurosurgical techniques due to the risk of rupture of emissary veins during surgical procedures [14, 16]. The present study has a similar range, 4.44–18.20 mm, of the location of the PF from the sagittal suture when compared to previous studies such as Yoshioko et al. [20] and Murlimanju et al. [14] which reported ranges of 3.00––12.00 mm and 0.50–15.00 mm, respectively (Table 3). However, the mean distance reported by the present

study, 9.02 mm, was found to be higher in comparison to previous studies such as Halagatti and Sagar [8] and Shantharam and Manjunath [16] who reported mean distances of 6.60 mm and 7.34 mm, respectively (Table 3).

Information on skull foraminal size is imperative due to radiological advancements by use of magnetic resonance imaging and computed tomography to make diagnoses of pathological conditions [2, 16]. With respect to diameter, the range of 0.74–3.08 mm, recorded in the present study is similar to that of studies conducted by Yoshioko et al. [20] (0.40––4.30 mm) and Shantharam and Manyjunath [16] (0.86–5.57 mm), respectively; however, this range was greater than that of Mann et al. [11] (1.80–2.00 mm) (Table 4). The mean diameter reported by present study, 1.55 mm, was found to be lower than that of Yoshioko et al. [20] (1.80 mm), yet higher than studies conducted by Berge and Bergman [2] (0.67 mm) and Singh and Raibagkar [17] (0.91 mm) (Table 4).

Shantharam and Manjunath [16] stated that perhaps differences in studies conducted by Yoshioko et al. [20] and Boyd [4] were due to racial differences. Furthermore, Berry and Berry [3], in a study of variations of the human cranium, stated that the frequency of any particular variant is consistent in any given race. Thus, a need for population specific data of the anatomical parameters of the PF has been highlighted; therefore, the present study aimed to partially fill this gap since a thorough review of the literature has revealed the paucity of data regarding the PF within a South African population.

Variations of skull foramina are important for their disease associations and surgical implications [12, 17]. Therefore, due to the high incidence of the PF as reported by the present study, and since the emissary veins of the cranium will be encountered by the neurosurgeon, knowledge of the anatomy of the emissary PF is imperative.

Conflict of interest: None declared

REFERENCES

1. Agarwal P, Baranwal S, Pandey M, et al. Large midline persistent parietal foramina with occipital encephalocele and abnormal venous drainage. JCLPA. 2015; 2(1): 66–69, doi: 10.4103/2348-2125.150757.
2. Berge JK, Bergman RA. Variations in size and in symmetry of foramina of the human skull. Clin Anat. 2001; 14(6): 406–413, doi: 10.1002/ca.1075, indexed in Pubmed: 11754234.
3. Berry AC, Berry RJ. Epigenetic variation in the human cranium. J Anat. 1967; 101(Pt 2): 361–379, indexed in Pubmed: 4227311.
4. Boyd GI. The emissary foramina of the cranium in man and the anthropoids. J Anat. 1930; 65(Pt 1): 108–121, indexed in Pubmed: 17104299.
5. Collipal E, Silva H, Quintas F, et al. Morphometry study of the parietal foramen. Int J Morphol. 2009; 27: 481–484.
6. Debbarma S, Zaidi SHH, Mishra A, et al. A study of parietal foramen in North Indian population. JMS. 2015; 5(2): 143–145.
7. Gangmei G, Devi HS, Daimei T, et al. Variations of parietal foramen in dried adult human skulls. IOSR-JDMS. 2018: 26–29.
8. Halagatti M, Sagar S. An anatomical study of parietal emissary foramina in dry adult human skulls. IJARS. 2018: 20.
9. Keskil S, Gözil R, Calgüner E. Common surgical pitfalls in the skull. Surg Neurol. 2003; 59(3): 228–231, doi: 10.1016/s0090-3019(02)01038-8, indexed in Pubmed: 12681561.
10. Makandar UK, Kulkarni PR, Suryakar AN. Comparative study of incidence of parietal foramina in north and south indian human crania. Indian J Forensic Med Toxicol. 2013; 7(2): 123–127, doi: 10.5958/j.0973-9130.7.2.027.
11. Mann R, Manabe J, Byrd J. Relationship of the Parietal Foramen and Complexity of the Human Sagittal Suture. Int J Morphol. 2009; 27(2), doi: 10.4067/s0717-95022009000200040.
12. Mortazavi MM, Tubbs RS, Riech S, et al. Anatomy and pathology of the cranial emissary veins: a review with surgical implications. Neurosurgery. 2012; 70(5): 1312–8; discussion 1318, doi: 10.1227/NEU.0b013e31824388f8, indexed in Pubmed: 22127046.
13. Moore KL, Dalley AF. Clinically Oriented Anatomy, 5th Ed. Lippincott Williams & Wilkins, Philadelphia 2006: 897.
14. Murlimanju BV, Saralaya VV, Somesh MS, et al. Morphology and topography of the parietal emissary foramina in South Indians: an anatomical study. Anat Cell Biol. 2015; 48(4): 292–298, doi: 10.5115/acb.2015.48.4.292, indexed in Pubmed: 26770881.
15. Pereira GA, Lopes PT, Santos AM, et al. Study of landmarks in dried skulls in a Brazil population. J Morphol Sci. 2013; 30(2): 94–97.
16. Shantharam V, Manjunath KY. Anatomical study of parietal emissary foramina in human skulls. IJARS. 2018; 7(1): A011–A014.
17. Singh PR, Raibagkar CJ. Study of variation in atypical foramina of dry human skull. NJIRM. 2011; 2(2): 1–5.
18. Wysocki J, Reymond J, Skarzyński H, et al. The size of selected human skull foramina in relation to skull capacity. Folia Morphol. 2006; 65(4): 301–308, indexed in Pubmed: 17171609.
19. Yılmaz E, Yetim A, Erol OB, et al. Multiple occipital, parietal, temporal, and frontal foramina: a variant of enlarged parietal foramina in an infant. Balkan Med J. 2014; 31(4): 345–348, doi: 10.5152/balkanmedj.2014.14528, indexed in Pubmed: 25667790.
20. Yoshioko N, Rhoton AL, Abe H. Scalp to meningeal arterial anastomosis in the parietal foramen. Neurosurgery. 2006; 58(1 Suppl): ONS123–ONS126, doi: 10.1227/01.NEU.0000193516.46104.27, indexed in Pubmed: 16543869.

VIA MEDICA

ORIGINAL ARTICLE

Protective effect of resveratrol on acrylamide-induced renal impairment

M.M. Nasralla[1], S.M. Zaki[1, 2], R.A. Attia[1]

[1]Faculty of Medicine, Cairo University, Cairo, Egypt
[2]Fakeeh College for Medical Sciences, Jeddah, Saudi Arabia
[3]Department of Pharmacology, Fakeeh College for Medical Sciences, Jeddah, Saudi Arabia

Background: Acrylamide (ACR) has a wide range of uses. It possesses a renal impairment effect. The work aimed to study the possible protecting role of resveratrol (RVS) over the ACR-mediated renal impairment in rats. The suggested underlying mechanisms participating in such protection were investigated.

Materials and methods: Thirty Sprague-Dawley adult albino rats were divided into three groups: control, ACR, and RVS. After 4 weeks, the kidney was removed and prepared for histological, immunohistochemical, and biochemical studies. The activity of tissue oxidative (malondialdehyde [MDA]) and anti-oxidative (glutathione [GSH]) markers were assessed.

Results: Acrylamide induced glomerular renal affection in the form of shrinkage and distortion of the glomeruli with wrinkling of their basement membranes and widening of the urinary spaces. Degenerative tubular changes were markedly present in the proximal convoluted tubules. The necrotic tubular cells exhibited cytoplasmic vacuolation with desquamated epithelial cells within the tubular lumen. ACR increases the deposition of collagen fibres in the basement membrane of the glomerular capillaries and induced thickening of the basement membranes of the renal corpuscles and renal tubules. The administration of RVS affords high protection to the kidney. The glomeruli and renal tubules were nearly normal. The content of collagen fibres and the periodic acid Schiff reaction of the basement membrane of the renal tubules were 70% and 19% lower linked to the ACR group. The creatinine and urea levels decreased by 51% and 47%. RVS induced such a protective role through its antioxidant effect as the MDA level decreased by 45%, while the GSH level increased by 83% compared with the ACR group.

Conclusions: Acrylamide causes structural and functional disorders of the kidney. It induces kidney damage through oxidative stress and apoptosis. With the use of RVS, normal kidney architecture was preserved with little structural changes. Adding, functional kidney test became normal. RVS exerts its protective effect through its anti-apoptotic and antioxidant features. (Folia Morphol 2021; 80, 4: 985–993)

Key words: resveratrol, acrylamide, kidney

Address for correspondence: Dr. S.M. Zaki, Fakeeh College for Medical Sciences, Jeddah, Saudi Arabia, e-mail: zaky.sherif@yahoo.com

INTRODUCTION

Acrylamide (ACR) is a well-known environmental pollutant that exerts a range of systemic toxic effects on people after both occupational and dietary exposure [2, 22]. It possesses a variety of harmful properties: carcinogenicity, genotoxicity, neurotoxicity, and reproductive toxicity [5, 7]. ACR and its analogues are widely used in various chemical and environmental applications and are produced by heating plant tissue-derived biological material [25]. ACR formation occurs during food processing due to exposure of carbohydrates to temperatures above 200°C [12]. High levels of ACR have been found in foodstuffs commonly consumed, in particular; potato chips and bread [31].

Acrylamide is absorbed from the gastrointestinal tract and dispersed widely in body fluids and stored in the liver and kidney [28]. The ACR is known to cause structural and functional changes in many organs. The renal tubular cells undergo degenerative vacuolar changes, inflammatory cell infiltration and periglomerular oedema [28]. Furthermore, ACR administration in rats raises the levels of serum urea, creatinine, uric acid, and renal proinflammatory cytokine [1].

The metabolism of ACR triggers the release of free radicals (ROS), which initiates oxidative stress leading to an imbalance in the development and degradation of ROS [19]. It also induces lipid peroxidation and DNA harm [1].

The effects of many antioxidants and anti-inflammatory compounds such as olive oil, vitamin E and 5-aminosalicylic acid were studied to prevent and treat ACR-induced renal impairment [9, 19].

Resveratrol (RVS) is a phytoalexin found in at least 72 species of plants, many of which are eaten by humans, including mulberries, peanuts, and grapes [8]. RVS has anti-inflammatory, antiplatelet, antioxidant, and anti-carcinogenic activity, as well as the ability to reduce kidney damage caused by chemical compounds [8, 10]. However, it is unclear whether RVS can defend against ACR-induced renal impairment or not. Therefore, we studied the oxidative and apoptotic damaging effect of the ACR over the kidney and investigated the protecting role of RVS over such renal impairment in rats.

MATERIALS AND METHODS

Animals

Thirty Sprague-Dawley adult albino rats weighing 170–200 g were encompassed in our study. The animals were maintained in spacious wire mesh cages in a special room with direct daylight and natural ventilation. The rats had free access to standard rat chow and water.

All the animals were treated according to the standard guidelines for the care and use of laboratory animals. The study was permitted by the Ethics Committee, Faculty of Medicine, Cairo University, Egypt. The procedures followed were following the ethical standards of the responsible organization and with the Helsinki Declaration of 1975 as revised in 1983.

Experimental design

The rats were distributed into three groups (10 in each group): control (given distilled water at a dose of 1 mL), ACR group, and RVS group (concomitant ACR + RVS).

Chemicals

Acrylamide was obtained in a container of powder purchased by Biostain Company (United Kingdom) weighing 500 g. It was dissolved in distilled water, in a concentration of 10 g/L. It was given at a dose of 1 mL of distilled water containing 40 mg/kg/day orally via gastric gavage [9].

Resveratrol (purity, > 99%) was purchased from Sigma-Aldrich (St. Louis, MO, USA). It was dissolved in dimethyl sulfoxide and diluted in 0.9% physiological saline. It was given at a daily dose of 20 mg/kg/day orally via gastric gavage [18].

By the end of the experiment (after 4 weeks), each animal was weighed, and a blood sample was withdrawn from the tail vein using a fine heparinized capillary tube. The kidney was extracted, washed with saline, and left to dry on a plot paper.

Light microscopic study

Kidney specimens were fixed in formalin 10%, dehydrated in ethyl alcohol, cleared in xylol, and embedded in paraffin wax. Sections of 5 μm thickness were cut and mounted on glass slides. Other sections were mounted on positively charged slides for immunohistochemistry. The sections were subjected to the following:

— haematoxylin and eosin (H&E) and Masson's trichrome stained sections were prepared according to Suvarna et al. [24];
— histochemical evaluation: periodic acid Schiff (PAS) stain: PAS stained sections were prepared according to Suvarna et al. [24];

— immunohistochemistry analysis of Bcl-2-associated X protein (BAX) [20].

Paraffin sections were prepared. Then, a suitable quantity of serum was added to the sections for 30 min. Endogenous peroxidase was inactivated with a methanol solution containing H_2O_2 (1:50) for 10 min and washed with phosphate buffered saline (PBS). The tissue sections were blocked with 1.5% serum for 30 min. The sections were incubated with the primary antibody BAX (anti-human BAX protein, DakoCytomation, Denmark), followed by the secondary antibody (biotinylated link universal from the commercial kit LSAB: DakoCytomation, Denmark). Subsequently, samples were incubated with AB enzymes for 30 min and rinsed in PBS. Positive signals were detected using peroxidase chromogenic substrates. The negative control included PBS instead of the secondary antibody.

Image analysis and morphometric measurements

Using the Leica LAS V3.8 image analyser computer system (Switzerland), the following parameters were assessed: the diameters of the renal glomeruli and proximal convoluted tubules, the width of the renal space, and the height of the lining proximal tubular epithelium. Adding, the number of structurally altered glomeruli was assessed as a percentage of the total number of glomeruli. The content of the collagen fibres was also assessed.

In PAS-stained histological sections, the optical density of the basement membrane of the proximal convoluted tubules and the parietal layers of Bowman's capsules was additionally determined.

In the BCL2 immunohistochemical staining area percentage of the immune reaction was also measured.

Biochemical study

Blood samples withdrawn from the rats before sacrifice were used for biochemical assessment in the Biochemistry and Molecular Biology Department, Faculty of Medicine, Cairo University, Egypt.

The serum urea and creatinine levels were estimated by the conventional colorimetric method using Quanti Chrom TM Assay Kits (DIUR-500 and DICT-500), based on the improved Jung and Jaffe methods, respectively [32]. The mean values of these biochemical parameters were calculated and subjected to statistical analysis.

Tissue level of malondialdehyde (MDA) and reduced glutathione (GSH). The renal tissue was homogenised in 5–10 mL cold buffer (50 mM potassium phosphate, pH 7.5. 1 mM EDTA) per gram tissue then it was centrifuged at 100,000 g for 15 min at 4°C. The supernatant was removed for assay and stored on ice.

Malondialdehyde assay was performed with thiobarbituric acid (TBA) test in the supernatant, according to the method suggested by Buege and Aust [4]. MDA reacts with TBA to give a red compound absorbing at 535 nm.

Measurement of GSH was based on the reduction of 5,5-dithiobis (2-nitrobenzoic acid) (DTNB) with reduced GSH to produce a yellow compound [6].

Statistical analysis

The mean values of relative kidney weight, histomorphometric measurements, and biochemical levels were analysed using SPSS version 22. Statistical estimation was done using ANOVA followed by Bonferroni pairwise comparisons.

RESULTS

Light microscopic evaluation

The examination of the control group showed intact architecture of the renal cortex. The renal cortex is formed of renal corpuscles, and proximal and distal convoluted tubules (Fig. 1A).

The examination of the renal cortex of the ACR group revealed marked structural changes. The renal glomeruli showed moderate to marked shrinkage, distortion, segmentation, and vacuolation with widened urinary spaces. The renal tubules were dilated with marked diminution of their epithelial height and widening of their lumina. Their lining cells showed cytoplasmic vacuolation, cellular fragmentation, and intraluminal cast formation were observed in many convoluted tubules. The interstitium showed congested blood vessels with intimal thickening and massive cellular infiltration could be also seen (Fig. 1B–D).

Examination of the RVS group revealed the almost normal appearance of most of the glomeruli and the tubules. Minimal interstitial inflammatory cellular infiltration was encountered (Fig. 1E).

Content of collagen fibres

The content of the fibres was minimal in the control group. The content increased around the parietal layers of Bowman's capsules and the basement membranes of the renal tubules in ACR (9-fold) and RVS
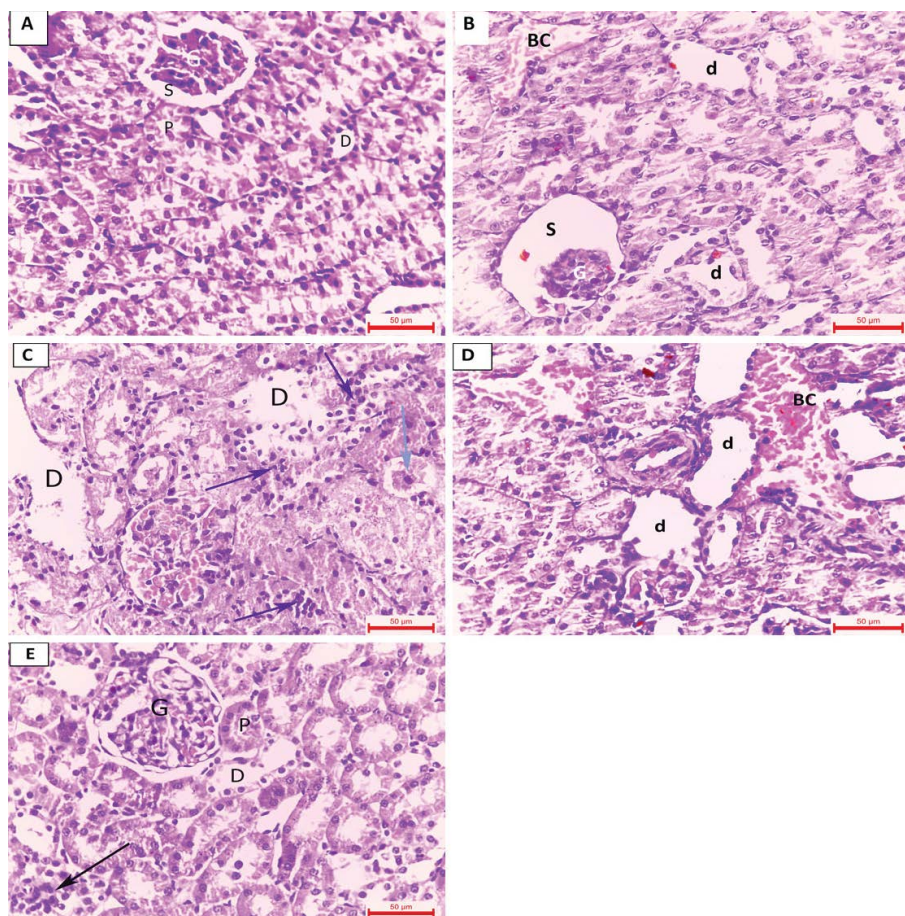
Figure 1. A. Normal renal architecture in the control group showing normal architecture with normal renal glomeruli (G), Bowman's spaces (S), proximal convoluted tubules (PCT) (P), and distal convoluted tubules (DCT) (D); **B–D.** Shrinkage and distortion of renal glomeruli (G) with glomerular congestion and interstitial cellular infiltration (arrow) in the acrylamide group. Note vacuolation and degenerated nuclei of the PCT (P); **E.** Normal appearance of renal glomeruli (G), Bowman's spaces (S), PCT (P), and DCT of the resveratrol group. Note minimal interstitial cellular infiltration (arrow) (haematoxylin and eosin; ×400); d — distal convoluted tubules; BC — blood capillary.

(2-fold) groups when related to the control group. The content in the RVS group was 70% lower when related to the ACR group (Fig. 2A–C, Table 1).

Histochemistry of the kidney

In the control group, the basement membranes of the renal tubules and the parietal layers of Bowman's capsules demonstrated a weak PAS reaction. Adding, the apical brush borders of the proximal convoluted tubules (PCT) were intact and partially occluding the tubular lumina (Fig. 3A).

The basement membranes of the renal tubules and the parietal layers of Bowman's capsules of the ACR group showed an intense PAS reaction (42% higher than the control group). Adding, the apical brush borders of the PCT were attenuated (Fig. 3B). With the use of RVS, the PAS reaction became comparable to the control group and was 19% lower than the ACR group (Fig. 3C, Table 1).

Immunohistochemical staining BAX

BAX showed a weak reaction in the control group (Fig. 4A). The area percentage of BAX immunopositive cells increased 4.5-fold in the ACR group matched to the control group (Fig. 4B, C, Table 1). With the use of RVS, the area percentage of the immunopositive cells decreased 56% equated to the ACR group; however, the area percentage in the RVS group was 1.4-fold higher than the control group (Fig. 4D, Table 1).

Biochemical and oxidative/antioxidative markers

The serum creatinine and urea levels increased in the ACR group by 2.75-fold, 1.9-fold linked to the control group. With the concomitant use of RVS, the levels of creatinine and urea decreased by 51%, 47% allied to the ACR. Nevertheless, the levels of creatinine and urea in the RVS group were 83%, 55% higher than the control group (Table 1).
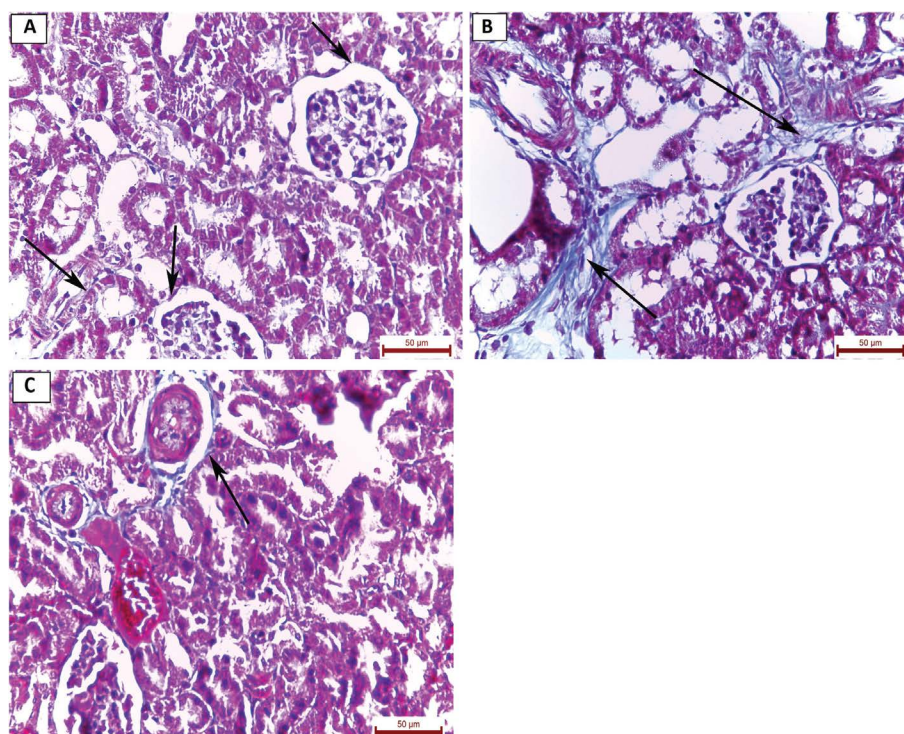
Figure 2. A. The control group with normal basement membranes of renal tubules (arrows) and parietal layers of Bowman's capsules (arrow);
B. Acrylamide group with thickened basement membranes of the renal tubules (arrows) and parietal layer of Bowman's capsules (arrowheads). Note augmented interstitial collagen fibres (arrow); **C.** Resveratrol group with normal appearance of renal tubules (arrows) and parietal layer of Bowman's capsules (arrow). Note a slight increase of interstitial collagen fibres (Masson's trichrome; ×400).

Table 1. Content of collagen fibres, periodic acid Schiff (PAS) reaction, apoptotic, biochemical and oxidative/antioxidative markers

Group		Content of collagen fibres	Optical density of PAS reaction	Area percentage of BAX immunopositive cells	Serum creatinine [mg/dL]	Serum urea [mg/dL]	Malondialdehyde [nmol/g protein]	Glutathione [µmol/g protein]
Control	Mean ± SD	3.51 ± 0.46	0.47 ± 0.01	1.35 ± 0.15	0.12 ± 0.01	36.1 ± 2.0	17.52 ± 2.4	0.28 ± 0.02
Acrylamide group	Mean ± SD	30.46 ± 0.50	0.67 ± 0.01	7.45 ± 0.37	0.45 ± 0.03	106.6 ± 2.2	42.18 ± 3.6	0.12 ± 0.02
	Versus control group	< 0.001*	< 0.001*	< 0.001*	< 0.001*	< 0.001*	< 0.001*	< 0.001*
	Versus resveratrol group	0.003*	0.005*	< 0.001*	< 0.001*	< 0.001*	< 0.001*	< 0.001*
Resveratrol group	Mean ± SD	9.63 ± 0.60	0.54 ± 0.01	3.24 ± 0.21	0.22 ± 0.03	56.6 ± 2.4	23.16 ± 1.8	0.22 ± 0.01
	Versus control group	0.002*	0.144	0.052	0.007*	< 0.001*	< 0.001*	0.259
	Versus acrylamide group	0.003*	0.005*	< 0.001*	< 0.001*	< 0.001*	< 0.001*	< 0.001*

*p-value significant; SD — standard deviation; BAX — Bcl-2-associated X protein

The values of the oxidative marker (MDA) in the ACR group increased by 1.4-fold, while the anti-oxidative marker (GSH) decreased by 1.3-fold compared with the control group. With the use of RVS, the MDA level decreased by 45%, while the GSH level increased by 83% compared with the ACR group. Still, the level of both markers was away from the control group (Table 1).

Morphometric glomerular and PCT changes

The percentage of the affected glomeruli in the ACR group increased 8.8-fold matched to the control group. With the use of RVS, the per cent of the affected glomeruli decreased 71% equated to the ACR group; however, the percentage in the RVS group was 1.6-fold higher than the control group (Table 2).
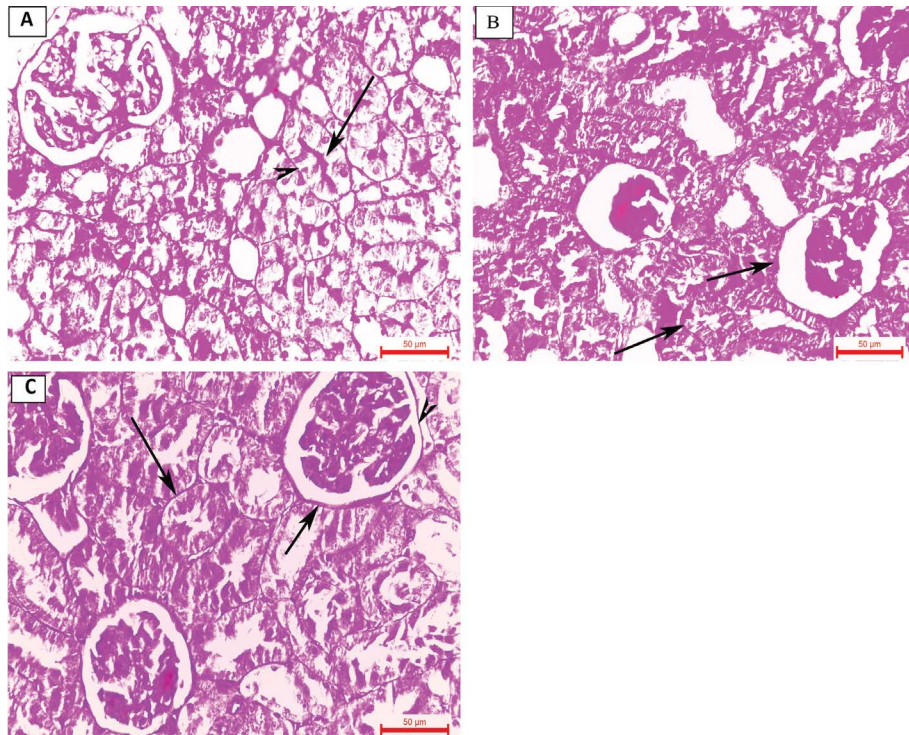
Figure 3. A. Apical brush borders (arrowheads) of proximal convoluted tubules (PCT) of the control group occluding the tubular lumina. Note weak periodic acid Schiff (PAS) reaction of parietal layers of Bowman's capsules and basement membranes of PCT; **B.** Intense PAS reaction of parietal layers of Bowman's capsules and the basement membranes of the renal tubules (arrows) of the acrylamide group; **C.** Moderate PAS reaction of the resveratrol group (PAS; ×400).
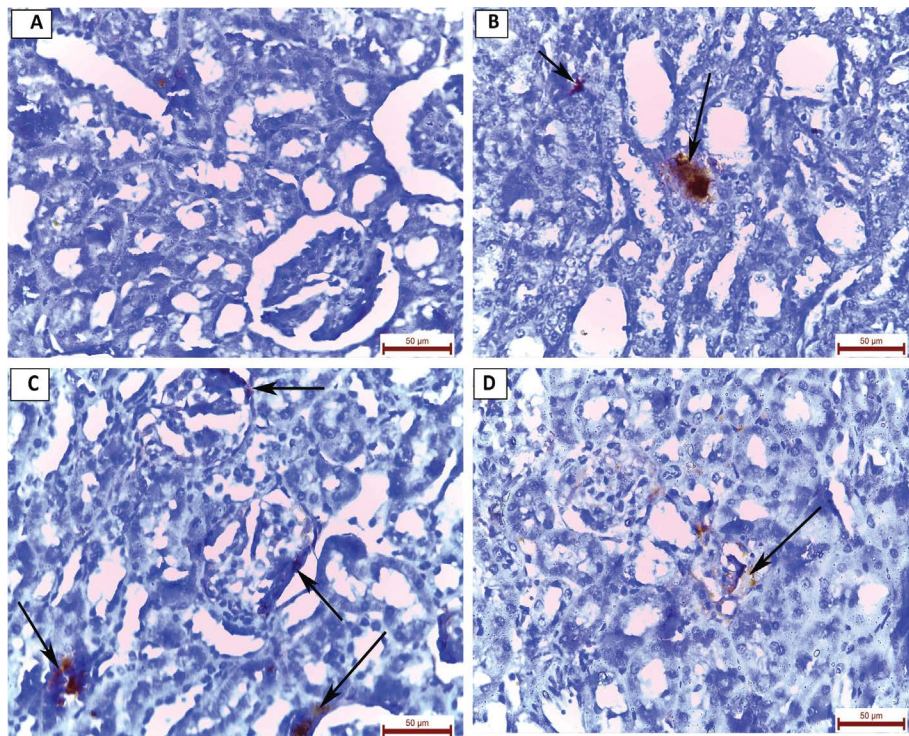

Figure 4. A. A negative immunoreactivity of the control group; **B, C.** A positive immunoreactivity of the acrylamide group; **D.** A negative immunoreactivity of the resveratrol group (BAX; ×400).

Table 2. Morphometric glomerular and proximal convoluted tubules (PCT) changes

Group		Percentage of the affected glomeruli	Glomerular diameter [μm]	Width of urinary space [μm]	PCT diameter [μm]	PCT epithelial height [μm]
Control	Mean ± SD	5.23 ± 1.78	353.29 ± 1.39	24.93 ± 1.6	180.38 ± 1.24	134.59 ± 2.21
Acrylamine group	Mean ± SD	49.15 ± 2.7	146.45 ± 2.09	83.40 ± 2.05	237.13 ± 1.64	50.80 ± 2.77
	Versus control group	< 0.001*	< 0.001*	< 0.001*	< 0.001*	< 0.001*
	Versus resveratrol group	< 0.001*	< 0.001*	< 0.001*	< 0.001*	< 0.001*
Resveratrol group	Mean ± SD	13.2 ± 2.2	330.74 ± 1.12	35.69 ± 1.38	193.46 ± 1.35	120.64 ± 3.01
	Versus control group	0.003*	0.01*	0.01*	< 0.001*	< 0.001*
	Versus acrylamide group	< 0.001*	< 0.001*	< 0.001*	< 0.001*	< 0.001*

*p-value significant; SD — standard deviation

In the ACR group, the glomerular diameter decreased 58% with an increase in the width of the urinary space 2.4-fold matched to the control group. With the use of RVS, the glomerular diameter increased 1.26-fold with a decrease in the width of the urinary space 57% equated to the ACR group. The glomerular diameter and width of urinary space in RVS and control groups were alike (Table 2).

In the ACR group, the diameter of the PCT increased 31%, while the height of their lining epithelium decreased 62% compared to the control group. With the use of RVS, the diameter of the PCT decreased 18%, while the height of their lining epithelium increased 1.4-fold equated to the ACR group. Both parameters were comparable in RVS and control groups (Table 2).

DISCUSSION

Acrylamide induced glomerular renal affection in the form of shrinkage and distortion of the glomeruli with wrinkling of their basement membranes and widening of the urinary spaces. Adding, degenerative tubular changes were markedly present in the PCT. The necrotic tubular cells exhibited cytoplasmic vacuolation with desquamated epithelial cells within the tubular lumen. Adding, ACR induced massive inflammatory cellular infiltration with congestion of glomerular blood vessels.

Acrylamide induced fibrosis that was established by a 9-fold increase deposition of collagen fibres in the basement membrane of the glomerular capillaries. Such collagen fibres can be the result of the epidermal growth factor that stimulates fibroblast proliferation and collagen synthesis [14].

The basement membranes of the renal corpuscles and renal tubules of the ACR group showed an intense PAS reaction (42% higher than the control group). Thickening of the tubular basement membrane is a common feature of atrophy and may be associated with hyalinosis [14]. Thickening is also a possible cause of reduced active transport in PCT causing micro-albuminuria [14].

The brush border of the PCT in the ACR group was interrupted. Loss of the brush border is the earliest morphological sign of impaired proximal tubular function [17, 27]. Furthermore, loss of the brush border affects the reabsorptive power of the PCT with loss of glucose, salts, and large amounts of water in urine [17, 27]. This mostly explains the observed serological changes (the elevated serum levels of urea and creatinine). The diameter of the PCT increased 31% in the ACR group which mostly is a compensatory mechanism to conserve the renal function [15].

Oxidative stress is the main pathogenic mechanism through which ACR induces renal damage. Oxidative stress is a shift in the balance between oxidants and antioxidants in favour of oxidants [3]. Many researchers proved the oxidative stress role of ACR over the kidney [23]. The values of the oxidative marker (MDA) in the ACR group increased by 1.4-fold, while the anti-oxidative marker (GSH) decreased by 1.3-fold. Oxidative stress creates oxygen free radical (ROS) that reacts with numerous biomolecules in the cell, leading eventually to oxidative damage [16]. ROS is scavenged by several cellular defence mechanisms involving non-enzymatic (GSH). GSH peroxidase proteins convert hydrogen peroxide to water and lipid peroxides to their respective alcohols [30]. The prolonged use of ACR decreased the activities GSH. This consequence in augmented production of the O_2^- and H_2O_2 that outcomes the production of OH^- [11]. Many researchers believed that MDA's level is sufficient

proof of oxidative stress [13] and higher value of MDA revealed an increase in lipid peroxidation.

Apoptosis is also another pathogenic mechanism through which ACR induced renal affection [23]. BAX reaction increased 4.5-fold in the ACR group. BAX exerts proapoptotic activity [29].

Resveratol, as one of the flavonoids, affords a high protection to the kidney as the glomeruli and renal tubules were nearly normal. Compared to ACR group, the content of collagen fibres and the PAS reaction of the renal tubules decreased by 70, 19%. Adding, the levels of creatinine and urea decreased by 51, 47%.

Many researchers recorded the exogenous antioxidant protective effect of RVS over the kidney [21]. RVS induced such protective role through its antioxidant effect as the MDA level decreased by 45%, while the GSH level increased by 83% compared with the ACR group. RVS prevents superoxide production from uncoupled endothelial nitric oxide synthase and increases the expression of various antioxidant enzymes [30]. The antioxidant activity of many flavonoids is due to direct scavenging of oxygen-free radicals or excited oxygen species as well as inhibition of oxidative enzymes producing ROS [26].

Another protective mechanism to RVS is through its anti-apoptotic effect. With the use of RVS, the area percentage of the immunopositive BAX cells decreased 56% equated to the ACR group.

CONCLUSIONS

In conclusion, ACR causes structural and functional disorders of the kidney. It induces kidney damage through oxidative stress and apoptosis. With the use of RVS, the normal kidney architecture was preserved with little structural changes. RVS exerts its protection through its anti-apoptotic and antioxidant features.

Conflict of interest: None declared

REFERENCES

1. Abdel-Daim MM, Abd Eldaim MA, Hassan AGA. Trigonella foenum-graecum ameliorates acrylamide-induced toxicity in rats: Roles of oxidative stress, proinflammatory cytokines, and DNA damage. Biochem Cell Biol. 2015; 93(3): 192–198, doi: 10.1139/bcb-2014-0122, indexed in Pubmed: 25607344.
2. Baskar G, Aiswarya R. Overview on mitigation of acrylamide in starchy fried and baked foods. J Sci Food Agric. 2018; 98(12): 4385–4394, doi: 10.1002/jsfa.9013, indexed in Pubmed: 29572830.
3. Birben E, Sahiner UM, Sackesen C, et al. Oxidative stress and antioxidant defense. World Allergy Organ J. 2012; 5(1): 9–19, doi: 10.1097/WOX.0b013e3182439613, indexed in Pubmed: 23268465.
4. Buege J, Aust S. [30] Microsomal lipid peroxidation. Methods Enzymol. 1978: 302–310, doi: 10.1016/s0076-6879(78)52032-6.
5. Carere A. Genotoxicity and carcinogenicity of acrylamide: a critical review. Ann Ist Super Sanita. 2006; 42(2): 144–155, indexed in Pubmed: 17033134.
6. Crowley C, Gillham B, Thorn MB. A direct enzymic method for the determination of reduced glutathione in blood and other tissues. Biochem Med. 1975; 13(3): 287–292, doi: 10.1016/0006-2944(75)90087-3, indexed in Pubmed: 1203068.
7. Dearfield KL, Abernathy CO, Ottley MS, et al. Acrylamide: its metabolism, developmental and reproductive effects, genotoxicity, and carcinogenicity. Mutat Res. 1988; 195(1): 45–77, doi: 10.1016/0165-1110(88)90015-2, indexed in Pubmed: 3275881.
8. Dudka J, Gieroba R, Korga A, et al. Different effects of resveratrol on dose-related Doxorubicin-induced heart and liver toxicity. Evid Based Complement Alternat Med. 2012; 2012: 606183, doi: 10.1155/2012/606183, indexed in Pubmed: 23258992.
9. Ghorbel I, Elwej A, Fendri N, et al. Olive oil abrogates acrylamide induced nephrotoxicity by modulating biochemical and histological changes in rats. Ren Fail. 2017; 39(1): 236–245, doi: 10.1080/0886022X.2016.1256320, indexed in Pubmed: 27846768.
10. Gülçin İ. Antioxidant activity of food constituents: an overview. Arch Toxicol. 2012; 86(3): 345–391, doi: 10.1007/s00204-011-0774-2, indexed in Pubmed: 22102161.
11. Halliwell B, Gutteridge JM. Free radicals and antioxidant protection: mechanisms and significance in toxicology and disease. Hum Toxicol. 1988; 7(1): 7–13, doi: 10.1177/096032718800700102, indexed in Pubmed: 3278973.
12. Kjuus H, Hansteen IL, Ryberg D, et al. Chromosome aberrations in tunnel workers exposed to acrylamide and N-methylolacrylamide. Scand J Work Environ Health. 2005; 31(4): 300–306, doi: 10.5271/sjweh.886, indexed in Pubmed: 16161713.
13. Kurt A, Tumkaya L, Turut H, et al. Protective effects of infliximab on lung injury induced by methotrexate. Arch Bronconeumol. 2015; 51(11): 551–557, doi: 10.1016/j.arbres.2015.03.018, indexed in Pubmed: 26071367.
14. Liu Y. Epithelial to mesenchymal transition in renal fibrogenesis: pathologic significance, molecular mechanism, and therapeutic intervention. J Am Soc Nephrol. 2004; 15(1): 1–12, doi: 10.1097/01.asn.0000106015.29070.e7, indexed in Pubmed: 14694152.
15. McCance KL, Huether SE. Pathophysiology: the biologic basis for disease in adults and children. 7th ed. Elsevier, St. Louis, Missouri 2014.
16. McCord JM. Human disease, free radicals, and the oxidant/antioxidant balance. Clin Biochem. 1993; 26(5): 351–357, doi: 10.1016/0009-9120(93)90111-i, indexed in Pubmed: 8299205.
17. Nangaku M. Chronic hypoxia and tubulointerstitial injury: a final common pathway to end-stage renal failure. J Am Soc Nephrol. 2005; 17(1): 17–25, doi: 10.1681/asn.2005070757.

18. Qiao Y, Gao Ke, Wang Y, et al. Resveratrol ameliorates diabetic nephropathy in rats through negative regulation of the p38 MAPK/TGF-β1 pathway. Exp Ther Med. 2017; 13(6): 3223–3230, doi: 10.3892/etm.2017.4420, indexed in Pubmed: 28588674.

19. Rajeh NA, Al-Dhaheri NM. Antioxidant effect of vitamin E and 5-aminosalicylic acid on acrylamide induced kidney injury in rats. Saudi Med J. 2017; 38(2): 132–137, doi: 10.15537/smj.2017.2.16049, indexed in Pubmed: 28133684.

20. Ramos-Vara JA, Kiupel M, Baszler T, et al. Suggested guidelines for immunohistochemical techniques in veterinary diagnostic laboratories. J Vet Diagn Invest. 2008; 20(4): 393–413, doi: 10.1177/104063870802000401, indexed in Pubmed: 18599844.

21. Rašić D, Micek V, Klarić MS, et al. Oxidative stress as a mechanism of combined OTA and CTN toxicity in rat plasma, liver and kidney. Hum Exp Toxicol. 2019; 38(4): 434–445, doi: 10.1177/0960327118819049, indexed in Pubmed: 30545268.

22. Semla M, Goc Z, Martiniaková M, et al. Acrylamide: a common food toxin related to physiological functions and health. Physiol Res. 2017; 66(2): 205–217, doi: 10.33549/physiolres.933381, indexed in Pubmed: 27982682.

23. Sengul E, Gelen V, Yildirim S, et al. The effects of selenium in acrylamide-induced nephrotoxicity in rats: roles of oxidative stress, inflammation, apoptosis, and DNA damage. Biol Trace Elem Res. 2021; 199(1): 173–184, doi: 10.1007/s12011-020-02111-0, indexed in Pubmed: 32166561.

24. Suvarna SK, Layton C, Bancroft JD. Bancroft's theory and practice of histological techniques. 8th ed. Elsevier, Oxford 2019.

25. Tareke E, Rydberg P, Karlsson P, et al. Acrylamide: a cooking carcinogen? Chem Res Toxicol. 2000; 13(6): 517–522, doi: 10.1021/tx9901938, indexed in Pubmed: 10858325.

26. Terao J. Dietary flavonoids as antioxidants. Forum of Nutr. 2009: 87–94, doi: 10.1159/000212741.

27. Tirapelli LF, Barione DF, Trazzi BFM, et al. Comparison of two models for evaluation histopathology of experimental renal ischemia. Transplant Proc. 2009; 41(10): 4083–4087, doi: 10.1016/j.transproceed.2009.09.061, indexed in Pubmed: 20005345.

28. Totani N, Yawata M, Ojiri Y, et al. Effects of trace acrylamide intake in Wistar rats. J Oleo Sci. 2007; 56(9): 501–506, doi: 10.5650/jos.56.501, indexed in Pubmed: 17898518.

29. Tsujimoto Y. Role of Bcl-2 family proteins in apoptosis: apoptosomes or mitochondria? Genes Cells. 1998; 3(11): 697–707, doi: 10.1046/j.1365-2443.1998.00223.x, indexed in Pubmed: 9990505.

30. Xia N, Daiber A, Förstermann U, et al. Antioxidant effects of resveratrol in the cardiovascular system. Br J Pharmacol. 2017; 174(12): 1633–1646, doi: 10.1111/bph.13492, indexed in Pubmed: 27058985.

31. Zhang Y. Study on reduction of acrylamide in fried bread sticks by addition of antioxidant of bamboo leaves and extract of green tea. Asia Pac J Clin Nutr. 2007; 16(Suppl 1): 131–136.

32. Zhang L, Yang J, Eastwood GM, et al. Extended daily dialysis versus continuous renal replacement therapy for acute kidney injury: a meta-analysis. Am J Kidney Dis. 2015; 66(2): 322–330, doi: 10.1053/j.ajkd.2015.02.328, indexed in Pubmed: 25843704.

ORIGINAL ARTICLE

VIA MEDICA

Pterional variable topography and morphology. An anatomical study and its clinical significance

K. Natsis[1], I. Antonopoulos[2], C. Politis[3, 4], E. Nikolopoulou[2], N. Lazaridis[1], G.P. Skandalakis[2], D. Chytas[5], M. Piagkou[2]

[1]Department of Anatomy and Surgical Anatomy, School of Medicine, Faculty of Health Sciences, Aristotle University of Thessaloniki, Greece
[2]Department of Anatomy, School of Medicine, Faculty of Health Sciences, National and Kapodistrian University of Athens, Greece
[3]OMFS-IMPATH Research Group, Department of Imaging and Pathology, Faculty of Medicine, Katholieke Universiteit Leuven, Belgium
[4]Department of Oral and Maxillofacial Surgery, University Hospitals Leuven, Belgium
[5]School of Medicine, European University of Cyprus, Engomi, Nicosia, Cyprus

Background: Pterion is the junction of the frontal, parietal, greater wing of the sphenoid and the squamous part of the temporal bone. The sphenoparietal, frontotemporal, stellate and epipteric pteria were described. The current study determines pterion topography, morphology (variant types' frequency) and morphometry, as well as epipteric bones presence in dried skulls. Gender impact is underlined as well.

Materials and methods: Ninety Greek adult dried skulls were observed. The distances in between pterion and the zygomatic arch midpoint and in between pterion and the frontozygomatic suture were measured.

Results: The sphenoparietal pterion was the commonest (58.3%), following by the stellate (25%), epipteric (15.5%) and by the frontotemporal pterion (1.1%). Twenty-eight (15.5%) skulls had epipteric bones, further categorised as quadrisutural (35.7%), trisutural (57.1%), bisutural and multiple (3.57%). The mean distances between pterion and the midpoint of zygomatic arch were 4.13 ± 0.45 cm on the right and 4.09 ± 0.47 cm on the left side and between pterion and the frontozygomatic suture were 3.47 ± 0.61 cm on the right and 3.52 ± 0.65 cm on the left side. Both distances were symmetrical. Male skulls showed slightly higher values on the left side for the distance (pterion–midpoint of zygomatic arch).

Conclusions: Pterion is a commonly used neurosurgical landmark and thus in depth knowledge of the pteric area and its variants could be valuable. Recognition of the possible variability in pterion location, morphology and morphometry, as well as possible occurrence of epipteric bones may render pterional craniotomy safer among different population groups. (Folia Morphol 2021; 80, 4: 994–1004)

Key words: pterion, skull, zygomatic arch, frontozygomatic suture, epipteric bone, variation, anatomy

Address for correspondence: Assoc. Prof. M. Piagkou, DDS, MD, MSc, PhD, Department of Anatomy, School of Medicine, Faculty of Health Sciences, National and Kapodistrian University of Athens, M. Asias 75, Street, 11527 Greece, tel: +30 210 7462427, fax: +30 210 7462398, Mob: +306984316353, e-mail: mapian@med.uoa.gr; piagkoumara@gmail.com

INTRODUCTION

Pterion, an H-shaped small circular area, is a point of convergence of the frontal (F), sphenoid (S), parietal (P), and squamous part of the temporal bone (T) (articulation of the coronal, sphenoparietal, squamosal, sphenofrontal and sphenosquamosal sutures) [36, 56]. It corresponds to the site of the anterolateral (sphenoidal) fontanelle which disappears approximately 3 months after birth [50]. Although the sutures contributing to pterion, exhibit a wide variability [11], their relationships are not yet elucidated. Variant sutural patterns in pterional area are the outcome of combination of various environmental and epigenetic factors [7, 55].

From the morphometric point of view, as the classical anatomical textbooks refer, the pterion is located approximately 3.0–3.5 cm behind the frontozygomatic suture (FZMS) and 4.0 cm above the midpoint of the zygomatic arch (MPZ) forming the temporal fossa floor [36, 50].

Pterion is a reference cranial landmark for the anterior branch of the middle meningeal artery, the Broca's motor speech area, the insula, the stem of lateral sulcus and the anterior cisterns of the encephalon base [14, 16, 23, 40]. In addition, age and gender determination in forensic and archaeological cases could be based on pterion [29].

Although suboptimal pterion localisation may compromise surgical access and therefore treatment outcome, studies focusing on pterion morphology and surgical anatomy are scarce. Knowledge of pterion location, presence and distribution of sutural bones convergence, the so-called epipteric bones (EBs), as well as different types of classified pteria are important to prevent complications when drilling burr pterional holes [24, 46]. In such cases, (i.e. in a penetrating orbital injury) surgery should be minimally invasive, while gaining access to the sphenoid ridge and optic canal [59].

The current study underlines morphological variability of the bones forming pterional area, taking into consideration variant distribution of EBs, their frequency and relationship with pterion sutures. A terminology of the EBs is proposed. Exact pterion location in relation to FZMS and MPZ was also recorded. Both morphological and morphometric observations were analysed taking into account laterality, gender and age as well.

MATERIALS AND METHODS

Ninety (49 male and 41 female) Greek adult dried skulls from the osseous collections of the Department of Anatomy and Surgical Anatomy of the Aristotle University and the Department of Anatomy of the National and Kapodistrian University were investigated on the right (R) and left (L) sides (180 sides). Exclusion criteria included children skulls, unknown gender and age skulls, damaged and deformed skulls and skulls with pathology and trauma affecting measurement landmarks. Thus, 180 (98 male and 82 female) pteria were subdivided in three age groups: 20–39 years (46 pteria), 40–59 years (40 pteria), over 60 years of age (94 pteria) to examine age effect in pterion topography, morphology and morphometry. All skulls were derived from body donation, before death, after written informed consent.

Pterion morphology. Various pteria frequencies were recorded and all pteria were classified into four types, based on Murphy's classification [37]. Sphenoparietal (SP), frontotemporal (FT), stellate (St) and epipteric (E) pteria appear in Figure 1A, B, C, and D, respectively. A circle was drawn to locate the adjacent bones forming pterion area.

Epipteric bones number and distribution. Skulls with E pterion (EBs) were further classified having as a guide the number of sutures converging to the EB. A novel epipteric terminology, based on the number and name (frontal — F, parietal — P, temporal — T, and sphenoidal — S) of sutures articulating with EB, is proposed:
— single EB articulating with 4 sutures (FPTS) (a typical quadrisutural EB) (Fig. 2A);
— a single EB articulating with 3 sutures (trisutural EB) was further subclassified as superior (FPT) (Fig. 3A), inferior (FTS) (Fig. 3B), anterior (FPS) (Fig. 3C), and posterior (PTS) (Fig. 3D);
— an EB articulating with two sutures (PS or ST) (bisutural EB) (Fig. 2B);
— several EBs or multiple (in the form of multiple fragments) (Fig. 2C).

Pterion morphometry. Two distances, in between pterion centre and MPZ and pterion centre and FZMS were bilaterally measured using a digital calliper (Mitutoyo, ABSOLUTE 500-196-20 Digital Calliper, 0.001 mm accuracy) (Fig. 4). The study was conducted in accordance to the Ethical Committee standards and with the 1964 Helsinki declaration and its later amendments. Measurements' reliability was assessed by examining the interobserver and intraobserver reliabilities using interclass and intraclass correlation coefficient. The intraclass correlation coefficient (ICC) was interpreted as poor if it
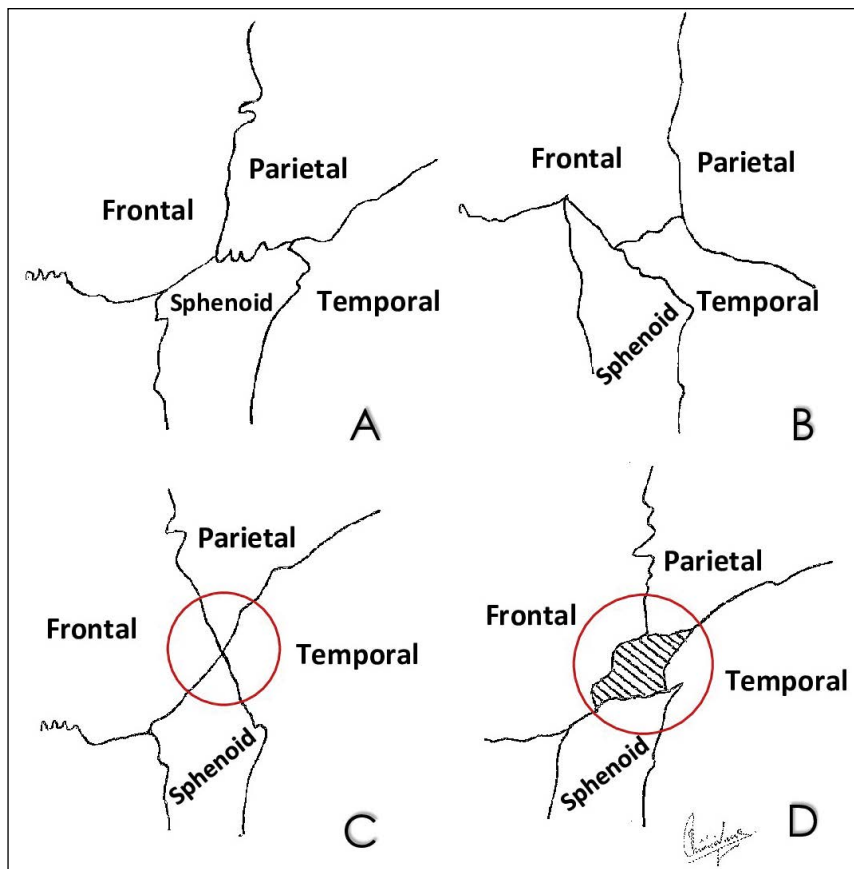
Figure 1. The frequency of various types of pterion based on Murphy's classification as modified accordingly, sphenoparietal (**A**), frontotemporal (**B**), stellate (**C**), and epipteric (**D**).
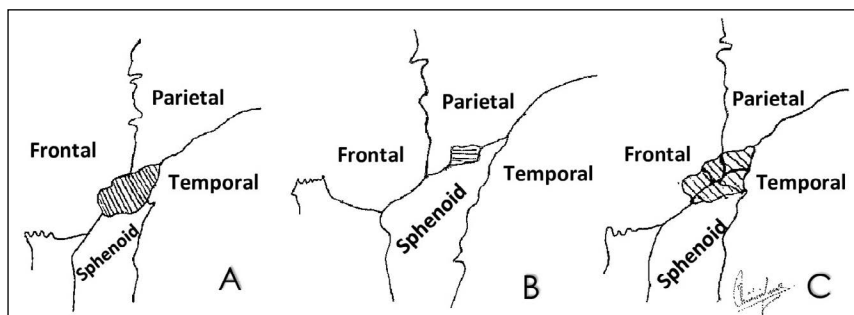

Figure 2. Classification of epipteric bones as quadrisutural (**A**), bisutural (**B**) and multiple (**C**).

was less than 0.4; as marginal when it was between 0.4 and 0.75; and as good when it was greater than 0.75. Descriptive statistics were evaluated for pterion morphometric measurements and their statistical distribution was analysed. Data normality was evaluated with Kolmogorov-Smirnov test. Wilcoxon signed ranks test was applied to investigate side asymmetry, Mann-Whitney U test and t test for gender dimorphism, and Kruskal-Wallis and one-way ANOVA tests to evaluate correlation with age. For all analyses, p value < 0.05 was consid-

ered statistically significant. Statistical analysis was carried out using IBM SPSS Statistics for Windows, version 21.0.

RESULTS

Pterion morphology. All pteria types (SP, FT, St and E) were identified (Fig. 5). SP pterion was the predominant type (58.3%, 105 skulls), St the second most common (25%, 45 skulls) following by the E (15.5%, 28 skulls) and the FT type (1.1%, 2 skulls on the R). Pterional symmetry was detected (57 skulls,
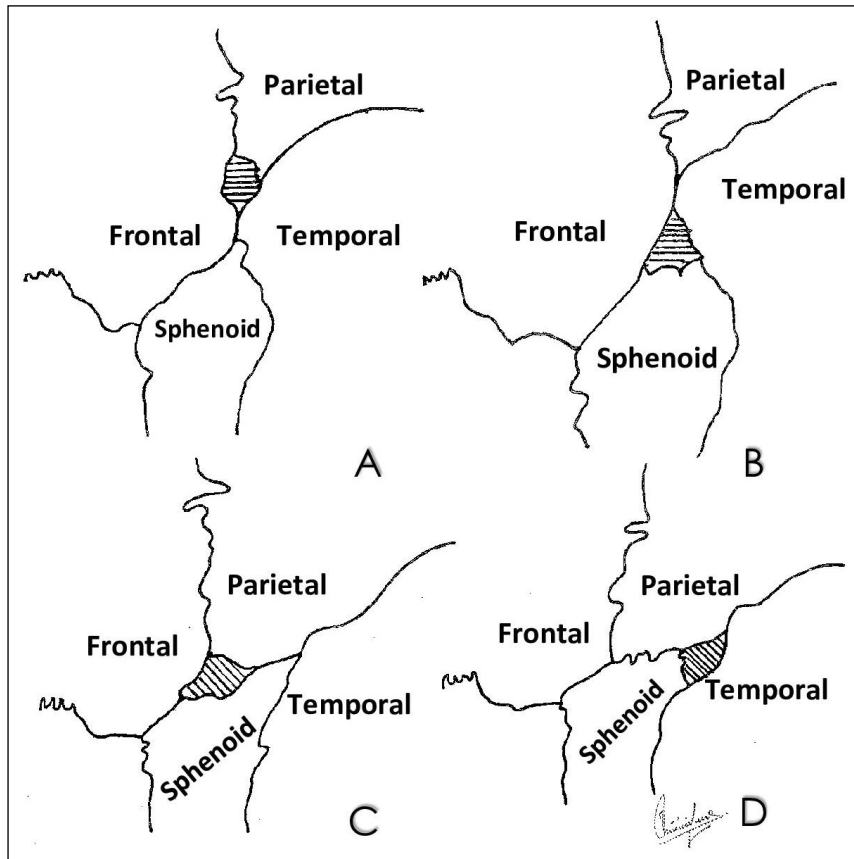
Figure 3. Classification of the trisutural epipteric bones observed according to their location as superior (**A**), inferior (**B**), anterior (**C**) and posterior (**D**).
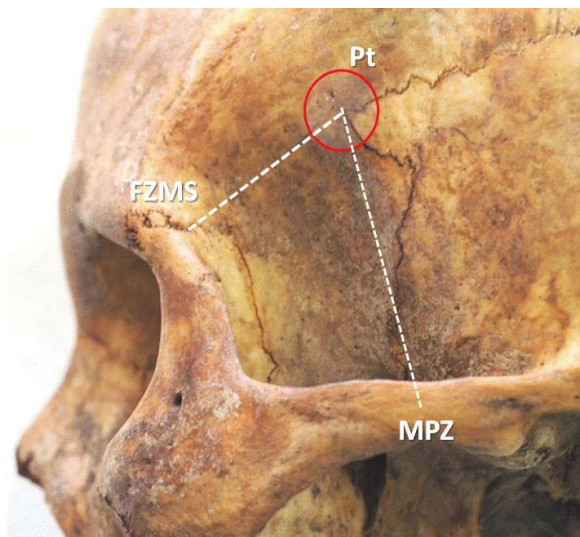

Figure 4. Distances from the pterion (Pt) centre to the midpoint of zygoma (MPZ) and from the Pt centre to the frontozygomatic suture (FZMS).

63.3%) (SP in 43, St in 10 and E in 4 skulls). In asymmetrically pairing skulls, the commonest pterion types were the SP-St (16.7%, 15 skulls) and the SP-E

(12 skulls). Age and gender had no significant impact on pterion type (Table 1).

Epipteric bone morphology. Twenty-eight (15.5%) skulls with EBs were further classified as quadrisutural (FPTS) (Fig. 6A) (35.7%, 10 skulls, 1 skull bilaterally and 9 skulls unilaterally — 5L and 4R), trisutural (Fig. 6B) (57.1%, 16 skulls unilaterally — 11L and 5R), bisutural (3.57%, 1 skull on the L) (Fig. 6C) and multiple EBs (3.57%, 1 skull on the L) (Fig. 6D).

Pterion morphometry. The mean distances (pterion-MPZ) and (pterion-FZMS) were symmetrical (R: 4.13 ± 0.45 cm, L: 4.09 ± 0.47 cm) and (R: 3.47 ± ± 0.61 cm, L: 3.52 ± 0.65 cm). No gender dimorphism was detected for all measured distances, except for the mean distance (pterion-FZMS) on the L (males 3.65 ± 0.72 vs. females 3.37 ± 0.51 cm, p = 0.039) (Table 2). No statistically significant difference was detected for both measurements among different age groups (Table 3). ICC for the interobserver and intraobserver reliabilities was 0.892 and 0.901 for pterion-MPZR, 0.879 and 0.845 for pterion-MPZL, 0.908 and 0.897 for pterion-FZMSR and 0.867 and 0.856 for pterion-FZMSL, respectively.
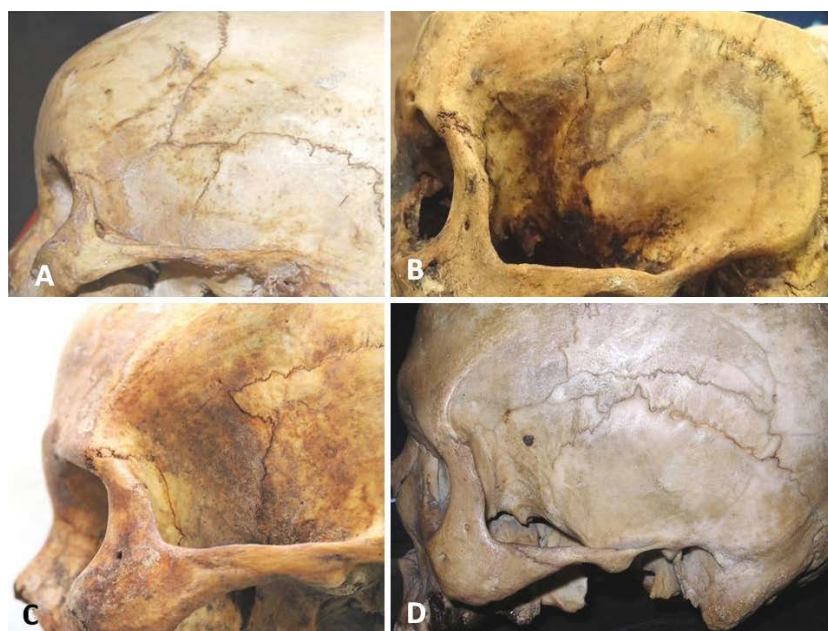
Figure 5. Depiction of various pterion types in Greek skulls, sphenoparietal (**A**), frontotemporal (**B**), stellate (**C**), and epipteric (**D**).

Table 1. Pterion types' frequency observed on the right (R) and left (L) sides of the skulls, combination types on asymmetrical skulls, gender (M — males, F — females) and age impact

Independent variables	Pterion types					
	Sphenoparietal type (SP)	Frontotemporal type (FT)	Epipteric type (E)		Stellate type (S)	
Laterality						
Right side (R)	50 (55.5%)	2 (2.2%)	11 (12.2%)		27 (30%)	
Left side (L)	55 (61.1%)	—	17 (18.9%)		18 (20%)	
Total	105 (58.3%)	2 (1.1%)	28 (15.5%)		45 (25%)	
Combination types of pterion						
SP-SP	**SP-S**	**SP-E**	**S-S**		**E-E, SP-FT**	**E-S**
43 (47.8%)	15 (16.7%)	12 (13.3%)	10 (11.1%)		4 (4.44%)	2 (2.22%)

Gender	Type SP		Type FT		Type E		Type S		P
	R	L	R	L	R	L	R	L	
Males	30 (61.2%)	31 (63.26%)	1 (2.04%)	—	2 (4.08%)	10 (20.4%)	16 (32.65%)	8 (16.32%)	0.187, 0.829
Females	20 (48.78%)	24 (58.53%)	1 (2.43%)	—	9 (21.95%)	7 (17.07%)	11 (26.82%)	10 (24.39%)	
Total	61 sides in M, 44 sides in F		1 side in M, 1 side in F		12 sides in M, 16 sides in F		24 sides in M, 21 sides in F		

DISCUSSION

Pterion morphology. Pterion variable morphology is classified into SP, FT, St and E types and has been extensively studied among different populations (Table 4). In depth knowledge of pterion type and location could be an extremely useful tool in neurosurgical procedures, skull identification and forensics. Yasargil et al. (1975) [58] first introduced the pterional approach and its extension. Pterional approach achieves more accurate and safer outcomes for sellar or suprasellar lesions, brain arterial circula-

tion and lateral sulcus, as well as for aneurysms of the distal internal carotid artery, as the conventional craniotomy was replaced from mini-craniotomy and to contemporary keyhole surgery [12].

Although classical anatomical textbooks describe St pterion as the typical pattern, this pterion was found with a frequency of 25% in the current study, while the predominant pterion was the SP (58.3%), similarly to all the other studies summarized in Table 4. In Asians, the SP pterion frequency ranged between 71.7% and 93.55% and among them Indians have the highest fre-
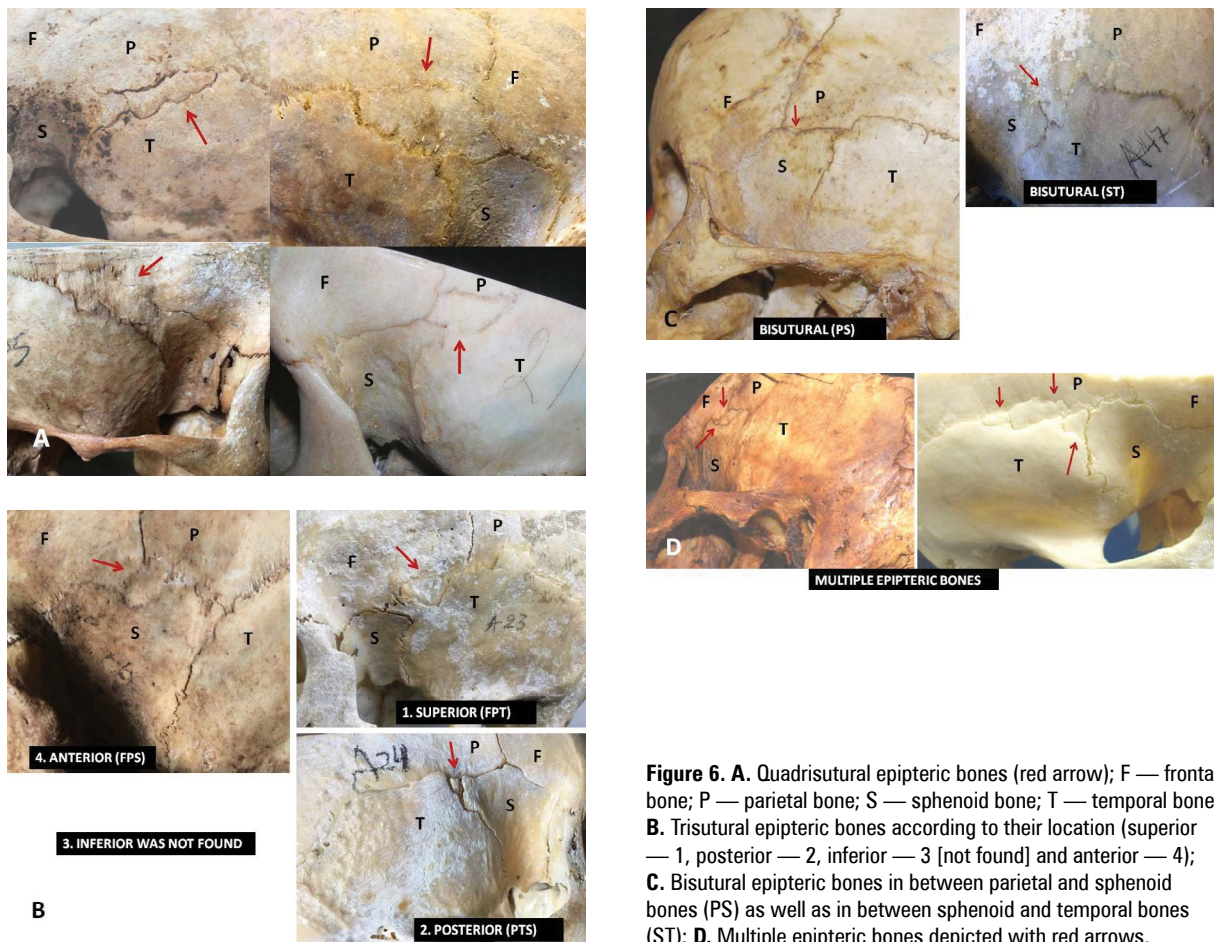
Figure 6. A. Quadrisutural epipteric bones (red arrow); F — frontal bone; P — parietal bone; S — sphenoid bone; T — temporal bone; **B.** Trisutural epipteric bones according to their location (superior — 1, posterior — 2, inferior — 3 [not found] and anterior — 4); **C.** Bisutural epipteric bones in between parietal and sphenoid bones (PS) as well as in between sphenoid and temporal bones (ST); **D.** Multiple epipteric bones depicted with red arrows.

Table 2. Mean ± standard deviation (SD), minimum and maximum distances of pterion (Pt) to the midpoint of zygoma (MPZ) and to the frontozygomatic suture (FZMS) [cm] on the right (R) and left (L) sides of the skulls, male and female incidence

Values	Distances according to side				Distances according to gender							
					Males		Females		Males		Females	
	Pt-MPZ R	Pt-MPZ L	Pt-FZMS R	Pt-FZMS L	Pt-MPZ R	Pt-MPZ L	Pt-MPZ R	Pt-MPZ L	Pt-FZMS R	Pt-FZMS L	Pt-FZMS R	Pt-FZMS L
Mean ± SD	4.13 ± 0.45	4.1 ± 0.47	3.47 ± 0.61	3.52 ± 0.65	4.19 ± 0.44	4.12 ± 0.55	4.04 ± 0.46	4.07 ± 0.42	3.51 ± 0.62	3.65 ± 0.73	3.43 ± 0.59	3.37 ± 0.51
Minimum	2.87	3.11	2.0	1.73	3.29	3.11	2.87	3.16	2.09	1.73	2.0	2.48
Maximum	5.32	5.7	4.81	5.2	5.32	5.7	5.2	5.1	4.63	5.2	4.81	4.78
P	p = 0.608 (symmetry)		p = 0.471 (symmetry)		p = 0.133 right ANOVA, p = 0.619 left ANOVA				p = 0.517 right ANOVA, p = 0.039 left (gender dimorphism)			

quencies (69.25–93.5%) (Southern [80–93.55%] and Western Indians [91.7%] showed higher frequencies compared to Northern [71.7–89.2%]), while Koreans have the lowest (76.5%) [26]. Kenyans had the lowest reported frequency (66%) [38]. The high frequency of SP pterion could be a result of evolution [28], given that it is the commonest type in primates [8, 47].

The second commonest pterion type is the FT [54], with a varying incidence among different populations:

Nigerians (10.1% and 23.6%) [46], Northern Indians (10%) [62], Turkish (10%) [40] and Kenyans 15% [38]. In the current study, the frequency of FT pterion was significantly lower (2.2% on the R), whereas no skull was found with a FT pterion on the L. However, the frequency is similar to those of Indian (Western [31] and Southern [36]) populations. In the present study, St pterion was the second most common type on the R (30%) and L (20%). The frequency of the E type of

Table 3. Mean values standard deviation (SD), minimum and maximum distances (in cm) from the pterion to the midpoint of zygoma (MPZ) and to the frontozygomatic suture (FZMS) on the right (R) and left (L) sides of the skulls among the three age groups

N	Age groups [years]											
	20–39				40–59				Over 60			
	MPZ R	MPZ L	FZMS R	FZMS L	MPZ R	MPZ L	FZMS R	FZMS L	MPZ R	MPZ L	FZMS R	FZMS L
Mean ± SD	4.15 ± 0.43	4.12 ± 0.44	3.40 ± 0.7	3.37 ± 0.75	4.1 ± 0.45	4.1 ± 0.5	3.38 ± 0.66	3.46 ± 0.71	4.13 ± 0.48	4.1 ± 0.48	3.54 ± 0.53	3.62 ± 0.56
Minimum	3.51	3.44	2.0	2.25	3.29	3.11	2.09	1.73	2.87	3.16	2.3	2.4
Maximum	5.2	5.1	4.81	4.69	4.73	4.93	4.32	4.90	5.32	5.70	4.40	5.2
P	p = 0.916 right MPZ, p = 0.522 right FZMS, p = 0.962 left MPZ and p = 0.319 left FZMS											

Table 4. Comparative review of pterion types in different populations among several studies, arranged in order by year of publication

Author(s)	Year	Population	Sample N = skulls (sides)	Type of pterion			
				Sphenoparietal (%)	Frontotemporal (%)	Stellate (%)	Epipteric (%)
Murphy [37]	1956	Australian	368	73.2	7.7	0.7	18.4
Agarwal et al. [2]	1980	North Indian	450 (900 sides)	71.7	3.3	1.7	23.3
Saxena et al. [47]	1988	Indian	72 (144)	82.6	2.8	1.4	13.2
Saxena et al. [47]	1988	Nigerian	40 (80)	81.2	11.3	5.0	2.5
Manjunath and Thomas [31]	1988	South Indian	172	93.5	3.5	2.9	17.3
Matsumura et al. [32]	1991	Japanese	614	82.4	2.9	0.7	14.0
Asala and Mbajiorgu [7]	1996	Nigerian	212	82.1	23.6	—	5.7
Lee et al. [26]	2001	Korean	149	76.5	—	—	40.3
Saxena et al. [46]	2003	North Indian	203	87.7	10.0	5.17	—
Ersoy et al. [14]	2003	Turkish	300 (490 sides)	96.0	3.8	0.2	9.0
Oguz et al. [40]	2004	Turkish	26 (52)	88.0	10.0	—	2.0
Mwachaka et al. [38]	2009	Kenyan	50	66.0	15.0	7.0	12.0
Ilknur et al. [22]	2009	Anatolian	28	89.2	3.6	3.6	3.6
Zalawadia et al. [62]	2009	West. Indian	42	91.7	2.4	1.2	4.7
Hussain Saheb et al. [20]	2010	Indian	125	69.25	17.35	9.7	3.7
Apinhasmit et al. [6]	2011	Thais	268 (536)	81.2	1.1	0.4	17.3
Natekar et al. [39]	2011	Indian	150 bones	85.3	8.0	10.6	51.4
Ma et al. [30]	2012	Australian	76	78.4	5.2	—	16.4
Praba and Venkatramaniah [41]	2012	Indian	50	74.0	3	9.0	14.0
Ukoha et al. [53]	2012	Nigerian	56	75.3	19.5	1.7	3.6
Adejuwon et al. [1]	2013	Nigerian	62	86.1	8.3	5.6	—
Kumar et al. [25]	2013	Indian	40	86.25	11.25	2.5	—
Sudha et al. [51]	2013	South Indian	150	80.0	3.0	5.3	11.3
Aksu et al. [3]	2014	Anatolian	128	85.2	1.1	5.5	8.2
Eboh and Obaroefe [13]	2014	Nigerian	50	83.0	5.0	6.0	6.0
Prasad et al. [42]	2015	North Indian	60	89.2	3.3	5.0	2.5
Modasiya and Kanani [35]	2018	North Indian	220	81	—	10.9	8.1
Present study	2019	Greek	90	58.4	1.1	25	15.5

Table 5. Comparative review of pterion (Pt) distances from the frontozygomatic suture (FZMS) and the midpoint of zygoma (MPZ) among different populations in several studies, in order by year of publication (in cm)

Author(s)	Year	Population	Sample N = skulls (sides)	Distances			
				Pt-FZMS R	Pt-FZMS L	Pt-MPZ R	Pt-MPZ L
Oguz et al. [40]	2004	Turkish male	26 (52)	3.3 ± 0.39	3.44 ± 0.40	4.05 ± 0.39	3.85 ± 0.25
Ilknur et al. [22]	2009	Anatolian	28	3.5 ± 0.5	3.5 ± 0.5	3.8 ± 0.4	3.9 ± 0.4
Mwachaka et al. [38]	2009	Kenyan	50	3.03 ± 0.34*	3.03 ± 0.43*	3.88 ± 0.35*	3.82 ± 0.35*
Bhargavi et al. [10]	2011	Indian	70	3.93 ± 0.37	3.8 ± 0.40	4.52 ± 0.32	4.45 ± 0.35
Ma et al. [30]	2012	Australian	76	2.6 ± 4.0	2.5 ± 4.0	3.4 ± 4.0	3.4 ± 4.0
Ukoha et al. [53]	2012	Nigerian	56	2.74 ± 0.07	2.74 ± 0.06	4.02 ± 0.05	4.01 ± 0.03
Adejuwon et al. [1]	2013	Nigerian	62	3.15 ± 0.67*	3.08 ± 0.80*	3.91 ± 0.58*	3.87 ± 0.63*
Aksu et al. [3]	2014	Anatolian	128	3.18 ± 0.45*	3.14 ± 0.47*	4.0 ± 0.40*	3.98 ± 0.40*
Eboh and Obavoefe [13]	2014	Nigerian	50	3.21 ± 0.26*	3.11 ± 0.22*	4.02 ± 0.29*	3.95 ± 0.33*
Present study	2019	Greek	90	3.47 ± 0.61*	3.52 ± 0.65*	4.13 ± 0.45*	4.09 ± 0.47*

*Studies with modified measurements into [cm] from [mm]; L — left; R — right

Pt is similar to that reported in Indians (11.8%) [8] and Kenyans (12%) [38].

Epipteric bone morphology. Ranke (1898) [43] proposed the most suitable hypothesis concerning the EBs occurrence. He supported that an EB appears in case of fusion failure of the postero-superior border of the greater sphenoidal wing (via its separate ossification centre) with the rest part of the greater wing, during the 4th month of the intrauterine life. The EBs occurrence and laterality is variable among different populations, as the result of genetic and epigenetic factors combination [9, 34, 45]. In the current study, among the 28 skulls with EBs (31.1%), trisutural EBs were found in 16 skulls (17.7%), quadrisutural in 10 skulls (11.1%), bisutural and multiple EBs in a single skull (1.11%) per each, on the L. Among Indian populations, a wide range of EBs frequency was reported ranging between 2.5% to 24% in Northern [42] and Karnataka Indians [5]. Saxena et al. (2003) [46] found the lowest frequency of EBs in Nigerians (3.79%), contrariwise to the present study reporting the highest frequency of 31.1%. Neurosurgeons should be aware of EBs occurrence and variant distribution, since their presence when making burr holes over the pterional area may lead to complications.

In such cases caution must be made, as the most anterior point of junction of four bones may be mistaken to be the pterion centre resulting in orbital penetration. High index of suspicion is required from both radiologists and neurosurgeons, since in pterional trauma the EBs may be mistaken as a skull fracture in X-rays [9, 62].

Pterion morphometry. The mean distances (pterion-MPZ) and (pterion-FZMS) in different populations are summarized in Table 5. In the present study, the mean (pterion-MPZ) distance was 4.13 ± 0.45 cm on the R and 4.09 ± 0.49 cm on the L, similarly to Nigerian (4.02 ± 0.05 cm on the R and 4.01 ± 0.03 cm on the L) [53] and Turkish population (4.05 ± 0.39 cm on the R and 3.85 ± 0.25 cm on the L) [40] (4.0 ± ± 0.40 cm on the R and 3.98 ± 0.40 cm on the L) [3]. A lower mean distance has been reported in Australian (3.4 ± 4.0 cm) [30] and Anatolian (3.8 ± 0.4 cm) populations [22]. However, a higher mean distance has been reported in Indians (4.52 ± 0.32 cm on the R and 4.45 ± 0.35 cm on the L) [10].

In the present study, the pterion was detected behind FZMS up to 3.51 cm in males and up to 3.39 cm in females. This slight difference may be explained by the larger male skulls. The mean distance (pterion-FZMS) was 3.47 ± 0.61 cm on the R and 3.52 ± ± 0.65 cm on the L. The highest mean values were reported in Indians [10] (3.93 ± 0.37 cm on the R and 3.80 ± 0.40 cm on the L) and the lowest in Australians (2.6 ± 4.0 cm on the R and 2.5 ± 4.0 cm on the L) [30] and Nigerians (2.74 ± 0.07 cm on the R and 2.74 ± ± 0.06 cm on the L) [53]. Since significant differences were observed for pterion-MPZ and pterion-FZMS distances among various studies' populations, the pterion topography may vary due to epigenetic, environmental factors and evolution [10, 21, 44].

Pterion could be safely used as a surface landmark in neurosurgical approaches and interventions [40], even in neonates [14]. Its clinical importance derives from the fact that it overlies the anterior (frontal)

branch of the middle meningeal artery, which is the most frequent source of acute traumatic epidural haematoma [30]. The knowledge of pterional typical anatomy, as well as its variants is important to neurosurgeons during pterional craniotomy [18], especially during extradural haematoma evacuation [49]. If the ophthalmic artery originates from the frontal branch of the middle meningeal artery [27, 48], pterional craniotomy could cause ophthalmic artery occlusion, which may end up in blindness [48]. Pterion is also used in various neurosurgical approaches treating anterior and middle skull base lesions [33], such as anterior and posterior cerebral circulation lesions, middle cerebral artery or upper basilar complex aneurysms, optic nerve and sellar and parasellar area lesions, sphenoidal wing, cavernous sinus, orbit, anterior and medial temporal lobe, midbrain, and posterior-inferior frontal lobe tumours, as well as cerebral tumours [4, 12, 15, 17, 19, 52, 57–61].

Information obtained from the current study may be of significant value in preoperative planning and perioperative navigation. Furthermore, recognition of the possible variants in location, morphology and morphometry of the pterion, as well as EBs occurrence may render pterional craniotomy safer among different population groups.

CONCLUSIONS

All pteria types were found in the current study and SP pterion was the predominant one, while FT was the less frequently observed. Pterional symmetry existed in the majority of cases, while gender and age had no significant impact on pterion type. EBs were observed in 15.5% of the skulls, and in the majority of the cases were tri- and quatrisutural. The distances of the pterion from MPZ and FZMS were symmetrical and gender dimorphism was found only in pterion-FZMS distance on the L. Information obtained from the current study may be of significant value in preoperative planning and perioperative navigation. Such data are especially mandatory to achieve the optimum craniotomy when neuronavigation is not available. Based on osseous landmarks, the neurosurgeon should be familiar with the sutural junctions, as well as with EBs variants which may be complicate the orientation. Furthermore, recognition of possible variants in pterion location, morphology and morphometry, as well as possible EBs occurrence may render pterional craniotomy safer among different population groups.

REFERENCES

1. Adejuwon SA, Olopade FE, Bolaji M. Study of the location and morphology of the pterion in adult nigerian skulls. ISRN Anat. 2013; 2013: 403937, doi: 10.5402/2013/403937, indexed in Pubmed: 25938098.
2. Agarwal AK, Singh PJ, Gupta SC, et al. Pterion formation and its vriations in the skulls of Northern India. Anthropol Anz. 1988; 38(4): 265–269.
3. Aksu F, Akyer SP, Kale A, et al. The localization and morphology of pterion in adult West Anatolian skulls. J Craniofac Surg. 2014; 25(4): 1488–1491, doi: 10.1097/SCS.0000000000000790, indexed in Pubmed: 25006922.
4. Al-Mefty O. Supraorbital-pterional approach to skull base lesions. Neurosurgery. 1987; 21(4): 474–477, doi: 10.1227/00006123-198710000-00006, indexed in Pubmed: 3683780.
5. Annam S, Bajpe R. A prospective anatomic study of epipteric bones in dry human skulls of Karnataka. Int J Biomed Adv Res. 2016; 7(6): 262, doi: 10.7439/ijbar.v7i6.3301.
6. Apinhasmit W, Chompoopong S, Chaisuksunt V, et al. Anatomical consideration of pterion and its related references in Thai dry skulls for pterional surgical approach. J Med Assoc Thai. 2011; 94(2): 205–214, indexed in Pubmed: 21534368.
7. Asala SA, Mbajiorgu FE. Epigenetic variation in the Nigerian skull: sutural pattern at the pterion. East Afr Med J. 1996; 73(7): 484–486.
8. Ashley-Montagu MF. The anthropological significance of the pterion in the primates. Am J Phys Anthropol. 1933; 18(2): 159–336, doi: 10.1002/ajpa.1330180216.
9. Bellary SS, Steinberg A, Mirzayan N, et al. Wormian bones: a review. Clin Anat. 2013; 26(8): 922–927, doi: 10.1002/ca.22262, indexed in Pubmed: 23959948.
10. Bhargavi C, Saralaya V, Saralaya V, et al. Pterion: a site for neurosurgical approach. Int J Biomed Res. 2012; 2(12), doi: 10.7439/ijbr.v2i12.207.
11. Broek A. On pteric sutures and pteric bones in the human skull. Kon Acad Wetenesch Amsterdam. Proc Sect Sci. 1914; 6: 634–639.
12. Cheng WY, Lee HT, Sun MH, et al. A pterion keyhole approach for the treatment of anterior circulation aneurysms. Minim Invasive Neurosurg. 2006; 49(5): 257–262, doi: 10.1055/s-2006-954575, indexed in Pubmed: 17163337.
13. Eboh D, Obaroefe M. Morphometric study of pterion in dry human skull bones of nigerians. Int J Morphol. 2014; 32(1): 208–213, doi: 10.4067/s0717-95022014000100035.
14. Ersoy M, Evliyaoglu C, Bozkurt MC, et al. Epipteric bones in the pterion may be a surgical pitfall. Minim Invasive Neurosurg. 2003; 46(6): 363–365, doi: 10.1055/s-2003-812434, indexed in Pubmed: 14968406.

15. Fahlbusch R, Schott W. Pterional surgery of meningiomas of the tuberculum sellae and planum sphenoidale: surgical results with special consideration of ophthalmological and endocrinological outcomes. J Neurosurg. 2002; 96(2): 235–243, doi: 10.3171/jns.2002.96.2.0235, indexed in Pubmed: 11838796.

16. Feng Wf, Qi St, Huang Sp, et al. [Surgical treatment of anterior circulation aneurysm via pterion keyhole approach]. Di Yi Jun Yi Da Xue Xue Bao. 2005; 25(12): 1546–1551, indexed in Pubmed: 16361160.

17. Figueiredo EG, Deshmukh P, Nakaji P, et al. The minipterional craniotomy: technical description and anatomic assessment. Neurosurgery. 2007; 61(5 Suppl 2): 256–64; discussion 264, doi: 10.1227/01.neu.0000303978.11752.45, indexed in Pubmed: 18091240.

18. Havaldar P, B.N S, Saheb S, et al. Morphological study on shapes of pterion. Int J Anat Res. 2015; 3(4): 1555–1558, doi: 10.16965/ijar.2015.279.

19. Hendricks BK, Spetzler RF. Pterional craniotomy for anterior temporal artery to middle cerebral artery bypass: 2-dimensional operative video. Oper Neurosurg (Hagerstown). 2020; 19(1): E43, doi: 10.1093/ons/opaa053, indexed in Pubmed: 32171008.

20. Hussain-Saheb S, Haseena S, Prasanna LC. Unusual wormian bones at pterion-three case reports. J Biomed Sci Res. 2010; 2(2): 116–118.

21. Ikeda T, Nakamura M, Itoh M. Sex differences in the zygomatic angle in japanese patients analyzed by MRI with reference to Moiré fringe patterns. Aesthetic Plast Surg. 1999; 23(5): 349–353, doi: 10.1007/s002669900297, indexed in Pubmed: 10541849.

22. Ilknur A, Mustafa K, Sinan B. A comparative study of variation of the pterion of human skulls from 13th and 20th century anatolia. Int J Morphol. 2009; 27(4), doi: 10.4067/s0717-95022009000400051.

23. Kalthur S, Vangara S, Kiruba L, et al. Metrical and non-metrical study of the pterion in South Indian adult dry skulls with notes on its clinical importance. Marmara Med J. 2017; 30(1): 30–30, doi: 10.5472/marumj.299387.

24. Khatri CR, Gupta DS, Soni DJS. Study of pterion and incidence of epipteric bones in dry human skulls of Gujarat. NJIRM. 2012; 3(2): 57–60.

25. Kumar S, Anurag A, Munjal S, et al. Pterion its location and clinical implications: a study compared. J Evol Med Dent Sci. 2013; 2(25): 4599–4608, doi: 10.14260/jemds/885.

26. Lee U, Park D, Kwon S, et al. Morphological analysis of the pterion in Korean. J Phys Anthropol. 2001; 14(4): 281, doi: 10.11637/kjpa.2001.14.4.281.

27. Liu Q, Rhoton A. Middle meningeal origin of the ophthalmic artery. Neurosurgery. 2001; 49(2): 401–407, doi: 10.1227/00006123-200108000-00025.

28. Liu YH, Tang Z, Kundu RK, et al. Msx2 gene dosage influences the number of proliferative osteogenic cells in growth centers of the developing murine skull: a possible mechanism for MSX2-mediated craniosynostosis in humans. Dev Biol. 1999; 205(2): 260–274, doi: 10.1006/dbio.1998.9114, indexed in Pubmed: 9917362.

29. Lovejoy CO, Meindl RS, Mensforth RP, et al. Multifactorial determination of skeletal age at death: a method and blind tests of its accuracy. Am J Phys Anthropol. 1985; 68(1): 1–14, doi: 10.1002/ajpa.1330680102, indexed in Pubmed: 4061595.

30. Ma S, Baillie LJM, Stringer MD. Reappraising the surface anatomy of the pterion and its relationship to the middle meningeal artery. Clin Anat. 2012; 25(3): 330–339, doi: 10.1002/ca.21232, indexed in Pubmed: 21800374.

31. Manjunath KY, Thomas IM. Pterion variants and epipteric ossicles in South Indian skulls. J Anat Soc India. 1993; 42: 85–94.

32. Matsumura G, Kida K, Ichikawa R, et al. Pterion and epipteric bones in jpanese adults and fetuses, with special reference to their formation vriations. Kaibogaku Zasshi. 1991; 66(5): 462–471.

33. McLaughlin N, Cutler A, Martin NA. Technical nuances of temporal muscle dissection and reconstruction for the pterional keyhole craniotomy. J Neurosurg. 2013; 118(2): 309–314, doi: 10.3171/2012.10.JNS12161, indexed in Pubmed: 23140151.

34. Mishra A, Mishra P, Bezbaruah N, et al. Study of variations of bony pattern and presence of wormian bone at pterion in dry human skulls. Int J Biomed Res. 2014; 5(11): 668–670, doi: 10.7439/ijbr.v5i11.748.

35. Modasiya UP, Kanani SD. Study of pterion and asterion in adult human skulls of north Gujarat region. Ind J Clin Anat Physiol. 2020; 5(3): 353–356, doi: 10.18231/2394-2126.2018.0082.

36. Moore KL, Dalley AF. Clinical Oriented Anatomy. 5th ed. Lippincott Williams & Wilkins, Philadelphia 2006: 887–903.

37. Murphy T. The pterion in the Australian aborigine. Am J Phys Anthropol. 1956; 14(2): 225–244, doi: 10.1002/ajpa.1330140218, indexed in Pubmed: 13362489.

38. Mwachaka PM, Hassanali J, Odula P. Sutural morphology of the pterion and asterion among adult Kenyans. Braz J Morphol Sci. 2009; 26: 4–7.

39. Natekar P, Natekar S, DeSouza F. Pterion: an anatomical variation and surgical landmark. Ind J Otol. 2011; 17(2): 83, doi: 10.4103/0971-7749.91045.

40. Oguz O, Sanli SG, Bozkir MG, et al. The pterion in Turkish male skulls. Surg Radiol Anat. 2004; 26(3): 220–224, doi: 10.1007/s00276-003-0210-2, indexed in Pubmed: 14648037.

41. Praba AMA, Venkatramaniah C. Morphometric study of different types of Pterion and its relation with middle meningeal artery in dry skulls of Tamil Nadu. JPBMS. 2012; 21(4): 1–4.

42. Prasad H, Bezbaruah NK, Mishra A, et al. Morphometric analysis of pterion: A clinic-anatomical study in north Indian dry skulls. Inn J Med Health Sci. 2015; 5(5): 201–205, doi: 10.15520/ijmhs.2015.vol5.iss5.91..

43. Ranke J. Der Stirnfortsatz der Schlafenschuppe bei den Primaten — Sitz, Mathem. Phys Cl Akad Wiss Munchen. 1898; 27: 227–270.

44. Ruiz C, Souza G, Scherb T, et al. Anatomical variations of pterion: analysis of the possible anatomical variations of pterion in human skulls. J Morphol Sci. 2018; 33(04): 200–204, doi: 10.4322/jms.094615.

45. Sanchez-Lara PA, Graham JM, Hing AV, et al. The morphogenesis of wormian bones: a study of craniosynostosis and purposeful cranial deformation. Am J Med Genet Part A. 2007; 143A(24): 3243–3251, doi: 10.1002/ajmg.a.32073, indexed in Pubmed: 18000970.

46. Saxena RC, Bilodi AKS, Mane SS, et al. Study of pterion in skulls of Awadh area — in and around Lucknow. Kathmandu Univ Med J (KUMJ). 2003; 1(1): 32–33, indexed in Pubmed: 16340258.

47. Saxena SK, Jain SP, Chowdhary DS. A comparative study of pterion formation and its variations in the skulls of Nigerians and Indians. Anthropol Anz. 1988; 46(1): 75–82, indexed in Pubmed: 3389768.

48. Shima K, Kawasaki T, Shimizu A, et al. An Ophthalmic Artery Occlusion after a Craniotomy Using the Pterional Approach : A Report of Three Cases, One resulting in Blindness. Jpn J Neurosurg. 1995; 4(2): 163–169, doi: 10.7887/jcns.4.163.

49. Shimizu S, Hagiwara H, Utsuki S, et al. Bony tunnel formation in the middle meningeal groove: an anatomic study for safer pterional craniotomy. Minim Invasive Neurosurg. 2008; 51(6): 329–332, doi: 10.1055/s-0028-1085430, indexed in Pubmed: 19061142.

50. Standring S, Ellis H, Healy JC, Johnson D. Gray's anatomy, 39th ed. Elsevier Churchill Livingstone, London 2005: 442–471.

51. Sudha R, Sridevi C, Ezhilarasi M. Anatomical variations in the formation of pterion and asterion in south Indian population. Int J Cur Res Rev. 2013; 5(09): 92–101.

52. Turazzi S, Cristofori L, Gambin R, et al. The pterional approach for the microsurgical removal of olfactory groove meningiomas. Neurosurgery. 1999; 45(4): 821–5; discussion 825, doi: 10.1097/00006123-199910000-00016, indexed in Pubmed: 10515476.

53. Ukoha U, Oranusi CK, Okafor JI, et al. Anatomic study of the pterion in Nigerian dry human skulls. Niger J Clin Pract. 2013; 16(3): 325–328, doi: 10.4103/1119-3077.113455, indexed in Pubmed: 23771454.

54. Vasudha TK, Divya Shanthi D, Sadashivana G, et al. Study of morphology of pterion and its clinical implications. Int J Anat Res. 2017; 5(4.3): 4674–4678, doi: 10.16965/ijar.2017.434.

55. Wang Q, Opperman LA, Havil LM, et al. Inheritance of sutural pattern at the pterion in Rhesus Monkey skulls. Anat Rec Discov Mol Cell Evol Biol. 2006; 288: 1042–1049.

56. Williams L, Bannister L, Berry M, Collins P, Dyson M, Dussek E. Gray's anatomy. 38th ed. Churchill Livingston, London 1988.

57. Yasargil M. Interfascial pterional (frontotemporosphenoidal) craniotomy. Microneurosurg. 1984; 1: 217–220.

58. Yasargil M, Fox J, Ray M. The operative approach to aneurysms of the anterior communicating artery. Adv Tech Stand Neurosurg. 1975; 2: 113–170.

59. Yasargil MG, Antic J, Laciga R, et al. Microsurgical pterional approach to aneurysms of the basilar bifurcation. Surg Neurol. 1976; 6(2): 83–91, indexed in Pubmed: 951657.

60. Yaşargil MG, Boehm WB, Ho RE. Microsurgical treatment of cerebral aneurysms at the bifurcation of the internal carotid artery. Acta Neurochir (Wien). 1978; 41(1-3): 61–72, doi: 10.1007/BF01809137, indexed in Pubmed: 665339.

61. Yasargil MG, Fox JL. The microsurgical approach to intracranial aneurysms. Surg Neurol. 1975; 3(1): 7–14, indexed in Pubmed: 1111150.

62. Zalawadia A, Vadgama J, Ruparelia S, et al. Morphometric study of pterion in dry skull of Gujarat Region. NJIRM. 2010; 1(14): 25–29.

ORIGINAL ARTICLE

Age-related histological changes in rat tibia

Q. Ni[1], H. Chen[1], Y. Tan[1], J. Qin[1], H. Wang[2], L. Chen[1]

[1]Department of Orthopaedic Surgery, Zhongnan Hospital of Wuhan University, Hubei Provincial Key Laboratory of Developmentally Originated Disease, Wuhan, China
[2]Department of Pharmacology, Basic Medical School of Wuhan University, Hubei Provincial Key Laboratory of Developmentally Originated Disease, Wuhan, China

Background: At present, studies on osteochondral morphogenesis only focus on a certain period of time or only provide a pattern diagram, but lack of dynamic tracking observation from the initiation of development to maturity. This study was aimed to dynamically observe the changes of skeleton morphology and structure from embryo to adult, to provide research data for enriching the knowledge of bone and cartilage tissue structure.
Materials and methods: In the intrauterine experiment, 5 normal pregnant Wistar rats were sacrificed under anaesthesia at gestational day (GD) 14, 17, 20, respectively. One of their offspring was randomly selected, and a total of 5 offspring were obtained at each time point. In the postnatal experiment, on the 7th and 10th day after birth and at postnatal weeks (PW) 2, 3, 6, 12, 28, 5 offspring rats from 5 different pregnant Wistar rats were randomly selected and sacrificed under anaesthesia at each time point. After obtaining the above offspring, the soft tissue was removed, and the tibia of hind limbs was retained for paraffin-embedded section. After stained with Safranin-O-fast-green and haematoxylin, the morphological development of the tibia was observed under an optical microscope.
Results: At GD14, there was no obvious joint space, the whole hind limb was cartilage and bone tissue was not visible. At GD17, visible joint space was seen and the chondrocytes in the centre region appeared to hypertrophy. At GD20, the primary ossification centre was obvious, and a typical epiphysis growth plate structure could be seen. On the 7th day after birth, the chondrocytes in the centre of epiphysis cartilage were hypertrophic and differentiated, the cartilage canal grows from the cartilage surface toward the centre of the epiphysis cartilage, at postnatal day 14, the secondary ossification centre was formed. At this time, the tibia had typical morphological characteristics of the metaphysis, however, there was no obvious layered structure of articular cartilage; the stratified structure of articular cartilage could be seen at PW6, but its mature marker (tidemark) was still not visible; however, at PW12, typical 4 layers of articular cartilage appeared, and the tidemark was visible. The growth plates were clearly visible at PW2, 6 and 12. At PW28, growth plates could still be observed, but its morphology is abnormal.
Conclusions: Our results, for the first time, dynamically observed the morphological changes of osteochondral at critical period of development from embryo to adult, especially the process of cartilage canal participating in the formation of secondary ossification centre. (Folia Morphol 2021; 80, 4: 1005–1019)

Key words: osteochondroplasia, cartilage anlage, primary ossification centre, secondary ossification centre, cartilage canal

Address for correspondence: Dr. L.B. Chen, Department of Orthopaedic Surgery, Zhongnan Hospital of Wuhan University, Wuhan 430071, China, tel: +86-13618610516, fax: +86 2767812892, e-mail: lbchen@whu.edu.cn; Dr. H. Wang, Department of Pharmacology, Basic Medical School of Wuhan University, Wuhan 430071, China, tel: +86-13627232557, fax: +86 2768758665, e-mail: wanghui19@whu.edu.cn

INTRODUCTION

Bone and cartilage are important structures which form the framework of the body, supporting, protecting and moving the body. Bones in different parts of the skeleton develop through two distinct processes [10], intramembranous ossification and intracartilaginous ossification. In intramebranous ossification, bones ossify directly without passing from the connective tissue structure to the cartilage tissue. In the intracartilaginous ossification type, which occurs in the axial and appendicular skeleton of vertebrates, the bones first turn into hyaline cartilage tissue and then into bone tissue [26]. Intracartilaginous ossification is initiated during foetal life, and continues until growth ceases in early adulthood. Limb development begins as a mesenchymal cell proliferation from the lateral plate mesoderm. These cells give rise to a circular bulge, known as the limb bud. Mesenchymal cells in the limb bud first undergo cellular condensation. This condensation results in a dramatically increased cell density that is a prerequisite for chondrogenesis. Following condensation, cells at the centre begin to differentiate into the chondrogenic lineage and turn the mesenchymal condensation into a primordial cartilage anlage. The cartilage anlage represents the moulds of the future skeletal elements; the entire model of the bone is still in a cartilage phase. When mesenchymal condensations form, several layers of mesenchymal cells at the boundary become fibroblast-like cells and eventually establish the perichondrium [30]. Shortly after the initiation of the cartilage anlage, chondrocytes at the centre of individual cartilage anlages undergo hypertrophy. These pre- and early hypertrophic chondrocytes in the cartilage anlage secret Indian hedgehog protein to directly stimulate differentiation of their surrounding perichondrial cells into osteoblast lineage cells [23], including osteoprogenitors and osteoblasts, these secrete a characteristic matrix, forming a bone collar [20]. The bone collar surrounding the central region of cartilage anlage and eventually establishes the midshaft (diaphyseal) cortical bone. Blood vessels, osteoclasts, as well as bone marrow and osteoblast precursors then invade the model from the bone collar and proceed to form the primary ossification centre (POC) [36]. In long bones, the secondary ossification centre (SOC) subsequently forms shortly after birth at each end of the cartilage anlage, leaving a cartilaginous growth plate between the POC and SOC, as well as the prospective permanent articular cartilages at each end of the bone [26]. The growth plate is responsible for longitudinal growth of bones. Skeletal maturity occurs when the expanding POC meets the SOC, thus obliterating the growth plate [9].

As an important tissue type in vertebrates, chondrocytes are involved in the whole process of the genesis and development of bone and cartilage system [30], so it is of great significance to study the biological mechanism of bone growth and development to explore the morphological characteristics and rules of chondrocyte differentiation in the process of osteochondrogenesis, and to uncover the pathogenesis of skeletal system diseases. However, there are few studies on characteristics of chondrocyte changes during chondrogenic formation, differentiation and intracartilaginous ossification.

In bone research, rat is the most important model system at present, rat is more similar to humans in their philicity and their skeletal phylogenetic processes are more similar, so it remains the main animal model [2, 4]. Therefore, the purposes of the present study were to determine the sequential change of histologic events involved in the formation of long bones and their epiphysis from the embryonic limb-bud stage to skeletal maturity, to classify the various stages, and to define the time at which each event occurs in the rat. This study can provide research data for enriching the knowledge of bone and cartilage tissue structure. It also has positive significance for the healthy development of bone during the development period.

MATERIALS AND METHODS

Chemicals and reagents

Fast green (catalogue no. 2353-45-9; Sigma-Aldrich, St. Louis, MO, USA) and Safranin-O (catalogue no. CI-50240; Junsei Chemical Co. Tokyo, Japan); haematoxylin-eosin (H&E; Sigma).

Animals and treatment

Specific pathogen free Wistar rats (female: 180– –220 g, male: 260–300 g) were obtained from the Experimental Centre of Hubei Medical Scientific Academy (No. 2010-2012, Hubei, China). This experiment was performed in the Centre for Animal Experimentation of Wuhan University (Wuhan, China), which has been accredited by the Association for Assessment and Accreditation of Laboratory Animal Care International (AAALAC International). All animal experimental procedures were approved by the Chinese Animal Welfare

Committee and performed in accordance with their Guidelines for the Care and Use of Laboratory Animals.

Animals were housed (room temperature: 18–22°C; humidity: 40–60%), acclimated, and mated. Upon confirmation of mating by the appearance of sperm in a vaginal smear, the day was taken as gestational day (GD) 0. Pregnant rats were transferred to individual cages.

In the intrauterine experiment, 5 normal pregnant Wistar rats with 10–14 live foetuses were anesthetized with isoflurane and euthanized on GD 14, 17, 20, respectively. One of their offspring was randomly selected, and a total of 5 offspring were obtained at each time point. For experiments on postnatal rats, 5 pregnant rats were kept until normal delivery on GD21. On postnatal day 1 (PD1), the numbers of pups were normalised to 8 pups per litter to assure adequate and standardised nutrition until weaning (postnatal week 4, PW4). On the 7th and 10th day after birth and at PW 2, 3, 6, 12, 28, 5 offspring rats from 5 different pregnant Wistar rats were randomly selected and sacrificed under anaesthesia at each time point. After obtaining the above offspring, the soft tissue was removed, and the tibias of hind limbs were retained and fixed in 4% paraformaldehyde solution for 24 h before being decalcified in EDTA, dehydrated in alcohol and embedded in paraffin until further histological examination.

Histological assays

Foetal rat tibia specimens were fixed in 4% paraformaldehyde at pH 7.4 for 3 days and then processed for paraffin embedding. Adult knee joints were fixed in 4% paraformaldehyde, decalcified in a 20% ethylenediamine tetraacetic acid solution for 21 days, and then embedded in paraffin wax. After each paraffin wax was cut to the bone tissue layer, 5 layers were removed and the subsequent layers were retained for staining. The tibias were sectioned sagittally at a thickness of 5 μm. Safranin-O-fast green staining and H&E staining were performed by standard procedures [27]. The photo images of histology were captured using the Nikon NIS Elements BR light microscope (Nikon, Tokyo, Japan).

RESULTS

Dynamic development of osteochondral from intrauterine to postnatal

As shown in Figure 1, at GD14, the mesenchymal cells aggregate to form a limb bud, which was a car-

tilage anlage. There was no joint space at both ends of the cartilage anlages, the chondrocytes homing in the centre of cartilage anlages where the POC is about to form. At GD17, the homing chondrocytes in the centre of cartilage anlages differentiated into hypertrophic chondrocytes, the joint space was clearly visible, but the morphological difference between articular cartilage and epiphysis cartilage was not obvious. At GD20, the POC expanded and the typical epiphysis growth plate cartilage structure was formed at both ends. 10–14 days after birth, the chondrocytes in the central area of the epiphysis cartilage at both ends of the cartilage anlages were hypertrophic and apoptotic, several cartilage canals elongated from different areas of epiphysis cartilage toward the location where the SOC would appear. At PW2, the SOC could be clearly identified. At PW3, the cartilage canals disappeared, forming a typical bone shape during development. At PW6, the articular cartilage had not formed the standard 4-layer structure at maturity, and the tidemark and subchondral bone were not visible. At PW12, articular cartilage was mature with a typical 4-layer structure, the tidemark and subchondral bone could be clearly identified. As the growth plate of rats existed for life, the residual growth plate could still be seen at PW28.

Morphological overview of cartilage anlages and primary ossification centre

GD14, the cartilage anlages formed by the aggregation of mesenchymal cells was clearly visible, all of it was cartilage, bone tissue was not visible, and all the stains were Safranin-O-fast-green without staining. At this time, there was no obvious joint space, the position where the joint will form was still the dense mesenchymal cells, undifferentiated chondrocytes were the main cells in the cartilage anlages. The chondrocytes in the centre of the cartilage anlages became bigger and formed clusters, the intercellular space was larger than that at both ends, and begin to differentiate into prehypertrophic chondrocytes.

GD17, the joint space at both ends of the cartilage anlages was clearly visible and the anatomical structure of the tibia was clearly defined, the whole tibia was still cartilage, and bone tissue was not visible, all of it was stained with Safranin-O. However, at this time, the volume of the middle segment cells of cartilage anlages increased, showing the typical morphology of hypertrophic chondrocytes, indicating that the
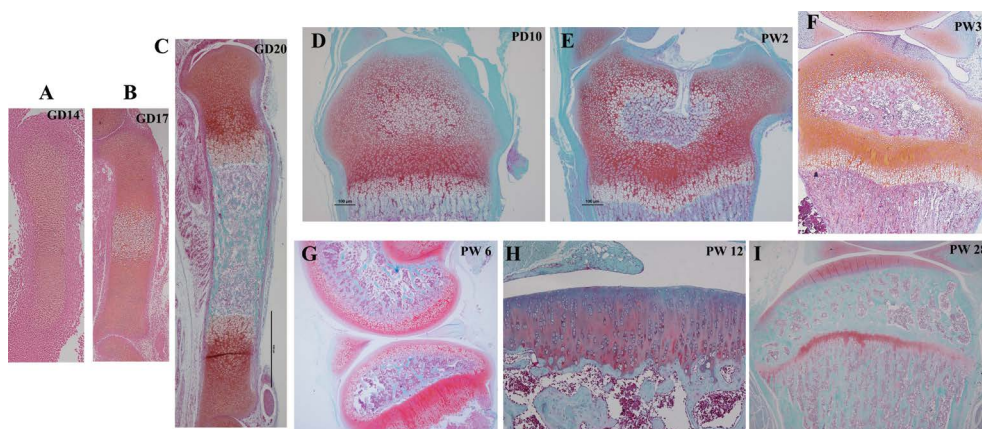
Figure 1. Safranine and fast green double dyeing demonstrates the dynamic development process of osteochondral from intrauterine to postnatal; **A.** Tibia of offspring rats at gestational day (GD) 14, cartilage anlages is present; **B.** Tibia of offspring rats at GD17, primary ossification centres appear; **C.** Tibia of offspring rats at GD20; **D.** Development of epiphysis at postnatal weeks (PW) 10; **E.** Development of secondary ossification centre formation at PW2; **F.** Development of secondary ossification centre formation at PW3; **G.** Development of articular cartilage at PW6; **H.** Development of articular cartilage at PW12; **I.** The whole osteochondral was observed at PW28.
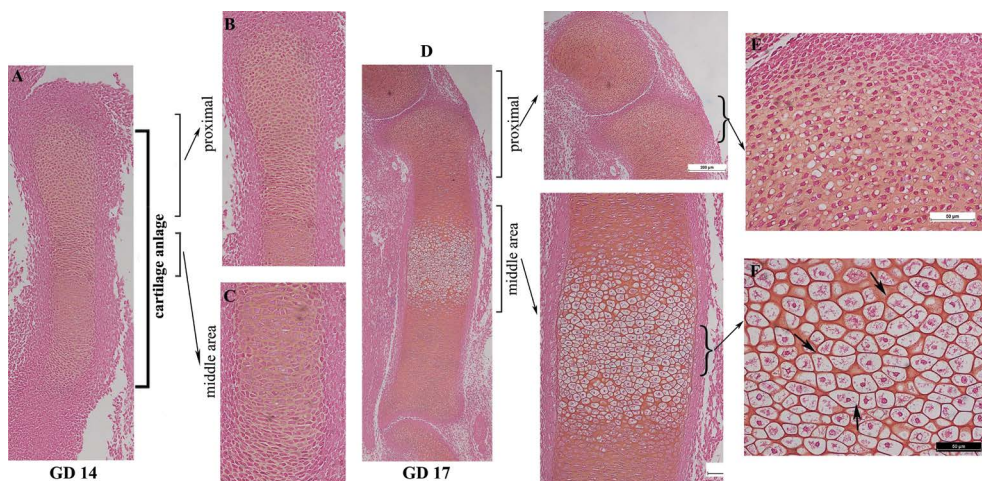
Figure 2. Morphology of the tibial cartilage anlage at gestational day (GD) 14, 17; **A.** Gross morphology of cartilage anlage at GD14; **B.** Development of cartilage anlage in the proximal at GD14; **C.** Development of the middle segment of cartilage anlage at GD14; **D.** Gross morphology of cartilage anlage at GD17; **E.** Development of cartilage primordium in the proximal at GD17; **F.** Development of the middle segment of cartilage anlage at GD17 (the black arrow refers to hypertrophic chondrocytes).

POC was about to be formed. With the hypertrophy of chondrocytes in the central position, the cartilage anlages began to stratify, the cells close to the joint surface were densely arranged and uniform in shape and size, with the characteristics of stem cells. From the joint to the centre, the cell volume gradually increased and hypertrophied. The results showed that the cartilage anlage was a model of the future skeletal elements, and the chondrocytes in the middle of the cartilage anlage developed hypertrophy before the cartilage anlage ossified. When the cartilage anlage was ossified, the chondrocytes in the middle were the first to become hypertrophy (Fig. 2D–F).

Osteochondral development on the day before birth

GD20, which is the day before birth, the bone further developed and matured, the longitudinal length of the tibia became longer and the transverse width increased, the two ends were still cartilage and stained with Safranin-O. At this time, a mature POC with fast-green coloured bone tissue and typical medullary cavity structures could be observed. A typical epiphysis growth plate structure located at both ends of tibia could be seen. From the surface to the deep layer of cartilage, chondrocytes gradually matured; cells varied in morphology, with distinct cell layers, more regular,
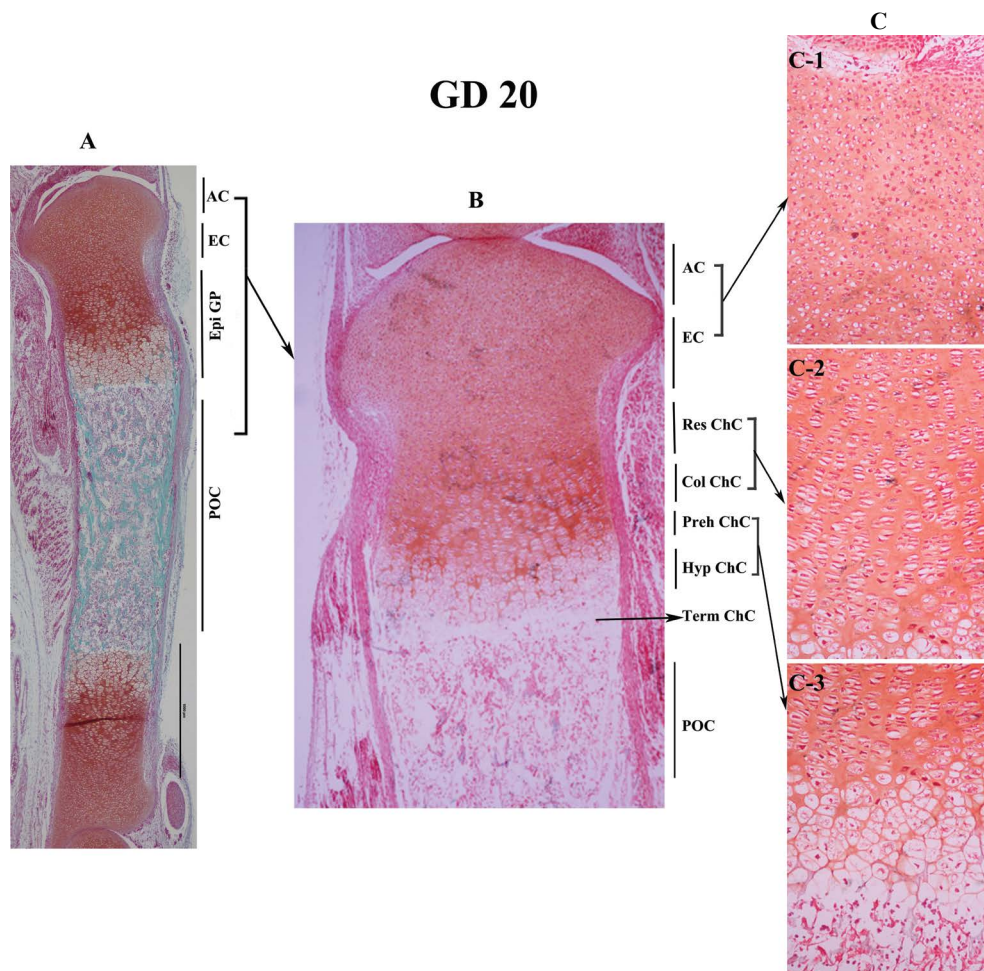
GD 20

Figure 3. Morphological structure of the tibia and epiphysis at gestational day (GD) 20 (the day before birth); **A.** In general view of the whole tibia, the primary ossification centre in the centre and epiphysis growth plates at both ends were clearly visible; **B.** General view of epiphysis growth plate adjacent to knee joint; **C.** General view of cells in different regions of epiphysis; AC — articular cartilage; EC — epiphysis cartilage; Epi GP — epiphysis growth plate; POC — primary ossification centre; Res ChB — resting zone chondroblast; Col ChB — columnar chondroblast; Preh ChC — prehypertrophic chondrocyte; Hyp ChC — hypertrophic chondrocyte; Term ChC — terminal chondrocyte (chondro-osseous junction).

orderly arrangement, and regular distribution. It could be roughly divided into articular cartilage, epiphysis cartilage, epiphysis growth plate, terminal chondrocyte (chondro-osseous junction) and POC (Fig. 3B). In addition, the epiphysis growth plate could be further subdivided into resting zone, proliferating zone, prehypertrophy and hypertrophy zone (Fig. 3B). In the cartilaginous reserve region, chondrocytes were elliptic, with a large number and dense arrangement, the arrangement direction was parallel to the articular surface, and still retains the characteristics of stem cells. The chondrocytes in the proliferating zone were proliferated by the reserved chondrocytes and arranged in series. The cell volume increased, the cells appeared in pairs and groups, and the intercellular space increased. Subsequently, the hypertrophic chondrocytes became round and enter the morphology of the pre-hyper-

trophy chondrocytes, which were further differentiated into hypertrophic chondrocytes. The hypertrophic chondrocytes were close to the POC and have the largest volume (Fig. 3C). Each cell existed independently, and eventually apoptosis and osteogenesis. At the same time, there was a layer of terminal chondrocyte (chondro-osseous junction) in the interface between hypertrophy chondrocytes and osteoblasts.

Formation and morphological characteristics of secondary ossifying centres

In rats, SOC is often found in PW2, but the formation of SOC is a dynamic process, which may start from PW1. Similar to the formation of POC, partial chondrocyte that in the region where the ossification centre is about to appear are hypertrophic and apoptotic, but what is different is that the formation
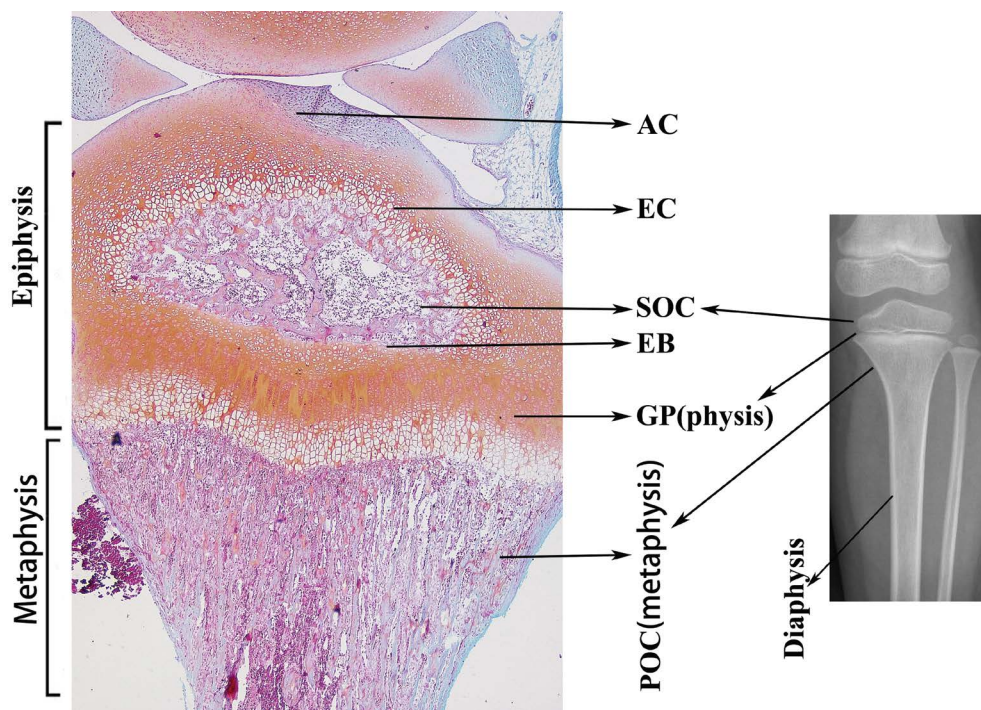
Figure 4. The histologic structure of the epiphysis of the proximal tibia is illustrated. The entire developing end of the bone from the articular cartilage surface to the last cells of the hypertrophic zone of the growth plate is the epiphysis. This encompasses three regions that are initially cartilage: (a) the articular cartilage (AC), (b) the growth plate (GP), also referred to as the epiphysis growth plate or the physis and (c) the epiphysis cartilage (EC) which refers to the cartilage mass between the articular cartilage and the growth plate cartilage. The secondary ossification centre (SOC) forms by the endochondral mechanism within the epiphysis cartilage. The epiphysis border (EB) is the boundary between the growth plate and the SOC; POC — primary ossification centre.

of SOC involves the participation of cartilage canal. In the early stage of SOC formation, several vascular-like cartilage canals elongate from different areas of epiphysis cartilage toward the location where the SOC will appear. These cartilage canals communicate with the tissue with abundant blood supply on the surface of cartilage, and allow for the arrival of blood vessels, vasoactive substances and osteoprogenitors to the centre of the epiphysis cartilage to promote the SOC formation. However, the cartilage canal was no longer visible at PW3 (Fig. 4). Once the SOC is formed, there were more than three ossification centres in the long bone, one in the centre of the diaphysis and the other at both ends. At this stage, the typical bone morphology of the development period was formed, that was, from the joint space to the centre of the diaphysis, in the order of articular cartilage, epiphysis cartilage, SOC, growth plate and POC (Fig. 4).

Cartilage canal, as shown in Figure 5A, the formation of cartilage canal generally began at multiple points simultaneously, the initial structure of the cartilage canal was similar to the structure of the ossification centre, and gradually expanded to

form a tubular structure. It joined the SOC with the tissue with abundant blood vessels on the surface of cartilage. Cartilage canal is a tubular structure surrounded by loose connective tissue, with a diameter of 50–150 μm; the cartilaginous wall is continuous with the pericardium, and there are red blood cells in the lumen, it's ends like a capillary bulb. When the SOC was mature, the cartilage canal which passed through the non-vascular tissue was closed again, so as to maintain the vascularization of cartilage in the proximal joint area (Fig. 1F).

Articular cartilage, at PW2, a large SOC could be seen in the centre of epiphysis, the cartilage between the ossification centre and the cartilaginous surface was articular cartilage (Fig. 5C, D). The volume of chondrocytes was larger than that of GD20, and the intercellular space increased. However, it was still difficult to distinguish articular cartilage from the underlying epiphysis cartilage by histology. They could be roughly divided into 3 layers: the chondrocytes in the surface layer were flat and densely arranged, the volume of chondrocytes in the middle layer increased and show the oval-shape,

A   Formation of SOC and dynamic change of CC
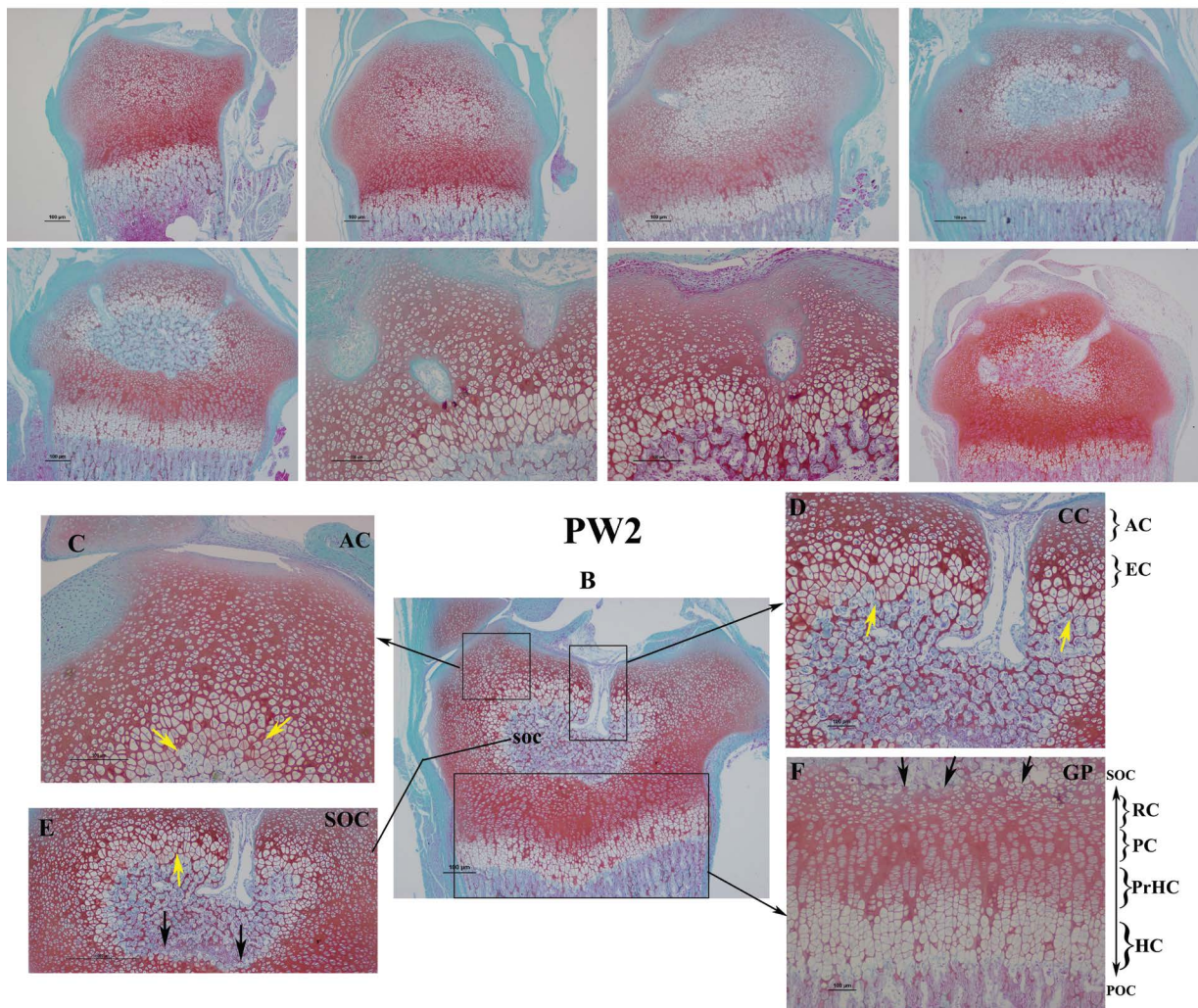
Figure 5. The dynamic process of secondary ossification centre (SOC) formation and its characteristics; **A.** The dynamic process of SOC formation and the dynamic change of cartilage canal (CC) at different developmental time; **B.** Gross morphology of epiphysis at postnatal weeks (PW) 2; **C.** Gross morphology of articular cartilage (AC) at PW2; **D.** Gross morphology of cartilage canals at PW2; **E.** Gross morphology of SOC at PW2 (the yellow arrow shows the hypertrophic chondrocytes near the articular side, and the black arrow indicates the border of the epiphysis border near the growth plate side); **F.** Gross morphology of growth plate cartilage at PW2 (the black arrow indicates the border of the bone plate near the growth plate side); RC — resting cartilage; PC — proliferative cells; PrHC — prehypertrophic chondrocyte; HC — hypertrophic chondrocyte; POC — primary ossification centre.

and agglomerated into clusters, the deep layer was adjacent to the SOC, and the chondrocytes were hypertrophic (Fig. 5C). Vascular invasion could be seen at the edge of articular cartilage, and cartilage canal could be seen in the centre of articular cartilage, and the cells around the cartilage canal were hypertrophic chondrocytes.

Secondary ossification centre, from 7th day after birth, chondrocytes at the centre of the epiphysis cartilage underwent hypertrophy and matrix mineralisation, the cartilage canals extended to this region from different positions, and finally the inner ends of the canal fused and expanded by continued excavation of surrounding hypertrophic chondrocytes to create the space for bone and bone marrow, thus establishing the SOC. After the formation of ossification centre, with the invasion of a large number of blood vessels, the SOC began a centripetal and continuous process of chondrocyte proliferation, hypertrophy, transformation, apoptosis, vascular invasion and other new bone formation processes from the inside to the outside. The SOC had a process of gradual ossification and expansion. When the SOC expanded close to the epiphysis plate, its shape changed from spherical to
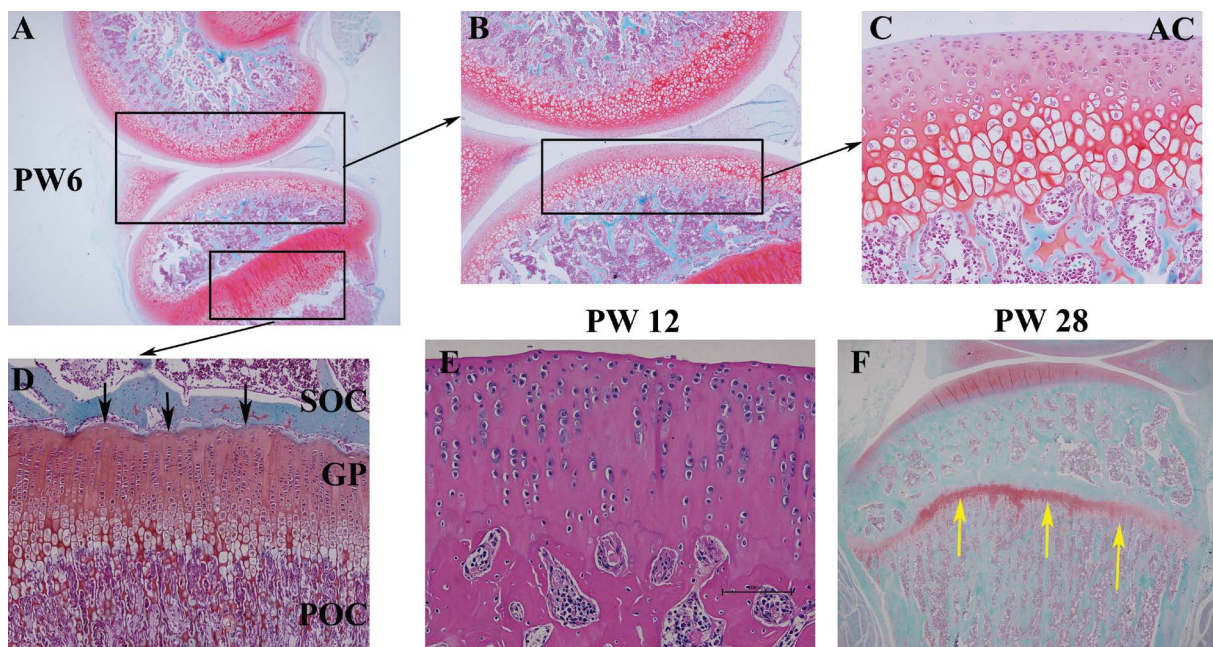
Figure 6. Morphological characteristics of mature osteochondral; **A.** The gross morphology of metaphysis at postnatal weeks (PW) 6;
B. Gross morphology of articular cavity and articular cartilage during at PW6; **C.** General morphology of articular cartilage (AC) at PW6;
D. General morphological view of the growth plate (GP) at PW6 (the black arrow indicates the boundary of the epiphysis border near the side
of the growth plate); SOC — secondary ossification centre; POC — primary ossification centre; **E.** Gross morphology of articular cartilage
at PW12; **F.** General morphological view of metaphysis at PW28 (the yellow arrow refers to the degenerated growth plate).

flat, and its longitudinal axis gradually parallel to the
metaphyseal. Morphological observation showed that
the osteogenesis of the SOC adjacent to the articular
space was different from that of the growth plate,
chondrocytes directly differentiate into hypertrophic
chondrocytes from resting chondrocytes, there was
no longitudinal proliferation and division process. In
the above process, chondrocytes did not experience
the obvious proliferation stage and pre-hypertrophy
stage. Compared with the process of epiphysis os-
sification, we found that chondrocytes in epiphysis
cartilage did not undergo columnar chondrocyte pro-
liferation. However, no obvious hypertrophic chon-
drocytes could be observed in the side of the SOC
near the growth plate, and there was a well-defined
osseous boundary, which was called epiphysis border,
which might be related to the prevention of ossifi-
cation of the reserved cartilage layer of the growth
plate (Fig. 5E).

Growth plate, as shown in Figure 5F, at PW2, the
growth plate had a clearer 4 discrete zones, and its
morphology was consistent with that of the epiphysis
growth plate at GD20, which was located between
the SOC and the POC.

Morphological characteristics of mature osteochondral

As shown in Figure 6, at PW6, the structure of the
joint (meniscus, cruciate ligament) was clearly visible,
and the joint structure was mature. The ossification
centre continues to expand, and there was no car-
tilage canal in the articular cartilage. However, the
articular cartilage was still not fully developed at this
time, the 4-layer structure of the articular cartilage
was still unclear, and the cell arrangement had no
obvious characteristics, the area near the SOC was
still hypertrophic chondrocytes (Fig. 6C). Calcified
cartilage layer, tidemark, subchondral bone was still
not recognised (Fig. 6C). At this time, the growth
plate was still clearly visible, and its shape, length
and width were not significantly different from those
of PW2, but the epiphysis border that is the bound-
ary between the growth plate and the SOC, was
clearer. At PW12, H&E staining showed that articular
cartilage was mature, and its 4-layer structure was
clearly visible. In addition, the tidemark, a mark-
er of mature articular cartilage, was clearly visible,
and the subchondral bone could be clearly identified
(Fig. 6E). In rats, we observed that the growth plate

still existed until PW28 (the structure of growth plate exists for life in rats), but at this time the growth plate morphology was abnormal, the thickness was obviously thinner (Fig. 6F), which can't continue to promote the growth of limb length.

DISCUSSION

Dynamic changes of cartilage anlages morphology

Skeletogenesis initiates at around mid-gestation in the mouse embryo. Limb development begins as mesenchymal cells form condensations from the lateral plate mesoderm. During this process, mesenchymal progenitor cells first move to the future bone sites and then differentiate into chondrocytes to form a cartilage anlage [34]. The cartilage anlage represents the moulds of the future skeletal elements and is gradually replaced by bone during intracartilaginous ossification [8]. When mesenchymal condensations form, several layers of mesenchymal cells at the boundary become fibroblast-like cells and eventually establish the perichondrium, chondrocytes at the centre of individual cartilage anlages undergo hypertrophy. The hypertrophic chondrocyte, simply through its size, is the principal engine of bone growth, and is also a master regulatory cell. Hypertrophic chondrocytes direct the mineralisation of their surrounding matrix, attract blood vessels through the production of vascular endothelial growth factor and other factors, and attract chondroclasts (closely related or identical to osteoclasts, which are cells of the macrophage lineage that digest matrix) [20]. Hypertrophic chondrocytes then undergo apoptotic cell death. Bone-forming cells then invade their lacunae and form POC [30]. This study found that, by GD14, chondrocytes in the centre of the cartilage anlage then stop proliferating, enlarge (hypertrophy). At GD17, the chondrocytes in the centre of the cartilage anlage have gone almost immediately from prehypertrophy to the terminal stage, without undergoing overt hypertrophy. Meanwhile, the joint cavity is formed and the complete model of the developing bone and joint has been formed. The cartilage model of the developing bone then increases in size by both interstitial and appositional growth of the chondrocytes. By GD20, a POC can be clearly distinguished.

Once the POC has formed and early intracartilaginous and intramembranous bone formation has proceeded toward either end of the bone, it is at this stage that the entire cartilaginous region at the developing end of each long bone is referred to as the epiphysis (Fig. 3) [32]. The epiphysis is sometimes referred to as the chondroepiphysis, but use of this term should be restricted to the time prior to formation of the SOC. That part of the epiphysis adjacent to the joint is referred to as the articular cartilage. This merges in indistinguishable fashion histologically with the underlying epiphysis cartilage and only reaches its definitive structure at skeletal maturity when the lowest zone of the articular cartilage calcifies persisting in the adult as the zone of calcified cartilage [32]. The epiphysis growth plate, which is also referred to as the physis or simply the growth plate (Fig. 3), is the cytologically and functionally specialised region of the epiphysis responsible for most of the longitudinal growth of a long bone [32].

While POC formation is an embryonic event, SOC formation occurs shortly after birth at the two ends (epiphysis regions) of rat long bones. At this time, the long bone has three ossification centres, one in the diaphysis and the other two are in each end of the cartilage model. SOC separating permanent articular cartilages from growth plates. When the SOC initiates, the typical epiphysis that refer to the entire developing end of the bone appear at both ends of the cartilage model (Fig. 4). This encompasses 3 regions that are initially cartilage: the articular cartilage, the growth plate, also referred to as the epiphysis growth plate or the physis and the epiphysis cartilage which refers to the cartilage mass between the articular cartilage and the growth plate cartilage [32]. The remaining cartilage between the ossification centres now forms a true "growth plate", driving further longitudinal bone growth, as well as the prospective permanent articular cartilages at each end of the bone [13]. During development, the growth plate is still a transient cartilage tissue. The continuous replacement of this cartilage by trabecular bone and bone marrow leads to its pivotal function as the primary source of longitudinal growth of long bones. In humans, the deposition of cartilage ceases at puberty; the metaphysis fuses with the epiphysis and growth stops. In mouse, longitudinal growth slows dramatically at puberty, but the growth plates do not completely disappear [13]. So the growth plate still exists at PW28 in this study, but it has no function of promoting limb growth.

Morphological changes in the development of articular cartilage

Articular cartilage is a layer of hyaline cartilage that covers the ends of the bone. It is a highly special-

ised connective tissue. Within each synovial joint, the articular cartilage is uniquely adapted to bear dynamic compressive loads and shear forces throughout the joint's range of motion [12]. Adult articular cartilage is typically avascular, alymphatic and aneural, it only depends on its unique cellular component — chondrocytes to construct, maintain and remodel extracellular matrix (ECM), with a low cell density and the limited ability of chondrocytes to proliferate [21]. The cells were surrounded by a large number of ECM (type II collagen, proteoglycan). This cartilage can perform continuous functions, such as painless joint activity and elastic recovery.

Most scholars hold the intermediate compartment of the histological interzone gave rise to articular cartilage, while cells in outer interzone layers participate in the initial epiphysis lengthening of long bones [17]. Derived from interzone cells, these periarticular, non-hypertrophic chondrocytes remain as chondrocytes during SOC formation and at the same time develop into articular cartilage with a lubricated surface for smooth joint articulation and load absorption and transmission [11]. Its underlying epiphysis cartilage is completely remodelled into subchondral trabecular bone and the subchondral bone plate. Resorption of the joint interzone leads to formation of the joint cavity and articular cartilage surface. Before the SOC appeared, that part of the epiphysis adjacent to the joint is referred to as the articular cartilage. This merges in indistinguishable fashion histologically with the underlying epiphysis cartilage [18]. SOC form postnatally, separating permanent articular cartilages from transitional growth plate cartilages. The skeletal structure of the limb during development is an ideal model to study the generation of transitional cartilage and permanent cartilage. Articular chondrocytes usually display a stable phenotype and do not undergo the processes characteristic of the growth-plate chondrocytes, such as rapid proliferation followed by cell-cycle exit, hypertrophy and apoptosis [19]. The growth plate is a transient structure and its physiological fate is to be replaced by bone; it is markedly different from articular cartilage that is designed to be permanent, ideally lasting unblemished for the entire lifetime of the individual [18].

Postnatal growth, the articular cartilage undergoes a series of tremendous structural and functional changes [12]. The final structural-maturation change at the undersurface of the articular cartilage, at skeletal maturation, the lowest level of the articular carti-

lage becomes calcified and this layer persists through adult life, after formation of the subchondral bone plate, involves calcification of the lowest zone of articular cartilage and appearance of the tidemark that separates the radial zone of the articular cartilage from the calcified zone. In this study, the formation of the tibia and the differentiation of chondrocytes in Wistar rats were firstly observed at GD 14, 17, 20 and PW 2, 6, 28. The results showed that: at GD14, there was no obvious joint space in the limb bud, the whole cartilage anlage is composed of hyaline cartilage, and the articular cartilage can't be recognised in morphology. At GD17, the joint cavity is visible, and the articular cartilage is closely connected to the epiphysis growth plate, but the morphology of articular chondrocytes is indistinguishable from that of the resting area of the epiphysis growth plate. At PW2, cartilage canals appeared in articular cartilage and epiphysis cartilage (Fig. 5), there is no typical layered structure of mature articular cartilage, which can be roughly divided into 3 layers: the surface chondrocytes were flat, the middle layer chondrocytes were large in size and aggregated in groups; the deep layer was adjacent to the SOC, and the chondrocytes were hypertrophic. It is worth mentioning that the chondrocytes in the SOC of epiphysis are lack of proliferative phase, chondrocytes directly differentiate into hypertrophic chondrocytes from resting chondrocytes, without obvious proliferation stage and pre-hypertrophy stage. At PW6, the articular cartilage gradually became thinner, the layers of chondrocytes decreased, the number of hypertrophic chondrocytes decreased, at this time, the articular cartilage appears layered structure, but it still does not have the typical 4 layers structure of mature articular cartilage, the tidemark is not visible and there is no typical subchondral bone morphology. With increasing age, the articular cartilage becomes thinner; at PW12 typical 4-layered structures of articular cartilage can be observed, they are shallow, radioactive, deep and calcified layers, the tidemark between the deep layer and the calcified layer is clearly visible, indicating that the articular cartilage has matured (Fig. 6).

Formation and development of POC

Our observation showed that, at GD14, at the position where the POC is about to appear in the cartilage anlages, chondrocytes are clustered and distributed in a nest-like manner. The volume is larger than that at both ends, and the intercellular space is enlarged (Fig. 2). With the continuous growth and

development, the chondrocytes in this area became hypertrophic at GD17. And by GD20, the typical POC structure could be seen. These data suggest that chondrocyte hypertrophy began on GD14, intracartilaginous ossification began on embryo GD15, and POC appeared on GD18–GD19.

Ossification in developing long bones starts in the perichondrium, the connective tissue surrounding the cartilage anlage [13]. At 14 days, chondrocyte hypertrophy occurs in the centre of the developing model of the major long bones, the cellular tissue surrounding the hypertrophic cartilage differentiates into periosteum with an outer fibrous layer and an inner osteoprogenitor-cell layer [13]. At this time, intramembranous periosteal-bone formation begins at the periphery of the middle of the model of the developing bone. The hypertrophic chondrocytes direct adjacent perichondrial cells to become osteoblasts; where cells differentiate into osteoblasts that start to deposit and mineralise a structure called the "bone collar" around the cartilage anlage [20]. This bone collar forms the initiation site of the cortical bone, the dense outer envelope of compact bone that provides most of the strength and rigidity to the long bones. Meanwhile, prehypertrophic chondrocytes in the centre of the cartilage anlage become hypertrophic chondrocytes and finally reach a terminal differentiation stage. Hypertrophic chondrocytes direct the mineralisation of their surrounding matrix, attract blood vessels through the production of vascular endothelial growth factor and other factors, and attract chondroclasts [20]. The actual process of "intracartilaginous ossification" is triggered shortly thereafter, around GD14–GD15 in mouse, when the hypertrophic chondrocytes in the centre of the cartilage anlage become invaded by blood vessels along with osteoclasts and osteoprogenitors from the surrounding perichondrium [13]. As a result, the cartilage anlage is progressively eroded and replaced by trabecular bone and bone marrow, a region initially termed the POC [3]. The ends of the long bones (with the exception of the metatarsals and phalanges) start to show epiphysis shaping (Fig. 3). In the metaphysis, hypertrophic cartilage of the epiphysis growth plate is continually replaced with trabecular bone, a process that relies heavily on angiogenesis and mediates longitudinal bone growth [13]. The intracartilaginous and intramembranous bone formation then extend proximally and distally toward the ends of the bone. The physes at the end of the bone and the surrounding periosteal intramembranous bone-formation sequence finally reach their farthest relative extent. However, in terms of actual bone-tissue formation, the intramembranous sequence is always slightly in advance of the intracartilaginous sequence, both temporally and spatially. These sequences may be separated by only a few hours.

Formation and development of SOC

Developing epiphysis consists of articular cartilage, epiphysis cartilage and epiphysis growth plate or physis. The SOC develops within the epiphysis cartilage of developing long bones. The cartilage canal development stage is the initial event preceding the appearance of SOC. When the SOC initiates, several cartilage canals appear at the proximal of the epiphysis cartilage, the epiphysis cartilage is excavated by canals invaginating from the periarticular region. The canals carry nutrients, blood vessels, growth factors and hormones to the centre of the epiphysis cartilage. At this time, chondrocytes at the centre of the epiphysis cartilage undergo hypertrophy and matrix mineralisation. The cartilage canals are oriented toward the position where the SOC was about to form. Finally, the inner ends of the canal fuse and expand by continued excavation of surrounding hypertrophic chondrocytes to create the space for bone and bone marrow, thus establishing the SOC [5]. Once SOC is formed, it separates permanent articular cartilages from transitional growth plate cartilages. It was concluded that the cartilage canals of foetus play great roles in formation of SOC. But with the continuous development and maturity, the cartilage canals in the cartilage eventually disappeared. In this study, we observed that chondrocytes in the central region of epiphysis cartilage began to differentiate and hypertrophy at 7 days after birth. Shortly afterward, several cartilage canals appear at the proximal of the epiphysis cartilage. The chondrocytes around the ends of the cartilage canal are hypertrophy, degeneration, ECM calcification. But the cartilage canal disappeared without being visible at PW3.

When the SOC appears, a centripetal and continuous new bone formation process begins in the epiphysis cartilage, which includes the process of chondrocyte proliferation, hypertrophy, transformation, apoptosis and vascular tissue invasion, with the growth of epiphyses, bone can continue to develop. Generally, the formation of SOC plays an important role in normal joint function. The formation and nor-

mal development of SOC is the guarantee of normal development of limb morphology and function. The development disorder of ossification centre in different parts may cause different limb deformity, skeletal developmental disorders or joint movement disorder. If the formation or development of cartilage canal is damaged for some reason, the development and growth of epiphysis cartilage and the formation of ossification centre will be seriously damaged, leaving the deformity that is difficult to be corrected, such as absence of femoral head, pathological dislocation of hip, etc. If the epiphysis border between the SOC and the growth plate is not formed, the growth plate lacks a blood supply barrier [29, 33], the infection of epiphysis and metaphysis spreads through the communication tube, which is the anatomical basis for the pathological evolution of acute haematogenous osteomyelitis in infants. Osteochondrosis of the epiphysis is an ischemic disease, and Carlson et al. [7] believe that it is associated with abnormal degeneration of cartilage canals. It is expected that through further research, to reveal its aetiology, so as to put forward targeted treatment measures. Therefore, the cartilage canals in epiphysis cartilage has important significance for the growth and development of cartilage.

Howship first described the vascular channel in cartilage in 1815 and named it "cartilage canals" [15]. As for the formation of cartilage canals, some scholars advocate the theory of "passive inclusion", they think that part of the connective tissue in the perichondrium differentiates into new cartilage, which wrapped the blood vessels and surrounding connective tissue in the original pericardium in cartilage and became the rudiment of the cartilage canals, and it grows and expands as the cartilage develops. Other scholars advocated the theory of "active invasion" and believed that cartilage canals were formed by the dissolution of cartilage matrix and the subsequent active extension of pericarpium vessels and surrounding connective tissue [31]. In this study, we observed that the perichondrium in the epiphysis cartilage in the superficial part of the epiphysis cartilage has an inner depression, or the structure is simple, the deep cartilage tube branches are complex, and the cartilage canals wall is continuous with the perichondrium. These phenomena support the "active invasion" theory of cartilage tube formation. Cartilage canals formation is due to invagination developing at specific sites on the perichondrium. However, the reason why these outbreaks occur in some parts of the perichondrium

and not in others remains unknown. The first epiphysis development pattern begins with cartilage canal formation in epiphysis cartilage have proposed three stages of spatial cartilage canal development: superficial, intermediate and deep. Short canals are formed in the superficial stage where the cartilage matrix is not calcified and chondrocytes are not hypertrophied. The canals increase in length during the intermediate stage; the matrix is not mineralised and chondrocytes obtain their level of hypertrophy. The cartilage matrix becomes mineralised during the deep stage.

While POC and SOC formation share many similarities, several key characteristics exist to distinguish these two processes. During POC initiation, invading vessels originate from the perichondrium that has already become the bone collar containing osteoprogenitors and mature osteoblasts. This bone collar eventually expands to become the cortical bone. In contrast, during SOC initiation, invading vessels originate from periarticular region consisting of several layers of flattened fibroblast-like chondrocytes aligned parallel to the surface [34]. While hypertrophic chondrocytes, mineralised ECM, and vessel invasion appear to be involved in both processes, these events are coupled in POC formation but uncoupled in the invagination and cartilage canal stages of SOC formation. As a result, the molecular and cellular mechanisms involved in the early initiation of SOC canal initiation remain unknown [34].

Growth plate and intracartilaginous osteogenesis

During the formation of POC, the central replacement of hypertrophic chondrocytes with deposition of bone on the calcified cartilage cores encompasses what is referred to as the intracartilaginous mechanism. In the periosteal region intramembranous bone formation extends the periosteal new bone sleeve. The periosteal development is always spatially somewhat more advanced toward either end of the bone than the central endochondral development. As this developmental sequence works its way toward either end of the bone, the cartilage forms itself into a specifically structured region referred to as the epiphysis growth plate (physis) (Fig. 3) [32]. Nilsson et al. [28] divided the epiphysis growth plate into: epiphysis cartilage, resting zone, proliferative zone, proliferation-hypertrophic transition zone and hypertrophic zone by histological characteristics. The chondrocytes in the epiphysis cartilage are round and have no regular orientation. The resting area is

adjacent to the epiphysis cartilage. The resting zone is populating by undifferentiated chondrocytes serving as a reservoir of stem-like progenitor cells which can rapidly generate proliferating chondrocytes [1]. Next is the proliferation zone which appears as a series of columns aligned parallel to the long axis of the bone. As these cells replicate, the two daughter cells line up parallel to the long axis, to maintain the columnar organization. Type II collagen represents a major component of the cartilage matrix in the resting and proliferative zones [6]. Chondrocytes then exit the cell cycle to become prehypertrophic and switch to produce type X collagen. Prehypertrophic chondrocytes increase in size and become hypertrophic cells that stop expressing type II collagen but continuously express type X collagen [16]. Eventually, hypertrophic chondrocytes reach the terminal stage with matrix mineralisation at the metaphyseal side. At the chondro-osseous junction, the invasion of hypertrophic cartilage by blood vessels, osteoclasts, and osteoprogenitors, together with the terminal differentiation of hypertrophic chondrocytes, leads to degradation and remodelling of the hypertrophic cartilage ECM into trabecular bone [34]. Calcification occurs in the matrix of the lower margins of the hypertrophic zone but involving almost exclusively the longitudinal septae along the long axis of the bone, whereas the transverse septae are either not mineralised or only slightly mineralised. The vascular invasion from below progresses two or three cells deep into the lower margin of the hypertrophic zone and in association with this vascular invasion of the hypertrophic cell regions there is deposition of bone by osteoblasts on the persisting calcified cartilage matrix [32].

After birth, in the long bone, the SOC is successively formed at the end of the cartilage models, the remaining cartilage between the ossification centres now forms a true "growth plate", driving further longitudinal bone growth that is the intracartilaginous ossification, as well as the prospective permanent articular cartilages at each end of the bone. Similar to the epiphysis growth plate, the growth plate is comprised of four discrete zones easily identifiable by histological analyses (Fig. 4). The chondrocytes in the growth plate like the chondrocytes in the epiphysis growth plate undergo stepwise maturation from resting, proliferative, prehypertrophic, and finally hypertrophic and mineralized stages [34]. The growth plate, which increases in width with age, but hardly changes in thickness, is entirely occupied by successive zones leading to intracartilaginous ossification [22]. At the top of the growth plate, round chondrocytes no longer proliferate rapidly and are called resting or reserve chondrocytes, and probably serve as precursors for the flat proliferating columnar chondrocytes [20]. There is a well-defined subchondral bone plate, which is called epiphysis border, on the side of the SOC adjacent to the growth plate, which can prevent the epiphysis vessels from invading the growth plate and thus avoid its premature differentiation and maturation [22]. When the POC and the SOC expand and eventually fuse, the growth plate disappears, which means the maturation of the skeleton. In humans, the growth plate fuses in late puberty, in rodents, this closure can either be greatly delayed or never fully complete [14]. Because of its important role in skeletal growth, any disturbance of signalling pathways required for growth plate development would likely cause skeletal dysplasia. In human, this often presents as a short stature. Mutations in the genes encoding these regulatory molecules result in abnormal chondrocyte behaviour and skeletal dysplasias, most of which are associated with dwarfism, i.e. inadequate growth of the bones that form by intracartilaginous ossification [25, 35].

Intracartilaginous ossification is one of the main ways of bone development in mammals, it starts from embryonic period and continues to develop and grow until the end of adolescence. Intracartilaginous ossification is a dynamic process of chondrocytes proliferation and differentiation. The agglutination of mesenchymal cells into the cartilage models is the starting point of intracartilaginous ossification, with the growth and development, mesenchymal cells differentiate into chondrocytes, and chondrocytes further differentiation, hypertrophy, apoptosis and eventually remodelled into bone after vascular invasion [24]. The ECM and angiogenesis stimulants produced by hypertrophic chondrocytes are the key factors to induce vascular invasion and angiogenesis. Neovascularisation transports nutrients to cells involved in ECM absorption and mineral deposition, and provides the necessary signalling factors for the normal development of bone. Studies have shown that osteoclasts and osteoprogenitor cells are always attached to endothelial cells when new blood vessels are formed in the osteogenic zone of the growth plate, and then enter the osteogenic region. Vascular invasion is an essential step in the process

of intracartilaginous osteogenesis, the invasion of blood vessels provides the necessary nutrients and corresponding cells and factors for the formation of cartilage. Therefore, the invasion of blood vessels is also a sign of cartilage transforming into bone. The proliferation and differentiation of chondrocytes can be orderly carried out in different time and space, which depends on the close regulation of chondrocytes themselves, surrounding matrix, systemic circulation factors, paracrine factors and transcription factors, as well as the precise coordination of activation and inhibition of corresponding pathways. The invasion of blood vessels brings osteoblasts to the cartilage models and forms ossification centre. The expansion and erosion of the ossification centres led to the cartilage anlages eventually developing into bone and permanent articular cartilage.

CONCLUSIONS

As far as we know, this is the first morphological study to dynamically observe the entire process of cartilage anlages development into articular cartilage and bone through a series of changes from embryo to adult. Our results especially show the formation of POC, the formation of SOC with the participation of cartilage canal and the dynamic process of articular cartilage maturation. The limitation of this study is that only morphological observation was carried out, but no qualitative, quantitative and related molecular mechanisms were studied. Meanwhile, due to the limited funds, continuous observation and comparative analysis of different genders were not carried out. However, the dynamic observation of osteochondral development and the results of morphological characteristics at various important time points in this study is conducive to a deeper understanding of the overall overview of the temporal and spatial regularity of osteochondral development. It is helpful to provide a reference for other research time node selection and morphological analysis.

Conflict of interest: None declared

REFERENCES

1. Abad V, Meyers JL, Weise M, et al. The role of the resting zone in growth plate chondrogenesis. Endocrinology. 2002; 143(5): 1851–1857, doi: 10.1210/endo.143.5.8776, indexed in Pubmed: 11956168.
2. Abubakar AA, Noordin MM, Azmi TI, et al. The use of rats and mice as animal models in ex vivo bone growth and development studies. Bone Joint Res. 2016; 5(12): 610–618, doi: 10.1302/2046-3758.512.BJR-2016-0102.R2, indexed in Pubmed: 27965220.
3. Baumgart M, Wiśniewski M, Grzonkowska M, et al. Morphometric study of the primary ossification center of the fibular shaft in the human fetus. Surg Radiol Anat. 2019; 41(3): 297–305, doi: 10.1007/s00276-018-2147-5, indexed in Pubmed: 30542927.
4. Blaker CL, Clarke EC, Little CB. Using mouse models to investigate the pathophysiology, treatment, and prevention of post-traumatic osteoarthritis. J Orthop Res. 2017; 35(3): 424–439, doi: 10.1002/jor.23343, indexed in Pubmed: 27312470.
5. Blumer MJF, Longato S, Fritsch H. Structure, formation and role of cartilage canals in the developing bone. Ann Anat. 2008; 190(4): 305–315, doi: 10.1016/j.aanat.2008.02.004, indexed in Pubmed: 18602255.
6. Burdan F, Szumiło J, Korobowicz A, et al. Morphology and physiology of the epiphyseal growth plate. Folia Histochem Cytobiol. 2009; 47(1): 5–16, doi: 10.2478/v10042-009-0007-1, indexed in Pubmed: 19419931.
7. Carlson CS, Hilley HD, Meuten DJ. Degeneration of cartilage canal vessels associated with lesions of osteochondrosis in swine. Vet Pathol. 1989; 26(1): 47–54, doi: 10.1177/030098588902600108, indexed in Pubmed: 2913703.
8. Chijimatsu R, Saito T. Mechanisms of synovial joint and articular cartilage development. Cell Mol Life Sci. 2019; 76(20): 3939–3952, doi: 10.1007/s00018-019-03191-5, indexed in Pubmed: 31201464.
9. Cohen MM. The new bone biology: pathologic, molecular, and clinical correlates. Am J Med Genet A. 2006; 140(23): 2646–2706, doi: 10.1002/ajmg.a.31368, indexed in Pubmed: 17103447.
10. Dash S, Trainor PA. The development, patterning and evolution of neural crest cell differentiation into cartilage and bone. Bone. 2020; 137: 115409, doi: 10.1016/j.bone.2020.115409, indexed in Pubmed: 32417535.
11. Decker RS, Um HB, Dyment NA, et al. Genesis and morphogenesis of limb synovial joints and articular cartilage. Matrix Biol. 2014; 39(1): 5–10, doi: 10.1016/j.matbio.2014.08.006, indexed in Pubmed: 25172830.
12. Decker R. Articular cartilage and joint development from embryogenesis to adulthood. Semin Cell Dev Biol. 2017; 62: 50–56, doi: 10.1016/j.semcdb.2016.10.005.
13. Dirckx N, Van Hul M, Maes C. Osteoblast recruitment to sites of bone formation in skeletal development, homeostasis, and regeneration. Birth Defects Res C Embryo Today. 2013; 99(3): 170–191, doi: 10.1002/bdrc.21047, indexed in Pubmed: 24078495.
14. Emons J, Chagin A, Sävendahl L, et al. Mechanisms of growth plate maturation and epiphyseal fusion. Horm Res Paediatr. 2011; 75(6): 383–391, doi: 10.1159/000327788.

15. Howship J. Experiments and observations in order to ascertain the means employed by the animal economy in the formation of bone. Med Chir Trans. 1815; 6: 263–676.5, doi: 10.1177/095952871500600116, indexed in Pubmed: 20895250.

16. Hunziker EB. Mechanism of longitudinal bone growth and its regulation by growth plate chondrocytes. Microsc Res Tech. 1994; 28(6): 505–519, doi: 10.1002/jemt.1070280606, indexed in Pubmed: 7949396.

17. Ito MM, Kida MY. Morphological and biochemical re-evaluation of the process of cavitation in the rat knee joint: cellular and cell strata alterations in the interzone. J Anat. 2000; 197 (Pt 4): 659–679, doi: 10.1046/j.1469-7580.2000.19740659.x, indexed in Pubmed: 11197539.

18. Iwamoto M, Higuchi Y, Enomoto-Iwamoto M, et al. The role of ERG (ets related gene) in cartilage development. Osteoarthritis Cartilage. 2001; 9 (Suppl A): S41–S47, doi: 10.1053/joca.2001.0443, indexed in Pubmed: 11680687.

19. Iwamoto M, Ohta Y, Larmour C, et al. Toward regeneration of articular cartilage. Birth Defects Res C Embryo Today. 2013; 99(3): 192–202, doi: 10.1002/bdrc.21042, indexed in Pubmed: 24078496.

20. Kronenberg HM. Developmental regulation of the growth plate. Nature. 2003; 423(6937): 332–336, doi: 10.1038/nature01657, indexed in Pubmed: 12748651.

21. Las Heras F, Gahunia H, Pritzker K. Articular cartilage development: a molecular perspective. Orthop Clin North Am. 2012; 43(2): 155–171, doi: 10.1016/j.ocl.2012.01.003.

22. Lee ER, Lamplugh L, Davoli MA, et al. Enzymes active in the areas undergoing cartilage resorption during the development of the secondary ossification center in the tibiae of rats ages 0-21 days: I. Two groups of proteinases cleave the core protein of aggrecan. Dev Dyn. 2001; 222(1): 52–70, doi: 10.1002/dvdy.1168, indexed in Pubmed: 11507769.

23. Long F, Chung Ui, Ohba S, et al. Ihh signaling is directly required for the osteoblast lineage in the endochondral skeleton. Development. 2004; 131(6): 1309–1318, doi: 10.1242/dev.01006, indexed in Pubmed: 14973297.

24. Long F, Ornitz DM. Development of the endochondral skeleton. Cold Spring Harb Perspect Biol. 2013; 5(1): a008334, doi: 10.1101/cshperspect.a008334, indexed in Pubmed: 23284041.

25. Macedo MP, Werner H, Araujo Júnior E. Fetal skeletal dysplasias: a new way to look at them. Radiol Bras. 2020; 53(2): 112–113, doi: 10.1590/0100-3984.2018.0140, indexed in Pubmed: 32336826.

26. Mackie EJ, Tatarczuch L, Mirams M. The skeleton: a multi-functional complex organ: the growth plate chondrocyte and endochondral ossification. J Endocrinol. 2011; 211(2): 109–121, doi: 10.1530/JOE-11-0048, indexed in Pubmed: 21642379.

27. Ni Q, Lu K, Li J, et al. Role of TGFβ signaling in maternal ethanol-induced fetal articular cartilage dysplasia and adult onset of osteoarthritis in male rats. Toxicol Sci. 2018; 164(1): 179–190, doi: 10.1093/toxsci/kfy080, indexed in Pubmed: 29617878.

28. Nilsson O, Weise M, Landman EBM, et al. Evidence that estrogen hastens epiphyseal fusion and cessation of longitudinal bone growth by irreversibly depleting the number of resting zone progenitor cells in female rabbits. Endocrinology. 2014; 155(8): 2892–2899, doi: 10.1210/en.2013-2175, indexed in Pubmed: 24708243.

29. Parvaresh KC, Upasani VV, Bomar JD, et al. Secondary ossification center appearance and closure in the pelvis and proximal femur. J Pediatr Orthop. 2018; 38(8): 418–423, doi: 10.1097/BPO.0000000000000836, indexed in Pubmed: 27442214.

30. Pazzaglia UE, Congiu T, Sibilia V, et al. Relationship between the chondrocyte maturation cycle and the endochondral ossification in the diaphyseal and epiphyseal ossification centers. J Morphol. 2016; 277(9): 1187–1198, doi: 10.1002/jmor.20568, indexed in Pubmed: 27312928.

31. Peinado Cortés LM, Vanegas Acosta JC, Garzón Alvarado DA. A mechanobiological model of epiphysis structures formation. J Theor Biol. 2011; 287: 13–25, doi: 10.1016/j.jtbi.2011.07.011, indexed in Pubmed: 21810429.

32. Shapiro F. Developmental bone biology. 2001: 3–128, doi: 10.1016/B978-012638651-6/ 50002-2.

33. Tong W, Tower RJ, Chen C, et al. Periarticular mesenchymal progenitors initiate and contribute to secondary ossification center formation during mouse long bone development. Stem Cells. 2019; 37(5): 677–689, doi: 10.1002/stem.2975, indexed in Pubmed: 30681752.

34. Tower R, Qin L. Chondrocyte cell fate analysis. Encyclopedia of Bone Biology. 2020: 621–631, doi: 10.1016/b978-0-12-801238-3.11190-0.

35. Wrmn ML, Cormier-Daire V, Hall C. Nosology nd clssifiction of genetic skeletl disorders: 2010 revision. Am J Med Genet A. 2011; 155A(5): 943–968, doi: 10.1002/ ajmg.a.33909.

36. Yang L, Tsang KY, Tang HC, et al. Hypertrophic chondrocytes can become osteoblasts and osteocytes in endochondral bone formation. Proc Natl Acad Sci U S A. 2014; 111(33): 12097–12102, doi: 10.1073/pnas.1302703111, indexed in Pubmed: 25092332.

CASE REPORT

Unusual formation of the musculocutaneous and median nerves: a case report refined by intraneural dissection and literature review

E. Clarke[1], R.S. Tubbs[2, 3, 4], M. Radek[5], R. Haładaj[1], M. Tomaszewski[1], G. Wysiadecki[1]

[1]Department of Normal and Clinical Anatomy, Chair of Anatomy and Histology, Medical University of Lodz, Poland
[2]Department of Neurosurgery, Tulane University School of Medicine, New Orleans, LA, United States
[3]Department of Neurosurgery and Ochsner Neuroscience Institute, Ochsner Health System, New Orleans, LA, United States
[4]Department of Anatomical Sciences, St. George's University, Grenada
[5]Department of Neurosurgery, Spine and Peripheral Nerve Surgery, Medical University of Lodz, University Hospital WAM-CSW, Lodz, Poland

This report presents a detailed anatomical investigation of an upper limb specimen showing an atypical formation of the musculocutaneous nerve (MCN) and median nerve (MN). The study was refined by intraneural dissection, which supplements earlier descriptions of similar anatomical variations and allows for revision of the accepted classification.

The case described in this report was an incidental finding during routine dissection of a fixed isolated upper limb. Intraneural dissection revealed partial fusion between the MCN and aberrant bundles of the MN. Those aberrant bundles joined the main steam of the MN at the level at which the MCN branched off as an independent nerve. The procedure allowed the aberrant fibres of the MN to be differentiated from the MCN. The presence of separate bundles in a territory corresponding to the MCN was confirmed, although those bundles and the aberrant MN bundles were covered by a common epineurium. The aberrant MN bundles running within the MCN did not contribute to innervation of the forearm muscles. They rejoined the main nerve trunk in the arm.

A comprehensive understanding of the diverse anatomical variations of the upper limb nerves could be crucial for the safety and success of surgical procedures, especially procedures for reconstructing the brachial plexus or its branches. (Folia Morphol 2021; 80, 4: 1020–1026)

Key words: anatomical variation, brachial plexus, median nerve, musculocutaneous nerve, peripheral nerves

INTRODUCTION

The musculocutaneous nerve (MCN) is typically derived from the C5, C6 and C7 spinal cord segments. It is a direct continuation of the lateral cord of the brachial plexus. Bergman et al. [3] reported that in about 90.5% of cases the MCN shows a typical origin. During its later course it pierces the coracobrachialis muscle at the lower border of the axillary cavity. It then runs between the biceps brachii and brachialis muscles. It provides branches to both those muscles

and travels to the lateral side of the biceps, where it pierces the brachial fascia lateral to biceps brachii muscle to emerge lateral to its distal tendon and brachioradialis muscle, and then continues as the lateral antebrachial cutaneous nerve, also known as the lateral cutaneous nerve of the forearm [22, 31].

In most cases (about 85%) the median nerve (MN) arises from two roots (the terms "branches", "heads" or "radices" are occasionally used), lateral and medial, which take origin from the lateral and medial cords of the brachial plexus, respectively [22]. The lateral root provides fibres derived from ventral roots of the C5–C7 spinal nerves, while the medial cord typically contains contributions from C8 and T1. Typically, the two roots merge within the axillary cavity anterior to the axillary artery. The V-shaped origin of the MN thus created is called "the loop of the median nerve" [6]. During its further course, the MN descends the arm, accompanying the brachial artery. It seldom provides muscular branches to the arm [22]. Its territory includes the anterior group of forearm muscles and it terminates by supplying the muscles and the skin of the hand [31].

Both the MCN and MN exhibit numerous anatomical variants with respect to their origins from the brachial plexus, topographical relationships, anastomotic connections with the neighbouring nerves, and branching patterns [3, 5–8, 10–23, 25, 27, 30, 33]. A comprehensive understanding of the diverse anatomical variations of the upper limb nerves could be crucial for the safety and success of surgical procedures, especially procedures for reconstructing the brachial plexus or its branches, particularly since the distribution of brachial plexus lesions is also highly variable [9, 11, 15, 18, 24, 29, 34]. As stressed by Sinha et al. [29], knowledge of the fascicular orientation of the nerves of the brachial plexus is important for neurosurgeons and can "improve the surgical outcome of nerve grafting in brachial plexus injuries by anastomosing related fascicles and avoiding possible axonal misrouting". In this context, refinement of gross anatomical descriptions of brachial plexus variations by intraneural dissection could help to deepen and organize existing knowledge about deviations from typical morphology and the targeting of nerves derived from that plexus. However, the technique of intraneural dissection is not commonly used.

The present report details the anatomical investigation of an upper limb specimen showing an atypical formation of the MCN and MN. The study was refined by intraneural dissection. It supplements earlier descriptions of similar anatomical variations and allows for revision of the accepted classification. One of our aims was to demonstrate the usefulness of intraneural dissection in anatomical research. Both clinical significance of the observed variation and surgical importance of the findings in this study were also discussed.

CASE REPORT

The case described in this report was an incidental finding during routine dissection of an isolated upper limb fixed in 10% formalin. Detailed examination of an atypical MCN and MN formation was supplemented by intraneural dissection using microsurgical instruments at a magnification of 2.5× under a HEINE® HR 2.5 × High Resolution Binocular Loupe (HEINE Optotechnik GmbH & Co. KG, Herrsching, Germany). The measurements were taken with a Digimatic Calliper (Mitutoyo Corporation, Kawasaki-shi, Kanagawa, Japan). Measurements were performed by two independent researchers. Each measurement was repeated twice and an average was calculated and as final result, with an accuracy of two decimal places.

In this case, the deviations from typical MCN and MN morphologies coincided. The variation involved partial fusion between the two nerves, which during initial assessment resembled a double loop of the MN (Fig. 1). The diameter of the lateral cord of the brachial plexus, measured at the level of the third part of the axillary artery, was 5.53 mm; the diameter of its medial cord, measured at the same level, was 6.58 mm. The first, typical loop of the MN covered the third part of the axillary artery (Fig. 1). The two roots of the MN merged just below the origin of the subscapular artery (the medial root was crossed anteriorly by this artery). The diameter of the lateral root was 3.12 mm and that of the medial root was 4.18 mm. An additional band of fascicles (1.75 mm in diameter), connecting the lateral cord of the brachial plexus to the medial cord of the plexus and the ulnar nerve, ran just above the two roots (Figs. 1, 2); this communication crossed the third part of the axillary artery anteriorly below the origin of the subscapular artery (Fig. 1). The MCN was remarkably thickened and resembled an elongated lateral cord of the brachial plexus (Fig. 1). Its diameter below the origin of the lateral root of the MN was 4.87 mm. It ran anterior to the brachioradialis muscle (which was one-headed and not pierced by any nerve), perpendicular to the
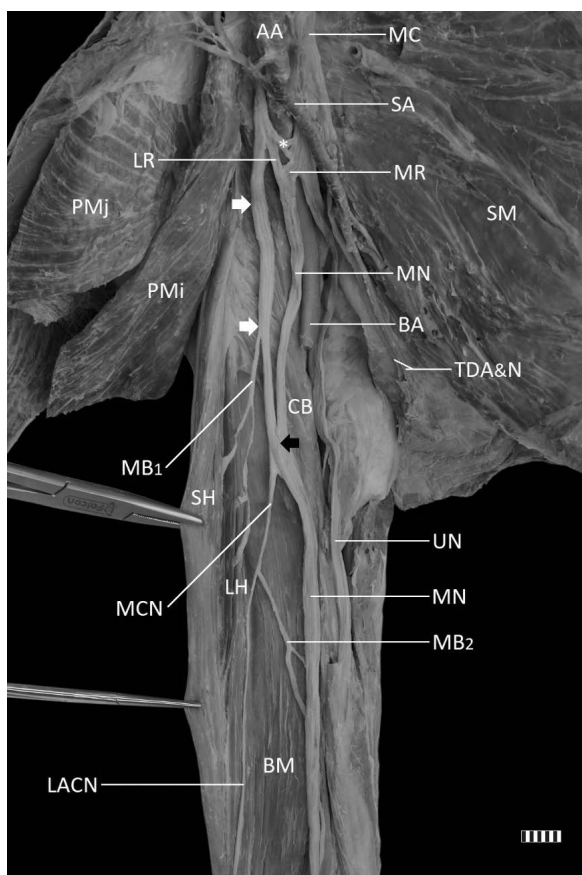
Figure 1. Co-occurrence of deviations from musculocutaneous (MCN) and median nerve (MN) typical morphology. Anterior view of the isolated right upper limb. The point at which those nerves merge is marked by a black arrow. An additional band of fascicles (marked by a white asterisk) connecting the lateral cord of the brachial plexus to the medial cord (MC) of the plexus and with the ulnar nerve (UN) runs just above the two roots of the MN. White arrows indicate an atypical thickened segment of the MCN accompanied by fibres of the MN; AA — axillary artery; BA — brachial artery (removed during dissection of the distal two-thirds of the arm); BM — brachialis muscle; CB — coracobrachialis muscle; LACN — lateral antebrachial cutaneous nerve; LH — long head of biceps brachii muscle; LR — lateral root of the MN; MR — medial root of the MN; MB₁ — branch to biceps brachii muscle; MB₂ — branch to brachialis muscle; SA — subscapular artery; SH — short head of biceps brachii muscle; SM — subscapularis muscle; PMi — pectoralis minor muscle (reflected); PMj — pectoralis major muscle (reflected); TDA&N — thoracodorsal artery and nerve.

Figure 2. Result of intraneural dissection performed to revise the variation observed in Figure 1. Posterior view of the isolated specimen of part of the right brachial plexus. The fascicular dissection revealed fusion between the musculocutaneous nerve (MCN) and aberrant fibres of the median nerve (MN); those aberrant fibres are marked by white arrows. They joined the mains team of the MN at the level at which the MCN branched off as an independent nerve (marked by a grey arrow); LACN — lateral antebrachial cutaneous nerve; LC — lateral cord of the MN; LR — lateral root of the MN; MC — medial cords of the MN; MR — medial root of the MN; MB₁ — muscular branch to the biceps brachii muscle; MB₂ — branch to brachialis muscle; UN — ulnar nerve; white asterisk — additional band of fascicles connecting the lateral cord of the brachial plexus to the medial cord of the plexus and the ulnar nerve.

proximal third of the MN (diameter 4.31 mm; Fig. 1). This anomalous, thickened segment of the MCN gave off one muscular branch (diameter 0.98 mm) to the coracobrachialis muscle and another to the biceps brachii muscle (1.16 mm diameter; Fig. 1). Fifty-seven millimetres below the inferior border of the pectoralis major muscle, the MCN rejoined the trunk of the MN, resembling a second loop of the MN (Fig. 1). Next, the MCN (with a smaller diameter of 2.39 mm) branched off again 9 mm below the level of its fusion

with the MN and 66 mm below the inferior border of the pectoralis major muscle. It soon entered between the biceps brachii and brachialis muscles and then followed a typical course. In the later part of its course the nerve gave a muscular branch (0.96 mm diameter) to the brachialis muscle and continued as the lateral cutaneous nerve of the forearm (1.74 mm diameter; Fig. 1). Just below the level of the fusion, the MN crossed the brachial artery and moved to its medial side. The subsequent course and branching pattern of the MN were typical.

The next stage of examination involved fascicular dissection to refine the classification of this varia-

tion. The brachial plexus was harvested (including the atypical MN and MCNs) and immersed in 10% acetic acid for 2 weeks to facilitate removal of the epineural sheath according to the fascicular dissection procedure [13]. This procedure revealed the fusion between the MCN and aberrant fibres of the MN (Fig. 2); those aberrant fibres joined the main steam of the MN at the level where the MCN branched off as an independent nerve (Fig. 2). It allowed the aberrant fibres of the MN to be differentiated from the MCN. It also revealed that the muscular branch to the biceps brachii muscle came from the nerve bundle (trunk) corresponding to the MCN (Fig. 2). Aberrant fibres of the MN running within the MCN did not contribute to innervation of the forearm muscles. They rejoined the main nerve trunk in the arm. The intraneural dissection results allowed the observed findings to be properly classified.

DISCUSSION

When neurovascular structures grow and differentiate within the developing limb bud, some deviations from the typical course of organogenesis are possible. These can lead to anatomical variations [4, 13, 14]. The case presented in this report describes an aberrant course of the nerve fibres derived from the brachial plexus and enables it to be analysed.

Anatomical variants can include the relationship of the first MCN segment to the coracobrachialis muscle; the MCN can lie anterior to that muscle instead of piercing it. Claassen et al. [6] estimated the incidence of this aberrant course of the nerve at 1.8%. In other variants, part of the MCN pierces the coracobrachialis muscle and then rejoins the main trunk after passing through it; or only the cutaneous branch of the MCN (i.e. the lateral cutaneous nerve of the forearm) pierces that muscle [3, 22].

Numerous variations have been reported in the courses and anatomical relationships of the MCN and MN. However, it is challenging to compare the different classifications applied by various authors because their criteria are not uniform [27, 30]. The literature is ambiguous about the classification of variations in which there is complete or partial fusion between the MCN and MN. The MCN can be fused with the MN over a certain distance and then branch off and continue its course as a single trunk or as several branches. Such cases are sometimes classified as the MCN being a branch of the MN, and sometimes as absence of the MCN [1, 7, 11, 15, 22, 30].

According to Bergman et al. [3], the prevalence of the MCN branching off the MN ranges from 0.6% to 2%. In research of Guerri-Guttenberg and Ingolotti [11], the MC was absent in 2 out of 54 cases and in 1 case the MC and the median nerve had a distal origin. Sirico et al. [30] noted in their extensive meta-analysis that fusion between the MCN and MN and the origin of the MCN from the MN can be placed in the same category, as reflected in some scientific reports. However, there are other approaches. For example, in series of Beheiry [2], the MN gave off muscular branches to the brachialis muscle as well as a branch from its lateral root to supply both heads of the biceps brachii muscle, while the MCN was reported to be absent. Thus, various cases can be classified as absence of the MCN when branches to the brachialis and biceps brachii muscles and the lateral antebrachial cutaneous nerve emerge from the MN. Our case resembles this variant, considering that an MCN following a typical course branched off only just below the place of fusion with the MN. However, in the light of the intraneural dissection results, it seems most justifiable to class this variant as "partial fusion between the MCN and MN". The presence of separate nerve bundles with territories corresponding to the MCN was confirmed, though those bundles and the aberrant MN fascicles were covered by a common epineurium. A recent report describing fascicular dissection of a case with absent MCN also revealed distinct fascicles corresponding to the MCN accompanying the MN [7]. Nerve fibres tracing of branches to the coracobrachialis muscle was also assessed by Kawashima et al. [18].

The MCN can also be accompanied by fibres derived from the MN. Such aberrant fibres can form an anastomosis between the MCN and the MN [27]. Cases of this kind could also resemble the one presented in our report. Sirico et al. [30] stress that variations in the communication between the MCN and MN may be classified as: communicating branches of the MCN; double lateral root of the MN; or "the third root of the median nerve". Communications with the MN usually appear in the lower third of the arm and can form a loop [3, 6, 17, 30, 33]. In research of Guerri-Guttenberg and Ingolotti [11], communications were seen between the MC and MN in 53.6% of the dissections from which 84.6% were proximal, 7.7% distal, and 7.7% had one proximal and one distal communication to the point of entry of the MC into coracobrachialis muscle. Loukas and Aqueelah [20],

in turn, identified four different patterns of communications between MN and MCN. Type I (45%): the communications were proximal to the point of entry of the MCN into the coracobrachialis, type II (35%): the communications were distal to the point of entry of the MCN into the coracobrachialis, type III (9%): the MCN did not pierce the coracobrachialis and type IV (8%): the communications were proximal to the point of entry of the MCN into the coracobrachialis and additional communication took place distally. Concomitantly the MCN was absent. Based on their own research, Maeda et al. [21] concluded, that the MCN and MN have the possibility of forming plexuses in the arm. Further studies supplemented by intraneural dissection on various cases of atypical MN and MCN formation should enable the distribution and origin of those aberrant nerve fibres to be traced. Fine dissection makes the nerve communications and separations clearly visible. For instance, studies of the MCN and MN by Kawashima et al. [18] and Maeda et al. [21] were performed with removing the epineurium under water immersion.

Bergman et al. [3] provide a concise and clear explanation of phenomena relating to atypical formations of nerves. The cited authors describe them as: "errors in the pathway (course) of some, inappropriately placed nerve fibres. For these nerve fibres to get to their proper endpoint, the bundle of nerve fibres leaves the inappropriate trunk and joins the proper nerve trunk". The background of anatomical variations among neurovascular structures based on molecular signals and factors was stressed by Carmeliet [4]. Comparative anatomical research could explain the occasional close relationship between the MN and MCN. Since the MCN is absent in lower vertebrates, the lack of a separate trunk of this nerve in humans could be considered a phylogenetic remnant [22]. Embryological studies also suggest that the MCN is derived from the MN [22]. Case of absence of the MCN associated with a supernumerary head of biceps brachii was described by Pacholczak et al. [25]. Thus, combinations of anatomical variations should be taken into account in the clinical practice [6, 7, 14, 19, 24–28].

Awareness of variable anatomy of the brachial plexus and its branches could influence the safety and success of surgical procedures [12, 16, 17, 32]. This is perhaps reflected in the case described by Hagemann et al. [12], who reported an adverse clinical outcome of a MN to MCN transfer abandoned because of

a neuroanatomical variation. Many surgical exposures of the humerus could potentially harm the MCN [9, 26, 32, 35]. An atypical MCN or an elongated lateral cord of the brachial plexus occupying an atypical position anterior to the coracobrachialis muscle seem to be at greater risk of injury during surgery [35].

Atypical formations of nerves can also influence the clinical manifestation of neurological lesions after repair of a nerve injury [13, 16, 29, 32]. Sinha et al. [29] emphasized that the first factor influencing repair of a nerve lesion is the number of axons that successfully cross the anastomotic site. According to those authors, approximately 30% of axons are lost while traversing one anastomotic site. In this regard, Sinha et al. [29] conclude that "The knowledge of exact fascicular location might be translatable to the operating room and can be used to anastomose related fascicles in brachial plexus surgery, thereby avoiding the possibility of axonal misrouting and improving the results of plexal reconstruction". Considering the numerous variations of the MN and MCN, advanced anatomical studies using intraneural dissection could fill the gaps in our knowledge of the origin of nerve fibres and help clinicians to deal with atypical cases [7]. It may be concluded, after Guerri-Guttenberg and Ingolotti [11], that the knowledge of these nerve's variations "will allow physicians to correctly interpret anomalous innervation patterns of the upper limb". It should also be noted that anatomical variability is the rule [36].

CONCLUSIONS

When the musculocutaneous nerve does not penetrate the coracobrachialis muscle, it may have a close relationship with the median nerve. The intraneural dissection confirmed the presence of separate fascicles corresponding to the MCN in cases of atypical formation of the MN and MCN. Awareness and detailed knowledge of anatomical variations can be crucial during clinical examination, brachial plexus repair or peripheral nerve surgeries (level of evidence IV, case series).

Conflict of interest: None declared

REFERENCES

1. Aydin ME, Kale A, Edizer M, et al. Absence of the musculocutaneous nerve together with unusual innervation of the median nerve. Folia Morphol. 2006; 65(3): 228–231, indexed in Pubmed: 16988921.
2. Beheiry EE. Anatomical variations of the median nerve distribution and communication in the arm. Folia Morphol. 2004; 63(3): 313–318, indexed in Pubmed: 15478107.
3. Bergman RA, Afifi AK, Miyauchi R. (2015) Illustrated encyclopedia of human anatomic variation, opus III: nervous system: plexuses: musculocutaneous nerve. https://www.anatomyatlases.org/AnatomicVariants/NervousSystem/Text/MusculocutaneousNerve.shtml.
4. Carmeliet P. Blood vessels and nerves: common signals, pathways and diseases. Nat Rev Genet. 2003; 4(9): 710––720, doi: 10.1038/nrg1158, indexed in Pubmed: 12951572.
5. Chentanez V, Jaruprat P, Udomchaisakul P, et al. Multiple variations in the course and motor branching pattern of the musculocutaneous nerve with unusual communication with the median nerve. Folia Morphol. 2016; 75(4): 555–559, doi: 10.5603/FM.a2016.0014, indexed in Pubmed: 27830893.
6. Claassen H, Schmitt O, Wree A, et al. Variations in brachial plexus with respect to concomitant accompanying aberrant arm arteries. Ann Anat. 2016; 208: 40–48, doi: 10.1016/j.aanat.2016.07.007, indexed in Pubmed: 27507152.
7. Clarke E, Wysiadecki G, Haładaj R, et al. Fusion between the median and musculocutaneous nerve: A case study. Folia Med Cracov. 2019; 59(3): 45–52, indexed in Pubmed: 31891359.
8. Darvishi M, Moayeri A. Anatomical variations of the musculocutaneous and median nerves: a case report. Folia Med (Plovdiv). 2019; 61(2): 327–331, doi: 10.2478/folmed-2018-0080, indexed in Pubmed: 31301650.
9. Das KK, Joseph J, Gosal JS, et al. "Undercutting of the corresponding rib": a novel technique of increasing the length of donor in intercostal to musculocutaneous nerve transfer in brachial plexus injury. Br J Neurosurg. 2019 [Epub ahead of print]: 1–4, doi: 10.1080/02688697.2019.1630554, indexed in Pubmed: 31208238.
10. Gelmi C, Pedrini F, Fermi M, et al. Communication between median and musculocutaneous nerve at the level of cubital fossa: a case report. Transl Res Anat. 2018; 11: 1–4, doi: 10.1016/j.tria.2018.04.001.
11. Guerri-Guttenberg RA, Ingolotti M. Classifying musculocutaneous nerve variations. Clin Anat. 2009; 22(6): 671–683, doi: 10.1002/ca.20828, indexed in Pubmed: 19637305.
12. Hagemann C, Stücker R, Breyer S, et al. Nerve transfer from the median to musculocutaneous nerve to induce active elbow flexion in selected cases of arthrogryposis multiplex congenita. Microsurgery. 2019; 39(8): 710–714, doi: 10.1002/micr.30451, indexed in Pubmed: 30891796.
13. Haładaj R, Wysiadecki G, Macchi V, et al. Anatomic variations of the lateral femoral cutaneous nerve: remnants of atypical nerve growth pathways revisited by intraneural fascicular dissection and a proposed classification. World Neurosurg. 2018; 118: e687–e698, doi: 10.1016/j.wneu.2018.07.021, indexed in Pubmed: 30010076.
14. Haładaj R, Wysiadecki G, Polguj M, et al. Hypoplastic superficial brachioradial artery coexisting with atypical formation of the median and musculocutaneous nerves: a rare combination of unusual topographical relationships. Surg Radiol Anat. 2019; 41(4): 441–446, doi: 10.1007/s00276-019-02183-1, indexed in Pubmed: 30652211.
15. Hayashi M, Shionoya K, Hayashi S, et al. A novel classification of musculocutaneous nerve variations: The relationship between the communicating branch and transposed innervation of the brachial flexors to the median nerve. Ann Anat. 2017; 209: 45–50, doi: 10.1016/j.aanat.2016.08.004, indexed in Pubmed: 27765675.
16. Isaacs J, Ugwu-Oju O. High median nerve injuries. Hand Clin. 2016; 32(3): 339–348, doi: 10.1016/j.hcl.2016.03.004, indexed in Pubmed: 27387077.
17. Kara AB, Elvan Ö, Öztürk NC, et al. Communications of the median nerve in foetuses. Folia Morphol. 2018; 77(3): 441–446, doi: 10.5603/FM.a2017.0107, indexed in Pubmed: 29131277.
18. Kawashima T, Yoshitomi S, Sasaki H. Nerve fibre tracing of branches to the coracobrachialis muscle in a Bornean orangutan (Pongo pygmaeus pygmaeus). Anat Histol Embryol. 2007; 36(1): 19–23, doi: 10.1111/j.1439-0264.2006.00714.x, indexed in Pubmed: 17266662.
19. Kimura S, Amatani H, Nakai H, et al. A novel case of multiple variations in the brachial plexus with the middle trunk originating from the C7 and C8. Anat Sci Int. 2020; 95(4): 559–563, doi: 10.1007/s12565-020-00541-3, indexed in Pubmed: 32333262.
20. Loukas M, Aqueelah H. Musculocutaneous and median nerve connections within, proximal and distal to the coracobrachialis muscle. Folia Morphol. 2005; 64(2): 101–108, indexed in Pubmed: 16121328.
21. Maeda S, Kawai K, Koizumi M, et al. Morphological study of the communication between the musculocutaneous and median nerves. Anat Sci Int. 2009; 84(1-2): 34–40, doi: 10.1007/s12565-008-0005-y.
22. Mahan MA, Spinner RJ. Nerves of the upper extremity. In: Tubbs RS, Shoja MM, Loukas M. Bergman's comprehensive encyclopedia of human anatomic variation. Wiley, Hoboken 2016: 1068–1112.
23. Nakatani T, Tanaka S, Mizukami S. Absence of the musculocutaneous nerve with innervation of coracobrachialis, biceps brachii, brachialis and the lateral border of the forearm by branches from the lateral cord of the brachial plexus. J Anat. 1997; 191 (Pt 3): 459–460, doi: 10.1046/j.1469-7580.1997.19130459.x, indexed in Pubmed: 9419004.
24. Olewnik Ł, Paulsen F, Tubbs RS, et al. Potential compression of the musculocutaneous, median and ulnar nerves by a very rare variant of the coracobrachialis longus muscle. Folia Morphol. 2021; 80(3): 707–713, doi: 10.5603/FM.a2020.0085, indexed in Pubmed: 32844391.
25. Pacholczak R, Klimek-Piotrowska W, Walocha JA. Absence of the musculocutaneous nerve associated with a supernumerary head of biceps brachii: a case report. Surg Radiol Anat. 2011; 33(6): 551–554, doi: 10.1007/s00276-010-0771-9, indexed in Pubmed: 21225427.
26. Pećina M, Bojanić I. Musculocutaneous nerve entrapment in the upper arm. Int Orthop. 1993; 17(4): 232–234, doi: 10.1007/BF00194185, indexed in Pubmed: 8407039.
27. Roy J, Henry BM, Pekala PA, et al. Median and ulnar nerve anastomoses in the upper limb: A meta-analysis. Muscle

Nerve. 2016; 54(1): 36–47, doi: 10.1002/mus.24993, indexed in Pubmed: 26599506.

28. Schwerdtfeger L, Pascoe M, Clapp T. High incidence of a third head of biceps brachii in females. Transl Res Anat. 2018; 12: 25–27, doi: 10.1016/j.tria.2018.08.001.

29. Sinha S, Prasad GL, Lalwani S. A cadaveric microanatomical study of the fascicular topography of the brachial plexus. J Neurosurg. 2016; 125(2): 355–362, doi: 10.3171/2015.6.JNS142181, indexed in Pubmed: 26654179.

30. Sirico F, Castaldo C, Baioccato V, et al. Prevalence of musculocutaneous nerve variations: Systematic review and meta-analysis. Clin Anat. 2019; 32(2): 183–195, doi: 10.1002/ca.23256, indexed in Pubmed: 30113088.

31. Standring S. Gray's anatomy: the anatomical basis of clinical practice. Churchill Livingstone 2016: 831–832.

32. Sunderland S. The anatomy and physiology of nerve injury. Muscle Nerve. 1990; 13(9): 771–784, doi: 10.1002/mus.880130903, indexed in Pubmed: 2233864.

33. Mat Taib CN, Hassan SNA, Esa N, et al. Anatomical variations of median nerve formation, distribution and possible communication with other nerves in preserved human cadavers. Folia Morphol. 2017; 76(1): 38–43, doi: 10.5603/FM.a2016.0045, indexed in Pubmed: 27665953.

34. Zapałowicz K, Radek M. The distribution of brachial plexus lesions after experimental traction: a cadaveric study. J Neurosurg Spine. 2018; 29(6): 704–710, doi: 10.3171/2018.5.SPINE171148, indexed in Pubmed: 30265223.

35. Zlotolow DA, Catalano LW, Barron OA, et al. Surgical exposures of the humerus. J Am Acad Orthop Surg. 2006; 14(13): 754–765, doi: 10.5435/00124635-200612000-00007, indexed in Pubmed: 17148623.

36. Żytkowski A, Tubbs R, Iwanaga J, et al. Anatomical normality and variability: Historical perspective and methodological considerations. Trans Res Anat. 2021; 23: 100105, doi: 10.1016/j.tria.2020.100105.

VIA MEDICA

CASE REPORT

An unusual anatomical variant of the left phrenic nerve encircling the transverse cervical artery

J.-H. Lee[1] , H.-T. Kim[2], I.-J. Choi[1], Y.-R. Heo[1], Y.-W. Jung[3]

[1]Department of Anatomy, School of Medicine, Keimyung University, Daegu, Republic of Korea
[2]Department of Anatomy, School of Medicine, Catholic University of Daegu, Republic of Korea
[3]Department of Anatomy, College of Medicine, Dongguk University, Gyeongju, Republic of Korea

During educational dissection of cadavers, we encountered anatomical variability of the left phrenic nerve (PN). In this cadaver, nerve fibres from C3 and C4 descended and crossed behind the transverse cervical artery (TCA), a branch of the thyrocervical trunk, at the level of the anterior scalene muscle. On the other hand, nerve fibres from C5 descended obliquely above the TCA and then joined the fibres from C3–C4 on the medial side of the anterior scalene muscle to form the PN. To our knowledge, the encircling of the TCA by the left PN in the neck has not yet been reported and may pose a potential risk for nerve compression during movement of the neck. We discuss several types of anatomical variants of the PN and the associated risk during thorax and neck dissection procedures. (Folia Morphol 2021; 80, 4: 1027–1031)

Key words: phrenic nerve, transverse cervical artery, variation

INTRODUCTION

The phrenic nerve (PN) is one of the most important nerves in the body, due to its role in respiration. The PN mainly arises from the fourth cervical ventral ramus (C4) and receives contributions from the third (C3) and fifth (C5) cervical ventral rami in the posterior triangle of the neck. It descends obliquely along the surface of the anterior scalene muscle from the posterior margin to the anterior, then enters the thorax by passing in front of the subclavian artery (SCA). Phrenic nerve injury can lead to diaphragmatic paralysis, temporary dyspnoea, and eventually worsen respiratory function due to the motor supply to the major respiratory muscles of the diaphragm; however, there is scarce literature on the anatomy of the nerve during neck dissection [23].

Unilateral diaphragmatic paralysis is frequently caused by an iatrogenic injury due to the anatomical variants of the PN that are encountered during thorax and neck procedures, including surgical, anaesthetic, or chiropractic complications [10, 19]. There are several anatomical variants of the PN that have been described; however, most are related to the duplication of the PN, as well as medial and lateral deviations of the PN [3]. Duplication of the PN is associated with early developmental events of the nascent diaphragm [20, 22], while aberrant origin and course of the thyrocervical trunk (TCT) arising in the SCA are thought to be the causes of deviations of the PN [16]. In practice, branches of the SCA, as well as branches of the TCT, can compress the PN and become potential sites of nerve impairment [9, 16].
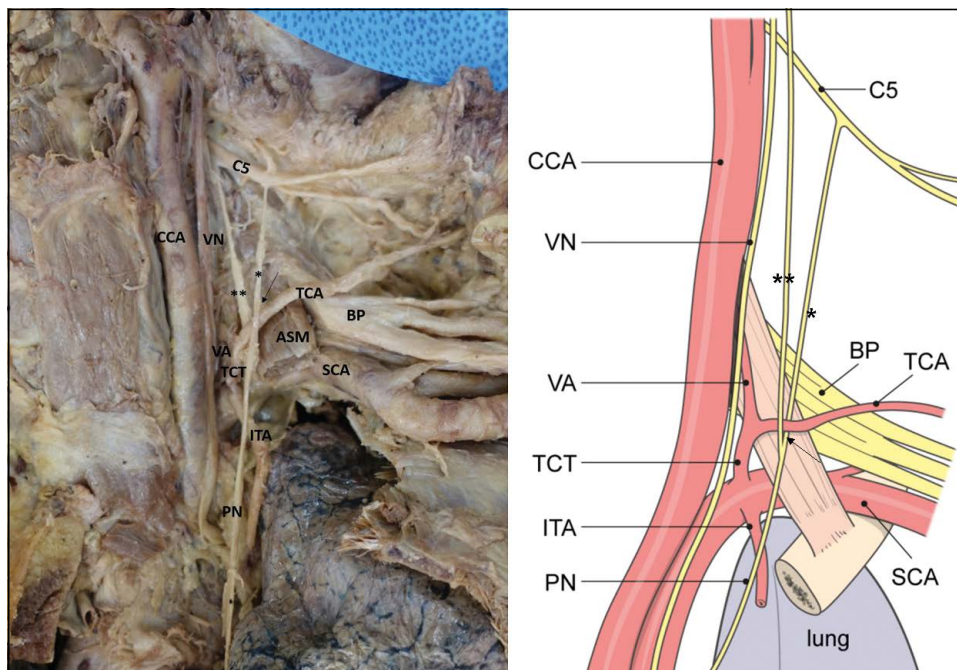
Figure 1. The common carotid artery (CCA) and subclavian artery (SCA) arise directly from the aortic arch. The vagus nerve (VN) enters the thorax between the CCA and SCA. The first portion of the SCA divided into the vertebral artery (VA), the internal thoracic artery (ITA), and the common trunk of thyrocervical trunk (TCT). The common trunk is located close to the medial edge of the anterior scalene muscle (ASM). The nerve fibres from C3 and C4 (**) descend passing the lateral side of VN and then cross the transverse cervical artery (TCA) posteriorly on the anterior scalene muscle. In contrast, the nerve fibres from C5 (*) descend obliquely above the TCA toward the thorax. The fibres from C3–C4 and C5 join together and then form a loop around the TCA. After encircling the TCA, the phrenic nerve (PN) accompanies the ITA descending toward the thorax; **nerve fibres from C3–C4; *nerve fibres from C5, C5 — ventral ramus of C5; BP — brachial plexus.

Injury to the PN caused by anatomic variations of the accessory PN have also been reported [15].

Recently, it has been suggested that the PN might be pulled more laterally by the transverse cervical artery (TCA), a branch of the TCT, based on changes in posture and movement of the neck [9]. In addition, disruption in the normal quality of the prevertebral fascia between the TCA and the PN on the anterior scalene muscle may result in adherence between the two structures and eventually lead to vascular compression of the nerve following surgical and interventional vascular procedures [11].

Thus, it is important to understand the anatomic relationship between anatomic variants of the PN and the TCT itself and/or the TCA in the neck region, in order to reduce postoperative complications. In this report, we present the potential risks of left PN injury, which is caused by the TCA, one of the branches of the TCT, which we believe has not yet been reported.

CASE REPORT

During a routine educational dissection, a rare encircling of the left PN around the TCA was found in an 83-year-old Korean male cadaver. The SCA and

common carotid artery arose directly from the aortic arch. The vagus nerve entered the thorax between the common carotid artery and SCA. The first portion of the SCA divided into the vertebral artery, the internal thoracic artery, the TCT, the common trunk of TCA, the suprascapular artery, and the inferior thyroid artery. The common trunk, close to the medial edge of the left anterior scalene muscle, continued to extend approximately 3 cm from the SCA and then divided into the TCA and the inferior thyroid artery (the inferior thyroid artery had already been removed by the students) (Fig. 1). The left anterior scalene muscle crossed under the TCA before being inserted into the first rib.

The left PN arose from ventral ramus of C3 to C5. The nerve fibres from C3 and C4 first descended passing the lateral side of the vagus nerve, and then crossed behind the TCA on the anterior scalene muscle. In contrast, the nerve fibres from C5 descended obliquely above the TCA toward the thorax. The fibres from the C3–C4 and C5 joined with each other, and then formed a loop around the TCA on the medial side of the anterior scalene muscle (Fig. 1). Therefore, the left PN may be greatly affected by the

movement of the neck and/or change in posture at the level of the anterior scalene muscle. In addition, TCA compressions can be one of the mechanisms of left PN injury, due to altered conditions that lead to changes in the course and calibre of the TCA occur, such as inflammation. After encircling the TCA, the left PN accompanied the internal thoracic artery and descended toward the thorax.

DISCUSSION

Diagnosis of PN injury requires great discretion due to non-specific signs and symptoms, including unexplained shortness of breath with exertion and/or supine position, increased fatigue, loss of energy, gastrointestinal reflux, bloating (left sided paralysis), and insomnia [6]. In unilateral diaphragmatic paralysis, the patient is often asymptomatic at rest and has dyspnoea only during exertion. In comparison, patients with bilateral paralysis always present shortness of breath [13]. However, mortality and morbidity associated with PN injury, and subsequent diaphragmatic paralysis, depend on the underlying causes and status of pulmonary function [12]

The motor fibres of the PN command the contraction of the diaphragmatic muscles and are controlled mainly by the C3–C5 segments of the neural tube. The axons of the right and left PNs descend along the vertebrae and pericardium, enter the diaphragm, and subdivide into several branches that innervate the respiratory muscles [20]. In the posterior neck, the cervical PN crosses obliquely to the anterior scalene muscle. It also traverses below the TCA and supra-scapular artery, a branch of the TCT arising from the SCA [9].

Considerable variation of the standard anatomy of the PN in the neck has not been extensively described in the literature. Interestingly, frequent PN variation occurs in patients with supraclavicular decompression surgery for neurogenic thoracic outlet syndrome; however, there are few reports based on cadaver research [3]. In this report, anatomic variations of the PN were identified in 28 (28%) patients with duplicated PNs, accessory PN, and medially or laterally displaced PNs. Duplicated PN is defined as the same-sized medial and lateral contributions of the PN, regardless of its relationship to the anterior scalene muscle. Phrenic nerve duplication may originate in early stages of ontogenesis, as a result of alternative developmental pathways, in which axons of the PN, specific to a given domain of the diaphragm, running separately at a specific stage of development, instead of forming a single stem [20, 22]. In addition, accessory PN arising from superior trunk of the brachial plexus, ansa cervicalis, or nerve to subclavius was reported [15]. The accessory PN usually lies lateral to the PN and traverses the neck with a highly variable course [4]. This variable course of the accessory PN increases the complexity of the surgical procedure performed in the neck. Displacement of the PNs have also been observed, specifically with a completely medial or lateral course relative to the belly of the anterior scalene muscle. Topographical studies of the relationship between the PN and variation of the origin of the TCT demonstrate that lateral displacement of the PN results from the unusual origin of the TCT, which arises from the third portion of the SCA [9, 16]. Lischka et al. [14] reported that the TCT arose from the third portion of the SCA in 2 among 166 possibilities (83 cases, 2 sides each). In general, the TCT is formed by the fusion of the suprascapular artery, TCA, and the inferior thyroid artery, which originate from the first portion of the SCA. The aberrant origin of the TCT can lead to potential impairment of the PN. Hamada et al. [5] also reported that lateral displacement of the PN could increase the risk of PN injury during internal jugular or subclavian venous catheter placement and brachial plexus block. In addition, marked lateral deviation and subsequent strain of the PN in the neck could increase the risk of nerve injury or nerve dysfunction [16]. Pretterklieber et al. [18] described that left PN passed the diaphragm dorsal to the apex of the pericardium, though its passage is described as the oesophageal hiatus in many textbooks. In present case, left PN passed not the oesophageal hiatus but the diaphragm. Anatomical study about the PN was rare, therefore, its further study should be performed with larger cases.

Post-procedural and post-surgical nerve injuries may result from direct nerve transection, stretching, or may be secondary to the fibrosis and scarring that occurs after inflammation. Loss of normal tissue properties and adherence between normally separate anatomical structures can lead to compression and nerve dysfunction [9]. In this case, the nerve fibres from the C3 and C4 ventral rami transverse the anterior scalene muscle superiorly in the posterior neck, just under the prevertebral fascia, before joining the nerve fibres from C5. We postulated that trauma or manipulation in the neck, including neck surgery, may result in inflammation of the prevertebral fascia,

scalene muscle induration, and, in association with an intramuscular haematoma, can sometimes cause adhesion and compression of the ventral rami of the left PN where it is interposed between the muscles and the inflammatory semi-rigid prevertebral fascia.

This case also shows that nerve fibres from C3–C4 and C5 separately cross the TCA posteriorly and superiorly on the anterior scalene muscle forming a loop around the TCA. Kaufman et al. [9] reported 3 patients with diaphragm paralysis caused by TCA compression of the PN. They described that this artery normally originated from the TCT in the first portion of the SCA. They called this condition the 'Red Cross Syndrome' and reported that one in three patients suffered severe dyspnoea when turning their head to the affected side. In our case, as in the report by Kaufman et al. [9], the root of TCA arose from the TCT. We postulated that the potential risk of PN compression by the TCA is based on the movement of the neck or change in posture. In addition, the left PN and/or PN loop might be pulled more laterally by the altered course and calibre of the ipsilateral TCA. Thus, a vascular nerve compression may result in either an ischaemic or demyelinating neurapraxia. Vascular compression of a central and peripheral nerve has been well examined in various locations throughout the body. Examples of such events include the vertebral artery compression of a cervical root, cerebral arterial compression of the intracranial trigeminal nerve, vascular compression of the vestibulocochlear nerve, vascular compression of the occipital nerve causing migraine headaches, and radial nerve palsy secondary to a thickened recurrent radial artery [2, 7, 8]. In particular, the radial nerve palsy condition may occur in a similar manner to our case in that, prior trauma or inflammation may alter the calibre or course of the TCA and/or the spatial relationship between it and the involved PN.

Iatrogenic damage to the PN is most commonly due to cardiothoracic or neck surgery and is described after interscalene brachial plexus block and central vein catheterisation [17]. Other studies have shown that carotid-subclavian bypass grafting (CSBG) procedures were associated with PN injury, with levels of morbidity after iatrogenic injury varying across patient types [21]. Cohen et al. [1] showed that patients with chronic obstructive pulmonary disease (COPD) and PN injury after CSBG had significantly worse survival rates than those of patients with only COPD or PN injury undergoing the same procedures.

CONCLUSIONS

In the present article, we described a variant of the left PN, which can be compressed by the TCA depending on the movement of the neck or even changes in posture. Additionally, variants of the PN can increase the risk of iatrogenic injury during neck procedures, including surgery. Moreover, PN injury can have a substantial negative impact on a patient's quality of life compared to that in other groups. Based on the increasing use of invasive procedures, accurate knowledge of the anatomic variants of the PN is of considerable importance for surgeries and interventional vascular procedures. Therefore, we believe that this case report will be helpful for clinicians who perform these procedures.

REFERENCES

1. Cohen AJ, Katz MG, Katz R, et al. Phrenic nerve injury after coronary artery grafting: is it always benign? Ann Thorac Surg. 1997; 64(1): 148–153, doi: 10.1016/s0003-4975(97)00288-9, indexed in Pubmed: 9236351.
2. Fink JR, Leung JY, Creutzfeldt CJ. Vertebral artery loop formation causing severe cervical nerve root compression. Neurology. 2010; 75(2): 192, doi: 10.1212/WNL. 0b013e3181e7ca44, indexed in Pubmed: 20625174.
3. Golarz SR, White JM. Anatomic variation of the phrenic nerve and brachial plexus encountered during 100 supraclavicular decompressions for neurogenic thoracic outlet syndrome with associated postoperative neurologic complications. Ann Vasc Surg. 2020; 62: 70–75, doi: 10.1016/j. avsg.2019.04.010, indexed in Pubmed: 31207398.
4. Graves MJ, Henry BM, Hsieh WC, et al. Origin and prevalence of the accessory phrenic nerve: a meta-analysis and clinical appraisal. Clin Anat. 2017; 30(8): 1077–1082, doi: 10.1002/ca.22956, indexed in Pubmed: 28726261.
5. Hamada T, Usami A, Kishi A, et al. Anatomical study of phrenic nerve course in relation to neck dissection. Surg Radiol Anat. 2015; 37(3): 255–258, doi: 10.1007/s00276-014-1343-1, indexed in Pubmed: 25026999.
6. Hart N, Nickol AH, Cramer D, et al. Effect of severe isolated unilateral and bilateral diaphragm weakness on exercise performance. Am J Respir Crit Care Med. 2002; 165(9): 1265–1270, doi: 10.1164/rccm.2110016, indexed in Pubmed: 11991876.
7. Janis JE, Hatef DA, Reece EM, et al. Neurovascular compression of the greater occipital nerve: implications for migraine headaches. Plast Reconstr Surg. 2010; 126(6): 1996–2001, doi: 10.1097/PRS.0b013e3181ef8c6b, indexed in Pubmed: 21124138.
8. Johnson RD, Mitchell R, Maartens N. Trigeminal neuralgia due to severe vascular compression of the trigeminal nerve. ANZ J Surg. 2011; 81(4): 289–290, doi: 10.1111/j.1445-2197.2011.05676.x, indexed in Pubmed: 21418476.

9. Kaufman MR, Willekes LJ, Elkwood AI, et al. Diaphragm paralysis caused by transverse cervical artery compression of the phrenic nerve: the Red Cross syndrome. Clin Neurol Neurosurg. 2012; 114(5): 502–505, doi: 10.1016/j.clineuro.2012.01.048, indexed in Pubmed: 22366245.

10. Kessler J, Schafhalter-Zoppoth I, Gray AT. An ultrasound study of the phrenic nerve in the posterior cervical triangle: implications for the interscalene brachial plexus block. Reg Anesth Pain Med. 2008; 33(6): 545–550, indexed in Pubmed: 19258969.

11. Kim HaY, Soh EY, Lee J, et al. Incidence of hemi-diaphragmatic paresis after ultrasound-guided intermediate cervical plexus block: a prospective observational study. J Anesth. 2020; 34(4): 483–490, doi: 10.1007/s00540-020-02770-2, indexed in Pubmed: 32236682.

12. Kokatnur L, Rudrappa M. Diaphragmatic Palsy. Diseases. 2018; 6(1), doi: 10.3390/diseases6010016, indexed in Pubmed: 29438332.

13. Kumar N, Folger WN, Bolton CF. Dyspnea as the predominant manifestation of bilateral phrenic neuropathy. Mayo Clin Proc. 2004; 79(12): 1563–1565, doi: 10.4065/79.12.1563, indexed in Pubmed: 15595343.

14. Lischka MF, Krammer EB, Rath T, et al. The human thyrocervical trunk: configuration and variability reinvestigated. Anat Embryol (Berl). 1982; 163(4): 389–401, doi: 10.1007/BF00305554, indexed in Pubmed: 7091707.

15. Loukas M, Kinsella CR, Louis RG, et al. Surgical anatomy of the accessory phrenic nerve. Ann Thorac Surg. 2006; 82(5): 1870–1875, doi: 10.1016/j.athoracsur.2006.05.098, indexed in Pubmed: 17062263.

16. Ogami K, Saiki K, Okamoto K, et al. Marked lateral deviation of the phrenic nerve due to variant origin and course of the thyrocervical trunk: a cadaveric study. Surg Radiol Anat. 2016; 38(4): 485–488, doi: 10.1007/s00276-015-1557-x, indexed in Pubmed: 26438272.

17. Pakala SR, Beckman JD, Lyman S, et al. Cervical spine disease is a risk factor for persistent phrenic nerve paresis following interscalene nerve block. Reg Anesth Pain Med. 2013; 38(3): 239–242, doi: 10.1097/AAP.0b013e318289e922, indexed in Pubmed: 23518866.

18. Pretterklieber B, Hader M, Hammer N, et al. When and why was the phrenicoabdominal branch of the left phrenic nerve placed into the esophageal hiatus in German textbooks of anatomy? An anatomical study on 400 specimens reevaluating its course through the diaphragm. Ann Anat. 2020; 227: 151415, doi: 10.1016/j.aanat.2019.151415, indexed in Pubmed: 31513915.

19. Schram DJ, Vosik W, Cantral D. Diaphragmatic paralysis following cervical chiropractic manipulation: case report and review. Chest. 2001; 119(2): 638–640, doi: 10.1378/chest.119.2.638, indexed in Pubmed: 11171749.

20. Sefton EM, Gallardo M, Kardon G. Developmental origin and morphogenesis of the diaphragm, an essential mammalian muscle. Dev Biol. 2018; 440(2): 64–73, doi: 10.1016/j.ydbio.2018.04.010, indexed in Pubmed: 29679560.

21. Tripp HF, Bolton JW. Phrenic nerve injury following cardiac surgery: a review. J Card Surg. 1998; 13(3): 218–223, doi: 10.1111/j.1540-8191.1998.tb01265.x, indexed in Pubmed: 10193993.

22. Wysiadecki G, Polguj M, Topol M. An unusual variant of the abducens nerve duplication with two nerve trunks merging within the orbit: a case report with comments on developmental background. Surg Radiol Anat. 2016; 38(5): 625–629, doi: 10.1007/s00276-015-1573-x, indexed in Pubmed: 26501961.

23. Yaddanapudi S, Shah SC. Bilateral phrenic nerve injury after neck dissection: an uncommon cause of respiratory failure. J Laryngol Otol. 1996; 110(3): 281–283, doi: 10.1017/s0022215100133432, indexed in Pubmed: 8730372.

CASE REPORT

VIA MEDICA

Hepatomesenteric trunk, gastrosplenic trunk, coiled splenic and hepatic arteries, and a variant of Bühler's arc

M. Şelaru¹*, M.C. Rusu²*, A.M. Jianu³*, F. Bîrsăşteanu⁴*, B.A. Manta⁵*

¹Department of Surgery, Faculty of Medicine, "Victor Babes" University of Medicine and Pharmacy, Timişoara, Romania
²Division of Anatomy, Faculty of Dental Medicine, "Carol Davila" University of Medicine and Pharmacy, Bucharest, Romania
³Department of Anatomy and Embryology, Faculty of Medicine, "Victor Babes" University of Medicine and Pharmacy, Timisoara, Romania
⁴Department of Radiology and Medical Imaging, Faculty of Medicine, "Victor Babes" University of Medicine and Pharmacy, Timisoara, Romania
⁵"Carol Davila" University of Medicine and Pharmacy, Bucharest, Romania

The coeliac trunk is normally divided into the left gastric artery (LGA), splenic artery, and common hepatic artery (CHA). The combination between these arteries and the superior mesenteric artery (SMA) generates various combinations. We report here such a rare anatomic variant, namely the hepatomesenteric trunk (HMT), combined with a gastrosplenic trunk (GST). The variant was identified using computed tomography angiograms of a 62-year-old woman. The GST emerged from the aorta within the aortic hiatus of the diaphragm, a previously unknown possibility. Further, an accessory left hepatic artery originated from the LGA. The phrenic arteries had independent aortic origins. The HMT divided into the CHA and the SMA posterior to the origin of the hepatic portal vein (PV), above the pancreas. The CHA initially had a right course, towards the superior border of the PV, then it descended with a transpancreatic course posterior to the PV, reached its inferior/right border, and divided antero-inferiorly to the PV into the proper hepatic and gastroduodenal arteries. The proper hepatic artery continued on the anterior side of the PV, sending off the left and right hepatic arteries. The HMT and the GST were connected by a rudimentary variant of the arc of Bühler, unreported previously. Arterial variations in the coeliac region are accurately distinguished on computed tomography angiograms. They should be evaluated by surgeons when different surgical procedures are evaluated. (Folia Morphol 2021; 80, 4: 1032–1036)

Key words: aorta, coeliac trunk, superior mesenteric artery, computed tomography, hepatic artery

---

INTRODUCTION

The coeliac trunk (CT) normally sends off the left gastric artery (LGA), splenic artery (SA) and common hepatic artery (CHA) [6, 26].

The presence of aberrant hepatic arterial anatomy increases the surgical complexity and subsequently the potential risk of injury to the hepatic arterial supply during pancreaticobiliary procedures and duodenopancreatectomies [24]. The aortic common origin of the CHA and superior mesenteric artery (SMA) is by a hepatomesenteric trunk (HMT) [9, 15, 16, 21, 22]. This is a rare anatomic variation [21, 24]. The HMT was encountered in 0.5% [1], 2% [5], 2.08% [15], and in 4.47% [33]. Just a couple of studies found the HMT by computed tomographic studies [13, 33]. There are two morphological possibilities when a HMT is formed: either the LGA and SA have independent aortic origins, or they have a common aortic origin — the gastrosplenic trunk (GST) [33].

We report here a HMT, characterised anatomically on computed tomography angiograms, with unusual topography of the co-existing GST, and a rudimentary arc of Bühler uniting the two trunks.

MATERIALS AND METHODS

The anatomic variants reported here were found during a retrospective study of computer tomography scans, in a 62-year-old woman. Briefly, the study consisted in injecting an iodine radiocontrast agent in the left brachial vein (100 mL, with 6 mL/s flow), followed by 50 mL iodine radiocontrast agent (Ultravist 370 mg/mL) in the brachial vein, and by 20 mL saline medium. The computed tomography was performed with a 32-slice scanner (Siemens Multislice Perspective Scanner), using a 0.6 mm collimation and reconstruction of 0.75 mm thickness with 50% overlap for multiplanar and three-dimensional (3D) volume rendering technique [26]. The arterial variant was documented using the Horos software and its 3D Volume Rendering application.

RESULTS

The abdominal aorta (AA) coursed retroperitoneally and was deviated to the right at the level of the third and fourth lumbar vertebrae. The aortic bifurcation into the common iliac arteries was at the level of the fifth lumbar vertebra.

A gastrosplenic trunk (GST) emerged on the anterior surface of the AA at 1.67 cm above the origin of the HMT. The GST runoff was from the anterior
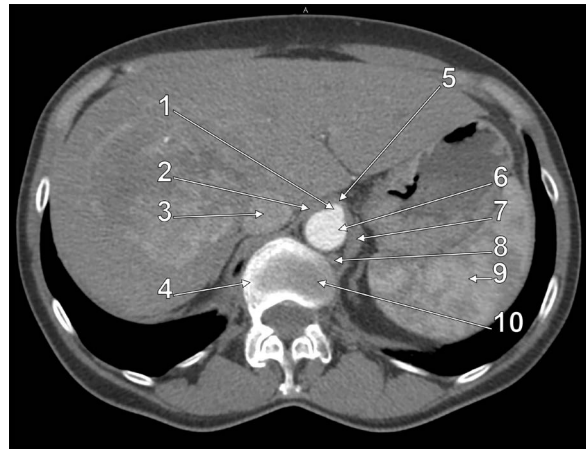
Figure 1. Axial coeliac trunk slice through the origin of the coeliac trunk which is located within the aortic hiatus of the diaphragm; 1 — coeliac trunk; 2 — right pillar of the diaphragm; 3 — inferior cava vein; 4 — first lumbar vertebra; 5 — median arcuate ligament; 6 — descending aorta; 7 — left pillar of the diaphragm; 8 — hemiazygos vein; 9 — spleen; 10 — intervertebral disc between T12 and L1.
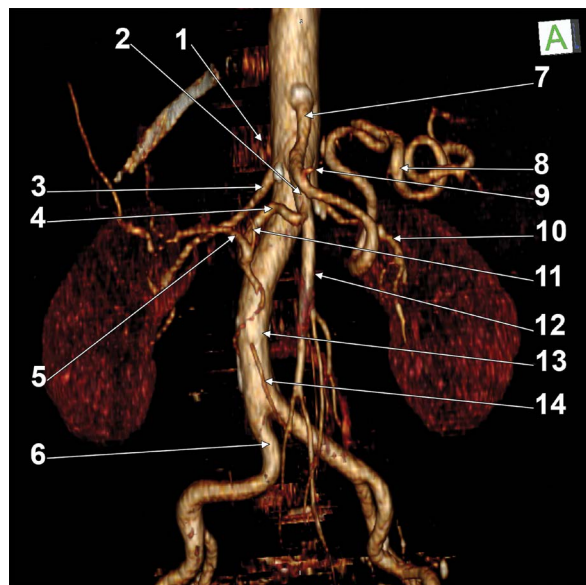
Figure 2. Three-dimensional volume renderisation of the abdominal aorta and its branches; 1 — first lumbar vertebra; 2 — hepatomesenteric trunk; 3 — right renal artery; 4 — common hepatic artery; 5 — right hepatic artery; 6 — right common iliac artery; 7 — gastrosplenic trunk; 8 — splenic artery; 9 — left gastric artery; 10 — left renal artery; 11 — left hepatic artery; 12 — superior mesenteric artery; 13 — abdominal aorta; 14 — inferior mesenteric artery.

midportion of the aorta. The origin of the GST was within, and not inferior to the aortic hiatus of diaphragm, at the level of the intervertebral disc between T12 and L1 (Fig. 1). Just above the origin of the GST was identified an atheromatous plaque of the anterior aortic wall. The GST further branched the LGA and continued with the SA (Fig. 2). The later had a kinked

and coiled morphology (Fig. 2). We could not find a dorsal pancreatic artery originating from the SA.

The two inferior phrenic arteries, right and left, originated independently from the posterior surface of the AA above the level of the origin of the GST.

The inferior mesenteric vein (IMV) extended toward the posterior left side of the SMA, circled the right side of the SMA, and united anteriorly with the superior mesenteric and splenic veins. It thus resulted the hepatic portal vein (PV) which inclined right abruptly towards the hilum of the liver (Fig. 3).

The AA was crossed anteriorly by the left renal vein at the level of the second lumbar vertebra. The HMT divided into the CHA and the SMA anterior to the left renal vein and posterior to the origin of the PV, above the pancreas. The initial segment of the CHA was directed to the right towards the superior border of the PV, then it descended with a transpancreatic course posterior to the PV, reached its inferior/right border, and divided antero-inferiorly to the PV into the proper hepatic (PHA) and gastroduodenal (GDA) arteries. The PHA continued on the anterior side of the PV, which was thus contained within an arterial coil of the CHA and PHA. From the initial segment of the PHA left a rudimentary left hepatic artery (LHA), the left lobe of the liver being also supplied by an accessory LHA emerging from the LGA. Then, the PHA continued as right hepatic artery (RHA) and was further divided in anterior and posterior branches (Fig. 2).

The aortic origins of the HMT and of the right renal artery were at the level of the inferior border of the first lumbar vertebra. The left renal artery emerged the abdominal aorta at the level of the superior border of the second lumbar vertebra.

The HMT and the GST had comparable lengths (Table 1), and were connected by a variant of the arc of Bühler (Fig. 4).

DISCUSSION

A combination of GST and HMT, such as in this case, was found in 1.1% [20], thus being rare. In one of the cases described in the scientific literature, the left phrenic artery branched from the GST, but in the other two the GST origin of a phrenic artery was not found [20]. Similar to our case, the phrenic arteries arose independently from the aorta. Nakamura et al. (2003) [20] documented different studies regarding the prevalence of the GST-HMT variant and found it varying from 0.4% to 1.6%. A recent multidetector computed tomography study on 1569 cases found
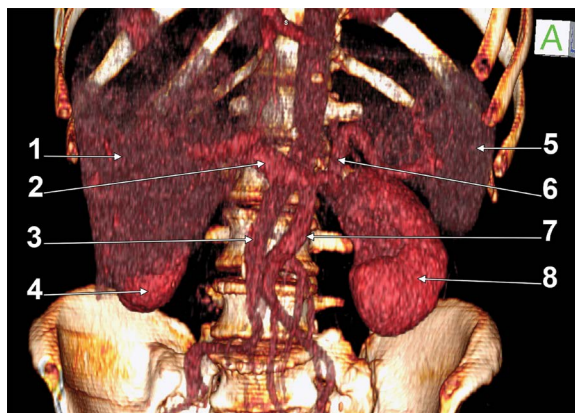
Figure 3. Three-dimensional volume renderisation of the hepatic portal venous system; 1 — liver (hepatomegaly); 2 — portal vein; 3 — superior mesenteric vein; 4 — right kidney; 5 — spleen; 6 — splenic vein; 7 — inferior mesenteric vein; 8 — left kidney.

Table 1. Vascular morphometry of the reported case

Blood vessel	Calibre [mm]	Length [cm]
Gastrosplenic trunk	5.902	2.859
Left gastric artery	1.931	
Splenic artery	5.441	
Hepatomesenteric trunk	5.49	2.983
Superior mesenteric artery	6.66	
Common hepatic artery	4.401	
Splenic vein	9.729	
Inferior mesenteric vein	9.204	
Superior mesenteric vein	8.921	
Portal vein	13.01	
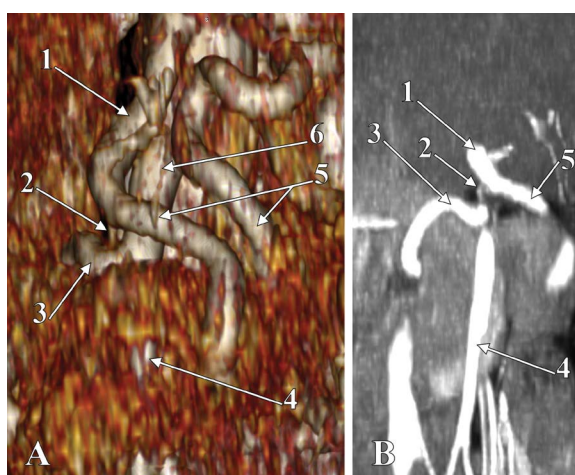
Figure 4. Three-dimensional volume renderisation (left antero-infero-lateral view, **A**), and multiplanar coronal slice (**B**) of the trunks emerging the upper segment of the abdominal aorta (AA). 1 — gastrosplenic trunk; 2 — arc of Bühler; 3 — common hepatic artery; 4 — superior mesenteric artery; 5 — splenic artery; 6 — hepatomesenteric trunk.

the GST in 4.1% of patients [31] but it was not found any GST associated with a HMT, such as in the present report. Uflacker (2006) [32] indicated that the GST might associate a middle hepatic artery origin from the aorta or the SMA. Wang et al. (2014) [33] listed two morphological possibilities in cases with HMT: HMT and GST, such as in this reported case, and HMT with distinct aortic origins for the LGA and SA.

The vertical insertion of the CT in the aortic wall is variable, as related to vertebrae, being found as high as the T11–12 intervertebral disc level [34]. Different studies reporting GSTs did not mention the vertebral level of origin of that trunk, nor related it with the aortic hiatus of the diaphragm [12, 20]. Kahraman et al. (2001) [15] reported the origin of the GST just below the aortic hiatus. In the case reported here the GST emerged within, and not below, the aortic hiatus, which implies a degree of the GST compression during the contractions of the diaphragm. It should be considered here the median arcuate ligament syndrome in which a low insertion of the ligament or a high origin of arterial trunks may cause extrinsic compressions [23].

Different topographical patterns were indicated as possible for a CHA emerged from the HMT [11], all of them describing an exclusively ascending course of the CHA and its variable placement in relation with the hepatic portal vein and the pancreas. However, none of these could be fitted with our findings, as the hepatic portal vein was horizontal and the CHA looped around it.

Common hepatic artery could ascend either anterior [8, 12, 14, 16, 20], or posterior [12, 20, 22, 28] of the PV. Higashi and Hirai (1995) [11] described four types of HMT morphology. In types I–III the course of the CHA was posterior to the PV but in type IV the CHA ascended behind the superior mesenteric vein, passed around in front from the right side of the PV, and reached the liver [10], as was found in our case.

Most HMTs were reported after anatomical dissections [1, 4, 5, 8, 9, 12, 14–16, 20, 22, 24, 28], the computed tomographic evidence being scarce [3, 13, 29, 33].

A HMT could be described as a replaced CHA originating the SMA [7]. This variant corresponds to Michels' type 9 of hepatic artery, in which the author indicated that the coeliac hepatic artery is absent and the entire hepatic trunk derived from the SMA [19]. That variant was found by Michels (1966) [19] in 5 of 200 dissections. There is, however, an incomplete

correspondence of our variant and Michels' type 9 of hepatic artery. This is because Michels indicated the origin of the GDA from the GST [19], while we found that the GDA left the CHA. Hicks et al. (2016) [10] indicated Michels' type 9 of hepatic arterial anatomy by a diagram in which the GDA leaves the LGA, and not the GST, as in Michels' original diagram (1966) [19]. The GDA origin from a replaced CHA, as in our case, corresponds to Tandler's type 5 of CT variation [30]. Therefore, Tandler's type 5 of hepatic artery and, respectively, Michels' type 9 of hepatic artery are reciprocally exclusive. Unlike in Tandler's type 5 we found here an arc of Bühler uniting the GST and HMT.

During development the segmental ventral branches of the abdominal aorta are united by longitudinal anastomoses that may either persist or disappear [12, 18, 25, 30]. There are three known possibilities of anastomoses between the CT and the SMA, the direct one, well known and rarely reported, being the arc that Bühler described in 1904 [2, 17]. We report here a variant of the Bühler's arc that unites the GST and HMT instead of the CT and the SMA. This variant was not reported previously, at least to our knowledge.

Michalinos et al. (2019) [18] reviewed the literature regarding the arc of Bühler and discussed that, although the arc of Bühler is regarded as a remnant of Tandler's ventral longitudinal anastomosis, its embryogenesis is related to that of the dorsal pancreatic artery. This is because that artery could either originate from the SA, or from the SMA, and when both origins are maintained, an arc of Bühler results [18]. This theory is supported by the present findings: an absent dorsal pancreatic artery, seemingly replaced morphologically by a short arc of Bühler.

CONCLUSIONS

Arterial variations in the coeliac region are accurately identified on computed tomography angiograms. They should be evaluated by surgeons when different surgical procedures are evaluated.

Conflict of interest: None declared

REFERENCES

1. Adachi B. Das arteriensystem der japaner: In 2 bdn: Maruzen Company; 1928.
2. Bergman RA, Tubbs RS, Shoja MM. Bergman's comprehensive encyclopedia of human anatomic variation. John Wiley & Sons, Hoboken, New Jersey 2016.

3. Bueschel P, Meyer F, Weber M, et al. Rare aneurysm of the hepatic artery with overlap to the gastroduodenal artery in very uncommon coincidence with occurence of hepatomesenteric trunk. Wien Klin Wochenschr. 2013; 125(3-4): 111–114, doi: 10.1007/s00508-012-0317-8, indexed in Pubmed: 23420527.

4. Chandramohan K, Abdulla FA, Thomas S. Periampullary carcinoma complicated by a transpancreatic hepatomesenteric trunk-a case report of an extremely rare vascular anomaly. Indian J Surg Oncol. 2020; 11(1): 142–146, doi: 10.1007/s13193-019-01001-9, indexed in Pubmed: 32205984.

5. Chitra R. Clinically relevant variations of the coeliac trunk. Singapore Med J. 2010; 51(3): 216–219, indexed in Pubmed: 20428743.

6. Grigoriță L, Damen NS, Vaida MA, et al. Unusual anatomical variation: tetrafurcation of the celiac trunk. Surg Radiol Anat. 2019; 41(11): 1399–1403, doi: 10.1007/s00276-019-02286-9, indexed in Pubmed: 31302730.

7. Ha HIl, Kim MJ, Kim J, et al. Replaced common hepatic artery from the superior mesenteric artery: multidetector computed tomography (MDCT) classification focused on pancreatic penetration and the course of travel. Surg Radiol Anat. 2016; 38(6): 655–662, doi: 10.1007/s00276-016-1618-9, indexed in Pubmed: 26758052.

8. Harada H, Yamaki K, Doi Y, et al. An anomalous case of the gastro-splenic and the hepato-mesenteric trunks independently arising from the abdominal aorta. Kurume Med J. 1996; 43(2): 181–184, doi: 10.2739/kurumemedj.43.181, indexed in Pubmed: 8755123.

9. Hemamalini A, Pushpalatha K. Absence of celiac trunk associated with a hepatomesenteric trunk: A case report. J Anat Soc India. 2017; 66: S94, doi: 10.1016/j.jasi.2017.08.296.

10. Hicks CW, Burkhart RA, Weiss MJ, et al. Management of type 9 hepatic arterial anatomy at the time of pancreaticoduodenectomy: considerations for preservation and reconstruction of a completely replaced common hepatic artery. J Gastrointest Surg. 2016; 20(7): 1400–1404, doi: 10.1007/s11605-016-3154-7, indexed in Pubmed: 27138326.

11. Higashi N, Hirai K, Higashi N, et al. [On the hepatic artery arising from the superior mesenteric artery]. Kaibogaku Zasshi. 1995; 70(4): 338–346, indexed in Pubmed: 8540282.

12. Hirai Y, Yamaki K, Saga T, et al. Two anomalous cases of the hepato-mesenteric and the gastro-splenic trunks independently arising from the abdominal aorta. Kurume Med J. 2000; 47(3): 249–252, doi: 10.2739/kurumemedj.47.249, indexed in Pubmed: 11059229.

13. Iacob N, Pureca A, Belic O, et al. A hepatomesenteric trunk, in association with left gastric and splenic arteries arising independently from the abdominal aorta: A case report using MDCT angiography. J Anat Soc India. 2014; 63(2): 179–182, doi: 10.1016/j.jasi.2014.07.001.

14. Iimura A, Oguchi T, Shibata M, et al. An anomalous case of the hepatic artery arising from the superior mesenteric artery. Okajimas Folia Anat Jpn. 2007; 84(2): 61–65, doi: 10.2535/ofaj.84.61, indexed in Pubmed: 17969994.

15. Kahraman G, Marur T, Tanyeli E, et al. Hepatomesenteric trunk. Surg Radiol Anat. 2001; 23(6): 433–435, doi: 10.1007/s00276-001-0433-z, indexed in Pubmed: 11963627.

16. Kardile PB, Ughade JM, Ughade MN, et al. Anomalous origin of the hepatic artery from the hepatomesenteric trunk. J Clin Diagn Res. 2013; 7(2): 386–388, doi: 10.7860/JCDR/2013/5304.2778, indexed in Pubmed: 23543854.

17. McNulty JG, Hickey N, Khosa F, et al. Surgical and radiological significance of variants of Bühler's anastomotic artery: a report of three cases. Surg Radiol Anat. 2001; 23(4): 277–280, doi: 10.1007/s00276-001-0277-6, indexed in Pubmed: 11694975.

18. Michalinos A, Schizas D, Ntourakis D, et al. Arc of Bühler: the surgical significance of a rare anatomical variation. Surg Radiol Anat. 2019; 41(5): 575–581, doi: 10.1007/s00276-018-2168-0, indexed in Pubmed: 30552487.

19. Michels NA. Newer anatomy of the liver and its variant blood supply and collateral circulation. Am J Surg. 1966; 112(3): 337–347, doi: 10.1016/0002-9610(66)90201-7, indexed in Pubmed: 5917302.

20. Nakamura Y, Miyaki T, Hayashi S, et al. Three cases of the gastrosplenic and the hepatomesenteric trunks. Okajimas Folia Anat Jpn. 2003; 80(4): 71–76, doi: 10.2535/ofaj.80.71, indexed in Pubmed: 14964466.

21. Nakano H, Kikuchi K, Seta Si, et al. A patient undergoing pancreaticoduodenectomy in whom involved common hepatic artery anomalously arising from the superior mesenteric artery was removed and reconstructed. Hepatogastroenterology. 2005; 52(66): 1883–1885, indexed in Pubmed: 16334799.

22. Nayak S. Hepatomesenteric trunk and gastro-splenicophrenic trunk. Int J Anat Variat. 2008; 1: 2–3.

23. Ozbülbül NI. CT angiography of the celiac trunk: anatomy, variants and pathologic findings. Diagn Interv Radiol. 2011; 17(2): 150–157, doi: 10.4261/1305-3825.DIR.3283-10.1, indexed in Pubmed: 20690078.

24. Rammohan A, Sathyanesan J, Palaniappan R, et al. Transpancreatic hepatomesenteric trunk complicating pancreaticoduodenectomy. JOP. 2013; 14(6): 649–652, doi: 10.6092/1590-8577/1641, indexed in Pubmed: 24216553.

25. Rusu MC, Jianu AM, Sztika D, et al. Three extremely rare anatomic variants of the hepatic artery. Ann Vasc Surg. 2011; 25(8): 1138.e1–1138.e7, doi: 10.1016/j.avsg.2011.03.011, indexed in Pubmed: 21680146.

26. Rusu MC, Manta BA. Novel anatomic variation: heptafurcation of the celiac trunk. Surg Radiol Anat. 2018; 40(4): 457–463, doi: 10.1007/s00276-018-1995-3, indexed in Pubmed: 29497808.

27. Rusu MC, Măru N, Rădoi PM, et al. Trifurcated external carotid artery and complete gamma-loop of its maxillary branch. Surg Radiol Anat. 2019; 41(2): 231–234, doi: 10.1007/s00276-018-2142-x, indexed in Pubmed: 30483866.

28. Saga T, Hirao T, Kitashima S, et al. An anomalous case of the left gastric artery, the splenic artery and hepato-mesenteric trunk independently arising from the abdominal aorta. Kurume Med J. 2005; 52(1-2): 49–52, doi: 10.2739/kurumemedj.52.49, indexed in Pubmed: 16119612.

29. Schwarz L, Huet E, Yzet T, et al. An extremely uncommon variant of left hepatic artery arising from the superior mesenteric artery. Surg Radiol Anat. 2014; 36(1): 91–94, doi: 10.1007/s00276-013-1131-3, indexed in Pubmed: 23652481.

30. Tandler J. über die Varietäten der Arteria coeliaca und deren Entwickelung. Beiträge und Referate zur Anatomie und Entwickelungsgeschichte. 1904; 25(2): 473–500, doi: 10.1007/bf02300762.

31. Torres K, Staśkiewicz G, Denisow M, et al. Anatomical variations of the coeliac trunk in the homogeneous Polish population. Folia Morphol. 2015; 74(1): 93–99, doi: 10.5603/FM.2014.0059, indexed in Pubmed: 25792402.

32. Uflacker R. Atlas of vascular anatomy: An angiographic approach. Wolters Kluwer Health 2006.

33. Wang Yi, Cheng C, Wang Lu, et al. Anatomical variations in the origins of the celiac axis and the superior mesenteric artery: MDCT angiographic findings and their probable embryological mechanisms. Eur Radiol. 2014; 24(8): 1777–1784, doi: 10.1007/s00330-014-3215-9, indexed in Pubmed: 24859597.

34. Yang IY, Oraee S, Viejo C, et al. Computed tomography celiac trunk topography relating to celiac plexus block. Reg Anesth Pain Med. 2011; 36(1): 21–25, doi: 10.1097/AAP.0b013e318203067f, indexed in Pubmed: 21455084.

C A S E   R E P O R T

"Popliteofascial muscle" or rare variant of the tensor fasciae suralis?

Ł. Olewnik[1], B. Gonera[1], K. Kurtys[1], R.S. Tubbs[2, 3, 4], M. Polguj[1]

[1]Department of Normal and Clinical Anatomy, Chair of Anatomy and Histology, Medical University of Lodz, Poland
[2]Department of Neurosurgery, Tulane University School of Medicine, New Orleans, LA, United States
[3]Department of Neurosurgery and Ochsner Neuroscience Institute, Ochsner Health System, New Orleans, LA, United States
[4]Department of Anatomical Sciences, St. George's University, Grenada

Anatomical variations are routinely encountered during dissections of muscles and in clinical practice, so anatomists and clinicians need to be aware of them. One such muscle is the tensor fascia suralis, a very rare muscle located in the popliteal fossa. It can originate from any of the hamstring muscles and it inserts into the fascia of the leg. This report presents a case of a variant muscle located very deep to the biceps femoris; it originated from the posterior surface of the femur and inserted into the fascia of the leg. It is unclear whether this is a rare variant of the tensor fascia suralis or a completely new muscle. (Folia Morphol 2021; 80, 4: 1037–1042)

Key words: tensor fascia suralis muscle, variant muscle, supernumerary muscles, new muscle, hamstring tendon, semitendinosus muscle, semitendinosus tendon, biceps femoris

INTRODUCTION

Anatomical variations are commonly encountered, and although some have been described extensively in the literature, many are still being reported for the first time. Such variations can include veins, arteries, innervation, muscles and even organs.

Although they are less common than variations in veins or arteries, muscle variants are nevertheless frequent and have been found to affect both lower and upper limbs and muscles of the chest, abdomen and back. These variants can include lack of a muscle, or the presence of supernumerary muscles, bifurcated muscles or tendons, deviation from the normal course, or a variable origin or insertion. They can affect routine clinical procedures or important and complex surgeries. For example, an additional

head of the gastrocnemius muscle can cause pain syndromes or popliteal artery entrapment [10, 25], the variable course of the plantaris tendon has been associated with a higher risk of mid-portion Achilles tendinopathy [18, 28], and an atypical arrangement of the belly of the plantaris muscle is believed to apply pressure to the tibial nerve [20]. In addition, if a muscle of the forearm or the foot has multiple tendons, stenosing tenosynovitis can be triggered [3, 5, 11, 14, 19]. Anatomical variations in muscles typically have genetic causes and reflect our ancient origins. Some arise from anomalies in embryological development or the persistence of an embryological condition; however, most are benign.

The tensor fascia suralis muscle (TFS), also known as the ischioaponeuroticus, is a sporadic accessory

---
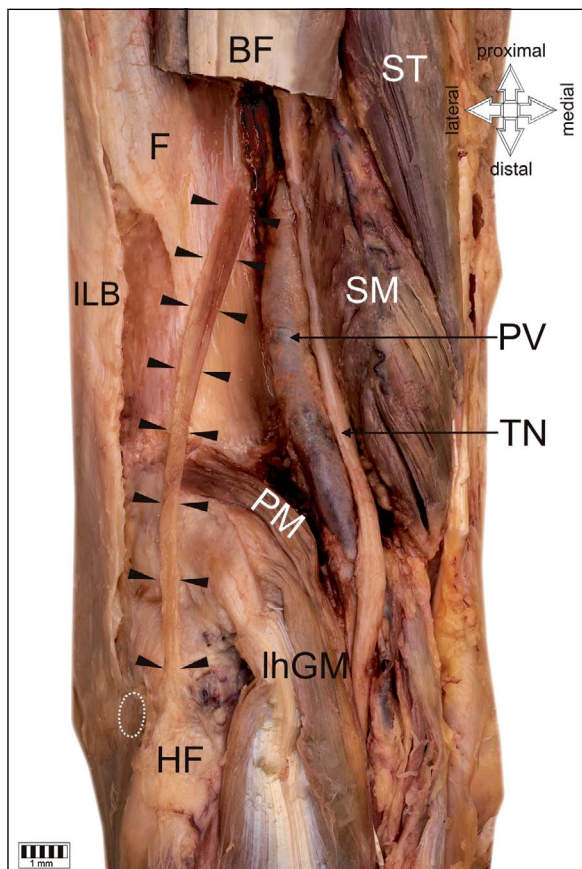
Figure 1. Rare anatomical type of tensor fascia suralis or new muscle. Left lower limb; BF — biceps femoris muscle; ST — semitendinosus muscle; SM — semimebranosus muscle; F — femur; ILB — ilio-tibial band; PV — popliteal vein; TN — tibial nerve; PM — plantaris muscle; lhGM — lateral head of the gastrocnemius muscle; HF — head of fibula; white dashed line shows the insertion of the biceps femoris, black arrowheads indicate the new muscle.
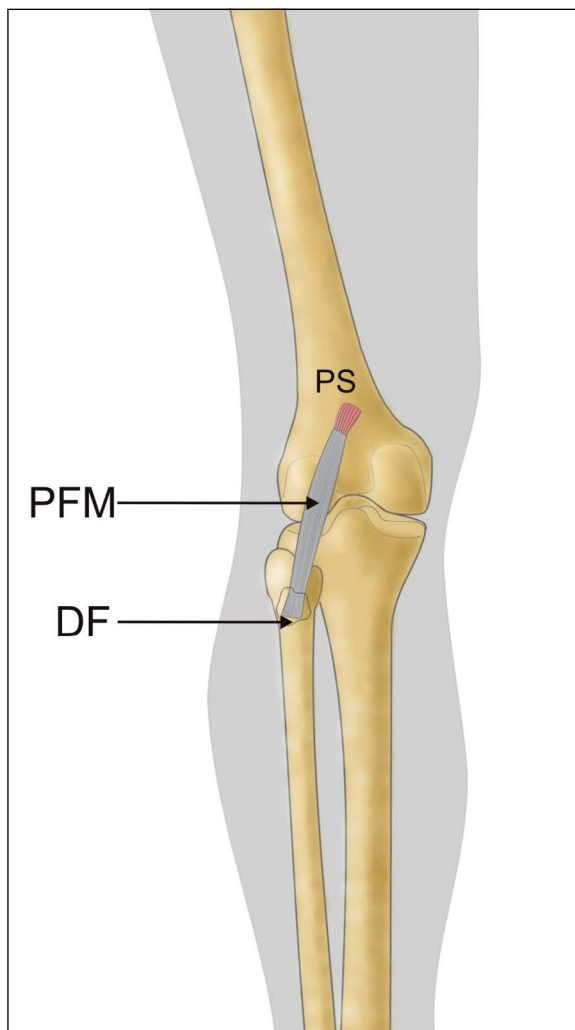
Figure 2. Schema of rare anatomical type of tensor fascia suralis or new muscle. Left lower limb; PS — popliteal surface of the femur; PFM — 'popliteofascial muscle'; DF — deep fascia.

muscle [2, 6, 9, 12, 22, 24, 27, 29]. It originates from the distal aspect of any of the hamstring muscles, typically the semitendinosus, and inserts into the sural fascia or the medial head of the gastrocnemius muscle or the calcaneal tendon [27].

This case report describes an extremely rare variant of the origin, insertion and course of the TFS, which could represent a completely new lower limb muscle. Our findings highlight the importance of muscle variants in the popliteal region and are significant for radiologists, anatomists, physiotherapists and surgeons specialising in the knee region.

CASE REPORT

A male cadaver, 71 years old at death (height: 184 cm), was subjected to routine anatomical dissection for research and teaching purposes at the Department of Normal and Clinical Anatomy, Medical University of Lodz, Poland. The left thigh, knee and crural region were dissected using standard techniques according to a strictly-specified protocol [15, 16, 18, 21]. During the dissection of the right posterolateral region of the knee, an unusual tendon was found. It inserted to the deep fascia of the leg, close to the origin of the fibularis longus and the insertion of the biceps femoris. The tendon was cleaned and gently separated from the biceps femoris. The distal part of the biceps femoris was then removed to reveal the 'new muscle', the origin of which was found on the popliteal surface of the femur (Figs. 1, 2).

The next step was to obtain morphometric measurements using digital photographic images processed through MultiScanBase 18.03 (Computer Scanning System II, Warsaw, Poland). The length of

Table 1. A comparison of case studies reporting the tensor fascia suralis muscle

Study	Type of study	Origin	Insertion	Figure
Chason et al. (1995)	Radiological	Semitendinosus muscle	Achilles tendon	Fig. 3A
Montet et al. (2002)	Radiological	Semitendinosus muscle	Achilles tendon	Fig. 3A
Tubbs et al. (2006)	Anatomical	Semitendinosus muscle	Fascia of the leg	Fig. 3B
Padmalatha et al. (2010)	Anatomical	Semitendinosus muscle	Sural fascia	Fig. 3C
Kim et al. (2015)	Radiological	Lateral aspect of the semitendinosus muscle	Medial head of the gastrocnemius muscle	Fig. 3D
Rajendiran et al. (2016)	Anatomical	Medial side of the long head of the biceps femoris	Deep fascia over the gastrocnemius muscle	Fig. 3E
Bale et al. (2017)	Anatomical	Long head of the biceps femoris	On to the fascia of both heads of the gastrocnemius muscle	Fig. 3F

the muscle belly was 33.1 mm, while the length of the tendon was 73.83 mm. The width at the origin was 7.51 mm. The width of the tendon was 5.63 mm at the myotendinous junction and 7.19 mm at the distal attachment. No other anatomical variations were identified.

Ethical approval and consent to participate

The cadaver belonged to the Department of Normal and Clinical Anatomy of the Medical University of Lodz, Poland.

DISCUSSION

Our case illustrates a potentially new structure of the popliteal region. It describes an accessory muscle (AM) located deep to the biceps femoris muscle, originating on the popliteal surface of the femur and inserting into the deep fascia of the leg, close to the origin of the fibularis longus and the insertion of the biceps femoris. On the basis of its origin, we propose the term "popliteofascial muscle" for this AM.

Accessory muscles and muscle variations are not uncommon in the lower and upper limbs. The most common AMs are accessory slips from the medial or lateral head of the gastrocnemius, accessory soleus, fibularis quartus and fibularis digiti quinti in the lower limb, and accessory lumbricals and extensor digitorum in the upper limb. In contrast, the TFS is one of the least frequently observed muscles in the lower limb. It has been identified using both sonography and magnetic resonance imaging [4, 9, 12] and during anatomical studies [1, 2, 6, 22, 24, 26, 29], and its origin and insertion are morphologically highly variable (Table 1; Fig. 3).

Accessory muscles are usually asymptomatic and encountered as incidental findings; however, some

have been implicated as potential sources of clinical symptoms [17]. When it occurs, the TFS is clinically significant because it can cause swelling in the popliteal fossa [1, 12]. In addition, its location between the hamstring tendons in the popliteal region can mimic a Baker's cyst on physical examination [4, 12]. Moreover, as the TFS is located close to the neurovascular bundle, it can compress the popliteal vein, popliteal artery, sciatic nerve, tibialis or sural nerve [1, 9, 26, 27]; this can be mistaken for soft tissue tumours or aneurysms of the popliteal artery or abscesses [12]. Although no electrostimulation research has been carried out, it has been suggested that the TFS assists in flexion of the leg and places tension on the fascia of the posterior leg [29].

The TFS is located superficially in the popliteal fossa; it is found medially between the semitendinosus and semimembranosus muscles, and laterally between the semitendinosus and biceps femoris. This is quite different from the case we have described, in which the muscle is located very deep to the femoris biceps muscle and originates at the posterior surface of the femur. It possesses a short (33.1 mm) muscle belly, which is 7.51 mm wide at the femur; the muscle belly later becomes a tendon, 73.83 mm long, which inserts into the fascia of the leg at a point close to the head of the fibula and medially to the biceps femoris insertion (Fig. 1).

This muscle arrangement has not been described before, even as a variant of the TFS. We speculate that it assists in flexing the knee joint and in providing tension to the fascia of the leg; previous studies have attributed these functions to the TFS. Furthermore, in view of its atypical location, it could help to stabilise the posterolateral corner of the knee joint; this has never been mentioned before. The presence of
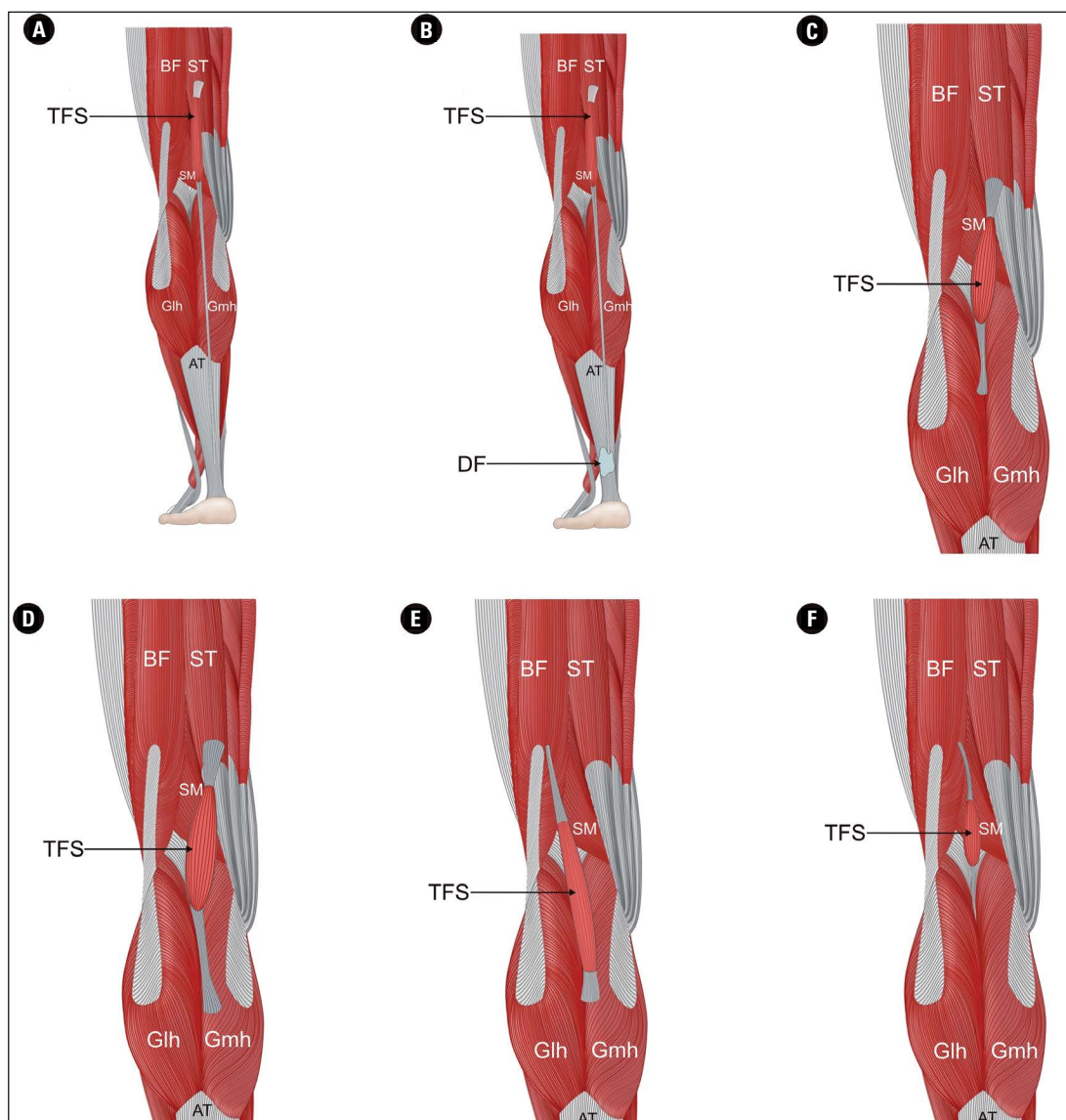
Figure 3. Schema of rare anatomical types of tensor fascia suralis (TFS); BF — biceps femoris muscle; ST — semitendinosus muscle; SM — semimembranosus muscle; Glh — lateral head of the gastrocnemius muscle; Gmh — medial head of the gastrocnemius muscle; AT — Achilles tendon; DF — deep fascia of the leg.

such a muscle in this location could be associated with clinical problems; for example, rupture of its distal part could be connected with femoris tendon biceps rupture. Owing to its close relationship with the fibular collateral ligament, injury to the ligament might affect the TFS and vice versa. In contrast to the 'typical' TFS described in earlier literature, it is doubtful that the muscle we have identified participates in compressing the tibial nerve or the popliteal vein and artery.

Other AMs have been reported in the area of the popliteal fossa [6, 13, 23, 26]. Somayaji et al. [26] describe an example originating by two slips, one

from the semitendinosus and another from the biceps femoris muscle, which then connect to a common tendon and insert into the calcaneal tendon (Fig. 4A). A very similar case was described by Gupta et al. [6] in which the origin also consisted of two slips from the semitendinosus and biceps femoris; however, the common tendon formed was attached at the junction of the two heads of gastrocnemius muscle (Fig. 4B). Cases have been described of AMs running transversely from the biceps femoris tendon to the medial head of the gastrocnemius muscle, innervated from the common fibular nerve [13, 23]. Another supernumerary muscle in the popliteal fossa was found
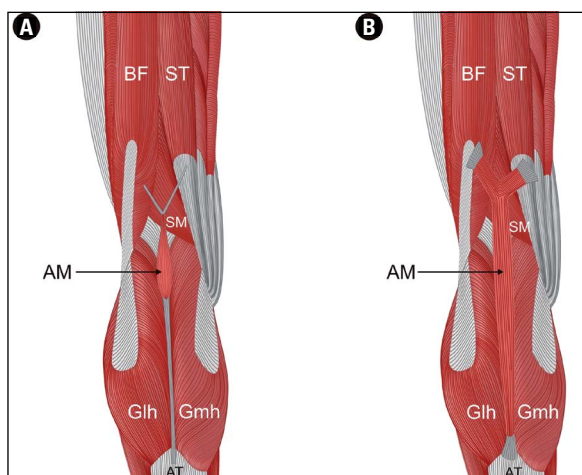
Figure 4. Schema of variant muscle in the popliteal region; AM — variant muscle; BF — biceps femoris muscle; ST — semitendinosus muscle; SM — semimembranosus muscle; Glh — lateral head of the gastrocnemius muscle; Gmh — medial head of the gastrocnemius muscle; AT — Achilles tendon.

to originate from the biceps femoris tendon and insert into the medial head of the gastrocnemius muscle; innervation was from the lateral sural nerve, a branch of the common fibular nerve [8]. Interestingly, all cases describing the TFS muscle have been found in men [1, 4, 9, 12, 22, 24, 29]; although two cases of AMs have been found in women [8, 13], one had previously been found in a man [6], and the present case description also concerns a man.

The question arises as to whether these "accessory, variant muscles" are completely new muscles or rare variants of the TFS. Further studies are also needed to confirm whether the TFS muscle occurs only in men, and whether other AMs occur in the popliteal region in both men and women. The key question is whether this present case represents a new muscle or a rare variant of the TFS. Its close relationship with the biceps femoris and the locations of the insertion suggests that it is a rare TFS variant; however, its deep arrangement and attachment (origin), located on the popliteal surface of the femur, could suggest a new muscle.

The appearance of AMs can be explained by embryonic development. The muscles of the limbs develop from myogenic precursor cells that arise from the ventral dermomyotome of somites. In these precursor cells, muscle regulatory genes such as Pax 3 and Myf 5 are activated, resulting in the expression of transcription factors including Myo D, myogenin and myogenic regulatory factors. The fusion of myoblasts and myotubes leads to further growth of the muscles

and their subsequent investment by connective tissue. Additional variations in the muscle pattern can also be caused by alterations in the signalling or stimuli among mesenchymal cells [7, 24]. The final configuration of a muscle is achieved though several apoptosis and growth cycles of the muscle primordia, and the failure of these primordia to disappear results in the presence of an AM or even an additional muscle.

CONCLUSIONS

This case report describes a possible variant of the 'tensor fascia suralis', as indicated by its close relationship to the biceps femoris and the location of its insertion. However, the deep positioning of this muscle could indicate that it is in fact a new muscle; hence, if the latter, we propose the name "popliteofascial muscle". Knowledge of such potential variations in the popliteal region is important for the surgeon when operating in and around the popliteal fossa, for the radiologist for correct radiological interpretations, and for the physiotherapist for correct diagnoses.

Conflict of interest: None declared

REFERENCES

1. Bale LSW, Herrin SO. Bilateral tensor fasciae suralis muscles in a cadaver with unilateral accessory flexor digitorum longus muscle. Case Rep Med. 2017; 2017: 1864272, doi: 10.1155/2017/1864272, indexed in Pubmed: 28210274.
2. Barry D, Bothroyd JS. Tensor fasciae suralis. J Anat. 1924; 58(Pt 4): 382–383, indexed in Pubmed: 17104034.
3. Bravo E, Barco R, Bullón A. Anatomic study of the abductor pollicis longus: a source for grafting material of the hand. Clin Orthop Relat Res. 2010; 468(5): 1305–1309, doi: 10.1007/s11999-009-1059-4, indexed in Pubmed: 19760470.
4. Chason DP, Schultz SM, Fleckenstein JL. Tensor fasciae suralis: depiction on MR images. Am J Roentgenol. 1995; 165(5): 1220–1221, doi: 10.2214/ajr.165.5.7572507, indexed in Pubmed: 7572507.
5. Fabrizio PA, Clemente FR. A variation in the organization of abductor pollicis longus. Clin Anat. 1996; 9(6): 371–375, doi: 10.1002/(SICI)1098-2353(1996)9:6<371::AID-CA2>3.0.CO;2-E, indexed in Pubmed: 8915615.
6. Gupta R, Kumar BSS. An anomalous muscle in the region of the popliteal fossa: A case report. J Anat Soc India. 2006; 55: 65–68.
7. Ilayperuma I, Nanayakkara G, Palahepitiya N. Incidence of humeral head of biceps brachii muscle: anatomical insight. Int J Morphol. 2011; 29(1): 221–225, doi: 10.4067/s0717-95022011000100037.
8. Kim DI, Kim HJ, Shin C, et al. An abnormal muscle in the superficial region of the popliteal fossa. Anat Sci Int. 2009; 84(1-2): 61–63, doi: 10.1007/s12565-008-0002-1, indexed in Pubmed: 19214656.

9. Kim K, Shim J, Lee G, et al. MR imaging and ultrasono-graphic findings of tensor fasciae suralis muscle: a case report. J Korean Soc Radiol. 2015; 73(4): 249, doi: 10.3348/jksr.2015.73.4.249.

10. Kwon YJ, Kwon TW, Gwon JG, et al. Anatomical popliteal artery entrapment syndrome. Ann Surg Treat Res. 2018; 94(5): 262–269, doi: 10.4174/astr.2018.94.5.262, indexed in Pubmed: 29732358.

11. Mahakkanukrauh P, Mahakkanukrauh C. Incidence of a septum in the first dorsal compartment and its effects on therapy of de Quervain's disease. Clin Anat. 2000; 13(3): 195––198, doi: 10.1002/(SICI)1098-2353(2000)13:3<195::AID-CA6>3.0.CO;2-V, indexed in Pubmed: 10797626.

12. Montet X, Sandoz A, Mauget D, et al. Sonographic and MRI appearance of tensor fasciae suralis muscle, an uncommon cause of popliteal swelling. Skeletal Radiol. 2002; 31(9): 536–538, doi: 10.1007/s00256-002-0496-x, indexed in Pubmed: 12195508.

13. Okamoto K, Wakebe T, Saiki K, et al. An anomalous muscle in the superficial region of the popliteal fossa, with special reference to its innervation and derivation. Ann Anat. 2004; 186(5-6): 555–559, doi: 10.1016/S0940-9602(04)80106-7, indexed in Pubmed: 15646291.

14. Olewnik Ł. Is there a relationship between the occurrence of frenular ligaments and the type of fibularis longus tendon insertion? Ann Anat. 2019; 224: 47–53, doi: 10.1016/j.aanat.2019.03.002, indexed in Pubmed: 30930196.

15. Olewnik Ł, Gonera B, Kurtys K, et al. The anterolateral ligament of the knee: a proposed classification system. Clin Anat. 2018; 31(7): 966–973, doi: 10.1002/ca.23267, indexed in Pubmed: 30144325.

16. Olewnik Ł, Podgórski M, Polguj M, et al. The plantaris muscle - rare relations to the neurovascular bundle in the popliteal fossa. Folia Morphol. 2018; 77(4): 785–788, doi: 10.5603/FM.a2018.0039, indexed in Pubmed: 29651792.

17. Olewnik Ł, Podgórski M, Ruzik K, et al. New classification of the distal attachment of the fibularis brevis: anatomical variations and potential clinical implications. Foot Ankle Surg. 2020; 26(3): 308–313, doi: 10.1016/j.fas.2019.04.002, indexed in Pubmed: 31031151.

18. Olewnik Ł, Wysiadecki G, Podgórski M, et al. The plantaris muscle tendon and its relationship with the achilles tendinopathy. Biomed Res Int. 2018; 2018: 9623579, doi: 10.1155/2018/9623579, indexed in Pubmed: 29955614.

19. Olewnik Ł, Wysiadecki G, Polguj M, et al. Anatomical variations of the palmaris longus muscle including its relation to the median nerve — a proposal for a new classification. BMC Musculoskelet Disord. 2017; 18(1): 539, doi: 10.1186/s12891-017-1901-x, indexed in Pubmed: 29258498.

20. Olewnik Ł, Podgórski M, Polguj M, et al. The plantaris muscle - rare relations to the neurovascular bundle in the popliteal fossa. Folia Morphol. 2018; 77(4): 785–788, doi: 10.5603/FM.a2018.0039, indexed in Pubmed: 29651792.

21. Olewnik Ł, Wysiadecki G, Polguj M, et al. The report on the co-occurrence of two different rare anatomic variations of the plantaris muscle tendon on both sides of an individual. Folia Morphol. 2017; 76(2): 331–333, doi: 10.5603/FM.a2016.0069, indexed in Pubmed: 27813626.

22. Padmalatha K, Prakash B, Mamatha Y, et al. Ischio-aponeuroticus/tensor fascia suralis. Int J Anat Var. 2011; 4: 104–105.

23. Parsons FG. Note on abnormal muscle in popliteal space. J Anat. 1920; 54(Pt 2-3): 170, indexed in Pubmed: 17103889.

24. Rajendiran R, Murugesan A. Unilateral tensor fascia suralis: a case report. Brunei Darussalam J Heal. 2016; 6: 94–98.

25. Rodrigues V, Rao MK, Nayak S. Multiple heads of gastrocnemius with bipennate fiber arrangement: a clinically significant variation. J Clin Diagn Res. 2016; 10(8): AD01––AD02, doi: 10.7860/JCDR/2016/20094.8340, indexed in Pubmed: 27656426.

26. Somayaji SN, Vincent R, Bairy KL. An anomalous muscle in the region of the popliteal fossa: case report. J Anat. 1998; 192 (Pt 2): 307–308, doi: 10.1046/j.1469-7580.1998.19220307.x, indexed in Pubmed: 9643434.

27. Sookur PA, Naraghi AM, Bleakney RR, et al. Accessory muscles: anatomy, symptoms, and radiologic evaluation. Radiographics. 2008; 28(2): 481–499, doi: 10.1148/rg.282075064, indexed in Pubmed: 18349452.

28. van Sterkenburg MN, Kerkhoffs GM, Kleipool RP, et al. The plantaris tendon and a potential role in mid-portion Achilles tendinopathy: an observational anatomical study. J Anat. 2011; 218(3): 336–341, doi: 10.1111/j.1469-7580.2011.01335.x, indexed in Pubmed: 21323916.

29. Tubbs RS, Salter EG, Oakes WJ. Dissection of a rare accessory muscle of the leg: the tensor fasciae suralis muscle. Clin Anat. 2006; 19(6): 571–572, doi: 10.1002/ca.20205, indexed in Pubmed: 16059929.

C O N T E N T S

←

Cover picture: Inferior mesenteric artery (IMA) branching type IC. Lack of left colic artery, ascending colic artery (AscCA) and descending colic artery (DscCA) originating directly from IMA; SB — sigmoidal branch; SRA — superior rectal artery. For details see: A. Balcerzak et al., Folia Morphol 2021; 80, 4: 827–838.